SCHOLARLY PUBLICATIONS

A CURRENT AWARENESS BULLETIN
OF RESEARCH OUTPUT

@DTU

(57th Edition)

SEPTEMBER, 2017

BY: CENTRAL LIBRARY

DELHI TECHNOLOGICAL UNIVERSITY
(FORMERLY *DELHI COLLEGE OF ENGINEERING)*
GOVT. OF N.C.T. OF DELHI
SHAHBAD DAULATPUR, MAIN BAWANA ROAD
DELHI 110042

PREFACE

This is the **Fifty seventh** Issue of Current Awareness Bulletin started by Delhi Technological University, Central Library. The aim of the bulletin is to compile, preserve and disseminate information published by the faculty, students and alumni for mutual benefits. The bulletin also aims to propagate the intellectual contribution of Delhi Technological University (DTU) as a whole to the academia.

The bulletin contains information resources available in the internet in the form of articles, reports, presentations published in international journals, websites, etc. by the faculty and students of DTU. The publications of faculty and student which are not covered in this bulletin may be because of the reason that the full text either was not accessible or could not be searched by the search engine used by the library for this purpose.

The learned faculty and students are requested to provide their uncovered publications to the library either through email or in CD, etc to make the bulletin more comprehensive.

This issue contains the information published during **September 2017**. The arrangement of the contents is alphabetical. The full text of the article which is either subscribed by the university or available in the web is provided in this bulletin.

Central Library

CONTENTS

1. A Hybrid Approach for Promoting Low Carbon Technologies in Distributed Generation Planing, Sandeep Kaur, Ganesh Kumbhar, ***8.Manmeet Kaur*** and Rintu Khanna, ECE, DTU

2. A Novel Carrier-Based Hybrid PWM Technique for Minimization of Line Current Ripple in Two Parallel Interleaved Two-Level VSIs, ***7.1.Kapil Shukla***, Varun Malyala, and Ramkrishan Maheshwari, Electrical, DTU

3. A Novel Load Balanced Energy Conservation Approach in WSN Using Biogeography Based Optimization, ***6.Ajay Kaushik***, ***3.Prof. Indu S*** and ***3.Prof. Daya Gupta,*** Computer Science and Engineering, DTU

4. Affinity of Metal Ions Incorporated Bentonite for Enantiomeric Interactions with Alanine, Pramod Pandey, Preeti Bhatt, Jia Yan, Le Peng, ***3.Mohan Singh Mehata*** and Chandra Kala Pant, Applied Physics, DTU

5. Alcohol Abuse and Related Health Issues, Geetanjali, ***3.Poonam***, ***6.Veer Babita*** and ***3.Singh Ram***, Applied Chemistry, DTU

6. An Intermediate Temperature Stable, Extracellular and Alkaline Lipase from Pseudomonas aeruginosa and Its Application in Biodiesel Production, ***7.Vineet Kumar Goswami*** and ***3.Jai Gopal Sharma***, Biotechnology, DTU

7. Analysing the interaction of factors for Flexibility in Supply Chains, Rajesh Singh, Saroj Koul and ***3.Pravin Kumar***, Mechanical, DTU

8. Application of Gaussian as Edge Detector for Image Enhancement of Ancient Manuscripts, ***3.N.Jayanthi*** and ***3.S.Indu***, ECE, DTU

9. Application of Soil Nailing for Landslide Mitigation in Bhutan: A Case Study at Sorchen Bypass, Dr. Raju Sarkar, ***8.1.Ritesh Kurar***, Sangay Zangmo, Ugyen Dema, Sujan Subba and Daman Kumar Sharma, Civil, DTU

10. Approximation by Kantorovich form of modified Szász–Mirakyan operators, Minakshi Dhamija, ***6.Ram Pratap*** and ***3.Naokant Deo***, Applied Mathematics, DTU

11. Biofunctionalized Graphene Oxide Wrapped Carbon Nanotubes Enabled Microfluidic Immunochip for Bacterial Cells Detection, Chandan Singh, Md. Azahar Ali, Venu Reddy, Dinesh Singh, Cheol Gi Kim, G.Sumana and ***3.B.D.Malhotra,*** Biotechnology, DTU

12. Compositional dependence of red luminescence from Eu3+ ions doped single and mixed alkali fluoro tungsten tellurite glasses, Ch. B Annapurna Devi, Sk. Mahamuda, K. Swapna, M. Venkateswarlu, ***3. Srinivasa Rao*** and G. Vijaya Prakash, Applied Physics, DTU

13. Dual Stator Induction Generator For Rural Electrification, ***3.Ramesh Singh*** and ***3.Vishal Verma***, Electrical, DTU

14. Dynamic frequency based parallel k-bat algorithm for massive data clustering (DFBPKBA), ***6.Ashish Kumar Tripathi***, ***3.Kapil Sharma*** and Manju Bala, Computer Science, DTU

15. DYNAMICS OF A PREY-PREDATOR SYSTEM WITH INFECTION IN PREY, ***6.SHASHI KANT*** AND ***3.VIVEK KUMAR***, Applied Mathematics, DTU

16. Effect of Malathion on Seed Germination and Photosynthetic Pigments in Wheat (Triticum aestivum L.), ***6.Satish Kumar*** and ***3.Jai Gopal Sharma***, Biotechnology, DTU

17. Effective sensitization of Eu3+ and energy transfer in Sm3+/Eu3+ co-doped ZPBT glasses for CuPc based solar cell and w-LEDs applications, ***6.Kaushal Jha*** and ***3.M. Jayasimhadri***, Applied Physics, DTU

18. Electronically Tunable Fractional Order All Pass Filter, ***6.RakeshVerma***, ***3.Neeta Pandey*** and ***3.Rajeshwari Pandey***, Electronics and Communication, DTU

19. Exergetic performance and parametric evaluation of simple linde liquefaction system using different gasses, ***3.R.S Mishra*** and ***6.Devender Kumar***, Mechanical, Production and Automobile, DTU

20. Exergy analysis of orc integrated combined cycle power plant with single pressure heat recovery steam generator, ***3.R.S. Mishra*** and ***6.Yunis Khan***, Mechanical Production and Automobiles, DTU

21. Friction stir welding/processing studies of aluminum alloy & titanium 64, ***3.R.S. Mishra*** & ***6.Preeti Rani***, Mechanical Production and Automobiles, DTU

22. Harmonic Reduction in Power Distribution Network using UPQC, ***3.J.N.Rai*** and ***3.Ram Bhagat***, Electrical, DTU

23. Major Issues of Post-earthquake Housing Construction during Resettlement, ***3.Raju Sarkar***, Karan Narang and Sonam Yangdhen, Civil, DTU

24. Methods for improving thermal performances of vapour absorption system using heat pipes, ***3.R.S. Mishra*** and ***6.Ankit Dwivedi***, Mechanical, Production and Automobile, DTU

25. Microporous Nanocomposite Enabled Microfluidic Biochip for Cardiac Biomarker Detection, Nawab Singh, Md. Azahar Ali, Prabhakar Rai, Ashutosh Sharma, ***3.B. D. Malhotra*** and Renu John, Biotechnology, DTU

26. NUMERICAL STUDY OF PRESSURE DROP AND HEAT TRANSFER IN A STRAIGHT RECTANGULAR AND SEMI CYLINDRICAL PROJECTIONS MICROCHANNEL HEAT SINK, ***3.M. Zunaid***, ***6.A.Jindal, 6.D. Gakhar*** and ***6.A. Sinha***, Mechanical, DTU

27. Performance Enhancement of Wind Energy System with Distribution Static Compensator, Manju Aggarwal, ***3.Madhusudan Singh*** and S. K. Gupta, Elec, DTU

28. PERFORMANCE EVALUATION OF MLP AND RBF CLASSIFIERS FOR HANDWRITTEN CHARACTER RECOGNITION USING HYBRID FEATURES, Amit Choudhary and ***3.Vinod Kumar***, Computer Science, DTU

29. Performance Evaluation of the Supercritical Organic Rankine Cycle (SORC) Integrated with Large Scale Solar Parabolic Trough Collector (SPTC) System: An Exergy Energy Analysis, ***6.Harwinder Singh*** and ***3.R.S. Mishra***, Mechanical, Production and Industrial, Automobile, DTU

30. Physical Modeling of Shear Behavior of Infilled Rock Joints Under CNL and CNS Boundary Conditions, ***3.Amit Kumar Shrivastava*** and·K. Seshagiri Rao, Civil, DTU

31. Second law analysis of super critical power plant using entropy generation method, ***3.R.S Mishra*** and ***6.Prashant Bansal***, Mechanical, Production and Automobile, DTU

32. Soft Switched High Voltage Gain Boost Integrated Flyback Converter Interfaced Single-Phase Grid Tied Inverter for SPV Integration, Amardeep B. Shitole, Shelas Sathyan, H. M. Suryawanshi, ***7.1.Girish G. Talapur*** and Pradyumn Chaturvedi, Elec, DTU

33. SOLAR TECHNOLOGY , FACTORS AFFECTING ITS PERFORMANCE AND ITS POTENTIAL MARKET IN INDIA, ***8.ANADI SHANKAR JHA***, Elec , DTU

34. STATIC ANALYSIS AND MASS OPTIMIZATION OF AUTOMOTIVE VALVE SPRING, ***8.Anant Jindal*** and ***8.Aatresha Biswas***, Mechanical, DTU

35. Thermo physical property of nano-refrigerant: preparation, thermal characteristics, and applications, ***3.R S Mishra*** and ***6.Rahul Jaiswal***, Mechanical Production and Automobiles, DTU

36. Thermodynamic (Energy-Exergy) Analysis of Combined Coal based Thermal Power Plant and Solar Integrated Double Bed Vapor Adsorption System for Heat Recovery and Space Cooling, ***6.Kaushalendra Kumar Dubey*** and ***3.R.S. Mishra***, Mechanical, DTU

37. Time Kinetics Studies of Enzyme Catalyzed Hydrolysis of Triolein and Transesterifications of Olive Oil for the Synthesis Major Olive Oil Methyl Esters Using Pseudomonas Aeruginosa Lipase, ***6.Vineet Kumar Goswami*** and ***3.Jai Gopal Sharma***, Environmental and Industrial Biotechnology, DTU

1. *Chancellor*

2. *Pro Vice Chancellor* — ***2.1.*** *Ex Pro Vice Chancellor*

3. *Faculty* — ***3.1.*** *Ex Faculty*

4. *Teaching-cum-Research Fellow* — ***4.1.****Asst. Librarian*

5. *Alumni*

6. *Research Scholar* — ***6.1.*** *Ex Research Scholar*

7. *PG Scholar* — ***7.1.*** *Ex PG Scholar*

8. *Undergraduate Student* — ***8.1.*** *Ex Undergraduate Student*

2017 IEEE International Conference on Smart Grid and Smart Cities

A Hybrid Approach for Promoting Low Carbon Technologies in Distributed Generation Planning

Sandeep Kaur
Electrical Engineering Department
PEC University of Technology,
Chandigarh (India)
e-mail: sandipsaroa@gmail.com

Manmeet Kaur
Electronics & Comm. Department
Delhi Technological University,
Delhi (India)
e-mail: mk2763119@gmail.com

Ganesh Kumbhar
Electrical Engineering Department
Indian Institiue of Technology,
Roorkee (India)
e-mail: dr.gbkumbhar@gmail.com

Rintu Khanna
Electrical Engineering Department
PEC University of Technology,
Chandigarh (India)
e-mail: rintukhanna1@rediffmail.com

***Abstract*—The greatest challenge for power utilities is to meet exponentially increasing energy demand subjected to the constraints of sustainable development with clean energy apart from economic viability. Renewable DGs, in spite of high investment cost and intermittent generation, are compulsive choice for environment friendly planning and sustainable growth. Clean energy DG technologies can provide solution to ever increasing power demand in sustainable and cost effective manner by adopting appropriate incentive mechanism. Clean energy technologies can also be encouraged by penalizing the conventional resources for harmful emissions. The proposed method minimizes the annual cost by maximizing the emission reduction and carbon credit revenue. The proposed formulation yields solution in terms of type, optimal size and location while fulfilling the criterion in terms of economic, technical or techno-economic. The objective function comprises of energy purchase, losses, capital, operational and GHG emission costs. Importance of each objective is mapped with optimal weight allocation, thereby maintaining the consistency among all objectives. A hybrid optimization technique based on Harmony Search integrated with Teaching-Learning is used to enhance the search process. The merit of the proposed algorithm is dynamic tuning of control parameters which enhances the convergence property of the solution algorithm. Results indicate that renewable DG technologies can become financially viable with appropriate price mechanism depending on planner's objective.**

Keywords- Clean energy planning, Harmony search Teaching-learning Optimization, Distributed generation

Nomenclature

$\|V_i\|_{\min}, \|V_i\|_{\max}$	Minimum and maximum bus voltages
$N_{DG}, N_{DG}^{\max}$	Number of DG units
$C_{tc}, C_{en}^{SS}, C_{Loss}$	Total, substation energy, loss, emission cost
$C_{cpt}^{DG}, C_{op}^{DG}, C_{o\&m}^{DG}$	Annual capital, operational, O&M costs of DG
$C_{emi}, C_{inc_emi}^{DG}, C_{cce}^{DG}$	Annual emission, emission-offset, and carbon credit earned by DG
$Cf^{bmg}, Cf^{wg}, Cf^{spv}$	Capacity factor of biomass, wind, & SPV DG
$P_n^{bmg}, P_n^{wg}, P_n^{spv}$	Power output of biomass, wind & SPV DG
$S_n^{bmg}, S_n^{wg}, S_n^{spv}$	Installed capacity of biomass, wind &SPV DG
$E_n^{bmg}, E_n^{wg}, E_n^{spv}$	Annual energy biomass, wind & SPV DG

I. INTRODUCTION

Power system planning is generally viewed as cost minimization problem for meeting load requirement subjected to the network constraint. In modern power system environmental sanctions such as GHG emission reduction, low carbon energy inclusion have gained equal importance in addition to the economical factor. Snoring load demand, deregulated market approach, and environmental considerations have led to the distributed generation (DG) resources. DGs comprise of dispatchable resources namely gas turbine driven synchronous generator, fuel cells, etc.) and non-dispatchable sources namely solar, wind, biomass, etc.). Both the DGs have benefits and drawbacks.. Non-dispachable DGs are suitable for sustainable energy planning, though sources are intermittent in nature, poor utilization factor and large installation cost. Dispatchable resources provide low cost efficient solution, but still pose threat to sustainable growth. DG sources improve the network performance by many ways. Research Studies have reiterated that planners can exploit the benefits in terms of reduced losses, improved voltage profile, and reduced line flows by the optimal placement of DG resources. Inadequate site and size of DG resources can result in higher losses and violation in network parameters. In addition, DG can be considered as a viable option to ease out problems such as network congestion, power quality and deferral network expansion.

Researchers have explored DG planning from different objectives [1]. Cost benefit analysis with DG integration is proposed by khattam et. al[2].Algorithm for Single and multi period modeling in deregulated environment is proposed for minimizing installation operational and loss cost [3].Multi-

objective DG planning model for promoting green energy by offering incentive in terms of emission reduction to obtain pareto-optimal solutions for cost and emission minimization is proposed in [4] [5] [6]. DG planning towards Low carbon energy model for China and Thailand is proposed in [7], [8].The optimization models aims to provide low carbon environment and economical generation settlement. Optimal DG planning model is mixed integer non-linear formulation to determine optimal location, size, type of technology and time of investment subjected to network, financial and environment constraints. This single or multi-objective optimization problem is solved using different techniques. Analytical approach proposed in [9], [10]for single and multiple DGs showed superior performance in terms of computational time but suffers in terms of multiple DG planning. Optimal DG allocation by genetic algorithm for network parameters improvement, from utility profit and consumer satisfaction perspective is investigated in [11],[12]. A hybrid approach for pre-specified number of DGs [13]is proposed. Hybrid approach is proposed for optimal DG placement for loss and cost minimization [1]. Other meta-heuristic techniques such as Ant colony, artificial bee colony and differential evolution for optimal allocation of DG are reviewed in [1].

A recently developed meta-heuristic algorithm that mimics the harmony process of musicians proved to be efficient for number of optimization problems [14], [15]. The conventional HS although possess good search mechanism but may get trapped in local minima. Search mechanism can be improved by iterative tuning and dynamically updating position vector in[16], [17]. Teaching-Learning based optimization (TLBO) is yet another population based, recently developed efficient algorithm in which solution is refined by iterative learning from teacher and learner group[18], [19]. A hybrid HS algorithm interlaced with teaching-learning is proposed for enhancing the performance of classical HS. The proposed formulation consists of minimizing the cost function subjected to network constraints. The key features of research paper are

-Optimal placement of renewable DGs towards low carbon energy planning for minimizing annual cost with incentive and penalty mechanism for reduction in cost and GHG emissions, respectively.

- Clean energy planning from planner's perspective using optimal weight allocation.

-A hybrid approach integrating harmony search and teaching learning to improve the exploration and exploitation process with four dynamically controlled improvisation choices.

The paper is organized as follows: the problem formation is explained in section II and III , optimal weight allocation and proposed algorithm in section IV. The results are discussed in section V followed by conclusions drawn in section VI.

II. METHODOLOGY

Modern DG planning requires for proper weightage to economic as well as environmental aspects for sustainable growth. The basic aim of the proposed optimization problem is planning from number of perspectives such as economic viability, resource availability, loss minimization and low carbon planning in terms of optimal location, size and technology. As per planner's objective, optimal weight allocation philosophy is adopted to ensure consistency among decision components. Total cost is comprised of capital, operational, emission and revenue earned in terms of emission offset and carbon trading. This incentive is offered to boost participation of renewable energy sources (RES). Power drawn from grid is penalized for creating health hazards due to harmful emissions. Optimal solution in terms of DG locations, technology type and DG sizes are obtained. Objective function and associated constraints are described as follows.

III. PROBLEM FORMULATION

A. Objective Function

The objective function of proposed work is minimization of annualized DG cost. It is comprised of grid energy, loss, capital, operating, operational and maintenance, emission cost incurred and incentive earned by offsetting emission and carbon credits earned. DG type, site and size are taken as decision variables. Mathematical formulation is described in terms of objective function and constraints.

The objective function for minimization of annual cost incurred is represented in terms of cost of grid energy, installation, operational, and emission cost of DG and profit earned by producing green energy is given as

$$Min\, C_{tc} = w_1 C_{en}^{SS} + w_2 C_{Loss} + w_3 (C_{cpt}^{DG} + C_{op}^{DG} + C_{o\&m}^{DG} + C_{emi}) - w_4 (C_{inc_emi}^{DG} + C_{cce}^{DG}) \quad (1)$$

where w1, w_2, w_3, and w_4 are weights for energy loss DG and incentive cost.

Network Constraints

(I) Power balance: Power inflow and outflow in terms of real and reactive power at every bus should be zero.

(II) System voltage: Voltage magnitude at all the buses must be within allowed upper and lower limits.

$$|V_i|_{\min} \le |V_i| \le |V_i|_{\max} \quad (2)$$

(III) Penetration limit for DG units: The total power penetration of DG units should be less than allowable penetration limit.

$$\sum_{n=1}^{N} Cf_n^{bmg} P_n^{bmg} + Cf_n^{wg} P_n^{wg} + Cf_n^{spv} P_n^{spv} \le \alpha P_{LD} \quad (3)$$

where α is DG injection to load ratio, P_{LD} is load demand

(IV) Installed DG capacity at each bus: DG capacity installed at each bus should be less than maximum permissible limit.

$$S_n^{bmg} + S_n^{wg} + S_n^{spv} \le S_n^{\max} \quad (4)$$

(V) Maximum number of DG units: The number of DG units installed on candidate buses should be within maximum allowable number of DG units.

$$0 \le N_{DG} \le N_{DG}^{\max} \qquad N_{DG} \in \{\text{No. of DG units}\} \quad (5)$$

B. Optimal Weight Allocation by AHP

Weight assignment is simple and convenient way for solving multi-objective problems. Generally a weight selection is random without giving much attention to inter-relationship of decision components in integrated plan [20]. Due to the multi-objective nature of proposed formulation, a systemic method for comparing different planning alternatives from planner point of view is proposed. Instead of random weight assignment to decision component, optimal weight allocation is performed using Analytical Hierarchy Process (AHP) so as to maintain the consistency and rationality among decision components. steps in AHP are

I. Priorities weight among the decision components such that summation of weights is unity.

II. Pair wise comparison matrix showing relative importance of different parameters is prepared as given in (5).

$$C = \begin{pmatrix} w_{11} & w_{12} & \cdots & w_{1n} \\ \vdots & & \ddots & \\ w_{m1} & w_{m2} & \cdots & w_{mn} \\ w_{n1} & w_{n2} & \cdots & w_{nn} \end{pmatrix} \quad (6)$$

where w_{ii}=1, w_{ij}=1/w_{ji} and w_{ij}=w_i/w_j.w_{ij} is relative importance of ith component to jth component.

III. Weighing vector w is computed as given below.

$$Cw = \lambda_{\max} w \quad (7)$$

λ_{max} is largest eigen value of C and w is corresponding eigen vector of C

IV. To calculate optimal weights for each decision component weighing factor w is normalized as

$$W_i = \frac{w_i}{\sum_{j=1}^{n} w_j} \quad (8)$$

Consistency check is performed by computing Consistency Ratio (CR) using expression (8)

$$CR = \frac{(\lambda_{\max} - n)}{(n-1)RI} \le 0.1 \quad (9)$$

where RI is random index for selected n. If CR <0.1 weight allocation is rational.

IV. Proposed Algorithm

A meta-heuristic harmony search is derivative free random search optimization technique which does not require initial setting of decision variables [14-15]. However classical approach has sluggish performance and less accurate solution due to the fixed tuning parameters [21]. In order to overcome this limitation, HS is further improved by integrating Teaching-Learning based optimization (TLBO) which has proved to have a strong search mechanism to improve exploration and exploitation [22].Novel Harmony Search with Teaching-Learning is proposed for solving above formulation. Parameter selection for HSTL are given in [22]. Flow chart of the proposed algorithm is shown in Fig. 1.

V. Simulation Results & Discussion

The proposed methodology is implemented on standard IEEE 33 bus test system. Three DG technologies namely biomass, wind and solar PV are considered as candidate DGs. Maximum DG injection cannot exceed 50% of system load.. Lower and upper limits for voltage are set at 0.90pu and 1.0pu for load buses and 1.0 pu for slack bus. DG is considered as negative PQ load. Line losses without DG injection with peak load of 3.7 MW and 2.3 MVAr is 211 kW.

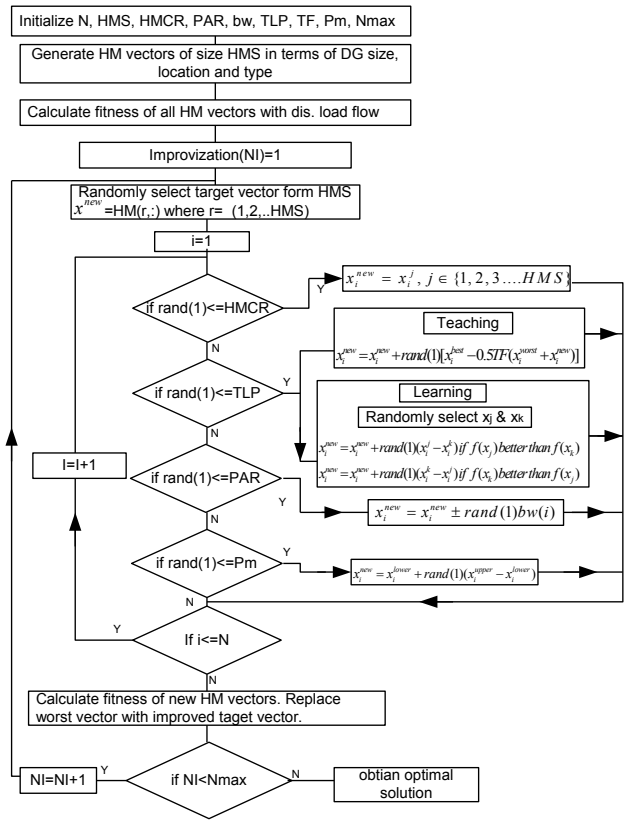


Figure 1. Flow chart of HSTL algorithm

Cost parameters in the simulation study are taken from [23-25]. As capacity factor for SPV is quite low and its capital cost is also high in comparison to biomass and wind generator, 20% subsidy on capital cost of SPV is considered in proposed formulation. Incentive in form of emission offset to promote cleaner environment is further proposed. Emission offset incentive can be offered for all pollutants e.g. carbon, nitrogen and sulphur, only carbon offset is considered in simulated results. Carbon emission reduction (CER) rate for biomass, wind and SPV generators are 6300,

1600, 1570 tones/annum respectively [26-29].Following case studies are performed.

A. *Case1: Planning without DG*

Planning without DG injection is considered in this case. Real & reactive power losses are 211kW and 143 kVAr respectively. Grid power required is 3.926+2.443i. Total annual cost incurred is $2.84M.

B. *Case I1: Cost Minimization Planning with DG*

DG planning with cost minimization aspect while maintaining the financial viability is achieved by selecting biomass and wind DG at bus 16 and 30 respectively. Optimal size for biomass and wind DG are .33 & 1.96 MVA and installed capacity is 0.4 & 4.9MVA respectively. It is observed from Fig. 2 that line loss cost is maximum in this case as the reactive power support is not sufficient due to the smaller size of biomass DG in comparison to case III and IV. Objective function value is minimum due to the maximum DG injection in this case. DG installation cost is max due to higher DG size. Minimum annual cost if attributed to the least operational cost of DG as wind DG has zero operational cost.

C. *Case II1: Loss Minimization Planning with DG*

Distribution system is responsible for considerable share of power losses. Line loss reduction is major concern distribution network operators (DNO) in deregulated environment. DG planning with loss reduction aspect while maintaining the financial viability is achieved by optimal weight allocation formulation. Weights assigned by AHP for different cost functions namely grid energy cost, loss cost, DG injection cost and DG earning cost is 0.01, 0.5, 0.15 and 0.25 respectively. Optimal results are shown in Fig. 2.
Biomass and wind DG combination contribute to the minimum losses. Optimal DG size of 0.84MVA (biomass) and 1.4MVA at bus no. 14 & 30 respectively is obtained. It is concluded that line losses reduction is maximum with optimal weight allocation to different objectives. Objective function value is more in this case in comparison to case II. Total cost incurred is more as compared to minimum cost objective due to the fact that the DG location and size are primarily decided by the loss reduction criteria and secondly biomass injection at bus number 14 is more in loss minimization scenario which leads to lower losses due to the reactive power support but increases the operational cost which results in increasing the total cost as evident from Fig. 2.

D. *Case IV: Planning from Clean Energy Prospective*

Due to stringent environment conditions and sustainable development compulsions, power system planners need to do planning with due weightage to clean energy phenomena. To assist system planners for this kind of planning, weighing factor of cost components in objective function are selected by AHP in such a manner that environment aspect gains importance over other cost factors while maintaining the economic aspect. Weights assigned by AHP for different cost component are 0.15, 0.15, 0.2 & 0.5 respectively. SPV DG could not be made economically viable in case II and III. Clean energy prospective encouraged the SPV injection. All the three DGs i.e biomass, wind, and SPV with installed capacity of 1.7, 1.3 and 0.6 MVA. Total cost incurred is more as compared to cost minimization and loss minimization criteria as observed in case II and III. Increased annual cost is attributed to higher DG operational cost due to larger biomass injection and high capital cost of SPV DG. This scenario results in maximum carbon credit earning and emission offset cost thereby increases DG earning cost out of the above discussed cases as shown in Fig. 2.

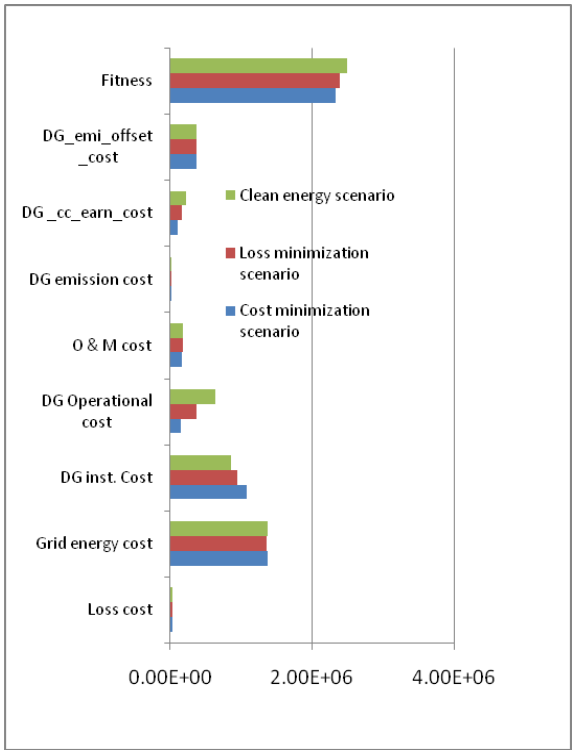


Figure 2. Comparison of DG planning for different planning schemes.

VI. CONCLUSION

An evolutionary approach for DG planning from different perspectives i.e. economy, resource availability, loss reduction and clean environment is proposed. Optimal weight allocation method is implemented for optimal solution from planner's perspective. Optimal solution in terms of DG type, optimal location and size to balance the economic and environment criteria is obtained. The proposed methodology is step to encourage techno-economic energy planning over traditional planning by incentive policy for emission offset and carbon credits earning. A hybrid optimization approach, interlacing teaching-learning with harmony search is used to exploit better search process. The adopted hybrid search algorithm is made robust by tuning control parameters dynamically thereby improving the success and convergence rate. Four improvisations harmony memory consideration rate, teaching-learning, pitch adjustment and mutation are adopted to maintain the balance

between explorative and exploitative potential. Findings suggest that low carbon planning can be made viable by designing appropriate subsidy and incentive schemes by planners for encouraging clean energy production. Proposed formulation is modeled without considering uncertainty. Algorithm is helpful for energy planners to decide the price mechanism for low carbon energy planning to maintain the financial and environment balance. More realistic model can be realized by considering uncertainty in generation, load and market price.

REFERENCES

[1] P. S. Georgilakis and N. D. Hatziargyriou, "Optimal Distributed Generation Placement in Power Distribution Networks: Models, Methods, and Future Research," *IEEE Trans. Power Syst.*, vol. 28, no. 3, pp. 3420–3428, 2013.

[2] W. El-Khattam, K. Bhattacharya, Y. Hegazy, and M. M. A. Salama, "Optimal Investment Planning for Distributed Generation in a Competitive Electricity Market," *IEEE Trans. Power Syst.*, vol. 19, no. 3, pp. 1674–1684, 2004.

[3] S. Porkar, P. Poure, A. Abbaspour-Tehrani-fard, and S. Saadate, "A novel optimal distribution system planning framework implementing distributed generation in a deregulated electricity market," *Electr. Power Syst. Res.*, vol. 80, no. 7, pp. 828–837, 2010.

[4] A. Zangeneh, S. Jadid, and A. Rahimi-Kian, "A fuzzy environmental-technical-economic model for distributed generation planning," *Energy*, vol. 36, no. 5, pp. 3437–3445, 2011.

[5] G. Celli, E. Ghiani, S. Mocci, and F. Pilo, "A multiobjective evolutionary algorithm for the sizing and siting of distributed generation," *Power Syst. IEEE Trans.*, vol. 20, pp. 750–757, 2005.

[6] A. Zangeneh, S. Jadid, and A. Rahimi-Kian, "Promotion strategy of clean technologies in distributed generation expansion planning," *Renew. Energy*, vol. 34, no. 12, pp. 2765–2773, 2009.

[7] Q. Chen, C. Kang, Q. Xia, and J. Zhong, "Power Generation Expansion Planning Model Towards Low-Carbon Economy and Its Application in China," *Power Syst. IEEE Trans.*, vol. 25, pp. 1117–1125, 2010.

[8] A. Phdungsilp and T. Wuttipornpun, "Analyses of the decarbonizing Thailand's energy system toward low-carbon futures," *Renew. Sustain. Energy Rev.*, vol. 24, pp. 187–197, 2013.

[9] C. Wang and M. H. Nehrir, "Analytical Approaches for Optimal Placement of Distributed Generation Sources in Power Systems," *IEEE Trans. Power Syst.*, vol. 19, no. 4, pp. 2068–2076, 2004.

[10] N. Acharya, P. Mahat, and N. Mithulananthan, "An analytical approach for DG allocation in primary distribution network," *Int. J. Electr. Power & Energy Syst.*, vol. 28, no. 10, pp. 669–678, 2006.

[11] C. L. T. Borges and D. M. Falcão, "Optimal distributed generation allocation for reliability, losses, and voltage improvement," *Int. J. Electr. Power & Energy Syst.*, vol. 28, no. 6, pp. 413–420, 2006.

[12] M. F. Shaaban, Y. M. Atwa, and E. F. El-Saadany, "DG Allocation for Benefit Maximization in Distribution Networks," *IEEE Trans. Power Syst.*, pp. 1–1, 2012.

[13] G. P. Harrison, A. Piccolo, P. Siano, and A. R. Wallace, "Hybrid GA and OPF evaluation of network capacity for distributed generation connections," *Electr. Power Syst. Res.*, vol. 78, no. 3, pp. 392–398, 2008.

[14] Z. W. Geem, J. H. Kim, and G. V. Loganathan, "A New Heuristic Optimization Algorithm: Harmony Search," *SIMULATION*, vol. 76, no. 2, pp. 60–68, 2001.

[15] K. S. Lee, Z. W. Geem, S. Lee, and K. Bae, "The harmony search heuristic algorithm for discrete structural optimization," *Eng. Optim.*, vol. 37, no. 7, pp. 663–684, 2005.

[16] M. Mahdavi, M. Fesanghary, and E. Damangir, "An improved harmony search algorithm for solving optimization problems," *Appl. Math. Comput.*, vol. 188, no. 2, pp. 1567–1579, 2007.

[17] K. Nekooei, M. M. Farsangi, H. Nezamabadi-Pour, and K. Y. Lee, "An Improved Multi-Objective Harmony Search for Optimal Placement of DGs in Distribution Systems," *IEEE Trans. Smart Grid*, vol. 4, no. 1, pp. 557–567, 2013.

[18] R. V. Rao, V. J. Savsani, and D. P. Vakharia, "Teaching–Learning-Based Optimization: An optimization method for continuous non-linear large scale problems," *Inf. Sci.*, vol. 183, no. 1, pp. 1–15, 2012.

[19] R. V. Rao, V. J. Savsani, and J. Balic, "Teaching–learning-based optimization algorithm for unconstrained and constrained real-parameter optimization problems," *Eng. Optim.*, vol. 44, no. 12, pp. 1447–1462, 2012.

[20] J. Jin, L. Rothrock, P. L. McDermott, and M. Barnes, "Using the Analytic Hierarchy Process to Examine Judgment Consistency in a Complex Multiattribute Task," *Syst. Man Cybern. Part A: Syst. Humans, IEEE Trans.*, vol. 40, pp. 1105–1115, 2010.

[21] S. Das, A. Mukhopadhyay, A. Roy, A. Abraham, and B. K. Panigrahi, "Exploratory Power of the Harmony Search Algorithm: Analysis and Improvements for Global Numerical Optimization," *IEEE Trans. Syst. Man, Cybern. Part B*, vol. 41, no. 1, pp. 89–106, 2011.

[22] L. Y. Shouheng Tuo and Tao Zhou., "An Improved harmony search based on teaching-learning strategy for unconstrained optimization problems," *Hindawi* 2013, [Online]. Available: http://dx.doi.org/10.1155/2013/413565

[23] K. Zou, A. P. Agalgaonkar, K. M. Muttaqi, and S. Perera, "Distribution System Planning With Incorporating DG Reactive Capability and System Uncertainties," *IEEE Trans. Sustain. Energy*, vol. 3, no. 1, pp. 112–123, 2012.

[24] N. Jain, S. N. Singh, and S. C. Srivastava, "A Generalized Approach for DG Planning and Viability Analysis Under Market Scenario," *Ind. Electron. IEEE Trans.*, vol. 60, pp. 5075–5085, 2013.

[25] Sandeep Kaur and G. B. Kumbhar, "Incentive driven distributed generation planning with renewable energy resources," *Int. J. Advances in Electrical and Computer Engineering*, vol.14, pp. 21-28,2014.

[26] http://greencleanguide.com/2011/12/02/solar-pv-and-carbon-credits/

[27] http://www.agricultureinformation.com/forums/consultancy-services/26781-carbon-credit-biomass-power-thermal-project.html/

[28] http://www.renewableenergyworld.com

[29] http://smallb.in/%20/environment%20/carbon-market

This article has been accepted for publication in a future issue of this journal, but has not been fully edited. Content may change prior to final publication. Citation information: DOI 10.1109/TIE.2017.2745438, IEEE Transactions on Industrial Electronics

A Novel Carrier-Based Hybrid PWM Technique for Minimization of Line Current Ripple in Two Parallel Interleaved Two-Level VSIs

Kapil Shukla, Varun Malyala, and Ramkrishan Maheshwari, *Member, IEEE*

Abstract— **A novel hybrid pulse-width modulation (PWM) technique is proposed in this paper for two parallel interleaved, two-level (2L), three-phase voltage source inverters (VSIs). The two parallel interleaved VSIs are analyzed as a three-level (3L) inverter. A 3L inverter provides minimum line current ripple when nearest three voltage vectors are applied. In this paper, a novel carrier-based PWM technique is developed that ensures application of nearest voltage vectors, keeping average circulating current to zero over a switching period. For carrier based implementation of the proposed PWM, generalized common-mode (CM) offsets are derived in terms of maximum and minimum values of reference signals. Each 3L space-vector sector is divided into seven sub-sectors. For each sub-sector, a CM offset is calculated, addition of which to reference signals ensures minimum line current ripple and zero average circulating current. Simulation and experimental results are provided to validate the proposed technique.**

***Index Terms*— Voltage-Source inverter (VSI), Interleaving, Two-level Inverter (2L), Pulse-width Modulation (PWM).**

I. INTRODUCTION

Parallel interleaved voltage source inverters (VSIs) are used for different applications such as high power renewable energy power conversion system [1], shunt active power filters, active front end rectifiers [2], etc. The main advantages of the parallel interleaved VSIs are reduced current stress on the switches, reduced current ripple, modularity, improved thermal management, increased power capability, redundancy, easy maintenance, increased efficiency [2] - [6]. Parallel interleaved VSIs have common dc-link, ac sides are connected through inductors, and carrier signals are interleaved. Due to this interleaving, ac side harmonic distortion and line current ripple is less [3]. However, the harmonic distortion in the ac side current depends on interleaving angle as well as pulse-width modulation (PWM) methods [4] - [9]. In [3], the effect of interleaving angle is analyzed, and it is recommended to operate the inverter with $2\pi/N$ angle between the carrier signals for N parallel-connected inverter system. The interleaving angle also impacts on the size of ac and dc passive components [10] - [11].

In addition to interleaved carrier signals, different PWM techniques are also used to reduce output current harmonic distortion. Analysis of the ac side current distortion for a single 2L VSI is presented in [7]. It has been shown that for lower modulation indices, conventional space-vector PWM (SVPWM) technique provides minimum THD, while for higher modulation indices, split clamping and advanced split clamping sequences PWM techniques should be used. In [4], active zero state PWM (AZSPWM) and near-state PWM (NSPWM) techniques are proposed for reducing line current distortion in parallel interleaved VSIs with 180° phase-shift between carrier signals. However, the effect of different interleaving angles between the carrier signals is discussed in [5], and a hybrid PWM technique employing multiple sequences is proposed for reducing ac side current total harmonic distortion (THD). The proposed technique in [5] implements different interleaving angles for different zones in a sector which makes the implementation of the technique quite complicated. Another PWM technique based on different CM offset addition for different modulation indices for parallel-connected VSIs is proposed in [6]. The proposed PWM technique reduces the flux linking in the inter-cell transformers connected to the ac side of parallel-connected VSIs, which in-turn reduces the output ac side current ripple. The above mentioned techniques consider the parallel interleaved inverters as two single VSIs.

In this paper, a new PWM technique is presented with following key features,

1) The two parallel interleaved 2L inverter system is analyzed as a single 3L inverter instead of treating them as two single VSIs.
2) A new hybrid PWM technique is developed for the two parallel interleaved 2L VSIs to minimize the ac side current ripple.
3) The difference of CM voltages of both the inverters averaged over a switching period is also kept to zero such that the circulating current averaged over a switching period will be zero.

Manuscript received January 19, 2017; revised May 6, 2017 and July 10, 2017; accepted August 6, 2017.

All authors are with the department of Electrical Engineering, Indian Institute of Technology Delhi, New Delhi, India (e-mail: kapilstriker@gmail.com, rkmahesh@ee.iitd.ac.in).

0278-0046 (c) 2017 IEEE. Personal use is permitted, but republication/redistribution requires IEEE permission. See http://www.ieee.org/publications_standards/publications/rights/index.html for more information.

This article has been accepted for publication in a future issue of this journal, but has not been fully edited. Content may change prior to final publication. Citation information: DOI 10.1109/TIE.2017.2745438, IEEE Transactions on Industrial Electronics

4) The proposed PWM is implemented using a carrier-based approach. For this, a CM offset is required to be added to the three-phase reference signal in a switching period. The required CM offset is also presented.

For minimization of line current ripple in a 3L inverter, three nearest voltage vectors should be applied [12] - [13]. However, in parallel interleaved system, there exists another problem of circulating current [14]. This current is caused by the common-mode (CM) voltage difference of the inverters [15]. The instantaneous CM voltage difference cannot be avoided in interleaved carrier signals. However, the CM voltage difference averaged over a switching period can be made zero for reducing the average circulating current. Another way of eliminating the circulating current is by providing high impedances path for the circulating current which is achieved by line frequency isolation transformer but it increases the size and cost of the overall system and hence decreases the power density. The circulating current could also be reduced by the use of coupled inductors [14], integrated inductors [16], and three limb inductors [17]. Different PWM techniques and control schemes are also been developed for mitigation of circulating current [18] - [27]. However, these techniques do not focus on minimizing the ac side current distortion. The proposed PWM technique ensures the zero average circulating current with minimization of the ac side current distortion.

The converter topology under consideration looks similar to the topology uses for the dual induction fed open end winding induction motor drive, and it is analyzed as a 3L inverter [28] - [32]. However, the dc-link is not common in [28] - [31], and the operation is also different. In the drive application, the average CM voltage is kept zero [28], [32]. On the other hand, the system considered in this paper requires difference of the CM voltage averaged over a switching period to be zero to make the average circulating current equal to zero in a switching period. In summary, the proposed PWM technique applies three nearest vectors of the 3L SV diagram to minimize the ac side current ripple keeping the average of the CM voltage difference zero. In this way, the ac side line current ripple can be kept same as that of the 3L VSI.

The carrier based implementation of the proposed PWM is also presented which ensures that no extra look-up tables are required for sector identification and CM offset signal addition. The proposed PWM requires multiple switching of a phase in a switching period. The carrier based implementation of PWM sequence with multiple phase switching is discussed in [33] for a single 2L inverter. However, the PWM technique used in [33] has one phase clamped to a dc-link terminal for a switching period, and different CM offsets are calculated for different sector. While, the technique proposed in this paper is used for two parallel interleaved VSIs without any phase clamped to the dc-link terminal in a switching period, and the generalized CM offsets applicable to each sector are calculated, which ensures fast and simple implementation.

The paper is organized as follows. Section II explains the functioning of parallel interleaved 2L inverters as a 3L inverter. Section III discusses about the proposed hybrid PWMstrategy. Simulation and experimental results are explained in section IV. Conclusions are provided in section V.

II. 2L Inverters As A 3L Inverter

A. Parallel Interleaved 2L Inverters As A 3L Inverter

The two parallel interleaved 2L inverters with a common dc-link of voltage V_{dc} are shown in Fig. 1. Each leg of the inverter is connected through an inductor to the ac side. The ac side inductors can be realized using a common-mode (CM) and differential-mode (DM) chokes. Here, the inductors are connected to a common point, which could be further connected to any ac load or grid. Now, considering phase A of each parallel interleaved inverters, the system could be visualized as shown in Fig. 2. The thevenin's equivalent circuit of Fig. 2 can be drawn as shown in Fig. 3. Using this equivalent circuit, the equivalent output pole voltage for phase A is given by [27]

$$v_{AO} = \frac{v_{A1O} + v_{A2O}}{2}. \quad (1)$$

where v_{A1O} is the inverter-1 pole voltage, and v_{A2O} is the inverter-2 pole voltage.

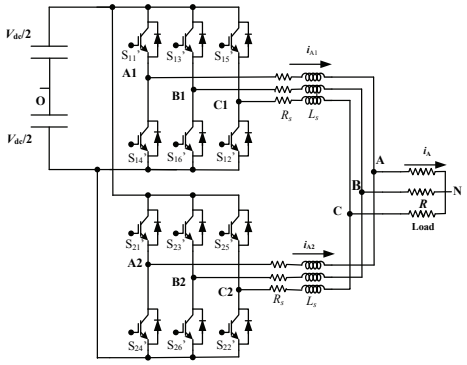


Fig. 1. Parallel interleaved inverters connected to load fed from a common dc-link.

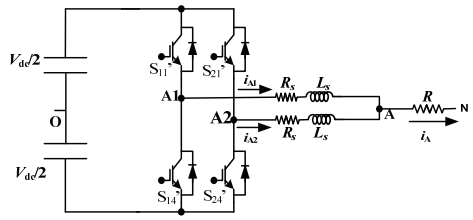


Fig. 2. Equivalent circuit of the system considering only phase A of both inverters.

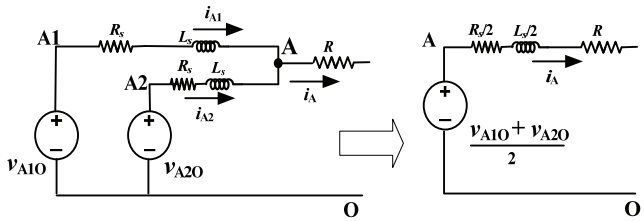


Fig. 3. Thevenin equivalent circuit of phase A.

Using (1), the values of equivalent pole voltages of phase A (v_{AO}) for different values of pole voltages of phase A of inverter 1 and 2 are listed in Table I. By looking at the

0278-0046 (c) 2017 IEEE. Personal use is permitted, but republication/redistribution requires IEEE permission. See http://www.ieee.org/publications_standards/publications/rights/index.html for more information.

This article has been accepted for publication in a future issue of this journal, but has not been fully edited. Content may change prior to final publication. Citation information: DOI 10.1109/TIE.2017.2745438, IEEE Transactions on Industrial Electronics

combinations, it is clear that the equivalent pole voltage, v_{AO}, can have three voltage levels. Similarly, it can be said that the equivalent pole voltages of other phases, phase B and C, can also have three voltage levels. Therefore, two parallel interleaved 2L inverters could be analyzed as a single 3L inverter. The different voltage levels of the equivalent pole voltage are denoted as

$$2 = +\frac{V_{dc}}{2};\quad 1 = 0\text{ V};\quad 0 = -\frac{V_{dc}}{2} \tag{2}$$

TABLE I
POLE VOLTAGE COMBINATIONS

v_{A1O}	v_{A2O}	v_{AO}
$-V_{dc}/2$	$-V_{dc}/2$	$-V_{dc}/2$
$-V_{dc}/2$	$+V_{dc}/2$	0
$+V_{dc}/2$	$-V_{dc}/2$	0
$+V_{dc}/2$	$+V_{dc}/2$	$+V_{dc}/2$

The space-vector diagram of two parallel interleaved system is shown in Fig. 4 which is similar to a 3L inverter space-vector diagram. The diagram is divided into 6 sectors/triangles, as displayed by bold lines. Each sector could be further divided into different sub-sectors, as displayed by dashed lines. The magnitude of the outermost vector ($\mathbf{V}_{13}$) is V_{dc}, while the inner middle vector ($\mathbf{V}_1$) has magnitude equal to $V_{dc}/2$.

B. Equivalent 3L Inverter Switching Sequence Generation from 2L Inverter Switching Sequences

The parallel interleaved system can be represented as a 3L inverter, and each inverter is modulated as a 2L inverter for generating switching sequences of equivalent 3L inverter. The 2L inverter space-vector diagram is shown in Fig. 5 and divided into six sectors. Here, '−' and '+', respectively, correspond to the pole voltage level of $-V_{dc}/2$ and $+V_{dc}/2$ of a phase. There are six active vectors ($\mathbf{V}_1^{2L}$- $\mathbf{V}_6^{2L}$) and two zero vectors ($\mathbf{V}_0^{2L}$ & $\mathbf{V}_7^{2L}$) in a 2L inverter space-vector diagram. Among these vectors, two active and both zero vectors are used to approximate a given reference vector ($\mathbf{V}_{ref}$), at an angle θ, in conventional SVPWM technique in a switching period (T_s), and the duration for which adjacent active vectors are applied (dwell time) are given by [13], [35]

$$T_1 = \frac{|\mathbf{V}_{ref}|\sin(60^\circ-\theta)}{V_{dc}\sin(60^\circ)}T_s = \frac{v_{max}-v_{mid}}{V_{dc}}T_s \tag{3}$$

and,

$$T_2 = \frac{|\mathbf{V}_{ref}|\sin(\theta)}{V_{dc}\sin(60^\circ)}T_s = \frac{v_{mid}-v_{min}}{V_{dc}}T_s \tag{4}$$

The duration, for which each zero vector is applied, are equal and is given by

$$T_z = \frac{T_s - T_1 - T_2}{2} \tag{5}$$

where, v_{max}, v_{min}, and v_{mid} are the maximum, minimum, and middle values of the three-phase reference signals ($v_{A,ref}$, $v_{B,ref}$, $v_{C,ref}$), respectively, sampled in a switching period. Due to the six-fold symmetry of the space vector diagram, (3) – (5) hold good for each sector.

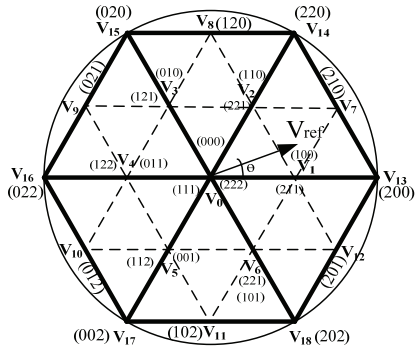


Fig. 4. Space-vector diagram using the equivalent pole voltages of two parallel interleaved inverter system.

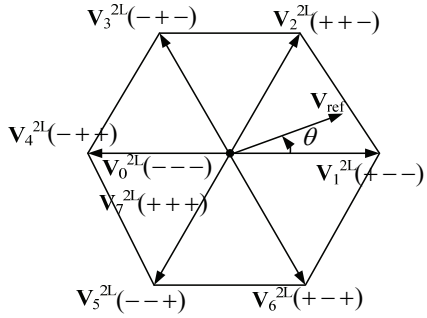


Fig. 5. Space-vector diagram of a 2L inverter.

This technique requires calculation of T1 and T2, which in turn are required to calculate the on and off times of individual switches of the inverters. However, the on and off times of the individual switches can be found directly using carrier-based approach [19]. In this approach, the reference signals are compared with the high frequency triangular carrier signals. The carrier based approach for implementing conventional SVPWM technique is described in [15], as shown in Fig. 6 for two parallel interleaved inverters. The carrier signals are interleaved and phase shifted by 180° to reduce the harmonic components of the load side current [3]. From Fig. 6, the switching sequences for both the inverters can be given as:

$(---),(+--),(+-+),(++-),(+++)$ and reverse for Inv.-1

$(+++),(++-),(+--),(+-+),(---)$ and reverse for Inv.-2

From abovementioned switching sequences, (1), and Table I, the equivalent pole voltages of the parallel interleaved inverter system can be calculated which yield the following switching sequence

(111), (210), (200), (210), (111), and reverse (6)

In a similar manner, the equivalent 3L switching sequences for different 2L PWM sequences could be determined. However, it is not feasible to apply any PWM sequence in the parallel interleaved system due to the circulating current. The circulating current is caused by the difference between the CM voltages of the inverters, as given by [15]

$$i_{CC} = \frac{i_{A1}+i_{B1}+i_{C1}}{3} = -\frac{i_{A2}+i_{B2}+i_{C2}}{3} = \frac{1}{L_s}\int(v_{cm1}-v_{cm2})dt \tag{7}$$

0278-0046 (c) 2017 IEEE. Personal use is permitted, but republication/redistribution requires IEEE permission. See http://www.ieee.org/publications_standards/publications/rights/index.html for more information.

This article has been accepted for publication in a future issue of this journal, but has not been fully edited. Content may change prior to final publication. Citation information: DOI 10.1109/TIE.2017.2745438, IEEE Transactions on Industrial Electronics

where i_{A1}, i_{B1}, and i_{C1} are the three phase currents of inverter 1, and i_{A2}, i_{B2}, and i_{C2} are the three phase currents of inverter 2. $v_{cm,1}$ and $v_{cm,2}$ are the CM voltages of inverter 1 and inverter 2, respectively. R_s is neglected in (7). From (7), if the CM voltage difference averaged over a switching period (T_s) is zero, i.e.

$$\left\langle v_{cm,1} - v_{cm,2} \right\rangle_{T_s} = 0 \tag{8}$$

the circulating current averaged over a switching period will also be zero. The above mentioned constraint is met for SVPWM as displayed in Fig. 6.

III. Proposed Hybrid PWM Technique

Different 3L switching sequences could be generated from different switching sequences of parallel interleaved 2L inverters. Now, when the conventional SVPWM technique is applied to 2L parallel interleaved inverters, the equivalent 3L switching states for ($0 \le \theta \le 30$) would be (111), (210), (200), (210), (111), as given by (6). For these equivalent 3L switching states, the error voltage vectors are shown in Fig. 7. (a). Now, if the switching sequences of 2L inverters are made such that the nearest three voltage vectors are applied for the same reference vector (Fig. 7. (b)), the error voltage vectors will reduce, which in turn reduces the ac side line current ripple [8]. The proposed PWM technique ensures application of three nearest voltage vectors.

A. Selection of the 3L Switching Sequences

In the equivalent 3L space-vector diagram (Fig. 4), there are 6 voltage vectors ($\mathbf{V}_1 - \mathbf{V}_6$) with even redundancy and one zero vector ($\mathbf{V}_0$) with odd redundancy. Redundancy provides the degree of freedom, which could be utilized for reducing the error vectors or ac side line current ripple to a great extent [12] – [13]. If the reference vector lies in sector-1 and the middle value of the given reference signals is negative, i.e. $v_{mid} < 0$, redundancy of middle voltage vector $\mathbf{V}_1$ (211, 100) is utilized. However, when $v_{mid} > 0$, redundancy of middle voltage vector $\mathbf{V}_2$ (110, 221) is utilized. Similarly, the redundancy of middle voltage vectors in other sectors is utilized for minimizing the ac side line current ripple.

In the proposed technique, the equivalent space-vector sector of two parallel interleaved inverter system is divided into seven sub-sectors (Fig. 8). Method of sector identification from the three-phase reference signals is displayed in Fig. 9. For each sub-sector, a switching sequence is found out purely on the basis of minimum error voltage vectors, satisfying the constraint given in (8). However, it is observed that one cannot achieve maximum possible reduction of ac side line current ripple as well as reduction of the circulating current with the same PWM sequence. So, a PWM technique with minimum line current ripple and zero average circulating current is presented. The equivalent 3L switching sequences for the proposed hybrid PWM technique are displayed in Table II. To generate the equivalent 3L switching sequence, the required 2L switching sequence for inverter 1 is shown in the second column of Table II, and the required 2L switching sequence for inverter 2 is the reverse of the switching sequence of inverter 1. The proposed PWM technique applies different switching sequences for difference reference vectors whose tips lie in Sector I, as shown in Table II, depending on its position in the sector. So, the proposed technique is named as a hybrid PWM technique.

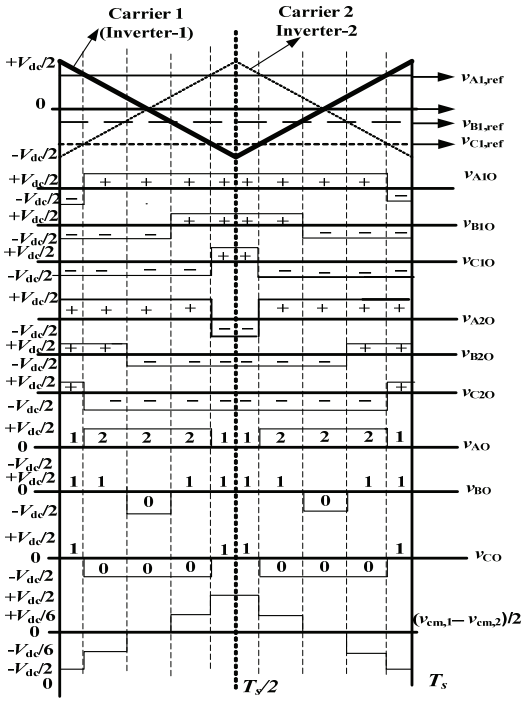


Fig. 6. Switching waveforms for parallel interleaved inverters using SVPWM.

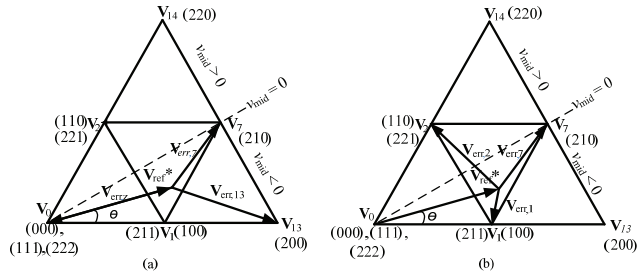


Fig. 7. Error voltage vectors.

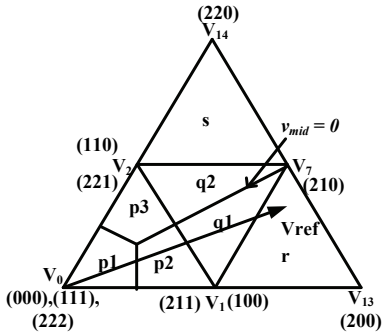


Fig. 8. Proposed hybrid PWM sub-sector division.

The proposed hybrid PWM technique is implemented using carrier-based approach. For implementing the conventional PWM techniques using carrier-based approach, a CM offset is added to the given reference signals. While, the proposed hybrid PWM technique is composed of the sequence with a

0278-0046 (c) 2017 IEEE. Personal use is permitted, but republication/redistribution requires IEEE permission. See http://www.ieee.org/publications_standards/publications/rights/index.html for more information.

This article has been accepted for publication in a future issue of this journal, but has not been fully edited. Content may change prior to final publication. Citation information: DOI 10.1109/TIE.2017.2745438, IEEE Transactions on Industrial Electronics

phase switching four times in a switching period (Table II). For implementing these sequences using carrier-based approach, the reference phase voltage signal which switches four times in a switching period is divided in two signals which are compared with the carrier signal. The output of the comparison is passed through an EX-NOR or EX-OR logic gate to obtain the desired switching sequence. The type of gate to be used would depend on the magnitude of the middle value of the three phase reference voltage signals. For $v_{mid} < 0$, EX-NOR gate is used, while for the remaining conditions EX-OR gate is utilized.

Now, let the voltage reference vector ($\mathbf{V_{ref}}$) lies in sector r (Fig. 8). The voltage waveforms corresponding to the switching sequence used in sector r are displayed in Fig. 10. Here, two interleaved carriers corresponding to each inverter and magnitudes of the updated reference signals ($v_{A1,ref}$, $v_{B1,ref}$, $v_{C1,ref}$) are displayed. As phase A is to be switched four times within a switching period, so two reference signals, $v_{A1,ref1}$ and $v_{A1,ref2}$, are generated. These two reference signals are used to generate two pulses gv_{A1O1} and gv_{A1O2}, which may have high and low levels. These pulses are passed through an EX-NOR gate to get the desired gate signal and the pole voltage signal (v_{A1O}) for phase A of inverter-1. Similarly, signals for inverter-2 (v_{A2O}) are generated. The generated signals keeps the average value of the CM voltages difference over a switching period to zero (Fig. 10).

The error vectors produced by the proposed hybrid PWM technique are similar to the error vectors generated by a 3L inverter using conventional SVPWM technique [13]. Therefore, the rms ac side line current ripple produced by the proposed PWM technique is same as that of a 3L inverter as displayed in Fig. 11.

B. Common-mode Offset Calculation

For better dc-link utilization, a CM offset (v_{off}) is added to the reference phase signals. To modulate parallel interleaved 2L inverters as a single 3L inverter using carrier based approach, the CM offset is added to the reference signals which ensures that the dwell times of redundant middle vectors are divided equally. Using this CM offset, the updated reference signals are generated for the phase switching four times which will make sure that the equivalent 3L switching sequence for minimum line current ripple is generated. The switching waveforms over a switching period (T_s) for the given reference signals (sub-sector r) are displayed in Fig. 10. The corresponding 2L switching sequences for parallel interleaved inverters are shown below:

$(+--),(+--),(+--),(---),(+--),(+--),(++-),(+++)$..Inv1

$(+++),(++-),(+--),(+--),(---),(+--),(+--),(+--)$..Inv2

Let T_{1_3}, T_{2_3}, T_{z_3} be the dwell times of the equivalent 3L voltage vectors $\mathbf{V}_{13}$, $\mathbf{V}_7$, and $\mathbf{V}_1$ (Fig. 8), respectively. Let T_{s_3} be the switching time of the equivalent 3L inverter. The point to be noted here is that the 3L inverter switching time period will be half that of the 2L inverter, i.e $T_{s_3} = T_s/2$ (Fig. 6). From similar triangle and volt-sec balance approach, the required CM offset can be easily calculated. For the given reference phase signals, using similar triangles approach (Fig. 10),

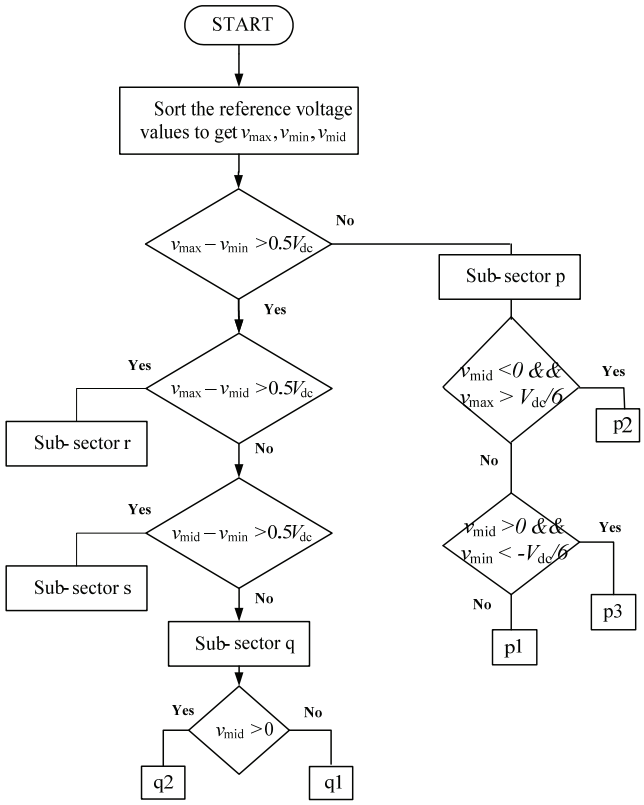


Fig. 9. Flowchart for sector identification.

TABLE II
PROPOSED HYBRID PWM TECHNIQUE SWITCHING SEQUENCES (SECTOR-I)

Sub-Sector		2L PWM Switching Sequence (Inverter 1)	Equivalent 3L PWM Switching Sequence
p	p1	(−−−), (−−−), (−−−),(−−−),	(111), (110), (100), (000),
		(−−−), (+−−), (++−), (+++)	(000), (100), (110), (111)
	p2	(+−−), (−−−), (−−−),(−−−),	(211), (111), (110), (100),
		(+−−), (++−), (+++), (+++)	(100), (110), (111), (211)
	p3	(−−−), (−−−), (+−−),(++−),	(110), (111), (211), (221),
		(+++), (+++), (+++), (++−)	(221), (211), (111), (110)
q	q1	(+−−), (+−−), (−−−),(−−−),	(211), (210), (110), (100),
		(+−−), (++−), (++−), (+++)	(100), (110), (210), (211)
	q2	(−−−), (+−−), (+−−),(++−),	(110), (210), (211), (221),
		(+++), (+++), (++−), (++−)	(221), (211), (210), (110)
r		(+−−), (+−−), (+−−),(−−−),	(211), (210), (200), (100),
		(+−−), (+−−), (++−), (+++)	(100), (200), (210), (211)
s		(−−−), (+−−), (++−),(++−),	(110), (210), (220), (221),
		(++−), (++−), (++−), (++−)	(221), (220), (210), (110)

$$\frac{\frac{V_{dc}}{2}+(v_{c,ref}+v_{off})}{T_7}=\frac{V_{dc}}{T_s/2} \tag{9}$$

where, T_7 is dwell time for switching state (+++).

Also, from switching sequences of 2L parallel interleaved inverters and equivalent 3L switching sequence,

$$T_7=\frac{T_{z_3}}{2} \tag{10}$$

$$2T_z = T_{z_3} \tag{11}$$

0278-0046 (c) 2017 IEEE. Personal use is permitted, but republication/redistribution requires IEEE permission. See http://www.ieee.org/publications_standards/publications/rights/index.html for more information.

This article has been accepted for publication in a future issue of this journal, but has not been fully edited. Content may change prior to final publication. Citation information: DOI 10.1109/TIE.2017.2745438, IEEE Transactions on Industrial Electronics

Using equations (3) – (5) and (9) – (11), the CM offset is given by

$$v_{\text{off}} = \frac{-v_{\text{A,ref}} - v_{\text{C,ref}}}{2} \tag{12}$$

Eq. (12) can be generalized as,

$$v_{\text{off}} = \frac{-v_{\max} - v_{\min}}{2} \tag{13}$$

This CM offset will be added to phase B and C reference signals. As phase A is to be switched four times within a switching period, so two reference signals are required. To summarize for sector 1, sub-sector r, modified reference signals for 2L parallel interleaved inverters are:

$$\begin{aligned} v_{\text{A1,ref1}} &= 0, v_{\text{A1,ref2}} = \frac{V_{\text{dc}}}{2} - (v_{\text{off}} + v_{\text{A,ref}}) \\ v_{\text{B1,ref}} &= v_{\text{B2,ref}} = (v_{\text{off}} + v_{\text{B,ref}}) \\ v_{\text{C1,ref}} &= v_{\text{C2,ref}} = (v_{\text{off}} + v_{\text{C,ref}}) \end{aligned} \tag{14}$$

The CM offsets are calculated in terms of maximum and minimum values of the reference signals for each sub-sector of a sector and due to six-fold symmetry, these signals could be used in all six sectors, as shown in Table III. The reference signal having maximum value or minimum value will switch four times in a switching period. Therefore, two reference signals are required for the phase which switches four times which are denoted by v_{max1ref} and v_{max2ref} if phase having maximum value switches four times or v_{min1ref} and v_{min2ref} if phase having minimum value switches four times.

TABLE III
COMMON-MODE OFFSET SIGNAL FOR PROPOSED HYBRID PWM TECHNIQUE

Sub-Sector		Common-mode offset
p	p1	$v_{\text{off}} = -0.25 \cdot V_{\text{dc}} - 0.5 \cdot v_{\max} - 0.5 \cdot v_{\min}$
	p2	$v_{\text{off}} = 0.5 \cdot v_{\min}$, $v_{\text{max1ref}} = 0$, $v_{\text{max2ref}} = v_{\max} + 0.5 \cdot V_{\text{dc}} - 2 \cdot v_{\max} - 0.5 \cdot v_{\min}$
	p3	$v_{\text{off}} = 0.5 \cdot v_{\max}$, $v_{\text{min1ref}} = 0$, $v_{\text{min2ref}} = v_{\min} - 0.5 \cdot V_{\text{dc}} - 2 \cdot v_{\min} - 0.5 \cdot v_{\max}$
q	q1	$v_{\text{off}} = -0.25 \cdot V_{\text{dc}} + 0.5 \cdot v_{\max}$, $v_{\text{max1ref}} = 0$, $v_{\text{max2ref}} = v_{\max} + 0.75 \cdot V_{\text{dc}} - 2.5 \cdot v_{\max}$
	q2	$v_{\text{off}} = 0.25 \cdot V_{\text{dc}} + 0.5 \cdot v_{\min}$, $v_{\text{min1ref}} = 0$, $v_{\text{min2ref}} = v_{\min} - 0.75 \cdot V_{\text{dc}} - 2.5 \cdot v_{\min}$
r		$v_{\text{off}} = -0.5 \cdot v_{\max} - 0.5 \cdot v_{\min}$, $v_{\text{max1ref}} = 0$, $v_{\text{max2ref}} = 0.5 \cdot V_{\text{dc}} - (v_{\max} + v_{\text{off}})$
s		$v_{\text{off}} = -0.5 \cdot v_{\max} - 0.5 \cdot v_{\min}$, $v_{\text{min1ref}} = 0$, $v_{\text{min2ref}} = 0.5 \cdot V_{\text{dc}} + (v_{\min} + v_{\text{off}})$

IV. Simulation And Experimental Results

A MATLAB-Simulink® model of the parallel interleaved 2L inverter system has been developed. The system parameters are shown in Table IV. A MATLAB code using error vectors [8] is developed for calculating normalized rms

TABLE IV
SYSTEM PARAMETERS

R	60 Ω
Rs	2.5 Ω
Ls	24 mH
Vdc	600 V
Ts	200 µs

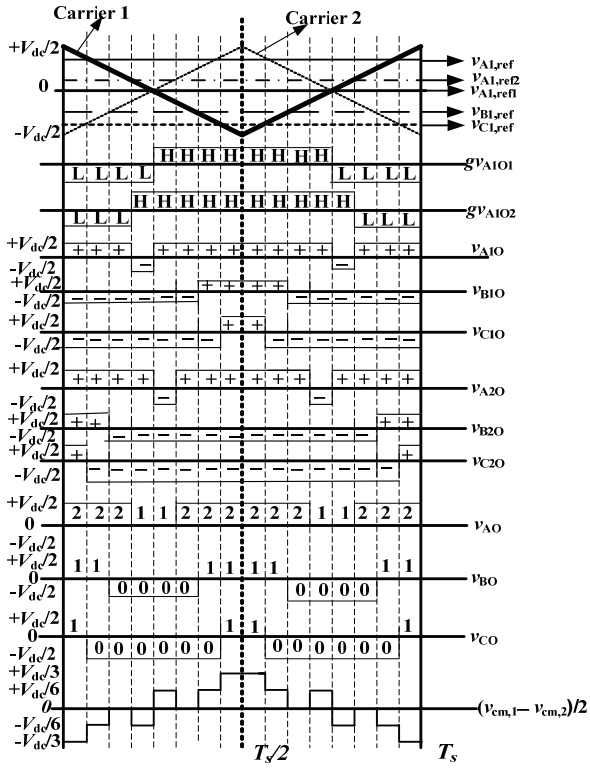


Fig. 10. Voltage waveforms for sub-sector r (H – High, L - Low).

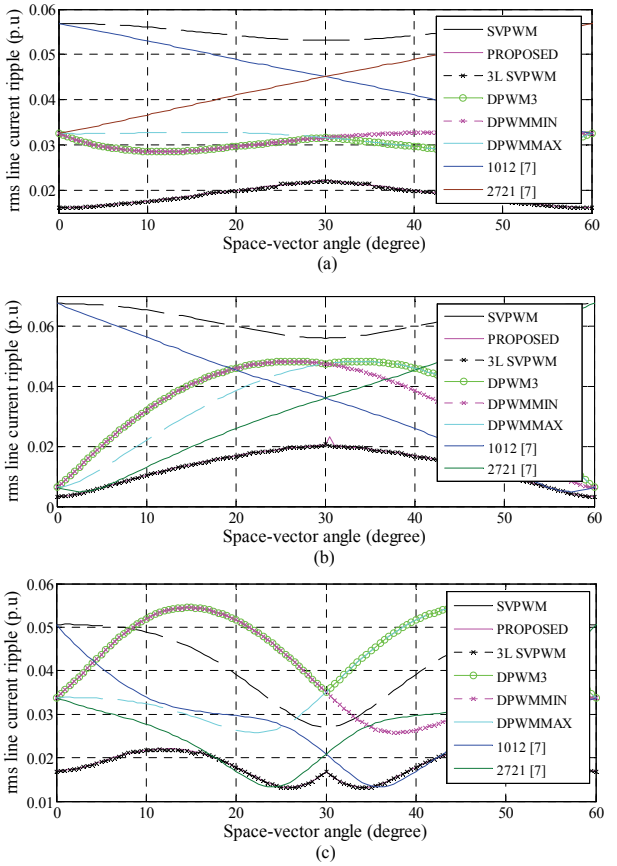


Fig. 11. Line current ripple (p.u) (a) m_a = 0.4, (b) m_a = 0.7, (c) m_a = 1.0.

0278-0046 (c) 2017 IEEE. Personal use is permitted, but republication/redistribution requires IEEE permission. See http://www.ieee.org/publications_standards/publications/rights/index.html for more information.

This article has been accepted for publication in a future issue of this journal, but has not been fully edited. Content may change prior to final publication. Citation information: DOI 10.1109/TIE.2017.2745438, IEEE Transactions on Industrial Electronics

(root mean square) ac side line current ripple computed over a switching period (T_s). The normalized rms ac side line current ripple of different PWM schemes for different modulation indices (m_a) for a sector is shown in Fig. 11. The rms ac side line current ripple remains minimum for the proposed hybrid PWM technique compared to other PWM techniques used in [8] as displayed in Fig. 11. The comparison of normalized rms ac side line current ripple w.r.t modulation indices (m_a) for different PWM techniques is also carried out and is displayed in Fig. 12. The variation of normalized rms ac side line current ripple for the proposed hybrid PWM technique at different modulation indices is shown in Fig. 13. Here, modulation index (m_a) is defined as ratio of peak of reference signal and $V_{dc}/2$.

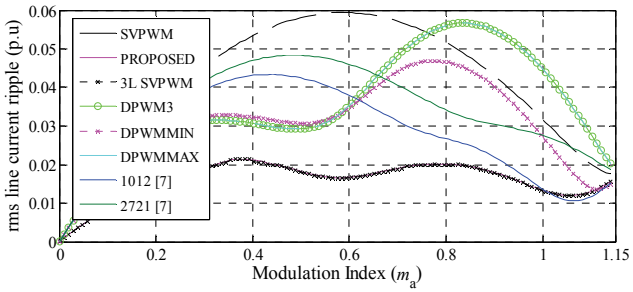


Fig. 12. Line current ripple (p.u) variation w.r.t modulation index (m_a).

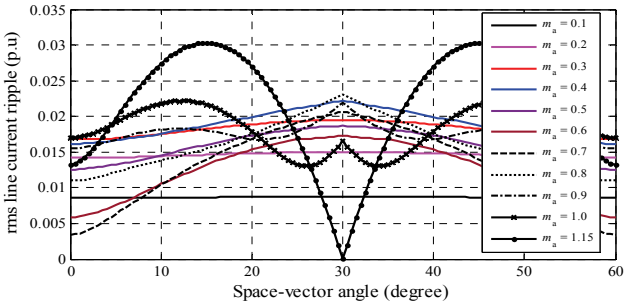


Fig. 13. Line current ripple (p.u) variation of proposed hybrid PWM technique for different modulation index (m_a) values.

Effectiveness of the proposed technique is also examined experimentally. The experimental implementation of the system is done with the help of the digital signal processor (DSP) TMS320F28335 from Texas Instruments. EPWM A and EPWM B channels are used for generating the gate signals of inverter 1 and inverter 2, respectively. The software code execution time for the proposed PWM technique is 5 µs as compared to the 4 µs required by the carrier-based SVPWM technique. A GPIO signal is toggled for switching the logic gate operation (EX-OR to EX-NOR and vice-versa). Same parameters are used for experimental purpose as applied in case of simulation. A picture of the experimental setup is shown in Fig. 14. The normalized total switching loss ($P_{SUB,TOT}$) variation over a switching period [9] for a single inverter with load power factor angle of 30° (lagging) is also displayed in Fig. 15. Due to the multiple switching of a phase in a switching period, the normalized total switching loss for the proposed PWM technique is increased by nearly 8% as compared to conventional SVPWM. This increase in switching loss could be treated as a disadvantage of the proposed PWM technique. However, the ac-side line current ripple for the proposed PWM technique reduces by more than 40% at lower m_a values and reduces nearly by 24% at higher m_a values as compared to the conventional SVPWM technique.

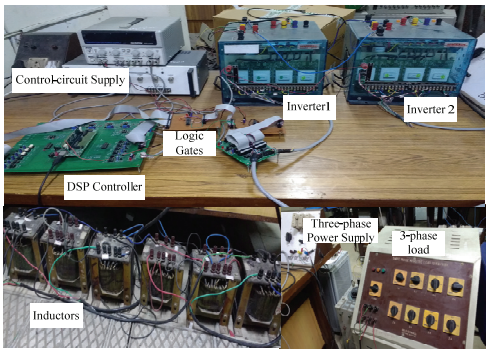


Fig. 14. Experimental Set-up.

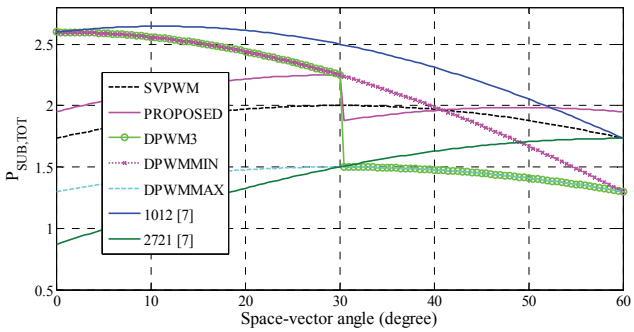


Fig. 15. Normalized total switching loss ($P_{SUB,TOT}$) variation over a sector.

Experimental results for SVPWM and proposed PWM technique are shown in Figs. 16-23. At all modulation indices, using the proposed PWM technique, ripple content in the ac side line current (i_A) turns out to be lower as compared to the commonly used PWM technique [8]. In FFT plots (Fig. 19 and Fig. 23), the fundamental component is scaled down by three to focus on harmonic components. The dominant harmonics are displayed separately in the FFT plots. The comparison of rms ac side ripple current for different modulation indices is displayed in Table V.

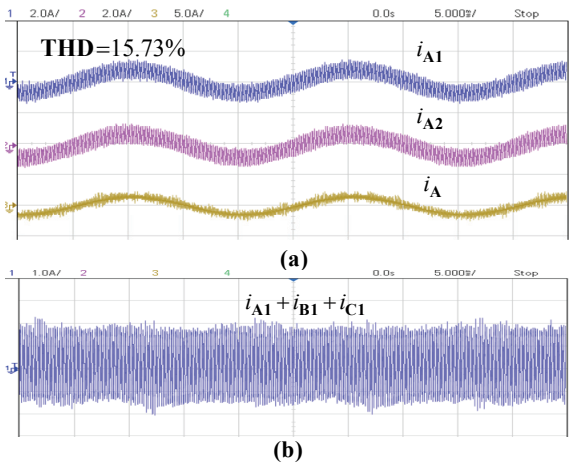


Fig. 16. Experimental result of SVPWM, m_a = 0.4. (a) Line currents (2A/div, 2A/div, and 5A/div) (b) 3·Circulating current (1A/div).

0278-0046 (c) 2017 IEEE. Personal use is permitted, but republication/redistribution requires IEEE permission. See http://www.ieee.org/publications_standards/publications/rights/index.html for more information.

This article has been accepted for publication in a future issue of this journal, but has not been fully edited. Content may change prior to final publication. Citation information: DOI 10.1109/TIE.2017.2745438, IEEE Transactions on Industrial Electronics

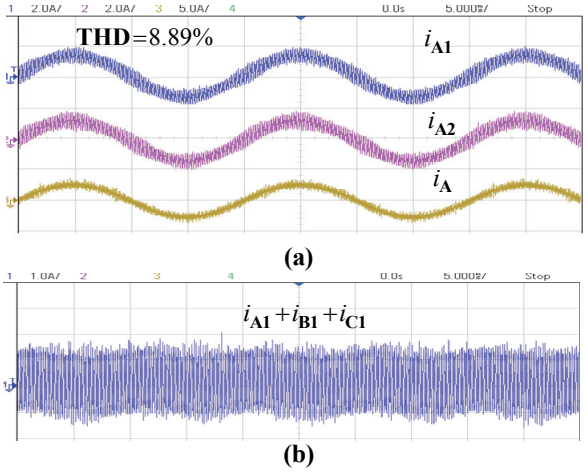


Fig. 17. Experimental result of SVPWM, m_a = 0.7. (a) Line currents (2A/div, 2A/div, and 5A/div) (b) 3·Circulating current (1A/div).

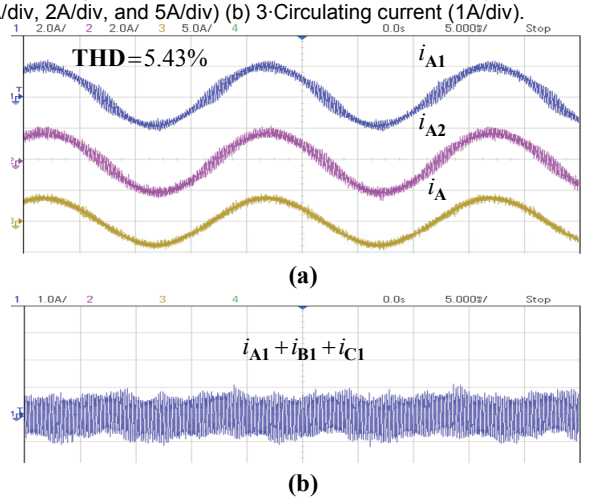


Fig. 18. Experimental result of SVPWM, m_a = 1.0. (a) Line currents (2A/div, 2A/div, and 5A/div) (b) 3·Circulating current (1A/div).

The circulating current produced by the proposed PWM technique also turns out to be lower than the SVPWM technique at all different values of modulation indices. The comparison of circulating current applying different PWM sequences for different modulation index values is shown in Table VI. Both experimental and simulated results accompany each other.

TABLE V
COMPARISON OF SVPWM AND PROPOSED PWM TECHNIQUE

Modulation Index (m_a)	RMS Ripple current (mA)	
	SVPWM	Proposed PWM
0.4	167	100
0.7	174	118
1.0	156	120

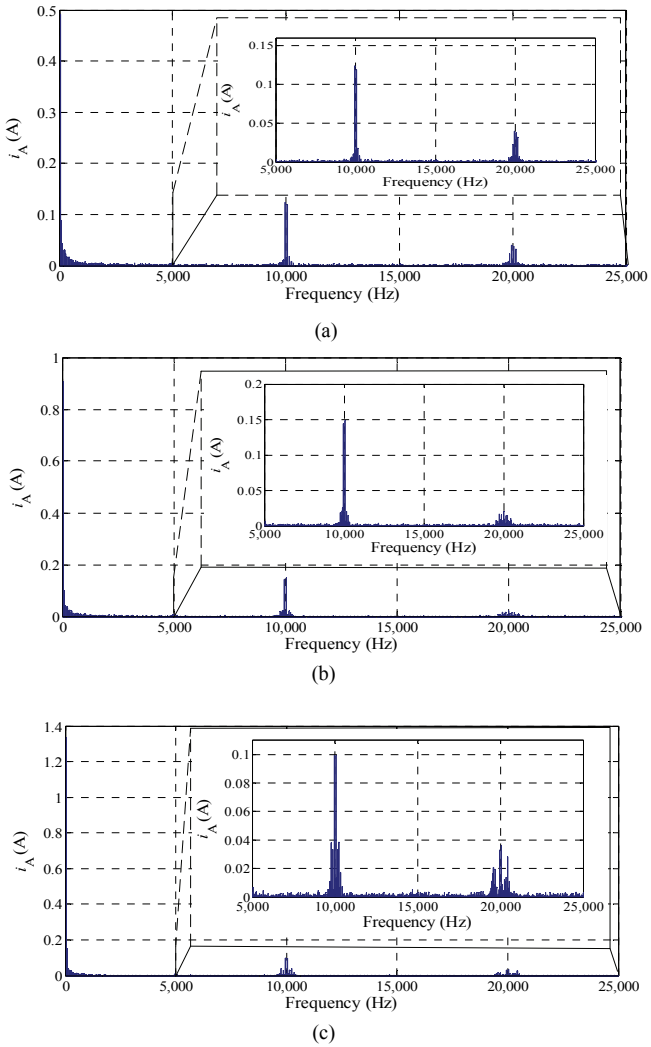


Fig. 19. FFT analysis of line current (i_A) for SVPWM, (a) m_a = 0.4, (b) m_a = 0.7, (c) m_a = 1.0.

V. Conclusion

In this paper, a novel hybrid PWM technique is developed for reducing ac side line current ripple in parallel interleaved inverter system. Here, two parallel interleaved 2L inverters are analyzed as a single 3L inverter. Since the proposed technique is carrier-based implemented, and the required subsector identification is done using the three-phase reference signals, the proposed PWM technique requires less computational effort. The updated reference signals for proposed switching sequences are calculated in terms of maximum and minimum values of reference signals. Hence, the updated reference signals could be used for each sector, for reducing the line

TABLE VI
RMS & PEAK-PEAK CIRCULATING CURRENT

Modualtion Index (m_a)	RMS Circulating Current (mA)			Peak-Peak Circulating Current (A)		
	SPWM	SVPWM	Proposed PWM	SPWM	SVPWM	Proposed PWM
0.4	337	330	290.5	1.1	1.09	1.03
0.7	275.1	271.4	207.9	0.88	0.87	0.855
1.0	187.46	180.43	139.56	0.826	0.813	0.776

0278-0046 (c) 2017 IEEE. Personal use is permitted, but republication/redistribution requires IEEE permission. See http://www.ieee.org/publications_standards/publications/rights/index.html for more information.

This article has been accepted for publication in a future issue of this journal, but has not been fully edited. Content may change prior to final publication. Citation information: DOI 10.1109/TIE.2017.2745438, IEEE Transactions on Industrial Electronics

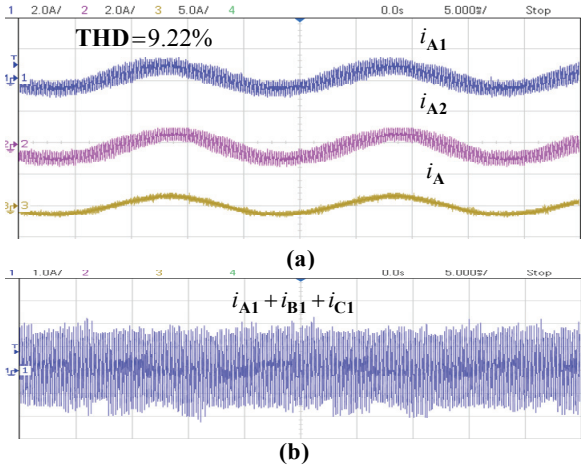


Fig. 20. Experimental result of proposed hybrid PWM technique, m_a = 0.4. (a) Line currents (2A/div, 2A/div, and 5A/div) (b) 3·Circulating current (1A/div).

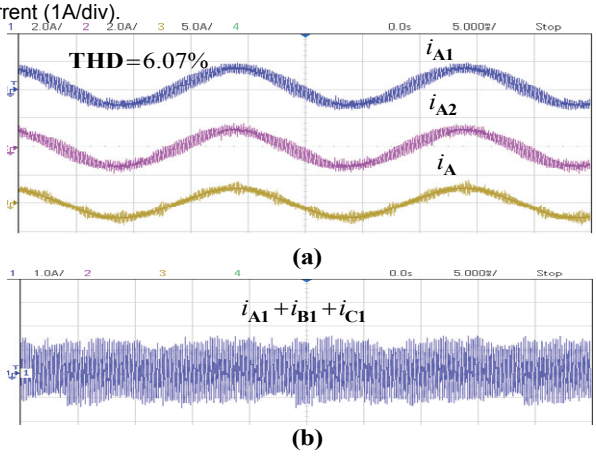


Fig. 21. Experimental result of proposed hybrid PWM technique, m_a = 0.7. (a) Line currents (2A/div, 2A/div, and 5A/div) (b) 3·Circulating current (1A/div).

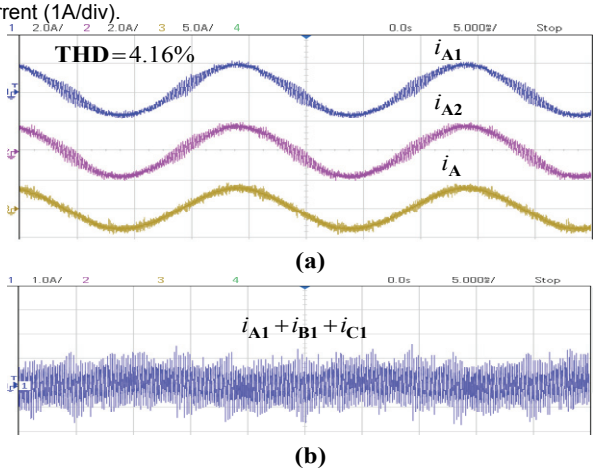


Fig. 22. Experimental result of proposed hybrid PWM technique, m_a = 1.0. (a) Line currents (2A/div, 2A/div, and 5A/div) (b) 3·Circulating current (1A/div).

current ripple. The ac side line current ripple is lower than the most commonly used PWM techniques. The circulating current is also lower than the conventional SPWM and SVPWM techniques for all modulation indices. However, the

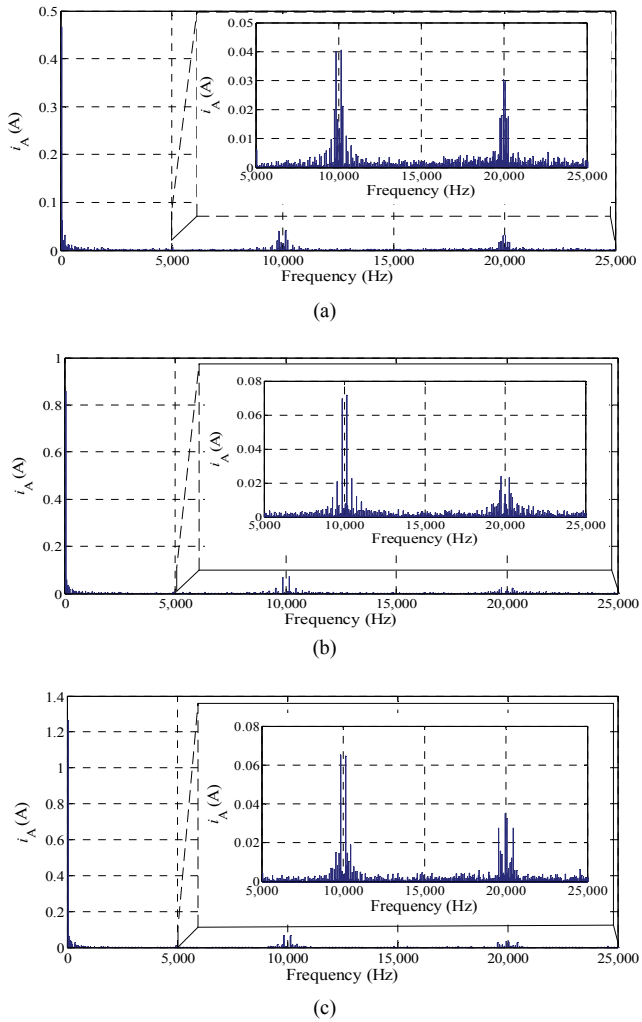


Fig. 23. FFT analysis of line current (i_A) for proposed hybrid PWM technique, (a) m_a = 0.4, (b) m_a = 0.7, (c) m_a = 1.0.

number of switching in a switching period is increased which causes higher switching losses as compared to the conventional SVPWM technique. The simulation and experimental results also verify the proposed PWM technique.

REFERENCES

[1] G. Gohil, L. Bede, R. Teodorescu, T. Kerekes, and F. Blaabjerg, "Line filter design of parallel interleaved VSCs for high power wind energy conversion system," *IEEE Trans. Power Electron*., vol. 30, no. 12, pp. 6775–6790, Dec. 2015.

[2] L. Asiminoaei, E. Aeloiza, P. N. Enjeti, and F. Blaabjerg, "Shunt active power- filter topology based on parallel interleaved inverters," *IEEE Trans. Ind. Electron.*, vol. 55, no. 3, pp. 1175–1189, Mar. 2008.

[3] J. S. S. Prasad and G. Narayanan, "Minimization of grid current distortion in parallel-connected converters through carrier interleaving," *IEEE Trans. Ind. Electron.,* vol. 61, no. 1, pp. 76-91, Jan. 2014.

[4] G. Gohil, L. Bede, R. Teodorescu, T. Kerekes, and F. Blaabjerg, "An integrated inductor for parallel interleaved VSCs and PWM schemes for flux minimization," *IEEE Trans. Ind. Electron.*, vol. 62, no. 12, pp. 7534-7546, Dec. 2015.

[5] M. Xiaolin, A. K. Jain, and R. Ayyanar, "Hybrid interleaved space Vector PWM for ripple reduction in modular converters," *IEEE Trans. Power Electron.,* vol. 26, no. 7, pp. 1954-1967, July 2011.

[6] B.Cougo, T. Neynard, and G. Gateau, "Parallel three-phase inverters: Optimal PWM method for flux reduction in intercell transformers," *IEEE Trans. Power Electron*., vol. 26, no. 8, pp. 2184-2191, Aug. 2011.

0278-0046 (c) 2017 IEEE. Personal use is permitted, but republication/redistribution requires IEEE permission. See http://www.ieee.org/publications_standards/publications/rights/index.html for more information.

This article has been accepted for publication in a future issue of this journal, but has not been fully edited. Content may change prior to final publication. Citation information: DOI 10.1109/TIE.2017.2745438, IEEE Transactions on Industrial Electronics

[7] T. Bhavsar and G. Narayanan, "Harmonic analysis of advanced bus-clamping PWM techniques," *IEEE Trans. Power Electron*., vol. 24, no. 10, pp. 2347-2352, Oct. 2009.

[8] G. Narayanan, V. T. Ranganathan, D. Zhao, H. K. Krishnamurthy, and R. Ayyanar, "Space vector based hybrid PWM techniques for reduced current ripple," *IEEE Trans. Ind. Electron.*, vol. 55, no. 4, pp. 1614-1627, April 2008.

[9] D. Zhao, V. S. S. P. K. Hari, G. Narayanan, and R. Ayyanar, "Space-vector-based hybrid pulsewidth modulation techniques for reduced harmonic distortion and switching loss," *IEEE Trans. Power Electron*., vol. 25, no. 3, pp. 760-774, Mar. 2010.

[10] D. Zhang, F. Wang, R. Burgos, L. Rixin, and D. Boroyevich, "Impact of interleaving on AC passive components of paralleled three-phase voltage-source converters," *IEEE Trans. Ind. Appl*., vol. 46, no. 3, pp. 1042-1054, May-June 2010.

[11] D. Zhang, F. Wang, R. Burgos, R. Lai, and D. Boroyevich, "DC-Link ripple current reduction for paralleled three-phase voltage-source converters with interleaving," *IEEE Trans. Power Electron*., vol. 26, no. 6, pp. 1741-1753, June 2011.

[12] S. Das, G. Narayanan, and M. Pandey, "Space- vector-based hybrid pulsewidth modulation techniques for a three-level inverter," *IEEE Trans. Power Electron*., vol. 29, no. 9, pp. 4580-4591, Sep. 2014.

[13] S. Das and G. Narayanan, "Novel switching sequences for a space-vector- modulated three- level inverter," *IEEE Trans. Ind. Electron*., vol. 59, no. 3, pp. 1477-1487, Mar. 2012.

[14] D. Shin, J. Lee, D. Yoo, and H. Kim, "Stability improvement of interleaved voltage source inverters employing coupled inductors for grid-connected applications", *IEEE Trans. Ind. Electron*., vol. 63, no. 10, pp. 6014-6023, 2015.

[15] R. Maheshwari, G. Gohil, L. Bede, and S. Munk-Nielsen, "Analysis and modelling of circulating current in two parallel-connected inverters," *IEEE IET Power Electron.,* vol. 8, no. 7, pp. 1273-1283, 2015.

[16] G. Gohil, L. Bede, R. Teodorescu, T. Kerekes, and F. Blaabjerg, "An integrated inductor for parallel interleaved three-phase voltage source-converters," *IEEE Trans. Power. Electron.*, vol. 31, no. 5, pp. 3400-3414, May. 2016.

[17] J. Ewanchuk, and J. Salmon, "Three-limb coupled inductor operation for paralleled multi-level three-phase voltage sourced inverters," *IEEE Trans. Ind. Electron.*, vol. 60, no. 5, pp. 1979–1988, Mar. 2013.

[18] M. Narimani and G. Moschopoulos, "Improved method for paralleling reduced switch VSI modules: harmonic content and circulating current," *IEEE Trans. Power Electron*., vol. 29, no. 7, pp. 3308-3317, July 2014.

[19] A. M. Hava, R. J. Kerkman, and T. A. Lipo, "Simple analytical and graphical methods for carrier-based PWM-VSI drives," *IEEE Trans. Power Electron*., vol. 14, no. 1, pp. 49-61, Jan. 1999.

[20] T. P. Chen, "Circulating zero-sequence current control of parallel three-phase inverters," *Electric Power Applications, IEE Proceedings*, vol. 153, no. 2, pp. 282-288, 2 March 2006.

[21] T. P. Chen, "Zero-sequence circulating current reduction method for parallel HEPWM inverters between AC bus and DC bus," *IEEE Trans. Ind. Electron.,* vol. 59, no. 1, pp. 290-300, Jan. 2012.

[22] C. C. Hou, C. C Shih, P. T. Cheng, and A. M. Hava, "Common-mode voltage reduction pulsewidth modulation techniques for three-phase grid-connected converters, " *IEEE Trans. Power Electron*, vol. 28, no. 4, pp. 1971-1979, April 2013.

[23] E. Ün and A. M. Hava, "A near-state PWM method with reduced switching losses and reduced common-mode voltage for three-phase voltage source inverters," *IEEE Trans. Ind. Appl*., vol. 45, no. 2, pp. 782-793, Mar./Apr. 2009.

[24] Vladimir Blasko, "Analysis of a hybrid PWM based on modified space vector and triangle comparison methods," *IEEE Trans. Ind. Appl*., vol. 33, no. 3, pp. 756-764, 1997.

[25] D. Zhang, F. Wang, R. Burgos and D. Boroyvich, "Total flux minimization control for integrated inter-phase inductors in paralleled, interleaved three-phase two-level voltage-source converters with discontinuous space-vector modulation,' *IEEE Trans. Power Electron*., vol. 27, no. 4, pp. 1679-1688, 2012.

[26] T. P. Chen, "Dual-modulator compensation technique for parallel inverters using space-vector modulation," *IEEE Trans. Ind. Electron*., vol. 56, no. 8, pp. 3004-3012, 2009.

[27] G. Konstantinou, J. Pou, G. J. Capella, K. Song, S. Ceballos, and V. G. Agelidis, "Interleaved operation of three-level neutral point clamped converter legs and reduction of circulating currents under SHE-PWM", *IEEE Trans. Ind. Electron*., vol. 63, no. 6, pp. 3323-3332, June 2016.

[28] S. Srinivas and K. R. Sekhar, "Theoretical and experimental analysis for current in a dual-inverter-fed open-end winding induction motor drive with reduced switching PWM," *IEEE Trans. Power Electron*., vol. 60, no. 10, pp. 4318–4328, Oct. 2013.

[29] K. R. Sekhar and S. Srinivas, "Discontinuous decoupled PWMs for reduced current ripple in a dual two-level inverter fed open-end winding induction motor drive," *IEEE Trans. Power Electron*., vol. 28, no. 5, pp. 2493–2502, May 2013.

[30] J. Kalaiselvi and S. Srinivas, "Bearing currents and shaft voltage reduction in dual-inverter-fed open-end winding induction motor with reduced CMV PWM methods," *IEEE Trans. Ind. Electron*., vol. 62, no. 1, pp. 144-152, Jan. 2015.

[31] M. Chen and D. Sun, "A unified space vector pulse width modulation for dual two-level inverter system," *IEEE Trans. Power Electron*., vol. 32, no. 2, pp. 889–893, Feb. 2017.

[32] A. Edpuganti and A. K. Rathore, "New optimal pulsewidth modulation for single DC-link dual-inverter fed open-end stator winding induction motor drive," *IEEE Trans. Power Electron*., vol. 30, no. 8, pp. 4386–4393, Aug. 2015.

[33] V. S. S. P. K. Hari, G. Narayanan, R. Joseph, and L. Umanand, "Analysis of the modulation process in advanced bus-clamping PWM techniques," *Industrial Electronics Society, IECON 2013- 39th Annual Conference of the IEEE*, Vienna, 2013, pp. 453-458.

[34] J. S. S. Prasad, R. Ghosh, and G. Narayanan, "Common-mode injection PWM for parallel inverters," *IEEE Trans. Ind. Electron*., vol. 62, no. 2, pp. 789-794, Feb. 2015.

[35] H. W. Van der Broeck, H. C. Skudelny, and G. V. Stanke, "Analysis and realization of a pulsewidth modulator based on voltage space vectors," *IEEE Trans. Ind. Appl.,* vol. 24, no. 1, pp. 142-150, Jan/Feb 1988.



Kapil Shukla was born in Dungarpur, India. He received the bachelor of technology (B.Tech.) degree in electrical engineering from the Rajasthan Technical University, Kota, India in 2010 and the master of technology (M.Tech.) degree in power systems from the Delhi Technological University (DTU), New Delhi, India in 2012. Since 2015, he has been working toward the Ph.D degree in the Department of Electrical Engineering, Indian Institute of Technology Delhi, New Delhi, India.

From 2012 to 2014, he was with the Department of Electrical and Electronics Engineering, Galgotias University, Greater Noida, U.P, India, as an Assistant Professor. He then joined the Electrical Engineering Department, Manipal University Jaipur, India as an Assistant Professor. His research interests include parallel operation of voltage source inverters and pulse-width modulation techniques.



Varun Malyala was born in Mahabubnagar, India. He received the Bachelor of Engineering (B.E.) degree in Electrical Engineering from Osmania University, Hyderabad, India in 2014, and the Master of Technology (M.Tech.) degree in Power Electronics, Electrical Machines and Drives (PEEMD) from Indian Institute of Technology (IIT) Delhi, India in 2016.

His research interests include parallel operation of voltage source inverters and pulse-width modulation techniques.



Ramkrishan Maheshwari (S'10 – M'11) was born in Allahabad, India. He received the master of engineering (M.E.) degree in electrical engineering from the Indian Institute of Science (IISc), Bangalore, India in 2005 and the Ph.D. degree in electrical engineering from Aalborg University, Aalborg, Denmark in 2012.

From 2005 to 2008, he was with Honeywell Technology Solution Lab, Bangalore, India. From 2012 to 2014, he was with the Department of Energy Technology, Aalborg University, Denmark. He is currently working as an assistant professor with the Department of Electrical Engineering, Indian Institute of Technology, Delhi, India. His research interests include modeling and control of power converters.

0278-0046 (c) 2017 IEEE. Personal use is permitted, but republication/redistribution requires IEEE permission. See http://www.ieee.org/publications_standards/publications/rights/index.html for more information.

A novel load balanced energy conservation approach in WSN using biogeography based optimization

Ajay Kaushik, Indu S., and Daya Gupta

Citation: AIP Conference Proceedings **1884**, 020003 (2017); doi: 10.1063/1.5002507
View online: http://dx.doi.org/10.1063/1.5002507
View Table of Contents: http://aip.scitation.org/toc/apc/1884/1
Published by the American Institute of Physics

Articles you may be interested in

Optimal design of high concentration reflected photovoltaic module
AIP Conference Proceedings **1884**, 020001 (2017); 10.1063/1.5002505

Property analysis into the formation of liquid falling thin film on a single channel of a vertical twisted and fluted tube
AIP Conference Proceedings **1884**, 020004 (2017); 10.1063/1.5002508

Humid free efficient solar panel
AIP Conference Proceedings **1884**, 020002 (2017); 10.1063/1.5002506

Preface: 2nd International Conference on Energy Engineering and Smart Materials (ICEESM 2017)
AIP Conference Proceedings **1884**, 010001 (2017); 10.1063/1.5002504

Relation between plastic surface microtexturation and Ag film percolation and resistivity
AIP Conference Proceedings **1884**, 030001 (2017); 10.1063/1.5002511

Analysis of seasonal exergy efficiency of an air handling unit
AIP Conference Proceedings **1884**, 020005 (2017); 10.1063/1.5002509



A Novel Load Balanced Energy Conservation Approach in WSN Using Biogeography Based Optimization

Ajay Kaushik[1, a)], Prof. Indu S.[2, b)], Prof. Daya Gupta[3, c)]

[1]*Ph.D research scholar, Computer science and engineering, Delhi Technological University, Delhi, India*
[2] *Professor and Head, Electronics and communication, Delhi Technological University, Delhi, India*
[3]*Professor, Computer science and engineering, Delhi Technological University, Delhi, India*

[a)] Corresponding author-ajaykaushik777@gmail.com
[b)]s.indu@dce.ac.in
[c)]dgupta@dce.ac.in

Abstract – Clustering sensor nodes is an effective technique to reduce energy consumption of the sensor nodes and maximize the lifetime of Wireless sensor networks. Balancing load of the cluster head is an important factor in long run operation of WSNs. In this paper we propose a novel load balancing approach using biogeography based optimization (LB-BBO). LB-BBO uses two separate fitness functions to perform load balancing of equal and unequal load respectively. The proposed method is simulated using matlab and compared with existing methods. The proposed method shows better performance than all the previous works implemented for energy conservation in WSN

Keywords – Wireless sensor networks, load, gateway, habitat**.**

INTRODUCTION

Wireless sensor networks (WSNs) are widely used in many applications such as weather monitoring, disaster management, intrusion detection and crop forecasting [1].WSN consist of tiny sensor nodes that are manually or arbitrarily deployed in an area. [2-4]. Clustering helps in reducing the energy consumption of WSN as only one sensor node is communicating with the sink. Clustering preserves commutation bandwidth as communication channel is not flooded with redundant messages from the sensor nodes.[5]

In [6] GA is used for routing of aggregated data between cluster head and sink. In this algorithm roulette wheel selection is used for selection of individuals and fitness of an individual is taken in terms of network lifetime. In [7] another routing algorithm is proposed in which attempt is made to reduce the communication distance between the sink and gateway using GA.

One thing to be noted in both [6] and [7], focus is only on sending data from cluster head to the sink, there is no emphasis on energy consumption in data transfer between individual node to cluster head. All other work specified before except Kulia et. Al [8] did not use non linear programming for energy efficient clustering. NLP formation helps in extending the network lifetime. Kulia et. Al [8] used NLP for PSO based clustering considering the distance between a sensor node and the gateway. They did not consider distance of a gateway to the sink in clustering.

Author's Contributions

- LB-BBO prolongs lifetime of the WSN by achieving optimum load balancing of the gateways.
- Improves network lifetime by non linear mapping of gateway identification. LB-BBO minimizes the inter gateway distance, load on the gateway closest to the sink and also minimizes the number of hops taken by a gateway to forward data to the sink for both equal and unequal load of sensor nodes.

2017 The 2nd International Conference on Energy Engineering and Smart Materials
AIP Conf. Proc. 1884, 020003-1–020003-4; doi: 10.1063/1.5002507
Published by AIP Publishing. 978-0-7354-1564-5/$30.00

- BBO introduces the concept of immigration and emigration of species. New species keep evolving and poor species keep getting extinct.

The proposed algorithm is compared with kulia et al [8] and three other evolutionary algorithms namely sajid GA [9], simple GA [10], differential evolution [11] and LDC [12].

PROBLEM FORMULATION

Gateways are battery operated and hence load assigned to each gateway is an important factor in efficient working of a WSN. Our goal is to maximize the network lifetime by balancing the load assigned to each gateway in the network by optimizing distance between any 2 gateways and average load assigned to each gateway with emphasis on gateways which are closer to the sink. Mathematically it can be explained as follows. In this multi hop routing

$$E(g_{sink})\frac{1}{\alpha}\ N_{wall} \tag{1}$$

$$E(g_{sink})\ \alpha\ S_{close} \tag{2}$$

$$g_{diss}\ \alpha\ \beta \tag{3}$$

$$g_{diss}\ \alpha\ H_{gat(i)} \tag{4}$$

Also

$$L_{total}\frac{1}{\alpha}d_{gat(i)} \tag{5}$$

In the article, S_N is the total number of sensor nodes, G_N is the total number of gateways, β is inter gateway distance between any 2 gateways, l is average load on a gateway, g_{sink} gateway which is closest to the sink, S_{close}number of sensor nodes that are assigned to the gateway closest to the sink, $g_{diss}$is energy dissipated by a gateway, $H_{ga(i)}$ is number of hops taken by ith gateway to transmit its data to the sink, L_{total} total load on a gateway, $d_{gat(i)}$ is distance of ith gateway to the sink, N_{wall} is number of gateways present in the wall nearby the sink.

PROPOSED ALGORITHM

S_N sensor nodes and gateways are randomly distributed in the deployment area.

Calculation of HSI.

BBO is analogous to the genetic algorithm [13]. In BBO we calculate habitat suitability index value of each habitat of the population just like we calculate fitness in GA. For equal and unequal load the HSI values calculated are given in equation 6 and 7.

For equal load of sensor nodes.

$HSI_{equal} =$

$$\left(\frac{1}{L}+\frac{1}{\beta}+\frac{1}{H_{gat(i)}}\right) * N_{wall} \tag{6}$$

For unequal load of sensor nodes.

$HSI_{unequal} =$

$$\left(\frac{1}{L}+\frac{1}{\beta}+\frac{1}{H_{gat(i)}}+\frac{1}{S_{close}}\right) * N_{wall} \tag{7}$$

Maximization of the fitness function leads to minimization of L, β and $H_{gat(i)}$. Problem faced in the past works is that energy of the gateway which is closest to the sink get exhausted very quickly as it has to bear the load of relaying the information of trailing gateways to the sink. With the use of parameter N_{wall} multiple gateways are deployed in close proximity of the sink giving all the trailing gateways an alternate path to transfer information to the sink. This shares the load on a single gateway and ensures that the gateway which is closest to the sink is not exhausted quickly. Parameter S_{close} is used to further share the load of the overloaded gateway. Sensor nodes assigned to the gateways which are close to the sink are kept to minimum levels to ensure long working of those gateways. Efficient routing is done using Dijkastra algorithm to find $H_{gat(i)}$.

Each habitat/vector contains entries equal to number of sensor nodes in the network. After calculating fitness for each habitat, rank is assigned to ach habitat on the basis of their HSI value.

Rank = sort (HSI value of every habitat)

Migration operator. Habitats having high HSI value will have a low immigration rate and high emigration rate. SIV will migrate from high HSI value or high emigration rate habitat to the low HSI value of high immigration rate habitat.[13] Recalculated HSI values of habitats show improvement in their HSI value which shows that a better network performance is obtained. Habitat with the best HSI value is the optimum solution.

EXPERIMENTAL RESULTS

We simulated our algorithm using Matlab based on parameters used in [8]. We consider two network scenario WSN 1 and WSN 2. WSN 1 considers equal distribution of load and WSN 2 considers unequal distribution of load among the gateways.

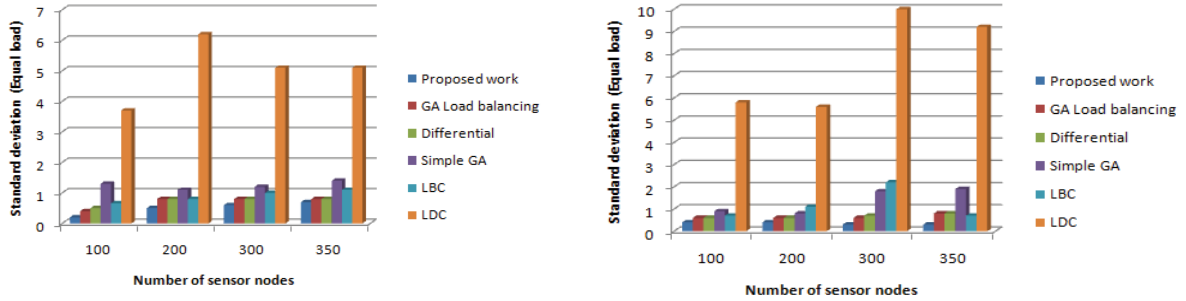


FIGURE 1. Comparison of the proposed work with existing work in terms of load balancing for WSN 1 for (a) 15 gateways (b) 30 gateways.

The comparison of the proposed work with existing algorithms is shown in figure 1. Standard deviation of the proposed work is less than the other algorithms. For WSN 2 scenario, standard deviation of load is calculated for 15 and 30 gateways for varying number of sensor nodes ranging from 100 to 350 as shown in figure 2. For unequal distribution of load as well proposed algorithm performs better than the existing work.

Proposed work performs better than previous works in number of inactive nodes as shown in figure 3.[8] Proposed work is compared with the existing work in terms of total energy consumed in the network as shown in figure 3. Energy consumption of the proposed work is more than most of the existing works because of the reason that in proposed work number of active sensor nodes present at any instant of time are more. Thus consuming more energy.

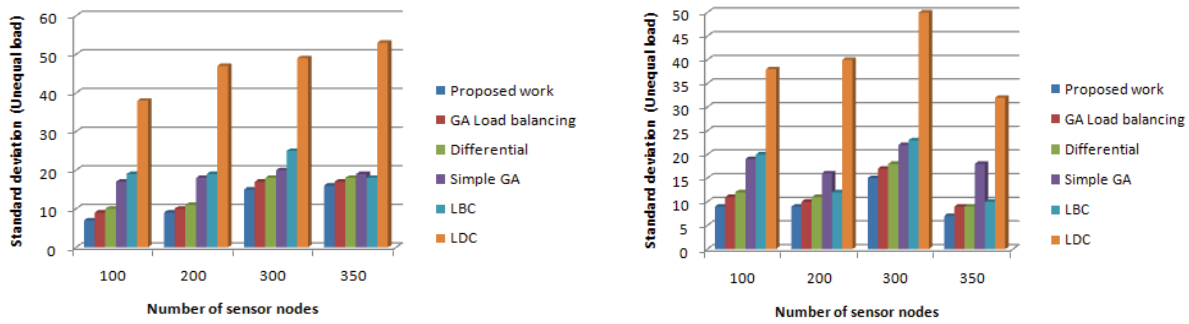


FIGURE 2. Comparison of the proposed work with existing work in terms of load balancing for WSN 2 for (a) 15 gateways (b) 30 gateways

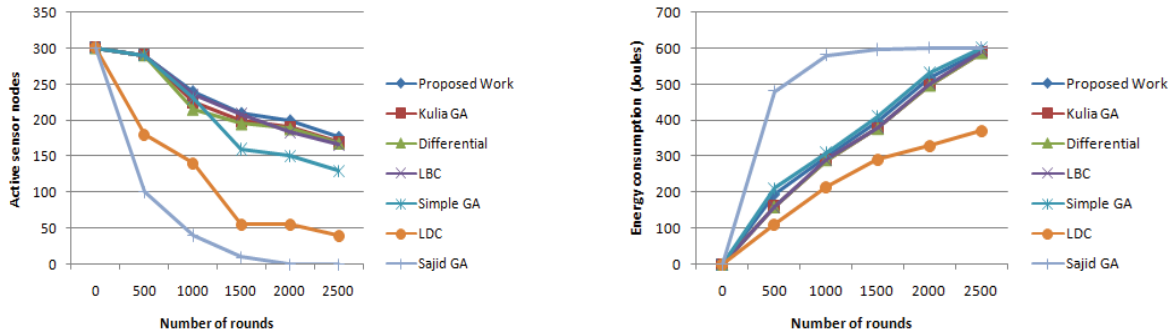


FIGURE 3. Comparison of the proposed work in terms of number of active sensor nodes and energy consumed in the network.

CONCLUSION

In this paper we have presented a BBO based load balancing algorithm for WSNs. The sensor nodes are properly represented by habitats, initial population, calculation of HSI for each habitat and migration using MPX crossover. The experimental results have shown that performance of the proposed algorithm is better than LDC, LBC, simple GA based clustering, differential approach and GA based load balancing respectively

REFERENCES

1. Indu Sreedevi, Santanu Chaudhury, Asok Bhattacharyya and Shubham Mankhand "Bio-Inspired Distributed Sensing using a Self-Organizing Sensor Network", Journal of Engineering, Hindawi, 2013.
2. S.Indu, Nikhil. R. Mittal, Santanu Chudhury and Asok Bhattacharyya "Optimal Sensor Placement for Surveillance of large spaces" Proceedings of ACM/IEEE International conference on Distributed Smart cameras, (pp.66-73), September 2009
3. C.Y.Chong,S.P.Kumar, Sensor networks: evolution, opportunities, and challenges, Proceedings of the IEEE 91(8)(2003)1247–1256.
4. L.Emanuele, et al.,Energetic sustainability of routing algorithms for energy- harvesting wireless sensor networks, *Computer Communication,* 30, 2976–2986, 2007.
5. A.Hamed Abbasi, Y.A.Mohamad, Survey on clustering algorithms for wireless sensor networks, Computer Communications, 30, 2826–2841, 2007.
6. Bari et al, A genetic algorithm based approach for energy efficient routing in two-tiered sensor networks. Ad Hoc Netw.7, 665–676, 2009.
7. Gupta et al, GAR: an energy efficient GA-based routing for wireless sensor networks. In: ICDCIT, LNCS 7753, pp.267–277, 2013.
8. Kuila et al., A novel evolutionary approach for load balanced clustering problem for wireless sensor networks, Swarm and Evolutionary Computation, p 48–56, 2013.
9. S. Hussain, et al., Genetic Algorithm for hierarchical wireless sensor networks, Journal of Networks2(5)87–97, 2007.
10. S. Das, P.N. Suganthan, Differential evolution: a survey of the state-of-the-art, IEEE Transaction on Evolutionary Computation15(1) 4–31, 2011.
11. R. Storn, K. Price, Differential evolution—a simple and efficient heuristic for global optimization over continuous spaces, Journal of global optimization. 11 , 341–359, 1997.
12. B.Ataul et al. ,Clustering strategies for improving the lifetime of two-tiered sensor networks, Computer Communications 31 , 3451–3459, 2008.
13. D. Simon, Biogeography-based optimization, IEEE Transactions on Evolutionary Computation (IEEE Computer Society Press) 12 (6) , 702–713., 2008.

ResearchGate

See discussions, stats, and author profiles for this publication at: https://www.researchgate.net/publication/319621204

Affinity of Metal Ions Incorporated Bentonite for Enantiomeric Interactions with Alanine

Article · September 2017

DOI: 10.26434/chemrxiv.5383627.v1

CITATIONS
0

READS
19

6 authors, including:



Pramod Pandey
Dalian Institute of Chemical Physics
10 PUBLICATIONS **13** CITATIONS
SEE PROFILE



Preeti Bhatt
Kumaun University
5 PUBLICATIONS **1** CITATION
SEE PROFILE

Some of the authors of this publication are also working on these related projects:



Study of Structural Complexity for Neurdegenerative Disorders in Human View project

All content following this page was uploaded by Pramod Pandey on 10 September 2017.

The user has requested enhancement of the downloaded file.

Affinity of Metal Ions Incorporated Bentonite for Enantiomeric Interactions with Alanine

Pramod Pandey[†,‡], Preeti Bhatt[†], Jia Yan[‡], Le Peng[‡], Mohan Singh Mehata[¶], and Chandra Kala Pant[†*]

[†] Chemical Laboratory, Department of Chemistry, DSB Campus, Kumaun University, Nainital 263002 Uttarakhand, India

[‡] State Key Laboratory for Molecular Reaction Dynamics, Dalian Institute of Chemical Physics, Chinese Academy of Sciences, 457 Zhongshan Road, Dalian, Liaoning, China

[¶] Department of Applied Physics, Delhi Technological University, Bawana Road, New Delhi 110042, India

* Prof. Chandra Kala Pant ckp.astrochem@gamil.com

Abstract

Explanation of the homochirality of amino acids in the biosphere is one of the most important mysteries in the origin of life. Following the abiotic evolution of life on Earth, possible role of prebiotically available mineral and metal ion have been widely studied. In this communication an effort has been made to investigate the surface interaction of L-alanine (L-ala) and D-alanine (D-ala) on Bentonite (BNT) and its divalent metal ion (M=Ca^{2+}, Mg^{2+}, Ni^{2+}, Cu^{2+} and Zn^{2+}) incorporated BNT for the optimal condition of pH, time, concentration and enantiomeric selectivity for D- and L-ala. Cu^{2+}, $Ni^{2+}$and Zn^{2+}exchanged BNT have higher affinity for both the ala but Mg^{2+} exchanged BNT have shown the selective adsorption of L-ala in comparison to the D-ala at pH 4.0±0.1. Further, absolute value of metal ion affinities with ala (ala—M^{2+}) and hydration effect on the relative stability and geometry of the individual species of ala—$M^{2+}\times(H_2O)n$, (n =2 and 4) has also been evaluated using DFT calculation. Possible implications for the stability and selectivity of biomolecules in prebiotic era of Earth has been discussed.

Key Words Metal ions, Bentonite, Enantiomer, Surface Interaction and Origin of Life

Introduction

The well accepted theories [1,2] behind the origin of life in planet Earth, generally envisioned as having proceeded from the formation of organic compounds from environmentally supplied precursors, to their self-organization under various environmental conditions into self-replicating and energy-transducing systems, and their further evolution into modern biochemical systems [3,4,5].

However, the concentration of endogenous (i.e. chemicals synthesized in the Earth) as well as exogenous (i.e. chemicals synthesized outside from the Earth) amino acids (AAs), nucleic acid bases (NBs) and pentose sugars (PSGs) are very low. Total concentration of amino acids (AAs) in the prebiotic era is supposed to be 40×10^{-1} mM to 10^{-7} mM [6,7], while stability of newly formed biomolecules is also questioned in presence of the drastic conditions of energy (viz. ultra-violet, thermal, electric discharge etc.) at the contemporary period of planet Earth, when life is supposed to be started ~4.4–3.5 Ga ago [1,3]. Thus, concentration and stabilization of biologically significant chemicals from 'super-dilute solution' was hitherto unfolded till J.D. Bernal (1951) put forwarded the possible solution for the above said problems and postulated the prebiotic bimolecular concentration by surface interaction onto materials like silicates, metal oxides, abundantly available on the planet Earth [8]. Today, there are ~4500 known, naturally occurring minerals and each year ~50 new unknown minerals are discovered [9,10]. The basic question regarding the selection of minerals in relevance to origin of life must be considered while selecting a mineral as an adsorbent for surface interaction studies and catalyst for biomolecular formation from prebiotically available precursors. As life is supposed to be started on before 3.6 Ga., so, minerals only synthesized before this period are to be considered [10].

Bentonite (BNT) from the Smectite (SMT) group of aluminosilicates, is octahedral alumina sandwiched between tetrahedral layers of silica (T-O-T), had been widely investigated

at different conditions of pH, temperature and concentration to explore the Bernal's view regarding their role as a surface provider for local concentration as well as catalyst for their subsequent polymerization and are also well known for their cation exchanged capacities [11-12]. SMT clay minerals combine a wide range of physicochemical properties that result in strong surface interaction capacities. These include high surface area, swelling and hydration properties, as well as strong cation exchange capacities (CEC). These characteristic properties, thus, enhance its capabilities as adsorbent, catalysis as well as in drug delivery [13].

Metal ions are found to be vital for biological systems as they participate in several functions such as enzyme regulation, stabilization of structural elements, cellular transportations etc. [14-15]. Nearly a third of all known enzymes requires one or more metal ions for catalytic activity [16] since metals are the good reflectors of biogenic activities in present day living system, which initially functions as the neutralizing agent for the negative sites of proteins, enzymes, nucleic acids etc. Divalent cations are found to have their peculiar contribution in the physiology of biological system and are also known for their affinity to form peptide bonds in relevance to the prebiotic evolution of biomolecules [17-20]. Metal ions exchanged SMT are reported as good surfactants which justify their role in the adsorption studies of AAs NBs PGS etc. and also as a catalyst for biomolecular formation [3,10-11,21].

Further, explanation of the homochirality of biomolecules in the biosphere is one of the most important mysteries in the origin of life [22-24]. Biological systems are highly specific in nature and only a particular stereospecific type of chemical is responsible for the assigned functioning in the cellular systems. A change in stereospecificity i.e. D-isomer instead of L-isomer of amino acids and L-isomer instead of D-isomer of pentose sugar) can alter the fate of whole biochemical reaction. The functional aspects of the biochemistry of all living systems depend on proteins as they function as enzymes, a biological catalyst and any change in the isomeric form of L-AAs can prevent it for its assigned functioning [25]. So, the question of

stereospecificity of amino acids i.e. why only L-amino acids instead of D-amino acids are present in living system is also necessary to answer from the point of view of prebiotic mineral evolution and role of clays in the selection of stereospecific isomers.

Enantiomeric selectivity of AA in the prebiotic era of Earth, can be investigated considering the experimental routes using 1; Surface interaction of AA on minerals and effect of pH, concentration, 2; Role of different metal ions using metal ion exchanged minerals, and computational routes involving thermodynamic and kinetic parameters of 1; AA-metal complex formation, 2; solvation dynamics of AA-metal complex, 3; interaction of AA on the various available crystallographic sites in minerals.

Prebiotic simulation experiments have shown the formation of some bio-essential AAs, NBs, PSGs. Ala (ala) is a major constituent of several simulation experiments as well as the organics reported in meteorites and cosmic dust. [10,23,27-28]. The first chiral and neutral amino acid (i.e. ala), out of twenty amino acids, which are the building blocks of proteins in present day living system, has been chosen as a model for its surface interaction (i.e. adsorption) on plently available solid clay surface (e.g. BNT) on planet Earth, with a view to understand the stabilization properties of biomarkers and the possibility to answer the enantiomeric selectivity of AA. The plausibility to trace out the metal ion interaction with biomolecules is widely investigated using quantum mechanical calculations which provide a better insight into the complex formation, solvation dynamics and counter ions effects for biomolecules [12,20]. So, computational studies to explore the thermodynamic parameters of reactions systems as well as biomolecule-metal ions affinities is an essential step, for the chemistry behind chemical evolution of life in Earth and possibilities of biomarkers formation in another planets like Mars.

Therefore, an effort has been made to explore the role of the bentonite (BNT) and different metal dictation (Ca^{2+}, Mg^{2+}, Ni^{2+}, Cu^{2+} and Zn^{2+}) exchanged BNT for their affinity

towards the surface interaction with L-ala and D-ala. The chemical structure of D- and L-ala has been given in Fig. 1. Computational studies of metal-amino acid complexes (ala—M^{2+}) were conducted using Gaussian 16 to understand the affinity of metal ions with biomolecules and the effect of hydration on ala—$M^{2+}\times (H_2O)_n$, (n =0,2 and 4) complex formation. Moreover, investigation of the stability of AA under given conditions of study is also important from the prebiotic point of view as these minerals and metal ions play a catalytic role in polymerization and decomposition of biomolecules [29].

Experimental

All reagents were of analytical grade. BNT clay was purchased from E. Merck and Loba Chemicals, India, while L-alanine (L-ala), D-alanine (D-ala) and $CaCl_2$ from CDH, India. H_2O_2, $MgCl_2$, $NiCl_2$, $CuCl_2$, $ZnCl_2$ were procured from Qualigens, India. Triple distilled-deionized water (pH 6.8 ±0.1) was used throughout the study. All containers, measuring equipment and assemblies were of borosilicate glass. A JascoV-550, UV/VIS/NIR spectrophotometer was used for the absorbance measurements. The pH was recorded on Hanna pH meter (model pHep, accuracy: ±0.1 pH unit).

The sequential steps involved in the preparation/purification of adsorbents during analysis are shown in scheme I. Mg^{2+} Ca^{2+}, Ni^{2+}, Cu^{2+} and Zn^{2+} exchanged BNT (i.e. BNT-M^{2+})was prepared by the saturation method as mentioned in our earlier work [12]. All the adsorbents (Scheme I) were ground, sieved using a 100 mesh size sieve (SETHI BSS 100) and then dried in vacuum desiccators. The color of BNT has been found to be 7.5YR7/2 (light brown) on Munsell Notations.

The purity of BNT and their divalent cation-exchanged forms, as described in our previous work [12], were determined by X-ray diffraction and energy-dispersive X-ray

spectrometry (EDS) using Hitachi S-3700N Instrument with an acceleration voltage 15.0 kV with a take-off angle 44.1°, and also with ZEISS EHT 20kV instrument.

The adsorption of L-ala and D-ala on different adsorbents in aqueous medium was studied as function of pH (3.0-9.2), time (1 min – 72 hrs) and concentration (1 mM to 10 mM) of adsorbate. Solution of ala (5 ml) at different pH values was added to the adsorbents (50 mg) in separate conical flasks (10 ml) under air, stirred mechanically using magnetic stirrer and allowed to stand at room temperature (298K) for different time intervals to determine the optimum conditions for adsorption. The solutions were then centrifuged at 2000 rpm for 25 min. The supernatant was decanted leaving the BNT/BNT-M as a residue. The supernatant in each experiment was used for quantitative estimation of ala content after adsorption and the adsorbent was separated, washed and then, dried at ambient temperature under vacuum. Further, it was ground/ sieved and used for SEM/EDS (Scheme I). The concentration of adsorbate before and after adsorption was determined using UV difference spectra in quartz cuvettes with a 1 cm path length using $_{td}H_2O$ as reference. Same amount of respective buffer had also been added into the $_{td}H_2O$ which was used as reference.

The amount of ala adsorbed under different conditions of pH, time and concentration was calculated from the difference between the initial ala concentration and the concentration after adsorption in each case. The initial concentration of ala and the quantity adsorbed were used to obtain the adsorption isotherms. Percentage binding was calculated as follows-

$$\% \text{ binding} = \frac{C_e - C_f}{C_e} \times 100 \qquad \text{eq. 1}$$

Where, C_e is the initial concentration of adsorbate and C_f is the final concentration after adsorption.

Chromatographic techniques (Paper chromatography and HPLC) were used to measure the degradation products (if any) of ala after adsorption studies as described in our previous work using PC and HPLC [30].

Computational Study

Density functional theory (DFT) was used to investigate the interaction of ala with metal cations (Mg^{2+} Ca^{2+}, Ni^{2+}, Cu^{2+} and Zn^{2+}). Becke's three parameter exchange functional with a Lee, Yang and Parr type nonlocal correlation functional hybrid Hartee-Fock DFT method (B3LYP), was applied for metal ions and ala (Zwitterion) with the all-electron 6-311G++(2d,2p) internal basic set with integral equation formalism (IEF) polarizable continuum model (PCM) for water [31-33] (Becke 1993; Lee et al. 1988; Hohenberg and Kohn 1964). Open shell calculations using a spin-unrestricted formalism have been used for ala—Cu^{2+}complexas Cu^{2+} is an open shell system with a d^9(^{2}D) ground state. All the computational analysis was carried out using gaussian 16(A.03) software package [34]. The formation of ala—$M^{2+}\times (H_2O)_n$, (n =0, 2 and 4) complexes can be described following, which has been used to compute the metal ion affinity as a negative enthalpy variation (ΔH) for the reaction-

$$ala + M^{2+} + (H_2O)_n \rightarrow ala—M^{2+}\times (H_2O)_n \qquad \text{eq. 2}$$

M = Mg^{2+} Ca^{2+}, Ni^{2+}, Cu^{2+} and Zn^{2++}, n = 0, 2 and 4.

Result and Discussion

Interaction behaviour of D- and L-ala on the surface of BNT and BNT-M (M = Mg^{2+}, Ca^{2+}, Ni^{2+}, Cu^{2+} and Zn^{2+}) in aqueous medium has been studied as a function of pH, contact time and concentration. The surface interaction has been carried out at variant pH from 3.0-9.2, concentration ranges from 1 mM to 10 mM with a contact time of 5 min - 72 hrs at ambient temperature to find the optimum conditions of these variables. The amount of adsorbate

adsorbed (D- and L-ala) has been determined from the standard concentration curve obtained from the optical density of the different L-ala solutions monitored at their respective peak (λ_{max} = 201 nm ±2nm) of absorption spectrum. Linear behaviour (r^2 = ~0.97) was observed between the absorbance and concentration of ala solutions.

The maximum adsorption capacity of adsorbates (i.e. D- and L-ala) has been found at lower pH (pH 4.0) in comparison to its isoelectric point (pH 6.2). Zwitterionic form of ala is dominated at pH 6.2 while at pH 4.0 it has both the cationic as well as zwitterionic forms present in solution. Further, the optimum time for the adsorption of both the adsorbates separately (i.e. D- and L-ala) onto BNT and BNT-M has been found ~4 hrs, whereas after this contact time an equilibrium has been stabilized between adsorbent and aqueous solution of adsorbate. A graph showing the relationship between percentage adsorption of L-ala with Cu^{2+} exchanged BNT (BNT-Cu^{2+}) with time (only 30 min to 6 hrs) has been provided in Fig. 2.

Langmuir adsorption isotherm has been applied to evaluate the adsorption behaviour along with different adsorption parameters from the eq.3, while percentage adsorption has been calculated using eq. 1.

$$\frac{\boldsymbol{C_{eq}}}{\mathbf{X_e}} = \frac{\mathbf{1}}{K_L.\boldsymbol{X_m}} + \frac{\boldsymbol{C_{eq}}}{\boldsymbol{X_m}} \qquad \text{eq. 3}$$

Where C_{eq} is the equilibrium concentration of ala. K_L is a constant which is a function of the adsorption energy *i.e.* the enthalpy of adsorption coefficient ($K_L = Ae^{-\Delta H/RT}$); X_e is amount of ala (mg) adsorbed per gram of BNT/BNT-M; X_m is the amount of ala required for a definite weight of BNT/BNT-M for complete surface coverage.

Adsorption isotherms (Fig.3-6) have shown a linear relation between the equilibrium molar concentration (C_{eq}) and quantity adsorbed (mg/g) from 1 mM to ~7 mM adsorbate solution while above this concentration range, saturation point has been achieved for the uptake of adsorbate by different adsorbents from aqueous solution. Adsorption parameters along with

the percentage adsorption for D- and L-ala at pH 4.0 ±0.2 and 6.0 ±0.2, in presence of BNT and divalent metal exchanged BNT (BNT-M) have been provided in Table 1-2.

Table 1 shows the percentage affinity of L- and D-ala with different adsorbents under investigation at pH 4.0±0.2. Cu^{2+} exchanged BNT (BNT-Cu) have shown highest affinity for the uptake of ala from its solution while it is minimum on the surface of BNT-Mg. A comparative uptake of L- and D-ala from its aqueous solution by BNT-Mg at pH 4.0 shows 5.12 % higher adsorption of L-ala on its surface in comparison to the D-ala.

SEM images of BNT clay, L-Ala and their adsorption adducts (BNT-ala) at pH 4.0 ±0.2 are provided in Fig. 7, where (a) and (b) represent the BNT surface, (c) and (d) are the figures of the L- and D-ala, while (e) and (f) are the adsorption adducts (BNT-L-ala and BNT-D-ala) of adsorbents and adsorbates, respectively. The surface of the BNT has been accumulated with the adsorbates (Fig. 7 e and f).

The adsorption affinity of ala with different adsorbents (e.g. BNT/BNT-M) in its zwitterionic form (pH 6.0±0.2), has been found less in comparison to the affinity at pH 4.0 ±0.2 (Table 1-2) but a similar trend has been observed for the different adsorbents at both the pH, under consideration except no preferential uptake of L-ala over D-ala.

The effectiveness of various adsorbents towards the surface interaction of D- and L- ala at both the pH (4.0 ±0.2 and 6.0 ±0.2) has been found in the order of BNT-Cu^{2+} > BNT-Ni^{2+} > BNT-Zn^{2+} > BNT-Ca^{2+} > BNT> BNT-Mg^{2+}

Addition of Ca^{2+}, Mg^{2+}, Ni^{2+}, Cu^{2+} and Zn^{2+} divalent metal ions into the BNT increases the surface affinity throughout the entire concentration range of isotherm which shows that divalent metal ions increase the ionic strength of BNT which increase the ionic interactions between adsorbate and adsorbents. Further, this higher percentage of adsorption affinity towards the metal incorporated BNT may be attributed to increase in an interlamilar space

between two successive layers of clay [13]. An increase in the interlamilar space may facilitate the absorption of higher numbers of adsorbate molecules.

Although, a comparative analysis of the adsorption trends for D- and L-alanine towards various adsorbents (BNT/BNT-M) was found almost similar, yet Mg^{2+} exchanged bentonite has shown more affinity for L-ala at pH 4.0±0.2.

Computational Study

Complexation modes between M^{2+} and ala with greater attractive interactions between electron rich (─COO^-) and electron deficient sites (M^{2+}) have been considered [20,35], for AAs (H_3N^+—CH(R)—COO^-). Here, only L-ala has been considered for the metal ions interaction and effect of hydration as D-ala and L-ala have similar energy parameters in absence of any external perturbation in three dimensional space, distinguish them for their specific isomerism. The respective atoms of zwitterionic L-ala are numbered for hydrated or non-hydrated metal complexes L-ala—M × $(H_2O)_n$, (M = Mg^{2+}, Ca^{2+}, Ni^{2+}, Cu^{2+} and Zn^{2+}, n = 0, 2 and 4) according to the scheme presented in Fig. 8a.

For hydrated system of L-ala—M^{2+}, metal cations are coordinated with two water molecules (I and II) using a supermolecule modelling of hydration (Fig. 8b) while other two water molecules were placed at the polar part of the AA (III and IV of Fig. 8b), where the water molecule form intermolecular hydrogen bonds with the polar proton donor (—NH_3^+) [12].

Geometrical parameters (bond length, bond angles and dihedral angles) of the L-ala—M × $(H_2O)_n$, (M = Mg^{2+}, Ca^{2+}, Ni^{2+}, Cu^{2+} and Zn^{2+}, n = 0, 2 and 4) complexes have been given in Table 3-5, while net charges on the metal, oxygen, nitrogen atoms, dipole moment, total energies, relative energies including ZPE and thermodynamic parameters of different nine complexes of L-ala—M^{2+} × $(H_2O)_n$ (n = 0, 2 and 4) complexes are summarized in Tables 6 and 7.

Preliminary structural investigations of L-ala have shown its stable complexes with M^{2+} may be formed in two different ways. First, binding of M^{2+} with O3 of carboxylic end and N5 of amine in neutral AA while, another, its interaction with both the oxygen (O3 and O4 ends) of carboxylate ion of zwitterionic AA (Fig. 8). The bicoordinated complexes of M^{2+} with simultaneous interaction with carbonyl oxygen (O3) and amine nitrogen (N5) is not possible as the lone pair of electron have already been associated with the proton (H^+) liberated from –COOH group to form zwitterions. The zwitterionic form of amino acid (H_3N^+—CH(R)—COO^-) may be stabilized by the presence of counter-ions and/or water molecules [35-36].

The selected geometrical changes for the L-ala—M (M = Mg^{2+}, Ca^{2+}, Ni^{2+}, Cu^{2+} and Zn^{2+}) complexes indicate that the O(4) ····M(9) bonds (Å) are slightly shorter for Ca^{2+}, Ni^{2+}, Cu^{2+} and Zn^{2+} than O(3)····M(9) bonds in comparison of L-ala—Mg^{2+} complex , indicating that these metal ions form stronger bonds with O(4) which are farther away from the ammonium group (—NH_3^+) of L-ala. The equilibrium distance of O(4)····M(9) and O(3)····M(9) increases in the order: $Ni^{2+} < Cu^{2+} < Mg^{2+} < Zn^{2+} < Ca^{2+}$. The M^{2+} in both the non-hydrated (L-ala—M^{2+}) as well as hydrated (L-ala—M × $(H_2O)_n$, n = 2 or 4) lie in the same plane of carboxylate groups of L-ala.

Table 7 summarizes the different energies and thermodynamic parameters which reflect that stability of L-ala—M can substantially be modified by the specific metal ion and hydration. Energy parameters have been calculated using eq. 2 and ΔH for all the fifteen complexes studied are found to be exothermic. L-ala—Cu^{2+} have been found most stable complex while its hydration has further increases its stability with a maximum enthalpy, 165.808 kcal/mol for L-ala—Cu^{2+} × $(H_2O)_4$, among all fifteen complexes studied (Table 7). Gibbs energies, a scale to measure the tendency to associate in real molecular complexes, are found negative except for L-ala—Ca^{2+} × $(H_2O)_4$.

The ΔG for the non-hydrated L-ala—M complexes are 21.462 k.cal/mol, 9.186 kcal/mol, 68.155 kcal/mol, 98.848 kcal/mol and 23.098 kcal/mol for Mg^{2+}, Ca^{2+}, Ni^{2+}, Cu2+ and Zn^{2+} complexes respectively. To analyze the affinity of hydration with the L-ala—M complexes, first two water molecules have been coordinated with M^{2+} ions (I and II system in Fig. 8b), which stabilized (-ΔG) the complexes of Mg^{2+}, Ni^{2+} and Cu^{2+} with a magnitude of 1.716 k.cal/mol, 48.342 k.cal/mol and 29.19 k.cal/mol respectively (Table 7). Addition of another two water molecules (III and IV system of 8b) on the L-ala—M^{2+} (i.e. L-ala—M × $(H_2O)_4$) has further showed a partial change in Gibbs free energy (-ΔG) to stabilize for the hydrated complex of Ni^{2+} only(Table 7).

The net atomic charges on different atoms of the complexes studied, have been investigated by the natural population analysis using the NBO program [37]. The amounts of metal ion charge transfer (CT) for the M^{2+} along with dipole moments are summarized in Table 6. The magnitude of CT contribution in L-ala—Ca^{2+} is much lower (0.051 to 0.099*e*) for its non-hydrated as well as hydrated complexes while CT for all L-ala—Ni^{2+} complexes are maximum from 0.588*e* to 0.995*e*.

Conclusion:

In conclusion, surface interaction of ala enantiomers (D- and L-ala) has been studied on BNT and BNT-M with a view to understand the role of minerals and metal ions for their adsorption selectivity under the condition of different pH and concentration. Metal ion interaction with ala and role of hydration has also been studied. Transition metal ion exchanged (Ni^{2+}, Cu^{2+} and Zn^{2+}) BNT have more affinity for ala than alkaline earth metal ions (Mg^{2+} and Ca^{2+}). Out of 6 adsorbents, Mg^{2+} exchanged BNT has been observed to have higher selectivity for biologically available L-ala as compare to D-ala at pH 4.0. So, such studies might be helpful for a better insight into the enantiomeric selection of molecules present in living system and role of pH

with a view to understand the abiotic evolution of life on the surface of minerals in prebiotic era of Earth.

Acknowledgement

Author (PP) acknowledge Head of the Chemistry Department and Prof. Sanjay Pant, Photophysics Lab, D.S.B. Campus, Kumaun University, Nainital 263002, Uttarakhand, India for providing the necessary research facility. PP also thankful to Prof. Ke-Li Han, State Key Laboratory for Molecular Reaction Dynamics, Dalian Institute of Chemical Physics, Chinese Academy of Sciences, 457 Zhongshan Road, Dalian, Liaoning, China for providing the computational facilities.

References

[01] Oparin, A.I. and Haldane, J.B.S., **(1938)** The Origin of Life, McMillan, London.

[02] Eschenmoser, A., **(2007)** Tetrahedron, (63), 12821-12844.

[03] Cleaves, II H. J., Scott, A.M., Hill, F.C., Leszczynshi, J., Sahai, N. and Hazen, R., **(2012)** Chem. Soc. Rev., (41), 5502-5525.

[04] Schopf, J.W., **(1993)** Science,(260), 640-646.

[05] Lazcano, A.M.S., **(1994)** Abstr. Pap. Am. Chem. S., (207), 24-GEOC.

[06] Lahav, N., Chang, S., **(1976)** J Mol Evol, (8), 357–380.

[07] Stribling, R., Miller, S.L., **(1987)** Orig Life Evol Biosph, (17), 261–273.

[08] Bernal, J.D., **(1951)** Proc Phys Soc London A, (62), 537-558.

[09] Hazen, R.M., Papineau, D., Bleeker, W., Downs, R.T., Ferry, J.M., McCoy, T.J., Sverjens, D.A. and Yang, H., **(2008)** Am. Miner., (93),1693-1728.

[10] Zaia, D.A.M., **(2012)** Int. J. Astrobiology, 1-6.

[11] Lambert, J.F., **(2008)** Orig Life Evol Biosph, (38), 211-242.

[12] Aranda, P., Darder, M., Ogawa, M., **(2011)** Chem. Soc. Rev., (40), 801.

[13] Park, J-H et al., **(2016)** Journal of Pharmaceutical Investigation, (46), 363–375

[14] Marino, T., Russo, N., Toscano, M., **(2001)** Inorg. Chem., (40), 6439-6443.

[15] Nelson, D.L., Cox, M.M., **(2005)** Lehninger, Principles of Biochemistry, Fourth edition, W H Freeman and Company, New York.

[16] Rode, B.M., Bujdak, J., Eder, A.H., **(1993)** Trends Inorg Chem, (3), 45-62.

[17] Remko, M., Rode, B.M., **(2000)** Chem Phys Lett, (316), 489-494.

[18] Pant, C.K., Lata, H., Pathak, H.D., Mehata, M.S., **(2009)** Int. J. of Astrobiology, (8), 107-115.

[19] Gururani, K., Pant, C.K., Pandey, N., Pandey, P., **(2012a)** Int J Scie Techno Res (8), 159–163.

[20] Remko, M., Fitz, D., Broer, R., Rode, B.M., **(2011)** J Mol Model, (17), 3117-3128.

[21] Gururani, K., Pant, C.K., Pandey, P., Pandey, N., **(2012b)** Asian J Res Chem (9), 1150–1155.

[22] Kojo, S., (**2010**) Symmetry, (*2*), 1022-1032.

[23] Avalos, M., Babiano, R., Cintas, P., Jimenez, J.L., Palacios, J.C., **(1998)** Chem. Rev., (98), 2391–2404.

[24] Pizzarello, S., **(2006)** Acc. Chem. Res, (39), 231–237.

[25] Nelson, D.L., Cox, M.M., **(2005)** Lehninger, Principles of Biochemistry, Fourth edition, W H Freeman and Company, New York.

[26] Emiliani C., **(1997)** Planet Earth cosmology, geology and the evolution of life and environment, Cambridge University Press, Low price editions, pp. 373 (Table 19.2).

[27] Glavin, D.P., Aubrey, A., Dwokin, J.P., Botta, O., Bada, J.J., **(2005)** Lunar and Planetary Science XXVI.

[28] Yi-Jehng, K., Steven, B.C., Hui-Chun, H., Wei-Ling, T., Zbigniew, K., **(2003)** The Astrophysical Journal, (593), 848.

[29] Marshall-Bowman, K., Ohara, S., Sverjensky, D.A., Hazen, R.M., Cleaves, H.J., **(2010)** Geochim Cosmochim Acta (74), 5852–5861.

[30] Pandey, P., Pant, C.K., Gururani, K., Arora, P., Kumar, S., Sharma, Y., Pathak, H.D., Mehata, M.S., **(2013)** Orig Life Evol Biosph, (43), 331–339

[31] Becke, A.D., **(1993)** J Chem Phys, (98), 5648.

[32] Lee, C., Yang, W., Parr, R.G., **(1988)** Phys Rev B (37), 785.

[33] Hohenberg, P., Kohn, W., **(1964)** Phys Rev B, (136), 864–871

[34] Gaussian 16, Revision A.03, M. J. Frisch, G. W. Trucks, H. B. Schlegel, G. E. Scuseria, M. A. Robb, J. R. Cheeseman, G. Scalmani, V. Barone, G. A. Petersson, H. Nakatsuji, X. Li, M. Caricato, A. V. Marenich, J. Bloino, B. G. Janesko, R. Gomperts, B. Mennucci, H. P. Hratchian, J. V. Ortiz, A. F. Izmaylov, J. L. Sonnenberg, D. Williams-Young, F. Ding, F. Lipparini, F. Egidi, J. Goings, B. Peng, A. Petrone, T. Henderson, D. Ranasinghe, V. G. Zakrzewski, J. Gao, N. Rega, G. Zheng, W. Liang,

M. Hada, M. Ehara, K. Toyota, R. Fukuda, J. Hasegawa, M. Ishida, T. Nakajima, Y. Honda, O. Kitao, H. Nakai, T. Vreven, K. Throssell, J. A. Montgomery, Jr., J. E. Peralta, F. Ogliaro, M. J. Bearpark, J. J. Heyd, E. N. Brothers, K. N. Kudin, V. N. Staroverov, T. A. Keith, R. Kobayashi, J. Normand, K. Raghavachari, A. P. Rendell, J. C. Burant, S. S. Iyengar, J. Tomasi, M. Cossi, J. M. Millam, M. Klene, C. Adamo, R. Cammi, J. W. Ochterski, R. L. Martin, K. Morokuma, O. Farkas, J. B. Foresman, and D. J. Fox, Gaussian, Inc., Wallingford CT, 2016.

[35] Marino, T., Russo, N., Toscano, M., **(2001)** Inorg. Chem., (40), 6439-6443

[36] Bush, M.F., Oomens, J., Saykally, R.J., Williams, E.R., **(2008)** J. Am Chem Soc., (130), 6463-6471.

[37] Glendening ED, Reed AE, Carpenter JE, Weinhold F. The NBO program, Version 3.1.

Scheme, Figures and Tables:

Scheme I: Sequential steps involved in the preparation/purification of adsorbents and adsorption studies

Fig. 1: Chemical structure of L- and D-alanine.

Fig. 2: Time optimization of L-ala (5 mM aqueous solution) on BNT-Cu, showing relationship between percentage adsorption (y-axis shown in right side of the graph) with time (x-axis) while total amount of L-ala available for adsorption in 5 mM aqueous solution has been provided in y-axis (left one).

Fig. 3: Adsorption behaviour of L-alanine as a function of concentration versus quantity adsorbed at pH 4.0 ±0.2.

Fig. 4: Langmuir adsorption isotherm of L-alanine at pH 4.0 ±0.2

Fig. 5: Adsorption behaviour of D-alanine as a function of concentration versus quantity adsorbed at pH 4.0 ±0.2.

Fig. 6: Langmuir adsorption isotherm of D-alanine at pH 4.0 ±0.2 (adsorbents have been denoted same as in the above figures5.1.6-5.1.8).

Fig. 7: Scanning electron microscopic (SEM) images of (a), (b) of adsorbent BNT; (c), (d) of adsorbate (L-ala and D-ala) and (e), (f) of adsorption adducts (BNT-L-ala and BNT-D-ala) for L-alanine and D-alanine respectively.

Fig. 8: Chemical structures of (a) L-ala—M complexes, with numbering, and (b) L-ala—M with addition of different water molecules.

Table 1: Adsorption parameters and percentage adsorption of L- and D-alanine at pH 4.0 ±0.2 in presence of BNT and BNT-M.

Table 2: Adsorption parameters and percentage adsorption of L- and D-alanine at pH 6.0 ±0.2 in presence of bentonite and divalent metal ion exchanged bentonite.

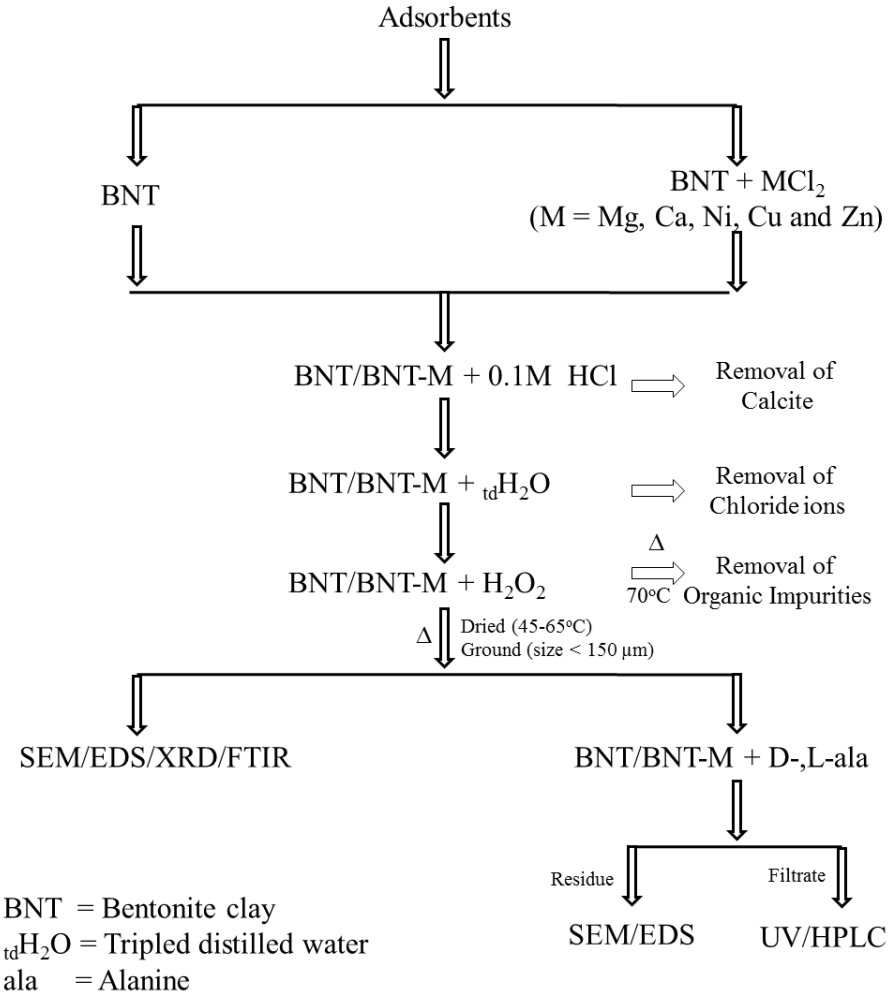
Table 3: B3LYP/6-311++G(2d,2p) optimized relevant bond lengths (Å), bond angles (deg) and dihedral angles (deg) for L-ala—M complex.

Table 4: B3LYP/6-311++G(2d,2p) optimized relevant bond lengths (Å), bond angles (deg) and dihedral angles (deg) for L-ala—M —2H_2O complex.

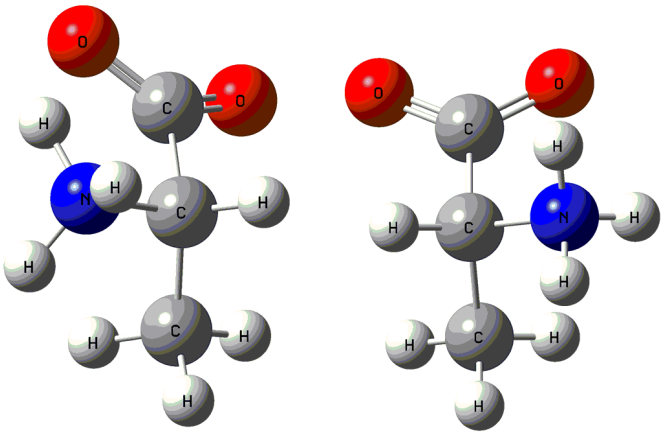
Table 5: B3LYP/6-311++G(2d,2p) optimized relevant bond lengths (Å), bond angles (deg) and dihedral angles (deg) for L-ala—M —4H_2O complex.

Table 6: B3LYP/6-311++G(2d,2p) calculated net charge of metal (q_M), two oxygen ($q_{O(3)}$ and $q_{O(4)}$), nitrogen ($q_{N(5)}$) in |e|, dipole moments (μ in Debye) and amount of metal ion charge transfer (CT) for different L-ala—M × $(H_2O)_n$, (n = 0, 2 and 4) systems calculated at 298.15K and 1 atm. pressure.

Table 7: B3LYP/6-311++G(2d,2p) calculated absolute energy (E in au), energy change (ΔE in k.cal/mol), metal ion affinities (ΔH in k.cal/mol), Gibbs free energies (ΔG in k.cal/mol) and entropies (ΔS in cal/mol.K) for different L-ala—M × $(H_2O)_n$, (n = 0, 2 and 4) systems calculated at 298.15K and 1 atm pressure.


Adsorbents
BNT
BNT + MCl2
(M = Mg, Ca, Ni, Cu and Zn)
BNT/BNT-M + 0.1M HCl
Removal of Calcite
BNT/BNT-M + tdH2O
Removal of Chloride ions
BNT/BNT-M + H2O2
Δ
70°C
Removal of Organic Impurities
Δ
Dried (45-65°C)
Ground (size < 150 μm)
SEM/EDS/XRD/FTIR
BNT/BNT-M + D-,L-ala
Residue
Filtrate
SEM/EDS
UV/HPLC
BNT = Bentonite clay
tdH2O = Tripled distilled water
ala = Alanine

Scheme I



L-alanine **D-alanine**

Fig. 1

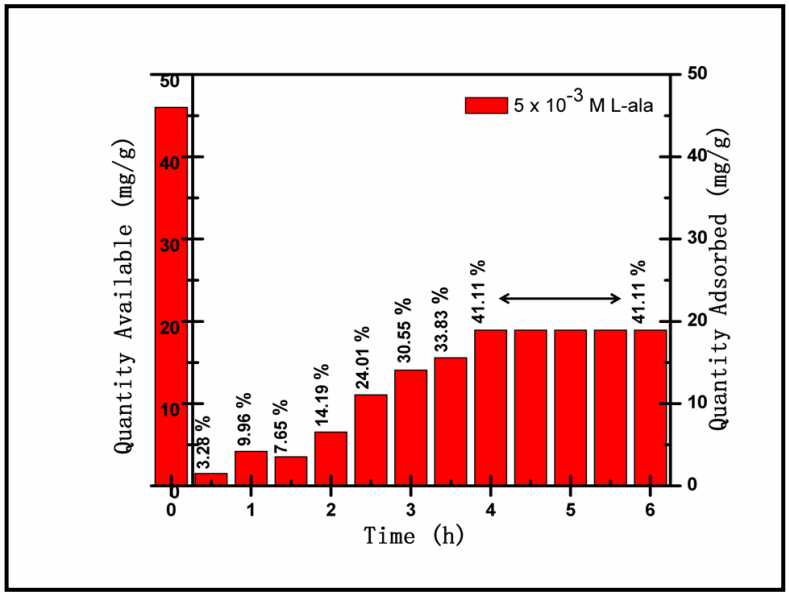

5 x 10-3 M L-ala
Quantity Available (mg/g)
Quantity Adsorbed (mg/g)
Time (h)
3.28 %
9.96 %
7.65 %
14.19 %
24.01 %
30.55 %
33.83 %
41.11 %
41.11 %
0
10
20
30
40
50
0
1
2
3
4
5
6

Fig. 2

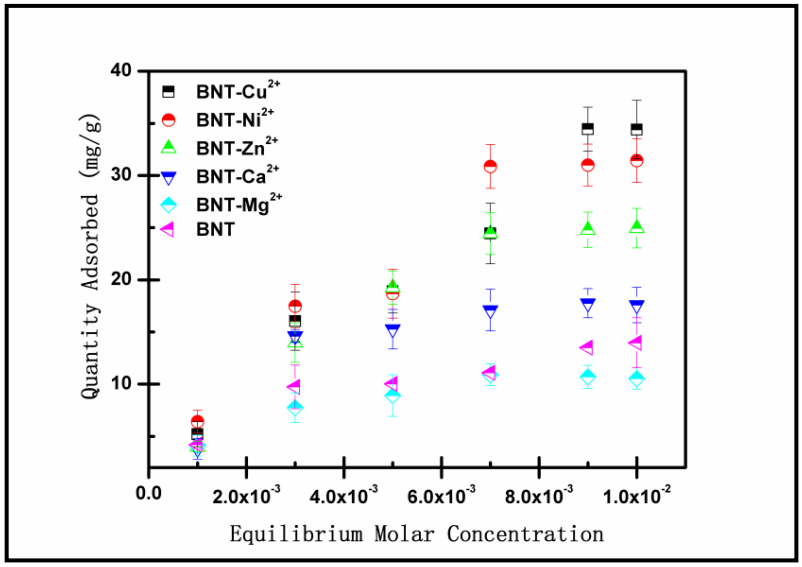

BNT-Cu2+
BNT-Ni2+
BNT-Zn2+
BNT-Ca2+
BNT-Mg2+
BNT
Quantity Adsorbed (mg/g)
40
30
20
10
0.0
2.0x10-3
4.0x10-3
6.0x10-3
8.0x10-3
1.0x10-2
Equilibrium Molar Concentration

Fig. 3

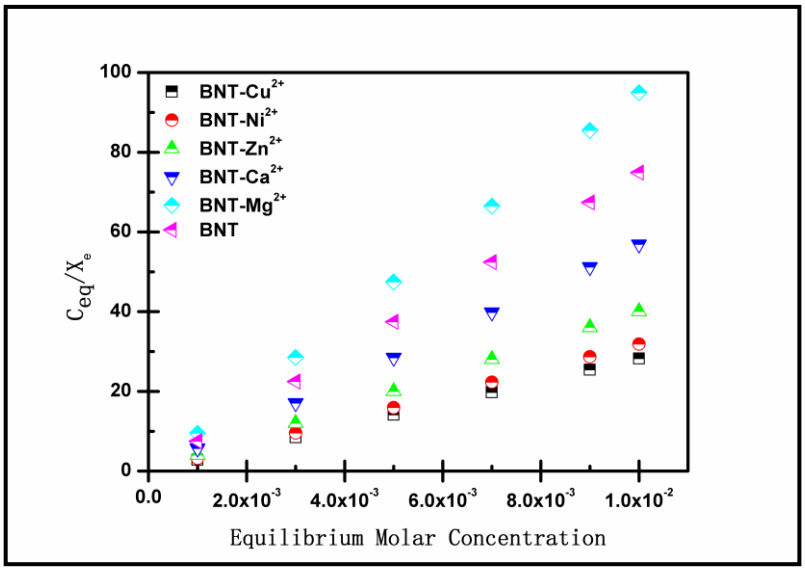

BNT-Cu2+
BNT-Ni2+
BNT-Zn2+
BNT-Ca2+
BNT-Mg2+
BNT
Ceq/Xe
100
80
60
40
20
0
0.0
2.0x10-3
4.0x10-3
6.0x10-3
8.0x10-3
1.0x10-2
Equilibrium Molar Concentration

Fig. 4

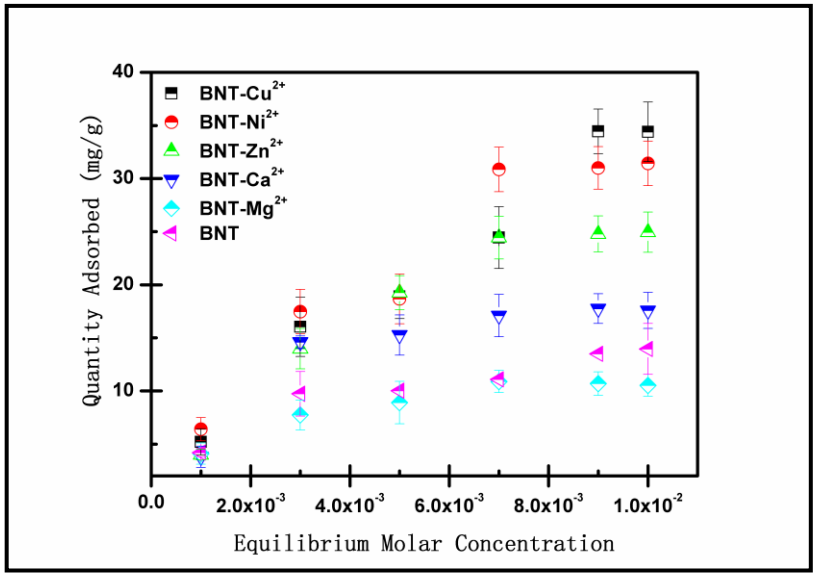

BNT-Cu2+
BNT-Ni2+
BNT-Zn2+
BNT-Ca2+
BNT-Mg2+
BNT
Quantity Adsorbed (mg/g)
Equilibrium Molar Concentration
0.0
2.0x10-3
4.0x10-3
6.0x10-3
8.0x10-3
1.0x10-2
10
20
30
40

Fig. 5

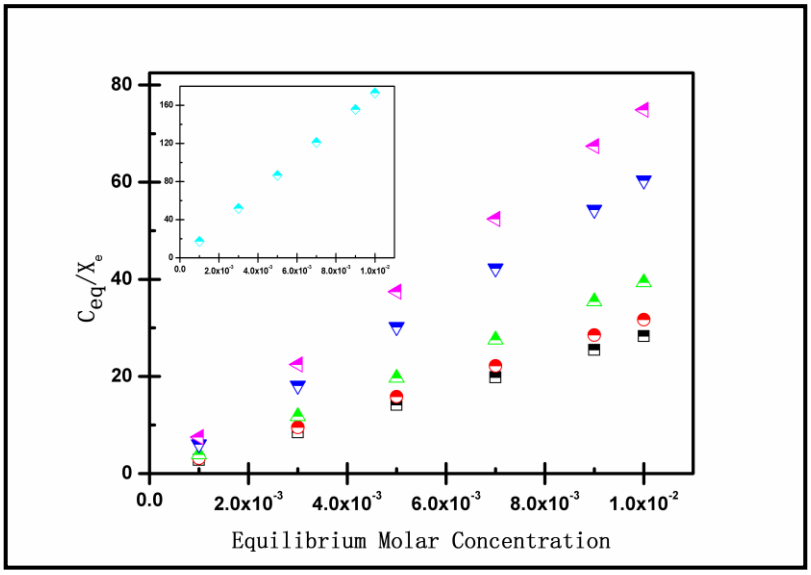

Ceq/Xe
Equilibrium Molar Concentration
0.0
2.0x10-3
4.0x10-3
6.0x10-3
8.0x10-3
1.0x10-2
0
20
40
60
80

Fig. 6

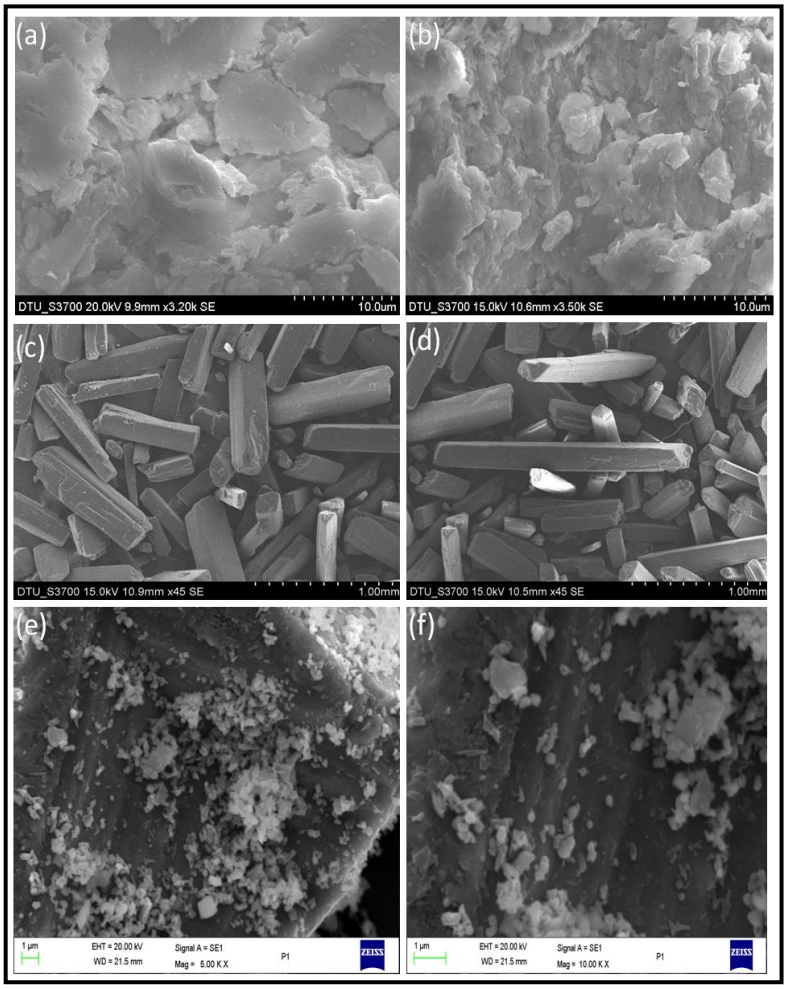

(a)
DTU_S3700 20.0kV 9.9mm x3.20k SE
10.0um
(b)
DTU_S3700 15.0kV 10.6mm x3.50k SE
10.0um
(c)
DTU_S3700 15.0kV 10.9mm x45 SE
1.00mm
(d)
DTU_S3700 15.0kV 10.5mm x45 SE
1.00mm
(e)
1 µm
EHT = 20.00 kV
WD = 21.5 mm
Signal A = SE1
Mag = 5.00 K X
P1
ZEISS
(f)
1 µm
EHT = 20.00 kV
WD = 21.5 mm
Signal A = SE1
Mag = 10.00 K X
P1
ZEISS

Fig. 7

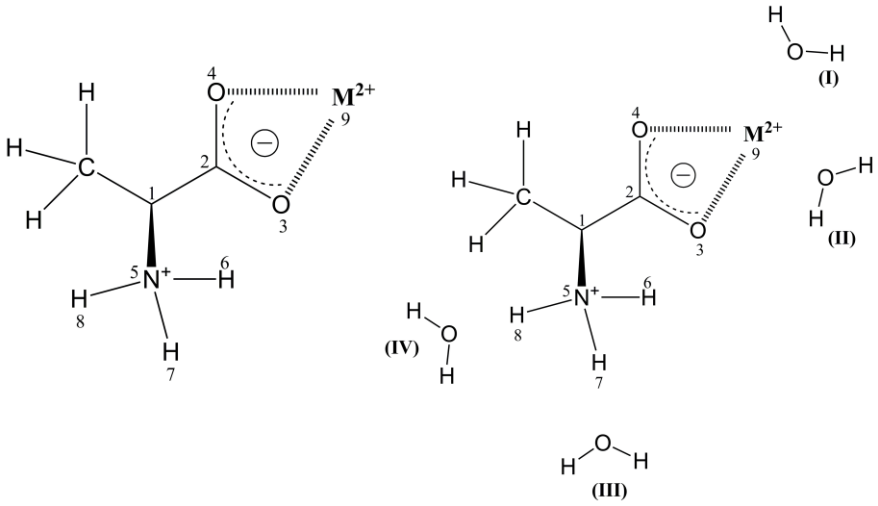


Fig. 8

Table 1

		Adsorbents					
		BNT-Cu	BNT-Ni	BNT-Zn	BNT-Ca	BNT-Mg	BNT
L-alanine	X_m	35.41	31.38	24.95	17.58	10.53	13.35
	K_L ($\times 10^2$)	11.36	04.49	11.28	56.88	66.83	13.18
	% Adsorption	38.85	33.85	26.91	18.96	11.36	14.40
D-alanine	X_m	35.32	31.56	25.40	16.56	5.78	13.35
	K_L ($\times 10^2$)	03.98	04.46	15.83	28.32	121.83	—
	% Adsorption	38.01	34.04	27.40	17.86	06.24	14.40

Table 2

		Adsorbents					
		BNT-Cu	BNT-Ni	BNT-Zn	BNT-Ca	BNT-Mg	BNT
L-alanine	X_m	24.32	19.34	17.31	15.26	10.18	10.83
	% Adsorption	26.24	20.86	18.67	16.46	10.98	11.68
D-alanine	X_m	24.10	19.47	16.67	15.28	08.43	11.13
	% Adsorption	26.00	21.00	17.98	16.48	09.04	12.01

Table 3

Parameters	L-ala—M Complexes					
	ala	**Mg^{2+}**	**Ca^{2+}**	**Ni^{2+}**	**Cu^{2+}**	**Zn^{2+}**
***d*[C(1)−C(2)]**	1.561	1.523	1.536	1.505	1.505	1.520
***d*[C(2)−O(3)]**	1.263	1.267	1.265	1.271	1.270	1.263
***d*[C(2)−O(4)]**	1.242	1.257	1.253	1.270	1.269	1.259
***d*[C(1)−N(5)]**	1.513	1.510	1.512	1.507	1.507	1.508
***d*[N(5)−H(6)]**	1.048	1.024	1.029	1.022	1.022	1.021
***d*[N(5)−H(7)]**	1.016	1.021	1.018	1.022	1.022	1.021
***d*[N(5)−H(8)]**	1.017	1.019	1.019	1.021	1.021	1.020
***d*[O(3)−H(6)]**	1.764	2.177	1.987	2.511	2.563	2.365
***d*[O(3)⋯M(9)]**	-	**2.077**	2.426	1.888	1.953	2.114
***d*[O(4)⋯M(9)]**	-	**2.093**	2.417	1.868	1.946	2.081
***Θ*[C(1)–C(2)−O(3)]**	115.049	119.169	117.541	123.377	122.730	120.104
***Θ*[C(2)–C(1)−N(5)]**	105.680	107.756	106.900	108.529	108.779	108.559
***Θ*[O(3)–C(2)−O(4)]**	128.685	121.245	123.577	114.477	115.915	121.427
***Θ*[C(1)–O(4)⋯M(9)]**	-	120.733	125.144	120.177	120.768	122.397
***Θ*[C(1)–O(3)⋯M(9)]**	-	121.236	125.001	118.535	119.625	119.863
***Θ*[C(2)–O(3)⋯M(9)]**	-	87.753	90.560	87.629	88.349	86.868
***Θ*[O(3)⋯M(9)⋯O(4)]**	-	63.664	54.538	69.324	67.020	63.265
***ϕ*[O(3)−C(2)−C(1)−N(5)]**	0.872	8.821	10.287	6.985	1.625	6.421
***ϕ*[C(1)−C(2)−O(4)⋯M(9)]**	-	178.337	175.150	179.716	179.668	179.793
***ϕ*[C(1)−C(2)−O(3)⋯M(9)]**	-	178.344	175.190	179.726	179.664	179.821

Table 4

Parameters	L-ala—M—2H$_2$O Complexes					
	ala	**Mg^{2+}**	**Ca^{2+}**	**Ni^{2+}**	**Cu^{2+}**	**Zn^{2+}**
***d*[C(1)−C(2)]**	1.561	1.526	1.537	1.508	1.512	1.522
***d*[C(2)−O(3)]**	1.264	1.265	1.264	1.271	1.268	1.251
***d*[C(2)−O(4)]**	1.242	1.257	1.252	1.266	1.253	1.268
***d*[C(1)−N(5)]**	1.513	1.510	1.512	1.507	1.508	1.509
***d*[N(5)−H(6)]**	1.048	1.025	1.030	1.022	1.022	1.021
***d*[N(5)−H(7)]**	1.016	1.021	1.018	1.022	1.021	1.021
***d*[N(5)−H(8)]**	1.017	1.019	1.020	1.020	1.020	1.020
***d*[O(3)−H(6)]**	1.764	2.121	1.978	2.48	2.417	2.410
***d*[O(3)⋯M(9)]**	-	2.127	2.453	1.907	1.996	2.286
***d*[O(4)⋯M(9)]**	-	2.098	2.441	1.906	1.994	2.038
***Θ*[C(1) –C(2)−O(3)]**	115.049	118.856	117.516	121.936	120.974	119.931
***Θ*[C(2) –C(1)−N(5)]**	105.680	107.379	106.888	108.116	108.126	107.801
***Θ*[O(3) –C(2)−O(4)]**	128.685	121.564	123.938	116.343	118.324	122.032
***Θ*[C(1) –O(4)⋯M(9)]**	-	121.973	125.643	119.438	120.501	127.986
***Θ*[C(1) –O(3)⋯M(9)]**	-	120.800	125.249	119.041	120.045	116.413
***Θ*[C(2) –O(3)⋯M(9)]**	-	87.088	90.639	87.299	87.706	83.149
***Θ*[O(3)⋯M(9)⋯O(4)]**	-	62.799	53.983	68.848	66.021	60.935
***ϕ*[O(3)−C(2)−C(1)−N(5)]**	0.872	15.307	8.728	0.301	5.749	0.574
***ϕ*[C(1)−C(2)−O(4)⋯ M(9)]**	-	178.051	178.829	179.483	178.179	178.687
***ϕ*[C(1)−C(2)−O(3)⋯ M(9)]**	-	178.064	178.843	179.482	178.176	178.727

Table 5

Parameters	L-ala—M—4H$_2$O Complexes					
	ala	**Mg^{2+}**	**Ca^{2+}**	**Ni^{2+}**	**Cu^{2+}**	**Zn^{2+}**
***d*[C(1)−C(2)]**	1.561	1.522	1.533	1.507	1.510	1.521
***d*[C(2)−O(3)]**	1.264	1.266	1.264	1.272	1.269	1.251
***d*[C(2)−O(4)]**	1.242	1.260	1.257	1.269	1.267	1.273
***d*[C(1)−N(5)]**	1.513	1.499	1.501	1.496	1.497	1.498
***d*[N(5)−H(6)]**	1.048	1.021	1.024	1.019	1.020	1.019
***d*[N(5)−H(7)]**	1.016	1.039	1.036	1.043	1.042	1.040
***d*[N(5)−H(8)]**	1.017	1.039	1.037	1.044	1.043	1.040
***d*[O(3)−H(6)]**	1.764	2.250	2.086	2.527	2.431	2.458
***d*[O(3)···M(9)]**	-	2.095	2.429	1.902	1.991	2.275
***d*[O(4)···M(9)]**	-	2.091	2.390	1.899	1.986	2.024
***Θ*[C(1) –C(2)−O(3)]**	115.049	119.777	118.474	122.550	121.547	120.735
***Θ*[C(2) –C(1)−N(5)]**	105.680	109.094	108.546	109.373	109.458	109.154
***Θ*[O(3) –C(2)−O(4)]**	128.685	120.964	123.383	115.816	117.761	121.602
***Θ*[C(1) –O(4)···M(9)]**	-	121.432	126.079	119.630	120.660	128.112
***Θ*[C(1) –O(3)···M(9)]**	-	120.733	123.794	118.829	119.830	115.975
***Θ*[C(2) –O(3)···M(9)]**	-	87.662	89.878	87.459	87.869	83.180
***Θ*[O(3)···M(9)···O(4)]**	-	63.370	54.833	69.008	66.173	61.342
***ϕ*[O(3)−C(2)−C(1)−N(5)]**	0.872	3.971	7.666	4.006	4.505	1.730
***ϕ*[C(1)−C(2)−O(4)··· M(9)]**	-	176.073	175.268	179.296	177.169	178.962
***ϕ*[C(1)−C(2)−O(3)··· M(9)]**	-	176.064	175.296	179.300	177.158	178.967

Table 6

System	Species		q_M	$q_{O(3)}$	$q_{O(4)}$	$q_{N(5)}$	μ	CT/e
Alanine			-	-0.810	-0.778	-0.699	12.91	-
(L-ala···M) × $(H_2O)_n$		n = 0	1.926	-0.813	-0.845	-0.589	9.80	0.074
	M =Mg^{2+}	n = 2	1.852	-0.830	-0.830	-0.669	5.84	0.148
		n = 4	1.848	-0.833	-0.818	-0.719	8.48	0.152
		n = 0	1.949	-0.836	-0.805	-0.675	10.47	0.051
	M=Ca^{2+}	n = 2	1.913	-0.830	-0.800	-0.676	5.85	0.087
		n = 4	1.901	-0.829	-0.815	-0.725	7.42	0.099
		n = 0	1.412	-0.630	-0.610	-0.664	5.17	0.588
	M=Ni^{2+}	n = 2	1.012	-0.629	-0.606	-0.663	5.83	0.988
		n = 4	1.005	-0.627	-0.611	-0.719	2.33	0.995
		n = 0	1.434	-0.647	-0.627	-0.665	5.53	0.566
	M=Cu^{2+}	n = 2	1.230	-0.681	-0.659	-0.663	6.09	0.770
		n = 4	1.220	-0.679	-0.665	-0.719	5.97	0.780
		n = 0	1.805	-0.790	-0.779	-0.663	4.79	0.195
	M=Zn^{2+}	n = 2	1.554	-0.736	-0.770	-0.663	4.31	0.446
		n = 4	1.562	-0.741	-0.784	-0.717	5.81	0.438

Table 7

System	Species		Parameters				
			-E	**-ΔE**	**-ΔH**	**-ΔG**	**-ΔS**
(L-ala$^{\cdots}$M) × (H_2O)$_n$							
		n = 0	523.797	30.466	29.080	21.462	25.55
	M=Mg^{2+}	n = 2	676.772	54.017	49.003	23.178	86.62
		n = 4	829.730	65.859	58.182	16.687	139.18
		n = 0	1000.371	17.631	16.634	9.186	24.98
	M=Ca^{2+}	n = 2	1154.328	29.017	24.870	0.596	81.51
		n = 4	1307.284	40.513	33.750	+5.321	152.30
		n = 0	1831.838	78.337	76.741	68.155	28.80
	M=Ni^{2+}	n = 2	1984.846	122.655	116.497	116.497	97.20
		n = 4	2137.806	135.848	127.169	127.169	152.30
		n = 0	1964.007	108.372	106.946	98.848	27.16
	M=Cu^{2+}	n = 2	2117.029	161.015	155.467	128.038	92.00
		n = 4	2269.988	173.938	165.809	122.314	145.89
		n = 0	2102.952	32.490	31.011	23.098	26.54
	M=Zn^{2+}	n = 2	2255.925	53.986	48.433	20.546	93.53
		n = 4	2408.880	64.622	56.723	13.378	56.72

View publication stats

ResearchGate

See discussions, stats, and author profiles for this publication at: https://www.researchgate.net/publication/307122769

Alcohol Abuse and Related Health Issues

Article · August 2016

CITATIONS
0

READS
45

4 authors, including:



Geetanjali ..
University of Delhi
43 PUBLICATIONS **202** CITATIONS
SEE PROFILE



Ram Singh
Delhi Technological University
72 PUBLICATIONS **532** CITATIONS
SEE PROFILE

Some of the authors of this publication are also working on these related projects:

Project Working on neurodegenerative diseases View project

Project working on biomimetic reactions View project

All content following this page was uploaded by Ram Singh on 29 August 2016.

The user has requested enhancement of the downloaded file.

International Research Journal of Medical Sciences _____E- ISSN 2320 –7353
Vol. **4(8),** 18-23, August **(2016)** *Int. Res. J. Medical Sci.*

Review Paper

Alcohol Abuse and Related Health Issues

Geetanjali[2], Poonam[1], Veer Babita[1] and Singh Ram[1*]
[1]Department of Applied Chemistry, Delhi Technological University, Delhi - 110 042, India
[2]Department of Chemistry, Kirori Mal College, University of Delhi, Delhi-110 007, India
singh_dr_ram@dce.ac.in

Available online at: www.isca.in, www.isca.me
Received 2nd July 2016, revised 23rd July 2016, accepted 11th August 2016

Abstract

Alcohol abuse and related health issues are an age old problem. Alcoholism is the reflection of socio-cultural factors of an individual and sometimes society as a whole. For some people, this is a part of daily life. Use and abuse travel on the very tight rope. People who have been drinking excess amounts of alcohol for longer periods of time come under the category of alcohol abuse. These people put themselves in the risk of developing serious and persistent changes in various organs including the brain. The effect of alcohol on the organs may be direct or indirect depending upon the general health status of the person. The studies have suggested that the brain functions are affected due to the interaction of alcohol with multiple neurotransmitter systems. Alcohol abuse also leads to different nutritional deficiencies and diseases. This article will discuss the effect of alcohol abuse and related health issues.

Keywords: Alcohol, Ethanol, Alcoholism, Acetaldehyde, CNS, Nutritional deficiencies.

Introduction

Alcohol, in chemistry, is symbolized as R-OH, where R is an alkyl group. Drinking alcohol is an age-old practice and is thought to be the reflection of socio-cultural factors of the individual and society as a whole[1]. All alcohols are not appropriate for drinking purposes. Only the ethyl alcohol (CH_3CH_2OH; ethanol) has been found to be suitable for drinking. Ethanol is being used in the production of alcoholic beverages and is the most widely consumed chemical worldwide. This alcohol is produced by the fermentation of grains and fruits. All the rural and urban societies are involved in the alcohol abuse. People have a total misconception that drinking alcohol releases their stress and tension and makes them happy. But the fact is different. Ethanol is a psychoactive substance and causes more adverse effect on human health which includes various disorders and diseases. Also drinking alcohol is responsible for negative social and economic burden on alcoholics[1].

As per the report of the National Institute on Alcohol Abuse and Alcoholism, in a year, the alcohol related problem takes the life of about 88,000 people. This data makes it the fourth leading cause of death in the United States[2,3]. Globally, about 3.3 million deaths in 2012 were attributable to alcohol abuse and related health issues[4]. Alcohol directly does not contributes to many diseases but over 200 diseases and injury-related health conditions are alcohol dependent diseases which also includes liver cirrhosis, cancers, and other injuries[4]. The alcohol consumption is directly linked with the economic condition of the country. The higher economic wealth of a country showed more alcohol consumption.

Ethanol is classified as depressant[5]. The damaging effects of this in CNS are possible due to its direct toxic effect. This also damages by an indirect effect through its metabolites or ROS generation (Reactive Oxygen Species). The ethanol drinking slows down the vital functions and results in uneven movement that causes an inability to react quickly, slurred speech and disturbed precipitations. The amount of ethanol consumed determines the type of the effect and health issues. Its overdose causes a more severe depressant effect such as an inability to feel pain, unconsciousness, worse, coma or even death. Ethanol can travel anywhere in our body as they contain both hydrocarbon chain and hydroxyl group and hence the hydrophobic part allows them to move into fat while the hydroxyl group (hydrophilic part) allows moving into water[4]. This article presents an overview of the correlation of alcohol consumption and its impact on our health.

Effect of Alcohol

Effect of alcohol in the brain: The brain gets damaged due to the chronic and excessive consumption of alcohol, i.e. ethanol[6]. The quantity and time period of ethanol consumption plays leading role in the damage and neuro-behavioral changes of any alcoholic person. The effect also depends on age, gender, family history and level of education of the person. The effects of ethanol consumption on brain have been studied by a number of research groups.[7,8] They have postulated that the effect is basically mediated through the formation of acetaldehyde (CH_3CHO), the first metabolite of ethanol[8].

Acetaldehyde plays a crucial role in damaging the health of alcoholic people and is responsible for the behavioural,

neurochemical and neurotoxic actions[8]. However, this hypothesis has several doubts and is still under investigation; however, several groups have reported the oxidation of ethanol to acetaldehyde in the brain[9]. The three enzymes that are involved in the metabolic reaction of ethanol to acetaldehyde in the brain are *Catalase*, *Cytochrome P450* and *Alcohol dehydrogenase*[10]. The quantity of acetaldehyde in the brain at a particular time period is based on the comparative rate of removal and formation of acetaldehyde. This is because the oxidation of acetaldehyde to acetate is taking place in large quantity. Hence, the exact damage done by the acetaldehyde in the brain is still under investigation.

Effect of alcohol on astrocytes: The entire central nervous system (CNS) is covered by astrocytes which are specialized glial cells[11]. The population of these cells are 10 to 50 times more than the neurons in the CNS. Ethanol has several targets in astrocytes. This tempts astroglial activation, in combination with up-regulation of several pro-inflammatory cytokines that is responsible for cell apoptosis, neuroinflammation and neurodegeneration[12]. Ethanol also affects the synthesis, distribution, intracellular transport, and secretin of N-glycoproteins in astrocytes and neurons resulting in the hindrance of brain development[13].

Effect of ethanol on neurotransmitters: Neurotransmitters are the chemical compounds that act as messengers which enable neurotransmission by passing signals across a chemical synapse. The chronic alcoholism affects the synaptic structure[14]. The N-methyl-D-aspartate receptor (NMDA receptor or NMDAR) is the main target of ethanol in the brain. The interaction of this receptor with ethanol is associated with ethanol tolerance, dependence, withdrawal, craving, and relapse[15]. The low level of ethanol concentration inhibits the excitary activity of the NMDA receptor, which contributes towards the abnormalities like learning disabilities, neuronal losses and cognitive deficits.

The exact mechanism and direct action for changes in the functionality of this receptor by ethanol remains unclear[16]. The interference of ethanol with the phosphorylation and compartmentalization of NMDA receptor is a possible mechanism of action[17]. The inhibition of the NMDA receptors by ethanol is mainly restricted in the subset of neurons[18]. This is because; the different sub-units of the receptors have different sensitivity to ethanol[19].

Ethanol also interacts with another membrane receptor, γ-aminobutyric acid (4-aminobutyric acid, GABA). The three types of GABA receptors are $GABA_A$, $GABA_B$ and $GABA_c$. $GABA_A$ and $GABA_C$ receptors are ligand-gated whereas $GABA_B$ receptors are G protein-coupled receptors[20]. Ethanol does not affect all the subunits of all types of GABA. The interaction of ethanol is only restricted to certain subtypes of some subunits[21]. The chronic alcohol consumption leads to the decreased sensitivity of $GABA_A$ receptor-mediated responses[22]. The interaction of ethanol to GABA is allosteric which changes the shape of active site and modulates the receptor activity leading to the stimulation of the flow of chloride ion[23]. Some studies have also suggested that the modulation of the $GABA_A$ receptor is also due to phosphorylation / dephosphorylation mechanisms[21]. The ethanol dependence and withdrawal are also responsible for the various polymorphisms in the $GABA_A$ gene[24] and there is a possibility of significant functional consequences[25].

The enhancement of the $GABA_B$ induced synaptic responses by ethanol results in the inhibition of the cation channels. This results in the hyperpolarization of the membrane and a consequent decrease in neuronal excitability[26] and altered mental and motor performance in an acute intoxication phase[27].

Ethanol being small molecule interacts with many neurotransmitter systems in the brain like mesocorticolimbic dopamine and serotonin[28]. Ethanol acutely activates mesocorticolimbic dopamine (DA) system and leads to the functional changes in the brain reward system[29]. The polymorphic variations in many dopaminergic system genes including the dopamine transporter gene have been observed in alcoholics[30] along with severe alcohol withdrawal symptoms[31]. The alcoholism has also been associated with polymorphism of the serotonin transporter[32].

Vitamin and Mineral Deficiency due to Alcoholism

The vitamins and minerals that are essential for our life are severely got deficient due to chronic alcoholism. The deficiency is associated with inhibition in breakdown and lowering of absorption. Alcohol slows down the secretion of digestive enzyme from the pancreas and hence inhibits the breakdown of nutrients into usable molecules[33]. Also, alcohol damages the cells lining in the stomach and intestines and reduces the nutrient absorption[34]. Alcohol also affects the transport, storage, and excretion of the digested and absorbed nutrients[35].

The chronic alcoholic people have shown deficiencies of minerals like calcium (Ca), magnesium (Mg), iron (Fe), zinc (Zn) etc in their body[36]. A variety of diseases like skin lesions, zinc-related night blindness and calcium-related bone etc caused due to the mineral deficiencies and are also called mineral deficiency diseases[37].

Chronic alcoholics also showed vitamin deficiencies due to decreased food ingestion and impaired absorption, metabolism and utilization. This has been observed that the people who are addicted to ethanol suffer from thiamine (Vitamin B1) deficiencies[38]. Vitamin B1 is used in combination with other Vitamin B as Vitamin B complexes[38]. The deficiency of these vitamins has fatal outcome and mainly responsible for the diseases like Korasakoff's syndrome, optic neuropathy and beriberi. Three important pathways are involved in thiamine deficiency due to alcoholism: i. Inadequate nutritional intake, ii.

Decreased absorption of thiamine from the gastrointestinal tract and iii. Reduced uptake and impaired utilization in the cells[39]. Similarly, the chronic alcohol consumers showed deficiency in vitamin A and hence exposed to the vitamin A deficiency diseases[40]. The diseases like the loss of night vision (nyctalopia), xerophthalmia and blindness are associated with alcoholism[41].

Diseases due to Alcoholism

Alcohol consumption results in the initiation and development of many chronic diseases and conditions. Twenty-five chronic disease and condition codes in the International Classification of Disease (ICD)-10 are entirely attributable to alcohol[42]. Alcohol has been found to be associated with diseases like tumors, cancers, numerous cardiovascular and digestive diseases and neuropsychiatric conditions[42].

Cancer: Studies have proved that alcoholic beverages are carcinogenic to humans[43]. Generally alcohol increased the risk of cancers of the upper digestive track, the lower digestive track and the female breast[42]. The stomach cancer has also been linked to alcoholism[44]. Some studies have also shown some positive effect of alcohol, if taken in dose-dependent manner. It has been found that alcohol significantly decreased the risk of renal cell carcinoma[45], Hodgkin's lymphoma[46], and non-Hodgkin's lymphoma[47].

Alcoholic Liver Disease (ALD): ALD is a collection of various liver diseases that are directly or indirectly associated with the alcohol consumption. The three histological stages of ALD includes simple steatosis (fatty liver), alcoholic hepatitis, and chronic hepatitis with hepatic fibrosis or cirrhosis[48]. Cirrhosis is a condition in which the liver is damaged and does not function properly whereas hepatitis is an inflammation of the liver. The widely accepted mechanism for liver damage involves the oxidative and non-oxidative breakdown of ethanol in the liver leading to the formation of free radicals, acetaldehyde, and fatty acid ethyl esters. These chemical species are responsible for the damage[49].

Pancreatic problems: The inflammation of the pancreas (pancreatitis) is usually observed in alcoholics. The alcoholism increases the risk for acute and chronic pancreatitis[50]. The combination of alcohol drinking with smoking aggravates the pancreatic problem further. The damage pathway for the pancreas is almost similar to the liver[51].

Sexual dysfunction: The sexual dysfunction (SD) is associated with many types of problems that include decreased sexual desire, difficulty in erection and achieving orgasm, sexual aversion disorder and premature ejaculation[52]. Alcoholic people always complain of SD like testicular atrophy, inhibition of testosterone production, and inhibition of spermatogenesis, has been observed in the people with chronic alcohol drinking habit[53].

Infertility: The association of alcoholism and male/female infertility cannot be ruled out completely[54]. The exact relationship between alcohol and infertility is not clear. This has been observed that the chronic alcoholic female experienced irregularities in their menstrual cycles and ovulation and also unusual variation in the levels of estrogen and progesterone[55]. Infertility due to ovulatory disorders like anovulation and oligoovulation or endometriosis have been associated with alcohol abuse[56]. Alcoholism was found to be associated with decreased fecundability also[57].

In case of male, the semen quality is associated with alcoholism[58]. The vitality, survival rate and count of sperm have dose and time effect relationship with alcoholism[58]. The alcoholic nature increases the teratozoospermia and oligozoospermia significantly[59]. The teratozoospermia is a condition where sperm with abnormal morphology are present where as oligozoospermia refers to semen with a low concentration of sperm.

Neurological complications: The chronic and excessive alcohol consumption affects the nervous system. This causes disordered thinking, dementia, numbness and pain in hands and feet, and short-term memory loss[60]. Various studies have proved the association between alcohol and Alzheimer's disease (AD) and vascular dementia[61]. The high alcohol consumption is considered a risk for late-onset AD[62]. The initial studies with primary neuron culture had provided information about the ability of ethanol to exacerbate Aβ toxicity and neuron cell death mechanisms[63].

Conclusion

From the beginning of human civilization, ethanol remain one of the most commonly used and abused chemical compound on this earth. The alcoholic people develop various alcohol related health issues. The studies have suggested that the adverse effect of ethanol consumption is mainly due to its first metabolite, acetaldehyde. Acetaldehyde plays a crucial role in the alcoholic people and is responsible for the behavioural, neurochemical and neurotoxic actions. Also, ethanol has several targets in astrocytes and responsible for cell apoptosis neuroinflammation and neurodegeneration.

The interaction of ethanol with multiple neurotransmitter system is associated with ethanol tolerance, dependence, withdrawal symptoms, relapses etc. Alcoholic people suffer from vitamins and minerals deficiencies. Alcohol has been found to be associated with diseases like tumors, cancers, numerous cardiovascular and digestive diseases and neuropsychiatric conditions.

Acknowledgements

The authors are thankful to Council of Scientific & Industrial Research (CSIR), India, for financial support.

References

1. McGovern Patrick E. (2010). Uncorking the past: The quest for wine, beer, and other alcoholic beverages. Berkley (CA), University of California Press, 1-352, ISBN: 0520253795.

2. NIH (2016). National Institute on Alcohol Abuse and Alcoholism. www.niaaa.nih.gov; retrieved on May 22, 2016

3. Stahre M., Roeber J., Kanny D., Brewer R.D. and Zhang X. (2014). Contribution of excessive alcohol consumption to deaths and years of potential life lost in the United States. *Preventing Chronic Disease,* 11, E109.

4. World Health Organization (WHO) (2014). Global status report on alcohol and health. 13-14.

5. Hanson G.R., Venturelli P.J. and Fleckenstein A.E. (2012). Drugs and Society. Jones and Bartlett Learning, 201, ISBN-13: 978-1284036374.

6. Montoliu C., Sancho-Tello M., Azorin I., Burgal M., Valler S., Renan J. and Guerri C. (1995). Ethanol increases cytochrome P4502E1 and induced oxidative stress in astmcytes. *J. Neurochem.*, 65(6), 2561-2570.

7. Hashimoto T., Ueha T., Kuriyama T., Katsura M. and Kuriyama K. (1989). Acetaldehyde-induced alterations in metabolism of monoamines in mouse brain. *Alcohol Alcohol.*, 24, 91-99.

8. Hunt W. A. (1996). Role of acetaldehyde in the actions of ethanol on the brain: A review. *Alcohol*, 13, 147-151.

9. Wanga J., Du H., Jiang L., Ma X., de Graaf R.A., Behar K.L. and Mason G.F. (2013). Oxidation of ethanol in the rat brain and effects associated with chronic ethanol exposure. *Proc. Nat. Acad. Sci. USA*, 110(35), 14444-14449.

10. Deitrich R., Zimatkin S. and Pronko S. (2006). Oxidation of ethanol in the brain and its consequences. *Alcohol Res. Health*, 29(29), 266-273.

11. Sofroniew M.V. and Vinters H.V. (2010). Astrocytes: biology and pathology. *Acta Neuropathol.*, 119(1), 7-35.

12. Alfonso-Loeches S., Pascual-Lucas M., Blanco A.M., Sanchez-Vera I. and Guerri C. (2010). Pivotal role of TLR4 Receptors in alcohol-induced neuroinflammation and brain damage. *J. Neurosci.*, 30(24), 8285-8295.

13. Braza-Boïls A., Tomás M., Marín M.P., Megías L., Sancho-Tello M., Fornas E. and Renau-Piqueras J. (2006). Glycosylation is altered by ethanol in rat hippocampal cultured neurons. *Alcohol Alcohol*, 41(5), 494-504.

14. Zhou X., Su Z., Anishkin A., Haynes W.J., Friske E.M., Loukin S.H., Kung C. and Saimi Y. (2007). Yeast screens show aromatic residues at the end of the sixth helix anchor transient receptor potential channel gate. *Proc. Natl. Acad. Sci. USA.*, 104(39), 15555-15559.

15. Krystal J.H., Petrakis I.L., Mason G., Trevisan L. and D'Souza D.C. (2003). N-Methyl-D-aspartate glutamate receptors and alcoholism: reward, dependence, treatment, and vulnerability. *Pharmacol Ther.*, 99(1), 79-94.

16. Ron D. (2004). Signaling cascades regulating NMDA receptor sensitivity to ethanol. *Neuroscientist.,* 10(4), 325-336.

17. Ron D. and Messing R.O. (2013). Signaling pathways mediating alcohol effects. *Curr. Topics Behav. Neurosci.*, 13, 87-126.

18. Yang X., Criswell H.E., Simson P., Moy S. and Breese G.R. (1996). Evidence for a selective effect of ethanol on N-methyl-D-aspartate responses: ethanol affects a subtype of the ifenprodil-sensitive N-methyl-D-aspartate receptors. *J. Pharmacol. Exp. Ther.*, 278(1), 114-124.

19. Nagy J., Kolok S., Dezso P., Boros A. and Szombathelyi Z. (2003). Differential alterations in the expression of NMDA receptor subunits following chronic ethanol treatment in primary cultures of rat cortical and hippocampal neurones. *Neurochem. Int.*, 42(1), 35-43.

20. Lobo I.A. and Harris R.A. (2008). $GABA_A$ receptors and alcohol. *Pharmacol. Biochem. Behav.*, 90(1), 90-94.

21. Ravindran C.R.M. and Ticku M.K. (2006). Tyrosine kinase phosphorylation of GABA(A) receptor $\alpha1$, $\beta2$ and $\gamma2$ subunits following chronic intermittent ethanol (CIE) exposure of cultured cortical neurons of mice. *Neurochem. Res.,* 31(9), 1111-1118.

22. Silvers J.M., Tokunaga S., Mittleman G. and Matthews D.B. (2003). Chronic intermittent injections of high-dose ethanol during adolescence produce metabolic, hypnotic, and cognitive tolerance in rats. *Alcoholism: Clinical and Experimental Res.*, 27(10), 1606-1612.

23. Aguayo L.G., Peoples R.W., Yeh H.H. and Yevenes G.E. (2002). GABA(A) receptors as molecular sites of ethanol action. Direct or indirect actions?. *Curr. Top. Med. Chem.*, 2(8), 869-885.

24. Soyka M., Preuss U.W., Hesselbrock V., Zill P., Koller G. and Bondy B. (2008). GABA A2 receptor subunit gene (GABRA2) polymorphisms and risk for alcohol dependence. *J. Psychiat. Res.*, 42(3), 184-191.

25. Kumar S., Porcu P., Werner D.F., Matthews D.B., Diaz-Granados J.L., Helfand R.S. and Morrow A.L. (2009). The role of GABA (A) receptors in the acute and chronic effects of ethanol: a decade of progress. *Psychopharmacol.*, 205(4), 529-564.

26. Bowery N.G., Bettler B., Froestl W., Gallagher J.P., Marshall F., Raiteri M. and Enna S.J. (2002). International Union of Pharmacology. XXXIII. Mammalian gamma-aminobutyric acid(B) receptors: structure and function. *Pharmacol. Rev.*, 54(2), 247-264.

27. Federici M., Nistico R., Giustizieri M., Bernardi G. and Mercuri N.B. (2009). Ethanol enhances GABAB-mediated inhibitory postsynaptic transmission on rat midbrain dopaminergic neurons by facilitating GIRK currents. *Eur. J. Neurosci.*, 29(7), 1369-1377.

28. Lovinger D.M., White G. and Wright F.F. (1989). Ethanol inhibits NMDA-activated ion current in hippocampal neurones. *Science*, 243(4899), 1721-1724.

29. Boileau I., Assaad J.M., Pihl R.O., Benkelfat C., Leyton M., Diksic M. and Dagher A. (2003). Alcohol promotes dopamine release in the human nucleus accumbens. *Synapse*, 49(4), 226-231.

30. Dahmen N., Volp M., Singer P., Hiemke C. and Szegedi A. (2005). Tyrosine hydroxylase Val-81-Met polymorphism associated with early-onset alcoholism. *Psychiat. Genet.*, 15(1), 13-16.

31. Sander T., Harms H., Podschus J., Finckh U., Nickel B., Rolfs A. and Schmidt L.G. (1997). Allelic association of a dopamine transporter gene polymorphism in alcohol dependence with withdrawal seizures or delirium. *Biolog. Psychiat.*, 41(3), 299-304.

32. Feinn R., Nellissery M. and Kranzler H.R. (2005). Meta-analysis of the association of a functional serotonin transporter promoter polymorphism with alcohol dependence. *Amer. J. Med. Gen. Part B: Neuropsych. Gen.*, 133B(1), 79-84.

33. Korsten M.A. (1989). Alcoholism and pancreatitis: Does nutrition play a role?. *Alcohol Health and Res. World*, 13(3), 232-237.

34. Feinman L. (1989). Absorption and utilization of nutrients in alcoholism. *Alcohol Health and Res. World*, 13(3), 207-210.

35. Watson Ronald Ross and Preedy Victor R (2003). Nutrition and Alcohol: Linking Nutrient Interactions and Dietary Intake. CRC Press, 1-448, ISBN 9780849316807.

36. Marsano L. and McClain C.J. (1989). Effects of alcohol on electrolytes and minerals. *Alcohol Health and Res. World*, 13(3), 255-260.

37. Feinman L. (1989). Absorption and utilization of nutrients in alcoholism. *Alcohol Health and Res. World*, 13(3), 207-210.

38. Mahan L.K. and Escott-Stump S. (2000). Krause's food, nutrition, and diet therapy. 10th ed., W.B. Saunders Company, Philadelphia, ISBN: 0721679048.

39. Combs G.F. Jr. (2008). The vitamins: Fundamental Aspects in Nutrition and Health. (3rd ed.). Elsevier Academic Press, Amsterdam, Boston, ISBN: 978-01-21834-93-7.

40. Clugston R.D. and Blaner W.S. (2012). The Adverse Effects of Alcohol on Vitamin A Metabolism. *Nutrients*, 4(5), 356-371.

41. Roncone D.P. (2006). Xerophthalmia secondary to alcohol-induced malnutrition. *Optometry*, 77(3), 124-133.

42. Shield K.D., Parry C. and Rehm J. (2013). Chronic diseases and conditions related to alcohol use. *Alcohol Res.: Curr. Rev.*, 35(2), 155-173.

43. International agency for Research on Cancer (IARC) (2010). International Agency for Researchon Cancer Monographs on the Evaluation of Carcinogenic Risks to Humans. 96, Alcoholic Beverage Consumption and Ethyl Carbamate (Urethane).

44. Song D.Y., Song S., Song Y. and Lee J.E. (2012). Alcohol intake and renal cell cancer risk: a meta-analysis. *British J. Cancer*, 106(11), 1881-1890.

45. Tramacere I., Pelucchi C., Bonifazi M., Bagnardi V., Rota M., Bellocco R., Scotti L., Islami F., Corrao G., Boffetta P., La Vecchia C. and Negri E. (2012). Alcohol drinking and non-Hodgkin lymphoma risk: A systematic review and a meta-analysis. *Ann. Oncol.*, 23(11), 2791-2798.

46. Tramacere I., Negri E., Pelucchi C., Bagnardi V., Rota M., Scotti L., Islami F., Corrao G., La Vecchia C. and Boffetta P. (2012). A meta-analysis on alcohol drinking and gas-tric cancer risk. *Ann. Oncol.*, 23(1), 28-36.

47. Tramacere I., Pelucchi C., Bonifazi M., Bagnardi V., Rota M., Bellocco R., Scotti L., Islami F., Corrao G., Boffetta P., La Vecchia C. and Negri E. (2012). A meta-analysis on alcohol drinking and the risk of Hodgkin lymphoma. *Eur. J. Cancer Prevent.*, 21(3), 268–273.

48. MacSween R.N. and Burt A.D. (1986). Histologic spectrum of alcoholic liver disease. *Semin Liver Dis.*, 6(3), 221-232.

49. Tuma D.J. and Casey C.A. (2003). Dangerous byproducts of alcohol breakdown-focus on adducts. *Alcohol Res. Health*, 27(4), 285-290.

50. Chowdhury P. and Gupta P. (2006). Pathophysiology of alcoholic pancreatitis: An overview. *World J. Gastroenterol*, 12(46), 7421-7427.

51. Vonlaufen A., Wilson J.S., Pirola R.C. and Apte M.V. (2007). Role of *alcohol* metabolism in chronic pancreatitis. *Alcohol Res. Health*, 30(1), 48-54.

52. Moreira E.D., Glasser D.B., Nicolosi A., Duarte F.G. and Gingell C. (2008). Sexual problems and help-seeking behaviour in adults in the United Kingdom and continental Europe. *BJU Int.*, 101(8), 1005-1011.

53. Rivier C., Rivest S. and Vale W. (1992). Alcohol-induced inhibition of LH secretion in intact and gonadectomized male and female rats: Possible mechanisms. *Alcohol., Clinical and Exp. Res.*, 16(5), 935-941.

54. Grover S., Mattoo S.K., Pendharkar S. and Kandappan V. (2014). Sexual dysfunction in patients with alcohol and opioid dependence. *Ind. J. Psycholog. Med.*, 36(4), 355-365.

55. Silva P.D., Cool J.L. and Olson K.L. (1999). Impact of lifestyle choices on female infertility. *J Reprod. Med.*, 44(3), 288–296.

56. Grodstein F., Goldman M.B. and Cramer D.W. (1994). Infertility in women and moderate alcohol use. *Am. J. Public Health*, 84(9), 1429-1432.

57. Jensen T.K., Hjollun N.H.I., Henriksen T.B., Scheike T., Kolstad H., Giwercman A., Ernst E., Bonde J.P., Skakkebæk N.E. and Olsen J. (1998). Does moderate alcohol consumption affect fertility? Follow-up study among couples planning first pregnancy. *BMJ*, 317(7157), 505-510.

58. Gude D. (2012). Alcohol and fertility. *J. Human Reprod. Sci.*, 5(2), 226-227.

59. Gaur D.S., Talekar M.S. and Pathak V.P. (2010). Alcohol intake and cigarette smoking impact of two major lifestyle factors on male fertility. *Ind. J. Pathol. Microbiol.*, 53(1), 35-40.

60. Hillbom M., Pieninkeroinen I. and Leone M. (2003). Seizures in alcohol-dependent patients. *CNS Drugs*, 17(14), 1013-1030.

61. Freund G. and Ballinger W.E. Jr. (1992). Alzheimer's disease and alcoholism: Possible interactions. *Alcohol*, 9(3), 233-240.

62. Fratiglioni L., Ahlbom A., Viitanen M. and Winblad B. (1993). Risk factors for late-onset Alzheimer's disease: A population-based, case-control study. *Ann. Neuroi.,* 33(3), 258-266.

63. Sun A.Y., Lusiak B.D. and Sun G.Y. (2001). Oxidized lipoproteins, beta amyloid peptides and Alzheimer's disease. *Neurotoxicity Res.*, 3(2), 167-178.

View publication stats

Asian Journal of Applied Science and Technology (AJAST)

Volume 1, Issue 7, Pages 104-115, August 2017

An Intermediate Temperature Stable, Extracellular and Alkaline Lipase from *Pseudomonas aeruginosa* and Its Application in Biodiesel Production

Vineet Kumar Goswami[1] and Jai Gopal Sharma[2]

[1,2]Laboratory of Environmental and Industrial Biotechnology, Department of Biotechnology, Delhi Technological University, Shahbad- Daulatpur, Delhi, India. Email: sharmajaigopal@gmail.com

Article Received: 24 July 2017 *Article Accepted: 08 August 2017* *Article Published: 16 August 2017*

ABSTRACT

An intermediate temperature stable, alkaline lipase from a newly isolated *Pseudomonas aeruginosa* strain was produced on a defined minimal medium and was found to have 800 IU/L of lipase under un-optimized conditions. Crude lipase produced by *Pseudomonas aeruginosa* was characterized for its biochemical properties and it was found to have temperature optima of 60°C with broad range of temperature activity from 40°C to70°C and pH optima was found to be 9.0 with sudden decline in lipolytic activity at pH other than 9.0. Crude enzyme was concentrated by ammonium sulfate precipitation and it was immobilized onto Celite® for is application for biodiesel production.

Keywords: Biodiesel, Enzyme characterization, Lipase and Pseudomonas aeruginosa.

1. INTRODUCTION

Lipases (triacylglycerol acylhydrolases, E.C. 3.1.1.3) catalyze the hydrolysis of triacylglycerols into glycerol and fatty acids under aqueous conditions but under low water conditions and non- aqueous conditions they can catalyze the reverse reaction [1]. Apart from their activity over a broad range of pH, temperature and variety of substrate, their ability to catalyze enantioselective, chemoselective and regioselective [2] reactions make them the biotechnological tool of choice for biocatalysis and synthetic chemistry. Owning to their unique properties, they occupy a distinct position among all the enzymes and they have diverse applications in a wide variety of industries [3]. Although numerous applications of lipases have been documented in literature but it is still a challenge to identify the most suitable lipase for specific need such as enantioselectivity and regioselectivity, and best reaction conditions for an efficient application, because property of each lipase varies from other and its application is largely governed by its characteristic properties. Frequently used methods such as immobilization and optimization of the reaction medium cannot be transferred from one reaction system or substrate to another, this makes the task more challenging for finding a suitable lipase for a particular application. Industrial demand for highly active preparations of lipolytic enzymes with appropriate specificity and stability to pH, temperature, ionic strength and organic solvents continues to stimulate the search for new enzyme sources of their unique industrial applications [4]. One such application which has remarkably gained the momentum in recent decade is, its application in nano-biotechnology

© 2017 AJAST All rights reserved.

and biodiesel production, biodiesel being a renewable, biodegradable, and nontoxic fuel, has come up as a potential alternative fuel to meet the future fuel demands.

Biodiesel is defined as the fatty acid methyl esters (FAME) which are derived from triglycerides by transesterification with methanol [5]. Several successful attempts for biodiesel production have been made in past using soybean oil [6,7], sunflower oil [8,9], cotton seed oil [10], rapeseed oil [11], palm oil [12,13] restaurant kitchen waste [14] and Jatropha oil [15].

Here, we report an extracellular, alkaline and intermediate temperature stable lipase from *Pseudomonas aeruginosa* with its applicability and catalytic potential as biotechnological tool for biodiesel production.

2. MATERIALS AND METHODS

All analytical reagents and media components were locally purchased from established brands such as SRL, India; Hi-Media, India; Merck, India and Celite® 209 and standards (99.99% pure by GC) of methyl oleate and methyl linoleate were purchased from Sigma Aldrich, USA.

2.1 Bacterial strain and inoculum preparation

Strain of *Pseudomonas aeruginosa* was isolated from the soil of waste disposal site of Mic- Mac canteen of Delhi Technological University, Delhi and it was identified using Gaby-Hadley Reagents A and B [16-17] and was also confirmed as described by [18]. Initially, it was grown at 37°C in nutrient broth (pH 7.0) with shaking at 250 rpm for 24hrs. For lipase production, 1ml of 4hrs old culture was used to inoculate the production flasks containing 100ml production media (Table 1). The extracellular lipolytic potential of the isolated stain was confirmed by tributyrin agar plate assay and gel diffusion assay [19-20].

Table 1.: Defined minimal media for the production of lipase from *Pseudomonas aeruginosa*

S. No.	Media Component	Composition (%)
1.	Glucose	2.00
2.	Olive oil	1.50
3.	K_2HPO_4	0.30
4.	KH_2PO_4	0.10
5.	$MgSO_4.7H_2O$	0.01
6.	NH_4Cl	0.50

2.2 Enzyme production and lipase assay

The enzyme was produced at shake flask level in 250ml flasks on a defined minimal media (Table 1). pH of the production media was adjusted to 7.0 by 0.1N NaOH before autoclaving. Olive oil was used from the stock of 10% olive oil emulsion

© 2017 AJAST All rights reserved.

with water in presence of 2% gum acacia. After the inoculation, production media was incubated at 37°C, 250rpm for 24hrs. Cell free culture broth was collected as supernatant by centrifugation at 15,000g for 20min. at 4°C using Eppendorf® 5810R centrifuge (Eppendorf, Germany) and its extra cellular lipolytic activity was again confirmed as described in [21-24] and total protein was estimated by Lowry's method [25]. The supernatant was concentrated by 60% ammonium sulfate precipitation followed by dialysis against pH 9.0 Tris-HCl buffer before its immobilization onto Celite® 209 (Sigma Aldrich, USA) as described in [15, 26-27].

2.3 Lipase unit

One International Unit (IU) of lipase is defined as the amount of enzyme required to liberate 1 μmol of fatty acid per ml per minute under standard assay conditions.

2.4 Characterization of lipase

Temperature and pH optima

Using pNPP as a substrate [23], initially, lipase assay was performed at neutral pH and at different temperature ranging from 20°C-90°C for identifying the temperature optima of lipase activity and thereafter, lipase assay was performed at known optimal temperature and at varied pH (3.0- 11.0) range for ascertaining the pH optima of the lipase [28].

Substrate specificity

To study the substrate specificity, lipase activity on different emulsified oils was calculated against olive oil as the standard using the method as described in [29, 30] at defined optimal temperature and pH.

2.5 Application of lipase in biodiesel production

One of our previous report [31] suggested that the maximum conversion of olive oil into its respective methyl esters (methyl oleate and methyl linoleate) can take place just in six hours using 2000 IU of *Pseudomonas aeruginosa* lipase and hence six hours was fixed as reaction time. Synthesis of biodiesel under solvent conditions by transesterification was done by using 5ml of olive oil and 5ml of methanol and they were allowed to react in presence of varied lipase units (200- 3000 IU) of Celite immobilized *Pseudomonas aeruginosa* lipase at 60°C and 200 rpm for 6hrs and the final volume of methanol was raised to 15ml by adding first dose of 5 ml methanol after 2hrs of reaction and second dose of 5ml methanol after 4hrs of reaction so as to reach the final equimolar concentration of free fatty acid and methanol and to minimize the deactivation of lipase in presence of methanol.

The reaction was terminated by collection of solvent layer after separation by centrifugation at 15000g at 4°C for 10 minutes using Eppendorf® 5810R centrifuge (Eppendorf, Germany). Excess of solvent was evaporated by vacuum evaporation and the residue was dissolved in 1.0ml of n-hexane for GC analysis. The percentage yield was also estimated and percent yield was expressed as the percentage molar conversion of olive oil to ester after titrating the residual fatty acid against 0.01 N KOH using phenolphthalein as an indicator.

© 2017 AJAST All rights reserved.

2.6 Gas Chromatography analysis

GC analysis was done as described in [31]. For GC analysis, 1.0 µl aliquot of the sample was injected onto capillary column using AOC- 20i auto injector in split mode on a Shimadzu GC-2010 Gas Chromatography (Shimadzu, Japan). The GC was equipped with Restek® Rxi®-5Sil MS capillary column with 30-meter column length and 0.25 mm ID which was having a coating of 5% diphenyl and 95% dimethyl polysiloxane as stationary phase with uniform phase/ film thickness of 0.25µm. The column pressure cut off was kept at 130.0 kPa and a constant flow rate of 1.2 mL/min was maintained. The initial column oven temperature was kept at 140°C and the final temperature was raised to 280°C for a total run time of 40 min. The FID detector was used which was set at 270°C and hydrogen was used as carrier gas and the helium was used as makeup gas while air flow was maintained at 400ml/min.

3. RESULTS AND DISCUSSION

3.1 Temperature and pH optima

The extracellular lipase produced by *Pseudomonas aeruginosa* was purified 1.5-fold (Table 2) using ammonium sulfate precipitation followed by dialysis against pH 9.0 buffer and immobilization. The lipase was active over a broad range of temperature (40°C- 70°C) with temperature optima of 60°C (Fig. 1a). Similar trend has been observed for *Pseudomonas aeruginosa* MTCC 2488 lipase [32]. It has been observed that the lipases from various *Pseudomonas spp*. are active over a broad temperature range between 30°C- 80°C and some of them have been found to have temperature optima as high as 70°C [33, 34]. Some of the bacterial lipases have been found to be stable upto 70°C [35-36]. Although, a few lipases may operate at 100°C but they have short half-life as for example lipase from *P. fluorescens* [37].

Table 2: Summary of partial purification of *Pseudomonas aeruginosa* lipase

Purification steps	Total activity (IU/L)	Total protein (mg)	Specific enzyme activity (IU/mg protein)	Yield (%)	Fold purification	
					With respect to previous step	Over all
Cell free fermentation broth						
Crude	800.00	65.00	12.30	100.00	1.00	1.00
Ammonium Sulfate precipitation and dialysis						
Partially purified	720.00	48.00	15.00	90.00	1.21	1.21
Immobilization on Celite®209						
Immobilized	480.00	26.00	18.46	66.66	1.23	1.50

The pH optima and activity studies were performed at 60°C and the enzyme was found to be active within the narrow pH range of 7.0- 9.0 and there was a sharp decline in lipase activity on the either side of this pH range (Fig. 1b). This makes this enzyme alkaline in nature which can be used for various industrial processes and biocatalytic reactions operating at alkaline

© 2017 AJAST All rights reserved.

pH. The enzyme was optimally active at pH 9.0 and the activity at pH 9.0 was considered as 100% activity. Lipase from *Bacillus thermoleovorans* have been reported to be active at pH 9.0 [38] and lipases from *Bacillus pumilus* LV01 and *Pseudomonas fragi* have been reported to be optimally active at pH 9.0 [33, 39].

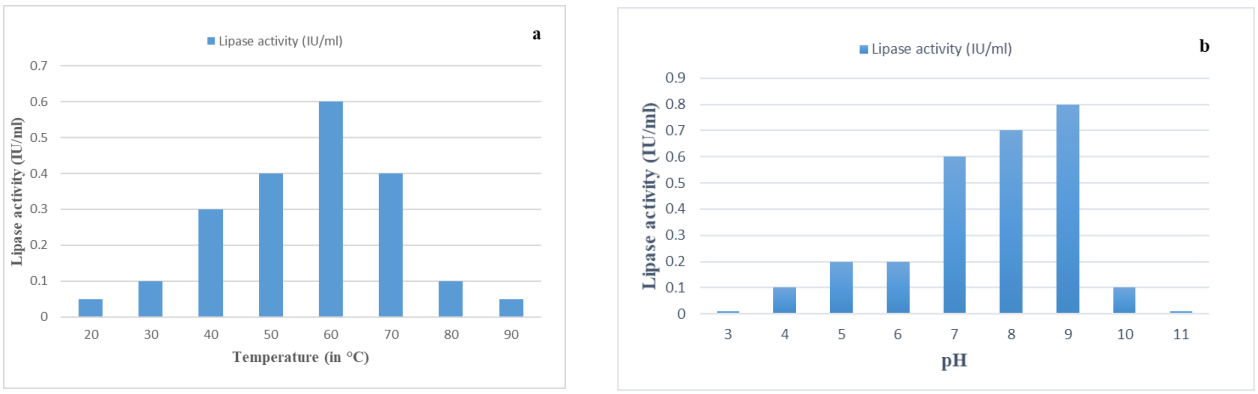


Fig. 1: *Pseudomonas aeruginosa* lipase activity at various (a) temperature and (b) pH

3.2 Substrate specificity

Activity using olive oil as substrate was considered as 100% and the relative activity was calculated for rest of the oils as substrate with respect to the activity on olive oil. Relative activity for castor oil was found to be 123.40% which was the highest among all the oils whereas lowest relative activity (4.4%) was observed in case of sunflower oil.

Thus, this lipase from *Pseudomonas aeruginosa* selectively catalyzes the hydrolysis of castor oil, mustard oil and olive oil whereas a decline in activity of 40% or more was observed in case of other oils (Table 3 and Fig. 2a). Since major fatty acid composition of castor oil is ricinoleic acid (12-hydroxy cis-Δ^9-octadecenoic acid) which is 18 carbon fatty acid and major fatty acid composition of olive oil is oleic acid (cis-Δ^9-octadecenoic acid) which is also 18 carbon fatty acid while for mustard oil, olive oil is second major constituent fatty acid after erucic acid.

This indicates that the *Pseudomonas aeruginosa* lipase is selective for the glycerides of 18 carbon fatty acids (ricinoleic acid and oleic acid). A similar affinity of *Pseudomonas* sp. lipase has been reported by Rathi *et al.* [40]. The higher affinity of the lipase for castor oil is of potential use in the castor oil based industry since the major component of castor oil is ricinoleic acid, which has numerous industrial application [41].

On olive oil as emulsified substrate, K_m and V_{max} for the *Pseudomonas lipase* were found to be 20µM and 12 µmol per ml per second respectively (Fig. 2b) which confirms its greater affinity towards the glycerides of cis-Δ^9-octadecenoic acid (olive oil) and its derivatives, such as 12-hydroxy cis-Δ^9-octadecenoic acid (castor oil).

© 2017 AJAST All rights reserved.

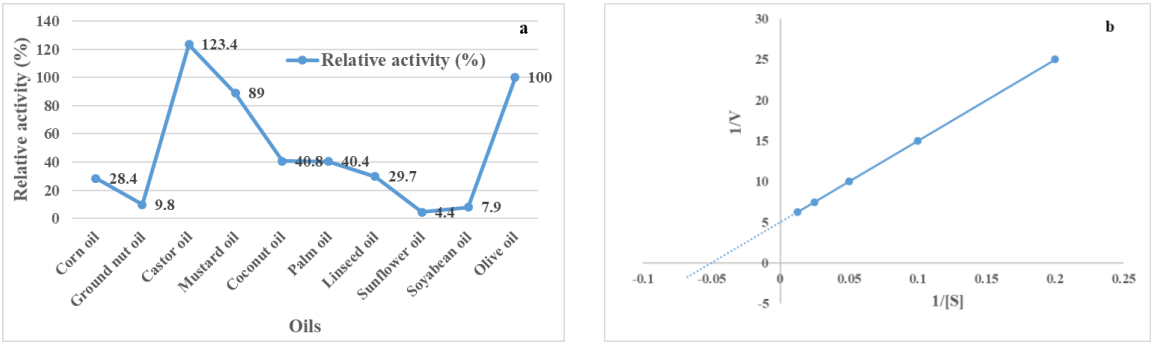


Fig. 2: *Pseudomonas aeruginosa* lipase (a) relative activity on various oils as emulsified substrate and (b) Lineweaver-Burk plot using emulsified olive oil as substrate

Table 3: Substrate specificity of *Pseudomonas aeruginosa* lipase at 60°C and pH 9.0 in aqueous conditions using various emulsified oils as substrate.

S.No.	Oil as substrate	Relative activity (%)		S.No.	Oil as substrate	Relative activity (%)
1.	Corn oil	28.40		6.	Palm oil	40.40
2.	Ground nut oil	9.80		7.	Linseed oil	29.70
3.	Castor oil	123.40		8.	Sunflower oil	4.40
4.	Mustard oil	89.00		9.	Soyabean oil	7.90
5.	Coconut oil	40.80		10	Olive oil	100.00

Table 4: Synthesis of biodiesel (major olive oil methyl esters) using immobilized *Pseudomonas aeruginosa* lipase and percent yield of biodiesel.

S. No.	Enzyme units (IU)	Percent yield	
		Methyl oleate	Methyl linoleate
1.	200	1.00	nd$^{\neq}$
2.	500	32.27	27.00
3.	1000	57.78	50.53
4.	1500	83.14	76.38
5.	2000	93.26	86.46
6.	2500	94.00	86.92
7.	3000	93.86	86.53

nd$^{\neq}$ not detected

3.3 Biodiesel production and GC analysis

Synthesis of biodiesel (FAME) by transesterification of major constituent fatty acids (oleic acid and linoleic acid) of olive oil with the help of Celite® 209 immobilized *Pseudomonas lipase* into their respective methyl esters revealed that the majority of biodiesel (methyl oleate and methyl linoleate) was synthesized while using 2000 IU of lipase and further

© 2017 AJAST All rights reserved.

increase in enzyme concentration could not enhance the conversion rate and over all yield whereas 200 IU lipase could not produce any significant results (Table 4 and Fig. 3). It is evident from the results that the *Pseudomonas aeruginosa* lipase can successfully mediate the esterification reactions for the synthesis of biodiesel.

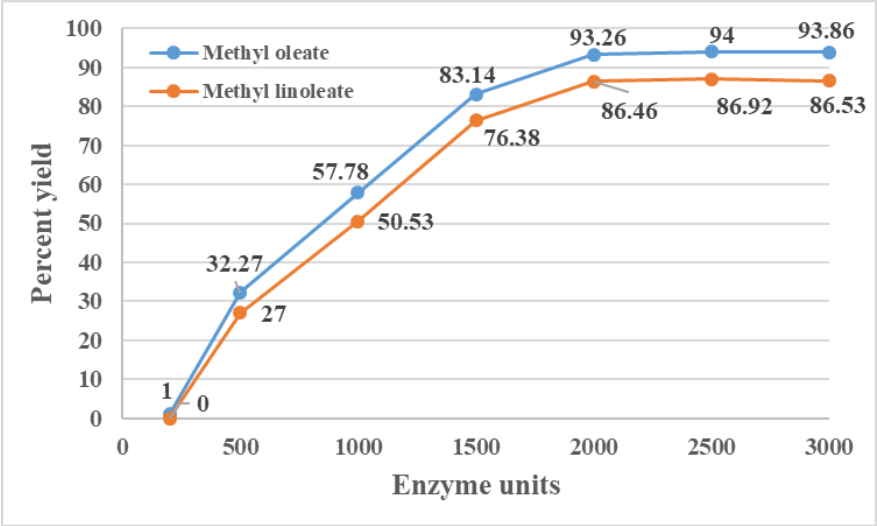
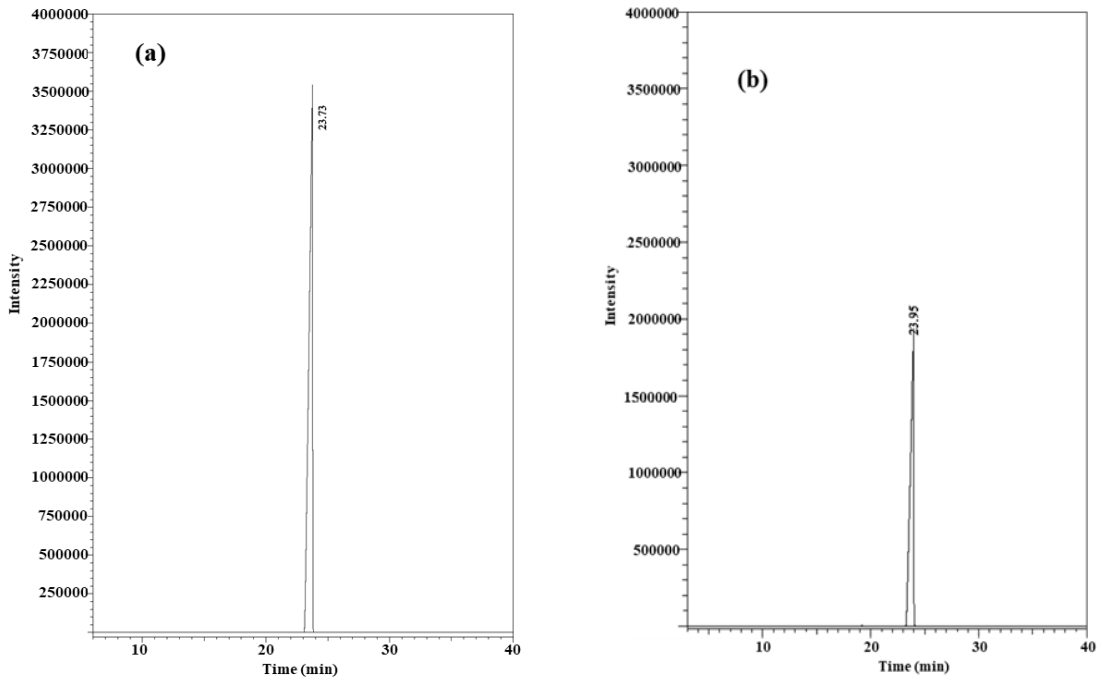


Fig. 3: Percent yield of biodiesel (methyl oleate and methyl linoleate) using olive oil and methanol as substrate in presence of *Pseudomonas aeruginosa* lipase



© 2017 AJAST All rights reserved. Online ISSN: 2456-883X Publication Impact Factor: 0.825 Website: www.ajast.net

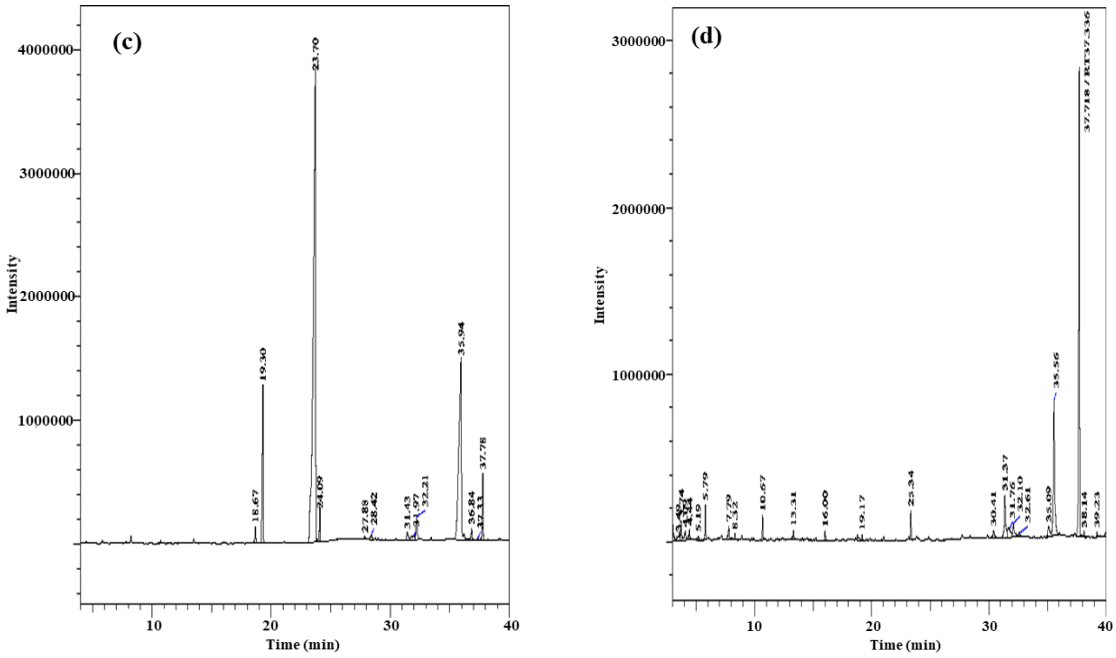


Fig. 4: GC chromatogram of standard (a) methyl oleate, (b) methyl linoleate and (c) test sample with 2000 IU lipase units (d) control.

GC analysis revealed that retention time (RT) of methyl oleate and methyl linoleate are very close (23.73 min and 23.95 min respectively) and this can be attributed to the fact that they do not differ much in chemical formula, structure and properties (Fig. 5) and hence their chemical behavior remains almost same towards the GC column stationary phase.

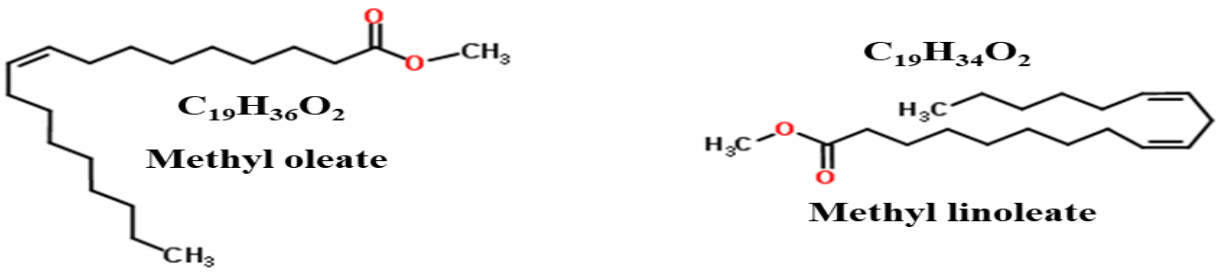


Fig. 5: Structure of methyl oleate and methyl linoleate

Synthesis of olive oil esters using various alcohols over a range of temperature (10- 90°C) have been reported by Kenz *et al.* [42] wherein they could achieve a maximum of 17.0% methyl oleate synthesis at 50°C in 3hrs while Marzuki *et al.* [43] reported 90.90% yield of methyl oleate using nano-bioconjugates *Candida rugusa* lipase.

© 2017 AJAST All rights reserved. Online ISSN: 2456-883X Publication Impact Factor: 0.825 Website: www.ajast.net

4. CONCLUSION

We have presented here lipase production under unoptimized conditions which indicates quite low levels of lipase and to make the process economical viable we need to further optimize the production conditions.

However, these are preliminary investigations with respect to the lipase production from the laboratory isolate of *Pseudomonas aeruginosa* but downstream processing and characterization of partially purified lipase indicates that it's an intermediate temperature stable alkaline lipase which can be used for the biocatalysis and other industrial process operating at alkaline pH. There are several similar reports for the production, downstream processing and characterization of lipase but all of them says either enzyme is active at pH 9.0 or 60°C but none of them suggests a lipase operating at alkaline pH and 60°C temperature simultaneously hence, it's a unique report with respect to the properties such as pH and temperature.

The downstream processing which we have tried could just enhance the purification of lipase by 1.5-fold. It has been observed that sometimes properties of enzymes vary with degree of their purity and hence we further need to enhance the purification of this lipase to escalate its catalytic efficacy to make it more suitable for industrial needs.

Affinity of this lipase for the glycerides of cis-Δ^9-octadecenoic acid (olive oil) and its derivatives, such as 12-hydroxy cis-Δ^9-octadecenoic acid (castor oil) makes it a suitable biocatalytic tool for the industries based on olive oil and castor oil.

Since this lipase can effectively and efficiently catalyze the synthesis of fatty acid methyl esters this indicates that it can be a potential enzyme for green chemistry for esterification and transesterification. Non-edible oils should to be tried for biodiesel production using this lipase so that its scope in biodiesel industry can be proposed.

5. ACKNOWLEDGEMENT

The authors sincerely thank Delhi Technological University for financial support to carry out this research and also thank Mr. Ajay, AIRF, JNU, New Delhi for GC analysis of samples.

REFERENCES

[1] Jaeger K.E., Ransac S., Dijkstra B.W., Colson C., van Heuvel M, Misset O., Bacterial lipases. *FEMS Microbiol. Rev.* 15, (1994), 29-63.

[2] Vulfson, E.N., Industrial application of lipases. In: Woolley P, Petersen SB, eds. Lipases: their structure, biochemistry and application, Cambridge, Cambridge University Press, (1994), 271-288.

[3] Ghosh P.K., Saxena R.K., Gupta R., Yadav R.P., Davidson W.S., Microbial lipases: production and applications, *Sci. Prog.* 79, (1996), 119-157.

[4] Lee S.Y., Rhee J.S., Production and partial purification of a lipase from *Pseudomonas putida* 3SK. *Enzyme Microb. Technol.* 15, (1993), 617-623.

© 2017 AJAST All rights reserved.

[5] Fukuda H., Kondo A., Noda, H., Biodiesel fuel production by transesterification of oils, *J. of Bio. Sci. and Bio. Engg.*, 92, 5 (2001), 405-416.

[6] Schwab A.W., Dykstra G.J., Selke E., Sorenson S.C., Pryde E.H., Diesel fuel from thermal decomposition of soybean oil. *J. Am. Oil Chem. Soc*. 65, (1988), 1781-1786.

[7] Samukawa T., Kaieda M., Matsumoto T., Ban K., Kondo A., Shimada Y., Noda H., Fukuda H., Pretreatment of immobilized *Candida antarctica* lipase for biodiesel fuel production from plant oil. *J. Bio Sci. and Bio Engg*., 90, (2000), 180- 183.

[8] Dossat V., Combes D., Marty A., Lipase-catalyzed transesterification of high oleic sunflower oil. *Enzyme Microbiol Technol*., 30, (2002), 90-94.

[9] Be´lafi-Bako´, K., Kova´cs, F., Gubicza, L., Hancso´k, J., Enzymatic biodiesel production from sunflower oil by *Candida antarctica* lipase in a solvent free system. *Biocatal Biotransform*. 20, 2002, 437- 439.

[10] Köse, Ö., Tüter, M., Aksoy, H.A., Immobilized *Candida antarctica* lipase catalyzed alcoholysis of cotton seed oil in a solvent-free medium. *Bioresource Technology* 83, 2, (2002), 125-129.

[11] Nelson L.A., Foglia T.A., Marmer W.N., Lipase catalyzed production of biodiesel. *J Am Oil Chem Soc*; 73, (1996), 191-195.

[12] Abigor R.P., Vadia P., Foglia T., Hass M., Jones K., Okefa E., Obibuzor J., Bator M., Lipase catalyzed production of biodiesel fuel from some Nigerian lauric oils. *Biochem Soc Trans* 28, (2000), 979-981.

[13] Crabbe E., Nolasco-Hipolito C., Kobayashi G., Sonomoto K., Ishizaki A., Biodiesel production from crude palm oil and evaluation of butanol extraction and fuel properties. *Process Biochem.* 37, (2001), 65-71.

[14] Hsu A.F., Jones K., Foglia T.A., Marmer W.N., Immobilized lipase-catalyzed production of alkyl esters of restaurant grease as biodiesel. *Biotechnol. App.l Biochem.*, 36, (2002), 181- 186.

[15] Shah S. and Gupta M. N., Lipase catalyzed preparation of biodiesel from Jatropha oil in a solvent free system, *Process Biochemistry* 42 (2007) 409-414.

[16] Gaby, W.L., and C. Hadley. Practical laboratory test for the identification of *Pseudomonas aeruginosa*. *J. Bacteriol.* 74, (1957), 356-358.

[17] Gaby W. L., and Free L., Differential diagnosis of *Pseudomonas* like microorganisms in the clinical laboratory. *J. Bateriol.* 76, (1958), :442-444.

[18] Reyes E.A.P., Bale M.J., Cannon W.H., Matesn J.M., Identification of *Pseudomonas aeruginosa* by pyocyanin production on Tech Agar, *J. clinical Microbiology*, 13, 3, (1881), 456-458.

[19] Lawrence R.C., Fryer T.F., Reiter B., Rapid method for quantitative estimation of microbial lipases, *Nature*, 25, (1967), 1264-1265.

[20] Singh R., Gupta N. Goswami V.K., Gupta, R., A simple activity staining protocol for lipases and esterases, *Appl. Microbiol. Biotechnol.* 70, (2006), 679-682.

[21] Gupta N., Rathi P., Gupta R. Simplified para-nitrophenyl palmitate assay for lipases and esterases. *Anal Biochem*., 311, (2002), 98-99.

© 2017 AJAST All rights reserved. Online ISSN: 2456-883X Publication Impact Factor: 0.825 Website: www.ajast.net

[22] Liu D., Yu Y., Wong W.K.R., Zhao X., Zhang J., An enzyme-like polyclonal antibody capable of catalyzing ester hydrolysis. *Enzyme and Microbial Technology*, 20, (1997), 24-31.

[23] Winkler U.K., Stuckmann M., Glycogen, hyaluronate, and some other polysaccharides greatly enhance the formation of exolipase by *Serratia marcescens*. *J Bacteriol*., 138, (1979), 663-670.

[24] Nahas E., Control of lipase production by *Rhizopus oligosporus* under various growth conditions. *J. Gen. Microbiol*., 134, (1988), 227-233.

[25] Lowry, O.H., Rosebrough, N.J., Farr, A.L., Randall, R.J., Protein measurement with the Folin Phenol reagent, *J. Biol. Chem.*,193, (1951), 265-275.

[26] Triantafyllou A.O., Aldercreutz P., Mattiasson B., Influence of the reaction medium on enzyme activity in bio-organic synthesis: behavior of lipase from *Candida rugosa* in the presence of polar additives 17, (1993), 167- 179.

[27] Tripathi R., Singh J., Bharti R.K., Thakur I.S., Isolation, purification and characterization of lipase from *Microbacterium* sp. and its application in biodiesel production, *Energy Procedia*, 54 (2014) 518- 529.

[28] Bussamara R., Fuentefria A.M., de Oliveira E.S., Broettoa L., Simcikova M., Valente P., Schrank A., Vainstein M.H., Isolation of a lipase secreting yeast for enzyme production in a pilot plant scale batch fermentation, *Bioresource Technology* 101 (2010) 268-275.

[29] Naka, Y. and Nakamura, T., The effect serum albumin and related amino acids on pancreatic lipase and bile salts inhibited microbial lipases, *Biosci. Biotechnol. Biochem.* 56, (1992), 1066-70.

[30] Ferrarezi A.L, Ohe T.H.K, Borges J.P., Brito R.R., Siqueira M.R., Vendramini P.H., Quilles Jr. J.C., da Costa C.N.C, Rodriguez G.O.B, Boscolo M., Da Silva R., Gomes E., Production and characterization of lipases and immobilization of whole cell of the thermophilic *Thermomucor indicae seudaticae* N31 for transesterification reaction, *Journal of Molecular Catalysis B: Enzymatic*, 107 (2014) 106-113.

[31] Goswami, V.K. and Sharma J.G., Time kinetics studies of enzyme catalyzed hydrolysis of triolein and transesterifications of olive oil for the synthesis major olive oil methyl esters using *Pseudomonas aeruginosa* lipase, Asian Journal of Applied Science and Technology, 1, 7 (2017), 38-46.

[32] Kukreja V. and Bern M.B., Lipase from *Pseudomonas aeruginosa* MTCC 2488: Partial purification, characterization and calcium dependent thermostability, *Indian Journal of Biotechnology*, 4, (2005), 222-226.

[33] Nishio T.; Chikano T.; Kamimura, M., Purification and some properties of lipase produced by *Pseudomons fragi* 22.39 B. *Agric. Biol. Chem*., 51, (1987), 181-186.

[34] Gilbert E.J., *Pseudomonas lipases*: biochemical properties and molecular cloning. *Enzyme Microb. Technol*., 15, (1993), 634-645.

[35] Nawani N., Dosanjh N.S., Kaur J., A novel thermostable lipase from a thermophilic *Bacillus* sp.: characterization and esterification studies. *Biotech. Lett.* 20, (1988), 997-1000.

[36] Kulkarni N. and Gadre R.V., A novel alkaline, thermostable, protease-free lipase from *Pseudomonas* sp. *Biotech. Lett.* 21, (1999), 897-899.

[37] Taipa M.A., Aires-Barros M.R., Cabral J.M.S., Purification of lipases. *J. Biotechnol.* 26, (1992), 111-142.

© 2017 AJAST All rights reserved.

[38] Lee D.W., Kim H.K., Lee K.W., Kim B.C., Choe A.C., Lee H.S., Purification and characterization of two distinct thermostable lipases from the gram-positive thermophilic bacterium *Bacillus thermoleovorans* ID-1, *Enzyme Microb. Tech.* 29, (2001), 363-71.

[39] Mariana N.G., Virginia A., Vargas H.A. Michal S., Lipolytic enzyme production by halophilic/halotolerant microorganisms isolated from laguna verde, Bolivia, *Revista Boliviana de Química*. 25, 1, (2008), 14-23.

[40] Rathi P., Bradoo S., Saxena R.K., Gupta R., A hyper-thermostable, alkaline lipase from *Pseudomonas* sp. with the property of thermal activation, *Biotechnology Letters* 22, (2000), 495–498.

[41] Ogunniyi D.S., Castor oil: A vital industrial raw material, *Bioresource Technology*, 97, (2006), 1086-1091.

[42] Kenz, Z., Leitgeb, M., Zavrsnik, D. Lavric, B., Synthesis of oleic acid esters with immobilized lipase, *Fat Sci Technol*., 92, 4, (1990), 169-172.

[43] Marzuki, N.H.C., Huyop, F., Enein, H.Y.A., Mahat N.A., Wahab, R.A., Modelling and optimization of *Candida rugosa* nanobioconjugates catalysed synthesis of methyl oleate by response surface methodology, Biotechnology & Biotechnological Equipment, 29, 6, (2015), 1113-1127.

© 2017 AJAST All rights reserved.

emeraldinsight

Journal of Modelling in Management

Analysing the interaction of factors for Flexibility in Supply Chains
Rajesh Singh, Saroj Koul, Pravin Kumar,

Article information:

To cite this document:
Rajesh Singh, Saroj Koul, Pravin Kumar, "Analysing the interaction of factors for Flexibility in Supply Chains", Journal of Modelling in Management, https://doi.org/10.1108/JM2-04-2016-0039
Permanent link to this document:
https://doi.org/10.1108/JM2-04-2016-0039

Downloaded on: 25 September 2017, At: 22:33 (PT)
References: this document contains references to 0 other documents.
To copy this document: permissions@emeraldinsight.com
The fulltext of this document has been downloaded 7 times since 2017*
Access to this document was granted through an Emerald subscription provided by emerald-srm:544911 []

For Authors

If you would like to write for this, or any other Emerald publication, then please use our Emerald for Authors service information about how to choose which publication to write for and submission guidelines are available for all. Please visit www.emeraldinsight.com/authors for more information.

About Emerald www.emeraldinsight.com

Emerald is a global publisher linking research and practice to the benefit of society. The company manages a portfolio of more than 290 journals and over 2,350 books and book series volumes, as well as providing an extensive range of online products and additional customer resources and services.

Emerald is both COUNTER 4 and TRANSFER compliant. The organization is a partner of the Committee on Publication Ethics (COPE) and also works with Portico and the LOCKSS initiative for digital archive preservation.

*Related content and download information correct at time of download.

Downloaded by Delhi Technological University At 22:33 25 September 2017 (PT)

Analysing the interaction of factors for Flexibility in Supply Chains

Structured Abstract

Purpose: In present scenario of global competition and economic recession, most of the organizations are facing tough challenge to survive in the market due to shortening product life cycle and reducing profit margin. Customers are seeking better design, production, and delivery, which have made firms concentrate on flexibility in supply chains. Therefore this study is aimed at identifying major factors and the development of a suitable framework for flexibility in supply chains.

Design and Research Methodology: Based on literature review, about fourteen factors have been identified. To develop relationship among these factors, a team of five experts from industry and academia was formed. Based on inputs from experts, different relationships are developed among factors to form Structural Self-Interaction Matrix (SSIM). Based on this matrix, a flexibility framework is devlopped by Interpretive Structural Modeling approach.

Findings: Top Management commitment, Strategy development for flexible SC, Application of Advance technology and IT Tools, Information sharing in SC members, Trust development among supply chain members have emerged as major driving factors. Logistics and warehouse management, suppliers flexibility, distribution flexibility and manufacturing flexibility have emerged as dependent factors.

Value: Findings of the study can be useful for industry professionals to develop strategies for flexible supply chains. It will help them in taking new initiatives for making supply chains more responsive and proactive for customers demand.

Limitations: The framework developed in this study is based on input given by team of experts while applying interpretive Structural Modelling. This framework can be further validated with some case analysis and empirical studies**.**

Keywords: Flexibility, Supply Chain Management, Performance, Product life cycle etc.

Downloaded by Delhi Technological University At 22:33 25 September 2017 (PT)

© Emerald Publishing Limited

This is a pre-print of a paper and is subject to change before publication. This pre-print is made available with the understanding that it will not be reproduced or stored in a retrieval system without the permission of Emerald Publishing Limited.

Analysing the interaction of factors for flexibility in supply chains

1. Introduction

Supply chain is a form of industrial organization that allows buyers and sellers, who are separated by time and space to progressively add value as products pass form one member of the chain to the next (Hughes 1994, Handfield and Nichols, 1999). Supply chains are effective networks of firms functioning in a particular product/service value chain (Stevenson, 2007). In present context of globalisation, customer requirements are changing continuously and product life cycle is shortening. Firms have acknowledged the importance of flexibility in meeting customer demands and improving responsiveness under uncertain conditionss (Vickery et al., 1999). Uncertainty in the supply chains can take many forms, e.g. uncertainty regarding the reliability of suppliers, the actions of competitors, or the quality of products. One of the key sources of uncertainty in the supply chain relates to the quantities, timings and specifications of end-customer demand and is a key cause of the bullwhip effect (Disney and Towill, 2003). Most literature on manufacturing and supply chain flexibility describes flexibility as a response to, or a means to cope with, uncertainty (Sheffi and Rice, 2005).
Flexibility is typically defined in terms of range, mobility and uniformity, i.e. the ability to move from making one product to making another and the ability to perform comparably well when making any product within a specified range (Slack, 1983; Upton, 1995). To meet emerging challenges of dynamic markets, flexibility in whole supply chain has become essential. Flexibility at a particular firm level will not be able to meet market challenges. All members of supply chain i.e. suppliers, manufacturers, distributors and retailers have to be flexible in their operations. By aligning flexibility with the external environment, organizations can ensure profit and sales performance.

Duclos et al. (2003) developed a conceptual model of supply chain flexibility consisting of six components. Lummus et al. (2003 have considered five elements such as operational systems, logistics processes, supply network, organizational design and information systems flexibility. Most notably, logistics (processes) flexibility relates to receiving and delivering products as sources of supply and customers change, while supply (network) flexibility refers to the ability to re-configure the supply chain, altering the supply of products in line with demand. Vickery et al.(1999) defines that supply chain flexibility comprises of those flexible dimensions that directly impact a firm and are shared among various functions i.e internal (marketing, manufacturing) or external (suppliers, channel members). Flexibility is most commonly associated with the literature on Manufacturing Flexibility which emerged in the 1980s and 1990s with seminal papers by Slack (1983, 1987), Gerwin (1987, 1993) and Upton (1995). Singh and Sharma (2014) have considered manufacturing, customers and suppliers flexibility as alternatives for improving overall flexibility of supply chains. Chiang et al. (2012) have observed that strategic sourcing and firm's strategic flexibility were significantly related to the firm's supply chain agility. According to Gunasekaran et al. (2001), flexibility refers to making available the the products/service to meet the individual demand of customers. According to them this has become possible as a result of the development of such technologies as flexible manufacturing systems, group technology, and computer-integrated manufacturing (CIM). In addition, other methods such as single minute exchange of die, as well as information technology (IT) and communication systems facilitate quick response and provide online information. A more detailed conceptual model on supply chain flexibility dimensions has been provided by Duclos et al. (2003). According to them, flexibility in the supply chain adds the requirement of flexibility within and between all partners in the chain, including departments within an organisation, and

Downloaded by Delhi Technological University At 22:33 25 September 2017 (PT)

© Emerald Publishing Limited
This is a pre-print of a paper and is subject to change before publication. This pre-print is made available with the understanding that it will not be reproduced or stored in a retrieval system without the permission of Emerald Publishing Limited.

the external partners, such as suppliers, carriers, third-party companies, and information systems providers.

With growth in outsourcing, companies are increasingly relying on service providers and sources of supply and realizing the need of management and integration of the whole value chain from vendor to consumer (Fisher, 1997; Lambert et al., 1998; Croom et al.,2000; Jack and Raturi, 2002), blurring the traditional boundaries of the firm. Due to high competence and responsiveness, it has become important to understand how certain organizational conditions enable firms to develop the ability to respond to the change. These conditions have been referred to as "Factors of flexibility" because their presence in the organization appears to support the ability to thrive in uncertain and dynamic environments (Dove, 1995; Goldman and Nagel, 1993). According to Vickery et al., (1999), Flexibility in supply chains may well represent a potential source to improve the company's efficiency and may be a significant measure of supply chain performance. The objectives of this paper are to identify major factors for flexible supply chain management (FSCM) and develop a structural model from an implementation perspective. Organization of this paper is as follows. Section two deals with literature review i.e. identification of factors, section three deals with research methodology i.e. Interpretive Structural Modelling (ISM), section four deals with the results and discussion and finally conclusion.

Downloaded by Delhi Technological University At 22:33 25 September 2017 (PT)

2. Literature Review

There are many factors influencing flexibility in supply chains. These may be related to people, machines and ICT (Vander and Beulens, 2002). Some of the crucial factors for analysing the interaction of factors for flexibility in supply chains are discussed in this section.

1. Top management commitment

According to Kumar et al. (2015), top management support is essential for success of any supply chain. Singh (2015) has observed that top management initiatives help in making supply chain responsive and flexible. Jennings and Kenley (1996) have found that total quality management, supply base management, customer driven corporate policy and other elements of supply chain management are the key strategic options available to achieve competitiveness. Top management commitment plays a key role in implementing different initiatives. However, efforts made by companies in order to implement these options have not been universally successful and have even failed in many cases to yield the desired results (Griffith, 2006). Regression models introduced by Kola and Latvala (2003) and Yee et al. (2005) have identified several factors that directly and positively impact corporate performance. These include the extent to which companies analyze the strategies of competitors and determine future customer requirements, and the commitment (Tan et al., 1999).

2. Strategy development for flexible SC

Managing the supply chains has become very important. Chandra and Kumar (2000) have discussed about the role of planning and coordination in an integrated system in creating a framework for the appropriate structure and better control. Firms are finding that they can no longer compete effectively in isolation of their suppliers or other entities in the supply chain (Spekman et al., 1998). Lummus and Vokurka (1999) have observed that linking a firm's supply

© Emerald Publishing Limited
This is a pre-print of a paper and is subject to change before publication. This pre-print is made available with the understanding that it will not be reproduced or stored in a retrieval system without the permission of Emerald Publishing Limited.

chain strategy to its overall business strategy and some practical guidelines can lead to successful supply chain management. Strategic flexibility is the capability of the company to respond quickly to changing competitive conditions in order to develop and sustain competitive advantage. Strategic flexibility allows the firm in developing future manufacturing strategies, which help them to react swiftly to the changing nature of internal and external conditions.

3. Information sharing among SC members

Sanchez and Perez (2005) have observed that information technology can help supply chain members in improving the performance of supply chain systems. Suarez et al., (1996) have derived optimal inventory policies under different information sharing scenarios. It is also found that information sharing reduces the level of behavioral uncertainty, which, in turn, improves the level of trust (Sanchez and Perez, 2005). Jennings and Kenley (1996) have presented a framework for understanding the evolution of buyer-supplier relationships during the last two decades from transaction processes based on arms-length agreements to collaborative processes based on trust and information sharing. Bhadani et al. (2016) have observed that organisations should invest in IT and telecommunication systems to improve information flow in supply chains.

4. Trust among supply chain partners

The presence of trust among supply chain partners can improve the chances of the supply chain to be flexible (Chan and Chan, 2009). A lack of trust among supply chain partners often results in inefficient and ineffective performance as the transaction costs (verification, inspections and certifications of their trading partners) increase (Singh, 2013). Firm's trust in its supply chain partner is highly associated with both sides' specific asset investments (positively) and behavioral uncertainty (negatively). A partner's reputation in the market should have a positive impact on the trust-building process, whereas partner's perceiving conflicts would lead to negative impact on trust (Gosain, 2005).

5. Collaborative decision making by SC members

Buyer-supplier relationships play an important role in an organization’s ability to respond to dynamic and unpredictable change. If the relationship is too restrictive, flexibility will be difficult to achieve and, if it is too lenient the risk of opportunism will be present. In order to achieve the objective of collaborative decision making , buyer-supplier relationship needs to be reviewed from the perspectives of transaction cost theory, strategy-structure theory and resource-based theory of the firm (Clarke and Varma, 1999). Singh (2013) has observed that flexibility in supply chain has the ability to change levels of production rapidly, to develop new products and to respond quickly to competitive threats. This requires managers to find the right balance between committing the resources necessary to carry out a decision and avoiding investment of good money in bad projects (Shimizu and Hitt, 2004).

6. Application of Advance technology and IT Tools

Advance Technology is a very important factor for all supply chains. Seamen (1995) have observed that applications of IT tools in the food industry have helped in reducing prices of

Downloaded by Delhi Technological University At 22:33 25 September 2017 (PT)

© Emerald Publishing Limited
This is a pre-print of a paper and is subject to change before publication. This pre-print is made available with the understanding that it will not be reproduced or stored in a retrieval system without the permission of Emerald Publishing Limited.

food items consistently. It is widely observed that the key differentiator between the successful and not so successful retailers is primarily in the area of technology. According to Mukhopadhyay (2009), technology can help the organized retailer to lead over the unorganized players, gaining both cost and service advantages. Karkkainen (2003) has showed that Radio-frequency identification (RFID) processes can be used to carry out continuous monitoring of backroom and shelf inventory, providing automated notification when replenishment is required. Hind (1994) has observed that RFID technology has been applied mainly in the organizational activities such as merchandise classification and tracking, data collection and analysis, production control, product authentication and authority identification. Both technological and design capabilities have a positive effect on technology commercialization. Upton (1995) has observed that the flexibility of the plants depends much more on people than on any technical factor.

According to Singh and Sharma (2014), flexibility in the supply chain can be enhanced by developing technological capabilities by making more investments in advanced technologies and giving more emphasis to human resource welfare related activities like training and education, recruitment policies, providing incentives on job training facilities and multi-skilling of the employees etc.

Downloaded by Delhi Technological University At 22:33 25 September 2017 (PT)

7. Logistics and Warehouse Management

The management of the flow and storage of materials and related information across supply chains is the fundamental feature of logistics management. Logistics services influences customers to evaluate firms on factors beyond the physical product. Hannon (2005) has emphasized the need for development of the proper Logistics system. A theoretical goal for facility location is identified: every plant should be located at the point of profit maximization (Smykay et al., 1961).

Richmond (2004) and Ahmed et al. (2005) have observed that the use of tools such as finite-element analysis (FEA) software can help packaging designers and engineers to study about complex packaging structure and optimise cost and performance effectively. They also observed that millions of dollars can be saved by substituting trial-and-error packaging design with rational math/science-based FEA. Agrawal et al. (2015) have felt the need for integrated logistic management for making supply chains more responsive and efficient.

8. Revenue and risk sharing

Jennings and Kenley (1996) have observed that risk Management has become a critical issue as a result of globalization. Revenue sharing is valuable in vertically separated industries in which demand is either stochastic (unpredictable) or variable (e.g., systematically declining). Unlike two-part tariffs, revenue sharing achieves the best outcome by softening retail price competition without distorting retailers. Supply chain risk management (SCRM) is of growing importance, as the vulnerability of supply chains increases. Fisher (1997); Lambert et al. (1998); Croom et al. (2000) and Jack and Raturi (2002) have tried to analyze, access and manage risk sources along the supply chain, partly by working closely with suppliers by placing formal requirements on them. It has been observed that risk related to traditional logistics concepts (time, cost, quality, agility and leanness) should be put into the trade-off analysis while evaluating new logistics solutions instead of minimizing risks (Norrman and Jansson, 2004).

9. Vendor Development

© Emerald Publishing Limited
This is a pre-print of a paper and is subject to change before publication. This pre-print is made available with the understanding that it will not be reproduced or stored in a retrieval system without the permission of Emerald Publishing Limited.

Many supply chains operate with poor forecasting and planning systems and operate with long cycle systems (Agarwal et al, 2014). They also have problems with unreliable inventory control systems, with no stock tracing and poor cost control. This can lead to excess, obsolete stock and eroding customer service levels (Gunasakeran et al., 2000).

Humphreys et al. (2004) and Singh et al. (2010) have observed that vendor development can help in improving the performance of not only buyers but of vendors also. By vendor development, buying firms can help their vendors in increasing their capabilities and improve their performance. It was found that higher rated vendors emphasize process management and employee satisfaction to a greater degree than lower rated vendors (Park et al., 2001). Voss (2013) has observed that purchasing managers prefer to purchase the highest quality product from their suppliers.

10. Training of Employees

Proper training of employees is considered a very important aspect for implementing new initiatives in a firm. According to Hui (2004) effective strategies and technologies can work to their optimum with proper leadership and trained employees. According to Boyer and Pagell (2000), new manufacturing capabilities can be only achieved when companies make infrastructural investments such as quality leadership, training and empowerment of employees.

11. Manufacturing flexibility

The process of choosing appropriate supply chain performance measures is difficult due to the complexity of these systems. Benita (1999) has considered manufacturing flexibility measures for supply chains performance. Singh and Sharma (2014) have observed that manufacturing flexibility is the most important alternative for supply chain flexibility. The availability of methods such as building smaller production units, cellular manufacturing systems, multipurpose machines, material handling and workforce agility has been cited as manufacturing flexibility approaches being integrated from shop floor to plant level (Upton, 1994; Vokurka and O'Leary, 2000). Gerwin (1993) and Upton (1995) have considered different aspect of flexible manufacturing system such as adoption of functions (flexibility in machine, labor, operation functions, logistics) or hierarchical (flexibility at shop-floor, plant and organization level) affecting the range of response towards the product volume and mix changes.

12. Supplier flexibility

It examines suppliers' ability to change as per market demands. Even though there has been a tremendous amount of research on the topic of flexibility, most of it has been confined to intra-firm flexibility concerns. JIT practices can help firms in achieving flexibility by reducing impediments of change. Gunasekaran et al. (2000) have observed that computer integrated manufacturing can help SMEs to reduce lead time, increase flexibility, reliability and customer service. Duclos et al. (2003) have identified opportunities for future cross-functional research that can build theoretical foundation and leads to more effective formulation of supply chain strategies. Girubha et al. (2016) have observed that selection of sustainable suppliers are crucial for ensuring success of supply chains.

13. Distribution Flexibility

Distribution Flexibility is used to guide organizations to measure and improve supply chain responsiveness and organizational performance. The research is carried out in order to identify that agile supply chain distribution enhances organizational performance. The critical distribution practices of supply chains that make supply chains agile are collaborative distribution, order commitment, distribution flexibility and inventory management. These practices have a significant impact on organizational performance (Khan et al., 2009). Changes

Downloaded by Delhi Technological University At 22:33 25 September 2017 (PT)

© Emerald Publishing Limited
This is a pre-print of a paper and is subject to change before publication. This pre-print is made available with the understanding that it will not be reproduced or stored in a retrieval system without the permission of Emerald Publishing Limited.

in overall warehouse locations, distribution of products among the warehouses, transportation network, and mode of transportation can emphasize the supply chain performance significantly. Chan and Chan (2009) conducted a number of simulation studies to investigate the effects on these two characteristics of the distributed supply chain, i.e. Flexibility and adaptability, which are subjected to uncertainty. Their research mainly focused on demand uncertainty and quality flexibility.

14. Flexible Supply Chain

To meet dynamic market requirements in terms of lead time, volume, variety, flexible supply chain is essential. Flexibility in supply chains represents a potential means of improving a company's efficiency and is one of significant measures of supply chain performance. Tummala et al. (2007) conducted a case study to identify important factors that are necessary for successful implementation of supply chain management (SCM) in an organization. Singh and Sharma (2015) have developed a TISM based framework to evaluate flexibility index of a supply chain. All above discussed factors for FSCM have been summarized in Table 1.

Downloaded by Delhi Technological University At 22:33 25 September 2017 (PT)

© Emerald Publishing Limited
This is a pre-print of a paper and is subject to change before publication. This pre-print is made available with the understanding that it will not be reproduced or stored in a retrieval system without the permission of Emerald Publishing Limited.

Table 1: Factors for Flexible Supply Chain Management (FSCM)

SN	**FACTORS**	**REFRENCES**
1	Top management commitment	Bhadani et al. (2016), Kumar et al. (2015), Singh (2015), Griffith, (2006), Yee et al., (2005), Kola and Latvala (2003), Tan et al. (1999), Jennings and Kenley (1996)
2	Strategy development for flexible SC	Singh and Sharma (2015), Kumar et al. (2015), Chandra and Kumar (2000), Spekman et al. (1998), Lummus et al (2003)
3	Information sharing in SC members	Bhadani et al. (2016), Chan and Chan (2009), Sanchez and Perez (2005), Suarez et al. (1996), Jennings and Kenley (1996), Duncan (1995)
4	Trust development among SC members	Singh, (2013), Chan and Chan (2009), Gosain (2005)
5	Collaborative decision making by SC members	Hoyt and Huq (2000), Laura, (2001) Clarke and Varma, (1999)
6	Application of Advance technology and IT Tools	Bhadani, et al. (2016), Mukhopadhyay (2009), Karkkainen (2003), Seamen (1995), and Hind (1994)
7	Logistics and Warehouse Management	Agrawal et al. (2015), Sharma and Bhat (2012b) Ralston et al. (2013), Hannon (2005), Smykay et al. (1961), Richmond (2004) and Ahmed et al. (2005)
8	Revenue and risk sharing	Sharma and Bhat (2012a), Jack and Raturi (2002), Norrman and Jansson (2004), Jennings and Kenley (1996), Fisher (1997); Lambert et al. (1998); Croom et al. (2000,
9	Vendor development	Bansal et al. (2014), Humphreys et al. (2005), Voss, (2013), Park et al. (2001), Gunasakeran et al. (2000)
10	Training of employees	Singh et al. (2007), Hui (2004), Boyer and Pagell (2000)
11	Manufacturing Flexibility	Singh and Sharma (2014), Sharma and Bhat (2013), Benita (1999), Upton (1995); Gerwin (1993); Upton (1995)
12	Supplier Flexibility	Girubha et al. (2016), Singh and Sharma (2014), Duclos et al. (2003), Leslie et al. (2003), Gunasekaran et al. (2000);
13	Distribution Flexibility	Agrawal et al. (2015), Khan et al., (2009), Chan and Chan (2009)
14	Flexible Supply Chain	Singh and Sharma (2015), Sharma and Bhat (2014), Chan and Chan (2009) Tummala et al. (2007), Christopher and Peck (2004)

Downloaded by Delhi Technological University At 22:33 25 September 2017 (PT)

© Emerald Publishing Limited
This is a pre-print of a paper and is subject to change before publication. This pre-print is made available with the understanding that it will not be reproduced or stored in a retrieval system without the permission of Emerald Publishing Limited.

3. Research methodology: The concept of Interpretive Structural Modeling (ISM) has been used for modeling Factors of FSCM. The basic idea of ISM is to decompose a complicated system into several subsystems (elements) by using practical experience of experts and their knowledge. The ISM process transforms unclear, poorly articulated mental models of systems into visible, well-defined models. Singh et al. (2007) have applied ISM for modeling of critical success factors for implementation of advanced manufacturing technologies in organizations. Bhadani et al. (2016) have used ISM for investment decision in the Indian mobile service sector. Steps involved in the ISM methodology are as follows:

1. Identification of Factors: The elements of the system are identified which are relevant to the problem or issue and then finalized with a group problem-solving technique like brainstorming sessions.
2. Contextual Relationship: From the factors identified in step 1, a contextual relationship is identified among factors. A structural self-interaction matrix (SSIM) is prepared based on pair-wise comparison of factors of the system under consideration.
3. Reachability matrix is developed from the SSIM and it is checked for transitivity. The transitivity of the contextual relation is a basic assumption made in ISM. It states that if a factor A is related to B and B is related to C, then A is necessarily related to C.
4. The reachability matrix obtained in step 3 is converted into the canonical matrix format by arranging the elements according to their levels.
5. From the canonical matrix form of the reachability matrix, a directed graph is drawn by means of vertices or nodes and lines of the edges and the transitive links are removed based on the relationships given above in the reachability matrix.
The resultant digraph is converted into an ISM, by replacing factors nodes with the statement.

3.1 Structural Self-Interaction Matrix (SSIM)

ISM methodology suggests the use of expert opinion in developing the contextual relationship among the factors. To develop a relationship among these factors, a team of five experts from industry and academia was formed. All experts were having more than ten years of experience. Three members were from industry and two members from academia. The majority view was considered as final decision. Based on the opinion of experts, Table 1 is developed. Four symbols are used to denote the direction of the relationship between the criterion (*i* and *j*):
V: criterion *i* will help to achieve criterion *j*;
A: criterion *j* will be achieved by criterion *i*;
X: criterion *i* and *j* will help to achieve each other
O: criterion *i* and *j* are unrelated.
The following statements would explain the use of the symbols V, A, X, and O in SSIM (Table 2):

- Factor 1 helps achieve Factor 2. This means that Factor namely "Top management commitment" will help to achieve factor "Strategy development for flexible SC". Thus, the relationship between factors 1 and 2 is denoted by "V" in the SSIM.
- Factor 3 can be achieved by factor 6, i.e. factor 6, namely, "Application of Advance technology and IT Tools" would help to achieve factor 3 i.e. "Information sharing among SC members". Thus, the relationship between these factors is denoted by "A" in the SSIM.

Downloaded by Delhi Technological University At 22:33 25 September 2017 (PT)

© Emerald Publishing Limited
This is a pre-print of a paper and is subject to change before publication. This pre-print is made available with the understanding that it will not be reproduced or stored in a retrieval system without the permission of Emerald Publishing Limited.

- Factors 4 and 3 help achieve each other. Factor 4, namely, "Trust development among SC members", and factor 3 namely, "Information sharing in SC members", help achieve each other. Thus, the relationship between these factors is denoted by "X" in the SSIM.
- No relationship exists between Trust development among SC members (Factor 4) and Application of Advance technology and IT Tools (Factor 6) and hence the relationship between these factors is denoted by "O" in the SSIM.

Table 2: Structural Self-Interaction Matrix (SSIM)

SN	Factors	1	2	3	4	5	6	7	8	9	10	11	12	13	14
1	Top management commitment		V	V	V	V	V	V	V	V	V	V	V	V	V
2	Strategy development for flexible SC			V	V	V	V	V	V	V	V	V	V	V	V
3	Information sharing among SC members				X	V	A	V	V	V	V	V	V	V	V
4	Trust development among SC members					V	O	V	V	V	O	O	V	V	V
5	Collaborative decision making by SC members						A	V	X	V	V	V	V	V	V
6	Application of Advance technology and IT Tools							V	O	V	V	V	V	V	V
7	Logistics and Warehouse Management								A	A	A	V	V	V	V
8	Revenue and risk sharing policies									V	O	V	V	V	V
9	Vendor development										A	V	V	V	V
10	Training of employees											V	V	V	V
11	Manufacturing Flexibility												X	X	V
12	Supplier Flexibility													X	V
13	Distribution Flexibility														V
14	Flexible Supply Chain														

Notes: Here for i< j; A: Factors j leads to Factors i; V: Factors i leads to Factors j; X: Factors i and j lead to each other; O: No relationship between i and j

3.2 Reachability Matrix

The SSIM is transformed into a binary matrix, called the initial reachability matrix by replacing V, A, X, O by 1 and 0 as per the case. The rules for the substitution of 1's and 0's are the following. Initial reachability matrix is given in Table 3.

- If the (i, j) entry in the SSIM is V, then the (i, j) entry in the reachability matrix becomes 1 and the (j, i) entry becomes 0.
- If the (i, j) entry in the SSIM is A, then the (i, j) entry in the reachability matrix becomes 0 and the (j, i) entry becomes 1.
- If the (i, j) entry in the SSIM is X, then the (i, j) entry in the reachability matrix becomes 1 and the (j, i) entry also becomes 1.

© Emerald Publishing Limited
This is a pre-print of a paper and is subject to change before publication. This pre-print is made available with the understanding that it will not be reproduced or stored in a retrieval system without the permission of Emerald Publishing Limited.

Downloaded by Delhi Technological University At 22:33 25 September 2017 (PT)

- If the (i, j) entry in the SSIM is O, then the (i, j) entry in the reachability matrix becomes 0 and the (j, i) entry also becomes 0.

Table 3: Initial Reachability Matrix

SN	FACTORS	1	2	3	4	5	6	7	8	9	10	11	12	13	14
1	Top management commitment	1	1	1	1	1	1	1	1	1	1	1	1	1	1
2	Strategic development for flexible SC	0	1	1	1	1	1	1	1	1	1	1	1	1	1
3	Information sharing in SC members	0	0	1	1	1	0	1	1	1	1	1	1	1	1
4	Trust development among link partners	0	0	1	1	1	0	1	1	1	0	0	1	1	1
5	Collaborative decision making by SC members	0	0	0	0	1	0	1	1	1	1	1	1	1	1
6	Application of Advance technology and IT Tools	0	0	1	0	1	1	1	0	0	1	1	1	1	1
7	Logistics and Warehouse Management	0	0	0	0	0	0	1	0	0	0	1	1	1	1
8	Revenue and risk sharing policies	0	0	0	0	1	0	1	1	1	0	1	1	1	1
9	Vendor development	0	0	0	0	0	0	1	0	1	0	1	1	1	1
10	Training of employees	0	0	0	0	0	0	1	0	1	1	1	1	1	1
11	Manufacturing Flexibility	0	0	0	0	0	0	0	0	0	0	1	1	1	1
12	Supplier Flexibility	0	0	0	0	0	0	0	0	0	0	1	1	1	1
13	Distribution Flexibility	0	0	0	0	0	0	0	0	0	0	1	1	1	1
14	Flexible Supply Chain	0	0	0	0	0	0	0	0	0	0	0	0	0	1

3.3 Level partitions

After considering transitivity effect, final reachability matrix is given in Table 4. From the final reachability matrix, the reachability and antecedent set for each factor are found. The reachability set consists of the element itself and other elements, which it may help achieve, whereas the antecedent set consists of the element itself and the other elements, which may help in achieving it. Then the intersection of these sets is derived for all elements. The element for which the reachability and intersection sets are same is the top-level element in the ISM hierarchy. The top-level element of the hierarchy would not help achieve any other element above their own level. Once the top-level element is identified, it is separated out from the other elements. Then, the same process finds the next level of element. This process continues till the levels of each element are found. All iterations for identification of levels of different factors are shown in Tables 5 to 12. These identified levels help in building the digraph and final model.

Downloaded by Delhi Technological University At 22:33 25 September 2017 (PT)

© Emerald Publishing Limited
This is a pre-print of a paper and is subject to change before publication. This pre-print is made available with the understanding that it will not be reproduced or stored in a retrieval system without the permission of Emerald Publishing Limited.

Table 4: Final Reachability Matrix

SN	FACTORS	1	2	3	4	5	6	7	8	9	10	11	12	13	14	D.P
1	Top management commitment	1	1	1	1	1	1	1	1	1	1	1	1	1	1	14
2	Strategy development for flexible SC	0	1	1	1	1	1	1	1	1	1	1	1	1	1	13
3	Information sharing in SC members	0	0	1	1	1	0	1	1	1	1	1	1	1	1	11
4	Trust development among SC members	0	0	1	1	1	0	1	1	1	1*	1*	1	1	1	11
5	Collaborative decision making by SC members	0	0	0	0	1	0	1	1	1	1	1	1	1	1	9
6	Application of Advance technology and IT Tools	0	0	1	1*	1	1	1	1*	0	1	1	1	1	1	11
7	Logistics and Warehouse Management	0	0	0	0	0	0	1	0	0	0	1	1	1	1	5
8	Revenue and risk sharing policies	0	0	0	0	1	0	1	1	1	1*	1	1	1	1	9
9	Vendor development	0	0	0	0	0	0	1	0	1	0	1	1	1	1	6
10	Training of employees	0	0	0	0	0	0	1	0	1	1	1	1	1	1	7
11	Manufacturing Flexibility	0	0	0	0	0	0	0	0	0	0	1	1	1	1	4
12	Supplier Flexibility	0	0	0	0	0	0	0	0	0	0	1	1	1	1	4
13	Distribution Flexibility	0	0	0	0	0	0	0	0	0	0	1	1	1	1	4
14	Flexible Supply Chain	0	0	0	0	0	0	0	0	0	0	0	0	0	1	1
	DEPENDENCE	1	2	5	5	7	3	10	7	9	8	12	13	13	14	109

D.P. - Driving Power, * - Transitivity Effect

Table 5: Iteration 1

Factor	Reachability Set	Antecedent set	Intersection set	Level
1	1,2,3,4,5,6,7,8,9,10,11,12,13,14	1	1	
2	2,3,4,5,6,7,8,9,10,11,12,13,14	1,2	2	
3	2,3,4,5,7,8,9,10,11,12,13,14	1,2,3,4,6	2,3,4	
4	2,3,4,5,7,8,9,10,11,12,13,14	1,2,3,4,6	2,3,4	
5	5,7,8,9,10,11,12,13,14	1,2,3,4,5,6,8	5,8	
6	3,4,5,6,7,8,10,11,12,13,14	1,2,6	6	
7	7,11,12,13,14	1,2,3,4,5,6,7,8,9,10	7	
8	5,7,8,9,10,11,12,13,14	1,2,3,4,5,6,8	5,8	
9	7,9,11,12,13,14	1,2,3,4,5,8,9,10	9	
10	7,9,10,11,12,13,14	1,2,3,4,5,6,8,10	10	

© Emerald Publishing Limited
This is a pre-print of a paper and is subject to change before publication. This pre-print is made available with the understanding that it will not be reproduced or stored in a retrieval system without the permission of Emerald Publishing Limited.

Downloaded by Delhi Technological University At 22:33 25 September 2017 (PT)

11	11,12,13,14	1,2,3,4,5,6,7,8,9,10,11,12,13	11,12,13	
12	11,12,13,14	1,2,3,4,5,6,7,8,9,10,11,12,13	11,12,13	
13	11,12,13,14	1,2,3,4,5,6,7,8,9,10,11,12,13	11,12,13	
14	14	1,2,3,4,5,6,7,8,9,10,11,12,13,14	14	I

Table 6: Iteration 2

Factor	Reachability set	Antecedent set	Intersection set	Level
1	1,2,3,4,5,6,7,8,9,10,11,12,13	1	1	
2	2,3,4,5,6,7,8,9,10,11,12,13	1,2	2	
3	2,3,4,5,7,8,9,10,11,12,13	1,2,3,4,6	2,3,4	
4	2,3,4,5,7,8,9,10,11,12,13	1,2,3,4	2,3,4	
5	5,7,8,9,10,11,12,13	1,2,3,4,5,6,8	5,8	
6	3,6,7,8,10,11,12,13	1,2,6	6	
7	7,11,12,13	1,2,3,4,5,6,7,8,9,10	7	
8	5,7,8,9,10,11,12,13	1,2,3,4,5,6,8	5,8	
9	7,9,11,12,13	1,2,3,4,5,8,9,10	9	
10	7,9,10,11,12,13	1,2,3,4,5,6,8,10	10	
11	11,12,13	1,2,3,4,5,6,7,8,9,10,11,12,13	11,12,13	II
12	11,12,13	1,2,3,4,5,6,7,8,9,10,11,12,13	11,12,13	II
13	11,12,13	1,2,3,4,5,6,7,8,9,10,11,12,13	11,12,13	II

Table 7: Iteration 3

Factor	Reachability set	Antecedent set	Intersection set	Level
1	1,2,3,4,5,6,7,8,9,10	1	1	
2	2,3,4,5,6,7,8,9,10	1,2	2	
3	2,3,4,5,7,8,9,10	1,2,3,4,6	2,3,4	
4	2,3,4,5,7,8,9,10	1,2,3,4	2,3,4	
5	5,7,8,9,10	1,2,3,4,5,6,8	5,8	
6	3,6,7,8,10	1,2,6	6	
7	7	1,2,3,4,5,6,7,8,9,10	7	III
8	5,7,8,9,10	1,2,3,4,5,6,8	5,8	
9	7,9	1,2,3,4,5,8,9,10	9	
10	7,9,10	1,2,3,4,5,6,8,10	10	

Downloaded by Delhi Technological University At 22:33 25 September 2017 (PT)

© Emerald Publishing Limited
This is a pre-print of a paper and is subject to change before publication. This pre-print is made available with the understanding that it will not be reproduced or stored in a retrieval system without the permission of Emerald Publishing Limited.

Table 8: Iteration 4

Factor	Reachability set	Antecedent set	Intersection set	Level
1	1,2,3,4,5,6,8,9,10	1	1	
2	2,3,4,5,6,8,9,10	1,2	2	
3	2,3,4,5,8,9,10	1,2,3,4,6	2,3,4	
4	2,3,4,5,8,9,10	1,2,3,4	2,3,4	
5	5,8,9,10	1,2,3,4,5,6,8	5,8	
6	3,6,8,10	1,2,6	6	
8	5,8,9,10	1,2,3,4,5,6,8	5,8	
9	9	1,2,3,4,5,8,9,10	9	IV
10	9,10	1,2,3,4,5,6,8,10	10	

Table 9: Iteration 5

Factor	Reachability set	Antecedent set	Intersection set	Level
1	1,2,3,4,5,6,8,10	1	1	
2	2,3,4,5,6,8,10	1,2	2	
3	2,3,4,5,8,10	1,2,3,4,6	2,3,4	
4	2,3,4,5,8,10	1,2,3,4	2,3,4	
5	5,8,10	1,2,3,4,5,6,8	5,8	
6	3,6,8,10	1,2,6	6	
8	5,8,10	1,2,3,4,5,6,8	5,8	
10	10	1,2,3,4,5,6,8,10	10	V

Table 10: Iteration 6

Factor	Reachability set	Antecedent set	Intersection set	Level
1	1,2,3,4,5,6,8	1	1	
2	2,3,4,5,6,8	1,2	2	
3	2,3,4,5,8	1,2,3,4,6	2,3,4	
4	2,3,4,5,8	1,2,3,4	2,3,4	
5	5,8	1,2,3,4,5,6	5	
6	3,6	1,2,6	6	
8	5,8	1,2,4,5,6,8	5,8	VI

Downloaded by Delhi Technological University At 22:33 25 September 2017 (PT)

© Emerald Publishing Limited
This is a pre-print of a paper and is subject to change before publication. This pre-print is made available with the understanding that it will not be reproduced or stored in a retrieval system without the permission of Emerald Publishing Limited.

Table 11: Iteration 7

Factor	Reachability set	Antecedent set	Intersection set	Level
1	1,2,3,4,5,6	1	1	
2	2,3,4,5,6	1,2	2	
3	2,3,4,5	1,2,3,4,6	2,3,4	
4	2,3,4,5	1,2,3,4	2,3,4	
5	5	1,2,3,4,5,6	5	VII
6	3,6	1,2,6	6	

Table 12: Iteration 8

Factor	Reachability set	Antecedent set	Intersection set	Level
1	1,2,3,4,6	1	1	XI
2	2,3,4,6	1,2	2	X
3	2,3,4	1,2,4,6	2,3,4	VIII
4	2,3,4	1,2,3,4	2,3,4	VIII
6	3,6	1,2,6	6	IX

Downloaded by Delhi Technological University At 22:33 25 September 2017 (PT)

4. Results and Discussion

Results have been discussed in two parts. The first part will try to develop ISM based framework for flexible supply chains and the second part will try to classify the factors based on driving and dependence power derived from final reachability matrix i.e. table 4.

4.1 Formation of ISM based Framework: Based on levels derived from different iterations and relations in final reachability matrix (Table 4), the structural framework is generated by means of vertices or nodes and lines of the edges. If there is a relationship between the factors i and j, this is shown by an arrow which points from i to j. This graph is called a directed graph or digraph. After removing the transitivities as described in ISM methodology, the digraph is finally converted into ISM as shown in Figure 1. Top management is at the bottom of framework i..e. major driving factor. It helps in strategy formulation for application of advanced technologies and developing trust in supply chains. Trust among members of supply chain helps in collaborative decision making and in sharing of revenue and risks. These initiatives help in developing vendors thereby improving flexibility in manufacturing and distribution and finally flexible supply chains. Flexible supply chains help organisations in meeting dynamic market requirements.

© Emerald Publishing Limited
This is a pre-print of a paper and is subject to change before publication. This pre-print is made available with the understanding that it will not be reproduced or stored in a retrieval system without the permission of Emerald Publishing Limited.

Downloaded by Delhi Technological University At 22:33 25 September 2017 (PT)

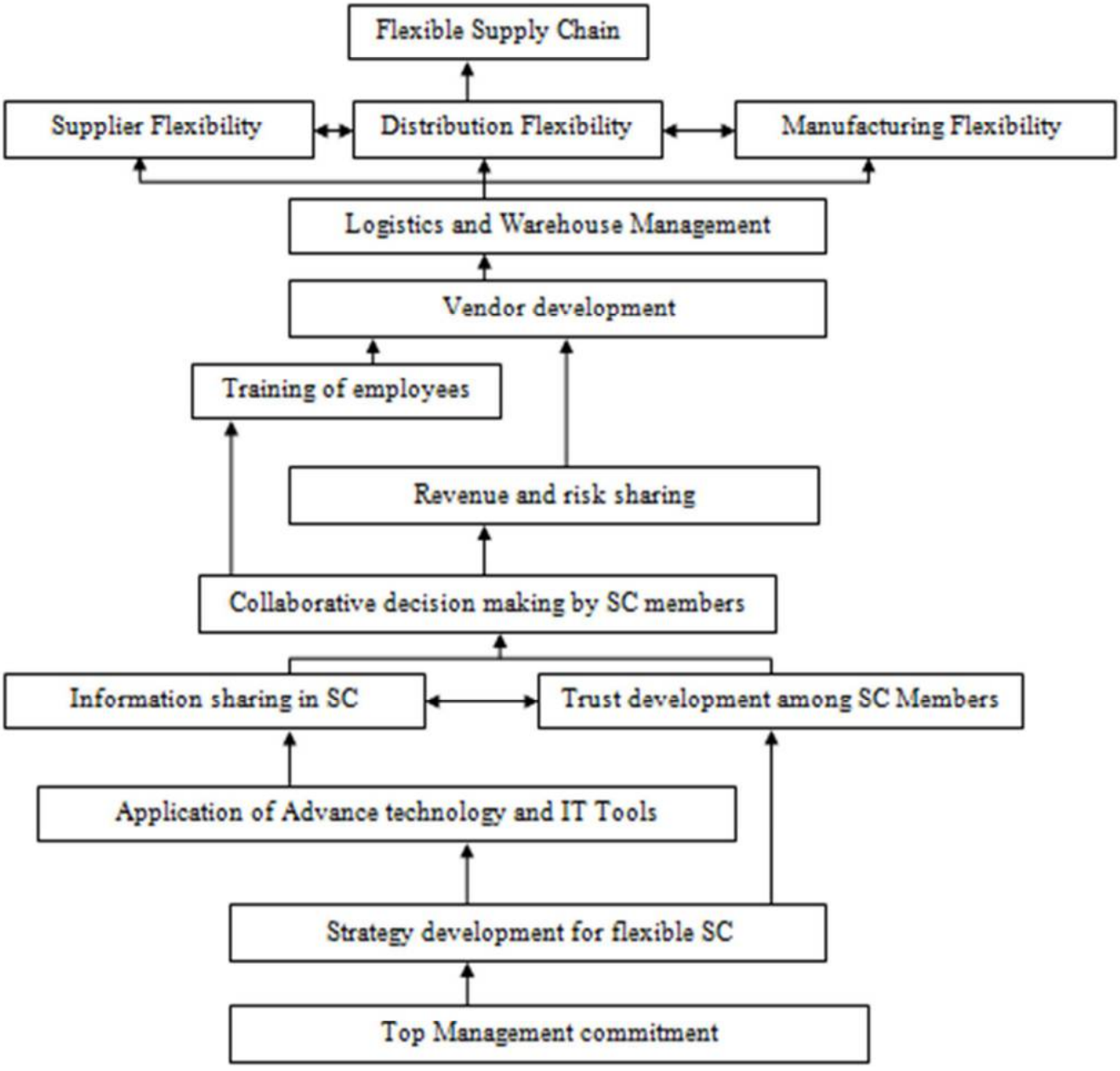


Figure 1- ISM based framework for Factors of Flexible Supply Chain Management

© Emerald Publishing Limited
This is a pre-print of a paper and is subject to change before publication. This pre-print is made available with the understanding that it will not be reproduced or stored in a retrieval system without the permission of Emerald Publishing Limited.

4.2 Classification of Factors: Based on the driving power and the dependence, these factors for flexible supply chain management have been classified into four clusters i.e (i) Autonomous (ii) Dependent (iii) Linkages (iv) Drivers. These factors are shown in figure 2.

Cluster I: Weak Driving Power and Weak Dependence
This group is called Autonomous or Excluded Factors. They appear quite out of line with the system. However, a distinction may be drawn within this group between the disconnected factors situated near the axis's origin, whose evolution, therefore, seems to be rather excluded from the system's global dynamics and secondary levers. These Factors are located in the south-west frame. The analysis reveals that factor 10 i.e. training of employees comes under this category (Figure 2).

Cluster II: Weak Driving Power and Strong Dependence:
These Factors are called dependent Factors, or result oriented factors. These factors, located in the south-east frame of the chart, are at the same time little influent and very dependent. So, they are especially sensitive to the evolution of influent factors. In this study factors 7,9,11,12,13,14 namely logistics and warehouse management, vendor development, supplier flexibility, distribution flexibility, manufacturing flexibility, flexible supply chain management fall in this cluster (Figure 2) . This finding implies that flexible supply chain management can be analyzed in terms of these results oriented factors.

Cluster III: Strong Driving Power and Strong Dependence:
These Factors are at the same time very influencing and very dependent. They are also called Linkages factors. These Factors are situated in the north-east frame of the chart and are unstable. Any action on these indicators will have impact on others and feedback effect on themselves which may amplify or support the initial pulse. These are usually unstable factors. In present study there is no factor in this cluster (Figure 2).

Cluster IV: Strong Driving Power and Weak Dependence:
These Factors are altogether very influential and very less dependent on others. These Factors are located in the north-west frame of the diagram (Figure 2) and known as drivers of the system. Most of the dependent factors or results dimensions depend on these Factors. “Top management commitment”(Factor-1) ,” Strategy development for flexible SC”(factor-2), “Information sharing in SC members”(factor-3), “Trust among SC members”(factor-4), “Application of advance technology ” (factor-6) , “Collaborative decision making”(factor-5), Revenue and risk sharing policies (Factor-8) are the factors in this zone and are ranked as independent factors as they are having the strong driving power.

© Emerald Publishing Limited
This is a pre-print of a paper and is subject to change before publication. This pre-print is made available with the understanding that it will not be reproduced or stored in a retrieval system without the permission of Emerald Publishing Limited.

Downloaded by Delhi Technological University At 22:33 25 September 2017 (PT)

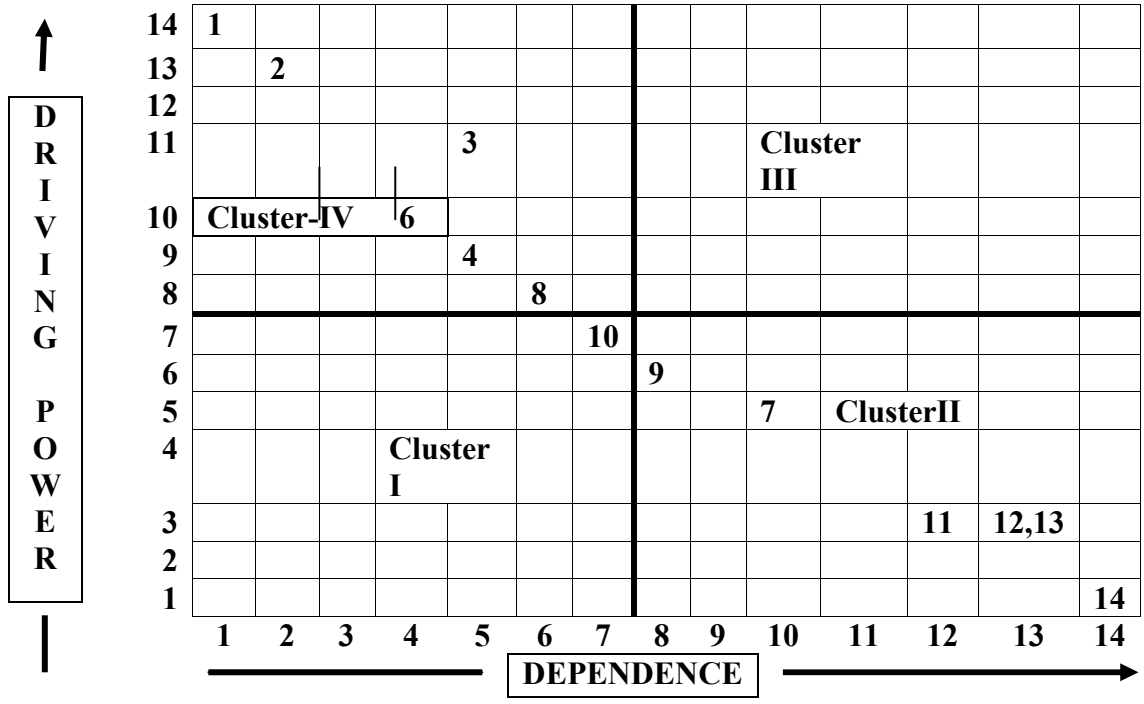


Figure 2: Classification of Factors

Conclusion

This study has tried to identify the different factors for flexible supply chain management. Total fourteen factors are identified from the literature. Then ISM approach is applied to develop a framework based on relationships among different factors. Based on driving and dependence power different factors are classified into four clusters, i.e. (i) Autonomous (ii) Dependent (iii) Linkages (iv) Drivers

It is observed from ISM framework, that top management commitment is a major driver for developing effective strategies to improve flexibility in supply chain. Strategies should focus on application of advanced IT systems to improve information flow and trust among supply chain partners. Information flow and mutual trust among supply chain members , will help in collaborative decision making to provide effective training for employees and for developing a mechanism to share the revenue and risk among supply chain partners. By taking these initiatives, organizations can improve vendors and logistics management capability. Vendors development and logistics management capability will improve suppliers' flexibility, distribution flexibility and manufacturing flexibility, which will ultimately lead to flexibility in

© Emerald Publishing Limited
This is a pre-print of a paper and is subject to change before publication. This pre-print is made available with the understanding that it will not be reproduced or stored in a retrieval system without the permission of Emerald Publishing Limited.

Downloaded by Delhi Technological University At 22:33 25 September 2017 (PT)

supply chains. These findings imply that top management should be proactive in improving information flow and in developing trust among supply chain members to make their supply chain opertaions flexible. As ISM is based on inputs given by team of experts, chances of bisaing may be there. To overcome biasedness, fuzzy ISM can be also applied as future scope of study. Apart from this, the ISM framework for flexible supply chain management can be further validated with some case studies and survey based empirical findings.

References

1. Agarwal, S., Singh, R.K., and Murtaza, Q. (2014) "Forecasting product returns for recycling in Indian electronics industry", Journal of Advances in Management Research, Vol. 11, No 1, pp. 102-114.
2. Agrawal, S., Singh, R.K. and Murtaza, Q., (2015), "Prioritizing critical success factors for reverse logistics implementation by using Fuzzy-TOPSIS methodology", Journal of Industrial Engineering International, pp. 1-13.
3. Ahmed A., Ahmed N. and Salman A. (2005)," Critical issues in packaged food business", British Food Journal ,Vol. 107, No 10, pp. 760-780.
4. Bansal , A., Singh , R. K., Issar ,S. and Varkey , J. (2014) "Evaluation of vendors ranking by EATWOS approach", Journal of Advances in Management Research, Vol. 11, No, 3, pp. 290 – 311
5. Benita M. B. (1999) "Measuring supply chain performance", International Journal of Operations & Production Management, Vol. 19, No 3, pp.275 – 292.
6. Bhadani, A.K., Shankar, R. and Rao, D.V. (2016),"Modeling the factors and their interdependencies for investment decision in Indian mobile service sector", Journal of Modelling in Management, Vol. 11, No. 1 pp. 189 – 212.
7. Boyer K. K and Pagell, M. (2000), "Measurement issues in empirical research: Improving measures of operations strategy and advanced manufacturing technology," Journal of Operations Management, Vol. 18, No. 3, pp.361–374.
8. Chan, H.K. and Chan F.T.S. (2009), "Effect of information sharing in supply chains with flexibility" International Journals of Production Research, Vol.47, No.1, pp. 213-232.
9. Chandra, C and Kumar, S (2000) "Supply chain management in theory and practice: a passing fad or a fundamental change?" Industrial Management & Data Systems, Vol. 100, No 3, pp.100 – 114.
10. Chiang, C. Y., Hillmer, C K and Suresh, N. (2012), "An empirical investigation of the impact of strategic sourcing and flexibility on firm's supply chain agility" International Journal of Operations & Production Management Vol. 32, No. 1, 2012 pp. 49-78.
11. Christopher, M and Peck, H (2004) "Building the Resilient Supply Chain", International Journal of Logistics Management, Vol. 15, No. 2, pp.1 - 14
12. Clarke, J and Varma, S (1999), "Strategic risk management: The new competitive edge", Long Range Planning, Vol. 32, No 4, pp. 414–424
13. Croom, S., Romano, P. and Giannakis, M. (2000), "Supply chain management: An analytical framework for critical literature review", European Journal of Purchasing & Supply Management, Vol. 6, pp. 67-83.
14. Disney, S.M. and Towill, D.R. (2003), "The effect of vendor managed inventory (VMI) dynamics on the bullwhip effect in supply chains", International Journal of Production Economics, Vol. 85, pp. 199-215.

Downloaded by Delhi Technological University At 22:33 25 September 2017 (PT)

© Emerald Publishing Limited
This is a pre-print of a paper and is subject to change before publication. This pre-print is made available with the understanding that it will not be reproduced or stored in a retrieval system without the permission of Emerald Publishing Limited.

15. Dove, R. (1995), “Measuring agility: the toll of turmoil”, Production, Vol. 107, No. 1, pp. 12-14.
16. Duclos, L., Vokurka, R. and Lummus, R. (2003), “A conceptual model of supply chain flexibility”, Industrial Management & Data Systems, Vol. 103, No. 6, pp. 446-56.
17. Duclos, L.K., Vokurka, R.J. and Lummus, R.R. (2003), “A conceptual model of supply chain management”, Industrial Management & Data Systems, Vol. 103, Nos 5/6, pp. 446-56.
18. Duncan, N.B. (1995), “Capturing flexibility of information technology infrastructure: a study or resource characteristics and their measure”, Journal of Management Information Systems, Vol. 12, No. 2, pp. 37-57.
19. Fisher, M. (1997), “What is the right supply chain for your product?” Harvard Business Review, March-April, pp. 105-16.
20. Gerwin, D. (1987), “An agenda for research on the flexibility of manufacturing processes”, International Journal of Operations & Production Management, Vol. 7, No. 1, pp. 38-49.
21. Gerwin, D. (1993), “Manufacturing flexibility: a strategic perspective”, Management Science, Vol. 39, No. 4, pp. 395-410.
22. Girubha, J., Vinodh, S. and Vimal K E K , (2016),"Application of Interpretative Structural Modelling integrated Multi Criteria Decision Making methods for sustainable supplier selection", Journal of Modelling in Management, Vol. 11, No. 2 (In press)
23. Goldman, S.L. and Nagel, R.N. (1993), “Management, technology and agility: the emergence of a new era in manufacturing”, International Journal of Technology Management, Vol. 8, Nos 1/2, pp. 18-38.
24. Gosain, S., Malhotra, A. and El Sawy, O.A. (2005), “Coordinating for flexibility in e-business supply chains”, Journal of Management Information Systems, Vol. 21, No. 3, pp. 7-45.
25. Griffith J C (2006), " Food safety: where from and where to?", British Food Journal. Vol. 108, No 1, pp. 6-15
26. Gunasakeran A., Forker L. and Kobu B., (2000)"Improving operation performance in a small company: a case study", International Journal of Operations & Production Management", Vol. 20, No. 3,pp. 316-36.
27. Gunasekaran, A., Patel, C. and Tirtiroglu, E. (2001), “Performance measures and metrics in a supply chain environment”, International Journal of Operations & Production Management, Vol. 21, Nos 1/2, pp. 71-87.
28. Handfield, R.B. and Nichols E.L., 1999, Introduction to Supply Chain management. Prentice Hall, N.J., Vol. 14, No 6.
29. Hannon, D. (2005), “Efficiency is key to global sourcing”, Purchasing, Vol. 134, No. 12, pp. 54-9.
30. Hind, D.J. (1994), "Radio frequency identification and tracking systems in hazardous areas", paper presented at the Fifth International Conference on Electrical Safety in Hazardous Environments, pp. 215-27.
31. Hoyt, J and Huq F, (2000) "From arms-length to collaborative relationships in the supply chain: An evolutionary process", International Journal of Physical Distribution & Logistics Management, Vol. 30, No 9, pp.750 – 764
32. Hughes, D., 1994, "Breaking with traditions: building partnerships and alliances in the European Food Industry". Wye, Wye College Press, Vol. 13, No. 4, pp. 409-438

Downloaded by Delhi Technological University At 22:33 25 September 2017 (PT)

© Emerald Publishing Limited
This is a pre-print of a paper and is subject to change before publication. This pre-print is made available with the understanding that it will not be reproduced or stored in a retrieval system without the permission of Emerald Publishing Limited.

33. Hui, L.T., (2004) "Business timeliness: the intersections of strategy and operations management", International Journal of Operations & Production Management, Vol. 24, No. 6, pp.605 – 624.
34. Humpherys, P.K., Mc Adam R. and Leckey J.(2005),"Longitudinal evaluation of innovation implementation in SMEs", European Journal of Innovation Management, Vol. 8, No. 3, pp. 283-304
35. Jack, E.P. and Raturi, A. (2002), "Sources of volume flexibility and their impact on performance", Journal of Operations Management, Vol. 20, pp. 519-48.
36. Kärkkäinen M. (2003), "Increasing efficiency in the supply chain for short shelf life goods using RFID tagging", International Journal of Retail & Distribution Management, Vol 31, No. 10.
37. Khan A, Bakkappa, Bhimaraya A, Metri and Sahay, B.S. (2009) "Impact of agile supply chains' delivery practices on firms' performance: Cluster analysis and validation", Supply Chain Management: An International Journal, Vol. 14, No 1, pp.41 - 48
38. Kola, J., and Latvala, T. (2003). Impact of information on the demand for credence characteristics. In: Proceedings 13th annual world food and agribusiness forum and symposium (IAMA) (pp. 1–10).
39. Kumar, R, Singh, R.K., and Shankar, R, (2015) "Critical success factors for implementation of supply chain management in Indian small and medium enterprises and their impact on performance", IIMB Management Review, Vol. 27, pp. 92-104.
40. Lambert, D.M., Cooper, M.C. and Pagh, J.D. (1998), "Supply chain management: implementation issues and research opportunities", International Journal of Logistics Management, Vol. 9 No. 2, pp. 1-19.
41. Laura H, (2001) "Collaboration: the key to value creation in supply chain management", Supply Chain Management: An International Journal, Vol. 6, No. 5, pp.205 - 207
42. Leslie K. Duclos, Robert J. Vokurka, Rhonda R. Lummus, (2003) "A conceptual model of supply chain flexibility", Industrial Management & Data Systems, Vol. 103, No. 6, pp.446 - 456
43. Lummus, R and Vokurka, R.J. (1999) "Defining supply chain management: a historical perspective and practical guidelines", Industrial Management & Data Systems, Vol. 99 No. 1, pp.11 - 17
44. Lummus, R.R., Duclos, L.K. and Vokurka, R.J. (2003), "Supply chain flexibility: building a new model", Global Journal of Flexible Systems Management, Vol. 4, No. 4, pp. 1-13.
45. Mukhopadhyay J.(2009), "Supply chain management: A Comparative study between large organised food and grocery retailer in india"
46. Norrman, A and Jansson, U (2004) "Ericsson's proactive supply chain risk management approach after a serious sub-supplier accident", International Journal of Physical Distribution & Logistics Management, Vol. 34, No 5, pp.434 – 456
47. Park S., Hartley J.L. and Wilson D. (2001)."Quality management practises and their relationship to buyer's supplier ratings: A case study in the Korean automotive industry", Journal of Operations Management, Vol. 19, No. 6 pp. 695-712.

Downloaded by Delhi Technological University At 22:33 25 September 2017 (PT)

© Emerald Publishing Limited
This is a pre-print of a paper and is subject to change before publication. This pre-print is made available with the understanding that it will not be reproduced or stored in a retrieval system without the permission of Emerald Publishing Limited.

48. Ralston, P.M., Iowa, A. and Daugherty, P.J. (2013), “Logistics salience impact on logistics capabilities and performance”, International Journal of Logistics Management, Vol. 24 No. 2, pp. 136-152.

49. Richmond, M. (2004), Opportunities in Packaging: Innovation and Savings, available at: http://pti-solutions.com/resources/articles/
50. Sanchez, A. and Perez, M. (2005), “Supply chain flexibility and firm performance: a conceptual model and empirical study in the automotive industry”, International Journal of Operations & Production Management, Vol. 25 No. 7, pp. 681-700.
51. Seamen C.(1995),” Computers in the food industry – new developments”, Nutrition and Food Science, No. 1, 33-37.
52. Sharma, S and Bhat, A. (2012a), "Potential barriers in supply chain risk management in Indian automobile industry", International Journal of Business Continuity and risk Management, Vol.3, No.3, pp. 206-220.
53. Sharma, S and Bhat, A. (2012b) , "An Empirical investigation of the Contribution of Supply chain design characteristics on supply chain risks in Indian Automobile Industry", International Journal of Business Continuity and risk Management, Vol.3, No.2, pp. 117-135.
54. Sharma, S and Bhat, A. (2013), "An Empirical exploration of supply chain design factors and studying their influence on supply chain performance", International Journal of Business Performance and Supply chain Modeling, Vol.5, No.3, pp. 239-257.
55. Sharma, S and Bhat, A. (2014), "Modelling supply chain agility enablers using ISM", Journal of Modelling in Management, Vol. 9, No.2, pp. 200-214.
56. Sheffi, Y. and Rice, J.B. Jr (2005), “A supply chain view of the resilient enterprise”, Sloan Management Review, Vol. 47 No. 1, pp. 41-8.
57. Singh, R.K and Sharma P.B. (2015), “IISM-Based model to evaluate the flexibility index of a supply chain” System Flexibility and Business Agility, pp.323-342.
58. Singh, R.K and Sharma, M.K (2014), “Prioritizing the alternatives for flexibility in supply chains”, Production Planning and Control, Vol.25, No.2, pp-176-192.
59. Singh, R.K. (2013) “Prioritizing the factors for coordinated supply chain using analytic hierarchy process (AHP)”, Measuring Business Excellence, Vol.17, No.1 pp.80-98.
60. Singh, R.K. (2015) “Modelling of Critical Factors for Responsiveness in Supply Chain” Journal of Manufacturing and Technology Management,Vol. 26, No.6, pp. 868 – 888.
61. Singh, R.K., Garg, S.K., Deshmukh, S.G. and Kumar, M. (2007) “Modelling of critical success factors for implementation of AMTs”, Journal of Modelling in Management. Vol. 2, No. 3, pp. 232-250.
62. Singh, R.K., Kumar, P and Gupta, V, (2010) “Fuzzy Statistical Approach for Vendor Selection in Supply Chain”, International journal of Logistic Systems and Management, Vol. 7, No.3. pp 286-301.
63. Slack, N. (1983), “Flexibility as a manufacturing objective”, International Journal of Operations & Production Management, Vol. 3 No. 3, pp. 4-13.
64. Slack, N. (1987), “The flexibility of manufacturing systems”, International Journal of Operations& Production Management, Vol. 7 No. 4, pp. 35-45.

Downloaded by Delhi Technological University At 22:33 25 September 2017 (PT)

© Emerald Publishing Limited
This is a pre-print of a paper and is subject to change before publication. This pre-print is made available with the understanding that it will not be reproduced or stored in a retrieval system without the permission of Emerald Publishing Limited.

65. Smykay, E.W., Bowersox, D.J. and Mossman, F.H. (1961), Physical Distribution Management – Logistics Problems of the Firm, The Macmillan Company, New York, NY.
66. Spekman, R. E., Kamauff, J and Myhr, N (1998) "An empirical investigation into supply chain management: a perspective on partnerships", Supply Chain Management: An International Journal, Vol. 3, No. 2, pp.53 - 67
67. Stevenson, W. (2007), Operations Management, McGraw-Hill/Irwin, New York, NY, Vol. 101 No 3, pp.114 - 121
68. Suarez, F.F., Cusumano, M.A. and Fine, C.H. (1996), "An empirical study of manufacturing flexibility in printed circuit board assembly", Operations Research, Vol. 44 No. 1, pp. 223-40.
69. Tan K.C., Kannan V.R., Handfield R.B. and Ghosh S, (1999) "Supply chain management: An empirical study of its impact on performance", International Journal of Operations & Production Management, Vol. 19 No. 10, pp.1034 -1052
70. Tummala, R., Phillips, C. and Johnson, M. (2007), "Assessing supply chain management success factors: a case study", Supply Chain Management: An International Journal, Vol. 11 No. 2, pp. 179-92.
71. Upton, D.M. (1995), "What really makes factories flexible?", Harvard Business Review, July-August, pp. 74-84.
72. Vander V and Beulens, A.J.M. (2002), "Identifying sources of uncertainty to generate supply chain redesign strategies", International Journal of Physical Distribution & Logistics Management, Vol. 32 No. 6, pp. 409-30.
73. Vickery, S., Calantone, R. and Droge, C. (1999), "Supply chain flexibility: an empirical study", Journal of Supply Chain Management, Vol. 35 No. 3, pp. 16-24.
74. Voss, D. (2013), "Supplier choice criteria and the security aware food purchasing manager", International Journal of Logistics Management, Vol. 24 No. 3, pp. 380-406.
75. Yee, W. M. S., Yeung, R. M. W., and Morris, J. (2005), "Food safety: building consumer trust in livestock farmers for potential purchase behaviour" British Food Journal, Vol. 107, pp. 841–854.

Dr. Rajesh Kr. Singh is Professor in Operations Management area at Management Development Institute, Gurgaon, India. His areas of interest include Supply Chain Management, Small Business Management and Quality Management. He has published around 125 research papers in reputed international/national journals and conferences. His papers have appeared in journals such as Resources, Conservation and Recycling, Production Planning and Control, Journal of Industrial and Production Engg, Industrial management and Data Systems, Singapore Management Review, International Journal of Productivity and Performance Management, Benchmarking: An International Journal, Journal of Modelling in Management, Competitiveness Review, Global Journal of Flexible Systems and Management, Journal of Advances in Management Research, International Journals of Productivity and Quality Management, International Journal of Services and Operations Management, Management Research Review, IIMB Management Review etc.
Email-rksdce@yahoo.com

© Emerald Publishing Limited
This is a pre-print of a paper and is subject to change before publication. This pre-print is made available with the understanding that it will not be reproduced or stored in a retrieval system without the permission of Emerald Publishing Limited.

Downloaded by Delhi Technological University At 22:33 25 September 2017 (PT)

Dr. Saroj Koul is Professor of Operations and SCM at Jindal Global Business School, OP Jindal Global University,Sonepat, Haryana, INDIA. She has published many papers in Operations and Supply Chain Management in reputed international journals and conferences.
Email- skoul@jgu.edu.in

Dr. Pravin Kumar is an Assistant Professor in Mechanical Engineering Department, Delhi Technological University, Delhi, India. He is Ph.D. in supply chain Management from IIT Delhi and M. Tech in Industrial Management from I.T., BHU, Varanasi (Now IIT BHU Varanasi). He has published many research papers in international and national journals and conferences. His area of research is supply chain and logistics management. He has more than 14 years of teaching and research experience. He has authored the books on Engineering Economics and Industrial Engineering and Management by Wiley India and Pearson Learning, respectively.
Email-pravin.dce@gmail.com

Downloaded by Delhi Technological University At 22:33 25 September 2017 (PT)

© Emerald Publishing Limited
This is a pre-print of a paper and is subject to change before publication. This pre-print is made available with the understanding that it will not be reproduced or stored in a retrieval system without the permission of Emerald Publishing Limited.

IOP Conference Series: Materials Science and Engineering

PAPER • **OPEN ACCESS**

Application of Gaussian as Edge Detector for Image Enhancement of Ancient Manuscripts

To cite this article: N. Jayanthi and S. Indu 2017 *IOP Conf. Ser.: Mater. Sci. Eng.* **225** 012149

View the article online for updates and enhancements.

Related content

- Advanced Digital Imaging Laboratory Using MATLAB® (Second edition) : Methods of image enhancement
  L P Yaroslavsky
- A manuscript written…
- Computerized image improvement in nuclear medicine using selected frequency band enhancement
  D S Gooden and C Farmer

This content was downloaded from IP address 14.139.251.107 on 17/09/2017 at 06:09

Application of Gaussian as Edge Detector for Image Enhancement of Ancient Manuscripts

N.Jayanthi[1] and S.Indu[2]
1. Assistant Professor, ECE Department, Delhi Technological University, Delhi-110042, India
2. Professor, ECE Department, Delhi Technological University, Delhi-110042, India

Abstract: Binarization is an essential step for the Digitization of Ancient Manuscript images. Degradations in the manuscripts, such as, uneven light, low complexity, smears and high noise densities frequently make thresholding of the manuscript images a troublesome task. The purpose of study is to preserve the information contained in documents in digital form. To improve the accuracy of machine reading for camera-based Manuscript images, a simple and novel approach has been proposed based on Difference of Gaussians: a second order edge detector, followed by modified Niblack's local thresholding. The proposed strategy has been correlated with existing techniques. The numerical result stating average PSNR value 19.21dB validates that the performance of proposed method is superior to other five well known binarization techniques.

Keywords: *Binarization, Difference of Gaussians, global thresholding, Local thresholding, edge detection.*

1. INTRODUCTION

The evolution of modern imaging devices for Image enhancement and restoration plays a key part in manuscript document processing related applications, for example text recognition and image retrieval. In many cases the documents are deteriorated because of age, dust or due to ink smudging. The fundamental task is to digitize a manuscript image so that, background and foreground content are unmistakably isolated. In binarization there is a need of segmenting the document into two grayscale levels, which can be performed either locally [4], [6], [9],[10] or globally [1], [7], [8].

In the past a great deal of global thresholding concepts were proposed (e.g. Otsu's method [2], Illingworth and Kittler's method [3]). But global thresholding fails to remove noise from highly degraded images because of local degradation, poor illumination and complex background texture. Local thresholding is being utilized in [7] to achieve the goal of extracting a foreground part (text) from background (non text). Local thresholding achieves binarization by considering each and every pixel with neighborhood pixels [4]. Niblack proposed a local thresholding procedure by computing a threshold factor using local statistical parameters namely mean and standard deviation [4].

Content from this work may be used under the terms of the Creative Commons Attribution 3.0 licence. Any further distribution of this work must maintain attribution to the author(s) and the title of the work, journal citation and DOI.
Published under licence by IOP Publishing Ltd

In this manuscript, we present a concept based on difference of Gaussian followed by modified Niblack's local thresholding [4] and morphological post processing. Where the difference of Gaussian results in preservation of the edge information and thresholding using modified Niblack's local algorithm produces binarized image, the final binarized image can be digitized with the help of OCR.

The paper is indexed as: Section 2.1 and 2.2 clarifies the importance of Gaussian Filter and difference of Gaussian also depicts Niblack's thresholding algorithm. Section 2.3 introduces the proposed algorithm. Section 3 states the results of proposed strategy to access the framework. Section 4 finally concludes the work.

2. METHODOLOGY

2.1 Gaussian Filter and Difference of Gaussians:

As a gray image is a two dimensional object, two dimensional Gaussian functions is defined below.

$$g(a,b) = \frac{1}{2\pi\sigma^2} e^{-\frac{a^2+b^2}{2\sigma^2}} \quad (1)$$

Where a and b are the distances from the origin in the horizontal axis and in the vertical axis respectively, and represents the standard deviation of the Gaussian distribution [5 6].

In image processing, difference of Gaussians (DoG) is a second order edge detection algorithm which performs the subtraction between two blurred versions of the image with different blur amounts ( ). Hence DoG acts as a band pass filter for preserving the edge information in an image. Application of Gaussian functions on an image causes reduction in only high frequency spatial information. Subtracting one image from the other conserves spatial information which falls between the ranges of frequencies conserved in the two blurred images.

2.2 Niblack's Local Thresholding Algorithm:

Niblack's thresholding algorithm computes a threshold factor to each pixel by moving a rectangular window over the gray level image [4]. The dimensions of rectangular window can be changed depending upon the complexity of the background. The threshold value is calculated using the local mean and standard deviation of all the pixels in the window and is given by following equations [4]:

$$T_{Niblack} = M + K * SD \quad (2)$$

$$T_{Niblack} = M + K * \sqrt{\frac{\sum (p_i - m)^2}{NP}} \quad (3)$$

Here NP is the total pixels present in gray scale image, T represents the threshold value, M is the mean of gray levels of pixels and k is fixed depending upon the noise in the background and is - 0.2.

2.3 Proposed Method:

The proposed method for enhancement and restoration for manuscript images is described in this section. The flow diagram is shown in Fig.1 and each step is explained in detail in sub-sections.

2.3.1 Difference in Gaussians:

The difference of Gaussian edge detector eliminates high frequency details that generally include random noise removal. It reduces noise in the image by blurring and also preserves the edge information in the image. DoG also removes the low frequency background blotches. Finally the resultant image is normalized to [0, 1].
Equation for DoG is:

$$\Gamma(x, y) = I * (g_{\sigma 1} - g_{\sigma 2}) \tag{4}$$

The output image after application of DoG is denoted by $\Gamma(x, y)$, I is the input gray scale image, $g_{\sigma 1}$ and $g_{\sigma 1}$ are Gaussian functions, provided $2 > 1$.

2.3.2 Modified Niblack's Local Thresholding Algorithm:

In the proposed method threshold value is calculated using variance instead of standard deviation and the constant k is chosen in the range 0.15 to 0.30. Hence modified equation for calculation of threshold is:

$$T_{Niblack} = M + K * Var \tag{5}$$

2.3.3 Post Processing:

In the last step, the binarized image is applied with morphological operation to sharpen the text details in the image.

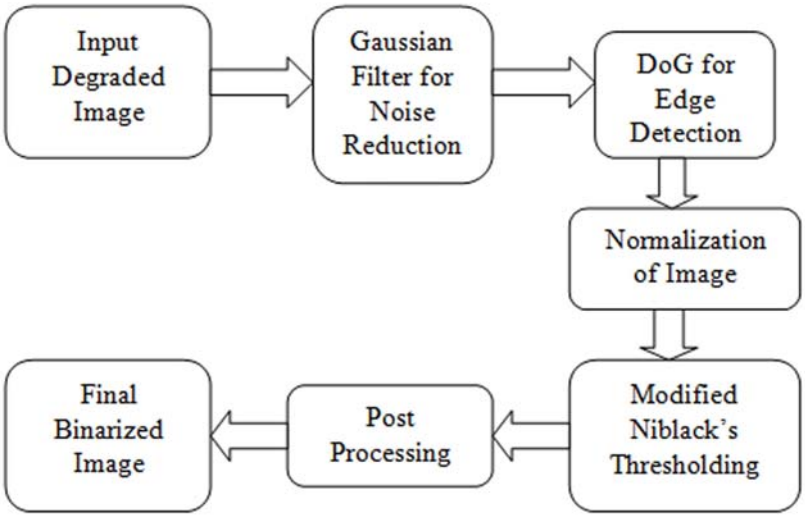
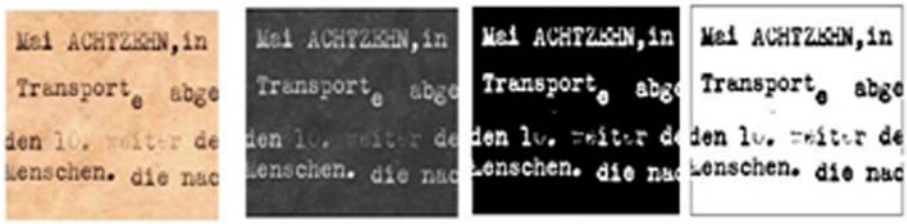


Fig. 1

3. EXPERIMENTAL RESULTS

The proposed method is evaluated on a set of 80 images including DIBCO-2009 [11] standard data set. Table 1 shows comparison of PSNR value of proposed technique with the existing binarization methods. Figure 4 and 5 shows that the proposed strategy is superior to contemporary Global and Local thresholding methods. Experimental results show that most of the documents are satisfactorily denoised. Figure 2 and 3 shows output and intermediate stages of the proposed method.



(a) (b) (c) (d)

Figure **2** (a) Input Image, (b) output after application of DoG (c) Result of applying modified Niblack thresholding on fig 2(b), (d) Final resultant image of proposed method

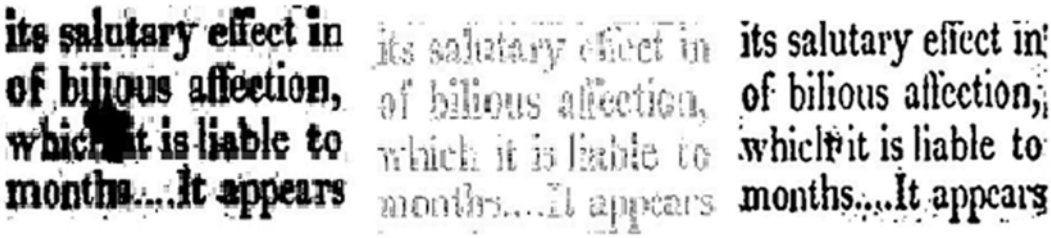


(a) (b) (c) (d)

Figure 3: (a) Input Image, (b) output after application of DoG (c) Result of applying modified Niblack thresholding on fig 2(b), (d) Final resultant image of proposed method

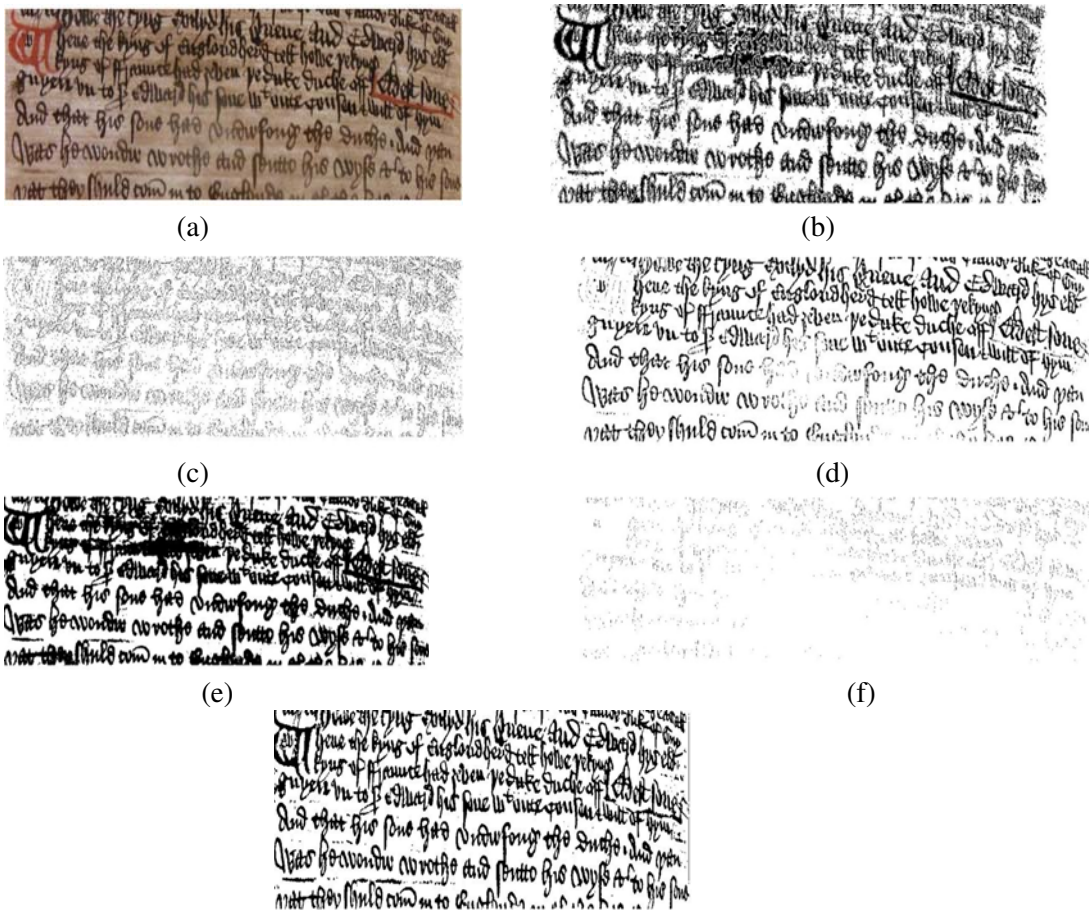


(a) (b) (c)



(d) (e) (f)

Figure 4: Result of proposed binarization method in comparison with some well known methods of fig 3a. (a) Bernsen's method, (b) Niblack's method, (c) Nick's method, (d) Otsu's method, (e) Sauvola's method and (f) proposed method.



(a) (b)

(c) (d)

(e) (f)

(g)

Figure 5: Result of proposed method in comparison with some well known methods. (a) Input image (b) Bernsen's method, (c) Niblack's method, (d) Nick's method, (e) Otsu's method, (f) Sauvola's method and (g) proposed method

The performance is validated by calculating Peak Signal Noise Ratio (PSNR) and Mean Square Error (MSE). The mathematical formula for MSE and PSNR are:

$$MSE = \frac{1}{MN}\sum\sum\left(k(x,y) - g(x,y)\right)^2 \quad (6)$$

$$PSNR = 10\log\left(\frac{mxi * mxi}{MSE}\right)dB \quad (7)$$

Where k(x, y), g(x, y) and mxi are the output image, input image and maximum intensity of the pixels in image respectively. In table 1 the PSNR value of proposed method (performed on DIBCO 2009 data set) is compared with some standard binarization methods. The numerical results stating average PSNR value 19.21dB validates that the execution of proposed strategy is better than other five binarization methods.

TABLE 1: COMPARATIVE RESULTS

Method	**PSNR(dB)**
OTSU [2]	15.89
NIBLACK'S [4]	10.89
SAUVOLA [9]	9.39
BERSEN [10]	15.01
NICK [12]	18.98
Proposed Method	19.21

4. CONCLUSION

In this paper, hybrid technique by linking the difference of Gaussian and modified Niblack's local thresholding method has been proposed to improve the legibility of manuscript images for better binarization. Results state that the proposed method is producing a binarized image in which background noise is eliminated and the texture information is enhanced. The performance is validated using MSE and PSNR values. Figure 4 and 5 also validates the superiority of proposed method over well known methods. However the method fails to produce better binarization if the manuscript images having very low contrast between text and the non text portion. Hence addressing the ancient manuscripts with the above said problem will be taken up as future work.

ACKNOWLEDGMENT

We would like to thank Mr. Abhilash Gaur for the data collection of the manuscript images.

REFERENCES

[1] P. K. Sahoo, S. Soltani, A. K. C. Wong, A survey of thresholding techniques, Computer Vision, Graphics Image Processing, 41 (2), 233&260, 1988

[2] N.Otsu, "A threshold selection method from a gray level histograms", IEEE Trans.Systems, Man, Cybernet., 9(1),1979, pp.62- 66

[3] J. Kittler and J. Illingworth , " Minimum error thresholding", Pattern Recogn. 19, 1986, pp. 41-47.

[4] W. Niblack, “An Introduction to Image Processing”, Prentice-Hall, Englewood Cliffs, NJ, 1986, pp. 115-116.
[5] R. C. Gonzalez., R. E. Woods, Digital Image Processing,Third Edition,Pearson Education Inc.,2008
[6]. B Gangamma, Srikanta Murthy K, Arun Vikas Singh, "Restoration of Degraded Historical Document Image", Journal of Emerging Trends in Computing and Information Sciences, Vol. 3,I ssue. 5,M ay 2012,I SSN 2079-8407,p ages 792-798
[7] B. Sankur and M. Sczgin. "Image thrcsholdirig techniques. A survey over categories", Pattern Recognition, :!001
[8] Oivind Due Trier , Torfinn Taxt, "Evaluation of Binarization Methods for Document lmages", IEEE Transactions on Pattern Analysis and Machine intelligence, v.17 n.3, p.312-315. March 1995.
[9] J. Sauvola and M. Pietikainen, “ Adaptive Document Image Binarization”, Pattern Recognition, 33(2), pp.255-236, 2000.
[10] J. Bersen, “Dynamic Thresholding of Gray-level Images”, Proc. International Conference on Pattern recognition, 1215-1255, 1986
[11] Document Image Binarization Contest DIBCO”, 2009.



N. Jayanthi received her M.Tech. degree in 2007 from Department of Electronics and Communication Engineering, National Institute of Technology, Tiruchirappalli, Tamilnadu. She had been working as a Assistant Professor for the past 9 years in the Department of Electronics and Communication Engineering, Delhi Technological University, Delhi. Currently she is working towards her Ph.D degree in Image Processing and Applications. Her area of interest is Image Processing, Machine Learning and Communication System.



Dr. S. Indu received her PhD. degree in 2012 from Department of Electronics and Communication Engineering, Delhi University, Delhi. She is working as Professor having 18 years of teaching experience and presently holds the position of Head of the Department in the Department of Electronics and Communication Engineering, Delhi Technological University, Delhi. Her area of interest is Image Processing, Computer Vision and Wireless Sensor Networks and in these areas she has published several research papers. She also holds position of Branch Counsellor IEEE DTU Branch and worked on several DST sponsored projects.

Applied Mathematics and Computation 317 (2018) 109–120

Contents lists available at ScienceDirect

Applied Mathematics and Computation

journal homepage: www.elsevier.com/locate/amc

Approximation by Kantorovich form of modified Szász–Mirakyan operators

Minakshi Dhamija[a], Ram Pratap[b], Naokant Deo[b,*]

[a] Shaheed Rajguru College of Applied Sciences for Women, Department of Mathematics, University of Delhi, Vasundhara Enclave, Delhi 110096, India

[b] Delhi Technological University, Formerly Delhi College of Engineering, Department of Applied Mathematics, Bawana Road, Delhi 110042, India

ARTICLE INFO

MSC:
41A25
41A36

Keywords:
Stancu operators
Szász–Mirakyan operators
Kantorovich
Modulus of continuity
Bounded variation

ABSTRACT

In the present article, we consider the Kantorovich type generalized Szász–Mirakyan operators based on Jain and Pethe operators [32]. We study local approximation results in terms of classical modulus of continuity as well as Ditzian–Totik moduli of smoothness. Further we establish the rate of convergence in class of absolutely continuous functions having a derivative coinciding a.e. with a function of bounded variation.

© 2017 Elsevier Inc. All rights reserved.

1. Introduction

In 1977, Jain and Pethe [32] generalized the well-known Szász–Mirakyan operators [40] as:

$$S_n^{[\alpha]}(f;x) = (1+n\alpha)^{-\frac{x}{\alpha}} \sum_{k=0}^{\infty} \left(\alpha+\frac{1}{n}\right)^{-k} \frac{x^{(k,-\alpha)}}{k!} f\left(\frac{k}{n}\right)$$
$$= \sum_{k=0}^{\infty} s_{n,k}^{[\alpha]}(x) f\left(\frac{k}{n}\right), \tag{1.1}$$

where

$$s_{n,k}^{[\alpha]}(x) = (1+n\alpha)^{-\frac{x}{\alpha}} \left(\alpha+\frac{1}{n}\right)^{-k} \frac{x^{(k,-\alpha)}}{k!},$$

$x^{(k,-\alpha)} = x(x+\alpha)\dots(x+(k-1)\alpha)$, $x^{(0,-\alpha)} = 1$ and f is any function of exponential type such that

$$|f(t)| \le Ke^{At} \quad (t \ge 0),$$

for some finite constants $K, A > 0$. Here $\alpha = (\alpha_n)_{n\in\mathbb{N}}$ is such that

$$0 \le \alpha_n \le \frac{1}{n}.$$

* Corresponding author.
E-mail addresses: minakshidhamija11@gmail.com (M. Dhamija), rampratapiitr@gmail.com (R. Pratap), naokantdeo@dce.ac.in, dr_naokant_deo@yahoo.com, naokant.deo@gmail.com (N. Deo).

http://dx.doi.org/10.1016/j.amc.2017.09.004
0096-3003/© 2017 Elsevier Inc. All rights reserved.

The operators $S_n^{[\alpha]}$ have also been considered by Stancu [39], Mastroianni [36], Della Vecchia and Kocic [17] and Finta [26,27].

Abel and Ivan [1] gave the following alternate form of operators (1.1) (by putting $c = \frac{1}{n\alpha}$):

$$S_{n,c}(f;x) = \sum_{k=0}^{\infty} \left(\frac{c}{1+c}\right)^{ncx} \binom{ncx+k-1}{k} (1+c)^{-k} f\left(\frac{k}{n}\right), \qquad x \geq 0, \tag{1.2}$$

where $c = c_n \geq \beta (n = 0, 1, 2, ...)$ for certain constant $\beta > 0$. Also, for a particular case $\alpha = \frac{1}{n}$, the operators (1.1) reduce to another form, which was considered by Agratini [2] as follows:

$$S_n^{[\frac{1}{n}]}(f;x) = 2^{-nx} \sum_{k=0}^{\infty} \frac{(nx)_k}{2^k k!} f\left(\frac{k}{n}\right), \tag{1.3}$$

where

$$(nx)_k = nx(nx+1)\dots(nx+k-1), \qquad k \geq 1,$$

and $(nx)_0 = 1$. These operators (1.3) are special cases of Lupaş operators [35]. The operators (1.3) have also been studied in [25] and [37].

Agratini [3] modified the operators (1.3) into integral form in Kantorovich sense as:

$$T_n(f;x) = n \sum_{k=0}^{\infty} 2^{-nx} \frac{(nx)_k}{2^k k!} \int_{k/n}^{(k+1)/n} f(t)dt, \tag{1.4}$$

and studied some approximation properties. Very recently, Deo et al. considered generalized positive linear operators based on Pólya–Eggenberger and inverse Pólya–Eggenberger distribution in [21] and furthermore, they gave Kantorovich variant of these generalized operators in [18]. Several researchers have given some interesting results on Kantorovich variant of various operators (see [7–16,30,38]). Motivated by above works, for any bounded and integrable function f defined on $[0, \infty)$, we also modify the operators (1.1) in Kantorovich form:

$$L_n^{[\alpha]}(f;x) = n \sum_{k=0}^{\infty} s_{n,k}^{[\alpha]}(x) \int_{\frac{k}{n}}^{\frac{k+1}{n}} f(t)dt. \tag{1.5}$$

Special cases:

(1) For $\alpha = 0$ in (1.5), we get Szász–Kantorovich operators given by Totik in [41].
(2) For $\alpha = \frac{1}{n}$ in (1.5), we obtain another Kantorovich operators considered by Agratini [3].

The focus of this paper is to study the approximation properties of modified Kantorovich operators (1.5). First we obtain local approximation formula via modulus of continuity of second order then we use Ditzian–Totik moduli of smoothness to discuss the rate of convergence of our operators. Finally, we establish the rate of convergence for functions having derivatives of bounded variation. The properties discussed in this article can be found in some recent papers like [4,6,19,20,24,28,29,31,33].

2. Auxiliary results

In order to prove the main convergence properties of operators (1.5), we need the following basic results:

Lemma 2.1 *[39]. For the generalized Szász–Mirakyan operators (1.1) hold*

$$S_n^{[\alpha]}(1;x) = 1, \qquad S_n^{[\alpha]}(t;x) = x,$$

and

$$S_n^{[\alpha]}\left(t^2;x\right) = x^2 + \left(\alpha + \frac{1}{n}\right)x.$$

Proposition 2.1. *For the operators (1.1), there hold the following higher order moments:*

$$S_n^{[\alpha]}\left(t^3;x\right) = x^3 + 3\left(\alpha + \frac{1}{n}\right)x^2 + \left(2\alpha^2 + \frac{3\alpha}{n} + \frac{1}{n^2}\right)x,$$

and

$$S_n^{[\alpha]}\left(t^4;x\right) = x^4 + 6\left(\alpha + \frac{1}{n}\right)x^3 + \left(11\alpha^2 + \frac{18\alpha}{n} + \frac{7}{n^2}\right)x^2 + \left(6\alpha^3 + \frac{12\alpha^2}{n} + \frac{7\alpha}{n^2} + \frac{1}{n^3}\right)x.$$

Proof. By definition we can write

$$S_n^{[\alpha]}\left(t^3;x\right) = (1+\alpha n)^{-\frac{x}{\alpha}} \sum_{k=1}^{\infty} \frac{x(x+\alpha)\dots(x+(k-1)\alpha)n^k}{k!(1+\alpha n)^k} \frac{k^3}{n^3}$$

$$
\begin{aligned}
&= \frac{(1+\alpha n)^{-\frac{x}{\alpha}}}{n^3}\sum_{k=1}^{\infty}\frac{\frac{x}{\alpha}\left(\frac{x}{\alpha}+1\right)\ldots\left(\frac{x}{\alpha}+k-1\right)\alpha^k n^k}{(k-1)!(1+\alpha n)^k}(k(k-1)+k)\\
&= \frac{(1+\alpha n)^{-\frac{x}{\alpha}}}{n^3}\sum_{k=2}^{\infty}\frac{\frac{x}{\alpha}\left(\frac{x}{\alpha}+1\right)\ldots\left(\frac{x}{\alpha}+k-1\right)\alpha^k n^k}{(k-2)!(1+\alpha n)^k}k+\frac{1}{n}S_n^{[\alpha]}\left(t^2;x\right)\\
&= \frac{(1+\alpha n)^{-\frac{x}{\alpha}}}{n^3}\sum_{k=3}^{\infty}\frac{\frac{x}{\alpha}\left(\frac{x}{\alpha}+1\right)\ldots\left(\frac{x}{\alpha}+k-1\right)\alpha^k n^k}{(k-3)!(1+\alpha n)^k}\\
&\quad+\frac{2(1+\alpha n)^{-\frac{x}{\alpha}}}{n^3}\sum_{k=2}^{\infty}\frac{\frac{x}{\alpha}\left(\frac{x}{\alpha}+1\right)\ldots\left(\frac{x}{\alpha}+k-1\right)\alpha^k n^k}{(k-2)!(1+\alpha n)^k}+\frac{1}{n}S_n^{[\alpha]}\left(t^2;x\right)\\
&= \frac{(1+\alpha n)^{-\frac{x}{\alpha}}}{n^3}\sum_{k=0}^{\infty}\frac{\left(\frac{x}{\alpha}+k+2\right)!\alpha^{k+3}n^{k+3}}{k!\left(\frac{x}{\alpha}-1\right)!(1+\alpha n)^{k+3}}\\
&\quad+\frac{2(1+\alpha n)^{-\frac{x}{\alpha}}}{n^3}\sum_{k=0}^{\infty}\frac{\frac{x}{\alpha}\left(\frac{x}{\alpha}+1\right)\ldots\left(\frac{x}{\alpha}+k+1\right)}{k!}\left(\frac{\alpha n}{1+\alpha n}\right)^{k+2}+\frac{1}{n}S_n^{[\alpha]}\left(t^2;x\right)\\
&= \frac{(1+\alpha n)^{-\frac{x}{\alpha}}}{n^3}\sum_{k=0}^{\infty}\frac{\left(\frac{x}{\alpha}+k+2\right)!\alpha^{k+3}n^{k+3}}{k!\left(\frac{x}{\alpha}-1\right)!(1+\alpha n)^{k+3}}\\
&\quad+\frac{2(1+\alpha n)^{-\frac{x}{\alpha}}}{n^3}\frac{x}{\alpha}\left(\frac{x}{\alpha}+1\right)\sum_{k=0}^{\infty}\frac{\left(\frac{x}{\alpha}+k+1\right)!}{k!\left(\frac{x}{\alpha}+1\right)!}\left(\frac{\alpha n}{1+\alpha n}\right)^{k+2}+\frac{1}{n}S_n^{[\alpha]}\left(t^2;x\right)\\
&= \frac{(1+\alpha n)^{-\frac{x}{\alpha}}}{n^3}\sum_{k=0}^{\infty}\frac{\left(\frac{x}{\alpha}+k+2\right)!\alpha^{k+3}n^{k+3}}{k!\left(\frac{x}{\alpha}-1\right)!(1+\alpha n)^{k+3}}\\
&\quad+\frac{2(1+\alpha n)^{-\frac{x}{\alpha}}}{n}\frac{x}{\alpha}\left(\frac{x}{\alpha}+1\right)\alpha^2\left(1-\frac{\alpha n}{1+\alpha n}\right)^{-\left(\frac{x}{\alpha}+2\right)}+\frac{1}{n}S_n^{[\alpha]}\left(t^2;x\right)\\
&= \frac{(1+\alpha n)^{-\frac{x}{\alpha}}}{n^3}\sum_{k=0}^{\infty}\frac{\left(\frac{x}{\alpha}+k+2\right)!\alpha^{k+3}n^{k+3}}{k!\left(\frac{x}{\alpha}-1\right)!(1+\alpha n)^{k+3}}+\frac{2}{n}\frac{x}{\alpha}\left(\frac{x}{\alpha}+1\right)\alpha^2+\frac{1}{n}\left[x^2+\left(\alpha+\frac{1}{n}\right)x\right]\\
&= x^3+3\left(\alpha+\frac{1}{n}\right)x^2+\left(2\alpha^2+\frac{3\alpha}{n}+\frac{1}{n^2}\right)x.
\end{aligned}
$$

Similarly, we can prove the expression for $S_n^{[\alpha]}\left(t^4;x\right)$. □

Lemma 2.2. *For Kantorovich operators (1.5), we have*

$$
\begin{aligned}
&L_n^{[\alpha]}(1;x)=1, \qquad L_n^{[\alpha]}(t;x)=x+\frac{1}{2n},\\
&L_n^{[\alpha]}\left(t^2;x\right)=x^2+\left(\alpha+\frac{2}{n}\right)x+\frac{1}{3n^2},\\
&L_n^{[\alpha]}\left(t^3;x\right)=x^3+3\left(\alpha+\frac{3}{2n}\right)x^2+\left(2\alpha^2+\frac{9\alpha}{2n}+\frac{7}{2n^2}\right)x+\frac{1}{4n^3},\\
&L_n^{[\alpha]}\left(t^4;x\right)=x^4+\left(6\alpha+\frac{8}{n}\right)x^3+\left(11\alpha^2+\frac{24\alpha}{n}+\frac{15}{n^2}\right)x^2\\
&\qquad\qquad+\left(6\alpha^3+\frac{16\alpha^2}{n}+\frac{15\alpha}{n^2}+\frac{6}{n^3}\right)x+\frac{1}{5n^4}.
\end{aligned}
$$

Proof. Taking into account of Lemma 2.1 and Proposition 2.1, we can easily get the desired result. □

Remark 2.1. By simply applying Lemma 2.2, we have

$$
\begin{aligned}
&L_n^{[\alpha]}(t-x;x)=x+\frac{1}{2n}-x=\frac{1}{2n},\\
&L_n^{[\alpha]}\left((t-x)^2;x\right)=L_n^{[\alpha]}\left(t^2;x\right)-2xL_n^{[\alpha]}(t;x)+x^2L_n^{[\alpha]}(1;x)\\
&\qquad\qquad=x^2+\left(\alpha+\frac{2}{n}\right)x+\frac{1}{3n^2}-2x\left(x+\frac{1}{2n}\right)+x^2\\
&\qquad\qquad=\left(\alpha+\frac{1}{n}\right)x+\frac{1}{3n^2},
\end{aligned}
$$

$$\begin{aligned}L_n^{[\alpha]}\left((t-x)^3;x\right) &= L_n^{[\alpha]}\left(t^3;x\right) - 3xL_n^{[\alpha]}\left(t^2;x\right) + 3x^2L_n^{[\alpha]}(t;x) - x^3L_n^{[\alpha]}(1;x)\\ &= x^3 + 3\left(\alpha+\frac{3}{2n}\right)x^2 + \left(2\alpha^2+\frac{9\alpha}{2n}+\frac{7}{2n^2}\right)x + \frac{1}{4n^3}\\ &\quad - 3x\left(x^2+\left(\alpha+\frac{2}{n}\right)x+\frac{1}{3n^2}\right) + 3x^2\left(x+\frac{1}{2n}\right) - x^3\\ &= \frac{3x^2}{n} + \left(2\alpha^2+\frac{9\alpha}{2n}+\frac{5}{2n^2}\right)x + \frac{1}{4n^3},\end{aligned}$$

and

$$\begin{aligned}L_n^{[\alpha]}\left((t-x)^4;x\right) &= L_n^{[\alpha]}\left(t^4;x\right) - 4xL_n^{[\alpha]}\left(t^3;x\right) + 6x^2L_n^{[\alpha]}\left(t^2;x\right)\\ &\quad - 4x^3L_n^{[\alpha]}(t;x) + x^4L_n^{[\alpha]}(1;x)\\ &= x^4 + \left(6\alpha+\frac{8}{n}\right)x^3 + \left(11\alpha^2+\frac{24\alpha}{n}+\frac{15}{n^2}\right)x^2\\ &\quad + \left(6\alpha^3+\frac{16\alpha^2}{n}+\frac{15\alpha}{n^2}+\frac{6}{n^3}\right)x + \frac{1}{5n^4}\\ &\quad - 4x\left(x^3+3\left(\alpha+\frac{3}{2n}\right)x^2+\left(2\alpha^2+\frac{9\alpha}{2n}+\frac{7}{2n^2}\right)x+\frac{1}{4n^3}\right)\\ &\quad + 6x^2\left(x^2+\left(\alpha+\frac{2}{n}\right)x+\frac{1}{3n^2}\right) - 4x^3\left(x+\frac{1}{2n}\right) + x^4\\ &= \left(3\alpha^2+\frac{6\alpha}{n}+\frac{3}{n^2}\right)x^2 + \left(6\alpha^3+\frac{16\alpha^2}{n}+\frac{15\alpha}{n^2}+\frac{5}{n^3}\right)x + \frac{1}{5n^4}.\end{aligned}$$

Lemma 2.3. *Let f be a bounded function defined on $[0,\infty)$ with $\|f\| = \sup_{x\in[0,\infty)} |f(x)|$, then*

$$\left|L_n^{[\alpha]}(f;x)\right| \le \|f\|.$$

Lemma 2.4. *For $n\in\mathbb{N}$, we have*

$$L_n^{[\alpha]}\left((t-x)^2;x\right) \le \frac{C}{n}\delta_n^2(x),$$

where $\delta_n^2(x) = \varphi^2(x) + \frac{1}{n}$ and $\varphi^2(x) = x$.

Now we can write the operators (1.5) in other form as:

$$L_n^{[\alpha]}(f;x) = \int_0^\infty K_n^{[\alpha]}(x,t)f(t)dt, \tag{2.1}$$

where

$$K_n^{[\alpha]}(x,t) = n\sum_{k=0}^{\infty} s_{n,k}^{[\alpha]}(x)\chi_{n,k}(t),$$

and $\chi_{n,k}(t)$ is the characteristic function of the interval $\left[\frac{k}{n},\frac{k+1}{n}\right]$ w.r.t $[0,\infty)$.

Lemma 2.5. *For $x\in(0,\infty)$ and sufficiently large n, we have*

(i) *Since $0\le y<x$, therefore*

$$\beta_n(x,y) = \int_0^y K_n^{[\alpha]}(x,t)dt \le \frac{C\delta_n^2(x)}{n(x-y)^2}.$$

(ii) *If $x<z<\infty$ then we get*

$$1-\beta_n(x,z) = \int_z^\infty K_n^{[\alpha]}(x,t)dt \le \frac{C\delta_n^2(x)}{n(z-x)^2}.$$

3. Direct results

Using the well-known Bohman–Korovkin–Popoviciu theorem (see [34]) we get the uniform convergence of the operators (1.5).

Theorem 3.1. *Let $f\in C[0,\infty)\cap E$ and $\alpha(n)$ be such that $\alpha\to 0$ as $n\to\infty$, then we have*

$$\lim_{n\to\infty} L_n^{(\alpha)}(f;x)=f(x)$$

uniformly on each compact subset of $[0,\infty)$, where $C[0,\infty)$ is the space of all real-valued continuous functions on $[0,\infty)$ and

$$E:=\left\{f: x\in[0,\infty), \frac{f(x)}{1+x^2}\text{is convergent as } x\to\infty\right\}$$

Proof. Taking Lemma 2.2 into the account and the fact that $\alpha\to 0$ as $n\to\infty$, it is clear that

$$\lim_{n\to\infty} L_n^{(\alpha)}(e_i;x)=x^i,\quad i=0,1,2$$

uniformly on each compact subset of $[0,\infty)$. Hence, applying the well-known Korovkin-type theorem [5] regarding the convergence of a sequence of positive linear operators, we get the desired result. □

Now we present local approximation formula via modulus of continuity of second order. For this let us start by recalling the following definitions:

Definition 3.1. *Let $f\in C_B[0,\infty)$, the space of all real-valued continuous and bounded functions on $[0,\infty)$ then Peetre's K-functional is defined as*

$$K_2(f,\delta)=\inf_{g\in W_\infty^2}\left\{\|f-g\|+\delta\|g''\|\right\}, \tag{3.1}$$

where $\delta>0$, $\|f\|=\sup_{x\in[0,\infty)}|f(x)|$ and $W_\infty^2=\left\{g\in C_B[0,\infty): g',g''\in C_B[0,\infty)\right\}$. Recall that, from ([22], p. 177, Theorem 2.4), there exists a positive constant M such that

$$K_2(f,\delta)\le M\omega_2\left(f,\sqrt{\delta}\right), \tag{3.2}$$

where $\omega_2\left(f,\sqrt{\delta}\right)$ is second order modulus of continuity given by

$$\omega_2(f,\delta):=\sup\{|f(x+h)-2f(x)+f(x-h)|: x, x\pm h\in[0,\infty),\ 0\le h\le\delta\}. \tag{3.3}$$

Moreover, we define the usual (first order) modulus of continuity as follows:

Definition 3.2. *Let $f\in C_B[0,\infty)$ then*

$$\omega(f,\delta):=\sup\{|f(x)-f(y)|: x,y\in[0,\infty),\ |x-y|\le\delta\}, \tag{3.4}$$

where $\delta>0$.

Theorem 3.2. *Let be $f\in C_B[0,\infty)$, then for any $x\in[0,\infty)$ it follows*

$$\left|L_n^{[\alpha]}(f;x)-f(x)\right|\le M\omega_2\left(f,\tfrac{1}{2}\delta_n(x)\right)+\omega(f,\beta_n),$$

where M is an absolute constant and

$$\delta_n(x)=\left(L_n^{[\alpha]}\left((t-x)^2;x\right)+\left(L_n^{[\alpha]}(t-x;x)\right)^2\right)^{\frac{1}{2}},\quad \beta_n=L_n^{[\alpha]}(t-x;x)$$

such that both terms δ_n and β_n tends to zero as $n\to\infty$.

Proof. For $x\in[0,\infty)$, consider the operators

$$\hat{L}_n^{[\alpha]}(f;x)=L_n^{[\alpha]}(f;x)-f\left(x+\frac{1}{2n}\right)+f(x). \tag{3.5}$$

Note that $\hat{L}_n^{[\alpha]}(1;x)=1$ and $\hat{L}_n^{[\alpha]}(t;x)=x$, i.e. constants and linear functions are preserved by the operators $\hat{L}_n^{[\alpha]}$. Therefore,

$$\hat{L}_n^{[\alpha]}(t-x;x)=0. \tag{3.6}$$

Let $g\in W_\infty^2$ and $x,t\in[0,\infty)$. By Taylor's expansion, we have

$$g(t)=g(x)+(t-x)g'(x)+\int_x^t(t-u)g''(u)du.$$

Applying $\hat{L}_n^{[\alpha]}$ on both sides of the above Taylor's expansion, we get

$$\hat{L}_n^{[\alpha]}(g;x)-g(x)=g'(x)\cdot\hat{L}_n^{[\alpha]}(t-x;x)+\hat{L}_n^{[\alpha]}\left(\int_x^t(t-u)g''(u)du;x\right)$$
$$=L_n^{[\alpha]}\left(\int_x^t(t-u)g''(u)du;x\right)-\int_x^{x+\frac{1}{2n}}\left(x+\frac{1}{2n}-u\right)g''(u)du.$$

Observe that

$$\left|\int_x^t(t-u)g''(u)\right|\le(t-x)^2\cdot\|g''\|.$$

Thus

$$\left|\hat{L}_n^{[\alpha]}(g;x)-g(x)\right|\le\left(L_n^{[\alpha]}((t-x)^2;x)+\left(L_n^{[\alpha]}(t-x;x)\right)^2\right)\cdot\|g''\|.$$

Making use of Definition (3.5) of the operators $\hat{L}_n^{[\alpha]}$ and Lemma 2.3, we have

$$\left|L_n^{[\alpha]}(f;x)-f(x)\right|\le\left|\hat{L}_n^{[\alpha]}(f-g;x)\right|+\left|\hat{L}_n^{[\alpha]}(g;x)-g(x)\right|$$
$$+|g(x)-f(x)|+\left|f\left(x+\frac{1}{2n}\right)-f(x)\right|$$
$$\le 4\|f-g\|+\delta_n^2(x)\left\|g''\right\|+\omega(f,\beta_n),$$

with $\delta_n^2(x)=L_n^{[\alpha]}\left((t-x)^2;x\right)+\left(L_n^{[\alpha]}(t-x;x)\right)^2$ and $\beta_n=L_n^{[\alpha]}(t-x;x)$.

Now taking infimum on the right-hand side over all $g\in W_\infty^2$ and using the relation (3.2), we get

$$\left|L_n^{[\alpha]}(f;x)-f(x)\right|\le 4K_2\left(f,\frac{{\delta_n}^2(x)}{4}\right)+\omega(f,\beta_n)$$
$$\le M\omega_2\left(f,\tfrac{1}{2}\delta_n(x)\right)+\omega(f,\beta_n).$$

Hence the proof. □

Now we obtain the convergence with the help of Ditzian–Totik moduli of smoothness which is defined as

$$\omega_{\varphi^\lambda}^2(f,t)=\sup_{0<h\le t}\sup_{x\pm h\varphi^\lambda\in[0,\infty)}\left|\Delta_{h\varphi^\lambda}^2f(x)\right|,\tag{3.7}$$

where

$$\varphi(x)=\sqrt{x}\qquad\text{and}\qquad 0\le\lambda\le 1,$$

$$\Delta_{h\varphi^\lambda}^2f(x)=f\left(x+h\varphi^\lambda(x)\right)-2f(x)+f\left(x-h\varphi^\lambda(x)\right),$$

and corresponding K-functional is

$$K_{\varphi^\lambda}\left(f,t^2\right)=\inf_{g\in D_\lambda^2}\left\{\|f-g\|+t^2\left\|\varphi^{2\lambda}g''\right\|\right\},\tag{3.8}$$

with

$$D_\lambda^2=\left\{f\in C[0,\infty),f'\in A.C_{loc},\left\|\varphi^{2\lambda}f''\right\|<\infty\right\}.$$

We have following relation:

$$\omega_{\varphi^\lambda}^2(f,t)\sim K_{\varphi^\lambda}\left(f,t^2\right).\tag{3.9}$$

Theorem 3.3. *Let $f\in C_B[0,\infty)$, then for any $x\in[0,\infty)$ we have*

$$\left|L_n^{[\alpha]}(f;x)-f(x)\right|\le C\omega_2^{\varphi^\lambda}\left(f,\frac{\delta_n^{(1-\lambda)}(x)}{\sqrt{n}}\right)+\omega\left(f,\frac{1}{2n}\right),$$

where C is an absolute constant and

$$\delta_n(x)=\left(L_n^{[\alpha]}\left((t-x)^2;x\right)+\left(L_n^{[\alpha]}(t-x;x)\right)^2\right)^{\frac{1}{2}}.$$

Proof. Consider the operators defined by (3.5)

$$\hat{L}_n^{[\alpha]}(f;x) = L_n^{[\alpha]}(f;x) + f(x) - f\left(x+\frac{1}{2n}\right) \tag{3.10}$$

For above considered operators, we can write $\hat{L}_n^{[\alpha]}(1;x) = 1$ and $\hat{L}_n^{[\alpha]}(t;x) = x$.

Therefore, Definition (3.10), Lemma 2.3 and Lemma 2.4 gives

$$\hat{L}_n^{[\alpha]}(t-x;x) = 0, \qquad \hat{L}_n^{[\alpha]}\left((t-x)^2;x\right) \le \frac{C}{n}\delta_n^2(x) \tag{3.11}$$

$$\text{and} \qquad \left\|\hat{L}_n^{[\alpha]}(f;x)\right\| \le 3\|f\|.$$

Again, from ([23], p. 141), for $t<u<x$, we have

$$\frac{|t-u|}{\varphi^{2\lambda}(u)} \le \frac{|t-x|}{\varphi^{2\lambda}(x)} \qquad \text{and} \qquad \frac{|t-u|}{\delta_n^{2\lambda}(u)} \le \frac{|t-x|}{\delta_n^{2\lambda}(x)}. \tag{3.12}$$

Now

$$\begin{aligned}\left|\hat{L}_n^{[\alpha]}(f;x) - f(x)\right| &\le \left|\hat{L}_n^{[\alpha]}(f-g;x)\right| + \left|\hat{L}_n^{[\alpha]}(g;x) - g(x)\right| \\ &\quad + |f(x)-g(x)| \\ &\le 4\|f-g\| + \left|\hat{L}_n^{[\alpha]}(g;x) - g(x)\right|.\end{aligned} \tag{3.13}$$

For $g \in D_\lambda^2$ and $t, x \in [0,\infty)$, using Taylor's expansion with integral remainder,

$$g(t) = g(x) + (t-x)g'(x) + \int_x^t (t-u)g''(u)du.$$

Operating $\hat{L}_n^{[\alpha]}$ and using (3.11) and (3.12), we get

$$\begin{aligned}\left|\hat{L}_n^{[\alpha]}(g;x) - g(x)\right| &= \left|\hat{L}_n^{[\alpha]}\left(\int_x^t (t-u)g''(u)du;x\right)\right| \\ &\le \left|L_n^{[\alpha]}\left(\int_x^t (t-u)g''(u)du;x\right)\right| + \left|\int_x^{x+\frac{1}{2n}} \left(x+\frac{1}{2n}-u\right)g''(u)du\right| \\ &\le \left\|\delta_n^{2\lambda}g''\right\| L_n^{[\alpha]}\left(\frac{(t-x)^2}{\delta_n^{2\lambda}(x)};x\right) + \left\|\delta_n^{2\lambda}g''\right\| \frac{\left(\frac{1}{2n}\right)^2}{\delta_n^{2\lambda}(x)} \\ &= \delta_n^{-2\lambda}(x)\left\|\delta_n^{2\lambda}g''\right\| L_n^{[\alpha]}\left((t-x)^2;x\right) + \left\|\delta_n^{2\lambda}g''\right\| \delta_n^{-2\lambda}(x)\frac{1}{(2n)^2} \\ &\le C\left(\frac{\delta_n^{2(1-\lambda)}(x)}{n}\left\|\delta_n^{2\lambda}g''\right\|\right) + \frac{\delta_n^{2(1-\lambda)}(x)}{n}\left\|\delta_n^{2\lambda}g''\right\| \\ &\le C\frac{\delta_n^{2(1-\lambda)}(x)}{n}\left\|\delta_n^{2\lambda}g''\right\|.\end{aligned} \tag{3.14}$$

From (3.13), (3.14) and then using definition of K-functional (corresponding to Ditzian–Totik) along with the relation (3.9),

$$\begin{aligned}\left|\hat{L}_n^{[\alpha]}(f;x) - f(x)\right| &\le 4\|f-g\| + C\frac{\delta_n^{2(1-\lambda)}(x)}{n}\left\|\varphi^{2\lambda}g''\right\| \\ &\le C\omega_{\varphi^\lambda}^2\left(f, \frac{\delta_n^{(1-\lambda)}(x)}{\sqrt{n}}\right).\end{aligned}$$

Hence

$$\begin{aligned}\left|L_n^{[\alpha]}(f;x) - f(x)\right| &\le \left|\hat{L}_n^{[\alpha]}(f;x) - f(x)\right| + \left|f\left(x+\frac{1}{2n}\right) - f(x)\right| \\ &\le C\omega_{\varphi^\lambda}^2\left(f, \frac{\delta_n^{(1-\lambda)}(x)}{\sqrt{n}}\right) + \omega\left(f, \frac{1}{2n}\right).\end{aligned}$$

Thus the proof is complete. □

3.1. Rate of convergence:

Here we estimate the rate of convergence of the operators (1.5) in the class $DBV[0,\infty)$, the class of all absolutely continuous functions f defined on $[0,\infty)$ having a derivative coinciding a.e. with a function of bounded variation on $[0,\infty)$. It can be observed that for $f\in DBV[0,\infty)$, we can write

$$f(x)=\int_0^x g(t)dt+f(0),$$

where $g(t)$ is a function of bounded variation on each finite subinterval of $[0,\infty)$.

Theorem 3.4. *Let $f\in DBV(0,\infty)$ then for all $x\in(0,\infty)$ and sufficiently large n, we have*

$$\begin{aligned}\left|L_n^{[\alpha]}(f;x)-f(x)\right| &\le \frac{1}{4n}\left|f'(x+)+f'(x-)\right|+\frac{1}{2}\sqrt{\frac{C}{n}}\left|f'(x+)-f'(x-)\right|\\ &\quad+\frac{C\delta_n^2(x)}{nx^2}\left|f(2x)-f(x)-xf'(x+)\right|\\ &\quad+\frac{x}{\sqrt{n}}\vee_{x-\frac{x}{\sqrt{n}}}^{x+\frac{x}{\sqrt{n}}}\left(f_x'\right)+\frac{C\delta_n^2(x)}{nx}\sum_{k=1}^{[\sqrt{n}]}\vee_{x-\frac{x}{k}}^{x+\frac{x}{k}}\left(f_x'\right)\\ &\quad+M(\gamma,r,x)+\frac{|f(x)|}{nx^2}C\delta_n^2(x)+\sqrt{\frac{C}{n}}\delta_n(x)f'(x+),\end{aligned}\tag{3.15}$$

where $\vee_a^b f(x)$ denotes the total variation of f on $[a,b]$, f_x is an auxiliary operator given by

$$f_x(t)=\begin{cases}f(t)-f(x-), & 0\le t<x\\ 0, & t=x\\ f(t)-f(x+), & x<t<\infty\end{cases}$$

and

$$M(\gamma,r,x)=M2^{\gamma}\left(\int_0^{\infty}(t-x)^{2r}K_n^{[\alpha]}(x,t)dt\right)^{\frac{\gamma}{2r}}$$

Proof. Because $L_n^{[\alpha]}(1;x)=1$, therefore for all $x\in(0,\infty)$, we obtain

$$\begin{aligned}L_n^{[\alpha]}(f;x)-f(x)&=\int_0^{\infty}(f(t)-f(x))K_n^{[\alpha]}(x,t)dt\\ &=\int_0^{\infty}K_n^{[\alpha]}(x,t)\int_x^t f'(u)dudt.\end{aligned}\tag{3.16}$$

For $f\in DBV(0,\infty)$, we may write

$$\begin{aligned}f'(u)&=\frac{1}{2}\left(f'(x+)+f'(x-)\right)+f_x'(u)+\frac{1}{2}\left(f'(x+)-f'(x-)\right)\operatorname{sgn}(u-x)\\ &\quad+\delta_x(u)\left(f'(u)-\frac{1}{2}\left(f'(x+)+f'(x-)\right)\right),\end{aligned}\tag{3.17}$$

where

$$\delta_x(u)=\begin{cases}1, & u=x\\ 0, & u\ne x.\end{cases}$$

It is easy to write that

$$\int_0^{\infty}\left(\int_x^t\left(f'(u)-\frac{1}{2}\left(f'(x+)+f'(x-)\right)\right)\delta_x(u)du\right)K_n^{[\alpha]}(x,t)dt=0.\tag{3.18}$$

Using (2.1), we obtain

$$\begin{aligned}&\int_0^{\infty}\left(\int_x^t\frac{1}{2}\left(f'(x+)+f'(x-)\right)du\right)K_n^{[\alpha]}(x,t)dt\\ &\quad=\frac{1}{2}\left(f'(x+)+f'(x-)\right)L_n^{[\alpha]}((t-x);x).\end{aligned}\tag{3.19}$$

Moreover,

$$\int_0^{\infty}\left(\int_x^t\frac{1}{2}\left(f'(x+)-f'(x-)\right)\operatorname{sgn}(u-x)du\right)K_n^{[\alpha]}(x,t)dt$$

$$= \int_0^\infty \frac{1}{2}\big(f'(x+) - f'(x-)\big)(t-x)K_n^{[\alpha]}(x,t)dt$$
$$\le \frac{1}{2}\big|f'(x+) - f'(x-)\big| \int_0^\infty |t-x|K_n^{[\alpha]}(x,t)dt$$
$$= \frac{1}{2}\big|f'(x+) - f'(x-)\big|L_n^{[\alpha]}(|t-x|;x)$$
$$\le \tfrac{1}{2}|f'(x+) - f'(x-)|\Big(L_n^{[\alpha]}\big((t-x)^2;x\big)\Big)^{1/2}. \tag{3.20}$$

Using Eqs. (3.16)–(3.20) with Lemma 2.4, we have

$$L_n^{[\alpha]}(f;x) - f(x) \le \frac{1}{2}\big(f'(x+) + f'(x-)\big)L_n^{[\alpha]}((t-x);x) + \frac{1}{2}\big|f'(x+) - f'(x-)\big|\Big(L_n^{[\alpha]}\big((t-x)^2;x\big)\Big)^{1/2} + \int_0^\infty \left(\int_x^t f_x'(u)du\right)K_n^{[\alpha]}(x,t)dt$$
$$\le \frac{1}{4n}\big(f'(x+) + f'(x-)\big) + \frac{1}{2}\sqrt{\frac{C}{n}}\delta_n(x)\big|f'(x+) - f'(x-)\big| + \int_0^\infty \left(\int_x^t f_x'(u)du\right)K_n^{[\alpha]}(x,t)dt.$$

Therefore

$$\Big|L_n^{[\alpha]}(f;x) - f(x)\Big| \le \frac{1}{4n}\big|f'(x+) + f'(x-)\big| + \frac{1}{2}\sqrt{\frac{C}{n}}\delta_n(x)\big|f'(x+) - f'(x-)\big| + A_{nx} + B_{nx}, \tag{3.21}$$

where

$$A_{nx} = \left|\int_0^x \left(\int_x^t f_x'(u)du\right)K_n^{[\alpha]}(x,t)dt\right|,$$

and

$$B_{nx} = \left|\int_x^\infty \left(\int_x^t f_x'(u)du\right)K_n^{[\alpha]}(x,t)dt\right|.$$

Applying Lemma 2.5, integrating by parts and taking $y = x - \frac{x}{\sqrt{n}}$, we obtain

$$A_{nx} = \left|\int_0^x \left(\int_x^t f_x'(u)du\right)d_t\beta_n(x,t)\right| = \left|\int_0^x \beta_n(x,t)f_x'(t)dt\right|$$
$$\le \int_0^y |\beta_n(x,t)|\big|f'_x(t)\big|dt + \int_y^x |\beta_n(x,t)|\big|f'_x(t)\big|dt$$
$$= \int_0^{x-\frac{x}{\sqrt{n}}} \beta_n(x,t)\big|f'_x(t)\big|dt + \int_{x-\frac{x}{\sqrt{n}}}^x \beta_n(x,t)\big|f'_x(t)\big|dt.$$

Since $f_x'(x) = 0$ and $\beta_n(x,t) \le 1$, it follows

$$\int_{x-\frac{x}{\sqrt{n}}}^x \big|f_x'(t)\big|\beta_n(x,t)dt = \int_{x-\frac{x}{\sqrt{n}}}^x \big|f_x'(t) - f_x'(x)\big|\beta_n(x,t)dt$$
$$\le \int_{x-\frac{x}{\sqrt{n}}}^x \vee_t^x\big(f_x'\big)dt \le \frac{x}{\sqrt{n}}\vee_{x-\frac{x}{\sqrt{n}}}^x\big(f_x'\big).$$

Again using Lemma 2.5 and substituting $t = x - \frac{x}{u}$,

$$\int_0^{x-\frac{x}{\sqrt{n}}} \big|f_x'(t)\big|\beta_n(x,t)dt \le \frac{C\delta_n^2(x)}{n}\int_0^{x-\frac{x}{\sqrt{n}}} \frac{\big|f_x'(t)\big|}{(x-t)^2}dt$$
$$\le \frac{C\delta_n^2(x)}{nx}\int_1^{\sqrt{n}} \vee_{x-\frac{x}{u}}^x\big(f_x'\big)du$$

$$\leq \frac{C\delta_n^2(x)}{nx}\sum_{k=1}^{[\sqrt{n}]}\vee_{x-\frac{x}{k}}^{x}(f_x').$$

Thus, $A_{nx}\leq \frac{x}{\sqrt{n}}\vee_{x-\frac{x}{\sqrt{n}}}^{x}(f_x')+\frac{C\delta_n^2(x)}{nx}\sum_{k=1}^{[\sqrt{n}]}\vee_{x-\frac{x}{k}}^{x}(f_x')$.

Now we can write

$$B_{n,x}\leq\left|\int_x^{2x}\left(\int_x^t f_x'(u)du\right)K_n^{[\alpha]}(x,t)dt\right|+\left|\int_{2x}^{\infty}\left(\int_x^t f_x'(u)du\right)K_n^{[\alpha]}(x,t)dt\right|$$

Also from part (ii) of Lemma 2.5, we have

$$K_n^{[\alpha]}(x,t)=d_t(1-\beta_n(x,t))\quad\text{for}\quad t>x$$

Thus,

$$B_{nx}\leq B_{1,n,x}+B_{2,n,x},$$

where

$$B_{1,n,x}=\left|\int_x^{2x}\left(\int_x^t f_x'(u)du\right)d_t(1-\beta_n(x,t))\right|$$

and

$$B_{2,n,x}=\left|\int_{2x}^{\infty}\left(\int_x^t f_x'(u)du\right)K_n^{[\alpha]}(x,t)dt\right|.$$

Applying integration by parts as well as using Lemma 2.5, (3.17), $1-\beta_n(x,t)\leq 1$ and putting $t=x+\frac{x}{u}$ successively,

$$\begin{aligned}
B_{1,n,x}&=\left|\int_x^{2x}f_x'(u)du(1-\beta_n(x,2x))-\int_x^{2x}f_x'(t)(1-\beta_n(x,t))dt\right|\\
&\leq\left|\int_x^{2x}\big(f'(u)-f'(x+)\big)du\right||1-\beta_n(x,2x)|\\
&\quad+\int_x^{2x}\left|f_x'(t)\right||1-\beta_n(x,t)|dt\\
&\leq\frac{C\delta_n^2(x)}{nx^2}\left|f(2x)-f(x)-xf'(x+)\right|\\
&\quad+\int_x^{x+\frac{x}{\sqrt{n}}}\left|f_x'(t)\right||1-\beta_n(x,t)|dt+\int_{x+\frac{x}{\sqrt{n}}}^{2x}\left|f_x'(t)\right||1-\beta_n(x,t)|dt\\
&\leq\frac{C\delta_n^2(x)}{nx^2}\left|f(2x)-f(x)-xf'(x+)\right|\\
&\quad+\frac{C\delta_n^2(x)}{n}\int_{x+\frac{x}{\sqrt{n}}}^{2x}\frac{\vee_x^t(f_x')}{(t-x)^2}dt+\int_x^{x+\frac{x}{\sqrt{n}}}\vee_x^t(f_x')dt\\
&\leq\frac{C\delta_n^2(x)}{nx^2}\left|f(2x)-f(x)-xf'(x+)\right|\\
&\quad+\frac{C\delta_n^2(x)}{n}\int_{x+\frac{x}{\sqrt{n}}}^{2x}\frac{\vee_x^t(f_x')}{(t-x)^2}dt+\frac{x}{\sqrt{n}}\vee_x^{x+\frac{x}{\sqrt{n}}}(f_x')\\
&\leq\frac{C\delta_n^2(x)}{nx^2}\left|f(2x)-f(x)-xf'(x+)\right|\\
&\quad+\frac{C\delta_n^2(x)}{nx}\sum_{k=1}^{[\sqrt{n}]}\vee_x^{x+\frac{x}{k}}(f_x')+\frac{x}{\sqrt{n}}\vee_x^{x+\frac{x}{\sqrt{n}}}(f_x').
\end{aligned}$$

Finally, Remark 2.1 implies

$$\begin{aligned}
B_{2,n,x}&=\left|\int_{2x}^{\infty}\left(\int_x^t\big(f'(u)-f'(x+)\big)du\right)K_n^{[\alpha]}(x,t)dt\right|\\
&\leq\int_{2x}^{\infty}|f(t)-f(x)|K_n^{[\alpha]}(x,t)dt+\int_{2x}^{\infty}|t-x|f'(x+)K_n^{[\alpha]}(x,t)dt
\end{aligned}$$

$$\leq M\int_{2x}^{\infty} t^{\gamma}K_n^{[\alpha]}(x,t)dt + |f(x)|\int_{2x}^{\infty} K_n^{[\alpha]}(x,t)dt + \sqrt{\frac{C}{n}}\delta_n(x)f'(x+).$$

As it is obvious that $t \leq 2(t-x)$ and $x \leq t-x$ when $t \geq 2x$, applying Holder's inequality, we get

$$B_{2,n,x} \leq M2^{\gamma}\left(\int_0^{\infty}(t-x)^{2r}K_n^{[\alpha]}(x,t)dt\right)^{\frac{\gamma}{2r}} + \frac{C\delta_n^2(x)|f(x)|}{nx^2} + \sqrt{\frac{C}{n}}\delta_n(x)f'(x+)$$

$$= M(\gamma,r,x) + \frac{C\delta_n^2(x)|f(x)|}{nx^2} + \sqrt{\frac{C}{n}}\delta_n(x)f'(x+).$$

Estimates of $B_{1,\,n,\,x}$ and $B_{2,\,n,\,x}$ results

$$B_{n,x} \leq \frac{C\delta_n^2(x)}{nx^2}\left|f(2x) - f(x) - xf'(x+)\right|$$

$$+ \frac{C\delta_n^2(x)}{nx}\sum_{k=1}^{[\sqrt{n}]}\vee_x^{x+\frac{x}{k}}\left(f_x{}'\right) + \frac{x}{\sqrt{n}}\vee_x^{x+\frac{x}{\sqrt{n}}}\left(f_x{}'\right)$$

$$+ M(\gamma,r,x) + \frac{C\delta_n^2(x)|f(x)|}{nx^2} + \sqrt{\frac{C}{n}}\delta_n(x)f'(x+).$$

Hence values of $A_{n,\,x}$ and $B_{n,\,x}$ in (3.21), we get the required result. □

Acknowledgment

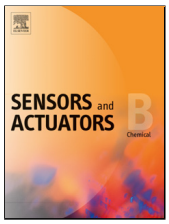
The authors are extremely thankful to the referees for their valuable comments and suggestions, leading to a better presentation of the paper. The authors are also thankful to Professor T. E. Simos for special attention.

References

[1] U. Abel, M. Ivan, On a generalization of an approximation operator defined by A. Lupaş, Gen. Math. 15 (1) (2007) 21–34.
[2] O. Agratini, On a problem of A. Lupaş, Gen. Math. 6 (1998) 3–11.
[3] O. Agratini, On the rate of convergence of a positive approximation process, Nihonkai Math. J. 11 (2000) 47–56.
[4] P.N. Agrawal, V. Gupta, A.S. Kumar, A. Kajla, Generalized Baskakov-Szász type operators, Appl. Math. Comput. 236 (2014) 311–324.
[5] F. Altomare, M. Campiti, Korovkin-type approximation theory and its application, de Gruyter Studies in Mathematics, vol. 17, Walter de Gruyter & Co., Berlin, 1994.
[6] F. Altomare, M.C. Montano, V. Leonessa, On a generalization of Szász-Mirakjan-Kantorovich operators, Results Math. 63 (3–4) (2013) 837–863.
[7] C. Bardaro, I. Mantellini, Voronovskaja formulae for Kantorovich generalized sampling series, Int. J. Pure Appl. Math 62 (3) (2010) 247–262.
[8] C. Bardaro, I. Mantellini, Linear combinations of multivariate generalized sampling type series, Mediterr. J. Math. 10 (4) (2013) 1833–1852.
[9] P.L. Butzer, On the extensions of Bernstein polynomials o the infinite interval, Proc. Am. Math. Soc. 5 (1954) 547–553.
[10] F. Cluni, D. Costarelli, A.M. Minotti, G. Vinti, Applications of sampling Kantorovich operators to thermographic images for seismic engineering, J. Comput. Anal. Appl. 19 (4) (2015) 602–617.
[11] L. Coroianu, S.G. Gal, Saturation results for the truncated maxproduct sampling operators based on sinc and Fejér-type kernels, Sampl. Theory Signal Image Process. 11 (1) (2012) 113–132.
[12] D. Costarelli, A.M. Minotti, G. Vinti, Approximation of discontinuous signals by sampling Kantorovich series, J. Math. Anal. Appl. 450 (2) (2017) 1083–1103.
[13] D. Costarelli, G. Vinti, Rate of approximation for multivariate sampling Kantorovich operators on some functions spaces, J. Integral Equ. Appl. 26 (4) (2014) 455–481.
[14] D. Costarelli, G. Vinti, Degree of approximation for nonlinear multivariate sampling Kantorovich operators on some functions spaces, Numer. Funct. Anal. Optim. 36 (8) (2015) 964–990.
[15] D. Costarelli, G. Vinti, Approximation by max-product neural network operators of Kantorovich type, Results Math. 69 (3) (2016) 505–519.
[16] D. Costarelli, G. Vinti, Convergence for a family of neural network operators in Orlicz spaces, Math. Nachr. 290 (2–3) (2017) 226–235.
[17] B. Della Vecchia, L.M. Kocic, On the degeneracy property of some linear positive operators, Calcolo 25 (4) (1988) 363–377.
[18] N. Deo, M. Dhamija, Generalized positive linear operators based on PED and IPED, 2016, arxiv:1605.06660v1.
[19] N. Deo, M. Dhamija, D. Miclăuş, Stancu-Kantorovich operators based on inverse Pólya-Eggenberger distribution, Appl. Math. Comput. 273 (2016) 281–289.
[20] M. Dhamija, N. Deo, Jain-Durrmeyer operators associated with the inverse Pólya-Eggenberger distribution, Appl. Math. Comput. 286 (2016) 15–22.
[21] M. Dhamija, N. Deo, Approximation by generalized positive linear-Kantorovich operators, Filomat, in press.
[22] R.A. DeVore, G.G. Lorentz, Constructive Approximation, Springer, Berlin, 1993.
[23] Z. Ditzian, V. Totik, Moduli of Smoothness, Springer Series in Computational Mathematics, vol. 9, Springer-Verlag, New York, 1987.
[24] O. Duman, M.A. Özarslan, B. Della Vecchia, Modified Szász-Mirakjan-Kantorovich operators preserving linear functions, J. Math. 33 (2) (2009) 15–158.
[25] A. Erençcin, G. Başcanbaz-Tunca, F. Taçsdelen, Some properties of the operators defined by Lupaş, Rev. Anal. Numér. Théor. Approx. 43 (2) (2014) 168–174.
[26] Z. Finta, Pointwise approximation by generalized Szász-Mirakjan operators, Stud. Univ. Babeş-Bolyai Math. 46 (4) (2001) 61–67.
[27] Z. Finta, On approximation properties of Stancus operators, Stud. Univ. Babes-Bolyai Math. XLVII (4) (4) (2002) 47–55.

[28] V. Gupta, N. Deo, X. Zeng, Simultaneous approximation for Szász-Mirakian-Stancu-Durrmeyer operators, Anal. Theory Appl. 29 (1) (2013) 86–96.
[29] N.K. Govil, V. Gupta, D. Soybaş, Certain new classes of Durrmeyer type operators, Appl. Math. Comput. 225 (2013) 195–203.
[30] V. Gupta, C. Radu, Statistical approximation properties of q-Baskakov-Kantorovich operators, Cent. Eur. J. Math. 7 (4) (2009) 809–818.
[31] N. Ispir, Rate of convergence of generalized rational type Baskakov operators, Math. Comput. Modell. 46 (5–6) (2007) 625–631.
[32] G.C. Jain, S. Pethe, On the generalizations of Bernstein and Szász-Mirakyan operators, Nanta Math. 10 (1977) 185–193.
[33] H.S. Jung, N. Deo, M. Dhamija, Pointwise approximation by Bernstein type operators in mobile interval, Appl. Math. Comput. 214 (1) (2014) 683–694.
[34] P.P. Korovkin, Convergence of linear positive operators in the spaces of continuous functions (Russian), Doklady Akad. Nauk. SSSR(N. N.) 90 (1953) 961–964.
[35] A. Lupaş, The approximation by means of some linear positive operators, in: M.W. Muller, M. Felten, D.H. Mache (Eds.), Approximation Theory (Proceedings of the International Dortmund Meeting IDoMAT 95, held in Witten, Germany, March 13–17, (1995), Akademie Verlag, Berlin, 1995, pp. 201–229. (Mathematical research, Vol. 86).
[36] G. Mastroianni, Una generalizzazione dell'operatore di Mirakyan, Rend. Accad. Sci. Fis. Mat. Napoli, Ser. IV XLVIII (1980/1981) 237–252.
[37] V. Miheşan, Approximation of continuous functions by linear and positive operators, 1997, (Romanian), Ph.D. thesis, Cluj.
[38] O. Orlova, G. Tamberg, On approximation properties of Kantorovich type sampling operators, Sampl. Theory Signal Image Process. 10 (2014).
[39] D.D. Stancu, A study of the remainder in an approximation formula using a Favard-Szász type operator, Stud. Univ. Babeş-Bolyai Math. XXV (1980) 70–76.
[40] O. Szász, Generalizations of S. Bernstein's polynomial to the infinite interval, J. Res. Nat. Bur. Stand. 45 (1950) 239–245.
[41] V. Totik, Approximation by Szász-Mirakyan-Kantorovich operators in $l_p\,(p>1)$, Anal. Math. 9 (2) (1983) 147–167.

Accepted Manuscript



Title: Biofunctionalized Graphene Oxide Wrapped Carbon Nanotubes Enabled Microfluidic Immunochip for Bacterial Cells Detection

Authors: Chandan Singh, Md. Azahar Ali, Venu Reddy, Dinesh Singh, Cheol Gi Kim, G. Sumana, B.D. Malhotra

PII: S0925-4005(17)31719-7
DOI: http://dx.doi.org/10.1016/j.snb.2017.09.054
Reference: SNB 23145

To appear in: *Sensors and Actuators B*

Received date: 26-4-2017
Revised date: 31-8-2017
Accepted date: 8-9-2017

Please cite this article as: Chandan Singh, Md.Azahar Ali, Venu Reddy, Dinesh Singh, Cheol Gi Kim, G.Sumana, B.D.Malhotra, Biofunctionalized Graphene Oxide Wrapped Carbon Nanotubes Enabled Microfluidic Immunochip for Bacterial Cells Detection, Sensors and Actuators B: Chemicalhttp://dx.doi.org/10.1016/j.snb.2017.09.054

This is a PDF file of an unedited manuscript that has been accepted for publication. As a service to our customers we are providing this early version of the manuscript. The manuscript will undergo copyediting, typesetting, and review of the resulting proof before it is published in its final form. Please note that during the production process errors may be discovered which could affect the content, and all legal disclaimers that apply to the journal pertain.

ACCEPTED MANUSCRIPT

Biofunctionalized Graphene Oxide Wrapped Carbon Nanotubes Enabled Microfluidic Immunochip for Bacterial Cells Detection

Chandan Singh[1,2], Md. Azahar Ali[1], Venu Reddy[3], Dinesh Singh[4], Cheol Gi Kim[5], G. Sumana[1*], B.D.Malhotra[6,£]

[1]Biomedical Instrumentation Section, CSIR-National Physical Laboratory, Dr. K.S.Krishnan Marg, New Delhi 110012,India.

[2]Academy of Scientific and Innovative Research (AcSIR), CSIR-National Physical Laboratory Campus, Dr. K.S.Krishnan Marg, New Delhi, 110012, India

[3]Nanotechnology Research Center, SRKR Engineering College, China Amiram, Bhimavaram -534204, India

[4]Sophisticated Analytical Equipment Division, CSIR-National Physical Laboratory, Dr. K.S.Krishnan Marg, New Delhi 110012,India

[5]Department of Emerging Materials Science, DGIST,Daegu-711873, South Korea

[6]Department of Biotechnology, Delhi Technological University, Shahbad Daulatpur, Main Bawana Road, Delhi110042, India.

Author Information

Corresponding Authors

*G.Sumana, E-mail:sumanagajjala@gmail.com ,Tel.: +91(011) 45602439.

[£]B. D. Malhotra, E-mail:bansi.malhotra@gmail.com .Tel.: +91-11-27871043, ext. 1609. Fax: +91-11-27871023.

Research Highlights

- Microfluidic Electrochemical immunosensor for *salmonella typhimurium* detection has been designed using soft lithography technique.
- Graphene Oxide (GO) wrapped caboxylated multiwalled carbon nanotubes (cMWCNTS) have been used as a transducer material for highly sensitive detection of *salmonella typhimurium*.
- Wrapping of cMWCNTs with GO leads to improved electrochemical performance of the composite as compared to GO, most probably due to the synergistic effect.

ACCEPTED MANUSCRIPT

- Abundant functional group available on GO and cMWCNTS were utilized for antibody functionalization using carbodiimide coupling using EDC-NHS chemistry results into the improved detection range.
- The designed microfluidic immunosensor offers label free, fast and reliable detection of *salmonella typhimurium* with negligible interference in presence of potential inteferent like *E.Coli*.

Abstract

A sensitive and selective microfluidic immunochip was fabricated for detection of *Salmonella typhimurium (S.typhimurium)* bacterial cells. In this sensor, graphene oxide (GO) nano sheets wrapped carboxylated multiwalled carbon nanotubes (cMWCNTs) composite acted as a transducer material. The colloidal solution of GO-cMWCNTs composite was selectively deposited onto patterned indium tin oxide (ITO) electrode and sealed with polydimethylsiloxane (PDMS) micro channels. The *S. typhimurium* antibodies (StAb) were *in situ* biofunctionalized followed by EDC-NHS covalent chemistry *via* amidation reaction. The presence of abundant functional groups at the GO-cMWCNTs composite improved the loading of antibodies (StAb) against *S. typhimurium* leading to improved biosensing characteristics. Wrapping of cMWCNTs with GO resulted in superior electron transfer behavior enhancing the sensitivity (162.47μA/CFU^{-1}/mLcm^{-2}) almost two folds as compared to that based on GO (89.16 μA/CFU^{-1}/mLcm^{-2}) sheets for bacterial cells detection. Besides this, GO wrapped cMWCNTs integrated microfluidics biosensor offers low detection limit as 0.376 CFU/mL and negligible interference due to presence of *Escherichia coli (E. coli* (O157:H7).

Keywords: Microfluidic Immunochip, Graphene Oxide, Carbon Nanotubes, *Salmonella typhimurium,* Synergistic effect, Sensitivity.

ACCEPTED MANUSCRIPT

1. Introduction

Salmonella, a Gram-negative facultative intracellular pathogen causes a wide range of illness in humans and animals, depending on the host susceptibility and the bacterial reservoir [1]. Some reservoirs may cause localized intestinal infection (gastroenteritis),while others are known to be responsible for systematic infection of a healthy host (typhoid) and systematic infection in susceptible host (non-typhoid salmonellosis) [1]. Among these, non-typhoid salmonellosis is considered to be the main cause for blood stream infection among children suffering from malaria, malnutrition and adults infected with human immunodeficiency virus [2, 3]. This has been found to result in annual incidence of 175-388/100,000 among children (<5yr) generating high fatality rate of 22-25%[2, 3]. Salmonellosis can be transferred from animals to humans due to consumption of infected foods. *S.Enteritidis*, *S.Heidelberg* and *S.typhimurium* are the most common reservoirs that are known to be responsible for salmonellosis infection. Among these, *S.typhimurium* is considered to be more fatal. *S.typhimurium* takes 12-36 h after the consumption of infected food resulting in symptoms like diarrhea, abdominal pain, nausea and vomiting. Conventional methods for *S.typhimurium* detection include selective enrichment and plating followed by biochemical tests that require 3-4 days to obtain results and another 6-7 days for the confirmation[4]. For the last two decades, many optical and electrochemical methods have been developed for rapid and reliable detection of *S.typhimurium*. Enzyme-linked immune magnetic electrochemical technique has been developed for *S.typhimurium* detection[5]. Similarly, a magneto-electrode has been designed for label free detection of *S.typhimurium* [6]. However, these techniques suffer from poor sensitivity, limited detection range and require a high volume of sample for the precise measurement.

ACCEPTED MANUSCRIPT

The application of microfluidics in biosensing may lead to significant improvements such as minimizing the sample volume, reducing the consumption of costly chemicals and the reduced processing time[7,8]. Combination of microfluidics with biosensing offers advantages of high throughput analysis, and portability resulting in the smart point-of-care diagnostics (POC). Due to comparable size of biomolecules, engineered nanomaterials can be used for functionalization and detection of different bioanalytes [9, 10]. With larger surface area and signal amplification capability of nanomaterials, the high aspect ratio of microfluidic devices may result in increased sensitivity and low limit of detection [11-14]. Zhou *et al.* reported gold nanoparticles integrated microfluidic chamber to detect the cardiac biomarkers [11]. Ali *et al.* reported a multiwalled carbon nanotubes integrated biosensor for the cholesterol detection with improved biosensing features[15].

GO is considered to be a potential candidate for sensing/diagnostic applications due to its excellent electron transport properties, very high specific surface area and availability of different functional groups on the edge and basal plane, [16, 17]. It is a derivative of carbon nanotubes (CNTs) cut along the axis and contains many conduction pathways per unit mass compared to the CNTs resulting in higher conductivity. However, the difficulties associated with the mechanical cleavage method and drawbacks in the reduction methods of GO (e.g hydrazine works only on the basal plane, while $NaBH_4$ results in incomplete reduction with aggregates) and is known to have poor conductivity[18, 19]. However, wrapping of GO nanosheets on CNTs may yield enhanced conductivity[20]. For diagnostics applications, solution process for GO is preferred as it allows easy fabrication of films using Langmuir-Blodgett technique, solution casting and filtration. However, these techniques suffer from lack of film architecture due to aggregation of GO, resulting in loss of the surface area [18]. The incorporation of CNTs may perhaps result in physical separation of two-dimensional GO sheets and decreased resistance, as electrical conductivity of the composite is known to depend on the percolated network of the CNTs formed in the composite film whereas GO

ACCEPTED MANUSCRIPT

acts as a carrier[21]. Additionally, intertwined GO with CNTs may result in improved electrochemical sensing of the target analyte [22].Romano *et al.* reported that GO-CNTs nanocomposite offers controlled porosity with maximized electroactive surface area that may provide enhanced surface for the immobilization of the biomolecules[23]. Many reports are available on the synergistic effect of GO and CNTs resulting in improved electrochemical and mechanical properties as compared to that of the individual components[24]. Cheng *et al*. have reported several fold increase in the electrochemical performance of the GO-CNTs composite mainly due to the synergistic effect[25].

We report results of the studies relating to fabrication of a sensitive, selective microfluidic immunosensor for detection of *S. typhimurium* via antigen-antibody interactions. The GO-cMWCNTs composite was electrophoretically deposited onto the hydrolyzed ITO microelectrode integrated with PDMS microchannels. Antibodies of *S. typhimurium* were immobilized using EDC-NHS coupling chemistry and the label-free detection of *S. typhimurium* was achieved using electrochemical technique. The schematic of fabrication of GO-cMWCNTs integrated microfluidic electrode is shown in **Fig. (1)**.

2. Experimental Section

2.1.Chemicals

Graphite powder flakes (45 μm, >99.99 wt%) were procured from Sigma Aldrich, USA. *S. typhimurium* antibody and antigen (heat killed S. *typhimurium* cells) were purchased from KPL Laboratory, USA. Bovine serum albumin (BSA), 1-ethyl-3-(3-dimethylaminopropyl) carbodiimide (EDC), and N-hydroxysuccinimide (NHS) were procured from Sigma, Aldrich, USA. The SU8-100 negative photoresist and SU-8 developer were purchased from Microchem (Newton, MA, USA). All other chemicals were of analytical grade and were used

ACCEPTED MANUSCRIPT

without further purification. During the entire experiments, Millipore water purification system was utilized for de-ionized water.

2.2. Characterization

The UV-visible spectroscopy (Perkin-Elmer, Lambda 950), Fourier transform infra-red spectroscopic (FT-IR, Perkin-Elmer, Model 2000) were used for characterization of the synthesized nanocomposite. The structural and morphological studies were carried out using scanning electron microscopy (SEM, LEO 440), transmission electron microscopy (HRTEM, Tecnaii-G2F30 STWIN). Electrochemical studies were performed on cyclic voltammetry (CV) conducted using Autolab, Potentiostat/Galvanostat (Eco Chemie, the Netherlands, Model AUT84275), Harvard syringe pumps and ILS microsyringes (Germany) were utilized to control the fluid flow into the microfluidic channels.

2.3.Device Fabrication

The PDMS microchannels were fabricated using a soft lithography technique as reported in literature[13]. The channel height and width were 200 µm each, and the length was 2.0 cm. The reservoirs of the microchannels at the end were fabricated by punching holes in the PDMS slab at the desired position. The fabricated channels were connected to reservoirs via a single inlet and outlet (**Fig.1**). The real image of the fabricated microfluidic device is shown in **Fig.2**. Microelectrodes were fabricated onto the ITO coated glass slides using wet chemical etching process using a home-made etchant [HNO_3:HCl:H_2O(1:10:10)].This was followed with washing with acetone and water, and were hydrolyzed using a solution containing H_2O:H_2O_2:NH_3(5:1:1) for about 1 h at 75ºC.

2.4 Fabrication of GO-cMWCNTs microelectrode

The synthesis of GO was achieved using the method proposed by Marcano *et al.*[26].The synthesis of MWCNTs was accomplished using catalytic chemical vapor deposition method

ACCEPTED MANUSCRIPT

using ferrocene as the catalyst and toluene as hydrogen source and further functionalized using nitric acid and sulphuric acid generating carboxylic group on MWCNTs surface [27].The synthesis of GO-cMWCNTs well-dispersed colloidal solution was accomplished using the a previously reported method[20].The optimum ratio of GO: cMWCNTs was determined on the basis of their elelctrochemical response. Five different GO-cMWCNTs electrodes having different mass ratio of GO: cMWCNTs such as 1:1, 1:2.5, 1:5 , 1:10 and 1:15 were used to measure the electrochemical response and the ratio of 1: 10 found to be most suitable, as it yielded the maximum electrochemical response as shown in the **Fig. (S1)**. This may be due to the fact that composites having ratio other than 1:10 were unable to generate effective π-π coupling between GO and cMWCNTs so that GO could not effectively wrap cMWCNTs resulting into the inefficient charge transfer properties of the composites [20].

The electrophoretic deposition (EPD) was accomplished for deposition of the GO-cMWCNTs composite. For EPD, colloidal solution of GO-cMWCNTs dissolved in acetonitrile (10 mg in 50 mL) was deposited onto the ITO (sheet resistance of 30 Ω cm^{-1}) coated microelectrodes by applying DC voltage of 60 V for 90 s to a two electrodes cell. In details, 10^{-5}–10^{-4} mol of $Mg(NO_3)_2.6H_2O$ was added into the colloidal solution of GO-cMWCNTs to obtain the overall charge on the composite positive for deposition onto the negatively charged hydrolyzed ITO microlectrodes under the influence of electric field [28]. In the EPD process, platinum (Pt) foil (1cm×2cm) acted as the cathode and a pre-cleaned ITO-coated glass substrate separated by 1.0 cm served as the anode. After successful deposition of the GO-cMWCNTs the microelectrode was washed with DI water three times followed by drying.

Prior to immobilization of the StAb, carboxylated groups (-COOH) at GO-cMWCNTs composite were activated using EDC-NHS coupling chemistry, where EDC (0.4M) acted as a

ACCEPTED MANUSCRIPT

coupling agent and NHS (0.1M) as an activator. For *in situ* immobilization, 130µL of StAb (100 µg/mL) dissolved in PBS (pH 7.4, 50 mM) solution was injected by syringe pump with a constant speed (10 µL/min) into the GO-cMWCNTs based microfluidic chip resulting in the formation of discrete regions for the capturing the *S.typhimurium* cells. Further, BSA (1 mg/mL) was used to block the non-specific sites present in the StAb/GO-cMWCNTs immmunochip.

3. Results and Discussions

3.1 UV-visible studies

Fig. 3(a) shows UV visible spectra of as-synthesized GO, cMWCNTs and GO-cMWCNTs composite. In curve (a), characteristic peak found at 230 nm for the GO nanosheets arose due to the π-π* transition of the aromatic C-C bond and a shoulder at 300 nm was attributed to the n-π* transitions of the C-O bonds. Similarly, the peak for the cMWCNTs found at 260 nm was due to π-π* transitions of aromatic C-C bonds of the cMWCNTs [29]. After the formation of the nanocomposite strong, π-π* transition was shifted to higher wavelength (248 nm) indicating strong interaction in the hydrophobic aromatic regions between cMWCNTs and the aromatic basal plane of GO resulting in wrapping of the GO nanosheets onto cMWCNTs [30].

3.2 FT-IR Analysis

FT-IR spectra recorded for GO, cMWCNTs and GO-cMWCNTs are shown in **Fig. 3(b)**. Curve (a) shows characteristic peak for the cMWCNTs shown at 1245cm^{-1} arising due to the C-O stretching, 1404 cm^{-1} is attributed to the aromatic C-C (in ring) stretching,1600 cm^{-1}may be assigned to the C=C stretching and 1750 cm^{-1} is due to C=O stretching due to the carboxylation of MWCNTs. In the spectra (b), the peak 980 cm^{-1} is assigned to C-H stretching, peak at 1251 $cm^{-1}$is due to the C-O of the various carboxylic groups available on

ACCEPTED MANUSCRIPT

its basal plane while the peak at 1530 cm^{-1}corresponds to C-C stretching of the aromatic carbon ring. Further, Curve(c) shows the spectra of GO wrapped cMWCNTs and the intense characteristic peak located at 1234 cm^{-1} is due to C=O groups, stretching at 1500 cm^{-1} arising from C-C available on both GO and cMWCNTs and a broad stretching at 1710 cm^{-1} may be assigned to C=O representing carboxylic groups of both GO and cMWCNTs. Further, the curve (d) shows the spectra for StAb/GO-cMWCNTs characteristic peak at 1660 cm^{-1} reveals the presence of secondary amide, while a broad peak at 3371 cm^{-1} represents the primary amide of the proteins from the StAb immobilized onto the GO-cMWCNTs/ITO electrode. Another peak at 980 cm^{-1} depicts the bending of alkene present in the GO-cMWCNTs composite.

3.3 Electron Microscopic Studies

The morphological studies for GO-cMWCNTs composite deposited onto the ITO microelctrode were performed using SEM reveal wrapping of cMWCNTs by GO nanosheets [**Fig.4(a&b)**]. The cMWCNTs having ~100 nm of diameter appeared to be wrapped with GO sheets through π-stacking interaction resulting in stable dispersion of high weight fraction cMWCNTs. SEM micrograph showed the well-defined network of the three dimensional composite having a clear image of cMWCNTs nanowires attached to the basal plane of the GO. In the GO-cMWCNTs composite, cMWCNTs nanowires may acted as additional route carrier for electrons generated during the electrochemical reactions. The SEM investigations revealed ample porosity in the network like structure due to the wrapping of GO and clustering of cMWCNTs and yielded enhanced area for immobilization of the StAb (**Fig 4b**). Carboxylic groups available on both GO and cMWCNTs offerred the possibility to form a strong amide bond (CO-NH) with amine (NH_2) group of the StAb enable higher loading of the StAb resulting in improved signal for the *S.typhimurium* cells detection. [27] As shown in the (**Fig 4c**), immobilization of StAb on the GO-cMWCNTs, resulted in a smooth surface as

ACCEPTED MANUSCRIPT

StAb have occupied all the available space in the GO-cMWCNTs electrode. Additional COOH groups arising due to the introduction of cMWCNTs provided an extra link for binding with the immobilized StAb. The energy dispersive spectroscopy (EDX) analysis of the StAb/GO-cMWCNTs revealed elemental composition for the GO-cMWCNTs composite and for the immobilized StAb. In addition to C and O, presence of the elements such as phosphorous (P) and potassium (K) demonstrated successful immobilization of StAb on the GO-cMWCNTs/ITO microelectrode (**Fig. 4d**). The SEM micrograph obtained for the GO based microelectrode is shown in the **Fig. S2**. GO sheets were found to be systematically deposited onto the ITO microelectrode due to the electrophoretic deposition as layer of the GO sheets are clearly visible (**Fig.S2a**). After immobilization with the StAb, it turned into the smooth surface (**Fig.S2b**).

The results of HRTEM investigations of the as-synthesized cMWCNTs, GO and GO-cMWCNTs composite are shown in **Fig.5**. The cMWCNTs having width upto 100 nm and length of a few micrometers are clearly visible in the **Fig.5a**. GO sheets on the holey carbon grid having some wrinkles and the overlapped regions are shown in the **Fig.5b**. Further, cMWCNTs were circularly arranged with on basal plane of the GO due to strong π-π interactions. It can be seen in **Fig.5d&e** circular dark grey lines (cMWCNTs) on the GO support, i.e clusters of the cMWCNTs nanowires were wrapped with the GO nanosheets. These images clearly demonstrated effective wrapping of the cMWCNTs with the GO as dark linear structures were surrounded by 2D structure. Further, cMWCNTs were arranged circularly and the GO offered effective wrapping/covering due to presence of strong π-π interaction between the cMWCNTs and the GO[25, 31]. An atomic scale image (**Fig.5f**) of GO-cMWCNTs composite revealed lattice fringes, where d_{002} value was obtained as 0.34 nm revealing graphitic nature of the composite. The presence of lattice fringes in cMWCNTs indicated multi-walled nature. The inset (**Fig.5f**) shows the selected area diffraction pattern of

ACCEPTED MANUSCRIPT

GO-cMWCNTs composite wherein two overlapped concentric rings appeared revealing presence of (002) and (004) crystalline planes in the GO-cMWCNTs composite.

3.4 Electrochemical Characterization

The electrochemical characterization of the cMWCNTs, GO,GO-cMWCNTs and StAb/GO-cMWCNTs electrodes were performed using CV technique (**Fig.6a**). The cMWCNTs integrated microfluidic chip revealed the peak current value as 20.87µA, while for GO the value was found to increase to 24.14µA. It could perhaps be due to the enhanced electron conductivity of the GO as compared to that of the cMWCNTs[16]. For the GO-cMWCNTs/ITO integrated chip the anodic peak current was much higher (29.38µA) as compared to that of both cMWCNTs/ITO and GO/ITO based microfluidic chips. The wrapping of the cMWCNTs with GO nanosheets resulted in increased electrochemical current due to higher charge transfer as it depended on the percolated network of cMWCNTs in the composite while GO played the role of carrier[21]. The synergistic effect of GO-cMWCNTs composite perhaps led to improved electrochemical performance of the microfluidic chip[25]. The high crystalline nature of GO coupled with improved charge transfer and the high aspect ratio of cMWCNTs resulted in enhanced acceleration of electrons that perhaps acted as electronic wires for the generated electrons from redox reaction resulting in higher magnitude of current [21]. The StAb covalently attached with the surface of GO-cMWCNTs provided an insulating layer to the current collector. This layer of StAb present on the matrix obstructed the electron transfer from redox reaction leading to decrease in the electrochemical reactivity (curve c).

The CV response of the StAb/GO-cMWCNTs based immuno-chips obtained as a function of scan rate (20–90 mV) is shown in **Fig.S3**.Both redox peak current and potential increased linearly with square root of the scan rate indicating that redox reaction was controlled by semi-infinite linear diffusion process leading to the improved electron transfer

ACCEPTED MANUSCRIPT

kinetics (inset of **Fig. S3**. The values of the slope, intercept and correlation coefficient are given by equation 1 and 2.

$Ia\ [A] = -5.99 \times 10^{-6}[A] + 3.30 \times 10^{-6}\ [A^2s/mV]^{1/2} \times [scanrate\left(\frac{mV}{s}\right)]^{½}$;R^2=0.99(1)

$Ic\ [A] = 3.01 \times 10^{-6}\ [A] - 2.60 \times 10^{-6}\ [A^2s/mV]^{1/2} \times [scanrate\left(\frac{mV}{s}\right)]^{½}$;$R^2$= 0.98 (2)

The diffusion coefficients of the redox species in GO/ITO, GO-cMWCNTs/ITO and StAb/GO-cMWCNTs were determined using Randles–Sevcik formula as given in equation (3).

$$I_p = 2.69 \times 10^5 (n^{3/2} A D^{1/2} v^{1/2} C) \quad (3)$$

Where, I_p is the peak current, A is an electrode area (200µm×0.6 cm^2), n is electron stoichiometry, D is diffusion coefficient (cm^2s^{-1}), c is concentration (mol cm^{-2}) and v is scan rate (mVs^{-1}). Using eq. (3), value of D for cMWCNTs, GO, GO-cMWCNTs and StAb/GO-cMWCNTs were found to be as 3.35×10^{-7} cm^2/s,$4.47\times10^{-7}$$cm^2$/s 6.65×10^{-7} cm^2/s and 2.27×10^{-7} cm^2/s, respectively. Wrapping of cMWCNTs with GO resulted in enhanced heterogeneous electron transfer constant ($k°$), as calculated by the modified Kochi's as given in the equation (4) [32]. The values of k° for cMWCNTs, GO and GO-cMWCNTs were calculated as 2.74×10^{-3}, $3.93 \times 10^{-3}$and 6.50×10^{-3} cm/s, respectively.

$$k^0 = (2.18)\left(\frac{\alpha DnFv}{RT}\right)^{\frac{1}{2}} exp\left[\frac{-\alpha^2 nF}{RT}\left(E_{pa} - E_{pc}\right)\right] \quad (4)$$

where, E_{pa}, E_{pc} are the anodic and cathodic peak potentials, D is diffusion coefficient calculated using Randles-Sevcik equation, v is scan rate and α is transfer co-efficient (0.5).

3.5 Incubation time

The effect of incubation time on the CV response was investigated with a constant concentration of 10^4 CFU/mL at different time intervals (**Fig.S4**). This study aimed at estimation of the minimal time that was required to bind *S.typhimurium* cells with the

ACCEPTED MANUSCRIPT

immobilized StAb. The value of response current obtained at 5, 10, 20, 30, 45 60 and 90 minutes are shown in the graph. It was observed that there was no significant change in the current value at 5 and 10 min, and significant change in the current value was found to be between 30 and 45 min. After this the current value was found to be constant, demonstrating the saturation of the binding event indicating that additional increase in the incubation time did not influence the binding event. CV response is known to depend on the thickness of the double layer formed due to the binding of *S.typhimurium* cells on the StAb/GO-cMWCNTs bioelectrode and 30 minutes were found to be the minimum time required to achieve the maximum binding resulting into the highest decrease in the current value.

3.6 Effect of pH on the response of StAb/GO-cMWCNTs immunochip

Optimum working pH condition for the StAb/GO-cMWCNTs immunochip were investigated at different pH conditions 6.0, 6.5, 7.0,7.2. 7.4, 7.6, 7.8 and 8.0 as shown in **Fig. (S5)**. Antigen binding capacity to the immobilized antibodies on the sensor surface depended on the pH of buffer solution used [33]. To perform the pH dependent binding of *S.typhimurium* cells on the StAb/GO-cMWCNTs immunochip,10^3CFU/mL concentration of *S.typhimurium* cells was prepared in PBS buffer having different pH mentioned above. It was observed that the optimum pH lied in the range of 7.0 to 7.6 and beyond this range the gradual shift in the response current was noticed. It could be assigned to the unsuitable binding environment for the *S.typhimurium* cells due to the extreme pH conditions.

3.7Electrochemical response studies

Fig. 6(b) shows results of the electrochemical response of StAb/GO-cMWCNTs based immuno-chip as a function of *S.typhimurium* concentration in the range of 10^1 to 10^7CFU/mL in PBS (50 mM, pH 7.4) containing 5 mM $[Fe(CN)_6]^{3-/4}$ as the redox probe. The magnitude of the anodic peak current of this microfluidic device decreased as the concentration of the *S.typhimurium* increased. Initially PBS was injected (10µL/min) into the inlet channel to

ACCEPTED MANUSCRIPT

remove the unbound StAb and to achieve the stable signal, and then the initial concentration of 10 CFU/mL was injected and incubated for 30 min following the measurement of electrochemical response and washing with the PBS. This procedure was repeated for different concentrations until 10^7 CFU/mL. The magnitude of electrochemical current was found to vary linearly upto 10^7 CFU/mL after which it became saturated. This could perhaps be attributed to the non-availability of the binding sites on the immobilized StAb onto the microfluidic immuno-chip. The decrease in the electrochemical current with increasing *S.typhimurium* concentrations was due to formation of the electrically insulating antigen–antibody complex[34]. This insulating layer worked as an insulating barrier for the transport of electrons via $[Fe(CN)_6]^{3-/4-}$ solution as reported in literature [35].The calibration plot for StAb/GO-cMWCNTs obtained as a function of concentration of *S.typhimurium* cells followed equation (5) [inset of **Fig. 6(b)**].

$$Ia(A) = 1.85 \times 10^{-5}\ A - 1.95 \times 10^{-6}\mathrm{Log}(S.typhimurium\ \mathrm{conc.});\ R^2 = 0.996 \quad (5)$$

The fabricated microfluidic immuno-chip showed excellent sensitivity of 162.47μA/CFU^{-1}mL/cm^{-2} that was the attributed to synergistic effect arising due to due to the wrapping of cMWCNTs with GO [36,37].On the other hand, the presence of cMWCNTs in the basal plane of the GO worked as a midrib to improve the conductivity of the GO. Kang *et.al.* reported improved electrochemical behavior due to wrapping with the GO [38]. The presence of cMWCNTs matrix provided enhanced loading of StAb via amide coupling utilizing -COOH groups of cMWCNTs and NH_2 groups of the StAb. The sufficient number of COOH groups available on the basal plane of the GO made strong amide bond (CO-NH) with the immobilized StAb leading to improved sensitivity of the immuno-chip. The detection limit of the microfluidic immuno-chip was estimated to be as 0.376CFU/mL using the standard formula (3×S.D/sensitivity). To confirm the synergistic effect in the electrochemical

ACCEPTED MANUSCRIPT

performance of the composite, a control experiment was performed using GO nano sheets integrated microfluidic immuno-chip, as a transducer material. As shown in the **Fig.6(c**), GO integrated immuno-chip did not yield enough change in the electrochemical current as compared to the GO-cMWCNTs based microelectrode. This resulted in decrease in the value of sensitivity (89.16µA/CFU^{-1}mL/cm^{-2}) as compared to that of the GO-cMWCNTs (162.47µA/CFU^{-1}mL/cm^{-2}). The enhanced sensitivity was due to introduction of cMWCNTs resulting in decreased resistance as the conductivity mainly depended on the percolated network of the cMWCNTs and GO worked as a carrier[21].The theoretical detection limit was found to be 0.75CFU/mL as compared to that of the GO-cMWCNTs (0.37 CFU/mL). In addition to this, the GO integrated immuno-chip could be used to detect the *S.typhimurium* cells upto 10^6 CFU/mL as compared to 10^7 CFU/mL for GO-cMWCNTs, indicating higher loading of the StAb due to the wrapping of cMWCNTs with the GO. To investigate the specificity of the microfluidic chip, we performed the control experiment with GO-cMWCNTs/ITO microelectrode without immobilization of the StAb. The injection of *S.typhimurium* cells in the GO-cMWCNTs/ITO microfluidic chip with the flow rate of 10µL/min did not exhibit any significant change in the output signal (**Fig. S6**). The GO-cMWCNTs/ITO did not respond to the *S.typhimurium* cells as compared to the StAb/GO-cMWCNTs/ITO microelectrode that revealed the role of StAb and *S.typhimurium* cells in signal generation. The insignificant fluctuation in the response current was mainly due to non-specific absorption of *S.typhimurium* cells (10^1 to 10^7 CFU/mL) onto the GO-cMWCNTs electrode.

3.8Selectivity and Shelf life studies

The effect of potential interferents such as *E.coli* was investigated on the performance of the microfluidic immuno-chip mixture of *S.typhimurium* and *E.coli* having concentration of 10^3 CFU/mL results into1.34% change in the electrochemical response due to the non-specific binding on StAb/GO-cMWCNTs. To investigate the influence of *E.coli* towards the detection

ACCEPTED MANUSCRIPT

of *S.typhimurium* more specifically higher concentration of *E.coli* (10^6 CFU/mL) was used and the observed change of 1.74 % may be due to the non-specific absorption on the StAb/GO-cMWCNTs microelectrode (**Fig.7a**). The interference in the electrochemical response was calculated using equation (6).

$$\%\ \text{Interference} = \left(\frac{I_{S.typhimurium} - I_{E.Coli}}{I_{S.typhimurium}}\right) \times 100 \qquad (6)$$

The similar protocol was used to investigate the specificity of StAb/GO immunochip. The change in the electrochemical response was recorded to be as 1.21 and 4.12% in the presence of 10^3 and 10^6 CFU/mL *E.Coli* concentration ((**Fig.7b**).

3.9. Stability and repeatability studies

The shelf-life of the immuno-chip was investigated at regular interval of one week as shown in (**Fig.S7**), when the immunochip was stored in the refrigerator at 4 ºC. Upto the fourth week, no significant change was observed as the difference in the current with the original value was only 1.67%.This was perhaps due to the effective loading of the StAb onto the GO-cMWCNTsvia strong amide bond and 3D structured network. However, after the 6^{th} week the change was 7.54%, as increased time, the amide linkage between StAb and COOH group of the GO-cMWCNTs got weakened. In case of the StAb/GO immunochip change of 2.87% and 12.43% was observed at the end of 4^{th} and 7^{th}week, respectively. The higher stability of StAb/GO-cMWCNTs indicated that microfluidic GO-cMWCNTs provided the favorable environment for the immobilization of the StAb and it was thus a suitable platform for the immobilization of other biomolecules like enzyme, DNA and proteins. The reproducibility studies for the StAb/GO-cMWCNTs immunochip were conducted. For this purpose, six different electrodes produced under similar conditions were used to measure the electrochemical response using 10^4 CFU/mL of *S.typhimurium* cells (**Fig.S8**). The electrode was found to be highly reproducible having low RSD value of 1.16%. While in the case of StAb/GO the RSD value was found to 1.74%.

ACCEPTED MANUSCRIPT

4. Conclusions

A highly sensitive, low cost and selective microfluidic immuno-chip has been fabricated using GO-cMWCNTs composite for detection of *S.typhimurium* cells. The wrapping of the cMWCNTs with GO nanosheets shows a synergetic effect resulting in improved sensing characteristics of *S.typhimurium* cells compared to those obtained using existing technologies. The wrapping of cMWCNTs with GO results into the superior biosening characteristics like sensitivity and detection limit as compared to the GO based immunochip. Easy functionalization and fabrication, portability, less reagents, sensitivity, and reproducibility are the main advantages of this fabricated microfluidic immuno-chip. Efforts should be made to conduct the clinical studies using this microfluidic immunosensor with real samples of *S.typhimurium* cells.This microfluidic immuno-chip can be utilized for quantification of other bacterial cells by immobilizing desired bio-receptors.

Supporting Information

CV studies for microfluidic immunosensor as a function of scan rate, incubation time, control experiment without immobilization of antibodies, determination of optimum ratio of GO: cMWCNTs, pH dependent response of GO-cMWCNTs, interference and stability studies of the fabricated microfluidic immune sensor designed using GO-cMWCNTs and GO have been given in the supplementary information sheet.

Notes

The authors declare no competing financial interest.

ACCEPTED MANUSCRIPT

Acknowledgements

Authors are thankful to Director CSIR-NPL for the facilities. Chandan Singh is thankful to CSIR, India for providing the Senior Research Fellowship. The authors thank Mr. Jay Talwade for SEM studies.

ACCEPTED MANUSCRIPT

References

[1] A.J. Griffin, S.J. McSorley, Development of protective immunity to Salmonella, a mucosal pathogen with a systemic agenda, Mucosal Immunol. 4, (2011) 371-82

[2] M.A. Gordon, Invasive Non-typhoidal Salmonella Diseaseepidemiology, pathogenesis and diagnosis, Curr Opin Infect Dis.24 (2011), 484–489.

[3] M.A. Gordon, S.M. Graham, A.L. Walsh, L. Wilson, A. Phiri, E. Molyneux, Epidemics of invasive Salmonella enterica serovar enteritidis and S. enterica Serovar typhimurium infection associated with multidrug resistance among adults and children in Malawi, Clin Infect Dis.46(2008) 963-9.

[4] S. Hoffmann, M.B. Batz, J.G. Morris Jr, Annual cost of illness and quality-adjusted life year losses in the United States due to 14 foodborne pathogens, J Food Prot. 75, (2012) Jul;75(7):1292-302 1292-302.

[5] A.G. Gehring, C.G. Crawford, R.S. Mazenko, L.J. Van Houten, J.D. Brewster, Enzyme-linked immunomagnetic electrochemical detection of Salmonella typhimurium, J Immunol Methods. 195(1996) 15-25.

[6] S. Liebana, A. Lermo, S. Campoy, M.P. Corta, S. Alegret, M.a.I. Pividori, Rapid detection of Salmonella in milk by electrochemical magneto-immunosensing, Biosens Bioelectron., 25(2009) 510-3.

[7] S. Choi, M. Goryll, L.Y.M. Sin, P.K. Wong, J. Chae, Microfluidic-based biosensors toward point-of-care detection of nucleic acids and proteins, Microfluidics and Nanofluidics, 10 (2011), 231-47.

[8] M. Medina-Sanchez, S. Miserere and A. Merkosi, Nanomaterials and lab-on-a-chip technologies, Lab Chip, 12 (2012) 1932-43.

ACCEPTED MANUSCRIPT

[9] C. Singh, A. Ali, G. Sumana, Green Synthesis of Graphene Based Biomaterial using Fenugreek Seeds for Lipid Detection, ACS Sustainable Chem. Eng., 4 (2016) 871–880

[10] K. Kalantar-Zadeh, J.Z. Ou, Biosensors Based on Two-Dimensional MoS2, ACS Sens., 1,2016, 5-16.[11] F. Zhou, M. Lu, W. Wang, Z.P. Bian, J.-R. Zhang, J.-J. Zhu, Electrochemical immunosensor for simultaneous detection of dual cardiac markers based on a poly (dimethylsiloxane)-gold nanoparticles composite microfluidic chip: a proof of principle, Clin Chem.56, (2010)1701-7.

[12] M. Pumera, Nanomaterials meet microfluidics, Chem. Commun., 47,(2011), 5671-80.

[13] M.A. Ali, P.R. Solanki, M.K. Patel, H. Dhayani, V.V. Agrawal, R. John, B.D. Malhotra, A highly efficient microfluidic nano biochip based on nanostructured nickel oxide, Nanoscale, 5 (2013) 2883-91.

[14] D.A. Boehm, P.A. Gottlieb, S.Z. Hua, On-chip microfluidic biosensor for bacterial detection and identification, Sens. Actuator B-Chem, 126(2007) 508-14.

[15] M.A. Ali, S. Srivastava, P.R. Solanki, V. Reddy, V.V. Agrawal, C. Kim, , Highly efficient bienzyme functionalized nanocomposite-based microfluidics biosensor platform for biomedical application, Sci Rep3 (.2013) 2661.

[16] J.Y. Tan, A. Avsar, J. Balakrishnan, G.K.W. Koon, T. Taychatanapat, E.C.T. O'Farrell, et al., Electronic transport in graphene-based heterostructures, Appl. Phys. Lett., 104 (2015) 183504.

[17] R. Ghosh, S. Santra, S.K. Ray, P.K. Guha, Pt-functionalized reduced graphene oxide for excellent hydrogen sensing at room temperature, Appl. Phys. Lett., 107 (2015) 153102.

[18] X. Li, G. Zhang, X. Bai, X. Sun, X. Wang, E. Wang, H.Dai, Highly conducting graphene sheets and Langmuir Blodgett films, Nat. Nanotechnol., 3(2008) 538-42.

[19] X. Wang, L. Zhi and K. Mallen, Nano Lett., Transparent, conductive graphene electrodes for dye-sensitized solar cells, Nano Lett, 8(2008) 323-7.

ACCEPTED MANUSCRIPT

[20] V.C. Tung, L. M. Chen, M.J. Allen, J.K. Wassei, K. Nelson, R.B. Kaner, et al., Low-temperature solution processing of graphene carbon nanotube hybrid materials for high-performance transparent conductors, Nano Lett,, 9(2009) 1949-55.

[21] D. Cai, M. Song, C. Xu, Highly Conductive Carbon • Nanotube/Graphite • Oxide Hybrid Films, Adv. Mater., 20(2008) 1706-9.

[22] S. Fang, L. Shen, H. Zheng, X. Zhang, Ge-Graphene carbon nanotube composite anode for high performance lithium-ion batteries, J. Mater. Chem. A, 3,(2015), 1498-1503 ,

[23] M.S. Romano, N. Li, D. Antiohos, J.M. Razal, A. Nattestad, S. Beirne, et al., Carbon nanotubereduced graphene oxide composites for thermal energy harvesting applications, Adv. Mater. 25 (2013) 6602.

[24] M.K. Shin, B. Lee, S.H. Kim, J.A. Lee, G.M. Spinks, S. Gambhir, et al., Synergistic toughening of composite fibres by self-alignment of reduced graphene oxide and carbon nanotubes, Nat. Commun,.3 (2012) 650.

[25] Y. Cheng, S. Lu, H. Zhang, C.V. Varanasi, J. Liu, Synergistic effects from graphene and carbon nanotubes enable flexible and robust electrodes for high-performance super capacitors, Nano Lett., 12 (2012) 4206-11.

[26] D.C. Marcano, D.V. Kosynkin, J.M. Berlin, A. Sinitskii, Z. Sun, A. Slesarev,W. Lu, and J. M. Tour., Improved synthesis of graphene oxide, ACS Nano., 4 (2010) 4806-14.

[27] C. Singh, S. Srivastava, M.A. Ali, T.K. Gupta, G. Sumana, A. Srivastava, R. B. Mathur, and B. D. Malhotra, Carboxylatedmultiwalled carbon nanotubes based biosensor for aflatoxin detection, Sens. Actuators, B.185 (2012) 258-64.

[28] A.R. Boccaccini, J. Cho, J.A. Roether, B.J.C. Thomas, E.J. Minay, M.S.P. Shaffer, Electrophoretic deposition of carbon nanotubes, Carbon, 44(2006) 3149-60.

[29] L. Lu, X. Zhu, X. Qiu, H. He, J. Xu, X. Wang, Graphene Oxide/Multiwalled Carbon Nanotubes Composites as an Enhanced Sensing Platform for Voltammetric Determination of Salicylic Acid, Int J Electrochem Sci, 9(2014) 8057-66.

ACCEPTED MANUSCRIPT

[30] M. Pumera, Graphene in biosensing, Mater.Today., 14 (2011) 308-15.

[31] J. Kuang, Z. Dai, L. Liu, Z. Yang, M. Jin, Z. Zhang, Synergistic effects from graphene and carbon nanotubes endow ordered hierarchical structure foams with a combination of compressibility, super-elasticity and stability and potential application as pressure sensors, Nanoscale, 7 (2015), 9252-9260.

[32] M. Velicky, D. F. Bradley, A.j.Cooper, E.W. Hill, I.A.Kinloch, A.Mishchenko, K.S. Novoselov, H.V.Patten , P.S.Toth, A.T.Valota, S.D.Worrall., Electron transfer kinetics on mono-and multilayer graphene. ACS Nano, 8(2014), 10089-10100

[33] Z. Pei Z, H. Anderson, A. Myrskog, G. Dunér, B. Ingemarsson, T. Aastrup. Optimizing immobilization on two-dimensional carboxyl surface: pH dependence of antibody orientation and antigen binding capacity.Anal. Biochem. 2 (2010)161-8.

[34]A. Kaushik, A. Yndart,R. D. Jayant, V. Sagar, V.Atluri, S.Bhansali,and M.Nai , Electrochemical sensing method for point-of-care cortisol detection in human immunodeficiency virus-infected patients,Int J Nanomedicine. 2015; 10: 677–685

[35] S. Srivastava, S. Abraham, C. Singh, M.A. Ali, A. Srivastava, G. Sumana, et al., Protein conjugated carboxylated gold@ reduced graphene oxide for aflatoxin B1 detection, RSC Advances, 5 (2015) 5406-14.

[36]Y. Cheng, S. Lu, H. Zhang, V. Chakrapania, J.Liu,Synergistic Effects from Graphene and Carbon Nanotubes Enable Flexible and Robust Electrodes for High-Performance Supercapacitors,Nano Lett.,12 (2012), 4206–4211.

[37] K. Y. Cho, H. Y. Seo, Y. S.Yeom, P. Kumar, A. S. Lee, K.Y. Baek, H. G. Yoon, Stable 2D-structured supports incorporating ionic block copolymer-wrapped carbonnanotubes with graphene oxide toward compact decoration of metal nanoparticles and high-performance nano-catalysis,Carbon, 105, (2016), 340–352

ACCEPTED MANUSCRIPT

[38] Y. Kang, F. Cai, H.Chen, M. Chen, Rui Zhang and Q. Li, Porous reduced graphene oxide wrapped carbon nanotube–manganese dioxide nanocables with enhanced electrochemical capacitive performance,RSC Adv., 5 (2015), 6136-6141.

ACCEPTED MANUSCRIPT

Author Biographies

Chandan Singh is working as a doctoral candidate at Biomedical Instrumentation section, CSIR-National Physical Laboratory, New Delhi, India. He received his M.Tech. degree in Biotechnology from Jaypee Universityof Information Technology, Waknaghat, H.P. Currently he is working as a doctoral candidate at Biomedical Instrumentation Section CSIR-National Physical laboratory, New Delhi, India. He is working on designing of microfluidics based electrochemical immumosensors for the detection of food borne pathogens like salmonella. He is also working on development of optofluidic biosensors using anisotropic nanostructures for the detection of different bioanalytes.

Dr.Md. Azahar Ali received his Ph.D. degree from the Biomedical Engineering Department at Indian Institute of Technology Hyderabad, India, in collaboration with the Biomedical Instrumentation Section at National Physical Laboratory, New Delhi, India, in 2014. He also received his Master of Technology degree from the Department of Electronics Engineering at Tezpur University, Assam, India, in 2009. Currently, he is doing Post-Doctoral Associate in the Department of Electrical and Computer Engineering at Iowa State University. He is actively engaged in the area of microfluidic and MEMS sensors in agriculture and biomedicine.

Mr. Dinesh Singh, currently working as Sr. Technical Officer in Sophisticated Analytical Equipment Division, CSIR-National Physical Laboratory, Dr. K.S. Krishnan Road, New Delhi 110012, India. He has completed his B. Sc degree (2000) and M. Sc degree (2002) from Hindu College Moradabad, MJP Rohilkhand University Bareilly, U.P., India in PCM group and Chemistry respectively. His research interested includes microscopic analysis of nanostructured materials. He has experience of more than 10 year in electron microscopy. He has also worked as Technical Assistant in department of Pharmaceutics in NIPER Mohali (Punjab) for more than 8 year.

Dr. Venu Reddy has completed his PhD from Chungnam National University, South Korea. Hi s research interest includes Nanomaterials Microfabrication and Biosensors. Currently he is working as DST-Inspire faculty at School of Engineering Sciences & Technology University of Hyderabad,India. He has also worked as Daegu Gyeongbuk Institute of Science and Technology (DGIST), South Korea.

ACCEPTED MANUSCRIPT

Prof.CheolGi Kim has completed his Ph.D. from KAIST in Korea and postdoctoral studies from NIST in USA. Now he is a professor and head of the department at DGIST. Prior to coming to DGIST, he has 24 years of research experience at KRISS in Korea, Sun Moon University in Korea, Tohoku University in Japan and Chungnam National University in Korea. Prof. CheolGi Kim has trained number of Ph.D. students who have gone on to successful researchers in their own related research fields. His research interests skate the intersection between technology and competitive strategy. During his Professional Period, he published ~ 300 articles in research journals, and 15 domestic and 6 international patents. For his contribution to the Scientific research, he has honoured by the bunch of awards.

Dr. Gajjala Sumana received her Ph.D. (1998) from Jiwaji University in Chemistry, India. She is currently working as a principal scientist with the DST Centre on Biomolecular Electronics at the National Physical Laboratory, New Delhi, India. She has a research experience of 15 years in controlled drug delivery, liquid crystal polymers, polymer dispersed liquid crystals and biosensors. She has published more than 80 publications in the area of biomedical applications.

Prof. B.D. Malhotra received his Ph.D. degree from the University of Delhi, Delhi, India in 1980. He has published 294 papers in peer-reviewed journals, filed 10 patents, and edited/co-edited books on biosensors and polymer electronics. After his stint as Chief Scientist and Head of the DST Centre on Biomolecular Electronics at the CSIRNational Physical Laboratory, New Delhi, India, he moved to Delhi Technological University (DTU), India. He has nearly 30 years of research experience in the field of biomolecular electronics and has guided 25 Ph.D. students to date. His current activities include biosensors, nanobiomaterials, conducting polymers, and ordered molecular assemblies including Langmuir–Blodgett films and self assembled monolayers among others. Dr. Malhotra is a Fellow of the Indian National Science Academy (INSA), the National Academy of Sciences, India (NASI) and an Academician of the Asia-Pacific Academy of Materials (APAM).

ACCEPTED MANUSCRIPT

Figure Captions

Figure 1: Schematic for the fabrication of GO-cMWCNTs integrated microfluidic chip, immobilization of StAb antibodies and detection of *S.typhimurium* cells using CV technique.

Figure 2: Real image of the as-fabricated GO-cMWCNTs integrated microfluidic immunochip.

Figure 3: UV-visible spectra of as synthesized GO (curve a) , cMWCNTs (curve b) and GO-cMWCNTs(curve c) (Fig. 3a), solutions dissolved in water, FT-IR Spectra of GO/ITO , cMWCNTs/ITO , GO-cMWCNTs/ITO and StAb/GO-cMWCNTs/ITO immunochip with labelled functional groups.(Fig. 3b).

Figure 4: SEM images of the GO-cMWCNTs/ITO microelectrode at 10µm scale (a). SEM image of GO-cMWCNTs/ITO microelectrode, demonstrating the wrapping of cMWCNTs with GO at 2µm scale (b).GO-cMWCNTs/ITO microelectrode after the immobilization of StAb (c), EDX investigation of StAb/GO-cMWCNTs/ITO immunochip demonstrating percentage distribution of different elements (d).

Figure 5: TEM images of as synthesized cMWCNTs (a), GO nanosheets on the holey carbon grid (b), GO wrapped cMWCNTs at 100 nm scale (c), Clear view of the cMWCNTs (in dark grey lines) attached to the basal plane of GO (d), High magnification image of GO-cMWCNTs showing the fine structures of cMWCNTs nanowires circularly arranged on the GO (e), Atomic scale image of GO-cMWCNTs with clear atomic fringes for GO and cMWCNTs and the SAED pattern (inset) (f).

Figure 6: Electrochemical characterization of cMWCNTs/ITO (curve a), GO/ITO (curve b),GO-cMWCNTs/ITO (curve c) and StAb/GO-cMWCNTs/ITO immunochip using CV (a). Electrochemical response of StAb/GO-cMWCNTs microfluidic electrode against *S.typhimurium* pathogen cells in the range of 10^1 to 10^7 CFU/mL at a constant flow rate of 10µL/min (b). Electrochemical response of StAb/GO/ITO microfluidic immunosensor against *S.typhimurium* pathogen cells in the range of 10^1 to 10^6 CFU/mL (c), Comparison

ACCEPTED MANUSCRIPT

curve for electrochemical response for only GO and GO wrapped cMWCNTs based bioelectrode for *S.typhimurium* detection.

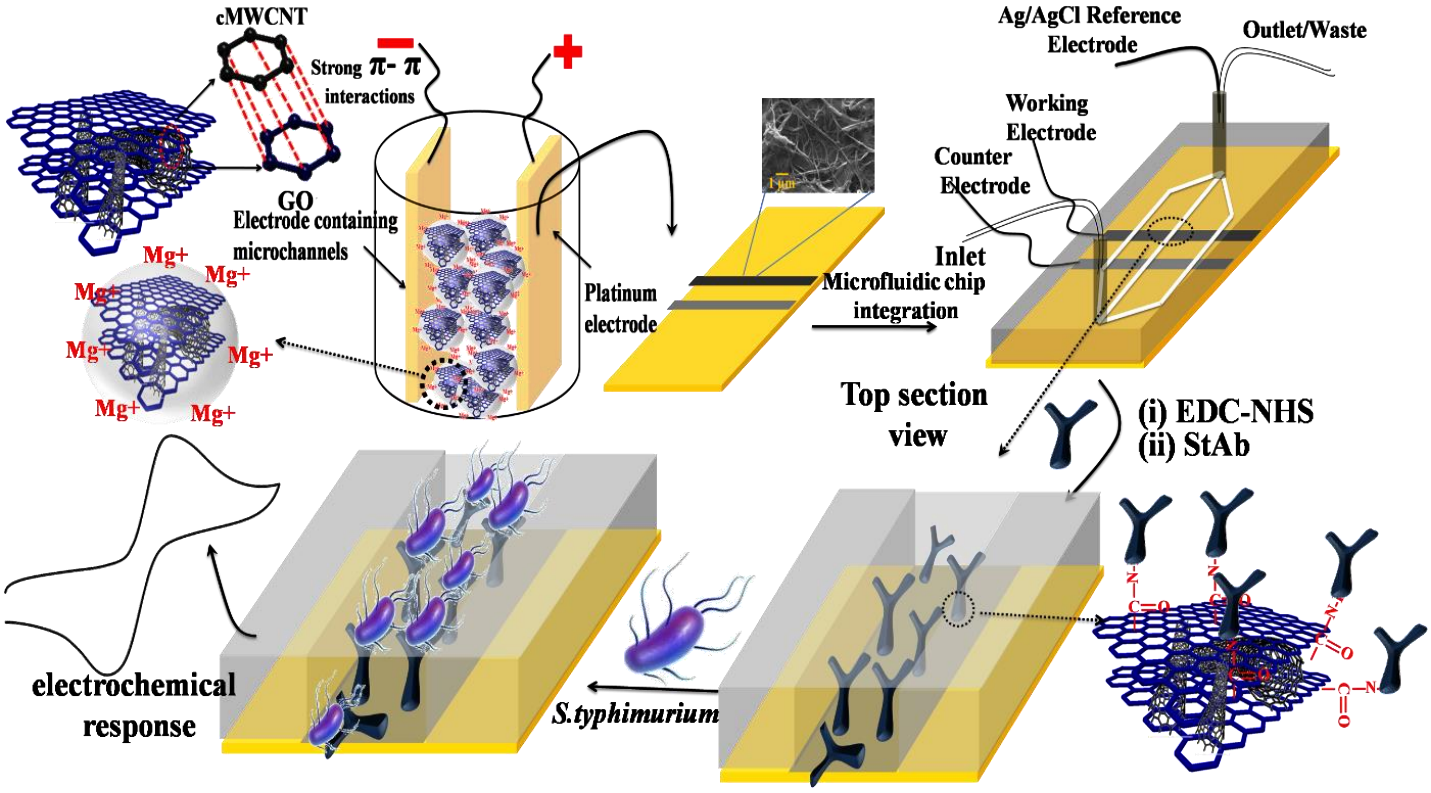


Figure7: Electrochemical response ofStAb/GO-cMWCNTs/ITO and StAb/GO/ITO microfluidic immunochip in presence of potential interference *E.Coli* having concentration of 10^3 and 10^6 CFU/mL, respectively (a & b).

Figures

Figure 1

ACCEPTED MANUSCRIPT

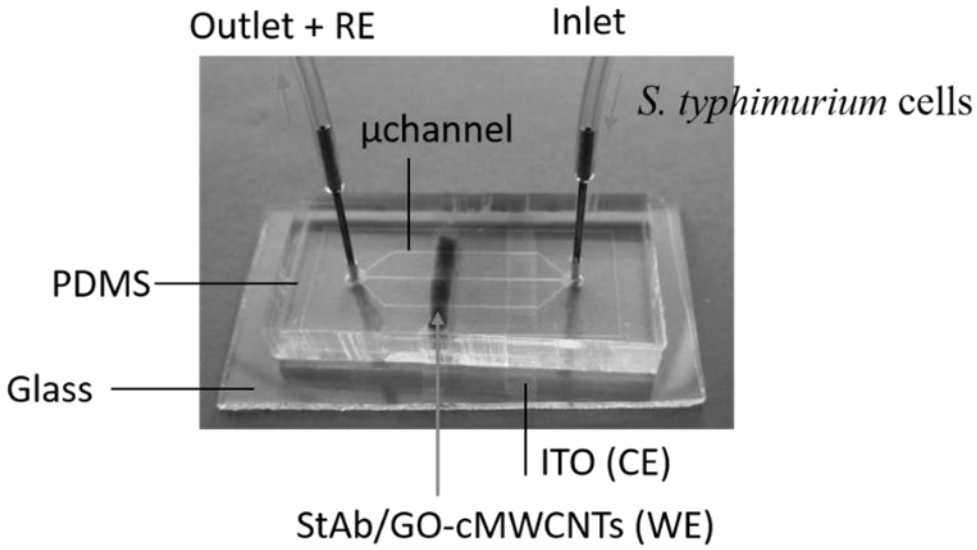
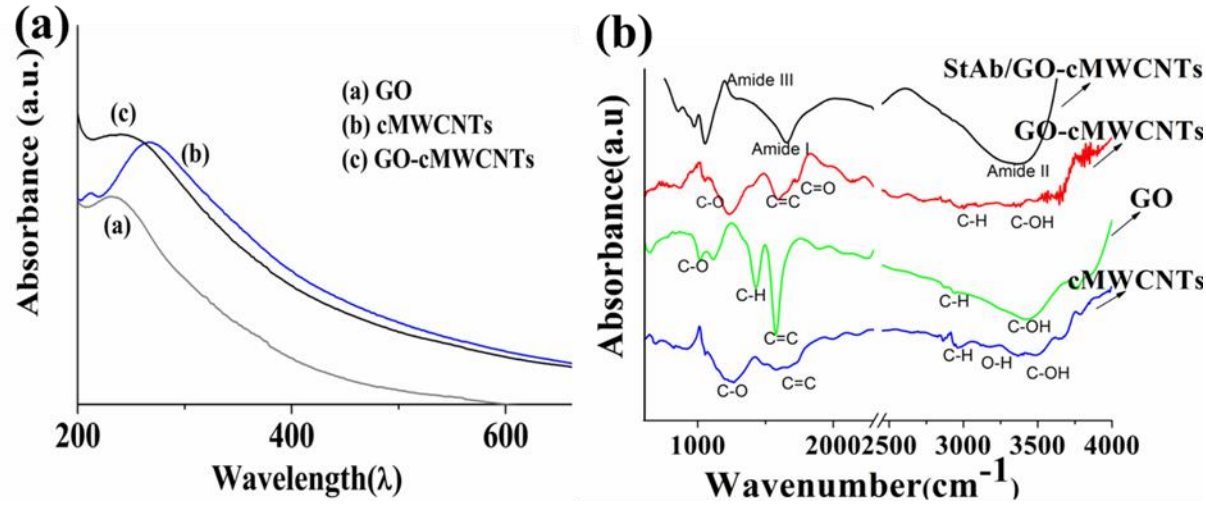


Figure 2

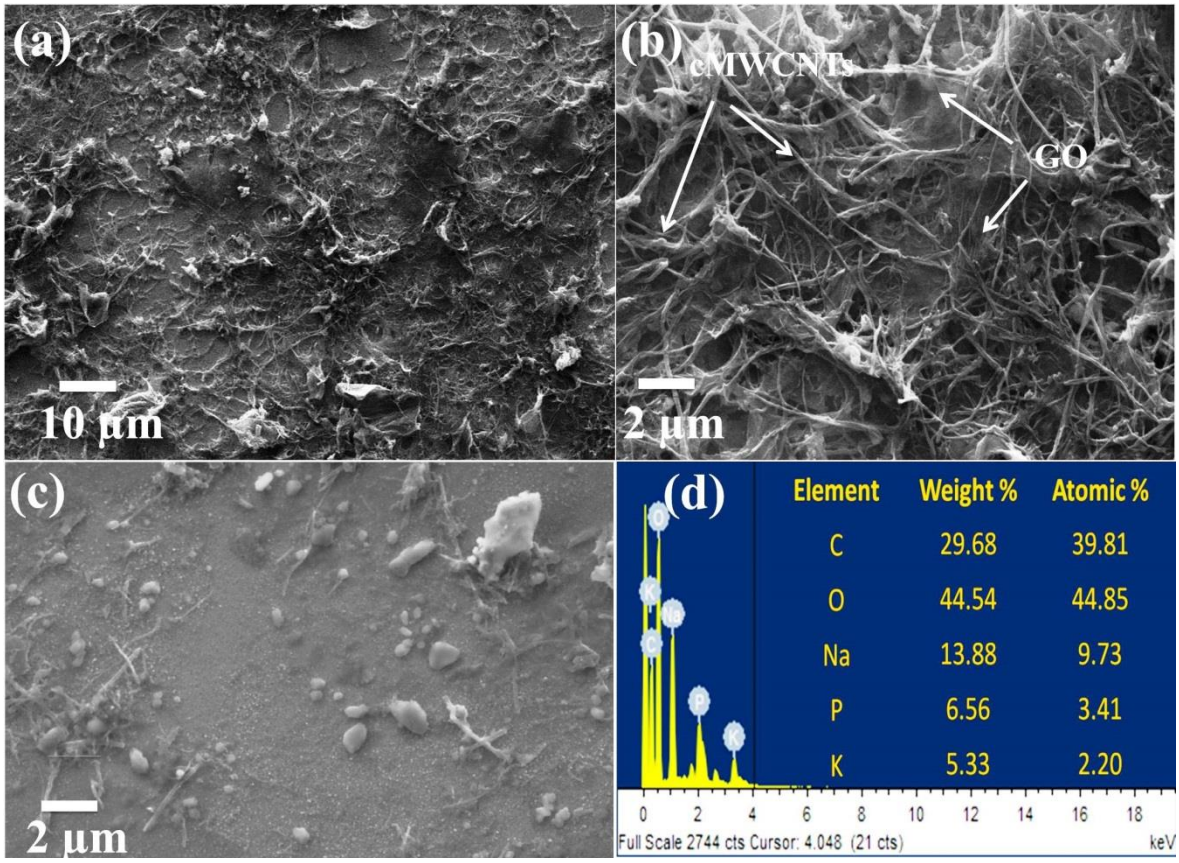
ACCEPTED MANUSCRIPT

Figure 3

Figure 4



ACCEPTED MANUSCRIPT



ACCEPTED MANUSCRIPT

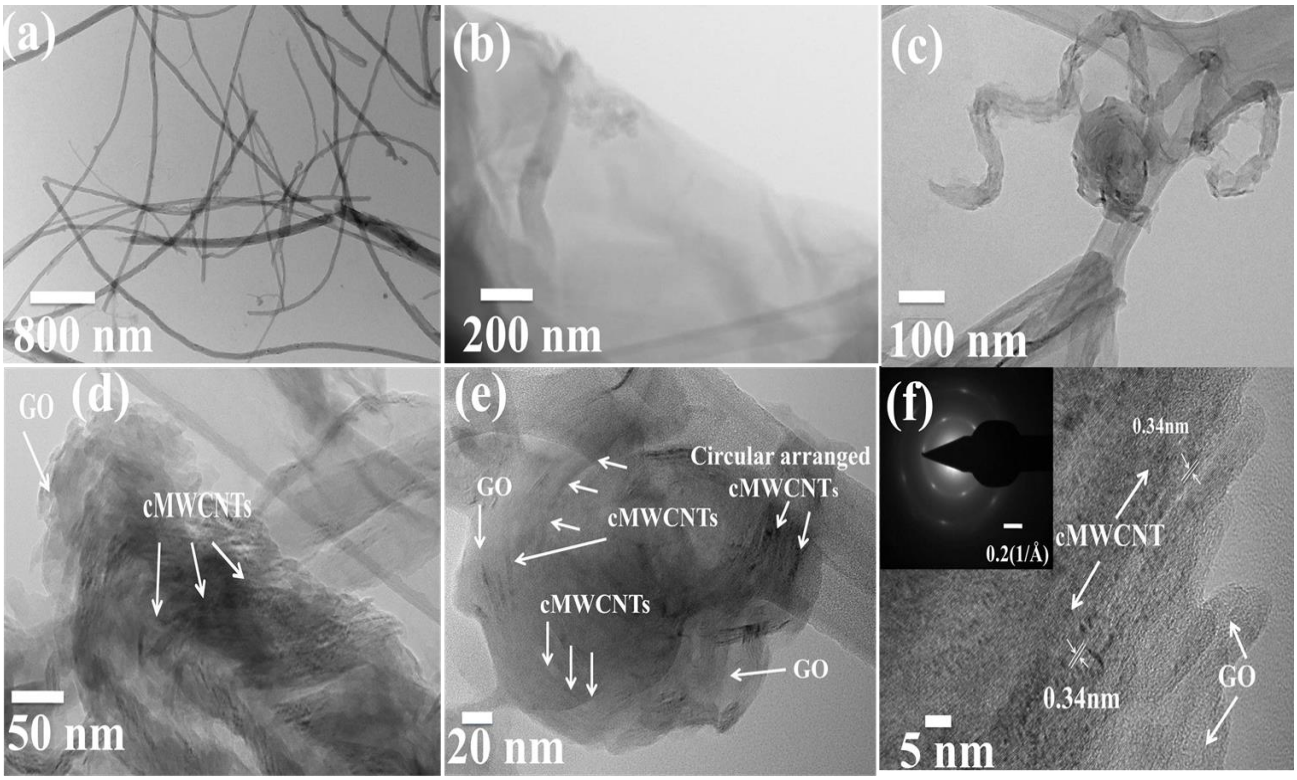
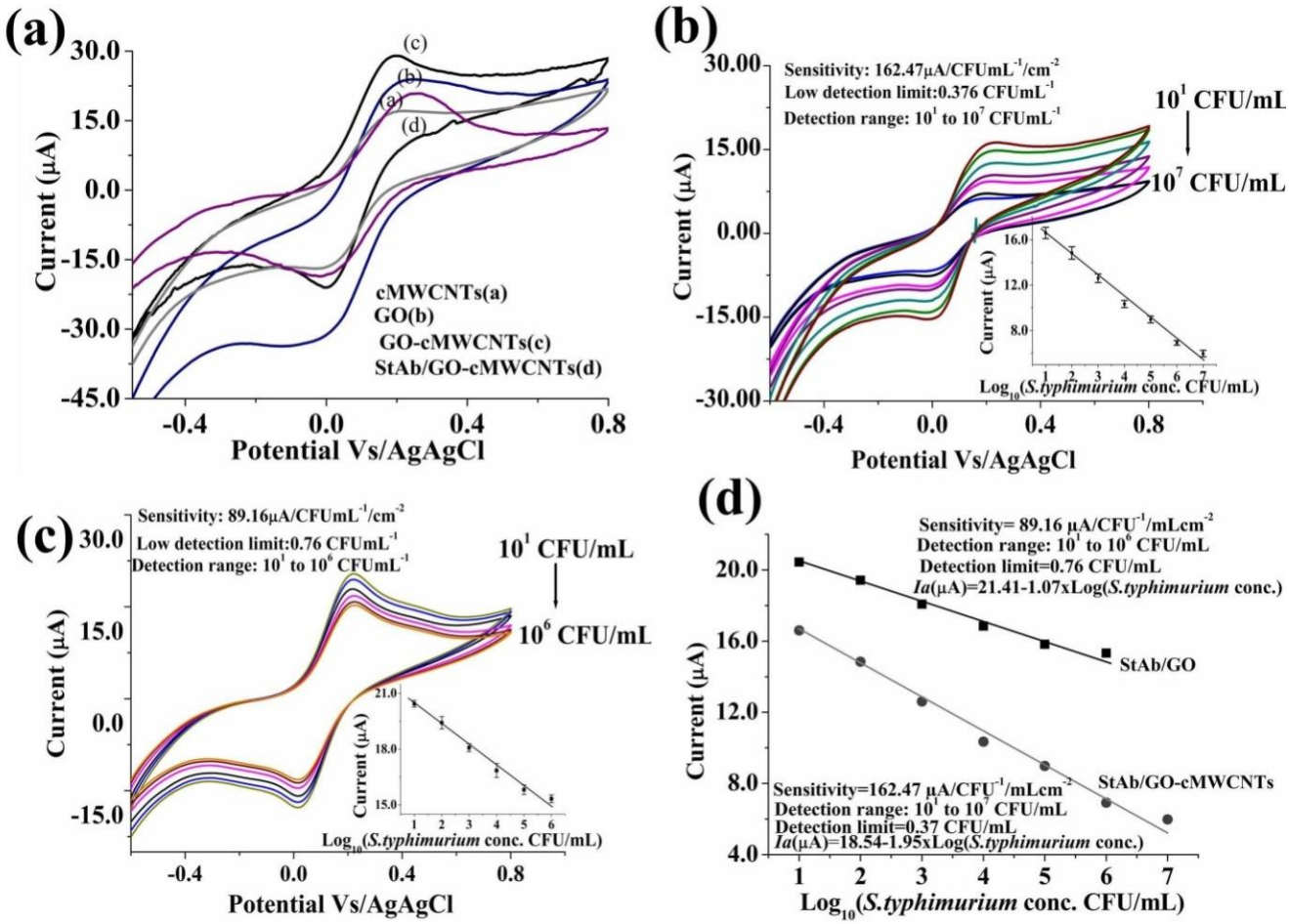


Figure 5

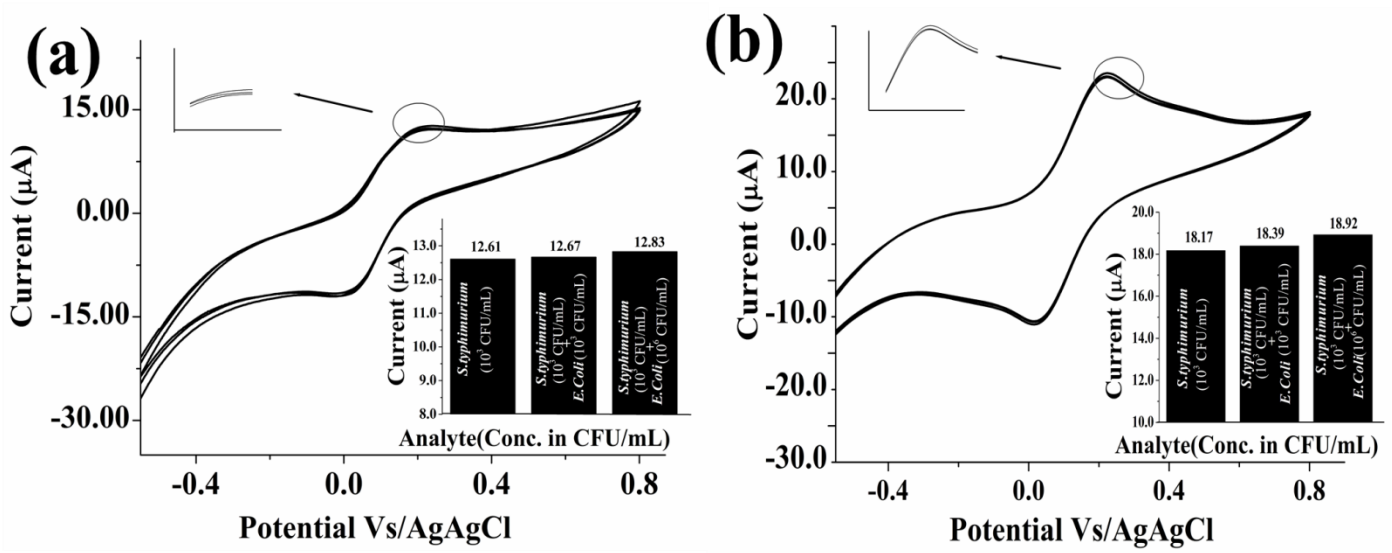
ACCEPTED MANUSCRIPT

Figure 6



ACCEPTED MANUSCRIPT

Figure 7



Optical Materials 73 (2017) 260–267

Contents lists available at ScienceDirect

Optical Materials

journal homepage: www.elsevier.com/locate/optmat

Compositional dependence of red luminescence from Eu^{3+} ions doped single and mixed alkali fluoro tungsten tellurite glasses

Ch. B Annapurna Devi [a, d], Sk. Mahamuda [a], K. Swapna [a], M. Venkateswarlu [a], A. Srinivasa Rao [a, b, *], G. Vijaya Prakash [c]

[a] Department of Physics, K L University, Vaddeswaram, Guntur (Dt), A.P, India
[b] Department of Applied Physics, Delhi Technological University, Bawana Road, New Delhi 110 042, India
[c] Nanophotonics Lab, Department of Physics, Indian Institute of Technology, Hauz Khas, New Delhi 110 016, India
[d] Vasireddy Venkatadri Institute of Technology, Namburu, Guntur (Dt.), A.P, India

ARTICLE INFO

Article history:
Received 1 May 2017
Received in revised form
4 August 2017
Accepted 8 August 2017

Keywords:
Europium
J-O parameters
Radiative properties
Photoluminescence

ABSTRACT

Trivalent europium ions doped single and mixed alkali fluoro tungsten tellurite glasses have been prepared via melt quenching method and characterized by using Raman, optical absorption, excitation, emission and time resolved spectral measurements to understand their utility in visible red emission. Raman spectrum is used to identify different functional groups present in the as prepared glasses. The optical absorption spectra recorded for all the glasses show six bands corresponding to the transitions $^7F_0 \rightarrow {}^6D_2$, $^7F_0 \rightarrow {}^6D_1$, $^7F_1 \rightarrow {}^6D_1$, $^7F_0 \rightarrow {}^6D_0$, $^7F_0 \rightarrow {}^7F_6$, and $^7F_1 \rightarrow {}^7F_6$. An excitation spectrum is used to measure the electron-phonon coupling strength 'g' and phonon energy of the glass host 'hω'. The photoluminescence (PL) spectra measured under 464 nm excitation show eight luminescence peaks related to the transitions $^5D_1 \rightarrow {}^7F_0$ (509 nm), $^5D_1 \rightarrow {}^7F_1$ (537 nm), $^5D_1 \rightarrow {}^7F_2$ (556 nm), $^5D_0 \rightarrow {}^7F_0$ (580 nm), $^5D_0 \rightarrow {}^7F_1$ (592 nm), $^5D_0 \rightarrow {}^7F_2$ (614 nm), $^5D_0 \rightarrow {}^7F_3$ (652 nm) and $^5D_0 \rightarrow {}^7F_4$ (701 nm) in all the glasses under investigation. Utilizing the Judd-Ofelt (J-O) parameters evaluated from the PL spectra, various radiative properties have been evaluated. From the decay spectra, experimental lifetimes were measured which are in turn used to evaluate the quantum efficiencies and non-radiatve decay rates in the as prepared glasses. The branching ratios, stimulated emission cross-section, quantum efficiency, colour co-ordinates and confocal images captured to confirm the suitability of these glasses for visible red luminescent devices.

© 2017 Elsevier B.V. All rights reserved.

1. Introduction

The necessity of developing solid-state optoelectronic devices, optoelectronic communication devices and white Light Emitting Diodes (w-LEDs) have escalated the research interest in rare earth (RE) ions doped glasses [1–5]. Especially, the demand for materials which are aptly suitable for w-LEDs are increasing day by day as they are playing a crucial role in solid state lighting applications. At present, RE doped phosphors are vigorously used in the production of w-LED. But they are not quite suitable for the excitation of InGaN-based LED chips in near-UV to blue region which finally leads to the low efficiency. Due to this reason, instead of Single w-LED, lots of w-LEDs are required to gain sufficient brightness for general lighting. To unravel this difficulty, so many studies have been done to enhance the output power of LED chips. But due to the increase in the chip temperature, the luminous efficiency and lifetime of the LED's decreases [6]. To avoid this problem, new phosphors without resin such as Ce-doped YAG glass ceramics are proposed [7]. Up to now, the major problem is lack of excellent red phosphors. To get efficient w-LED's, red phosphor is highly required in economic range [8]. But it is very intricate to get bright red colour emitting phosphors because of the sudden drop in quantum yield with increasing Stokes shift.

Europium ions are commonly used RE ions in several devices that can be used for lighting and displays. Europium ions can exist in several oxidation states and is a well-known activator with simple electronic transitions. A very interesting point in europium is, it gives strong visible luminescence in both the oxidation states

* Corresponding author. Department of Applied Physics, Delhi Technological University, Bawana Road, New Delhi 110 042, India. Tel.: +91 085860 39007; fax: +91 01127871023.
E-mail address: drsrallam@gmail.com (A. Srinivasa Rao).

http://dx.doi.org/10.1016/j.optmat.2017.08.010
0925-3467/© 2017 Elsevier B.V. All rights reserved.

i.e., Blue or green emission under near-UV excitation in Eu^{2+} state and red emission in Eu^{3+} state. Both are acting as efficient luminescent probes. The non-degenerate energy levels of Eu^{3+} ions are very crucial to understand the symmetry and inhomogeneity of the host material. The symmetry of the material depends upon the stark splitting of emission bands ($^5D_0 \rightarrow {}^7F_{1,\ 2}$). The trivalent europium ions possess prominent laser luminescence in the reddish-orange or bright red region and narrow band emission with higher lifetime [9]. However, the red luminescence of Eu^{3+} usually can't be efficiently excited by near-ultraviolet light because its excitation peaks in this region are due to parity-forbidden f-f transitions [10]. To obtain efficient red luminescence under near-UV excitation suitable host materials are required.

The end of the last decade is a strong evidence for the regeneration of RE ions doped luminescent materials. Glass materials are excellent option as luminescence materials because of their wide inhomogeneous line width, various compositions and easy mass production. Glasses based on heavy metal oxides like TeO_2 have always been an interesting area because of their typical structural and physical properties such as high refractive index, high density, high thermal expansion, low transformation temperature and excellent infrared transmission in the region 5–11 μm [11]. Comparatively high refractive indices with other glass systems like oxides are due to high polarizability of tellurium ions. Because of this property, the tellurite based glasses also have large values of third order non-linear optical susceptibilities that can be used to make the devices which can give femto second lasers [12]. These glasses are also used to improve the cross-sections because of their low vibrational frequencies which reduce the multiphonon radiations [13]. When these tellurite glasses are prepared in combination with tungsten ions, then these glasses become more suitable for optoelectronic devices because they show signs of photochromism and electrochromism. The main drawback of the TeO_2 is, it does not form a glass by itself and needs other compounds to form the glass. Hence the present system is prepared in combination with the compounds like WO_3, LiF, NaF and KF. The addition of WO_3 to the TeO_2 will improve the glass forming capacity and thermal stability because of conciliatory behaviour of octahedral sites present inWO_3. Tungsten ions can influence the photoluminescence behaviour of rare earth ions in tellurite glasses, because of their various valence states such as W^{6+}, W^{5+} and W^{4+}. These valence states participate in the glass network with different structural units like WO_4 and WO_6 and modify the tellurite network into TeO_4 to TeO_{3+1} structural units due to which remarkable changes can be produced in the photoluminescence behaviour of rare earth ions in a host matrix [14]. In addition, the presence of tungsten in a host matrix lowers their phonon energies and improves the luminescence efficiency or RE ions doped in them [15]. Single alkali and mixed alkali fluorides lend a hand to enhance the solubility of RE ions by creating the non-bridging oxygen ions [16]. They also decrease the melting temperature. They are also capable in reducing the water content in the glasses which in turn elevate the luminescence efficiency by reducing the phonon energies of glasses [16].

In the backdrop of the aforementioned various scientific patronages offered by the chemical constituents such as TeO_2, WO_3, LiF, NaF and KF, in the present work we prepared single and mixed alkali fluoro tungsten tellurite glasses doped with trivalent europium ions to understand their utility in visible red luminescence applications.

2. Experimental

In the present work, the single and mixed alkali fluoro tungsten tellurite glasses doped with trivalent europium ions have been prepared by using melt quenching technique with the following composition.

TeWLi: $59TeO_2$ - $20WO_3$ - 20LiF - $1Eu_2O_3$
TeWNa: $59TeO_2$ - $20WO_3$ - 20NaF - $1Eu_2O_3$
TeWK: $59TeO_2$ - $20WO_3$ - 20 KF - $1Eu_2O_3$
TeWLiNa: 59 TeO_2 - $20WO_3$ - 10LiF - 10NaF - $1Eu_2O_3$
TeWNaK: $59TeO_2$ - $20WO_3$ - 10NaF - 10 KF - $1Eu_2O_3$
TeWLiK: $59TeO_2$ - $20WO_3$ - 10LiF - 10 KF - $1Eu_2O_3$

High quality powders of 15 g for each batch of the composition of glass samples were melted at 750 °C in a silica crucible for about 2 h in an electrical furnace. The molten liquids have been quenched in air by pouring between two preheated brass moulds and later annealed at 400 °C for 4 h to remove internal thermal stresses. The prepared glasses have been polished before moving for characterization. The densities of the prepared glasses have been measured by Archimedes method using distilled water as an immersion liquid. The Raman spectrum of TeWKEu glass has been recorded in the range of 100–1000 cm^{-1} using Renishaw Invia Raman Microscope. The room temperature optical absorption spectra of all the glasses have been recorded in Visible to IR regions in the range of 450–2400 nm using a JASCO V-670 UV–vis–NIR spectrophotometer. The photoluminescence (PL) spectra were recorded using RF-5301PC Spectrofluorophotometer at room temperature. Edinburgh FLSP900 with a spectral resolution of 0.1 nm was used to measure the time resolved photoluminescence (TR-PL) spectra, where a xenon lamp was used as an excitation source.

3. Results and discussion

3.1. Raman spectral analysis

Fig. 1 shows the Raman Spectrum of TeWKEu glass which is recorded in the region 100–1000 cm^{-1}. The inset figure shows the Raman spectra for the remaining as prepared glasses. In all the glasses, nine peaks have been observed at 146, 183, 320, 395, 421, 463, 610, 733 and 924 cm^{-1} respectively. For the present series of glasses, there is no much variation in the intensity and no shifting of Raman peaks is observed. The peaks found in the range of 100–250 cm^{-1} are considered as boson peaks. These boson peaks are related to the scattering of light due to the thermal vibrations of disordered structure [17]. The Raman peaks observed at 320 and 395 cm^{-1} are due to vibrations of Tungsten anions and deformation vibrations of WO_6 octahedron [17,18]. The peaks observed at 421 cm^{-1} and 463 cm^{-1} are due to the bending vibrations of Te-O-Te linkages [17]. The peaks observed at 610 cm^{-1} are due to the vibrations of TeO_2 molecules and TeO_4 units. The peak observed at 733 cm^{-1} is due to the stretching vibrations of TeO_4 and TeO_3 groups or due to the stretching vibrations between Te and non-bridging oxygen (NBO) [19–21]. The peak observed at 924 cm^{-1} is due to the stretching vibrations of W–$O^-$and WO bonds associated with WO_4 and WO_6 units [22].

3.2. Optical absorption spectra

Fig. 2 show the optical absorption spectra of the trivalent Eu^{3+} ions doped single alkali and mixed alkali glasses. The absorption spectra have 6 peaks related to the transitions $^7F_0 \rightarrow {}^6D_2$, $^7F_0 \rightarrow {}^6D_1$, $^7F_1 \rightarrow {}^6D_1$, $^7F_0 \rightarrow {}^6D_0$, $^7F_0 \rightarrow {}^7F_6$, and $^7F_1 \rightarrow {}^7F_6$. Apart from all the trivalent RE ions, Eu^{3+} ions only possess two ground states such as $^7F_0$ and $^7F_1$. The energy gap between these two states is 360 cm^{-1}. Due to this reason, in Eu^{3+} ions doped materials, the absorption not only takes place from the ground level ($^7F_0$) but also takes place from the thermally excited level ($^7F_1$) [9]. Generally for all the

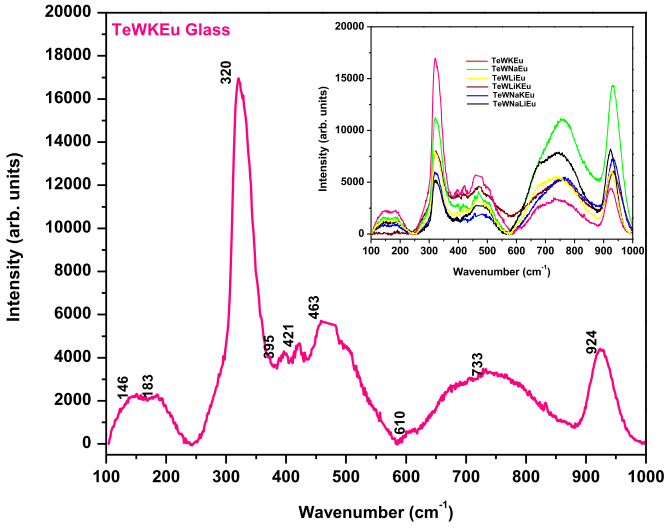


Fig. 1. Raman Spectrum of TeWKEu glass. The inset figure shows the Raman spectra of Eu^{3+} ions doped single and mixed alkali fluoro tungsten tellurite glasses.

trivalent RE ions doped glassy materials except Eu^{3+} ion, absorption spectra play a key role in calculating the Judd-Ofelt (J-O) intensity parameters (Ω_2, Ω_4 and Ω_6) using the J-O theory. Among these three parameters, Ω_2 is associated with the covalency and structural environment around the trivalent Eu^{3+} ion (short-range effect), while Ω_4 and Ω_6 parameters are associated with the long-range effects. For Eu^{3+} ion doped glass materials, except the two transitions such as $^7F_1 \rightarrow {}^5D_4$ and $^7F_1 \rightarrow {}^5D_3$, the square reduced matrix element $||U^4||$ is zero for all the other transitions [19]. For the present series of glasses most of the absorption peaks have low intensity value and most of the transitions observed in absorption spectrum of Eu^{3+} ion doped glasses have zero values of square reduced matrix elements ($||U^2||$ and $||U^6||$) except for the transitions like $^7F_0 \rightarrow {}^5D_2$, $^7F_0 \rightarrow {}^5D_4$ and $^7F_0 \rightarrow {}^5L_6$ [23]. Hence the data which is getting from the absorption spectra is not enough for the evaluation of the J-O intensity parameters. Hence in the present paper, the J-O parameters are evaluated from the PL spectral data. In fact this helps in rectifying the difficulty arising from the absorption of the first excited state $^7F_1$, which is situated just above the ground state $^7F_0$ [24].

3.3. Excitation and photoluminescence spectra

Fig. 3 illustrates the excitation spectra of trivalent europium ion doped single alkali and mixed alkali glasses monitoring emission at 614 nm. Several sharp inhomogeneous peaks have been observed in the wavelength region 350–600 nm corresponding to the transitions $^7F_1 \rightarrow {}^5L_7$ (384 nm), $^7F_0 \rightarrow {}^5L_6$ (394 nm), $^7F_0 \rightarrow {}^5D_3$ (408 nm), $^7F_1 \rightarrow {}^5D_3$ (416 nm), $^7F_0 \rightarrow {}^5D_2$ (464 nm), $^7F_1 \rightarrow {}^5D_2$ (472 nm), $^7F_0 \rightarrow {}^5D_1$ (526 nm), $^7F_1 \rightarrow {}^5D_1$ (535 nm), $^7F_0 \rightarrow {}^5D_0$ (580 nm) and $^7F_1 \rightarrow {}^5D_0$ (589 nm). The assignment of the bands has been done based on the Carnall paper [25]. Among all the glasses, TeWKEu glass has highly intensified peaks compared with other glasses. When Compared with other transitions, the transition $^7F_0 \rightarrow {}^5D_2$ (464 nm) is highly intense and is used as an excitation wavelength to record the PL spectra of the as prepared glasses at RT. The sharp and highly intense transition $^7F_0 \rightarrow {}^5D_2$ at 464 nm is known as Pure Electronic Transition (PET). A Phonon Side Band transition (PSB) is associated with this PET. From these two transitions, several crucial parameters have been evaluated like electron-phonon coupling strength 'g' and phonon energy of the glass host hω. The electron coupling strength can be measured by taking the intensity ratio of PSB and PET whereas the phonon energy is measured by taking the difference between the positions of PSB and PET using the following expressions [26].

$$\text{Electron} - \text{phonon coupling strength } 'g' = \frac{\int I_{PSB} d\vartheta}{\int I_{PET} d\vartheta}$$

$$= 33.14 \times 10^{-3}$$

$$\text{Phonon energy } h\omega = \text{PSB} - \text{PET} = 719\text{cm}^{-1}$$

This low phonon energy (~750 cm^{-1}) is a key feature of tellurite based glasses with the combination of alkali fluorides.

Fig. 4 represents the PL spectra of all the glasses which have eight luminescence peaks related to the transitions $^5D_1 \rightarrow {}^7F_0$ (509 nm), $^5D_1 \rightarrow {}^7F_1$ (537 nm), $^5D_1 \rightarrow {}^7F_2$ (556 nm), $^5D_0 \rightarrow {}^7F_0$ (580 nm), $^5D_0 \rightarrow {}^7F_1$ (592 nm), $^5D_0 \rightarrow {}^7F_2$ (614 nm), $^5D_0 \rightarrow {}^7F_3$ (652 nm) and $^5D_0 \rightarrow {}^7F_4$ (701 nm). Inset figure shows the maximized PL spectra in the region 500–570 nm which includes the luminescence transitions $^5D_1 \rightarrow {}^7F_0$ (509 nm), $^5D_1 \rightarrow {}^7F_1$ (537 nm) and $^5D_1 \rightarrow {}^7F_2$ (556 nm). Among all the emission transitions, the transition $^5D_0 \rightarrow {}^7F_2$ (614 nm) is highly intense in bright red region and is considered as an induced/forced electric dipole transition. This transition is also known as hypersensitive transition or pseudo quadrupole transition and it is considered as an admixture of odd-parity character into the $4f^6$ wave functions. These transitions obey the selection rule $|\Delta S| = 0$, $|\Delta L| \leq 2$ and $|\Delta J| \leq 2$ [27]. The intensity of this hypersensitive transition is strongly affected by the local symmetry of the trivalent europium ion and the nature of the ligands. The transition $^5D_0 \rightarrow {}^7F_1$ (592 nm) is a magnetic dipole transition and it is spin-forbidden. This is permissible only due to spin-orbit interactions. In general the intensity of this transition is almost constant for different materials doped with trivalent europium ions. The intensity of this transition is controlled by J-mixing [27]. The transition $^5D_0 \rightarrow {}^7F_3$ is forbidden according to J-O theory. The minimum intensity whatever observed in the PL spectra is due to J-mixing [27]. The transition $^5D_0 \rightarrow {}^7F_4$ (701 nm) observed at NIR region is having less intensity when compared with $^5D_0 \rightarrow {}^7F_2$ transition. The PL transitions $^5D_1 \rightarrow {}^7F_0$ (509 nm), $^5D_1 \rightarrow {}^7F_1$ (537 nm) and $^5D_1 \rightarrow {}^7F_2$ (556 nm) are having very less intensity. The intensity of the transitions that took place from $^5D_1$ excited state is low when compared with the $^5D_0$ excited state due to depopulation from higher excited state.

By using the PL spectra, J-O parameters of trivalent europium ion doped single alkali and mixed alkali tungsten tellurite glasses are evaluated and are given in Table 1 along with the other reported values [28–34]. The J-O parameters of all the glasses follow the trend $\Omega_2 > \Omega_4$. The Ω_2 J-O parameter indicates the bonding nature between Eu^{3+} ions and surrounding ligands as predominantly covalent. From the values of J-O parameters, it is observed that TeWK glass is having less magnitude comparatively other glasses. Hence TeWK glass is less covalent in nature when compared with other glasses. By using these J-O parameters various radiative parameters like transition probabilities (A_R), total Transition probabilities (A_T), radiative and experimental branching ratios (β_R & β_{exp}), stimulated emission cross-sections (σ_{se}), gain band width ($\sigma_{se} \times \Delta\lambda_p$) and optical gain ($\sigma_{se} \times \tau_R$) for $^5D_0 \rightarrow {}^7F_2$ luminescence transition are evaluated and are given in Table 2 using the expressions given in literature [35]. Branching ratios and stimulated emission cross-sections are the two major parameters which can decide the laser performance of a material [36]. From Table 2 it is observed that TeWK possesses higher magnitudes of branching ratios and stimulated emission cross-sections. The stimulated emission cross-

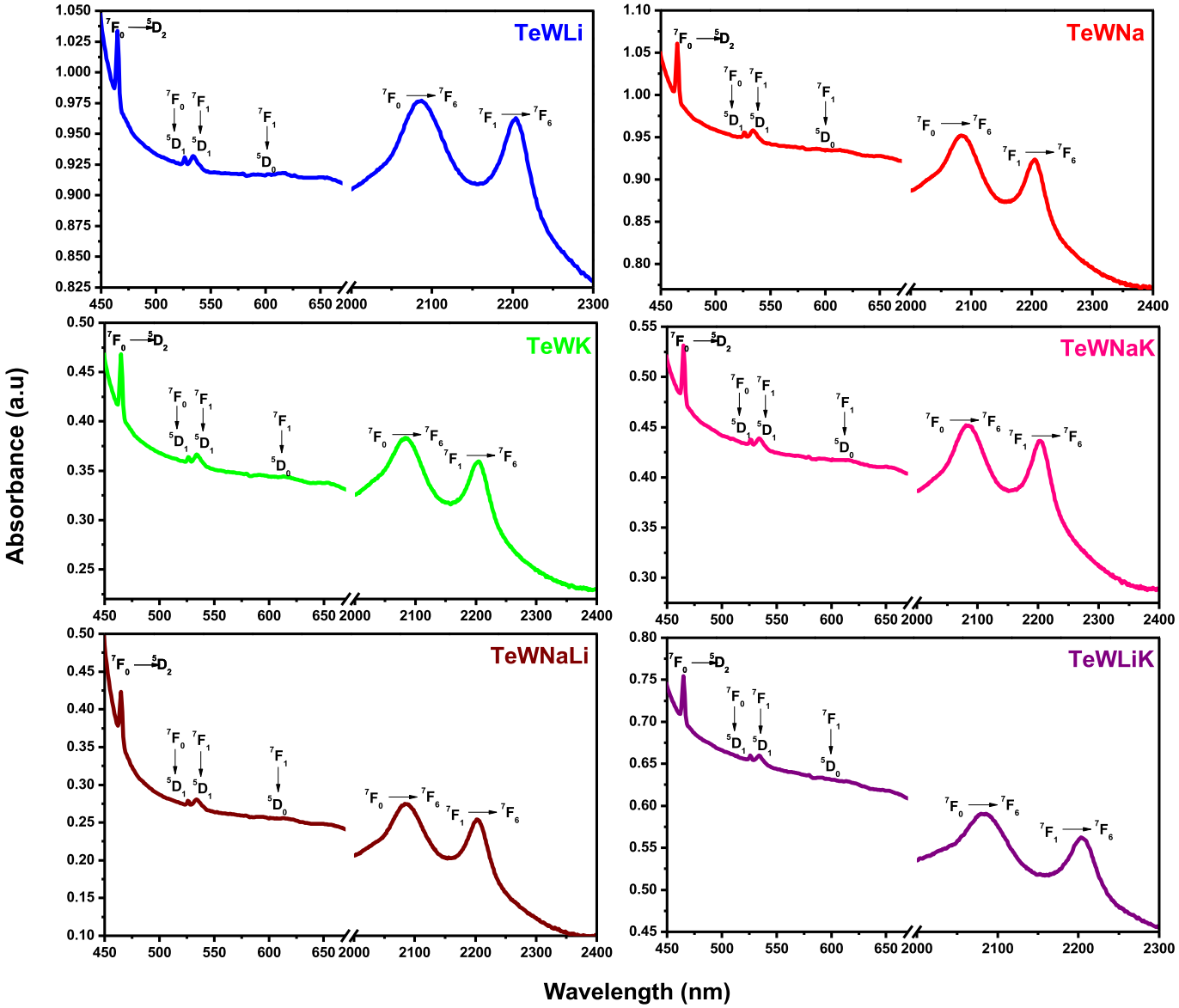


Fig. 2. Optical absorption spectra of Eu^{3+} ions doped single and mixed alkali fluoro tungsten tellurite glasses.

section values are also compared with other reported values [36–41]. Hence from the results obtained, it is suggested that, TeWK glass is suitable for laser in bright red region.

The luminescence intensities are improved when the chemical bond in between the Eu^{3+} ions and oxygen is more covalent in nature. In order to understand the covalent/ionic strength between Eu^{3+} ions and the surrounding ligands and also to found the degree of asymmetry around the local environment of dopant ions, the luminescence intensity ratio, $R = ({}^5D_0 \rightarrow {}^7F_2)/({}^5D_0 \rightarrow {}^7F_1)$ was evaluated. The R values are calculated from the area under various ${}^5D_0 \rightarrow {}^7F_J$ luminescence bands for all the glasses. These R values are high and some are incomparable with the other reported values [TeWLi (4.05), TeWNa (4.54), TeWK (4.97), TeWNaLi (4.25), TeWNaK (4.33) and TeWLiK (4.38)] [42–47]. From the obtained R values of all the glasses, it is concluded that the present series of glasses have higher degree of covalency in Europium-Oxygen bond. Among all the glasses, TeWK glass has highest intensity ratio 4.97, which is a representation of formation of strong Europium-Oxygen bond in that glass. Due to the higher degree of covalency in the present glasses, the emission intensity of ${}^5D_0 \rightarrow {}^7F_2$ transition is more. Comparison of stimulated emission cross-section values and Intensity ratios of Eu^{3+} ions doped single and mixed alkali fluoro tungsten tellurite glasses also represented in Fig. 5.

3.4. Time resolved photoluminescence (TR-PL) spectral analysis

Fig. 6 shows the TR-PL curves of Eu^{3+} ions doped single and mixed alkali fluoro tungsten tellurite glasses. All the decay curves are recorded at an excitation wavelength 464 nm related to the transition ${}^5D_0 \rightarrow {}^7F_2$. The decay curves of all the prepared glasses are fitted double exponentially as follows.

$$I(t) = A_1 \exp\left(\frac{t}{\tau_1}\right) + A_2 \exp\left(\frac{t}{\tau_2}\right)$$

Here τ_1 & τ_2 are the slow and fast decay times components, A_1 and A_2 are the amplitudes of slow and fast components respectively. Experimental lifetimes (τ_{exp}) are measured by considering the slow

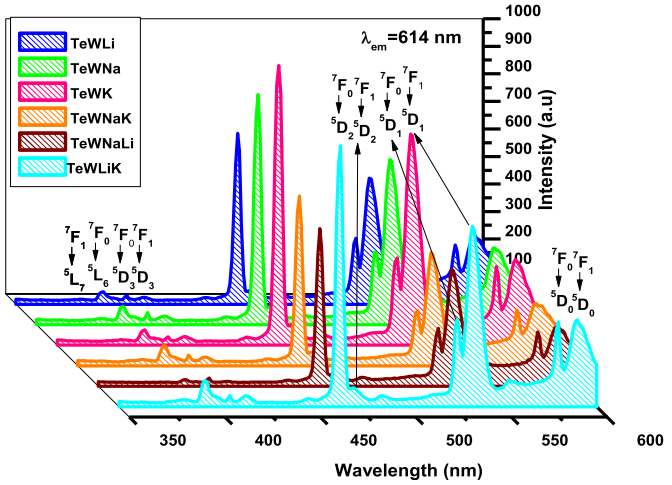


Fig. 3. Excitation spectra of Eu^{3+} ions doped single and mixed alkali fluoro tungsten tellurite glasses.

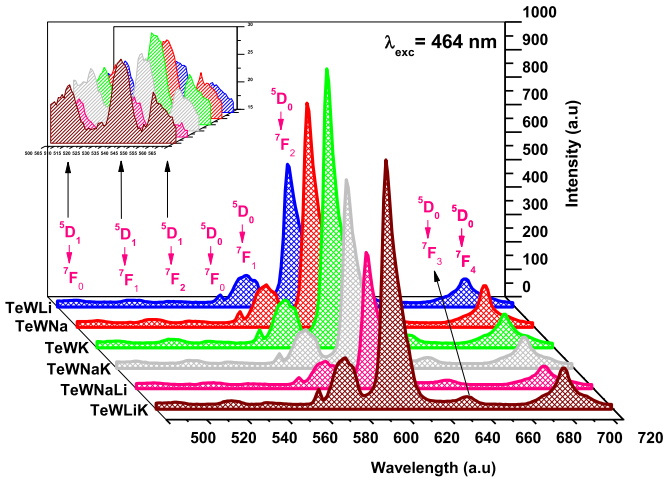


Fig. 4. Emission spectra of Eu^{3+} ions doped single and mixed alkali fluoro tungsten tellurite glasses. Inset figure shows the peaks (magnified) corresponding to the transitions $^5D_1 \rightarrow {}^7F_{0,1,2}$.

Table 1
JO Parameters ($\Omega_\lambda \times 10^{-20} cm^2$) evaluated from the photoluminescence spectra of the Eu^{3+} ions doped single and mixed alkali fluoro tungsten tellurite glasses.

Name of the Glass	Ω_2	Ω_4	Ω_6	References
TeWLi	2.5258	2.2492	–	Present Work
TeWNa	3.3005	2.3029	–	Present Work
TeWK	2.0802	0.8928	–	Present Work
TeWNaLi	2.9850	2.4850	–	Present Work
TeWNaK	3.1248	2.3587	–	Present Work
TeWLiK	3.0787	2.1418	–	Present Work
GICZPSEu	1.36	0.25	–	[28]
Lithium borate glasses	2.54	1.61	–	[29]
LNaFB	3.62	1.43	–	[30]
PKAlCaFEu10	2.52	3.64	–	[31]
CdLFB	2.46	0.126	–	[32]
BTBa0.05Eu	3.66	0.15	–	[33]
SPbKNLFEu 10	3.75	0.18	–	[34]

and fast decay time components and are given in Table 3 along with the radiative lifetimes (τ_R). By considering experimental and radiative lifetimes (τ_{exp} & τ_R), the luminescence quantum efficiency (η) for all the glasses have been evaluated using the following

Table 2
Transition probabilities (A_R) (s^{-1}), Total Transition probabilities (A_T) (s^{-1}), radiative and experimental branching ratios (β_R & β_{exp}), stimulated emission cross-sections (σ_{se})($\times 10^{-21}$ cm^2), gain band width ($\sigma_{se} \times \Delta\lambda_p$) ($cm^3$) and optical gain ($\sigma_{se} \times \tau_R$) ($cm^2$ s) for $^5D_0 \rightarrow {}^7F_2$ luminescence transition of Eu^{3+} ions doped single and mixed alkali fluoro tungsten tellurite glasses.

Name of the Glass	A_R	A_T	β_R	β_{exp}	σ_{se}	References
$^5D_0 \rightarrow {}^7F_2$ (614 nm)						
TeWLi	466	889	0.5245	0.5034	14.8	Present Work
TeWNa	583	994	0.5862	0.5432	16.8	Present Work
TeWK	363	646	0.5911	0.6123	18.9	Present Work
TeWNaLi	544	968	0.5700	0.5571	13.9	Present Work
TeWNaK	552	983	0.5531	0.5834	15.9	Present Work
TeWLiK	537	929	0.5775	0.5813	17.5	Present Work
ZnAlBiB2.0Eu	–	–	–	–	6.71	[36]
BSMN	–	–	–	–	6.89	[37]
1EPbFB	–	–	–	–	13.46	[38]
1.0LBTPE	–	–	–	–	10.6	[39]
TFB1Eu	–	–	–	–	19.6	[40]
NaTFP	–	–	–	–	13.42	[41]

expression and are given in Table 3 along with the other reported values [36,38–41].

$$\eta = \left(\frac{\tau_{exp}}{\tau_R}\right) \times 100$$

Among all the glasses, the TeWK glass possesses maximum quantum efficiency (83%) when compared with other glasses. Among the alkali ions, K^+ has less ionization energy when compared with Li^+ and Na^+ ions. This helps potassium ions to act as a relatively good network modifier when compared with lithium and sodium ions. Consequently, the presence of potassium in a glass can produce more number of non-bridging oxygens when compared with the lithium and sodium ions [48–50]. Such glass modifier networks leading to increase in the solubility of rare earth ions and reduces the phonon energy cross-sections in the glasses. Such high concentration solubility with low phonon energies results into less cross-relaxation (non-radiative) and/or self-quenching effects, which eventually may help in getting better radiative properties. The variation of experimental and radiative lifetimes (τ_{exp} & τ_R) are also shown in Fig. 7.

The populated europium ions in the higher excited state can undergo both radiatve and non-radiative decay transitions. The rate

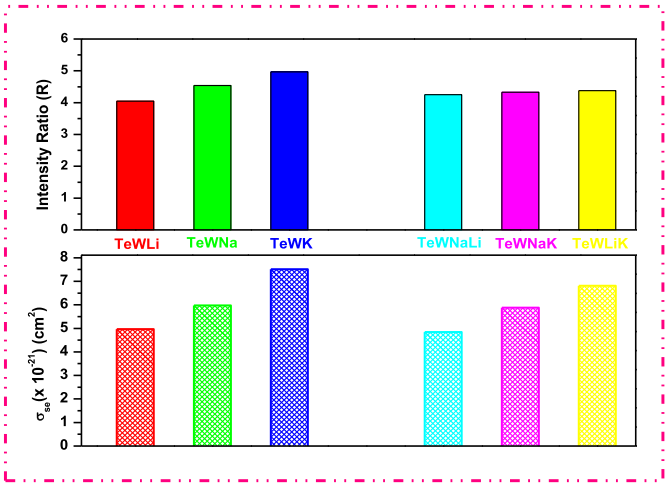


Fig. 5. Comparison of Stimulated emission cross-section values and Intensity ratios of Eu^{3+} ions doped single and mixed alkali fluoro tungsten tellurite glasses.

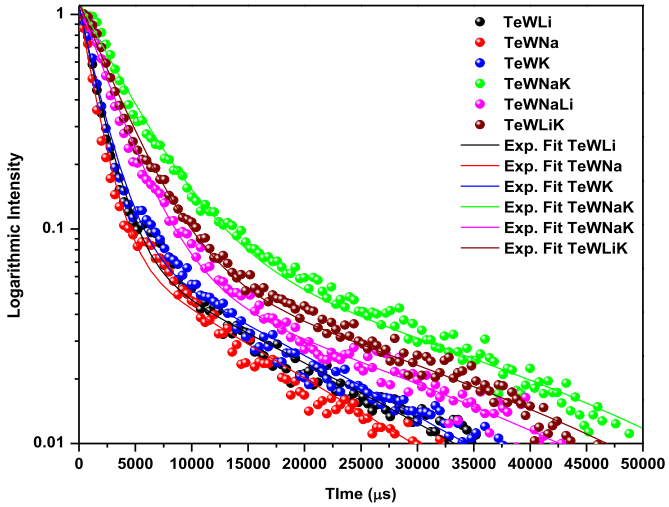


Fig. 6. The decay curves for $^5D_0 \rightarrow {}^7F_2$ (614 nm) emission of Eu^{3+} ions doped single and mixed alkali fluoro tungsten tellurite glasses when excited at 464 nm.

Table 3
The Experimental (τ_{exp}) (μs), radiative (τ_R) (μs) lifetimes, quantum efficiencies (η) non-radiative decay rates (W_{NR}) (s^{-1}) and colour chromaticity co-ordinates (x,y) for Eu^{3+} ions doped single and mixed alkali fluoro tungsten tellurite glasses excited at a wavelength of 464 nm.

Glass	τ_{exp}	τ_R	η	W_{NR}	(x, y)	Reference
TeWNa	1382	1005	60	271	(0.65, 0.34)	Present Work
TeWLi	1408	1124	72	179	(0.64, 0.35)	Present Work
TeWK	1737	1526	83	79	(0.65, 0.39)	Present Work
TeWLiNa	2842	1016	35	632	(0.63, 0.35)	Present Work
TeWNaK	4018	1032	25	720	(0.64, 0.34)	Present Work
TeWLiK	3241	1075	33	622	(0.64, 0.35)	Present Work
ZnAlBiB2.0Eu	–	–	55	–	–	[36]
1EPbFB	–	–	58	–	–	[38]
1.0LBTPE	–	–	41	–	–	[39]
TFB1Eu	–	–	63	–	–	[40]
NaTFP	–	–	70	–	–	[41]

of non-radiative decay can be evaluated using the following expression.

$$W_{NR} = \frac{1}{\tau_{exp}} - \frac{1}{\tau_R}$$

The non-radiative decay rates for all the glasses are given in Table 3. From Table 3, it is observed that TeWKEu glass possesses low rate of non-radiative decay. Depending upon the non-radiative decay value, one can predict the lifetime of a particular excited state. If the non-radiative decay rates are very high, then the lifetime of that particular excited level is reduced due to the involvement of more number of phonons. From the obtained values of non-radiative decay rates, it can be confirmed that the probability of multiphoton relaxation rates is less and whatever non-radiative decay takes place in the present series of glasses is due to the interactions between Eu^{3+}- Eu^{3+} ions [39].

3.5. Colour chromaticity co-ordinates

The assessment of colour given by a material is considered as colorimetry or the 'science of colour'. This is closely interacted with human colour vision. Mixing of two colours will appear to the human eye as one colour and the eye is unable to recognize the original dichromatic composition of that colour [47]. The red light

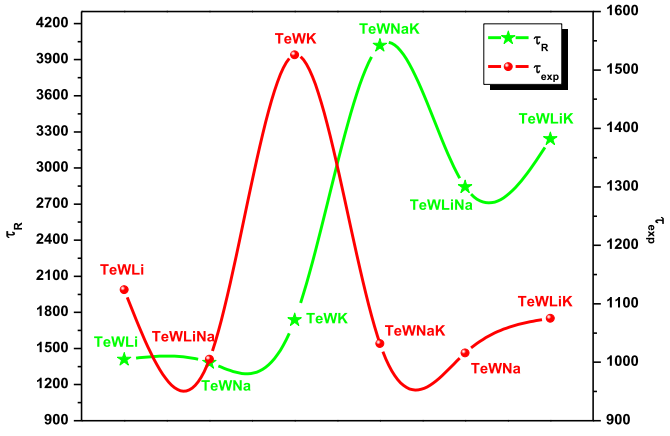


Fig. 7. Variation of radiative and experimental lifetimes (τ_R and τ_{exp}) of Eu^{3+} ions doped single and mixed alkali fluoro tungsten tellurite glasses when excited at 464 nm.

generation from the present series of glasses was confirmed through the CIE1931colour chromaticity co-ordinates shown in Fig. 8. The CIE colour space had provided a priceless evidence for LED makers who have developed such products, because it considers the eye's varying sensitivity to light of different colour and introduces a key reference for artificial lighting in the form of the Planckian locus delineating the colour of emissions from black bodies of increasing temperature. The colour of the luminescent source can be determined from the colour matching function values $\overline{X}(\lambda)$, $\overline{Y}(\lambda)$*and* $\overline{Z}(\lambda)$ and the degree of stimulation is essential to match the colour of the spectral power density $P(\lambda)$. These tristimulus values are used to evaluate the CIE1931colour chromaticity co-ordinates $\left(x = \frac{X}{X+Y+Z},\ y = \frac{Y}{X+Y+Z}\right)$. All the colour chromaticity co-ordinates of all the glasses are fall in the red colour region. Among all the glasses, the colour co-ordinates of TeWKEu glass exactly fall in the bright red colour region. This red light emission is also confirmed by confocal image of TeWKEu glass in Fig. 8. Hence from all the results obtained it is concluded that the TeWKEu glass is apposite for the emission of laser in bright red region.

4. Conclusions

Trivalent europium ions doped single and mixed alkali fluoro

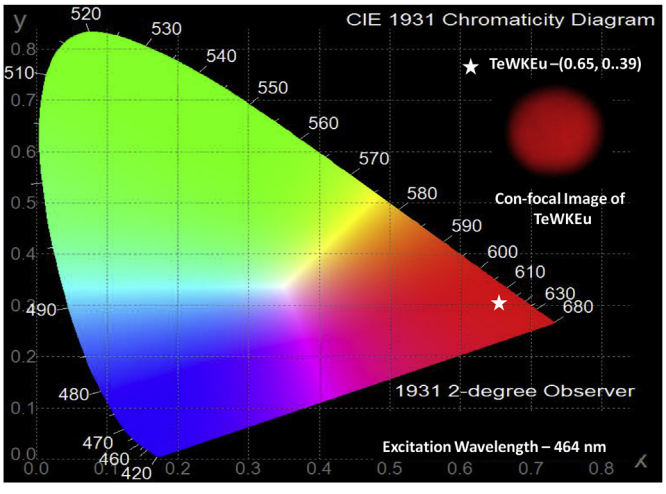


Fig. 8. Colour chromaticity diagram of TeWKEu glass.

tungsten tellurite glasses have been prepared by using conventional melt quenching technique at room temperature. The Raman spectra gives the information pertaining to different functional groups present in the as prepared glasses. Since the square reduced matrix element $||U^4||$ is zero for majority of the absorption transitions, the J-O parameters are evaluated from the PL spectra and they are following the trend $\Omega_2 > \Omega_4$. This trend shows the nature of bonding between the Eu^{3+} ions and surrounding ligands as covalent in nature. From the PL spectra, luminescence intensity ratio have been evaluated for all the glasses. From the obtained R values of all the glasses, it is concluded that the present series of glasses have higher degree of covalency in Europium-Oxygen bond which confirm the asymmetry around the local environment of the dopant ions. The PL spectra have eight luminescent peaks of which the peak at 614 nm corresponding to the transition $^5D_0 \rightarrow {}^7F_2$ is highly intense for the TeWK glass. Using the JO parameters, branching ratios, stimulated emission cross-sections, quantum efficiencies have been evaluated. From all the obtained results, it is concluded that TeWK glass possesses highest magnitudes of branching ratios, stimulated emission cross-section and quantum efficiency for the transition $^5D_0 \rightarrow {}^7F_2$ (614 nm). This can also be confirmed by the colour co-ordinates and confocal images. Hence TeWK glass is aptly suitable as a luminescent material to give bright red colour at 614 nm.

Acknowledgements

This work is partly supported by High-impact Research initiative of IIT-Delhi, UK-India Education Research Initiative (UKIERI) and Department of Science and Technology (DST), Govt. of India, New Delhi. The authors Dr. A. S. Rao, Dr. Sk. Mahamuda (File Number: ECR/2016/000376) and Dr. K. Swapna (File Number: ECR/2016/000335) are thankful to DST, Govt. of India, New Delhi for the award of a major research project to them.

References

[1] Sk. Mahamuda, K. Swapna, M. Venkateswarlu, A. Srinivasa Rao, Suman Shakya, G. Vijaya Prakash, Spectral characterisation of Sm^{3+} ions doped Oxy-fluoroborate glasses for visible orange luminescent applications, J. Lumin. 154 (2014) 410–424.
[2] K. Swapna, Sk. Mahamuda, M. Venkateswarlu, A. Srinivasa Rao, M. Jayasimhadri, Suman Shakya, G. Vijaya Prakash, Visible, up-conversion and NIR (~1.5 μm) luminescence studies of Er^{3+} doped zinc alumino bismuth borate glasses, J. Lumin. 163 (2015) 55–63.
[3] Sk. Mahamuda, K. Swapna, P. Packiyaraj, A. Srinivasa Rao, G. Vijaya Prakash, Lasing potentialities and white light generation capabilities of Dy^{3+} doped oxy-fluoroborate glasses, J. Lumin. 153 (2014) 382–392.
[4] M. Venkateswarlu, M.V.V.K.S. Prasad, K. Swapna, Sk. Mahamuda, A. Srinivasa Rao, A. Mohan Babu, D. Haranath, Pr^{3+} doped lead tungsten tellurite glasses for visible red lasers, Ceram. Int. l40 (2014) 6261–6269.
[5] Nisha Deopa, A.S. Rao, Sk. Mahamuda, Mohini Gupta, M. Jayasimhadri, D. Haranath, G. Vijaya Prakash, Spectroscopic studies of Pr^{3+} doped lithium lead alumino borate glasses for visible reddish orange luminescent device applications, J. Alloys Compd. 708 (2017) 911–921.
[6] Y. Shimizu, K. Bandou, Development of White LED light source, Rare Earth 40 (2002) 150–151.
[7] S. Fujita, S. Yoshihara, A. Sakamoto, S. Yamamoto, S. Tanabe, YAG glass-ceramic phosphor for white LED (I): background and development, in: Proc. SPIE 5941, 2005, p. 594111.
[8] I. Abramov, Retinal mechanism of color vision, in: M.G.F. Fuortes (Ed.), Handbook of Sensory Physiology, vol. 7, Springer-Verlag, Berlin, Heidelberg, and New York, 1972, pp. pp.567–607.
[9] R.V. Deun, K. Binnemans, C. Gorller-Walrand, J.L. Adam, Optical properties of Eu3þ-doped fluorophosphate glasses, J. Phys. Condens. Matter 10 (1998) 7231–7241.
[10] G. Blasse, B.C. Grabmaier, Luminescent Materials, Springer-Verlag, Berlin, 1994.
[11] Dirk Larink, Matthias T. Rinke, Hellmut Eckert, Mixed network former effects in tellurite glass systems: structure/property correlations in the system (Na2O)1/3[(2TeO2)x(P2O5)1−x]2/3, J. Phys. Chem. C 119 (2015) 17539–17551.
[12] J. Wasylak, K. Ozga, I.V. Kityk, J. Kucharski, IR optical limiting in europium and thulium doped oxide glasses, Infrared Phys. Technol. 45 (4) (2004) 253–263.
[13] M. Zambelli, M. Abril, V. Lavın, A. Speghini, M. Bettinelli, Fluorescence line narrowing spectroscopy of Eu^{3+} in a niobium tellurite glass, J. Non-Cryst. Solids 345&346 (2004) 386–390.
[14] Y. Gandhi, I.V. Ityk, M.G. Brik, P. Raghava Rao, N. Veeraiah, Influence of tungsten on the emission features of Nd^{3+}, Sm^{3+} and Eu^{3+} ions in ZnF_2–WO_3–TeO_2 glasses, J. Alloys Compd. 508 (2010) 278–291.
[15] Aline M. Farias, Marcelo Sandrini, José Renato M. Viana, Mauro L. Baesso, Antonio C. Bento, Jurandir H. Rohling, Yannick Guyot, Dominique De Ligny, Luiz Antonio O. Nunes, Flávio G. Gandra, Juraci A. Sampaio, Sandro M. Lima, Luis Humberto C. Andrade, Antonio N. Medina, Emission tunability and local environment in europium-doped OH^--free calcium aluminosilicate glasses for artificial lighting applications, Mater. Chem. Phys. 156 (2015) 214–219.
[16] R. Narro-García, H. Desirena, T. López-Luke, J. Guerrero-Contreras, C.K. Jayasankar, R. Quintero-Torres, E. De la Rosa, Spectroscopic properties of Eu^{3+}/Nd^{3+} co-doped phosphate glasses and opaque glass–ceramics, Opt. Mater. 46 (2015) 34–39.
[17] G. Upendera, C.P. Vardhania, S. Suresha, A.M. Awasthib, V.C. Chandra Moulia, Structure, physical and thermal properties of WO_3–GeO_2–TeO_2 glasses, Mater. Chem. Phys. 121 (2010) 335–341.
[18] J. Ozdanova, H. Ticha, L. Tichy, Optical band gap and Raman spectra in some $(Bi_2O_3)_x(WO_3)_y(TeO_2)_{100-x-y}$ and $(PbO)_x(WO_3)_y(TeO_2)_{100-x-y}$ glasses, J. Non-Cryst. Solids 355 (2009) 2318–2322.
[19] H. Burger, K. Kneipp, H. Hobert, W. Vogel, V. Kozhukharov, S. Neov, Glass formation, properties and structure of glasses in the TeO_2-ZnO system, J. Non-Cryst. Solids 151 (1992) 134–142.
[20] A.G. Kalampounias, G.N. Papatheodorou, S.N. Yannopoulos, A temperature dependence Raman study of the $0.1Nb_2O_5$–$0.9TeO_2$ glass-forming system, J. Phys. Chem. Solids 67 (2006) 725–731.
[21] Takao Sekiya, Norio Mochida, Atsushi Ohtsuka, Mamoru Tonokawa, Raman spectra of $MO_{1/2}$-TeO_2 (M=Li, Na, K, Rb, Cs and Tl) glasses, J. Non-Cryst. Solids 44 (1992) 128–144.
[22] V.O. Sokolov, V.G. Plotnichenko, V.V. Koltashev, E.M. Dianov, On the structure of tungstate–tellurite glasses, J. Non-Cryst. Solids 352 (2006) 5618–5632.
[23] T. Kalpana, M.G. Brik, V. Sudarsan, P. Naresh, V. Ravi Kumar, I.V. Kityk, N. Veeraiah, Influence of Al^{3+} ions on luminescence efficiency of Eu^{3+} ions in barium boro-phosphate glasses, J. Non-Cryst. Solids 419 (2015) 75–81.
[24] G. Mikhail, Brik Zelika M. Antic, Katarina Vukuvic, Miroslav D. Dramicanin, Judd-ofelt analysis of Eu^{3+} emission in TiO_2 anatase, Mater. Trans. 56 (2015) 1416–1418.
[25] W.T. Carnall, P.R. Fields, K. Rajnak, Electronic energy levels in the trivalent lanthanide aquo ions. I. Pr^{3+}, Nd^{3+}, Pm^{3+}, Sm^{3+}, Dy^{3+}, Ho^{3+}, Er^{3+}, and Tm^{3+}, J. Chem. Phys. 49 (1968) 4424–4442.
[26] Wojciech A. Pisarski, Lidia Zur, Martyna Kowal, Joanna Pisarska, Enhancement and quenching photoluminescence effects for rare earth – doped lead bismuth gallate glasses, J. Alloys Compd. 651 (2015) 565–570.
[27] Koen Binnemans, Interpretation of europium (III) spectra, Coord. Chem. Rev. 295 (2015) 1–45.
[28] M.A.K. Elfayoumi, M. Farouk, M.G. Brilk, M.M. Elokr, Spectroscopic studies of Sm^{3+} and Eu^{3+} co-doped lithium borate glass, J. Alloys Compd. 492 (2010) 712–716.
[29] B. Deva Prasad Raju, C.M. Reddy, Structural and optical investigations of Eu^{3+} ions in lead containing alkali fluoroborate glasses, Opt. Mater. 34 (2012) 1251–1260.
[30] S.N. Rasool, L.R. Moorthy, C.K. Jayasankar, Optical and luminescence properties of Eu^{3+} doped phosphate based glasses, Mater. Express 3 (2013) 231–240.
[31] S. Arun Kumar, K. Marimuthu, Structural and luminescence studies on Eu^{3+}: B_2O_3–Li_2O–MO–LiF (M=Ba, Bi_2, Cd, Pb, Sr_2 and Zn) glasses, J. Lumin. 139 (2013) 6–15.
[32] K. Marimuthu, R.T. Karunakaran, S. Surendra Babu, G. Muralidharan, S. Armugam, C.K. Jayasankar, Structural and Spectroscopic investigation on Eu3+ doped alkali fluoroborate glasses, Sol. Stat. Sci. 11 (2009) 1297–1302.
[33] K. Annapoorani, K. Marimuthu, Spectroscopic properties of Eu^{3+} ions doped Barium telluroborate glasses for red laser applications, J. Non-Cryst. Solids 463 (2017) 148–157.
[34] P. Manasa, C.K. Jayasankar, Luminescence and phonon side band analysis of Eu^{3+}-doped lead fluorosilicate glasses, Opt. Mater. 62 (2016) 139–145.
[35] Sk. Mahamuda, K. Swapna, A. Srinivasa Rao, M. Jayasimhadri, T. Sasikala, K. Pavani, L. Rama Moorthy, Spectroscopic properties and luminescence behavior of Nd^{3+} doped zinc alumino bismuth borate glasses, J. Phys. Chem. Solids 74 (2013) 1308–1315.
[36] K. Swapna, Sk. Mahamuda, A. Srinivasa Rao, T. Sasikala, P. Packiyaraj, L. Rama Moorthy, G. Vijaya Prakash, Luminescence characterization of Eu^{3+} doped Zinc Alumino Bismuth Borate glasses for visible red emission applications, J. Lumin. 156 (2014) 80–86.
[37] B. Naveen Kumar Reddy, B. Devaprasad Raju, K. Thyagarajan, R. Ramanaiah, Young-Dahl Jho, B. Sudhakar Reddy, Optical characterization of Eu^{3+} ion doped alkali oxide modified borosilicate glasses for red laser and display device applications, Ceram. Int. 43 (2017) 8886–8892.
[38] C.R. Kesavalu, K. Kiran Kumar, N. Vijaya, Ki-Soo Lim, C.K. Jayasankar, Thermal, vibrational and optical properties of Eu^{3+}-doped lead fluorophosphate glasses for red laser applications, Mater. Chem. Phys. 141 (2013) 903–911.
[39] S. Selvi, K. Marimuthu, N. SuriyaMurthy, G. Muralidharan, Red light generation through the lead boro–telluro–phosphate glasses activated by Eu^{3+} ions, J. Mol. Struct. 1119 (2016) 276–285.

[40] R. VijayaKumar, K. Maheshvaran, V. Sudarsan, K. Marimuthu, Concentration dependent luminescence studies on Eu^{3+} doped telluro fluoroborate glasses, J. Lumin. 154 (2014) 160–167.
[41] D. Uma Maheswari, T. Suresh Kumar, L. Rama Moorthy, Kiwan Jang, M. Jayasimhadri, Emission properties of Eu^{3+} ions in alkali telluro-fluorophosphate glasses, Phys. B 403 (2008) 1690–1694.
[42] A. Kumar, D.K. Rai, S.B. Rai, Optical studies of Eu^{3+} ions doped in tellurite glass, Spectrochim. Acta A 58 (2002) 2115–2125.
[43] P. Rehana, O. Ravi, B. Ramesh, G.R. Dillip, C. Madhukar Reddy, S.W. Joo, B. Deva Prasad Raju, Photoluminescence studies of Eu^{3+} ions doped calcium zinc niobium borotellurite glasses, Adv. Mater. Lett. 7 (2) (2016) 170–174.
[44] M. Bettinelli, A. Speghini, M. Ferrari, M. Montagna, Spectroscopic investigation of zinc borate glasses doped with trivalent europium ions, J. Non-Cryst. Solids 201 (1996) 211–221.
[45] M.V. Vijaya Kumar, B.C. Jamalaiah, K. Rama Gopal, R.R. Reddy, Novel Eu^{3+}-doped lead telluroborate glasses for red laser source applications, J. Solid State Chem. 184 (2011) 2145.
[46] E.W.J.L. Oomen, A.M.A. Van Dongen, Europium (III) in oxide glasses: dependence of the emission spectrum upon glass composition, J. Non-Cryst. Solids 111 (1989) 205–213.
[47] Y.C. Ratnakaram, V. Reddy Prasad, S. Babu, V.V. Ravi Kanth, Kumar, Luminescence performance of Eu^{3+} doped lead-free zinc phosphate glasses for red emission, Bull. Mater. Sci. 39 (2016) 1065–1072.
[48] J.E. Shelby, Introduction to Glass Science and Technology, second ed., Chapter 5, 72–95.
[49] Fuxi Gan, Optical Properties of fluoride glasses: a review, J. Non-Cryst. Solids 184 (1995) 9–20.
[50] T. Nakajima, B. Zemva, A. Tressaud, Advanced Inorganic Fluorides:Synthesis, Characterization and Applications, first ed., Elsevier, 2000.

International Journal of Applied Engineering Research ISSN 0973-4562 Volume 12, Number 16 (2017) pp. 5865-5871
© Research India Publications. http://www.ripublication.com

Dual Stator Induction Generator For Rural Electrification

Ramesh Singh[1] and Vishal Verma[2]

[1]*Electrical Engineering Department, Delhi Technological University, Delhi, India.*

[2]*Electrical Engineering Department, Delhi Technological University, Delhi, India.*

[1]*Orcid: 0000-0003-2545-890X*

Abstract

The paper presents an electromechanical auto synchronized wind energy conversion system (WECS) for larger penetration of renewable energy sources (RES) in the rural electrification systems. The architecture of the WECS uses two stator windings at power frequency which provides harvesting of power to flow from WECS to load and to grid side when the generated power is in access. Asymmetrical six phase machine is modeled and analyzed for power transaction between WECS to grid and load, grid to load in absence of energy harnessing from wind. A simulation study is done on a 3.75 KW Dual Stator Induction Generator (DSIG). The performance of the proposed system is evaluated and results show effective transfer of power to the load under perturbing load/source side conditions.

Keywords: DSIG; Wind Energy Conversion System; Renewable Energy; SCIG, THD.

INTRODUCTION

Demand for electrical power is increasing day by day so new and better ways of power generation and power transfer are being explored everywhere, but demand and supply parity is a distant dream for developing and underdeveloped countries. Use of renewable sources of power generation is highly encouraged for inducting power to fulfill the deficit demand. Amongst various renewable sources wind energy has proven to be a clearer and better solution [1]. Many types and topologies for wind generator systems have been practiced, each with its own advantage and disadvantage over the other scheme [1]. For having a deep penetration of renewable into the grid it is preferred to have distributed generating systems rather than larger units at specific places. Small induction generators are considered to be the promising solutions taking into consideration for larger penetration of power [1]. Low cost and maintenance free nature of squirrel cage induction generators (SCIG) give them a upper hand over doubly fed induction generators (DFIG) [2] [3]. Also in grid connected mode, reactive power demand is fully catered by grid itself or sometimes a capacitor is connected at point of common coupling to decrease the reactive power demand from grid side. Wide range of operating speed and rated back to back converter makes DFIG a suitable choice for higher generation ratings, but for low rating generating units DFIG becomes costly when compared with SCIG as the installation and running costs of DFIG are more making the payback period to become very long[4-5]. So for smaller generating units which can be installed for rural loads or at small community / residential areas fixed speed SCIG's offer suitable and sustainable solution, where their accumulated generation has an effect of reducing the overall average grid loading [4-5]. Pump loads are commonly occurring rural load in association with small residential loads. For improving power factor of the supply and limited voltage regulation a capacitor bank is often used. Tapped power from wind is utilized locally, but during light load conditions the excess power is transferred to the grid.

Induction generators directly connected to grid suffer from major drawback in terms of intermittency of power due to fluctuating wind speed and these are reflected in their electrical responses (like voltage and frequency fluctuation). Many a times due to larger variation in speed out of the cut-in and cut-off range, after the machine attains stall condition demanding large magnetizing current every time speed breaks into cut-in speed. Another problem the wind generator faces is due to low voltage at the point of common coupling. The low voltage ride through (LVRT) capability marks the merit of SCIG for its robust grid connection [2] [6] [7].

A new type of SCIG with two stators, with same number of poles, magnetically coupled via same air gap and single rotor (DSIG) is proposed as a new solution for such kind of smaller distributed wind energy generating units [8-9]. Grid is connected to one stator terminal of DSIG and local load is connected to other stator terminal of DSIG. Power is routed to the local load via air gap thus providing galvanic isolation. In case of low wind speed DSIG acts as transformer and transfers power from the grid to the local load. As power is transferred to load end via magnetic circuits there are least chances of grid side harmonic disturbances reaching the local loads or vice-versa. As wind speed goes post cut-in speed the DSIG generates and supplies power to its local load, for higher speed

the power after catering to the local loads pushed to the grid side to imitate/ use grid as storage. In all the cases DSIG always draw reactive power from the grid for its excitation, not only reduced in quantum due to coupling of only one side to the grid but also due to auto compensation because of loads on other side.

The paper presents DSIG connected to a three phase grid on one set of stator winding and with load on other side. The study on the effects of loading at one side of DSIG with different types and combinations of load like unity power factor load, lagging power factor load, non-linear load and dynamic load etc. has been considered. Prime mover enacting wind turbine is run at different speeds near synchronous speed with a slip of ± 4% to study the source side perturbations. This has been validated through simulation done using MATLAB/SIMULINK.

SYSTEM CONFIGURATION

Block diagram of considered system is shown in Fig. 1. The Figure shows that DSIG is connected to three phase grid through one set of three phase stator winding and the local loads are applied at the other three phase stator winding. Reactive power required by DSIG is provided by grid and thus requirement of any static or dynamic VAR compensator is eliminated. When local loads are connected to off grid side winding of DSIG and wind speed is less than synchronous speed and the DSIG is not generating any power the requisite power (active and reactive both) demanded by the load is drawn from grid side.

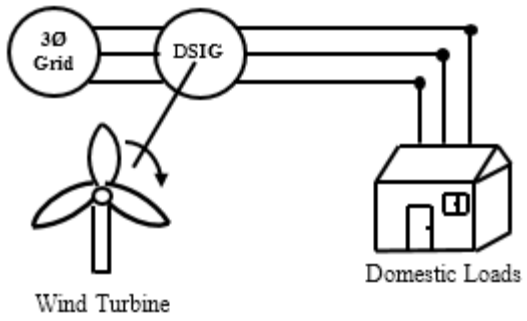


Figure 1: Block Diagram

MATHEMATICAL MODELLING

Two balanced three phase windings displaced to each other by 30˚ (asymmetrical) is assumed for modeling of DSIG; considering following assumptions:

- Air-gap is uniform and the windings are sinusoidally distributed around the air-gap.
- Magnetic saturation and core-losses are neglected.

The following voltage equations are written in d-q axis for DSIG in synchronous reference frame:

$$[V_{qs1}] = [R_{s1}].[i_{qs1}] + \text{þ}[\chi_{qs1}] + \omega[\chi_{ds1}] \quad (1)$$

$$[V_{ds1}] = [R_{s1}].[i_{ds1}] + \text{þ}[\chi_{ds1}] - \omega[\chi_{qs1}] \quad (2)$$

$$[V_{qs2}] = [R_{s2}].[i_{qs2}] + \text{þ}[\chi_{qs2}] + \omega[\chi_{ds2}] \quad (3)$$

$$[V_{ds2}] = [R_{s2}].[i_{ds2}] + \text{þ}[\chi_{ds2}] - \omega[\chi_{qs2}] \quad (4)$$

$$[V'_{qr}] = [R'_{r}].[i'_{qr}] + \text{þ}[\chi'_{qr}] + (\omega-\omega_r)[\chi'_{dr}] \quad (5)$$

$$[V'_{dr}] = [R'_{r}].[i'_{dr}] + \text{þ}[\chi'_{dr}] - (\omega-\omega_r)[\chi'_{qr}] \quad (6)$$

Where the flux linkages are expressed as:

$$[\chi_{qs1}] = [L_{ls}].[i_{qs1}] + [L_{lm}].[i_{qs1} + i_{qs2}] + [L_m].[\, i_{qs1} + i_{qs2} + i'_{qr}] \quad (7)$$

$$[\chi_{ds1}] = [L_{ls}].[i_{ds1}] + [L_{lm}].[i_{ds1} + i_{ds2}] + [L_m].[\, i_{ds1} + i_{ds2} + i'_{dr}] \quad (8)$$

$$[\chi_{qs2}] = [L_{ls}].[i_{qs2}] + [L_{lm}].[i_{qs1} + i_{qs2}] + [L_m].[\, i_{qs1} + i_{qs2} + i'_{qr}] \quad (9)$$

$$[\chi_{ds2}] = [L_{ls}].[i_{ds2}] + [L_{lm}].[i_{ds1} + i_{ds2}] + [L_m].[\, i_{ds1} + i_{ds2} + i'_{dr}] \quad (10)$$

$$[\chi'_{qr}] = [L'_{lr}].[i'_{qr}] + [L_m].[\, i_{qs1} + i_{qs2} + i'_{qr}] \quad (11)$$

$$[\chi'_{dr}] = [L'_{lr}].[i'_{dr}] + [L_m].[\, i_{ds1} + i_{ds2} + i'_{dr}] \quad (12)$$

Where, χ_{qs1}, χ_{qs2} are stator q-axis flux linkage components, χ_{ds1}, χ_{ds2} are stator d-axis flux linkage components, χ'_{qr}, χ'_{dr} are rotor q-axis and d-axis flux linkage components, i_{qs1}, i_{qs2} are stator q-axis current components, i_{ds1}, i_{ds2} are stator d-axis current components, i'_{qr}, i'_{dr} are rotor q-axis and d-axis current components, L_{ls} is stator leakage inductance, L_m is air gap inductance, L_{lm} is stator mutual leakage inductance, L'lr is rotor leakage inductance, þ is (d/dt), ω and ωr are synchronous flux and rotor speed, R_s and R_r are stator and rotor resistances, V_{qs1}, V_{ds1}, V_{qs2}, V_{ds2}, V'_{qr} and V'_{dr} are the stator and rotor q-axis and d-axis voltages respectively. The equivalent circuit of DSIG generator in d-q reference frame is shown in Fig. 2.

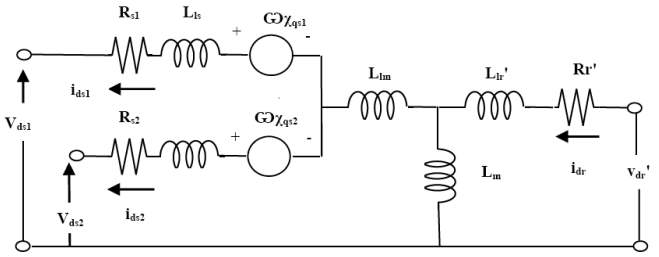


Figure 2 (a): Equivalent circuit in d-axis

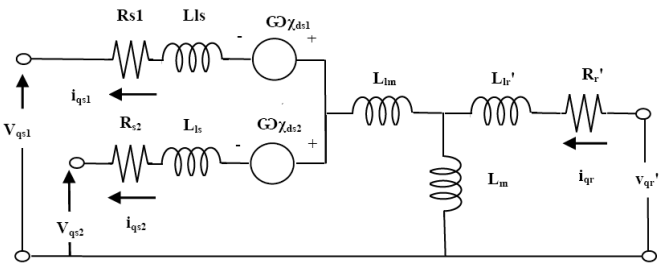


Figure 2 (b): Equivalent circuit in q-axis

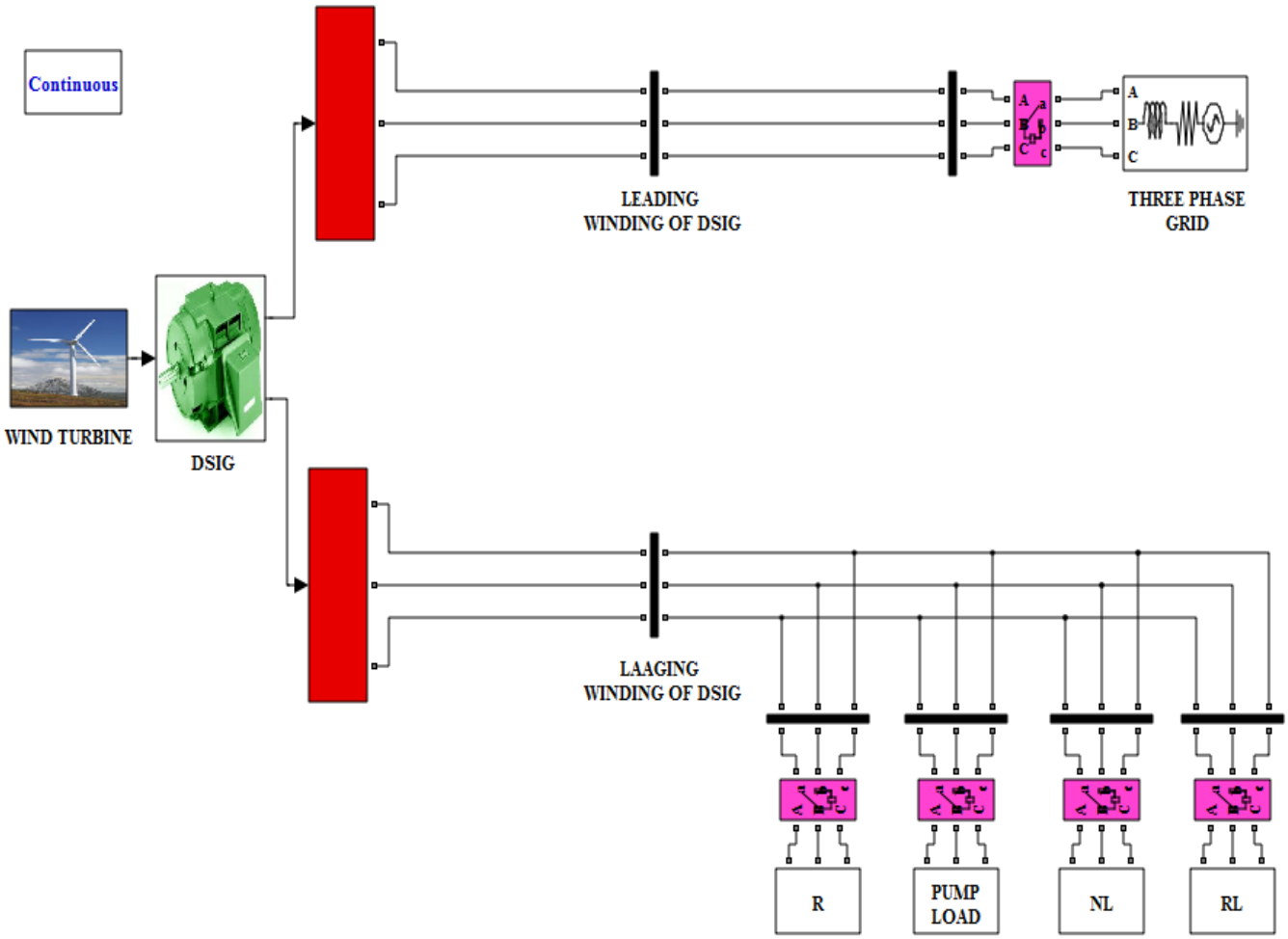


Figure 3: Simulation Diagram of Proposed System

MATLAB MODEL

The considered system is implemented under MATLAB/SIMULINK environment using SimPowerSystem toolbox as shown in Fig. 3. Leading side of DSIG is connected to a weak grid and various loadings are done on lagging side of DSIG. Two three phase stator winding sets act as filter to restrict the proliferation of harmonics to one side of DSIG to the other side of DSIG. Linear resistive load, inductive load, non-linear load and constant power load are applied to lagging side of DSIG and voltage, current; power and harmonic distortion are recorded for furthering the characteristics of DSIG. The details of different loads are given in Table 1.

Table 1: Rating of Different Loads

Type of Load	R	RL	NL	Pump Load
Value of Load	R= 180 Ω	Z= 180 Ω (0.8 pf)	R= 255Ω, C=50μF	1 kW

PERFORMANCE EVALUATION

DSIG connected to grid on leading winding side and variety of loads connected at the lagging wind side is analyzed in this paper. The analysis is done for seven different conditions pertaining to different wind speed and different types of load as shown in Fig.5 and Fig.6. Apart from Fig.5 and Fig.6 which show the voltage, current profile of grid and load side respectively, Fig. 7-10 show the total harmonic distortion (THD) of voltage and current at both sides of DSIG.

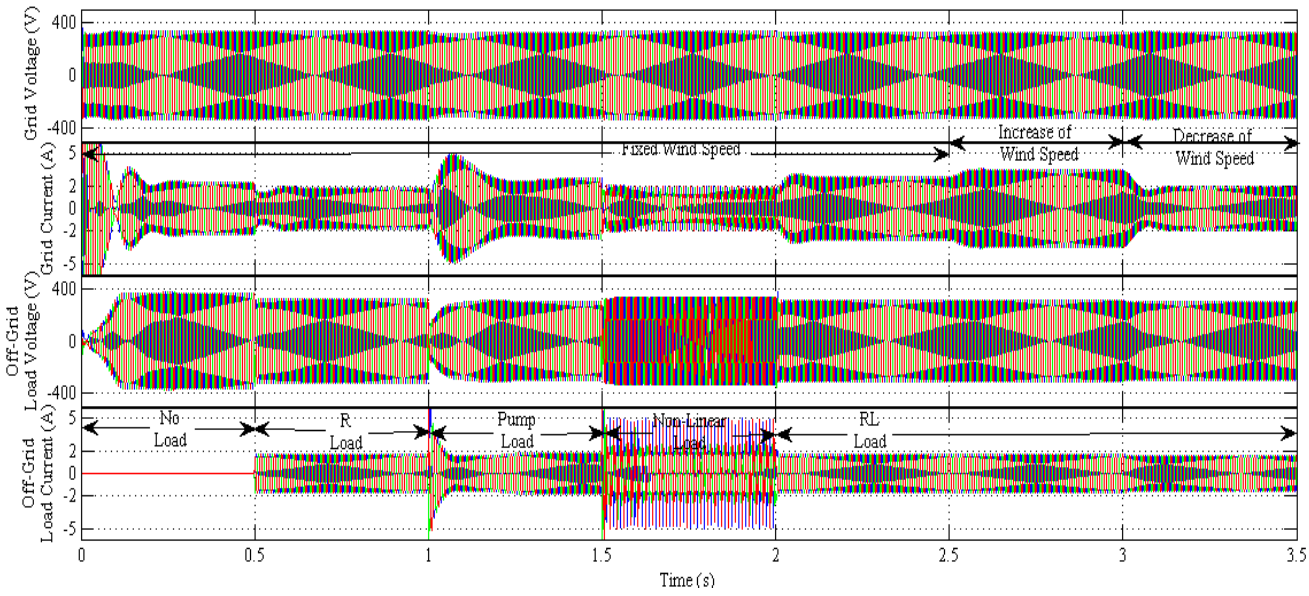


Figure 5: Voltage and Current of Grid and Load connected to both ends of DSIG

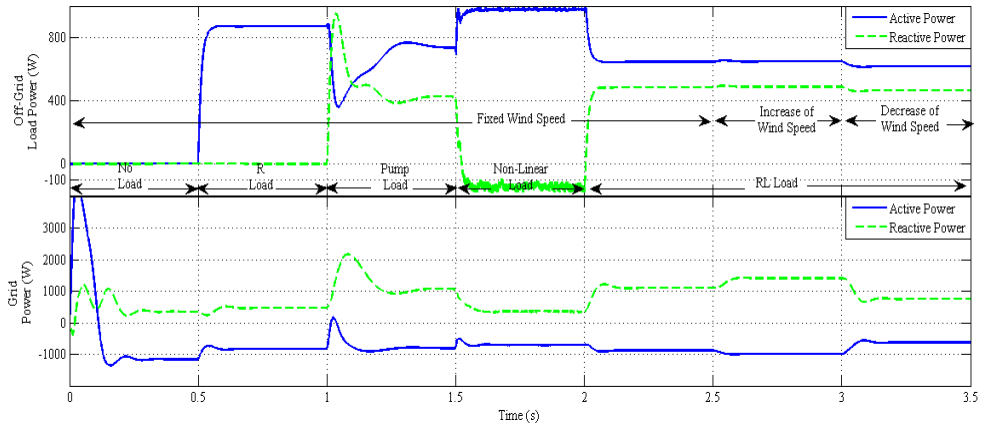


Figure 6: Active and Reactive Power of Grid and Load connected to DSIG

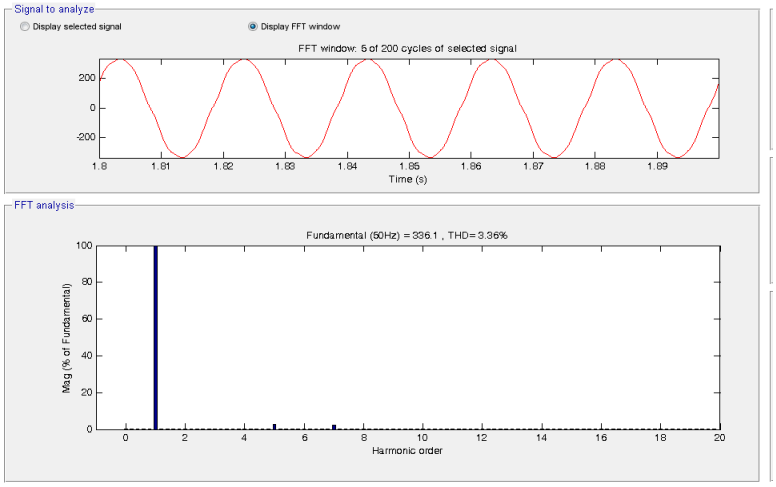


Figure 7: FFT of Grid Voltage when Non Linear Load is connected at off-grid side of DSIG

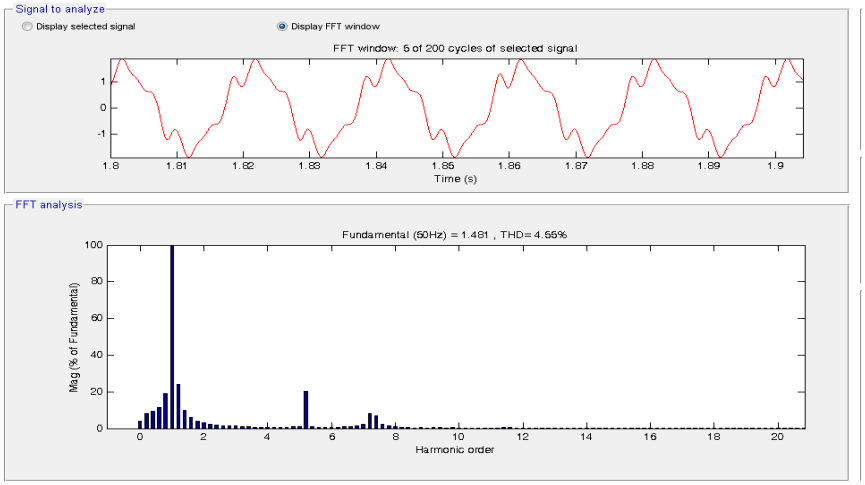


Figure 8: FFT of Grid Current when Non Linear Load is connected at off-grid side of DSIG

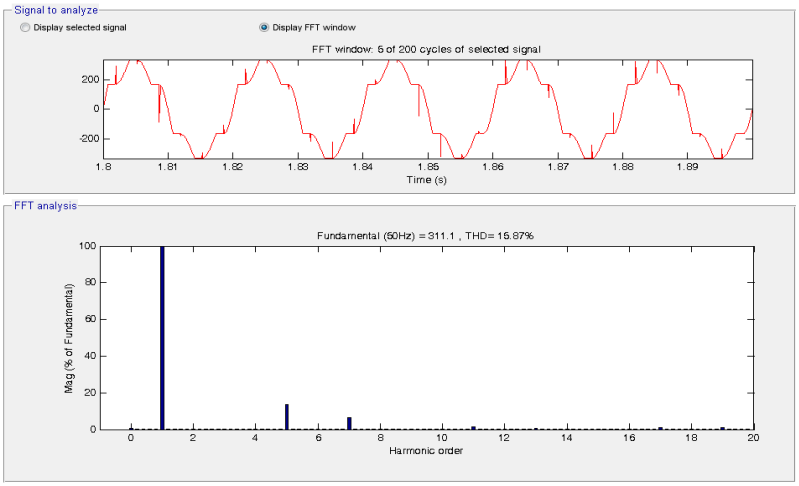


Figure 9: FFT of Load Voltage when Non Linear Load is connected at off grid side of DSIG

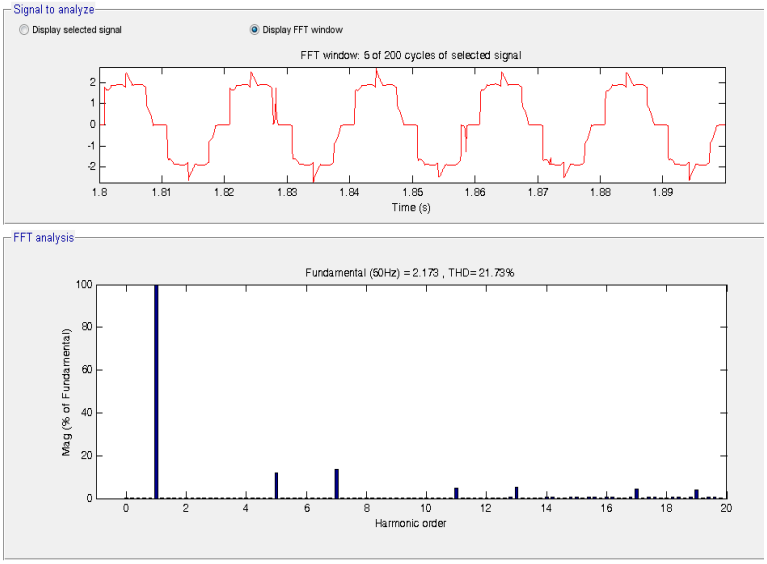


Figure 10: FFT of Load Current when Non Linear Load is connected at off grid side of DSIG

Condition 1: In this condition wind speed is sufficient for enabling the DSIG to generate electrical power and there is no load connected at the lagging winding side. The total active power generated by DSIG is fed to the grid and necessary reactive power is drawn from the grid.

Condition 2: In this condition wind speed remains same as previous and a resistive load of 180 ohms per phase is connected to lagging winding side of DSIG. The total power generated by DSIG is now divided in two portions and after catering to the local load demand the excess active power is fed to the grid. Necessary reactive power is still drawn from grid. Since the load is purely resistive the voltage and current profile are smooth and there is no harmonic distortion at grid side as well as load side.

Condition 3: With the condition of same wind speed driving DSIG and reactive power fed by grid, now the load is changed to pump load of 900 W. There is a dip in off-grid voltage instantaneously but the same recover quickly with no distortion in either voltage or current waveform of either load or grid. The active power left with DSIG after feeding the pump load is fed to grid.

Condition 4: The load is now changed and non-linear loading is applied to DSIG. The load comprises of a diode bridge rectifier feeding to a resistive load with 255 ohm resistance with 50 micro Farad capacitor on its DC bus. Wind speed is same as previous case and requisite reactive power is drawn from grid in this condition also. Due to non-linear load the voltage and current of load get distorted with more than 15 % THD in voltage and 20% THD in current. The winding structure and isolated stator windings of DSIG act as natural filter to restrict the flow of positive sequence harmonics component to the grid side. The FFT analysis of the grid side and off-grid side voltages and currents shown in Fig. 7 -10, depicts that except fifth all other harmonics have been reduced drastically. Table 2 shows the comparative values of THD for voltage and current of both grid and load.

Table 2 Voltage and Current THD with Non Linear Loading

Specification	Voltage THD	Current THD
Grid side	3.36	4.55
Load side (off grid side)	15.87	21.73

Condition 5: Wind speed is again kept constant and change in load condition is made by the application of resistive-inductive load of 0.8 power factor. The change in active and reactive component of power at load side is shown in Fig. 6. There is no distortion in voltage and current at both grid side and load side of DSIG. The remaining generated active power of DSIG after catering to the local load is fed to grid with a demand of necessary reactive power fulfilled by grid.

Condition 6: The loading condition is maintained same as previous one but the wind speed is increased resulting in more generation of active power and more requirement of reactive power by DSIG. Since the load is constant the excess power is fed to the grid, and the grid supplies the increased reactive power demanded for this condition due to increased voltage limited within the prescribed range.

Condition 7: Lastly the wind speed is decreased from in initial value, which was maintained in first five conditions, which shows that there is a decrease in active power generation and also decreases in reactive power demand raised by the DSIG. Since the generation is still more than the load requirement the remaining active power is fed to grid. The voltage and current waveforms are sinusoidal and there is no waveform distortion.

CONCLUSION

In the present scheme DSIG is connected to grid and when wind speed is good enough, i.e. above synchronous speed power is generated at power frequency as the reactive power is always supplied by grid. So this system always works on power frequency and there is no variation of frequency in the system. The total generated power of DSIG is supplied to off-grid side load and remaining to grid. Varieties of loads are applied and show that grid has a least impact of these loads when connected along with DSIG. This scheme is suitable for all those places where overall wind speed is sufficient for generation, thus it can reduce the loading on the grid. In all the modes of operation reactive power demanded by the DSIG is provided by the grid which can be reduced by using local VAR compensators / capacitor banks at either on one side or both sides of the DSIG.

REFERENCES

[1] Sajjad Tohidi, Hashem Oraee, Mohammad Reza Zolghadri, Shiyi Shao and Peter Tavner, "Analysis and Enhancement of Low-Voltage Ride-Through Capability of Brushless Doubly Fed Induction Generator," *IEEE Trans. Industrial Electronics*, vol. 60, no. 3, March 2013.

[2] Henk Polinder, Frank F. A. van der Pijl, Gert-Jan de Vilder, and Peter J. Tavner, "Comparison of Direct-Drive and Geared Generator Concepts for Wind Turbines," *IEEE Trans. Energy Conversion*,vol. 21, no. 3, pp. 725-73, September 2006.

[3] N. Budisan, O. Prostean, R. Boraci, I. Szeidert and V. Muller, "The Dual Induction Generator for Renewable Energy Conversion Systems. Experimental Results, Problems and Solutions," IEEE International Joint Conferences on Computational Cybernetics and Technical Informatics (ICCC-CONTI 2010), Timisora, Romania, May 27-29, 2010.

[4] Shiyi Shao, Teng Long, Ehsan Abdi and Richard A. McMahon, " Dynamic Control of the Brushless Doubly Fed Induction Generator Under Unbalanced Operation," *IEEE Trans. Industrial Electronics*, vol. 60, no. 6, June 2013.

[5] Roberto Cárdenas, Rubén Peña, Salvador Alepuz and Greg Asher, "Overview of Control Systems for the Operation of DFIGs in Wind Energy Applications," *IEEE Trans. Industrial Electronics*, vol. 60, no. 7, July 2013.

[6] Teng Long, Shiyi Shao, Paul Malliband, Ehsan Abdi and Richard A. McMahon, "Crowbarless Fault Ride-Through of the Brushless Doubly Fed Induction Generator in a Wind Turbine Under Symmetrical Voltage Dips," *IEEE Trans. Industrial Electronics*, vol. 60, no. 7, July 2013.

[7] R.Boraci, M.Babescu, N.Budisan, A.R.Boraci, "Mathematical Model of The Two Orthogonal Three-Phase Windings Stator Generator," 5th International Symposium on Applied Computational Intelligence and Informatics, Timişoara, Romania, May 28–29, 2009.

[8] Kostyantyn Protsenko and Dewei Xu, " Modeling and Control of Brushless Doubly-Fed Induction Generators in Wind Energy Applications," *IEEE Trans.Power Electronics,* vol. 23, no. 3, May 2008.

[9] Feifei Bu, Yuwen Hu, Wenxin Huang, Shenglun Zhuang, and Kai Shi, "Control Strategy and Dynamic Performance of Dual Stator-Winding Induction Generator Variable Frequency AC Generating System With Inductive and Capacitive Loads," *IEEE Trans.Power Electronics*, vol. 29, no. 4, pp. 1681- 1692, April 2014.

Int J Syst Assur Eng Manag
DOI 10.1007/s13198-017-0665-x

ORIGINAL ARTICLE

Dynamic frequency based parallel k-bat algorithm for massive data clustering (DFBPKBA)

Ashish Kumar Tripathi[1] · **Kapil Sharma**[1] · **Manju Bala**[2]

Received: 22 March 2017 / Revised: 12 June 2017
© The Society for Reliability Engineering, Quality and Operations Management (SREQOM), India and The Division of Operation and Maintenance, Lulea University of Technology, Sweden 2017

Abstract In the past one decade there has been significant increase in the growth of digital data. Therefore, good data mining techniques are important for the better decision making. Clustering is one of the key element in the field of data mining. K-means is a very popular algorithm present in the literature which is widely used for the clustering purpose. However k-means algorithm suffers from the problem of stucking into local optimum solution because of it's dependency on the random initialization of initial cluster center. In this paper a novel variant of Bat algorithm based on dynamic frequency is introduced. Further the proposed variant is hybridized with K-means to present a new approach for clustering in distributed environment. Since evolutionary computation is very computation intensive, traditional sequential algorithms are not able to provide satisfactory results within the reasonable amount of time for the large scale data problems. To mitigate this problem the proposed variant is parallelized using the MapReduce model in the Hadoop framework. The experimental results show that the proposed algorithm has outperformed K-means, PSO and Bat algorithm on eighty percent of the benchmark datasets in terms of intra-cluster distance. Further DBPKBA has also achieved significant speedup for dealing with massive datasets with increase in the number of nodes.

Keywords Bat algorithm · Hadoop · MapReduce · Large data sets · DFBPKBA

1 Introduction

With the progress of technology there has been a significant increase in the growth of the digital data. Data mining techniques have automated the task of deriving the meaningful conclusions from large datasets in a short time frame. Clustering is one of the popular data mining technique that groups data items in multiple clusters with maximum intra-cluster similarity and minimum inter-cluster similarity (Lin et al. 2004) . Data clustering is widely used in the many domains like image segmentation, data mining, bio-medical and information retrieval (Fayyad et al. 2002). The traditional clustering algorithms are failing with the increasing size of the data. Therefore, improvement in the traditional sequential computational model is required to cluster massive data sets in reasonable amount of time.

K-means is a popular and simple clustering algorithm used in the various clustering applications (Xu and Wunsch 2005). However, k-means algorithm suffers from the following problems:

- The quality of clusters in k-means algorithm is highly sensitive towards the initial cluster center values.
- There is no information sharing because of which this algorithm easily falls into the local optimum solution.

To overcome these problems, many researchers now a days are using nature inspired algorithms with k-means for the clustering purpose. This hybridization of k-means have shown ability to find the global best solution (Hatamlou

✉ Kapil Sharma
kapil@ieee.org

Ashish Kumar Tripathi
mail2ashish07@gmail.com

[1] Delhi Technological University, Delhi, India

[2] IP College of Women, Delhi, India

Published online: 06 September 2017

et al. 2012) and avoided the problem of trapping into local optima. Although these nature inspired algorithms have overcome the shortcoming of k-means algorithm but still not preferred for clustering massive datasets due to their computation intensiveness. Parallelization of the these algorithms is one of the promising solution to handle the large scale data. So, various distributed computing platforms such as cuda, gpu and Hadoop (Gong et al. 2015) are used to reduce the computational cost.

Gong et al. (2015) surveyed and compared different distributed models used in parallelization of nature inspired algorithms for handling large datasets. Among all studied models, hadoop map reduce architecture is one of the popular platform because of its simplicity scalability and robustness. It was concluded that parallelization with Master-Slave model of the Hadoop with MapReduce architecture has the highest fault tolerance and implementation simplicity while CUDA based model is difficult and less fault tolerant but have better execution time. Hadoop is an open source software developed by apache foundation which works on the MapReduce programming architecture that provides parallel computing environment on Hadoop distributed file system termed as HDFS (Frontpage 2016). MapReduce architecture works by dividing the data set into small blocks and send it to the map function running on various nodes. The map function calculate the distance of data point and decides that to which cluster the particular data point will belong. Reduce function then combines the Map function results from the various machines to calculate the final cluster center location.

This paper presents a novel algorithm for the efficient and fast clustering of large scale data using bat algorithm on Map-reduce architecture, namely dynamic frequency based parallel kbat algorithm (DFBPKBA).The proposed DFBPKBA algorithm is incorporated with the following capabilities.

- k means is used to initialize the cluster center to make convergence faster.
- Frequency tuning of the original Bat algorithm is modified to enhance the poor capability of exploitation and exploration of the of the Bat algorithm.
- The proposed Hybrid algorithm is parallelized using the MapReduce architecture to accelerate the speed of computation and reduce the computation time and find better results for the massive data sets.

The proposed algorithm leverages the strength of k-means by proposing a new variant of bat algorithm with the MapReduce programming model. This improved the clustering results in terms of and speed and quality of clusters generated. DFBPKBA has comparatively better exploration and exploitation capability than standard bat algorithm by modifying the frequency parameter. Rest of the paper is described as follows: Sect. 2 describes the work done in the field parallel clustering, Sect. 3 gives the background study of the clustering and k-means algorithm, Sect. 4 describes the proposed (DFBPKBA). The experimental settings and the results of the proposed approach are discussed in Sect. 5.

2 Related work

In this section various meta-heuristic algorithms used for the clustering purpose are discussed along with their parallelization on the MapReduce platform. Hadoop and MapReduce model have been widely used by a number of researchers for parallelization and solving computational intensive tasks (Khezr and Navimipour 2015; Wang et al. 2012). Paper (Khezr and Navimipour 2015) have given a survey of the MapReduce based parallel optimization algorithm. It was concluded in the paper that the MapReduce platform is being widely used now a days for the fast processing of the complex problems.

Paper (Wang et al. 2012) proposed k-PSO algorithm which combined Particle Swarm Optimization (PSO) with K-means using MapReduce. The proposed k-PSO made k-means parallel with MapReduce architecture for enhancing the possessing of massive data and improved global search with PSO. XY pang et al. proposed parallel genetic algorithm using the MapReduce architecture (Verma et al. 2009). In the proposed algorithm, population initialization and fitness calculation was done inside the Mapper. Each segment of chromosome was assumed to be the center of the cluster. In the second phase the reducer forms a new chromosome by joining the results received from the mapper. Process is repeated until all the centers of the chromosomes have not achieved the maximum inter cluster distance. Final chromosome contains the location of the optimal clusters.

Bhavani et al. (2011) proposed hybrid of k-means, differential evolution (DE) and ant colony optimization(ACO) using MapReduce architecture to identify species from their genome sequence. Feature descriptors for a genome sequence are identified using MapReduce architecture. Each feature descriptor is a three letter keyword, generated using A, T, C, G nucleotide bases. Genome sequences of related species are clustered by considering the feature descriptor count. It has been concluded that the inherent parallelism in the MapReduce model enhanced the execution time.

Aljarah and Ludwig (2013) used the MapReduce architecture for parallelization of particle swarm optimization and perform intrusion detection. Parallel architecture of the particle swarm optimization was able to handle and analyze high traffic data easily.

Nguyen et al. proposed a multi-objective firefly algorithm to solve the localization issues in WSN_s. The proposed approach improved the convergence rate and accuracy of the localization issues in the wireless sensor networks (Nguyen et al. 2016). Jagdish Chand Bansal et al. proposed spider monkey optimization algorithm for numerical optimization which mimics the foraging behavior of spider monkeys. The proposed algorithm was found to be competitive with PSO, DE, ABC and CMA-ES in terms of reliability, accuracy and efficiency (Bansal et al. 2014).

Tsai et al. proposed a variant of the original bat algorithm which was able to make a proper balance between exploration and exploitation. The proposed approach was tested on three bench mark functions with ten, thirty, fifty and hundred dimensions and it was concluded that new variant is able to enhance forty seven percent accuracy of the original bat algorithm (Tsai et al. 2016). The accuracy of the Evolved Bat algorithm was also improved in paper (Tsai et al. 2015; Cai and Tsai 2016). Kavita Sharma et al. developed a Fitness based particle swarm optimization to improve the slow convergence rate and stagnation in the local optima of the original PSO algorithm by incorporating a new position updating phase. The new phase was inspired from the onlooker phase of the Artificial Bee Colony algorithm. The proposed algorithm has outperformed original particle swarm optimization and artificial bee colony optimization in terms of mean fitness and convergence rate (Sharma et al. 2015).

Shimpi Singh Jadon et al. in their paper (Jadon et al. 2014) improved the problem of poor exploitation and slow convergence rate of Artificial Bee Colony Optimization. The proposed algorithm was compared with original ABC along with Best-So-Far ABC, Gbest guided, ABC, and Modified ABC on twenty four benchmark datasets. The proposed algorithm reduced up to half number of functions evaluations as compared to the original algorithm.

Jansen et al. (2009) investigated clustering of 150,000 microblog posts containing comments and sentiments regarding different brands and showed that microbiology can be a tool for marketing decisions. Ma et al. (2016) proposed a model based on neural network for identifying rumors in the large data sets like microblog.

B. Wu et al proposed MapReduced based ant colony optimization for solving combinatorial optimization problems (Wu et al. 2012) whereas paper (Xu et al. 2014; Lin et al. 2013) used MapReduce architecture for the parallelization of cuckoo search and concluded that MapReduce architecture is efficient for solving computation intensive problems. Paper (Moertini and Venica 2016) presented a parallel k-means algorithm for discovering knowledge from big data. The author showed that parallel k-means algorithm using MapReduce architecture can perform mining of big data in reasonable time.

In del Río et al. (2014), authors analyzed the techniques used for imbalanced big data processing using Random forest classifier.The problem of oversampling, under sampling and cost sensitive learning was adopted using MapReduce to handle the large data sets and to correctly identify the unrepresented class. It has been observed that the performance increases with increase in the number of mappers.

Meena et al. (2012) developed an enhanced parallel Ant Colony Optimization algorithm for text feature selection problem. However, the increased time complexity of the proposed algorithm was reduced by parallelizing with MapReduce architecture.

You et al. (2014) in their work proposed a parallel support vector machine (SVM) model for the prediction of large scale protein-protein interactions (PPI). Since the process of finding protein-protein interaction is computation intensive and complex, author employed the MapReduce based parallel architecture for training the SVM.This work achieved significant improvement in the training time and a good level of accuracy in predicting the PPI.

3 Background

3.1 Bat algorithm

The basic inspiration behind the bat algorithm is the echolocation behavior of the Micro-bats (Yang and He 2013). Microbats have ability to find their prey even in the darkness by using their echolocation behavior. Microbats emit sound pulses of different properties as per their hunting strategies and waits for emitted echo to bounced back from the surrounding objects (Yang 2010; Yang and He 2013). In bat algorithm, every bat at position X_i flies randomly in the search space to find the prey. The velocity V_i of bat is determined by fixed frequency f_i and loudness A_0. The loudness is assumed to vary from a large positive A_0 to a minimum constant value A_min. However, the wavelength and rate of pulse emission is adjusted automatically depending upon the distance from the prey. Bat algorithm makes a balance between exploration and exploitation through two parameters, i.e. frequency and emission rate. The frequency of ith bat is determined by Eq. (1)

$$freq_i = freq_{min} + (freq_{max} - freq_{min}) \times rand \quad (1)$$

$$vel_i^t = vel_i^{t-1} + (pos_i^{(t-1)} - pos^*) \times freq_i \quad (2)$$

$$pos_i^t = pos_i^{(t-1)} + vel_i^t \quad (3)$$

Here, x^* is the current global best solution among all the bats. The new equation of local search around the best is as follows:

$$pos_{new} = pos^{*} + \epsilon * 0.001 \tag{4}$$

Here, ϵ is a random number in the range $[-1, 1]$. Also, the average of loudness of bats has been skipped and instead the factor 0.001 has been used to multiply to the best solution. This has been done because searching for best solution should be done as close to the best value as possible. This is the base of exploitation. The equations for update of loudness and pulse rate are:

$$L_i^{t+1} = \alpha * L_i^t \tag{5}$$

$$rate_i^{t+1} = rate_0(1 - e^{-\gamma * t}) \tag{6}$$

In these equations, α is taken as 0.9 and λ is taken as 0.001 so that better exploitation can be done. Compared with the existing meta-heuristics, the bat algorithm has the advantage of dynamic control of exploitation and exploration by performing a local search around the best solution. When a random number generated becomes greater than the pulse rate value, the algorithm switches to exploitation around the best solution. But this structure of exploration and exploitation is not balanced as it should be. At the beginning of the algorithm, first exploitation is done and then exploration but it should be the other way round.

3.2 Clustering approach

Let $O = (o_1, o_2, o_3, \ldots, o_n)$ be a set of n data points where each data point is described by d features. These data points can be represented by a matrix of $O_{n \times d}$ that has n row vectors, where each row vector of d dimensions represents a particular data point. So, the ith row vector i.e $O_i = (o_i^1, o_i^2, o_i^3, \ldots, o_i^d)$ represents the ith data point of the data set, and each element o_i^j in O_i is scalar denoting the jth feature of the corresponding data point. The goal of a clustering algorithm is to find a set of cluster centers, $C = \{C_1, C_2, \ldots, C_k\}$ of k groups such that the data points belonging to the same cluster have maximum similarity, while the data points belonging to the different group have minimum similarity. The resulting group of data points is called clusters and should have the following properties:

- Every cluster should contain at least one data point, i.e . $C_i \neq \phi \forall i \in \{1, 2, 3, \ldots, k\}$
- Each data point must belong to a cluster i.e $U_{i=1}^{k} C_i = O$
- No data point should belong to more than one cluster i.e. $C_i = \phi, \forall i \neq$ and $i, j \in \{1, 2, 3, \ldots, k\}$.

A dataset is clustered when the above conditions get satisfied but quality clustering is done when clusters satisfy the fitness condition. The most widely used fitness condition to specify the quality of the clustering (Yang et al. 2010) is the total mean square quantization error(MSE) which is defined by Eq. (7).

$$f(O, C) = \sum_{l=1}^{k} \sum_{O_i \epsilon C_l} d(O_i, Z_l)^2 \tag{7}$$

where $d(o_i, z_l)$ is the measure of dissimilarity between the data point o_i and centroid of the cluster $c_l(z_l)$ which is the mean value of the data points belonging to the respective cluster. Dissimilarity between the clusters is calculated by different distance metric. The most common distance metric for calculating the dissimilarity is the Euclidean distance which is defined by Eq. (8).

$$(X_i, X_j) = \sqrt{\sum_{p=1}^{d} (x_i^p - x_i^p)^2} \tag{8}$$

3.3 k-mean algorithm

k-mean algorithm (Jain 2010; Forgy 1965; Kaufman and Rousseeuw 2009) is one of the popular clustering algorithm present in the literature that has been widely applied to many applications. It starts with random cluster centroids and then each data point is assigned to closest cluster based on its distance from the centroids. Centroids are updated with iterations by calculating the mean of the data points belonging to a particular cluster. Algorithm terminates either after completing the maximum number of iterations or the same cluster centroids repeat.

4 Proposed approach

In this section the proposed variant of the Bat algorithm along with its hybridization with k-means algorithm has been explained. The idea of the proposed DFBPKBA is to use the strength of bat algorithm for obtaining the global best solution and k-means algorithm for better population initialization. The clustering process of the proposed algorithm has been explained in the Sect. 4.1. Section 4.2 contains the parallelization of the proposed approach for the clustering using the hadoop and MapReduce.

4.1 Dynamic frequency based k-bat clustering

In the proposed DFBPKBA, two main operations are employed for performing the clustering task on large data sets. The first is, evaluation of the fitness value in the form of sum of square of mean Euclidean distance between each data object and centroid of the cluster. Secondly the cluster centroids are updated using the original bat algorithm described in Sect. 3.1 with dynamic frequency. The $freq_{max}$ parameter of the original bat algorithm is fix while the proposed DFBPKBA uses dynamic $freq_{max}$ value ,which

keep on decreasing with iterations using Eq. (5) that makes a good initial exploration followed by the exploitation. The fitness of each bat is calculated using the Eq. (8). The goal is to minimize the fitness value of each bat i.e sum of mean Euclidean distance. Further the quality of the clusters and convergence speed of the dynamic frequency based Bat algorithm has been enhanced by incorporating k-means algorithm. It is important to create a good initial population because the performance of the Bat algorithm and most of the meta-heuristic algorithm is much effected by the initial population.

$$freq_{max}(i) = (freq_{max} - itr_i * (freq_{max}/maxit)) \quad (9)$$

In Eq. (9) $freq_{max}$ is the initial maximum frequency, $freq_{max}(i)$ is the current maximum frequency, itr_i is the current iteration number and *maxit* is the maximum number of iterations for which the algorithm is run. The clustering process using the dynamic frequency based bat algorithm is based on the three main steps.

In the first step, ten iterations of k-means algorithm is applied to the dataset to get some nearby solution and also to avoid local optima. In the second step the population is initialized by the centroids produced by the ten iterations of the k-means algorithm. In the third step each data point is assigned a cluster using dynamic frequency based bat algorithm. The candidate solution in the proposed algorithm is represented by the one dimensional array to encode the centroids of the cluster centers. The size of the array is a*k where a is the number of the attributes of the data set and k is the number of predefined cluster. Let us consider $Pi = \{C_1, C_2, C_3 \ldots C_k\}$ as the i_{th} candidate solution, then $C_j = \{C_j^1, C_j^2, C_j^3, C_j^a\}$ is the Jth cluster centroid of the Ith candidate solution $(i = 1, 2, 3 \ldots N)$ and $j(1, 2, 3 \ldots a)$. N is the number of candidate solution or the population size of the algorithm. Table 1 contains population size taken for performing the clustering using the proposed DFBPKBA along with the other parameter values.

Table 1 Parameter values

Parameter name	BAT	PSO	DFBPKBA
Population size (pop)	40	40	40
$freq_{min}$	0	–	0
$freq_{max}$	10	–	10
alpha	0.9	–	.9
gamma	0.01	–	0.01
r0	0.5	–	0.5
Inertia weight	–	0.5	–
C1	–	0.5	–
C2	–	0.5	–

4.2 Parallelization of the proposed algorithm using MapReduce architecture

For the parallel processing to handle large scale data we have used Hadoop MapReduce model. Hadoop Shvachko et al. (2010) is an open source platform for distributed processing of large scale data sets. Hadoop works on the principle of distributing the large amount of work among the various machines to achieve speedup. The main reason for its popularity is its efficient task scheduling, concurrency control, robustness, scalability, and node failure recovery. MapReduce (Dean and Ghemawat 2008) is a parallel processing paradigm which have capability to process large scale data on the cluster of commodity hardware. In this programming model the large data set is broken into smaller chunks and distributed among various machines. Each machine have some part of the original data upon which map reduce job is rum independently. MapReduce framework process the data in the form of key, value pair. The whole work is done in two phases namely Map and Reduce phase. Map function is invoked for each input key,value pair and it generates intermediate output in the form of key,value. In the second phase reduce function is called for each key,value pair which was generated by the mappers of the first phase.The reduce function processes the key,value pair and produces the final output. For the clustering of large scale data set the main computation intensive task is to compute the fitness function since it involves visiting of each data object. Since in the MapReduce based approach each machine have a smaller part of the data so parallelism is achieved resulting in fast processing. Such approach becomes more important for the huge size data but when the data size is less, in such cases speedup may be reduced because of the hidden input output cost. As a whole, the procedure of DFBPKBA is described in Fig. 1.

4.2.1 Mapper

The job of each mapper is to calculate the distance from each data object from each cluster center. Thus map function finds the distance of data object from each centroid and compares those distances for one agent and one data point. After the calculation of the minimum distance of a data point from the centroids of the cluster, the mapper emits the batID and the computed minimum distance value as an output. Map process is thus used to compute the fitness of each bat. So the input to the mapper will be the data object and output will be the sum of the minimum distances of the data objects from the centroid. The map function is shown in Algorithm 1.

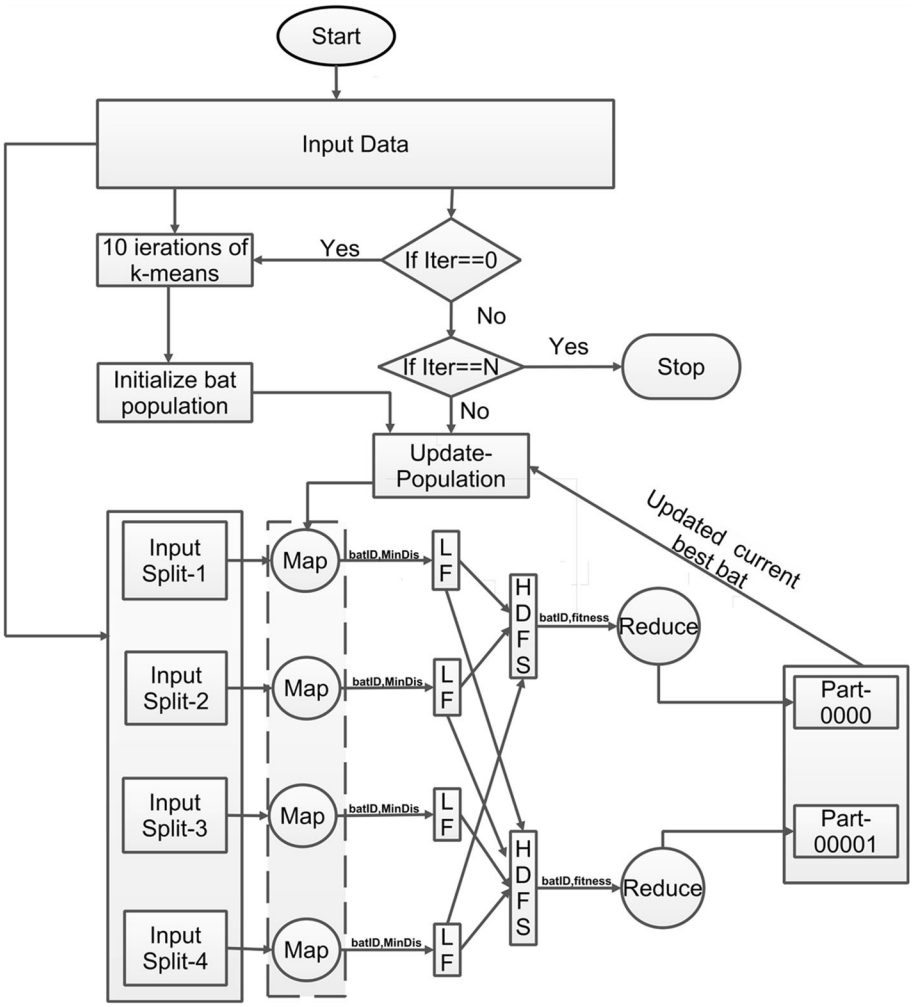


Fig. 1 The procedure of DFBPKBA based on MapReduce

Algorithm 1 Map Function

Input: $Key - data, Value - Dataobject.$
Output: .Key-BatId, Value-Minimum distance
Map (Key : dataId, Value : data)
Bat-list = read (file);
For each bat;
$Minimun - distance$= getMinDistance (bat, data);
$Min - Distance$=$Minimun - distance + centroid - index$
write (badID, Min-Distance);

4.2.2 Reduce

Reduce function starts with retrieving the batID and its fitness value i.e Min-Distance that is produced by the Map phase. The output key, value pair produced by the Map phase are sorted and grouped by key by the Hadoop. In our module bat-id is the key, therefore the values with the same batID will be grouped together. Finally the reducer will club the outputs got from the various mappers and emits the key with sum of mean squared Euclidean distance as value. The sum of mean squared Euclidean distance as value is the total intra-cluster distance that we aim to minimize. The pseudo code of this reducer module is given in Algorithm 2.

Algorithm 2 Reduce Function

Input: $Key - batId, Value - Min - Distance$
Output: .Key-Bat, Value-bat fitness
Reduce (Key: batID, Value: Min)
For each dist in Min-distance list
fitness=fitness+dist
if $(newfitness > oldfitness)$
$updateoldfitness = newfitness$
update position vector
decrease loudness
increase pulse rate
writeToFile (batID, fitness)

After mappers and reducers have finished working, the combine module is used to find the best bat. After getting the best bat, the population is updated in the driver code for the next iteration.

Table 2 Simulation results for the clustering algorithm

Dataset name	Criteria	K-means	PSO	BAT	DFBPKBA
Iris	Best	97.5674	96.9087	104.786	**96.5555**
	Average	105.129	98.8976	118.9807	**96.6767**
Glass	Best	214.5467	223.7685	341.3211	**198.8769**
	Average	227.9778	230.49328	380.9874	**201.7654**
Wine	Best	16,566.77	**16,304.48**	16,768.66	16,396.03
	Average	16,963.05	**16,316.27**	17,094.89	16,461.38
Magic	Best	1,650,422.68	1,659,260.50	2,205,689.82	**1,645,851.75**
	Average	1,660,311.11	1,659,210.50	2,635,125.55	**1,647,410.30**
Pokerhand	Best	6,652,657.44	6,750,253.48	6,675,069.58	**6,031,523.30**
	Average	6,669,935.77	6,887,355.11	6,698,433.00	**6,055,335.71**

The results (best and average) are represented in bold font

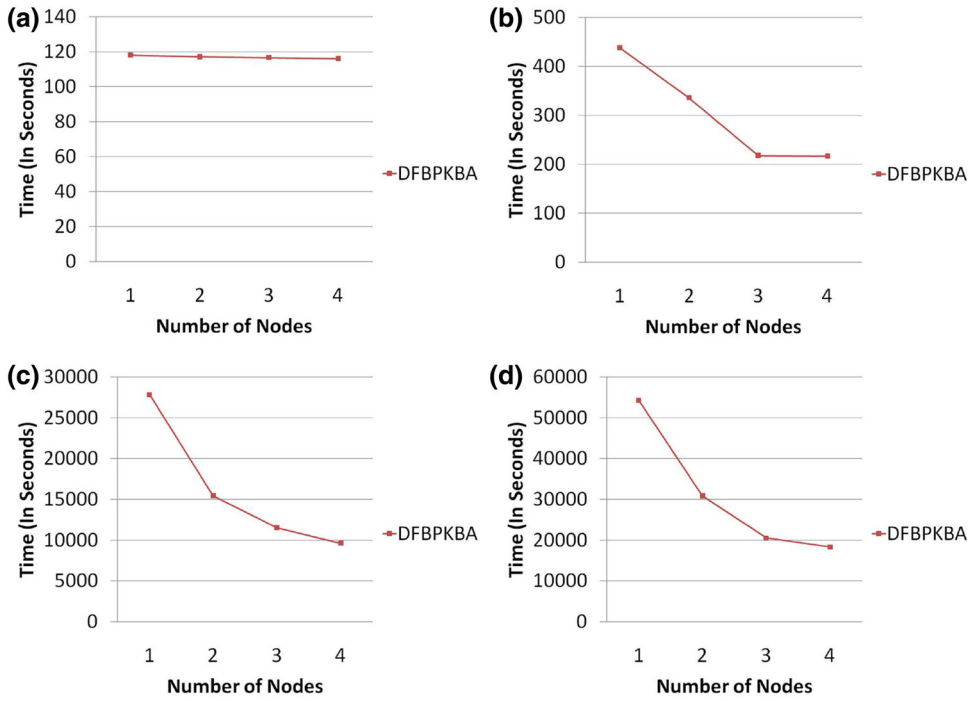


Fig. 2 The speedup graph of **a** wine **b** magic **c** Pokerhand **d** replicated wine

5 Experimental results

The proposed algorithm is tested on five benchmark datasets and compared with three algorithms, namely k-mean, particle swarm optimization (PSO) based clustering and original bat clustering. For the fair comparison, all the algorithms were run with 500 iterations and parameters setting of each algorithm is given in the Table 1. The performance of the proposed algorithms have been evaluated in terms of clustering quality and speedup. The DFBPKA is run on the cluster of 4 nodes having Intel Corei5-4570 processors with processing 3.20 GHz 4.32-bit configuration, Ubuntu 14.04 with Hadoop version 2.7.2. of replication value as 3. All the machines have the same configurations and same version of the Hadoop. The benchmark datasets are taken from UCI machine learning repository (Blake and Merz 1998). All these datasets are widely used to validate the efficiency of the algorithms for clustering.

5.1 Cluster quality

The cluster quality is measured with two parameters i.e best and average intra-cluster distance (Jain 2010; Hatamlou et al. 2012). Each algorithm is run thirty time on all the datasets. Table 2 contains the best and average intra-cluster distance of five datasets over thirty runs. It can be observed from the Table 2 that the proposed DFBPKBA has outperformed K-Means, PSO, BAT algorithm on the four datasets out of five in the terms of mean and average

Table 3 Speedup of the proposed algorithm on various data sets

Dataset name	No of records	Speedup on 2 nodes	Speedup on 3 nodes	Speedup on 4 nodes
Wine	178	1.008547009	1.012875536	1.017241379
Magic	19,020	1.305125149	2.011019284	2.023094688
PokerHand	1,000,000	1.800334185	2.41022842	2.887202766
Replicated wine	1,780,000	1.757780133	2.637304901	2.95502798

intra-cluster value. However for one data i.e Wine PSO has outperformed other algorithm for the mean and average value of intra-cluster distance.

5.2 Speedup test

The speedup of the proposed algorithm is tested on different sizes of the datasets. Two small size datasets are considered namely, Wine and Magic and two large size data sets are taken namely, Pokerhand and replicated wine which is made by replicating each record of the wine several time. In the experiment, the speedup of algorithm is calculated by Eq. (10).

$$Speedup = T_{base}/T_N \tag{10}$$

where T_{base} and T_N are the running time chosen as the baseline for the comparison and the running time of the system with N number of nodes, respectively. It is validated from the Fig. 2 that the proposed algorithm achieved good speedup on large scale data sets. It can also be depicted from the Fig. 2b–d that the running time of the DFBPKA decreases almost linearly with increasing number of nodes. However as we can see from the Fig. 2a that for the smaller data sets, the speedup performance is dropped because of the hidden input output cost. Table 3 shows the data sets taken and the corresponding speedup achieved by the proposed algorithm.

6 Conclusion

In this paper, a novel dynamic frequency based parallel bat algorithm (DFBPKBA), is proposed. The proposed algorithm takes the advantage of the bat algorithm to achieve global optimal solution and MapReduce architecture to handle large scale datasets. The DFBPKBA changes the max frequency parameter of original bat algorithm at each iteration to leverage the exploration at the starting stage followed by the exploitation at the later stage. The results shows that the proposed algorithm has outperformed PSO, k-means and Bat algorithm in the terms of quality of the clustering. The speedup performance results show that the DFBPKBA algorithm is able to handle large scale datasets efficiently in reasonable amount of time. We can conclude that the proposed DFBPKBA algorithm can serve as an useful alternative for clustering massive scale datasets. The future work includes the applicability of the proposed algorithm on real-world datasets of different domains like image or video.

References

Aljarah I, Ludwig SA (2013) Towards a scalable intrusion detection system based on parallel pso clustering using mapreduce. In: Proceedings of the 15th annual conference companion on Genetic and evolutionary computation, ACM, pp 169–170

Bansal JC, Sharma H, Jadon SS, Clerc M (2014) Spider monkey optimization algorithm for numerical optimization. Memet Comput 6(1):31–47

Bhavani R, Sadasivam GS, Kumaran R (2011) A novel parallel hybrid k-means-de-aco clustering approach for genomic clustering using mapreduce. In: 2011 world congress on information and communication technologies (WICT), IEEE, pp 132–137

Blake C, Merz CJ (1998) UCI repository of machine learning databases. Department of Information and Computer Science, Irvine

Cai S-J, Tsai P-W (2016) Echolocation guided evolved bat algorithm. J Inf Hiding Multimed Signal Process 7(1):153–162

Dean J, Ghemawat S (2008) Mapreduce: simplified data processing on large clusters. Commun ACM 51(1):107–113

del Río S, López V, Benítez JM, Herrera F (2014) On the use of mapreduce for imbalanced big data using random forest. Inf Sci 285:112–137

Fayyad UM, Wierse A, Grinstein GG (2002) Information visualization in data mining and knowledge discovery. Morgan Kaufmann, Burlington

Forgy EW (1965) Cluster analysis of multivariate data: efficiency versus interpretability of classifications. Biometrics 21:768–769

Frontpage–hadoop wiki. http://wiki.apache.org/hadoop/, (Accessed on 09/17/2016)

Gong Y-J, Chen W-N, Zhan Z-H, Zhang J, Li Y, Zhang Q, Li J-J (2015) Distributed evolutionary algorithms and their models: a survey of the state-of-the-art. Appl Soft Comput 34:286–300

Hatamlou A, Abdullah S, Nezamabadi-Pour H (2012) A combined approach for clustering based on k-means and gravitational search algorithms. Swarm Evolut Comput 6:47–52

Jadon SS, Bansal JC, Tiwari R, Sharma H (2014) Artificial bee colony algorithm with global and local neighborhoods. Int J Syst Assur Eng Manag 1–13

Jain AK (2010) Data clustering: 50 years beyond k-means. Pattern Recogn Lett 31(8):651–666

Jansen BJ, Zhang M, Sobel K, Chowdury A (2009) Twitter power: tweets as electronic word of mouth. J Am Soc Inform Sci Technol 60(11):2169–2188

Kaufman L, Rousseeuw PJ (2009) Finding groups in data: an introduction to cluster analysis. Wiley, New York

Khezr SN, Navimipour NJ (2015) Mapreduce and its application in optimization algorithms: a comprehensive study. Majlesi J Multimed Process 4(3)

Lin K-Y, Xu L-H, Wu J-H (2004) A fast fuzzy c-means clustering for color image segmentation. J Image Gr 2:005

Lin C-Y, Pai Y-M, Tsai K-H, Wen CH-P, Wang L-C (2013) Parallelizing modified cuckoo search on mapreduce architecture. J Electr Sci Technol 11(2):115–123

Ma J, Gao W, Mitra P, Kwon S, Jansen BJ, Wong K-F, Cha M (2016) Detecting rumors from microblogs with recurrent neural networks. In: IJCAI, pp 3818–3824

Meena MJ, Chandran K, Karthik A, Samuel AV (2012) An enhanced aco algorithm to select features for text categorization and its parallelization. Expert Syst Appl 39(5):5861–5871

Moertini VS, Venica L (2016) Enhancing parallel k-means using map reduce for discovering knowledge from big data. In: 2016 IEEE international conference on cloud computing and big data analysis (ICCCBDA), IEEE, pp 81–87

Nguyen T, Pan J, Chu S, Roddick JF, Dao TK (2016) Optimization localization in wireless sensor network based on multi-objective firefly algorithm. J Netw Intell 1(4):130–138

Sharma K, Chhamunya V, Gupta P, Sharma H, Bansal JC (2015) Fitness based particle swarm optimization. Int J Syst Assur Eng Manag 6(3):319–329

Shvachko K, Kuang H, Radia S, Chansler R (2010) The hadoop distributed file system. In: 2010 IEEE 26th symposium on mass storage systems and technologies (MSST). IEEE, 1–10

Tsai P-W, Zhang J, Zhang S, Istanda V, Liao L-C, Pan J-S (2015) Improving swarm intelligence accuracy with cosine functions for evolved bat algorithm. J Inf Hiding Multimed Signal Process 6:1194–1202

Tsai PW, Zhang J, Liu Y, He Y, Zhang S, Pan J-S (2016) Undulating swarm intelligence agents in wave increasing evolved bat algorithm. J Inf Hiding Multimed Signal Process 7(1):21–30

Verma A, Llorà X, Goldberg DE, Campbell RH (2009) Scaling genetic algorithms using mapreduce. In: 2009 ninth international conference on intelligent systems design and applications, IEEE, pp 13–18

Wang J, Yuan D, Jiang M (2012) Parallel k-pso based on mapreduce. In: 2012 IEEE 14th international conference on communication technology (ICCT), IEEE, pp 1203–1208

Wu B, Wu G, Yang M (2012) A mapreduce based ant colony optimization approach to combinatorial optimization problems. In: 2012 eighth international conference on natural computation (ICNC), IEEE, pp 728–732

Xu R, Wunsch D (2005) Survey of clustering algorithms. IEEE Trans Neural Netw 16:645–678

Xu X, Ji Z, Yuan F, Liu X (2014) A novel parallel approach of cuckoo search using mapreduce. In: 2014 international conference on computer, communications and information technology (CCIT 2014), Atlantis Press

Yang X-S (2010) A new metaheuristic bat-inspired algorithm. In: Nature inspired cooperative strategies for optimization (NICSO 2010), Springer, pp 65–74

Yang X-S, He X (2013) Bat algorithm: literature review and applications. Int J Bio-Inspired Comput 5(3):141–149

Yang S, Wu R, Wang M, Jiao L (2010) Evolutionary clustering based vector quantization and spiht coding for image compression. Pattern Recogn Lett 31(13):1773–1780

You Z-H, Yu J-Z, Zhu L, Li S, Wen Z-K (2014) A mapreduce based parallel svm for large-scale predicting protein-protein interactions. Neurocomputing 145:37–43

Electronic Journal of Differential Equations, Vol. 2017 (2017), No. 209, pp. 1–27.
ISSN: 1072-6691. URL: http://ejde.math.txstate.edu or http://ejde.math.unt.edu

DYNAMICS OF A PREY-PREDATOR SYSTEM WITH INFECTION IN PREY

SHASHI KANT, VIVEK KUMAR

Communicated by Zhaosheng Feng

Abstract. This article concerns a prey-predator model with linear functional response. The mathematical model has a system of three nonlinear coupled ordinary differential equations to describe the interaction among the healthy prey, infected prey and predator populations. Model is analyzed in terms of stability. By considering the delay as a bifurcation parameter, the stability of the interior equilibrium point and occurrence of Hopf-bifurcation is studied. By using normal form method, Riesz representation theorem and center manifold theorem, direction of Hopf bifurcation and stability of bifurcated periodic solutions are also obtained. As the real parameters are not available (because it is not a case study). To validate the theoretical formulation, a numerical example is also considered and few simulations are also given.

1. Introduction

The study of prey-predator systems has been a burning topic of research for several years. The pioneer work of Kermack and Mckendrick on Susceptible-Infective-Recovered-Susceptible (SIRS) models [9] have been widely accepted among researchers and scientific community. After the work of Kermack and Mckendrick [9] many mathematical models have been published ([3, 6, 16, 18, 21] etc. and references therein). M. Haque et al [3] proposed and analyzed a predator prey model using standard disease incidence. They observed that the disease in the prey may avoid extinction of predators and its presence can destabilize an otherwise stable configuration of species. In [16], Naji and Mustafa investigated the dynamical nature of an eco-epidemiological model by applying nonlinear disease incidence rate among living species of the ecosystem. They proposed and investigated with regards to local and global dynamical nature of Holling type-II model with Susceptible-Infective type of disease in prey [16]. Jang and Baglama [18] proposed a deterministic continues time ecological model with the effect of parasites, where it is assumed that intermediate host for the parasites are the prey species and observed the dynamics of it. They conclude that parasites are in position to affect the dynamics of the predator prey interaction due to infection. Jang and Baglama [18] have also proposed a stochastic version of the model and simulated

2010 *Mathematics Subject Classification.* 34C23, 34C25, 34C28.
Key words and phrases. Predator-prey model; linear Functional Response; Hopf-bifurcation; stability analysis; time delay.
©2017 Texas State University.
Submitted May 23, 2016. Published September 8, 2017.

the model numerically to verify the theoretical results. They performed asymptotic dynamics and compared the deterministic and stochastic models [18]. Jana and Kar [6] proposed and analyzed a three dimensional eco-epidemiological model consisting of susceptible prey, infected prey and predator. They introduced time delay in the model for considering the time delay as the time taken by a susceptible prey to become infected. Mathematically, they analyzed the dynamics of the model in terms of existence of non-negative equilibria, boundedness, local and global stability of the interior equilibrium point. They also studied Hopf bifurcation and by using central manifold reduction they investigated the direction of Hopf bifurcation and stability of limit cycles. Many mathematical models have been proposed to understand the evolution of diseases and provided valuable information for control strategies ([1, 11, 14, 4] and references therein). Hilker and Schmitz [4] proved that predator infection counteracts the paradox of enrichment. They discussed the implication for the biological control and resource management on more than one trophic level.

Ecology and epidemiology are two different major and important research areas. The basic work of Lotka [13] and Volterra [19] on predator-prey models in the form of coupled system of non-linear differential equations may be considered as the first break through in the modern mathematical ecology. Further, overlapping study of ecology and epidemiology termed as eco-epidemiology. In eco-epidemiology, we study prey-predator models with disease dynamics. Thus, eco-epidemiology may be considered as the study of interacting species in which disease spreads. Eco-epidemiology has very important ecological significance. Population growth models with disease spreading often provide complex non-linear mathematical dynamics. In these models the main concern is to study equilibrium points, their stability analysis, periodic solutions, bifurcations, chaotic nature etc. A large number of mathematical and statistical techniques are available to analyze the eco-epidemiological models.

While formulating a prey-predator model, it is a basic assumption that reproduction of predator species after the event of predation will not be instantaneous, but it will be mediated by some discrete time lag (delay) essential for the gestation of predator population [5]. To study mathematical models in ecology more scientifically, peoples coined a new word 'time delay'. Time delay has been used in large number of papers e.g. ([15, 20] are few name to). Mukhopadhyaya and Bhattacharyya [15] studied the effect of delay on a prey predator model with disease in prey. They have considered Holling type II functional response. Fengyan Wang et al [20] studied a predator prey model by assuming stages viz. mature and immature with both discrete and distributed delays. They considered delay as length of immature stage. For detailed study of delay differential equations we can refer reader to [22].

Chattopadhyay and Arino [2] proposed the following eco-epidemiological model with disease in prey

$$\begin{aligned} \frac{dS}{dt} &= r(S+I)(1-\frac{S+I}{K}) - \beta SI - \eta\gamma_1(S)Y, \\ \frac{dI}{dt} &= \beta SI - \gamma(I)Y - CI, \\ \frac{dY}{dt} &= (\varepsilon\gamma(I) + \eta\varepsilon\gamma_1(S) - d)Y, \end{aligned} \tag{1.1}$$

where, S is the number of sound prey, I is the number of infected prey population, Y is the number of predator population, $\gamma(I)$ and $\eta\gamma_1(S)$ are predator functional response functions. They analyzed the model (1.1) in terms of positivity, uniqueness, boundedness and the study the existence of the Hopf bifurcation. Model (1.1) may be re-written in simplified form as

$$\begin{aligned} \frac{dS}{dt} &= rS(1-\frac{S+I}{K}) - \beta SI, \\ \frac{dI}{dt} &= -cI + \beta SI - pIY, \\ \frac{dY}{dt} &= -dY + pqIY. \end{aligned} \tag{1.2}$$

Motivated by model (1.1), Samanta[17] proposed a diseased nonautonomous predator-prey system with time delay, which is given as

$$\begin{aligned} \frac{dx_1(t)}{dt} &= x_1(t)[r(t) - k_1(t)(x_1(t)+x_2(t)) - a_1(t)x_3(t) - \beta(t)x_2(t)], \\ \frac{dx_2(t)}{dt} &= x_2(t)[r(t) - k_2(t)(x_1(t)+x_2(t)) - a_2(t)x_3(t) + \beta(t)x_1(t)], \\ \frac{dx_3(t)}{dt} &= -d(t)x_3(t) - b(t)x_3^2(t) + c_1(t)x_3(t-\tau)x_1(t-\tau) \\ &\quad + c_2(t)x_3(t-\tau)x_2(t-\tau), \end{aligned} \tag{1.3}$$

where $x_1(t), x_2(t)$ and $x_3(t)$ are susceptible, infected and predator population respectively and the corresponding parameters has the meaning as defined in [17]. Time delay is considered as gestation period and disease can be transmitted by contact and spreads among prey species only. Author established some sufficient conditions for the permanence of the system by applying the method of inequality analytical techniques. By the well known method of Lyapunov functional,global asymptotic stability of model (1.3) has been derived in [17]. Author concluded that the time delay has no effect on the permanence of the system but it has an effect on the global asymptotic stability of model (1.3).

Model (1.2) was modified by Hu and Li (2012)[5] and proposed an autonomous model similar to (1.3), their model takes the form

$$\begin{aligned} \frac{dS}{dt} &= rS(1-\frac{S+I}{k}) - SI\beta - p_1SY, \\ \frac{dI}{dt} &= -cI + SI\beta - p_2IY, \\ \frac{dY}{dt} &= -dY + qp_1S(t-\tau)Y(t-\tau) + qp_2I(t-\tau)Y(t-\tau), \end{aligned} \tag{1.4}$$

where $S(t), I(t)$ and $Y(t)$ are susceptible, infected and predator population respectively and parameters used has the meaning as defined in [5]. They derived stability results and investigate Hopf-bifurcation analysis. They performed stability analysis by using Routh-Hurwitz criteria. The effect of delay on model (1.4) is considered as a bifurcation parameter for the purpose of the stability of the positive equilibrium. They investigated the Hopf bifurcation. By applying the normal form theory and the center manifold reduction method, the direction of Hopf bifurcations and the stability of bifurcated periodic solutions has been determined in [5].

The main motivation of the present study is to modify the models (1.2) and (1.4) by introducing suitable ecological and biological assumptions. We study the role of time delay as bifurcation parameter by using the normal form theory, Riesz representation theorem and central manifold theorem. The parameters are time independent as considered in [5, 2]. We have also analyzed the model with and without delay. Detailed ecological and biological assumptions for model formulation are listed in the next section.

Rest of the paper is organized as follows. Section 2 deals with mathematical model formation with help of some ecological and biological assumptions. In Section 3 we determine the stability of different equilibrium points for mathematical model without delay. In Section 4 we determine the stability of different equilibrium points for mathematical model with delay. In Section 5 we investigate Hopf-bifurcation and direction of the Hopf-bifurcation including stability of bifurcated periodic solutions. To verify the theoretical frame work, in Section 6 some numerical computation has been performed by considering suitable parameters and initial conditions followed by discussion and future directions in the last Section 7.

2. The model

For mathematical simplicity we impose the following ecological and biological assumptions:

(A1) We consider linear functional response as described in [19].

(A2) In the absence of disease and predation, prey population follow the logistic rule with the growth rate r ($r > 0$) and carrying capacity k ($k > 0$) [5].

(A3) In the presence of disease, prey population is divided into two parts: susceptible (S) and infective (I). Hence, total biomass of the prey population is $S(t) + I(t)$.

(A4) It is considered that by means of contact, disease spreads among the prey species only.

(A5) Only the susceptible prey is assumed to be reproducing offsprings with logistic law i.e. only S has growth rate. However, infected prey population contributes to the carrying capacity.

(A6) Prey population may have possible source of infection (external source) viz. viruses and other seasonal effects. After infection they converted into infected prey (I). The disease dynamics has been omitted.

(A7) Prey population (susceptible(S) and infective (I)) and predator population remains in the same environmental conditions and in the same terrestrial area and zone i.e in same ecosystem. In other words migration (in and out both) has been omitted here. Detail classification of an ecosystem has been ignored.

(A8) It is also assumed that infected prey has high probability of being predated (eaten) by the predator as compare to susceptible prey population. One of the reason of this may be that healthy prey population is more active than infected one.

(A9) It is also assumed that the coefficient of conversing of both the prey to predator are different. One is S-prey to predator and other one from I-prey to predator.

(A10) It is assumed that all the three species susceptive prey, infected prey and predator have their natural death rates.

(A11) Infected Prey has no growth i.e. they are declining only.
(A12) Motivated by studies in [14, 1, 7, 8, 10], that linear mass-action incidence is more appropriate than a proportional mixing one in case of direct transmission, we assume that the infection follow the simple law of mass action of the form βSI where β is the force of infection.
(A13) Initially there may not be infected Prey. It is also assumed that infected prey neither recover nor immune.
(A14) Time delay (τ) is the gestation period of predator.

In view of above assumptions, model (1.4) takes the form

$$\begin{aligned}
\frac{dS}{dt} &= rS(1-\frac{S+I}{k}) - SI\beta - p_1SY,\\
\frac{dI}{dt} &= SI\beta - p_2IY - (d_2+c)I,\\
\frac{dY}{dt} &= -d_3Y + q_1p_1S(t-\tau)Y(t-\tau) + q_2p_2I(t-\tau)Y(t-\tau).
\end{aligned} \tag{2.1}$$

We summarize the various nomenclature in Table 1.

Table 1. Biological/ecological meaning of the symbols

$S(t)$	Susceptible(healthy) prey population
$I(t)$	Infected prey population
$Y(t)$	Predator population
β	Disease contact rate (force of infection)
p_1, p_2	Predation coefficients of susceptible (S) and infected prey (I)
r	Intrinsic growth rate
k	Carrying capacity
τ	Gestation period(time delay)
c	Death rate of infected prey due to disease
d_2	Natural death rate of infected prey
d_3	Natural death rate of predator
q_1	Coefficient of conversing susceptible prey into predator
q_2	Coefficient of conversing infected prey into predator

On the basis of ecological and biological assumption that healthy prey are more active as compare to infected one, the relationship between q_1 and q_2 is established as under:

$$\begin{aligned}
q_2 \neq q_1 \text{ and } 0 < q_1 \leq 1,\\
q_2 > q_1 \text{ and } 0 < q_2 \leq 1
\end{aligned}$$

and the initial conditions for model (2.1) are $S(0) = \phi_1 > 0$, $I(0) = \phi_2 \geq 0$, $Y(0) = \phi_3 > 0$, where

$$\big\{\phi \in \mathbb{C}_+ : \phi = (\phi_1, \phi_2, \phi_3)\big\},$$

where $\mathbb{C}_+$ is the Banach space of positive continuous functions $\phi : [-\tau, 0] \to R^3_+$ with norm

$$\sup_{[-\tau,0]} \{|\phi_1|, |\phi_2|, |\phi_3|\},$$
$$\mathbb{R}^3_+ = \big\{\phi \in \mathbb{C}_+ : \phi_i \geq 0, \phi = (\phi_1, \phi_2, \phi_3),\ i = 1, 2, 3\big\}.$$

Model (1.3) is different with the proposed model (2.1) in the sense that parameters in (1.3) are time dependent as contrary to those in (2.1).

3. Model without delay

In absence of time delay τ, model (2.1) takes the form

$$\begin{aligned} \frac{dS}{dt} &= rS(1 - \frac{S+I}{k}) - SI\beta - p_1SY, \\ \frac{dI}{dt} &= SI\beta - p_2IY - (d_2 + c)I, \\ \frac{dY}{dt} &= -d_3Y + q_1p_1S(t)Y(t) + q_2p_2I(t)Y(t). \end{aligned} \tag{3.1}$$

3.1. **Equilibria and their feasibility.** Model (3.1) has the following equilibrium points

(1) $E_1 = (0, 0, 0)$, which is trivial equilibrium.
(2) $E_2 = (k, 0, 0)$, this provides the case where prey is infection free and predator is absent. This is called boundary equilibrium.
(3) $E_3 = (\widehat{S}, 0, \widehat{Y})$, where $\widehat{S}$ and $\widehat{Y}$ are given by

$$\begin{aligned} \widehat{S} &= \frac{d_3}{q_1p_1}, \\ \widehat{Y} &= \frac{r}{p_1}(1 - \frac{d_3}{kq_1p_1}), \end{aligned} \tag{3.2}$$

this provides the case where prey is infection free.
(4) $E_4 = (\overline{S}, \overline{I}, 0)$, where $\overline{S}$ and $\overline{I}$ are given by:

$$\begin{aligned} \overline{S} &= \frac{c + d_2}{\beta}, \\ \overline{I} &= \frac{r(k\beta - c - d_2)}{\beta(r + k\beta)} \end{aligned} \tag{3.3}$$

this provides the case where predator is absent.
(5) $E_5 = (\widetilde{S}, \widetilde{I}, \widetilde{Y})$, where $\widetilde{S}, \widetilde{I}, \widetilde{Y}$ are given by

$$\begin{aligned} \widetilde{I} &= \frac{d_3 - q_1p_1\widetilde{S}}{q_2p_2}, \\ \widetilde{Y} &= \frac{\beta\widetilde{S} - c - d_2}{p_2}, \end{aligned} \tag{3.4}$$

and

$$\begin{aligned} \widetilde{S}A + B &= 0, \\ A &= \big[-\frac{r}{K} + (\frac{r}{K} + \beta)\frac{q_1 p_1}{q_2 p_2} - \frac{p_1 \beta}{p_2} \big], \\ B &= \big[r - (\frac{r}{K} + \beta)\frac{d_3}{q_2 p_2} + \frac{p_1(c+d_2)}{p_2} \big]. \end{aligned} \tag{3.5}$$

Set E_5 provides the coexistence of all the three species. Existence (feasibility) conditions of equilibrium points of model ref3.1 are listed in Table 2.

TABLE 2. Existence conditions of equilibrium points of model (3.1)

Equilibrium Point	Existence Condition
$E_1 = (0, 0, 0)$	always
$E_2 = (k, 0, 0)$	always
$E_3 = (\widehat{S}, 0, \widehat{Y})$	$kq_1p_1 > d_3$
$E_4 = (\overline{S}, \overline{I}, 0)$	$k\beta > (c + d_2)$
$E_5 = (\widetilde{S}, \widetilde{I}, \widetilde{Y})$	$(d_3 - q_1p_1\widetilde{S}) > 0$, $(\beta\widetilde{S} - c - d_2) > 0$, either $A < 0$ or $B < 0$ but not both.

Remark 3.1. From Table 2 it is observed that:

(i) The existence of equilibrium points E_1, E_2 and E_4 is independent of parameters q_1 and q_2.
(ii) The existence of equilibrium point E_3 is dependent on q_1.
(iii) The existence of equilibrium point E_5 is dependent on q_1 and q_2 both.

3.2. **Stability analysis.** The variational matrix is given by

$$J = \begin{bmatrix} (r - \frac{2rS}{k} - \frac{rI}{k} - \beta I - p_1 Y) & (-\frac{rS}{k} - \beta S) & (-p_1 S) \\ (\beta I) & (\beta S - p_2 Y - c - d_2) & (-p_2 I) \\ (q_1 p_1 Y) & (q_2 p_2 Y) & (q_1 p_1 S + q_2 p_2 I - d_3) \end{bmatrix}.$$

It is very easy to prove from the above equality that the equilibrium points E_1, E_2, E_3 and E_4 are unstable.

Now, the jacobian matrix at E_5 is

$$J(E_5) = \begin{bmatrix} (r(1 - \frac{2\widetilde{S}}{k}) - \widetilde{I}(\frac{r}{k} + \beta) - p_1\widetilde{Y}) & (-\widetilde{S}(\frac{r}{k} + \beta)) & (-p_1\widetilde{S}) \\ (\beta\widetilde{I}) & (\beta\widetilde{S} - c - d_2 - p_2\widetilde{Y}) & (-p_2\widetilde{I}) \\ q_1 p_1 \widetilde{Y} & q_2 p_2 \widetilde{Y} & (q_1 p_1 \widetilde{S} + q_2 p_2 \widetilde{I} - d_3) \end{bmatrix}$$

and the characteristics equation of $J(E_5)$ is

$$\lambda^3 + C_1\lambda^2 + C_2\lambda + C_3 = 0.$$

By the Routh-Hurwitz criteria, we can conclude that equilibrium E_5 is locally stable provided the following conditions are satisfied

$$\begin{aligned} C_i &> 0, i = 1, 2, 3 \\ C_1C_2 - C_3 &> 0. \end{aligned} \tag{3.6}$$

The values of $C_i > 0, i = 1, 2, 3$ are listed at Appendix 1.

Remark 3.2. Stability of the non zero equilibrium point E_5 depends on $C_i > 0$, $i = 1, 2, 3$ (from Eq. (3.6)). Since $C_i > 0$, $i = 1, 2, 3$ involves q_1 and q_2 both (from Appendix 1). Hence, stability of E_5 depends on q_1 and q_2 both.

4. Model with time delay

Ecologically it is a fact that reproduction of predator after predation is not instantaneous but it will mediated by some time lag, so it may call as gestation period. We record this gestation period as time delay (τ) in our proposed model (2.1). It is also clear that since delay is gestation period of predator, hence delay term (τ) appears only in last equation of model (2.1). Time delay played a crucial role in analysis. In this section, we will observe the role of time delay.

4.1. **Equilibria and their feasibility.** It is remarkable that the two models (2.1) and (3.1) have the same equilibrium points ecologically. Because of the mathematical point of view we denote them differently. In R^3_+ the system (2.1) has several possible stationary states (equilibrium points) and they are summarized in Table 3. Table 3 provides a brief ecological meaning of equilibrium points and their applications to real ecosystems.

Table 3. Possible equilibrium points of model (2.1)

Equilibr. point	Name	Ecological meaning
$E_{10} = (0, 0, 0)$	Trivial	Species will die out. Ecologically not important
$E_{11} = (k, 0, 0)$	Boundary	Only sound prey survive.
		Infection fee. Predator will die out
$E_{12} = (\overline{S}, \overline{I}, 0)$	Boundary	Predator will die out. Infection exists
$E_{13} = (\widetilde{S}, 0, \widetilde{Y})$	Boundary	No infection. Co-existence of sound prey
		and predator
$E_* = (S_*, I_*, Y_*)$	Non zero	Co-existence of all species.
	(interior)	Ecologically very important

4.2. **Stability Analysis.** E_{13} and E_* play an important role in the controlling of epidemic. The variational matrix of system (2.1) is written as

$$J = \begin{bmatrix} (r(1-\frac{S+I}{k}) - \frac{rS}{k} - \beta I - p_1 Y) & (-\frac{rS}{k} - \beta S) & (-p_1 S) \\ (\beta I) & (\beta S - p_2 Y - c - d_2) & (-p_2 I) \\ 0 & 0 & (-d_3) \end{bmatrix} + \begin{bmatrix} 0 & 0 & 0 \\ 0 & 0 & 0 \\ (q_1 p_1 Y) & (q_2 p_2 Y) & (q_1 p_1 S + q_2 p_2 I) \end{bmatrix} e^{-\lambda\tau},$$

where λ being a complex number. In simplified form the above equation may be written as

$$J = \begin{bmatrix} (r(1-\frac{S+I}{k}) - \frac{rS}{k} - \beta I - p_1 Y) & (-\frac{rS}{k} - \beta S) & (-p_1 S) \\ (\beta I) & (\beta S - p_2 Y - c - d_2) & (-p_2 I) \\ (q_1 p_1 Y)(e^{-\lambda\tau}) & (q_2 p_2 Y)(e^{-\lambda\tau}) & (-d_3) + (q_1 p_1 S + q_2 p_2 I)(e^{-\lambda\tau}) \end{bmatrix}.$$

We will use the following lemma due to Hu and Li [5].

Lemma 4.1. *Let $A > 0, B > 0$. Then*

- *If $A < B$, all roots of the equation $\lambda + A - Be^{-\lambda\tau} = 0$ have positive real parts for $\tau < \frac{1}{\sqrt{B^2 - A^2}} \cos^{-1}(\frac{A}{B})$.*
- *If $A > B$, all roots of the equation $\lambda + A - Be^{-\lambda\tau} = 0$ have negative real parts for any τ.*

Now we study the dynamical behavior of system (2.1) about different equilibrium points with the help of variational matrix.

4.2.1. *Trivial equilibrium point (E_{10}).* Proceeding as in Sub-section 3.2.1, it is concluded that E_{10} is unstable.

4.2.2. *Boundary equilibrium point (E_{11}).* Variational matrix evaluated at E_{11} takes the form

$$J(E_{11}) = \begin{bmatrix} -r & -(r + k\beta) & (-p_1 k) \\ 0 & (\beta k - c - d_2) & 0 \\ 0 & 0 & (q_1 p_1 k)e^{-\lambda\tau} - d_3 \end{bmatrix},$$

with corresponding eigenvalues $-r$, $(\beta k - c - d_2)$ and $(q_1 p_1 k)e^{-\lambda\tau} - d_3$. Hence, the stability of E_{11} depends on $(\beta k - c - d_2)$ and $(q_1 p_1 k)e^{-\lambda\tau} - d_3$.

Now, if the following condition is satisfied

$$(q_1 p_1 k) < d_3, \tag{4.1}$$

and if delay τ satisfies

$$\tau < \frac{1}{\sqrt{(q_1 p_1 k)^2 - d_3^2}} \cos^{-1} \frac{d_3}{(q_1 p_1 k)},$$

by using Lemma 4.1, it is clear that $J(E_{11})$ has no eigenvalue λ with $Re(\lambda) \leq 0$. Hence, E_{11} is unstable in this case.

Further, if $(q_1 p_1 k) < d_3$ and $(\beta k - c - d_2) < 0$, then two eigenvalues are negative and third has the negative real part, (E_{11}) is stable in this case. If $(\beta k - c - d_2) > 0$, then E_{11} is unstable always.

4.2.3. *Predator free equilibrium (E_{12}).* Now as in previous section, we have $\overline{S} = \frac{(c+d_2)}{\beta}$ and $\overline{I} = \frac{r(k\beta - c - d_2)}{\beta(r + k\beta)}$. The variational matrix at E_{12} takes the form

$$J(E_{12}) = \begin{bmatrix} (r(1 - \frac{\overline{S}+\overline{I}}{k}) - \frac{r\overline{S}}{k} - \beta\overline{I}) & (-\frac{r\overline{S}}{k} - \beta\overline{S}) & (-p_1\overline{S}) \\ (\beta\overline{I}) & (\beta\overline{S} - c - d_2) & (-p_2\overline{I}) \\ 0 & 0 & (q_1 p_1 \overline{S} + q_2 p_2 \overline{I})e^{-\lambda\tau} - d_3 \end{bmatrix},$$

and the characteristics equation corresponding to $J(E_{12})$ is

$$[\lambda + d_3 - ((q_1 p_1 \overline{S} + q_2 p_2 \overline{I})e^{-\lambda\tau})][\lambda^2 + \lambda\big(c + d_2 + \frac{r(c + d_2)}{k\beta} + \frac{\beta}{(c + d_2)} - \frac{(c + d_2)}{k}\big)$$
$$- \frac{(c + d_2)^2 r}{k\beta} - \beta - r(c + d_2)] = 0.$$

If the following condition is satisfied

$$d_3 > (q_1 p_1 \overline{S} + q_2 p_2 \overline{I}),$$

then by Lemma 4.1, the root of the functions

$$\lambda + d_3 - ((q_1 p_1 \overline{S} + q_2 p_2 \overline{I})e^{-\lambda\tau})),$$

will have negative real part for any value of τ and for the equation

$$\lambda^2 + \lambda\Big((c+d_2) + \frac{r(c+d_2)}{K\beta} + \frac{\beta}{(c+d_2)} - \frac{(c+d_2)}{k}\Big) + \Big(-\frac{r(c+d_2)^2}{k\beta} - \beta - r(c+d_2)\Big) = 0,$$

the Routh-Hurwitz criteria, may be used for proving the fact that this equation will have roots with negative real parts. Hence, if the equilibrium E_{12} is asymptotically stable, it will mean that predator population will be die-out from system so considered.

4.2.4. *Infection free equilibrium* (E_{13}). $\widetilde{S}$ and $\widetilde{Y}$ are given by $\widetilde{S} = \frac{d_3}{q_1p_1}, \widetilde{Y} = [\frac{r}{p_1}(1 - \frac{d_3}{kq_1p_1})]$. The variational matrix at E_{13} takes the form

$$J(E_{13}) = \begin{bmatrix} (r(1-\frac{\widetilde{S}}{k}) - \frac{r\widetilde{S}}{k} - p_1\widetilde{Y}) & (-\frac{r\widetilde{S}}{k} - \beta\widetilde{S}) & (-p_1\widetilde{S}) \\ 0 & (\beta\widetilde{S} - p_2\widetilde{Y} - c - d_2) & 0 \\ (q_1p_1\widetilde{Y}e^{-\lambda\tau}) & (q_2p_2\widetilde{Y}e^{-\lambda\tau}) & (q_1p_1\widetilde{S}e^{-\lambda\tau} - d_3) \end{bmatrix},$$

One of the eigenvalue is $(\beta\widetilde{S} - p_2\widetilde{Y} - c - d_2)$ and two other eigenvalues are the roots of the expression

$$\Big[\lambda^2 - \lambda\big(r(1-\frac{2\widetilde{S}}{k}) - p_1\widetilde{Y} - d_3 + (q_1p_1\widetilde{Y}e^{-\lambda\tau})\big) + \big(-rd_3(1-\frac{2\widetilde{S}}{k}) - d_3p_1\widetilde{Y} + d_3 + rq_1p_1\widetilde{S}(1-\frac{2\widetilde{S}}{k})e^{-\lambda\tau}\big)\Big].$$

If the condition

$$\widetilde{S} > \frac{(c + d_2 + p_2\widetilde{Y})}{\beta}$$

is satisfied. Then one eigenvalue $(\beta\widetilde{S} - p_2\widetilde{Y} - c - d_2)$ corresponding to $J(E_{13})$ is positive. Hence, in this case E_{13} is unstable. Let us put, $\lambda = (u+iv)$ with condition for u as $u \geq 0$ in the expression

$$\Big[\lambda^2 - \lambda\big(r(1-\frac{2\widetilde{S}}{k}) - p_1\widetilde{Y} - d_3 + (q_1p_1\widetilde{Y}e^{-\lambda\tau})\big) + \big(-rd_3(1-\frac{2\widetilde{S}}{k}) - d_3p_1\widetilde{Y} + d_3 + rq_1p_1\widetilde{S}(1-\frac{2\widetilde{S}}{k})e^{-\lambda\tau}\big)\Big],$$

and on separating real and imaginary parts, we obtained

$$\text{Real part} = (u^2 - v^2) - \big(r(1-\frac{2\widetilde{S}}{k}) - p_1\widetilde{Y} - d_3 + (q_1p_1\widetilde{S}e^{-\lambda\tau}\cos v\tau\big) + \big(rq_1p_1\widetilde{S}(1-\frac{2\widetilde{S}}{K})e^{-\lambda\tau}\cos v\tau\big),$$

$$\text{Imaginary part} = 2uv + \Big(p_1\widetilde{Y} + d_3 - vr(1-\frac{2\widetilde{S}}{k}) - q_1p_1\widetilde{S}e^{-\lambda\tau}\cos v - uq_1p_1\widetilde{S}e^{-\lambda\tau}\sin v\tau - rq_1p_1\widetilde{S}(1-\frac{2\widetilde{S}}{k})e^{-\lambda\tau}\sin v\tau\Big).$$

Now, if the following condition is satisfied

$$\widetilde{S} < \frac{(c + d_2 + p_2\widetilde{Y})}{\beta},$$

and the real part is negative, we can conclude that equilibrium state E_{13} is stable.

4.2.5. *Non zero equilibrium* $(E_*(S_*, I_*, Y_*))$. S_*, I_*, Y_* are given by

$$S_* = \frac{-B}{A}, I_* = \frac{d_3 - q_1 p_1 S_*}{q_2 p_2}, Y_* = \frac{\beta S_* - c - d_2}{p_2},$$
$$A = \Big[-\frac{r}{k} + (\frac{r}{k} + \beta)\frac{q_1 p_1}{q_2 p_2} - \frac{p_1 \beta}{p_2}\Big] B = \Big[(r) - (\frac{r}{K} + \beta)\frac{d_3}{q_2 p_2} + \frac{p_1(c + d_2)}{p_2}\Big].$$

The variational matrix at E_* takes the form

$$J(E_*) = \begin{bmatrix} (r(1-\frac{S_*+I_*}{k}) - \frac{rS_*}{k} - p_1 Y_* - \beta I_*) & (-\frac{rS_*}{k} - \beta S_*) & (-p_1 S_*) \\ \beta I_* & (\beta S_* - p_2 Y_* - c - d_2) & p_2 I_* \\ (q_1 p_1 Y_* e^{-\lambda\tau}) & (q_2 p_2 Y_* e^{-\lambda\tau}) & (q_1 p_1 S_* + q_2 p_2 I_*) e^{-\lambda\tau} - d_3) \end{bmatrix},$$

and the characteristics equation corresponding to $J(E_*)$ is

$$(\lambda^3 + m_2\lambda^2 + m_1\lambda + m_0) + (n_2\lambda^2 + n_1\lambda + n_0)e^{-\lambda\tau} = 0, \tag{4.2}$$

where m_i, n_j, $i = 0, 1, 2$; $j = 0, 1, 2$ are listed in Appendix 2.

Now we put $\lambda = i\omega$ $(\omega > 0)$ in the above equation and separating real and imaginary parts, we obtain

$$\begin{aligned} \text{Real part} &= \{n_2\omega^2 + n_0\}\cos\omega\tau + \{n_1\omega\sin\omega\tau - m_2\omega^2 + m_0\}, \\ \text{Imaginary part} &= n_1\omega\cos\omega\tau - (-n_2\omega^2 + n_0)\sin\omega\tau + m_1\omega - \omega^3, \\ (\text{Real part})^2 + (\text{Imaginary part})^2 &= \omega^6 + p_0\omega^4 + q_0\omega^2 + r_0, \end{aligned} \tag{4.3}$$

where

$$\begin{aligned} p_0 &= (m_2^2 - 2m_1 - n_2^2), \\ q_0 &= (m_1^2 - 2m_2 m_0 + 2n_2 n_0 - n_1^2), \\ r_0 &= (m_0^2 - n_0^2). \end{aligned}$$

We refer the following lemma due to [5, 21]

Lemma 4.2. *For the polynomial*

$$h(z) = z^3 + p_0 z^2 + q_0 z + r_0 = 0, \tag{4.4}$$

(i) *If $r_0 < 0$, then this equation has at least one positive root;*
(ii) *If $r_0 \geq 0$ and $\triangle = (p_0^2 - 3q_0) \leq 0$, then this equation has no positive roots;*
(iii) *If $r_0 \geq 0$ and $\triangle = (p_0^2 - 3q_0) > 0$, then this equation has positive roots if and only if $z_1^* = \frac{-p_0 + \sqrt{\triangle}}{3}$ and $h(z_1^*) \leq 0$.*

If we put $z = \omega^2$ in $\omega^6 + p_0\omega^4 + q_0\omega^2 + r_0 = 0$, then we have the equation $z^3 + p_0 z^2 + q_0 z + r_0 = 0$. If $m_0^2 \geq n_0^2$, then we will have $r_0 \geq 0$, we have two situations for Δ:

(i) $\Delta = (p_0^2 - 3q_0) \leq 0$,
(ii) $\Delta = (p_0^2 - 3q_0) > 0$.

In situation (i), we have to say that E_* is stable thus E_* is absolutely stable if $r_0 \geq 0$ and $\Delta = (p_0^2 - 3q_0) \leq 0$ and also if we have and $r_0 \geq 0$ and $\Delta = (p_0^2 - 3q_0) > 0$ then equation has negative roots if and only if $h(z_1^*) > 0$ where $z_1^* = \frac{-p_0+\sqrt{\Delta}}{3}$, thus we have the following theorem for the stability of E_*

Theorem 4.3. *Equilibrium $E_*(S_*, I_*, Y_*)$ is absolutely stable if one of the following three conditions holds*

(i) $\Delta = (p_0^2 - 3q_0) \leq 0$;
(ii) $\Delta = (p_0^2 - 3q_0) > 0$ *and* $z_1^* = \frac{-p_0+\sqrt{\Delta}}{3} < 0$;
(iii) $\Delta = (p_0^2 - 3q_0) > 0$, $z_1^* = \frac{-p_0+\sqrt{\Delta}}{3} > 0$ *and* $h(z_1^*) > 0$ *provided* $r_0 \geq 0$.

Next if we consider the case when $r_0 < 0$ or $\{r_0 \geq 0, \Delta = (p_0^2 - 3q_0) > 0, z_1^* > 0, h(z_1^*) < 0\}$. Then according to lemma 4.2, (4.3) will have one positive root say ω_0 that is the characteristic equation has a pair of purely imaginary roots say $\pm i\omega_0$. Now assume that $i\omega_0$, $\omega_0 > 0$ is a root of $h(z)$. Solving the eq. (4.3) for τ, we have (by eliminating $\sin \omega\tau$, we obtain

$$\tau = \frac{1}{\omega_0} \cos^{-1}\Big(\frac{n_1\omega_0^2\{\omega_0 - m_1\} - \{m_2\omega_0^2 - m_0\}\{n_2\omega_0^2 - n_0\}}{n_1^2\omega_0^2 + n_2\omega_0^2 - n_0}\Big) + \frac{2k\pi}{\omega_0}, \tag{4.5}$$

for $k = 0, 1, 2, \dots$. We call it as a 'critical value' and is denoted by

$$\tau_k = \frac{1}{\omega_0} \cos^{-1}\Big(\frac{n_1\omega_0^2\{\omega_0 - m_1\} - \{m_2\omega_0^2 - m_0\}\{n_2\omega_0^2 - n_0\}}{n_1^2\omega_0^2 + n_2\omega_0^2 - n_0}\Big) + \frac{2k\pi}{\omega_0}, \tag{4.6}$$

for $k = 0, 1, 2, \dots$. This corresponds to the characteristic equation that has purely imaginary roots $\pm i\omega_0$. Which is a result similar to that is discussed in [5]. Transversality condition may also obtained as discussed in [5]. As discussed in [5, Theorem 2.4], the equilibrium point E_* of the system (2.1) is asymptotically stable when $\tau > \tau_0$. $\tau = \tau_k$ $(k = 0, 1, 2, 3, \dots)$ are Hopf-bifurcation values for the system (2.1) and τ_k is used as a point for direction of Hopf Bifurcation in next section.

Remark 4.4. From (4.5) and (4.6), it is observed that the delay term τ (here bifurcation parameter) depends on the values of m_i, n_j, $i = 0, 1, 2$; $j = 0, 1, 2$. Since m_i, n_j, $i = 0, 1, 2$; $j = 0, 1, 2$ depends on q_1 and q_2 (see Appendix 2), hence bifurcation parameter (τ) depends on q_1 and q_2 both. A little variation in the values of q_1 and q_2 may change the bifurcation parameter (τ). Hence, a little variation in the values of q_1 and q_2 may change the dynamics of the delayed model (2.1).

5. Direction and stability of the Hopf Bifurcation

With the symbols used in [5] and the procedure explained in [12]. System (2.1), can be translated to the following functional differential equation (FDE) system

$$\dot{u}(t) = L_\mu(\mu_t) + F(\mu, u_t), \tag{5.1}$$

where $u_t = u(t) \in R^3$ and $L_\mu : \mathbb{R} \times \mathbb{C} \to \mathbb{R}^3$ and $F : \mathbb{R} \times \mathbb{C} \to \mathbb{R}^3$ are given by,

$$L_\mu\phi = (\tau_k + \mu)(M_1\phi(0) + M_2\phi(-1)),$$
$$F(\mu, \theta) = \begin{bmatrix} -\frac{r}{k}\phi_1^2(0) - (\frac{r}{k} + \beta)\phi_1(0)\phi_2(0) - p_1\phi_1(0)\phi_3(0) \\ \beta\phi_1(0)\phi_2(0) - p_2\phi_2(0)\phi_3(0) \\ q_1p_1\phi_1(-1)\phi_3(-1) + q_2p_2\phi_1(-1)\phi_2(-1) \end{bmatrix},$$

where

$$M_1 = \begin{bmatrix} (r - \frac{2rS_*}{k} - (\frac{r}{k} + \beta)I_* - p_1Y_*) & -(\frac{r}{k} + \beta)S_* & (-p_1S_*) \\ \beta I_* & (\beta S_* - p_2Y_* - c - d_2) & -p_2I_* \\ 0 & 0 & -d_3) \end{bmatrix},$$

$$M_2 = \begin{bmatrix} 0 & 0 & 0 \\ 0 & 0 & 0 \\ q_1p_1Y_* & q_2p_2Y_* & q_1p_1S_* + q_2p_2I_* \end{bmatrix},$$

$$\phi(0) = (\phi_1(0), \phi_2(0), \phi_3(0))^T \in \mathbb{C},$$

$$\phi(-1) = (\phi_1(-1), \phi_2(-1), \phi_3(-1))^T \in \mathbb{C}.$$

We have considered, $\tau = (\tau_k + \mu)$, $\mu = 0$ which gives the Hopf bifurcation value for the mathematical model with delay as promised in previous section. Normalizing delay τ by the time scaling $t \to \frac{t}{\tau}$ then the model is written in the Banach Space $\mathbb{C} \equiv \mathbb{C}([-1, 0], \mathbb{R}^3)$.

By the Riesz representation theorem, we found that there exists a matrix function whose components are bounded variation function $\eta(\theta, \mu)$ in $\theta \in [-1, 0]$, such that $L_\mu\phi = \int_\Omega d\eta(\theta, \mu)\phi(\theta)$, $\phi \in \mathbb{C}$, $\Omega \in [-1, 0)$. We can choose

$$\eta(\theta, \mu) = (\tau_k + \mu)M_1\delta(\theta) - (\tau_k + \mu)M_2\delta(\theta + 1),$$

where $\delta(\theta)$ denotes the dirac delta function viz.

$$\delta(\theta) = \begin{cases} 0, & \theta \neq 0, \\ 1, & \theta = 0. \end{cases}$$

For $\phi \in \mathbb{C}^1([-1, 0], \mathbb{R}^3)$, we define

$$A(\mu)\phi(\theta) = \begin{cases} \frac{d\phi(\theta)}{d\theta}, & \theta \in [-1, 0), \\ \int_{-1}^{0} d\eta(\theta, \mu)\phi(\theta), & \theta = 0, \end{cases}$$

$$= \begin{cases} \frac{d\phi(\theta)}{d\theta}, & -1 \leq \theta < 0, \\ \int_{-1}^{0} d\eta(\theta, \mu)\phi(\theta), & \theta = 0. \end{cases}$$

and

$$\mathbb{R}(\mu)\phi(\theta) = \begin{cases} 0, & \theta \in [-1, 0), \\ F(\mu, \phi), & \theta = 0, \end{cases}$$

$$= \begin{cases} 0, & -1 \leq \theta < 0, \\ F(\mu, \phi), & \theta = 0, \end{cases}$$

with these symbols, FDE system (5.1) may be written in the form

$$\dot{u}(t) = A(\mu)(\mu_t) + \mathbb{R}(\mu)\mu_t,$$

which is an abstract differential equation where $u_t(\theta) = u(t + \theta), -1 \leq \theta < 0$. Now we come to operator theory, for $\psi \in \mathbb{C}^1\big([0, 1], (\mathbb{R}^3)^*\big)$ we define A^*, the adjoint operator of A, by

$$A^*\psi(S) = \begin{cases} -\frac{d\psi(S)}{dS}, & S \in (0, 1], \\ \int_{-1}^{0} d\eta^T(S, \mu)\psi(-S), & S = 0, \end{cases}$$

and a bilinear product

$$\langle \psi(S), \phi(\theta)\rangle = \overline{\psi}(0)\phi(0) - \int_1^0 \int_{\xi=0}^{\theta} \overline{\psi}^T(\xi-\theta)d\eta(\theta)\phi(\xi)d\xi, \tag{5.2}$$

where $\eta(\theta) = \eta(\theta, 0)$. Then $A(0)$ and A_* are adjoint operators. From previous section, it is noted that $\pm i\omega_0\tau_k$ are eigenvalues of $A(0)$. Hence they are also the eigenvalues of A^*.

To determine the poincare normal form of the operator A, we first need to evaluate the eigenvectors of $A(0)$ and A^* corresponding to $i\omega_0\tau_k$ and $-i\omega_0\tau_k$ respectively. Suppose that $q(\theta) = (1, \alpha_1, \alpha_2)^T \exp(i\omega_0\tau_k\theta)$ is the eigenvector of $A(0)$ corresponding to $i\omega_0\tau_k$, then we have $A(0)q(\theta) = i\omega_0 q(\theta)$ from the definition of $A(0)$, we have

$$\left[M_1 + M_2\exp(i\omega_0\tau_k)\right]\begin{bmatrix}1\\ \alpha_1\\ \alpha_2\end{bmatrix} = i\omega_0\begin{bmatrix}1\\ \alpha_1\\ \alpha_2\end{bmatrix},$$

or

$$M_1\begin{bmatrix}1\\ \alpha_1\\ \alpha_2\end{bmatrix} + M_2\begin{bmatrix}\exp(-i\omega_0\tau_k)\\ \alpha_1\exp(-i\omega_0\tau_k)\\ \alpha_2\exp(-i\omega_0\tau_k)\end{bmatrix} = i\omega_0\begin{bmatrix}1\\ \alpha_1\\ \alpha_2\end{bmatrix}.$$

By simple calculation, we obtain

$$\alpha_1 = \frac{-p_2I_*(i\omega_0 - (r - \frac{2rS_*}{K} - (\frac{r}{k}+\beta)I_* - p_1Y_*)) - p_1\beta S_*I_*}{p_2(\frac{r}{k}+\beta)S_*I_* - p_1S_*(i\omega_0 - \beta S_* + c + d_2 + p_2Y_*)},$$
$$\alpha_2 = \frac{q_1p_1Y_*\exp(-i\omega_0\tau_k + q_2p_2Y_*\exp(-i\omega_0\tau_k}{i\omega_0 + d_3 - q_1p_1S_* + q_2p_2I_*}.$$

Next, suppose that $q_*(s) = B(1, \alpha_1^*, \alpha_2^*)\exp(i\omega_0\tau_k s)$ is the eigenvector of A^* corresponding to $-i\omega_0\tau k$. Analogously, we have

$$\alpha_1^* = \frac{-p_1(\frac{r}{k}+\beta)S_* - p_2(i\omega_0 - (r - \frac{2rS_*}{k} - (\frac{r}{k}+\beta)I_* - p_1Y_*))}{p_2\beta I_* - p_1(i\omega_0 + \beta S_* - c - d_2 - p_2Y_*)},$$
$$\alpha_2^* = \frac{-p_1S_* - p_2I_*\alpha_1^*}{-i\omega_0 + d_3 - (q_1p_1S_* + q_2p_2I_*)\exp(-i\omega_0\tau_k}),$$

where B has to be calculated. We have the two conditions:

$$\langle q^*, q(\theta)\rangle = 1, \quad \langle q^*, \overline{q(\theta)}\rangle = 0,$$

which may be verified. By equation (5.2), we have

$$\begin{aligned}
&\langle q^*, q(\theta)\rangle\\
&= \overline{q^*}(0)q(0) - \int_{-1}^0\int_{\xi=0}^{\infty}\overline{q^*}^T(\xi-\theta)d\eta(\theta)q(\xi)d\xi\\
&= \overline{B}(1, \overline{\alpha_1}^*, \overline{\alpha_2}^*)(1, \alpha_1, \alpha_2)^T - \int_{-1}^0\int_{\xi=0}^{\infty}\overline{B}(1, \overline{\alpha_1}^*, \overline{\alpha_2}^*)\exp(-i\omega_0\tau_k(\xi-\theta))d\eta(\theta)\\
&\quad\times(1, \alpha_1, \alpha_2)^T\exp(i\omega_0\tau_k\xi)d\xi\\
&= \overline{B}\{1 + \alpha_1\overline{\alpha_1}^* + \alpha_2\overline{\alpha_2}^* - \int_{-1}^0(1, \overline{\alpha_1}^*, \overline{\alpha_2}^*)\exp(i\omega_0\tau_k)d\eta(\theta)(1, \alpha_1, \alpha_2)^T\}\\
&= \overline{B}\{1 + \alpha_1\overline{\alpha_1}^* + \alpha_2\overline{\alpha_2}^* + \tau_k[q_2p_2\overline{\alpha_2}^*Y_* + q_2p_2\alpha_1\overline{\alpha_2}^*Y_* + (q_1p_1S_* + q_2p_2I_*)\alpha_2\overline{\alpha_2}^*]\\
&\times\exp(-i\omega_0\tau_k)\},
\end{aligned}$$

and

$$1 = \overline{B}\{1 + \alpha_1\overline{\alpha_1}^* + \alpha_2\overline{\alpha_2}^* + \tau_k\big[q_2p_2\overline{\alpha_2}^*Y_* + q_2p_2\alpha_1\overline{\alpha_2}^*Y_* + (q_1p_1S_* + q_2p_2I_*)\alpha_2\overline{\alpha_2}^*\big]\exp(-i\omega_0\tau_k)\},$$

which gives

$$\overline{B} = \Big(1 + \alpha_1\overline{\alpha_1}^* + \alpha_2\overline{\alpha_2}^* + \tau_k[q_2p_2\overline{\alpha_2}^*Y_* + q_2p_2\alpha_1\overline{\alpha_2}^*Y_* + (q_1p_1S_* + q_2p_2I_*)\alpha_2\overline{\alpha_2}^*]\exp(-i\omega_0\tau_k)\Big)^{-1}.$$

5.1. **Stability of bifurcated periodic solutions.** Firstly, we will investigate the coordinates of the center manifold $\mathbb{C}_0$ at $\mu = 0$. Let u_t be the solution of (5.1) and define, $z(t) = \langle q^*, u_t\rangle$, q^* being the eigenvalue of A^* and $W(t,\theta) = u_t(\theta) - 2Re\{z(t)q(\theta)\}$ on the Center Manifold $\mathbb{C}_0$, we have

$$W(t,\theta) = W(z(t), \overline{z(t)}, \theta),$$

where

$$W(z,\overline{z},\theta) = W_{20}(\theta)\frac{z^2}{2} + W_{02}(\theta)\frac{\overline{z}^2}{2} + W_{11}(\theta)z\overline{z} + W_{30}\frac{z^3}{\lfloor 3} + \dots . \tag{5.3}$$

In fact, z and $\overline{z}$ are local coordinates for the center manifold $\mathbb{C}_0$ in the direction of q^* and $\overline{q}^*$ respectively. The existence of $\mathbb{C}_0$ will provide an opportunity to reduce the system $\dot{u}(t) = L_\mu(u_t) + F(\mu,\mu_t)$ into an ordinary differential equation ODE(in a single complex variable z) on $\mathbb{C}_0$ which is very interesting. u_t is the solution of system under consideration. $u_t \in \mathbb{C}_0$, we have

$$\begin{aligned}
\dot{z}(t) &= \langle q^*, \dot{u_t}\rangle \\
&= \langle q^*, A(u_t) + R(u_t)\rangle \\
&= \langle q^*, A(u_t)\rangle + \langle q^*, R(u_t)\rangle \\
&= \langle A^*q^*, (u_t)\rangle + \langle q^*, R(u_t)\rangle \\
&= i\omega_0\overline{\tau}z + \overline{q}^*\cdot F(0, W(t,0) + 2Re[z(t)q(\theta)]).
\end{aligned}$$

We rewrite it as

$$\dot{z}(t) = i\omega_0\overline{\tau}z + g(z,\overline{z}).$$

where

$$g(z,\overline{z}) = g_{20}(\theta)\frac{z^2}{2} + g_{02}(\theta)\frac{\overline{z}^2}{2} + g_{11}(\theta)z\overline{z} + g_{21}\frac{\overline{z}z^2}{\lfloor 3} + \dots .$$

The computation of coefficients of $g(z,\overline{z})$ is done at Appendix 3.

The coefficients g_{20}, g_{02}, g_{11} and g_{21} are used in calculating $\mathbb{C}_0$ etc. Since g_{21} (from Appendix 3) contains $W_{20}(\theta)$ and $W_{11}(\theta)$, we need to calculate them. Now $\dot{u}_t = A(\mu)u_t + R(\mu)u_t$ and $z(t) = \langle q^*, u_t\rangle$, $W(t,\theta) = u_t(\theta) - 2Re\{z(t)q(\theta)\}$ gives us

$$\dot{W} = \dot{u_t} - zq - \dot{\overline{z}}\overline{q} = \begin{cases} AW - 2Re\overline{q}^*(0)F_0q(\theta), & -1 \le \theta < 0, \\ AW - 2Re\overline{q}^*(0)F_0q(\theta) + F_0, & \theta = 0. \end{cases}$$

Rewriting the above equation, we obtain

$$\dot{W} = AW + H(z,\overline{z},\theta), \tag{5.4}$$

where

$$H(z,\overline{z},\theta)=H_{20}(\theta)\frac{z^2}{2}+H_{11}(\theta)z\overline{z}+H_{02}(\theta)\frac{\overline{z^2}}{2}+H_{21}(\theta)\frac{z^2\overline{z}}{2}+\dots. \tag{5.5}$$

Near the origin on $\mathbb{C}_0$, we have

$$\dot{W}=W_z\dot{z}+W_{\overline{z}}\overline{z},$$

by (5.4) and (5.5), we have

$$(A-2i\omega_0\tau_k)W_{20}(\theta)=-H_{20}(\theta),$$
$$AW_{11}(\theta)=-H_{11}(\theta),$$

hence for $-1\le\theta<0$ we have

$$H(z,\overline{z},\theta)=-2Re(\overline{q}^*(0)F_0q(\theta))=-g(z,\overline{z})q(\theta)-\overline{g}(z,\overline{z})\overline{q}(\theta).$$

By comparing the coefficients of z in $H(z,\overline{z},\theta)$, we have

$$H_{20}(\theta)=-g_{20}q(\theta)-\overline{g}_{02}\overline{q}(\theta),$$
$$H_{11}(\theta)=-g_{11}q(\theta)-\overline{g}_{11}\overline{q}(\theta).$$

Now, we have

$$\dot{W}_{20}(\theta)=2i\omega_0\tau_kW_{20}(\theta)+g_{20}q(\theta)+\overline{g}_{02}\overline{q}(\theta),$$
$$\dot{W}_{11}(\theta)=g_{11}q(\theta)+\overline{g}_{11}\overline{q}(\theta).$$

On integrating, we have

$$W_{20}(\theta)=\frac{ig_{20}}{\omega_0\tau_k}q(0)\exp(i\omega_0\tau_k\theta)+\frac{i\overline{g}_{20}\overline{q}(0)}{3\omega_0\tau_k}\exp(-i\omega_0\tau_k\theta)+E_1\exp(2i\omega_0\tau_k\theta),$$
$$W_{11}(\theta)=\frac{g_{21}}{i\omega_0\tau_k}q(0)\exp(i\omega_0\tau_k\theta)+\frac{i\overline{g}_{11}\overline{q}(0)}{\omega_0\tau_k}\exp(-i\omega_0\tau_k\theta)+E_2,$$

where E_1 and E_2 are to be determined. From definitions of A, the equation $(A-2i\omega_0\tau_k)W_{20}(\theta)=-H_{20}(\theta)$ gives us

$$\int_{-1}^{0}d\eta(\theta)W_{20}(\theta)=2i\omega_0\tau_kW_{20}(0)-H_{20}(0),$$

which gives us

$$H_{20}(0)=-g_{20}q(0)-\overline{g}_{02}\overline{q}(0)+2\tau_k\begin{bmatrix}-\frac{r}{k}-(\frac{r}{k}+\beta)\alpha_1-p_1\alpha_2\\ \beta\alpha_1-p_2\alpha_1\alpha_2\\ (q_1p_1\alpha_2+q_2p_2\alpha_1)\exp(-2i\omega_0\tau_k)\end{bmatrix}.$$

Now,

$$\Big(i\omega_0\tau_kI-\int_{-1}^{0}\exp(i\omega_0\tau_k\theta)d\eta(\theta)\Big)q(0)=0,$$
$$\Big(-i\omega_0\tau_kI-\int_{-1}^{0}\exp(-i\omega_0\tau_k\theta)d\eta(\theta)\Big)\overline{q(0)}=0.$$

We also have

$$\Big(2i\omega_0\tau_kI-\int_{-1}^{0}\exp(i\omega_0\tau_k\theta)d\eta(\theta)\Big)E_1=2\tau_k\begin{bmatrix}-\frac{r}{k}-(\frac{r}{k}+\beta)\alpha_1-p_1\alpha_2\\ \beta\alpha_1-p_2\alpha_1\alpha_2\\ (q_1p_1\alpha_2+q_2p_2\alpha_1)\exp(-2i\omega_0\tau_k)\end{bmatrix},$$

which leads to

$$\begin{bmatrix} a_{11} & S_*(\frac{r}{k}+\beta) & p_1S_* \\ -\beta I_* & a_{22} & p_2I_* \\ -q_1p_1Y_*\exp(-2i\omega_0\tau_k) & -q_2p_2Y_*\exp(-2i\omega_0\tau_k) & a_{33} \end{bmatrix} E_1 = 2\begin{bmatrix} -\frac{r}{k}-(\frac{r}{k}+\beta)\alpha_1-p_1\alpha_2 \\ \beta\alpha_1-p_2\alpha_1\alpha_2 \\ (q_1p_1\alpha_2+q_2p_2\alpha_1)\exp(-2i\omega_0\tau_k) \end{bmatrix},$$

where

$$a_{11}=2i\omega_0-(r-\frac{2rS_*}{k}-(\frac{r}{k}+\beta)I_*-p_1Y_*),\quad a_{22}=2i\omega_0-\beta S_*+c+d_2+p_2Y_*,$$
$$a_{33}=2i\omega_0+d_3-(q_1p_1S_*+q_2p_2I_*)\exp(-2i\omega_0\tau_k),$$

therefore,

$$\begin{aligned} E_1 &= 2\begin{bmatrix} -\frac{r}{k}-(\frac{r}{k}+\beta)\alpha_1-p_1\alpha_2 \\ \beta\alpha_1-p_2\alpha_1\alpha_2 \\ (q_1p_1\alpha_2+q_2p_2\alpha_1)\exp(-2i\omega_0\tau_k) \end{bmatrix} \\ &\quad\times\begin{bmatrix} a_{11} & S_*(\frac{r}{k}+\beta) & p_1S_* \\ -\beta I_* & a_{22} & p_2I_* \\ -q_1p_1Y_*\exp(-2i\omega_0\tau_k) & -q_2p_2Y_*\exp(-2i\omega_0\tau_k) & a_{33} \end{bmatrix}^{-1}. \end{aligned} \tag{5.6}$$

provided

$$\begin{bmatrix} a_{11} & S_*(\frac{r}{k}+\beta) & p_1S_* \\ -\beta I_* & a_{22} & p_2I_* \\ -q_1p_1Y_*\exp(-2i\omega_0\tau_k) & -q_2p_2Y_*\exp(-2i\omega_0\tau_k) & a_{33} \end{bmatrix}$$

is invertible.

Now, $\int_{-1}^{0} d\eta(\theta)W_{11}(\theta) = -H_{11}(0)$ and

$$H_{11}(0) = -g_{11}q(0)-\overline{g}_{11}\overline{q}(0)+2\tau_k\begin{bmatrix} -\frac{r}{k}-(\frac{r}{k}+\beta)Re(\alpha_1)-p_1Re(\alpha_2) \\ \beta Re(\alpha_1)-p_2Re(\alpha_1\alpha_2) \\ (q_1p_1Re(\alpha_2)+q_2p_2Re(\alpha_1) \end{bmatrix},$$

and hence this leads to the equation

$$\begin{bmatrix} b_{11} & S_*(\frac{r}{k}+\beta) & p_1S_* \\ -\beta I_* & b_{22} & p_2I_* \\ -q_1p_1Y_* & -q_2p_2Y_* & b_{33} \end{bmatrix} E_2 = 2\begin{bmatrix} -\frac{r}{k}-(\frac{r}{k}+\beta)Re(\alpha_1)-p_1Re(\alpha_2) \\ \beta Re(\alpha_1)-p_2Re(\alpha_1\alpha_2) \\ (q_1p_1Re(\alpha_2)+q_2p_2Re(\alpha_1) \end{bmatrix},$$

where

$$b_{11}=(r-\frac{2rS_*}{k}-(\frac{r}{k}+\beta)I_*-p_1Y_*),\quad b_{22}=-\beta S_*+c+d_2+p_2Y_*,$$
$$b_{33}=d_3-(q_1p_1S_*+q_2p_2I_*).$$

Then E_2 can be obtained as

$$E_2 = 2\begin{bmatrix} -\frac{r}{k}-(\frac{r}{k}+\beta)Re(\alpha_1)-p_1Re(\alpha_2) \\ \beta Re(\alpha_1)-p_2Re(\alpha_1\alpha_2) \\ (q_1p_1Re(\alpha_2)+q_2p_2Re(\alpha_1) \end{bmatrix}\begin{bmatrix} b_{11} & S_*(\frac{r}{k}+\beta) & p_1S_* \\ -\beta I_* & b_{22} & p_2I_* \\ -q_1p_1Y_* & -q_2p_2Y_* & b_{33} \end{bmatrix}^{-1}.$$

provided

$$\begin{bmatrix} b_{11} & S_*(\frac{r}{k}+\beta) & p_1S_* \\ -\beta I_* & b_{22} & p_2I_* \\ -q_1p_1Y_* & -q_2p_2Y_* & b_{33} \end{bmatrix}$$

is invertible.

By putting values of E_1 and E_2 we can obtain $W_{20}(\theta)$ and $W_{11}(\theta)$ and hence g_{21} is completely determined. Hence as stated in [12, 5], we can obtain the following values:

$$\begin{aligned} c_1(0) &= \frac{i}{2\omega_0\tau_k}(g_{11}g_{20} - 2 \mid g_{11} \mid^2 - \frac{\mid g_{02} \mid^2}{3}) + \frac{g_{21}}{2}, \\ \mu_2 &= -\frac{Re(c_1(0))}{Re(\lambda'(\tau_k))}, \\ \beta_2 &= 2Re(c_1(0)), \\ T_2 &= -\frac{1}{\omega_0\tau_k}[\mathrm{Im}(c_1(0)) + \mu_2\,\mathrm{Im}(\lambda'(\tau_k))], \end{aligned} \tag{5.7}$$

which determines the direction and stability of the model with delay at the critical value τ_k. Now, we state the following main theorem of this section due to [5, 12, 6]

Theorem 5.1. (i) *The sign of μ_2 determined the direction of Hopf bifurcation. If $\mu_2 > 0 (\mu_2 < 0)$, then the Hopf bifurcation is supercritical (sub critical).*

(ii) *The stability of bifurcated periodic solutions is determined by β_2. The periodic solutions are stable if $\beta_2 < 0$ and unstable if $\beta_2 > 0$.*

(iii) *The period of bifurcated periodic solutions is determined by T_2. The period increases if $T_2 > 0$ and decreases if $T_2 < 0$.*

6. Numerical example

In this section, we consider a numerical example and generate some numerical simulations to verify our theoretical calculations. As an example, we choose the set of parameters in Table 4. The initial values are taken as $S(0) = 0.9$, $I(0) = 0.9$, $Y(0) = 0.2$.

Table 4. Parameter values

Parameter	Numerical Value	Source
r	1/2	Hu and Li [5]
k	1	Hu and Li [5]
β	1	Hu and Li [5]
p_1	1/8	Hu and Li [5]
p_2	6	Hu and Li [5]
d_2	1/4	assumed
d_3	1/2	assumed
c	1/4	Hu and Li [5]
q_1	1/2	assumed
q_2	3/4	assumed

It is observed that the system has the equilibrium points $(0, 0, 0) = E_{10}$, $(1, 0, 0) = E_{11}$, $(\frac{1}{2}, \frac{1}{6}, 0) = E_{12}$ and $E_5 = (\frac{31}{48}, \frac{353}{1728}, \frac{7}{6}) = E_*$ and all are locally stable. The equilibrium point $(\frac{4}{3}, 0, \frac{-4}{3}) = E_{13}$ does not exist. By calculation, it is observed that $\omega_0 = 0.3694$ and $\tau_0 = 1.5326$. Thus positive equilibrium E_* is asymptotically

stable when $0 < \tau < \tau_0 = 1.5326$. The system undergoes a Hopf bifurcation when system crosses through τ_0. Few numerical simulations are represented by using MATLAB.

It is observed from numerical simulations that the phase diagram of the system changes with slight changes in the initial values. First two figures (1 and 2) are drawn for the value of $\tau = \tau_0 = 1.5326$ and $\tau = 3.6249 > \tau_0 = 1.5326$ respectively. From theoretical foundation it is observed that system is stable up to the critical value of time delay τ. Critical value is calculated in (4.6). Beyond the critical value of τ, Hopf bifurcation occurs. It is also observed in simulations. It is easy to see that system undergoes Hopf bifurcation (See Figures 1 and 2). The simulations are taken for the time interval $[0, 1000]$. For the simulation interval $[0, 1000]$. From Figure 1, it is found that all the three populations are unstable with respect to time. Similar explanation is concluded from Figure 3. Figure 3 shows the stable nature of positive equilibrium which is drawn for $\tau = 1.1026 < 1.5326 = \tau_0$, which is again consistent with the theoretical formulation. Therefore, numerical simulations are consistent with the theoretical formulation. If we choose the different set of values of the parameters q_1 and q_2 with the same other parameters and initial values, we may have different figures (see Remark 3.2, 4.4).

7. Discussion and future directions

In the present study, we have considered an eco-epidemiological model with disease in the prey population only. We have considered both cases with delay and without delay for analysis purpose. Local stability of all equilibrium points has been discussed. We have found the time delay as a game changer. This has been observed that time delay τ may change the stability and even bifurcation may occur. Hopf-bifurcation analysis is presented, by the application of famous normal form theory, Riesz representation theorem and central limit theorem, stability and direction of bifurcated periodic solutions have been investigated. Our analytical results has been compared with those in [5], when $d_2 = 0$ and $q_1 = q_2 = q$.

Stability of the non zero (positive) equilibrium E_5 indicates the existence and survival of all the three species in the ecosystem. Ecologically this equilibrium is very important, because it provides actual interaction among all the three living components of the ecosystem. Actual balance is maintained under this situation. Ecologists are interested to observe the stability of non zero equilibrium point. It is also remarkable that we classify our analysis in two parts (i) without delay (ii) with delay. Ecologically, corresponding equilibrium points listed for our models (2.1) and (3.1) are same. For example, ecologically, E_5 and E_* are same but mathematically both are different.

Theoretically, we can consider few examples of different ecosystems. If we consider Desert, Tundra, Savana geographical areas and consider an ecosystem from this area. Then positive equilibrium is more important, because in these areas many predators are going to decline or decay because their prey are also facing natural problems like climate changes, lake of water, low quality of oxygen etc. and they also decaying, therefore in such geographical areas the predator population is not in position to catch their prey as they are limited and therefore they remain hungry for most of the times, finally predator population starts decaying. For the ecological imbalance in such ecosystems, the main reason is the change in climate. Besides cutting of trees and global warming are also important environmental issues. Thus

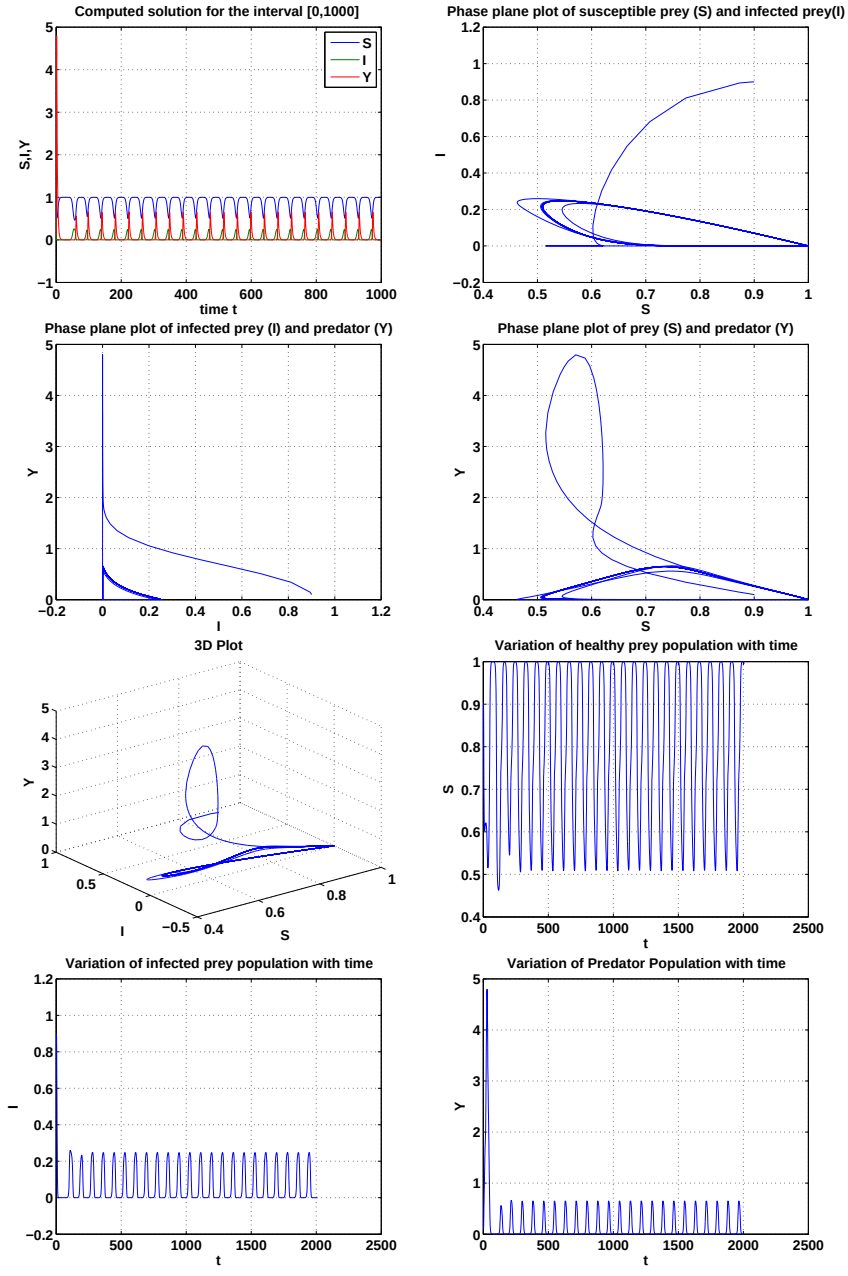


FIGURE 1. Phase portrait of model with parameter values in Table 4 with initial values $S(0) = 0.9$, $I(0) = 0.9$, $Y(0) = 0.2$

positive equilibrium can never exists, however if it exists, then not stable. If we consider hilly areas and consider an ecosystem from this area, then the cutting of trees and farming are two issues which are responsible for disturbance of climate in this

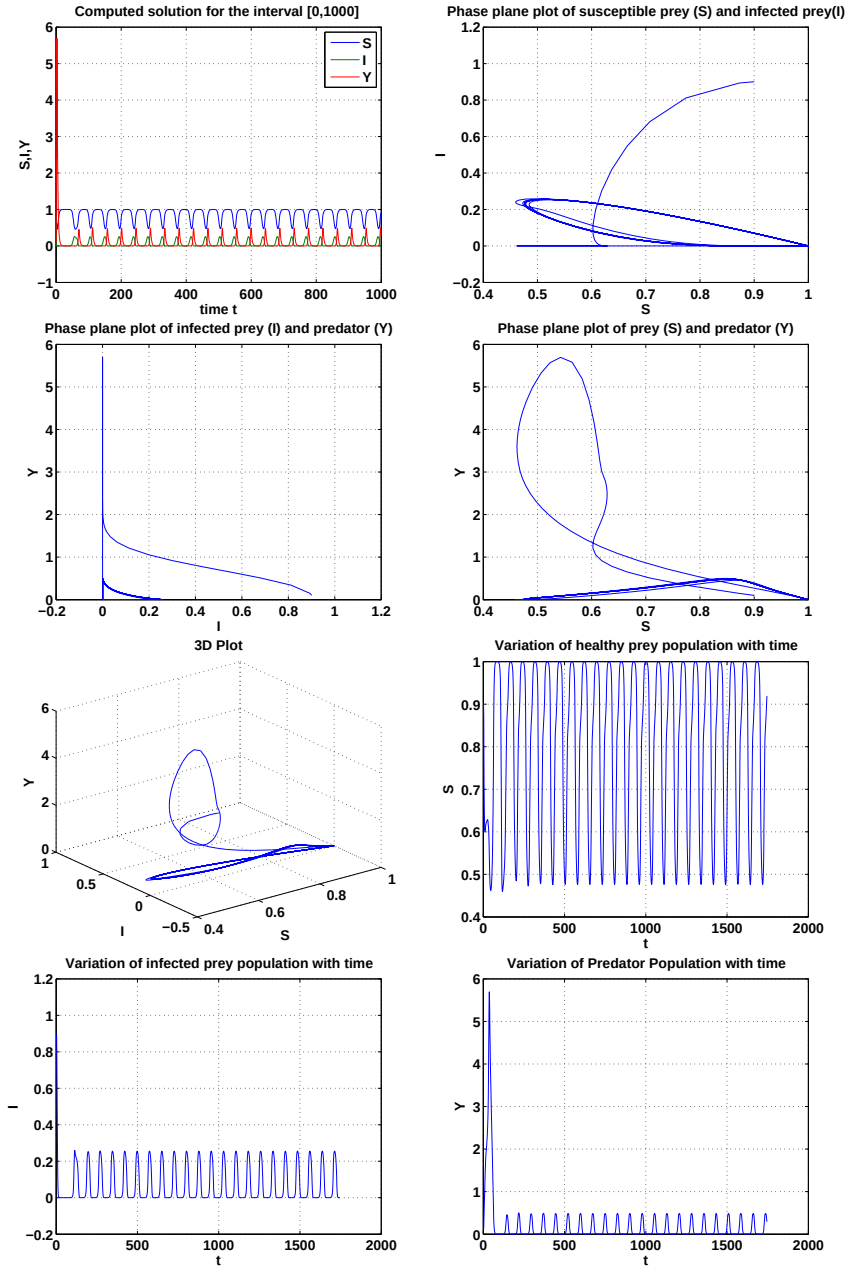


FIGURE 2. Phase portrait of model with parameter values in Table 4 with initial values $S(0) = 0.9$, $I(0) = 0.9$, $Y(0) = 0.2$

area. In near past, one natural disaster in Uttarakhand (India) occurred, possibly because of cutting of trees and other developmental projects. This changed the climate in hilly areas as well. This occurs the ecological imbalance in these areas and

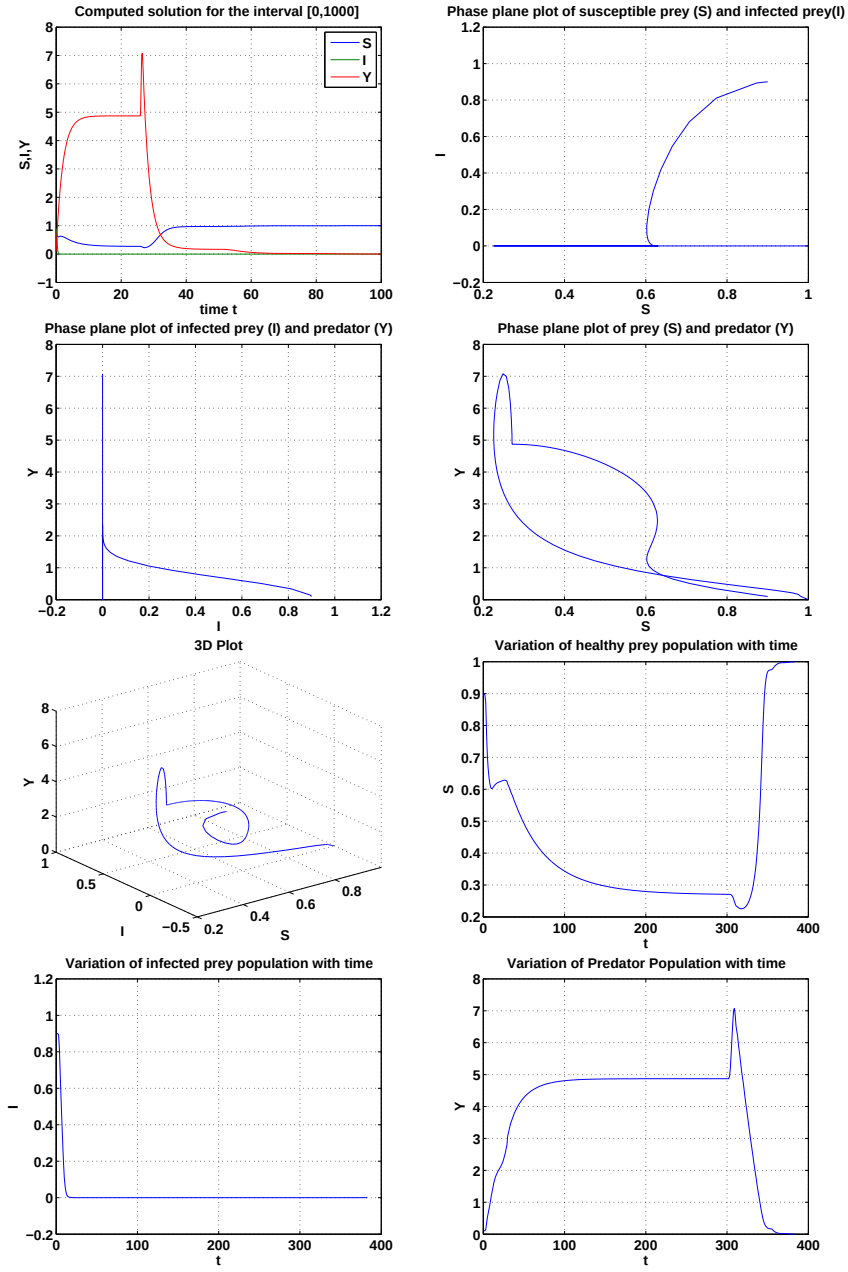


FIGURE 3. Phase portrait of model with parameter values in Table 4 with initial values $S(0) = 0.9$, $I(0) = 0.9$, $Y(0) = 0.2$

disturbs the natural ecosystems. Prey and predator both decays simultaneously due to unexpected mortality in the system. Thus if the positive equilibrium exists and is stable then the stability losses due to disaster. Similarly, if we choose the

aquatic ecosystem of any river in India, then the water pollution is a major factor in this ecosystem. Pollution disturbs the stability of the ecosystem and disturbs the ecological balance. Positive equilibrium may loose stability in such ecosystems as well. If we consider an ecosystem from green forest where pollution, weather conditions etc. are favorable for living species then actual prey-predation interaction will be occurred. In this situation, if the positive equilibrium exists and is stable this will provide the coexistence of all the three species. Thus equilibrium points E_5 and E_*, if exists, are stable for an ecosystem from a forest area.

The parameters considered for numerical computation are purely imaginary and are suitably selected and are quite similar to result discussed in [5]. An attempt may be done to estimate real parameters and these parameters may fit with the present mathematical model. This task may be achieved by real data collection from field. Further, to study the model more scientifically, control strategies may also be investigated. This study may have applications with real ecosystems and biomass available in the real world.

8. Appendix

Appendix 1: C_i, $i = 1, 2, 3$ **of** (3.6).

$$C_1 = -\Big((r - d_2 - d_3 - c) + \widetilde{S}[-\frac{2r}{k} + \beta + q_1p_1] + \widetilde{I}[-\frac{r}{k} + q_2p_2 - \beta] - \widetilde{Y}(p_1 + p_2)\Big),$$

$$\begin{aligned}
C_2 = {} & \widetilde{S}^2[\beta q_1p_1 - \frac{2rq_1p_1}{k} - \frac{2r\beta}{k}] + \widetilde{Y}^2[p_1p_2] + \widetilde{I}^2[(\frac{r}{k} + \beta)q_2p_2] \\
& + \widetilde{S}\widetilde{I}[\beta q_2p_2 - \frac{2rq_2p_2}{k} - (\frac{r}{k} + \beta)q_1p_1] + \widetilde{S}\widetilde{Y}[-q_1p_1p_2 - q_1p_1^2 + \frac{2rp_2}{k} - p_1\beta] \\
& + \widetilde{I}\widetilde{Y}[-q_2p_1p_2 + (\frac{r}{k} + \beta)p_2] + \widetilde{S}\Big[-\beta d_3 - (c + d_2)q_1p_1 + rq_1p_1 + \frac{2rd_3}{k} \\
& + r\beta + \frac{2r(c + d_2)}{k}\Big] \\
& + \widetilde{I}\Big[-(c + d_2)q_2p_2 + rq_2p_2 + (\frac{r}{k} + \beta)d_3 + (\frac{r}{k} + \beta)(c + d_2)\Big] \\
& + \widetilde{Y}\Big[d_3p_1 - rp_2 + p_1(c + d_2)\Big] + \Big[d_3(c + d_2) - rd_3 - r(c + d_2)\Big],
\end{aligned}$$

$$\begin{aligned}
C_3 = {} & -\Big(\widetilde{S}^3[-\frac{2rq_1p_1\beta}{k}] + \widetilde{S}^2\widetilde{Y}[\frac{2rq_1p_1p_2}{k}] + \widetilde{S}^2\widetilde{I}[\frac{2rq_1p_1p_2}{k}] + \widetilde{I}^2\widetilde{Y}[(\frac{r}{k} + \beta)q_2p_2^2] \\
& + \widetilde{Y}^2\widetilde{I}[q_2p_2^2p_1] + \widetilde{S}\widetilde{I}\widetilde{Y}\Big[-\frac{2rq_2p_2^2\beta}{k} + 2(\frac{r}{k} + \beta)q_1p_1p_2 - 2\beta q_2p_1p_2\Big] \\
& + \widetilde{S}^2\Big[\beta rq_1p_1 + \frac{2rd_3\beta}{k} + \frac{2rq_1p_1(c + d_2)}{k}\Big] \\
& + \widetilde{I}^2[(\frac{r}{k} + \beta)q_2p_2(c + d_2)] + \widetilde{Y}^2[d_3p_1p_2] \\
& + \widetilde{S}\widetilde{I}\Big[\beta rq_2p_2 + \frac{2rq_2p_2(c + d_2)}{k} + (\frac{r}{k} + \beta)(c + d_2)q_1p_1\Big] \\
& + \widetilde{S}\widetilde{Y}[-rq_1p_1p_2 + \frac{2rp_2d_3}{k} + d_3\beta p_1] \\
& + \widetilde{I}\widetilde{Y}\Big[-rq_2p_2^2 + (\frac{r}{k} + \beta)d_3p_2 + (c + d_2)q_2p_1p_2\Big]
\end{aligned}$$

$$
\begin{aligned}
&+\widetilde{S}\Big[-d_3r\beta - r(c+d_2)q_1p_1 - \frac{2r(c+d_2)d_3}{k}\Big]\\
&+\widetilde{I}\Big[-r(c+d_2)q_2p_2 - (\frac{r}{k}+\beta)(c+d_2)d_3\Big]\\
&+\widetilde{Y}\Big[-d_3p_2r - (c+d_2)d_3p_1\Big] + r(c+d_2)d_3\Big).
\end{aligned}
$$

Appendix 2: m_i, n_j**,** $i=0,1,2$**;** $j=0,1,2$ **of** (4.2)**.**

$$
m_2 = \Big(\frac{2r}{k} + \frac{p_1\beta}{p_2} - \frac{q_1p_1\beta}{q_2p_2}S_*\Big) + \Big(\frac{rd_3}{q_2p_2k} + d_3 - \frac{p_1(c+d_2)}{p_2} - r\Big),
$$

$$
\begin{aligned}
m_1 = \Big(&\{d_3(c+d_2) - r(c+d_2)\} + S_*\{-d_3\beta + \frac{2r}{k}d_3 + r\beta + \frac{2r}{k}(c+d_2)\}\\
&+ I_*\{(\frac{r}{k}+\beta)(d_3+c+d_2)\} + Y_*\{d_3p_2 + d_3p_1 + (c+d_2)p_1 + (r)p_2\}\\
&+ S_*^2(-\frac{2r\beta}{k}) + Y_*^2(p_1p_2) + S_*Y_*(-\beta p_1 + \frac{2r}{K}p_2) + I_*Y_*(\frac{r}{k}+\beta)p_2\Big),
\end{aligned}
$$

$$
\begin{aligned}
m_0 = \Big(&\{-r(c+d_2)d_3 + S_*\{d_3\beta r + \frac{2r}{k}d_3\}(c+d_2)\} + I_*\{d_3(c+d_2)(\frac{r}{k}+\beta)\}\\
&+ Y_*\{d_3(c+d_2)p_1 - rd_3p_2\} + S_*^2(-\frac{2r}{k}d_3\beta) + Y_*^2(d_3p_2p_1)\\
&+ S_*Y_*\{-d_3\beta p_1 - \frac{2r}{k}d_3p_2\} + I_*Y_*\{(\frac{r}{k}+\beta)p_2d_3\}\Big),
\end{aligned}
$$

$$
n_2 = -d_3,
$$

$$
\begin{aligned}
n_1 = \Big(&S_*^2\{q_1p_1\beta - \frac{-2r}{k}q_1p_1\} + I_*^2\{-(\frac{r}{k}+\beta)q_2p_2\}\\
&+ S_*Y_*\{-q_1p_2p_1\} + S_*I_*\{q_2p_2\beta + \frac{2r}{k}q_2p_2\} + Y_*I_*\{-q_2p_2p_1\}\\
&+ S_*\{\{-(c+d_2) - r\}q_1p_1\} + I_*\{-(c+d_2)q_2p_2 + rq_2p_2\}\Big),
\end{aligned}
$$

$$
\begin{aligned}
n_0 = -\Big(&S_*^2\{q_1p_1\beta(r - \frac{2r}{k}) + \frac{2r}{k}(c+d_2)q_1p_1 - q_1p_1^2\beta\} + I_*^2\{(\frac{r}{k}+\beta)(c+d_2)q_2p_2\\
&+ S_*^2Y_*\{\frac{2r}{k}q_1p_1p_2 + q_1p_1^2\beta\} + S_*^2I_*\{-\frac{2r}{k}q_2p_2\beta\} + S_*I_*Y_*\{(\frac{r}{k}+\beta)q_1p_1p_2\\
&- 2\beta q_2p_1p_2\} + S_*Y_*\{\{-r + (\frac{r}{k}+\beta)\}q_1p_1p_2\}\\
&+ S_*I_*\{\beta r q_2p_2 + \frac{2r}{k}(c+d_2)q_2p_2 + (c+d_2)(\frac{r}{k}+\beta)q_1p_1\}\\
&+ Y_*I_*\{(c+d_2)q_2p_2p_1\} + S_*\{(c+d_2)rq_1p_1\} + I_*\{-(c+d_2)rq_2p_2\}\Big).
\end{aligned}
$$

Appendix 3. We have

$$
g(z,\overline{z}) = g_{20}(\theta)\frac{z^2}{2} + g_{02}(\theta)\frac{\overline{z}^2}{2} + g_{11}(\theta)z\overline{z} + g_{21}\frac{\overline{z}z^2}{\lfloor 3} + \dots,
$$

$$
\begin{aligned}
g(z,\overline{z}) &= (\overline{q}^*)^T F(z,\overline{z})\\
&= \tau_k\overline{B}(1,\alpha_1^*,\alpha_2^*)\begin{pmatrix} -\frac{r}{k}u_1^2(t) - (\frac{r}{k}+\beta)u_1(t)u_2(t) - p_1u_1(t)u_3(t)\\ \beta u_1(t)u_2(t) - p_2u_2(t)u_3(t)\\ p_1q_1u_1(t-1)(t)u_3(t-1) + p_2q_2u_1(t-1)u_2(t-1),\end{pmatrix}
\end{aligned}
$$

further, it is noticed that

$$\begin{aligned}
u(t+\theta) &= W(t,\theta) + z(t)q(\theta) + \overline{z}(t)\overline{q}(\theta),\\
u_1(t) &= z + \overline{z} + W^{(1)}(t,0),\\
u_2(t) &= \alpha_1 z + \overline{\alpha_1 z} + W^{(2)}(t,0),\\
u_3(t) &= \alpha_2 z + \overline{\alpha_2 z} + W^{(3)}(t,0),\\
u_1(t-1) &= z\exp(-i\omega_0\tau_k) + \overline{z}\exp(i\omega_0\tau_k) + W^{(1)}(t,-1),\\
u_2(t-1) &= \alpha_1 z\exp(-i\omega_0\tau_k) + \overline{\alpha_1 z}\exp(i\omega_0\tau_k) + W^{(2)}(t,-1),\\
u_3(t-1) &= \alpha_2 z\exp(-i\omega_0\tau_k) + \overline{\alpha_2 z}\exp(i\omega_0\tau_k) + W^{(3)}(t,-1),
\end{aligned}$$

hence

$$\begin{aligned}
g(z,\overline{z}) &= \tau_k\overline{B}[-\frac{r}{k}u_1^2(t) - (\frac{r}{k}+\beta)u_1(t)u_2(t) - p_1u_1(t)u_3(t)\\
&\quad + \overline{\alpha_1}^*\{\beta u_1(t)u_2(t) - p_2u_2(t)u_3(t)\}\\
&\quad + \overline{\alpha_2}^*\{p_1q_1u_1(t-1)(t)u_3(t-1) + p_2q_2u_1(t-1)u_2(t-1)\}],
\end{aligned}$$

putting the values of u_1, u_2, u_3, $u_1(t-1)$, $u_2(t-1)$, $u_3(t-1)$ etc. in $g(z,\overline{z})$, we obtain

$$\begin{aligned}
g(z,\overline{z}) &= \tau_k\overline{B}\Big(-\frac{r}{k}[z+\overline{z}+W^{(1)}(t,0)]^2 - (\frac{r}{k}+\beta)[z+\overline{z}+W^{(1)}(t,0)][\alpha_1 z\\
&\quad + \overline{\alpha_1 z} + W^{(2)}(t,0)] - p_1[z+\overline{z}+W^{(1)}(t,0)][\alpha_2 z + \overline{\alpha_2 z} + W^{(3)}(t,0)]\\
&\quad + \overline{\alpha_1}^*(\beta[z+\overline{z}+W^{(1)}(t,0)][\alpha_1 z + \overline{\alpha_1 z} + W^{(2)}(t,0)]\\
&\quad - p_2[\alpha_1 z + \overline{\alpha_1 z} + W^{(2)}(t,0)][\alpha_2 z + \overline{\alpha_2 z} + W^{(3)}(t,0)])\\
&\quad + \overline{\alpha_2}^*(p_1q_1[z\exp(-i\omega_0\tau_k) + \overline{z}\exp(i\omega_0\tau_k) + W^{(1)}(t,-1)]\\
&\quad \times [\alpha_2 z\exp(-i\omega_0\tau_k) + \overline{\alpha_2 z}\exp(i\omega_0\tau_k) + W^{(3)}(t,-1)]\\
&\quad + p_2q_2[z\exp(-i\omega_0\tau_k) + \overline{z}\exp(i\omega_0\tau_k) + W^{(1)}(t,-1)]\\
&\quad \times [\alpha_1 z\exp(-i\omega_0\tau_k) + \overline{\alpha_1 z}\exp(i\omega_0\tau_k) + W^{(2)}(t,-1)])\Big),
\end{aligned}$$

from this equation we can find the values of the coefficients $g_{20}(\theta)$, $g_{02}(\theta)$, $g_{11}(\theta)$, $g_{21}(\theta)$ etc. by comparing the same powers of z, we have

$$\begin{aligned}
g_{20} &= 2\tau_k\overline{B}\{-\frac{r}{k} - (\frac{r}{k}+\beta)\alpha_1 - p_1\alpha_2 + \beta\overline{\alpha_1}^*\alpha_1 - \overline{\alpha_1}^*\alpha_1\alpha_2p_2\\
&\quad + \overline{\alpha_2}^*(p_1q_1\alpha_2 + p_2q_2\alpha_1)\exp(-2i\omega_0\tau_k)\},
\end{aligned}$$

$$\begin{aligned}
g_{11} &= \tau_k\overline{B}(-\frac{2r}{k} + (\overline{\alpha_1}^*)\beta + \overline{\alpha_2}^*p_2q_2 - \frac{r}{k}+\beta)(\overline{\alpha_1}+\alpha_1)\\
&\quad + (\overline{\alpha_2}^*p_1q_1 - p_1)(\overline{\alpha_2}+\alpha_2) - \overline{\alpha_1}^*p_2(\overline{\alpha_2}\alpha_1 + \overline{\alpha_1}\alpha_2)),
\end{aligned}$$

$$\begin{aligned}
g_{02} &= 2\tau_k\overline{B}\{-\frac{r}{k} - (\frac{r}{k}+\beta)\overline{\alpha_1} - p_1\overline{\alpha_2} + \beta\overline{\alpha_1}^*\overline{\alpha_1} - \overline{\alpha_1}^*\overline{\alpha_1\alpha_2}p_2\\
&\quad + \overline{\alpha_2}^*(p_1q_1\overline{\alpha_2} + p_2q_2\overline{\alpha_1})\exp(2i\omega_0\tau_k)\},
\end{aligned}$$

$$\begin{aligned}
g_{21} &= 2\tau_k\overline{B}\Big(-\frac{r}{k}(2W_{11}^{(1)}(0) + W_{20}^{(1)}(0)) - (\frac{r}{k}+\beta)[W_{11}^{(2)}(0) + \alpha_1W_{11}^{(1)}(0)\\
&\quad + \frac{1}{2}\overline{\alpha_1}W_{20}^{(1)}(0) + \frac{1}{2}W_{20}^{(1)}(0)] - p_1\big[W_{11}^{(3)}(0) + \frac{1}{2}W_{20}^{(3)}(0) + \alpha_2W_{11}^{(1)}(0)
\end{aligned}$$

$$+\frac{1}{2}W_{20}^{(1)}(0)]+\overline{\alpha_1}^*\beta[W_{11}^{(2)}(0)+\frac{1}{2}W_{20}^{(2)}(0)+\alpha_1W_{11}^{(1)}(0)+\frac{1}{2}\overline{\alpha_1}W_{20}^{(1)}(0)]$$
$$-\overline{\alpha_1}^*p_2[\alpha_1W_{11}^{(3)}(0)+\alpha_2W_{11}^{(2)}(0)+\frac{1}{2}\overline{\alpha_2}W_{20}^{(2)}(0)+\frac{1}{2}\overline{\alpha_1}W_{20}^{(3)}(0)]$$
$$+\overline{\alpha_2}^*p_1q_1[W_{11}^{(3)}(-1)e^{-i\omega_0\tau_k}+\alpha_2W_{11}^{(1)}(-1)e^{-i\omega_0\tau_k}+\frac{1}{2}W_{20}^{(3)}(-1)e^{i\omega_0\tau_k}$$
$$+\frac{1}{2}W_{20}^{(1)}(-1)e^{i\omega_0\tau_k}]+\overline{\alpha_2}^*p_2q_2[W_{11}^{(2)}(-1)e^{-i\omega_0\tau_k}+\alpha_1W_{11}^{(-1)}e^{-i\omega_0\tau_k}$$
$$+\frac{1}{2}W_{20}^{(2)}(-1)e^{i\omega_0\tau_k}+\frac{1}{2}W_{20}^{(1)}(-1)\overline{\alpha_1}e^{i\omega_0\tau_k}]\Big).$$

References

[1] Berthier, K.; Langlais, M.; Auger, P.; Pontier, D.; Dynamics of a feline virus with two transmission medels with exponentially growing host populations. *Proc. Roy. Soc. Lond.* 3267 (2000): 2049–2056 http: //www.ncbi.nlm.nih.gov/pubmed/11416908

[2] Chattopadhyay, J.; Arino, O.; A predator-prey model with disease in prey. *Non Linear Analysis* 36 (1999): 747–766 http: //repository.ias.ac.in/7560/1/411.pdf

[3] Haque, M; Zhen, J; Ventrino, E; An eco-epidemiological predator-prey model with standard disease incidence. *Mathematical Methods in the Applied Sciences* http: //dx.doi.org /10.1002/mma.1071, 2008.

[4] Hilker, F. M.; Schmitz, K.; Disease-induced stabilization of predator prey oscillations. *Journal of Theoretical Biology* 255 (2008): 299–306 http: //dx.doi.org/10.1016/j.jtbi.2008.08.018

[5] Hu, G.-P.; Li, X.-L.; Stability and Hopf bifurcation for a delayed predator-prey model with disease in the prey. *Chaos, Solitons and Fractals* 45 (2012): 229–237 http: //dx.doi.org/10.1016 /j.chaos.2011.11.011

[6] Jana, S.; Kar, T. K.; Modeling and Analysis of a prey-predator system with disease in the prey. *Chaos, Solitons and Fractals* 47 (2013): 42–53 http: //dx.doi.org/10.1016 /j.chaos.2012.12.002

[7] De Jong, M. C. M.; et al; How does infection depend on the population size? in D. Mollison(Ed.), Epidemic Models, their structure and Relation in data. *Cambridge University Press*, 1994. http: //igitur-archive.library.uu.nl/vet

[8] Greenhalgh, D.; Haque, M.; A predator-prey model with disease in the prey species only. *Math. Methods Appl. Sci.* 30 (2007): 911–929. http: //dx.doi.org/10.1002/mma.815

[9] Kermack, W. O.; Mckendrick, A. G.; Contributons to the mathematical Theory of Epidimics, Part 1. *Proc. Roy. Soc. A* 115 (1927): 700–721 http: //rspa.royalsocietypublishing.org /content/115/772/700.full.pdf+html

[10] Haque, M.; Venturino, E.; Increase of the prey may decrease the healthy prtedator population in presence of a disease in predator. *HERMIS* 7 (2006): 38-59 http: //www.aueb.gr /pympe/hermis/hermis-volume-7

[11] Litao, H.; Zhien, M. A.; Four Predator Prey Models with Infectious Diseases. *Mathematical and Computer Modeling* 34 (2001): 849–858 http: //homepage.math.uiowa.edu/ hethcote/PDFs/2001MathCompMod.pdf

[12] Karaaslanli, C. C.; Bifurcation Analysis and Its Applications, Chapter 1 in: Mykhaylo Andriychuk (Ed.),Numerical Simulation: From Theory to Industry. (2012) 1-34 http: //dx.doi.org/10.5772/50075

[13] Lotka, A.; Elements of Physical Biology. *Williams and Wilkins, Baltimore.*

[14] Maoxing, L.; Zhen, J.; Haque, M.; An Impulsive predator-prey model with communicable disease in the prey species only. *Non Linear analysis: Real World Applications* 10 (2009): 3098–3111 http: //dx.doi.org/10.1016/j.nonrwa.2008.10.010

[15] Mukhopadhyaya, B.; Bhattacharyya, R.; Dynamics of a delay-diffusion prey-predator Model with disease in the prey. *J. Appl. Math and Computing* 17 (2005): 361–377 http: //dx.doi.org/10.1007/BF02936062

[16] Naji, R. K.; Mustafa, A. N.; The Dynamics of an Eco-Epidemiological Model with Nonlinear Incidence Rate. *Journal of Applied Mathematics* http: //dx.doi.org/10.1155/2012/852631, 2012.

[17] Samanta, G. P.; Analysis of a delay nonautonomous predator-prey system with disease in the prey. *Non Linear Analysis: Modeling and Control* 15 (2010): 97–108.
[18] Sophia Jang, R.-J.; Baglama, J.; Continous-time predator-prey models with parasites. *J. Bio. Dyn* 3 (2009): 87–98 http: //dx.doi.org/10.1080/1751375080228325
[19] Volterra, V.; Variazioni e fluttauazionidel numero d individui in species animals conviventii. *Mem Acd. Linciei* (1926) 231–33.
[20] Wang, F.; Kuang, Y.; Ding, C.; Zhang, S.; Stability and bifurcation of a stage-structured predator-prey model with both discete and distributed delays, *Chaos, Solitons and Fractals* 46 (2013): 19–27 http: //dx.doi.org/10.1016/j.chaos.2012.10.003
[21] Yanni, X.; Chen, L.; Modeling and analysis of a predator-prey model with disease in the prey. *Mathematical Biosciences* 171 (2001): 59–82 http: /dx.doi.org/10.1016/S0025-5564(01)00049-9
[22] Yang, K.; Delay differential equations with applications in population dynamics. *Academic Press, INC.*, 1993.

Shashi Kant
Department of Applied Mathematics, Delhi Technological University, Delhi 110042, India
E-mail address: onlineskmishra@gmail.com

Vivek Kumar
Department of Applied Mathematics, Delhi Technological University, Delhi 110042, India
E-mail address: vivek_ag@iitkalumni.org

Asian Journal of Applied Science and Technology (AJAST)

Volume 1, Issue 7, Pages 158-167, August 2017

Effect of Malathion on Seed Germination and Photosynthetic Pigments in Wheat (*Triticum aestivum* L.)

Satish Kumar[1] and Jai Gopal Sharma[2*]

[1,2]*Department of Biotechnology, Delhi Technological University, Delhi- 110042, India.*
**Email: sharmajaigopal@gmail.com*

Article Received: 24 July 2017 *Article Accepted: 17 August 2017* *Article Published: 23 August 2017*

ABSTRACT

Background: Malathion belongs to organophosphates class of synthetic pesticide. It is widely used as an effective insecticide. The main purpose of this study is to evaluate the significant effect of malathion at different concentrations towards seed germination and estimate the content of various photosynthetic pigments in *Triticum aestivum* L.

Methods: Two different methods have been applied for this study, first moist sterile Whatman No. 2 filter paper in petri dish and second with sterile soil in plastic ice-cream cups. Qualitative and quantitative estimations of the photosynthetic pigments such as chlorophyll, xanthophyll and carotenoid etc. were performed by thin layer chromatography and biospectrophotometer respectively.

Results: The percentage germination and growth of seedling in term of shoot length were enhanced in lower concentrations (2ppm to 10ppm) as compared to control on filter paper. However soil morphogenic response significantly declined with increasing concentration. Photosynthetic pigments significantly reduced with increasing concentrations of malathion as compared to control.

Conclusion: We observed that malathion at 100 ppm shown adverse effect on germination and growth, but still growing the seedling.

Keywords: Malathion, Seed germination, Photosynthetic pigments, Thin layer chromatography, *Triticum aestivum*

1. INTRODUCTION

Malathion is an important member of organophosphates (OP), which is commonly known as carbophos, maldison and mercaptothion, and chemically known as [S-(1, 2-dicarbethoxyethyl)-O, O-dimethyl dithio-phosphate]. Malathion is a non-systemic, wide-spectrum insecticide that has been registered for use in the United States since 1956. Malathion is used in agriculture, residential gardens, public recreation areas, and in public health pest control programs [1]. Malathion may be found in some cosmetic items like special shampoos for the treating lice. When applied in accordance with the rate of application and safety precautions specified on the label, malathion can be used to kill mosquitoes without posing unreasonable risks to human health or the environment. However, at high doses, malathion, like other organophosphates, can over stimulate the nervous system causing nausea, dizziness, or confusion. Severe high-dose poisoning with any organophosphate can cause convulsions, respiratory paralysis, and death [2]. People who apply products containing malathion may be exposed if they do not wear the proper protective equipment. Consumption of food that has been treated with malathion may also result in detrimental effects. [3&4].

The higher concentration (300 ppm) of malathion has been shown to toxic effect on seeds germination, starch, amino acid and protein content. A person who was exposed to enough amount of malathion to responsible many health problem like vomited, weakness, shortness of breath, a slowed heart rate, headache and diarrhea [1&5]. Pets may be exposed to malathion if they get into contact by accident or eat plants that have just been sprayed. The

nervous system is very similar in people and other animals, so animals poisoned by malathion may show signs similar to those observed in people [6]. Bacteria may break down malathion in soil and sunlight can also break down malathion in the air. Less amount of malathion mixed with water and can move quickly through soil. Because of these properties, malathion can be found in surface waters such as streams, and sometimes it is found in well water. The time it takes for malathion to break down to half of the original amount in soil is about 17 days, depending on the soil type. This length of time is known as the half-life. In water, malathion has a half-life between 2 to 18 days, depending on conditions like temperature and pH. malathion vapor may also move long distances in air or fog. [7]

Cereals are one of the most traditional forms of carbohydrate and minerals intake amongst the Indian population. *Triticum aestivum* commonly known as wheat is one of the most important cereal crops cultivated since ancient times in India, with Uttar Pradesh followed by Punjab being the highest producer of wheat as a cereal crop. It is a carbohydrate and vitamin rich staple food containing about 23 % total carbohydrate content on dry weight basis, and 339 Calories per 100 gm. Apart from being an important source of carbohydrate in the human diet, wheat plants are also a source of fodder for cattle's. Some legume crop (*Lens culinaris*) was cultivated with wheat; legume plants play a key role in maintaining the fertility of the soil by fixing atmospheric nitrogen, thereby increasing nitrogen content in the soil. Its effect on crop plants such as *Triticum* was studied and employed to give a better understanding of its mode of action and toxicity towards seed germination and photosynthetic pigments [8&9].

2. MATERIALS AND METHODS

2.1. Chemicals and Seeds

Malathion (commercial formulation) was obtained from Davani crop science, Hapur, Utter Pradesh, India. For this study chemicals and reagents such as $CaCO_3$, $MgSO_4$, and acetone were used analytical grade and were purchased from authorized venders. Seeds of wheat (*Triticum aestivum*) were purchased from Agricultural seed store, Pusa complex, Delhi, India.

2.2. Soil and Filter Paper

Soil was collected from Delhi Technological University ground; most of organic matter was firstly removed and then dug around one cm deep. Whatman No.2 filter papers were used in the present study.

2.3. Sterilization

1 kg soil was sterilized by autoclaving at 121^oC for 40 min at 1.05 Kg/cm^2 (115 lb psi) pressure for three times every alternate day. Distilled water, glass wares and filter papers were sterilized by autoclaving at 121^oC for 20 min at 115 lb psi. Forceps, needle, petri-plates and plastic ice-cream cups were cleaned with 90% ethanol before use. The seeds were surface sterilized using liquid detergent teepol and then were thoroughly washed under running tap water for 10 min. The seeds were treated with 1% Citric acid solution, an antioxidant kept in flask and placed on rotary shaker for 10 min at 100 rpm and washed with distilled water. Subsequently, these seeds were surface sterilized with 0.1% (w/v) freshly prepared $HgCl_2$ solution for 5 min with constant shaking and was finally washed 4-5 times with

autoclaved distilled water. All materials like autoclaved distilled water, tissue paper, lamp, etc. except seeds, were exposed to ultra violet light in a laminar flow cabinet for 30 min prior to their use. Surface of laminar flow and working platform were cleaned with 90% ethanol before the start of seeds germination experiment.

2.4. Germination Test on Filter Paper

Sterile Whatman No. 2 filter papers, 10 cm round shape were placed on sterile petri-discs, 9 cm in diameter and covered by sterile petri-plate (10 cm diameter). The filter papers were moistened with sterile distilled water and then different concentrations (2 ppm to 100 ppm) from stock of pesticide along with control (without pesticide) were added. 10 seeds were placed on filter paper at equal distances. 1ml sterile distilled water was added in each petri-disc every day in morning to maintain moisture. The experiment was performed in the replicates of 10 with 10 seeds in each concentration. Rest of germination conditions was same to soil in cups experiment. The seedling was observed and measured after five days of experiment.

2.5. Germination Test on Soil

First of all 100 g of sterilized soil was filled in all the plastic cups with 8.0 cm diameter. Different concentrations (2 ppm to 100 ppm) from stock of pesticide were mixed thoroughly on plastic sheet along with control. Pesticide stock was prepared in organic solvent i.e. acetone. The sides and bottom of plastic ice-cream cups were punched with needle to facilitate air and also help in remove extra water if inside. 10 seeds per cups were propagated at 1 cm depth at equal distance with help of forceps. After the seeds propagated, 10 ml of sterile distilled water was dispensed with pipette for moisture. 10 plastic cups of each concentration were set aside at room temperature (28±2 ^{0}C) in air conditioned room under natural light. 2 ml sterile distilled water was added with pipette in each cup every day at evening time to maintain water content. After five days, the experiments were terminated and growth parameter of seedling such as morphogenesis, rhizogenesis and leaves surface area etc. were measured and calculated.

2.6. Analytical

2.6.1. Growth of seedling

Observations were recorded after 6 days of sowing of seeds. After recording the final data, the *in vivo* raised shoots were excised and preserved at 4 ^{0}C for further work like photosynthesis pigments and enzyme study. The data were recorded in terms of (i) Percentage of seed germination, (ii) Average shoot length in cm, (iii) Average root length in cm, (iv) Average No. roots per shoot, (v) Average No. of leaf per shoot.

2.6.2. Photosynthetic pigments

Chlorophyll pigments were estimated by using slightly modified Holden protocol (1960). 0.2g of plant samples from each concentration were weighed and homogenized individually using mortar-pestle in the presence of excess of acetone: water (70% : 30%) until all the color was released from the tissue. Few amount of CaCO3 was added to prevent pheophytin formation and this was then centrifuged at 5000 rpm for 10 minutes at room temperature. The

clear supernatant was collected and then made up to a known volume (10 ml). The test tubes were wrapped with black paper to protect chlorophyll degradation. The Biospectrophotometer (Eppendorf) was adjusted at wavelength of 663 nm, 645 nm, 665 nm, 434 nm, 480 nm, 486 nm for chlorophyll a, chlorophyll b, pheophytin 'a' pheophytin 'b', for carotenoid and xanthophyll respectively. The optical density was measured and the content of chlorophyll- a and chlorophyll- b (in mg/l) was calculated using optical density and standard formula [10]. For examples total chlorophyll, add value of chlorophyll a, chlorophyll b, and amount of carotenoid = (4×OD×total volume of sample)/ weight of fresh leaf.

2.6.3. Thin layer chromatography

200 mg of fresh green wheat with similar amount of anhydrous magnesium sulfate was grounded in a mortar and pestle in presence of acetone for 5-7 minutes. The light green solid was transferred into a micro-centrifuge tube with the help of acetone. This heterogeneous mixture was agitated to ensure complete mixing of the acetone and the semi-solid. This mixture was allowed to stand for 10 minutes and the green acetone solution was removed by pipette and transferred to a micro-centrifuge tube, then centrifuged at 5000 rpm for 10 minutes at room temperature (25 ^{0}C). The clear supernatant was collected (1 ml). Similar protocol follows with frozen wheat leaf. The 20 x 20 cm^2 plates were prepared by spreading a uniform layer of 0.25 mm thickness silica gel G using TLC kit in our lab. These plates were allowed to dry at RT and further activated at 120 ^{o}C for half an hour. The acetone extract was spotted in the standard manner and the plate was eluted in a closed TLC chamber saturated with the organic solvents as mobile phase (cyclohexane: petroleum ether: acetone: n-hexane **::** 5:2:2:1). The intensity of chromatogram was observed in normal light and retention factor was calculated.

2.6.4. Statistical analysis

All the experiments have been repeated with nine replicas and initially the experimental setup was performed with three replicas for every method and each concentration for average length of shoots, root. Average numbers of secondary roots per shoot have been represented as mean values along with standard error (mean ± SE).

3. RESULTS AND DISCUSSION

3.1 Effect of Malathion on Seeds of Wheat on Filter Paper

The wheat seeds were grown on the filter paper supplemented with 2, 5, 25, 50 and 100 ppm malathion. A maximum of 100% germination was observed with an average shoot length of 10.41±0.7 per seedling and roots per shoots were reported. It was also observed that the percentage germination and shoot lengths increased at lower concentration (5 ppm & 10 ppm) as compared to the controls (Fig. 1, Table 1). The morphogenic response in term of shoot length and percentage germination decreased with an increasing concentration (25 ppm to 100 ppm) of malathion. Higher level of malathion (100 ppm) proved toxic as seen a single leaf seedling with small and thick roots. However, seedling could survive on this concentration (100 ppm). The morphogenic response was variable at different concentrations (Table 1; Fig. 1).

Table 1: Effect of malathion on the germination of wheat seeds tested by filter paper (petri dish) method.

Sample	Germination (%)	Shoot length (cm)	Root length (cm)	Roots per shoot
Control	98	10.39±0.6	6.67±0.44	5.21±0.8
2ppm	100	10.41±0.7	6.25±0.4	5.4±0.65
5ppm	98.5	11.8±0.4	5.81±0.66	5.2±0.50
10ppm	99	12.68±0.55	4.70±0.7	4.66±0.6
25ppm	96	8.87±0.2	4.25±0.9	4.35±0.3
50ppm	88.2	7.87±0.3	4.85±0.48	4.25±0.4
100ppm	80	5.4±0.85	3.75±0.22	4.75±0.5

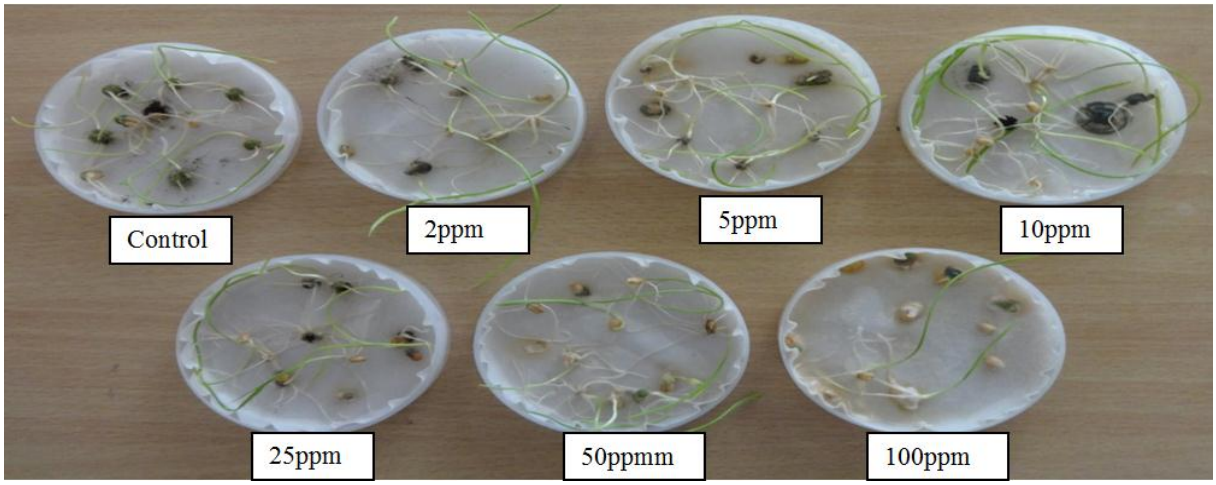


Fig.1. Seed germination on filter paper observed after 6 days at different concentrations of malathion

3.2 Effect of Malathion on Seeds of Wheat in Soil

The effect of malathion at different levels (2 ppm to 100 ppm) on the germination and growth of wheat seeds in soil was observed. The inhibitory effects towards seed germination and growth of seedling gradually increased with increase in concentration of malathion. A maximum of 97.5% seeds germinated with an average of 24.06 cm length of seedling on 2 ppm (Table 2). However, in control (without malathion) the percentage germination of seeds was less compared to the seeds grown on 2 ppm. Interestingly, the low toxicity towards seed germination was observed in higher concentration of malathion (50 &100 ppm). A low percentage of seed germination and survival was also observed at 100 ppm (Table 1, Fig 1). We observed that the malathion is less toxic in higher concentration as compare of organ-chlorine pesticides i.e. Lindane (17),because at lower concentrations most of seedlings survived and germination was around 64%.

Table 2**:** Average values of effect of malathion on the germination of wheat seeds tested by soil (cup) method.

Sample	Germination (%)	Shoot length (cm)	Root length (cm)	Roots per shoot
Control	97	13.41±0.55	11.98±0.6	5.74±0.084
2ppm	97.5	12.81±0.4	11.25±0.4	5.18±0.65
5ppm	96	11.88±0.7	11.11±0.8	4.83±0.55
10ppm	96	9.15±0.3	9.70±0.74	4.66±0.63
25ppm	96.5	9.0±0.2	9.45±0.9	4.35±0.37
50ppm	90.8	6.87±0.35	6.85±0.28	3.85±0.45
100ppm	64	5.08±0.6	0575±0.82	3.75±0.58

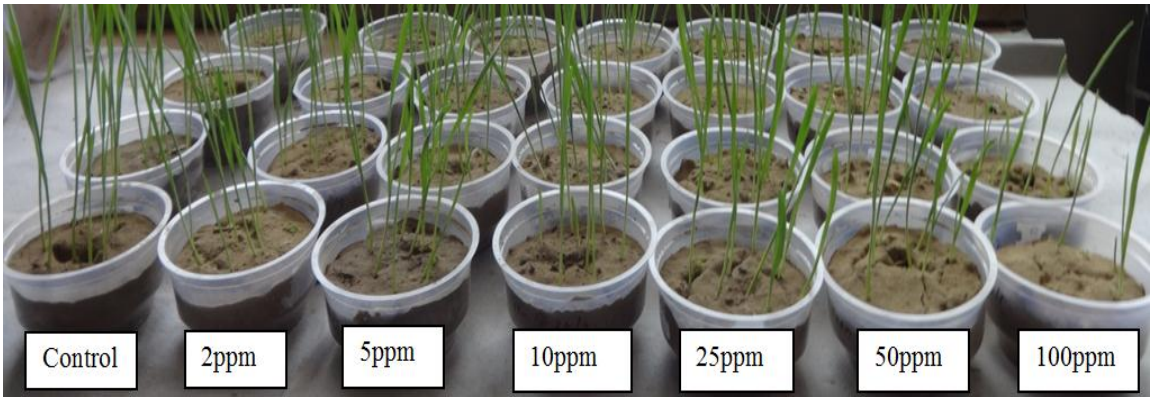


Fig.2. Seeds germinated at different concentrations of malathion after 6 days.

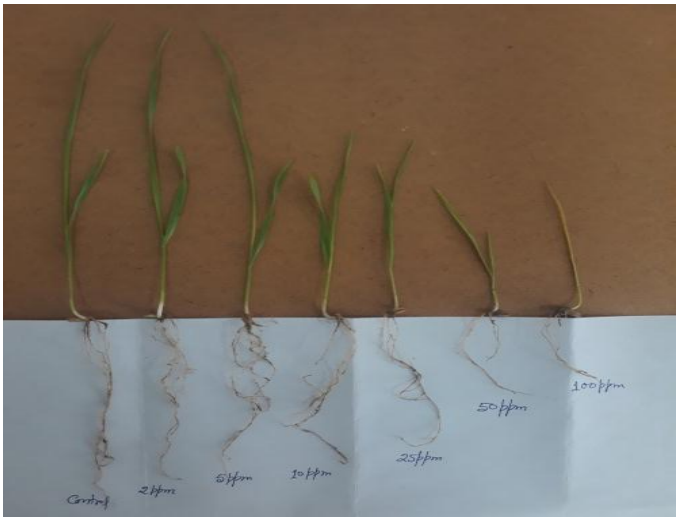


Fig.3. Seedling at different concentrations of malathion after 6 days.

3.3 Estimation of Photosynthetic Pigments in Green Leaf

In the present investigation, 6 days old seedling, which was cultivated by soil method, was evaluated qualitatively and quantitatively for the analysis of various photosynthetic pigments, total soluble chlorophyll and carotenoid. As we know chlorophyll is the most valuable primary metabolite of a plant. It is the center point for the capture of sunlight and is responsible for photosynthesis. Maximum amount of total chlorophyll was found in control i.e. 11.58 mg/g. and minimum in 100 ppm sample i.e. 2.16 mg/g. The effects of malathion on amount of total chlorophyll and carotenoid gradually decrease with increase in concentration (Table 3).

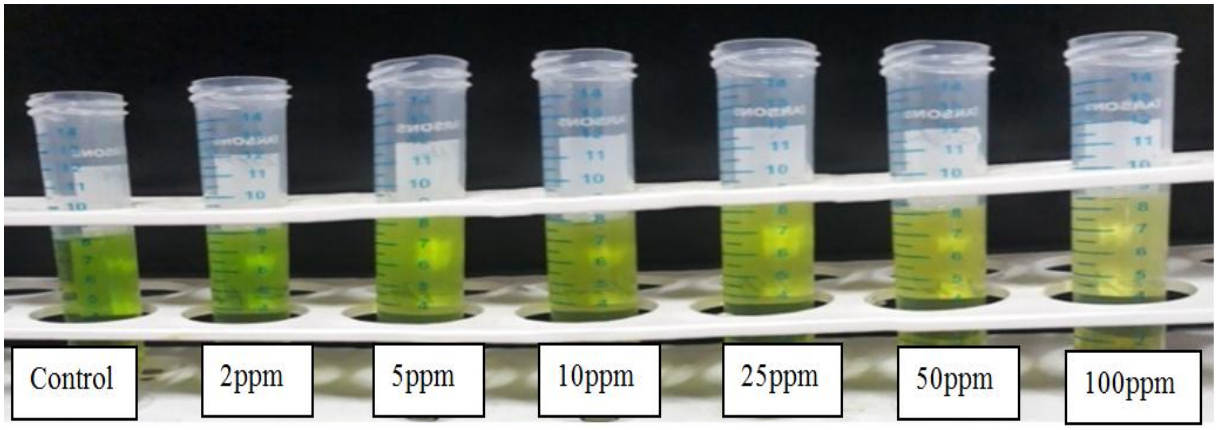


Fig.4. Intensity of photosynthetic pigments decrease with increasing concentration.

Table 3: Total content of photosynthetic pigments in green leaf.

Sample	**Chlorophyll a** (mg/l)	**Chlorophyll b** (mg/l)	**Total Chlorophyll** (mg/l)	**Carotenoid** (mg/l)
Control	8.42	3.16	11.58	0.211
2ppm	7.62	2.14	9.76	0.186
5ppm	6.18	2.30	8.48	0.154
10ppm	5.58	1.61	7.19	0.125
25ppm	3.47	1.15	4.62	0.093
50ppm	2.54	0.67	3.21	0.84
100ppm	1.45	0.71	2.16	0.60

The TLC for photosynthetic pigments was studied by using fresh and frozen leaf samples. The analysis of the various photosynthetic pigments on TLC plates showed the presence of xanthophyll, chlorophyll a, chlorophyll b and carotenoid (Fig. 5, 6) but no spot of pheophytin was observed on TLC plate for frozen sample (Fig. 6). However, TLC spots indicated that pheophytin was very minor spot in TLC plate in sample of fresh leaf (Fig. 5). Pigments pheophytin a and b were observed at *R*f values consistent with literature reports in addition to the

corresponding chlorophyll a and b when fresh or frozen leaves were used to prepare extract (Figure 5, 6). The demetalation of chlorophyll using strong acids has been previously described [11].The elution order using this elution solvent system was carotenoid (*R*f= 0.96), chlorophyll a (*R*f= 0.89), chlorophyll b (*R*f= 0.83), and xanthophyll (*R*f= 0.17).

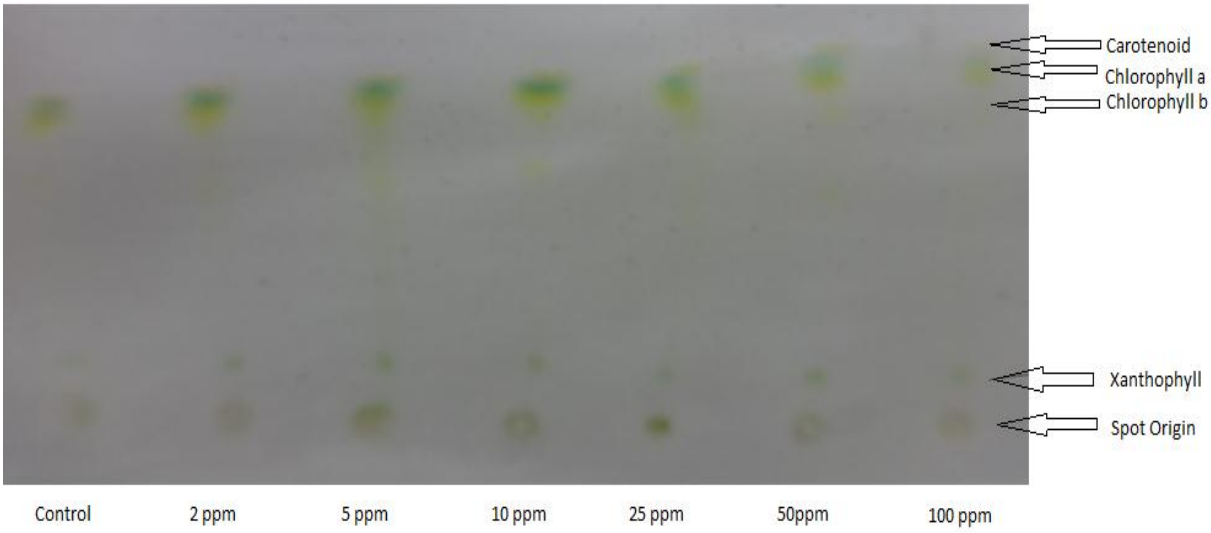


Fig.5. TLC analysis of photosynthetic pigmentsusingfresh green leaf of wheat

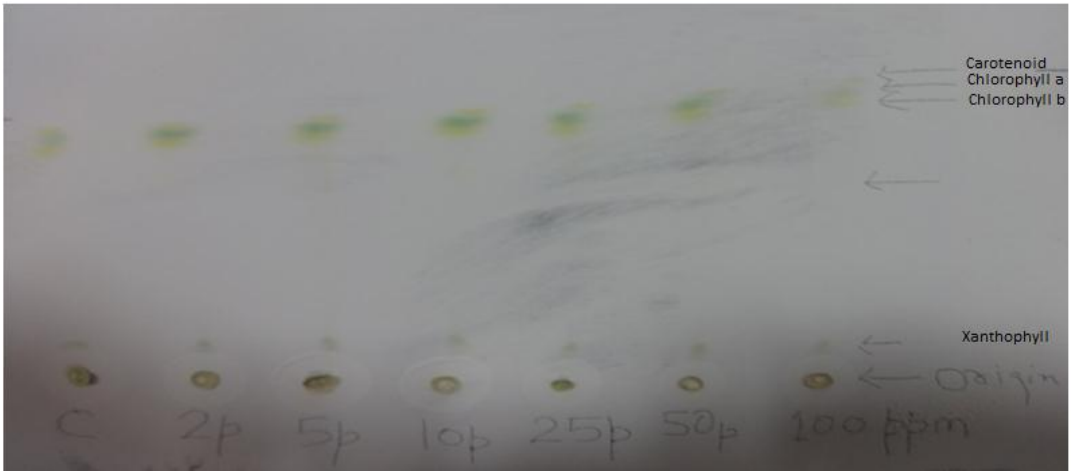


Fig.6. TLC analysis of photosynthetic pigments using frozen green leaf of wheat

On the basis of our result, we found that the low concentration of malathion may be used to promote the seeds germination and growth of seedling. However, it showed adverse effect on photosynthetic pigments. Even a low concentration of 1 ppm has been reported in reducing chlorophyll content [12, 13 &14]. Malathion inhibits the production of adenosine triphosphate (ATP) due to their effect on the photophosphorylation in the light reaction [15]. Similar results were obtained by Gafer *et al.* [3] on some other vegetables using the same pesticides and doses.

Also, pesticides affect crop growth and reduce its yield and quality due to their phytotoxicity. It even has detrimental effects on soil fertility and salinity [16 & 17].

4. CONCLUSION

This study confirmed that, malathion does not show toxicity towards seed germination and growth of seedling at higher concentration of 100 ppm, but shown adverse effect on growth of seedling and content of photosynthetic pigments. At lower levels, it was enhanced the germination and growth of seedling on filter paper. It has shown inhibitory effects towards seed germination and growth of seedling gradually increased with increase in concentration in soil method. Higher concentration of malathion inhibits the production of primary metabolites, like that photosynthetic pigments.

ACKNOWLEDGEMENTS

The first author would like to give vote of thanks to University Grants Commission, India for providing financial assistance as JRF/SRF. The authors would also like to thank the Hon'ble Vice Chancellor, Delhi Technological University for their valuable support. We are also thankful to Prof. D. Kumar, Dr. R. Bidlan and Mr. Puneet of Biotechnology Department, DTU for their timely support.

REFERENCES

[1] Srinivas, K. S. and Damani, J. "Effect of malathion on the concentration of primary metabolites from *Vigna radiate* and *Trigonellafoenum-graecum.*" Bull. Env. Pharmacol. Life Sci., 2016, Vol 5(7) 34-38.

[2] Gervais, J. A., Luukinen, B., Buhl, K. and Stone, D. "*Malathion General Fact Sheet*; National Pesticide Information Center". Oregon State University Extension Services. 2009.

[3] Gafar, M., Elhag, A. and Abdelgader, M. "Impact of Pesticides Malathion and Sevin on Growth of Snake Cucumber (*Cucumismelo L.* var. *Flexuosus*) and Soil." Universal Journal of Agricultural Research, 2013, 1(3), 81-84.

[4] Thirumaran, D. and Xavier, A. "Effect of methyl parathion (metacid. 50) on growth, proteins free amino acid and total polyphenol content of black gram (*Vigna mungo* L.) seedlings." Indian J Plant Physiol., 1987, 30(3): 289-292.

[5] Singh, S. P., Kumar, S. and Kishor, S.A. "Effect of malathion and carbendazim to the carbon and nitrogen metabolism in response of mustard." Biol J Patna, 1994, 6(1&2): 27-29.

[6] Nasrabadi, M. and Dhumal, K.N. "Effect of chloropyrifos and Malathion on stress and osmolyte parameters in Tomato and Brinjal." *Scholars Academic Journa for Biosciences.,* 2014, 2(11): 778-787.

[7] Srinivas, K. S. and Damani , J. "Effect of Malathion on the Concentration of Primary Metabolites from *Vigna radiata* and *Trigonella foenum-graecum.*" Bull. Env. Pharmacol. Life Sci., 2016, 5 (7): 34-38.

[8] Singh, B., Battu, S. and Dhaliwal, S. "Dissipation of Malathion on Fenugreek (*Trigonellafoenum-graecum L.*" Bull. Environ Contam. Toxicol, 2006, 77 (4): 521-523.

[9] Mersal, I. F., Ei-Ward, A., Ibrahim, A. and El-Emam, A.A.M. "Effect of malathion and plant extracts on seed quality of some wheat varities (*Triticum aestivum* L.) during storage." J. Plant Prod., 2011, 2 (8): 995-1007.

[10] Talreja, T. "Biochemical Estimation of Three Primary Metabolites from medicinally important plant *Moringaoliefera*." Int J Pharm Sci Rev Res, 2011. 7(2): 186-188.

[11] Mostafa Y. "Metabolism of Organophosphorus Insecticides: XIII Degradation of Malathion by *Rhizobium* spp." Arch Mikcrobiol, 1972, 86: 221-224.

[12] Singh, B., Kaur, J. and Singh, K. "Bioremediation of malathion in soil by mixed *Bacillus* culture." Adv. Biosci Biotechnol, 2013, 4: 674-678.

[13] Iriyama, K., Yoshiura, M., Shiraki, M., Yano, S. and Saito, S. *Anal. Biochem.* 1980, 106: 322–326.

[14] Lan, W.S., Gu, J.D., Zhang, J. L., Shen, B. C., Jiang, H., Mulchandani, A., Chen, W. and Qiao C. L, "Coexpression of Two Detoxifying Pesticide-degrading Enzymes in a Genetically Engineered Bacterium." Intern. Biod and Biodeg., 2006, 58(2), *pp.* 70-76.

[15] Suzuki, N., Saitoh, K. and Adachi, K. J. Chromatog. 1987, 408:181–190.

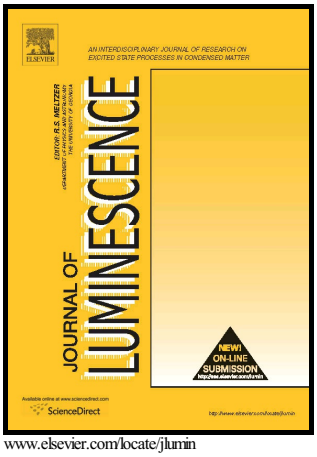
[16] Bollag, J.M. and Liu, S.Y. "Biological Transformation Processes of Pesticides. In:Pesticides in the Soil Environment Processes, Impacts and Modeling." Soil Science Society of America, Madison, Wisconsin, USA 1990. pp.169-211.

[17] Bidlan, R., Afsar, M. and Manonmani, H.K. "Bioremediation of HCH- contaminated soil: elimination of inhibitory effects of the insecticide on radish and green gram seed germination." Chemosphere. 2004, 56: 803- 811.

Author's Accepted Manuscript

Effective sensitization of Eu^{3+} and energy transfer in Sm^{3+}/Eu^{3+} co-doped ZPBT glasses for CuPc based solar cell and w-LEDs applications

Kaushal Jha, M. Jayasimhadri



www.elsevier.com/locate/jlumin

PII: S0022-2313(17)31294-2
DOI: http://dx.doi.org/10.1016/j.jlumin.2017.09.049
Reference: LUMIN15057

To appear in: *Journal of Luminescence*

Received date: 25 July 2017
Revised date: 19 September 2017
Accepted date: 19 September 2017

Cite this article as: Kaushal Jha and M. Jayasimhadri, Effective sensitization of Eu^{3+} and energy transfer in Sm^{3+}/Eu^{3+} co-doped ZPBT glasses for CuPc based solar cell and w-LEDs applications, *Journal of Luminescence,* http://dx.doi.org/10.1016/j.jlumin.2017.09.049

This is a PDF file of an unedited manuscript that has been accepted for publication. As a service to our customers we are providing this early version of the manuscript. The manuscript will undergo copyediting, typesetting, and review of the resulting galley proof before it is published in its final citable form. Please note that during the production process errors may be discovered which could affect the content, and all legal disclaimers that apply to the journal pertain.

ACCEPTED MANUSCRIPT

Effective sensitization of Eu^{3+} and energy transfer in Sm^{3+}/Eu^{3+} co-doped ZPBT glasses for CuPc based solar cell and w-LEDs applications

Kaushal Jha, M. Jayasimhadri*

Luminescent Materials Research Lab (LMRL), Department of Applied Physics, Delhi Technological University, Delhi 110 042, India

Abstract:

Sm^{3+}/Eu^{3+} co-doped transparent Zinc Phosphate Barium Titanate (ZPBT) glasses have been successfully prepared via melt quenching technique. The photoluminescence properties and energy transfer mechanisms of these glasses were investigated in detail. The addition of Sm^{3+} as sensitizer expanded the excitation spectrum of Eu^{3+} in the Sm^{3+}/Eu^{3+}co-doped ZPBT glasses. The mechanism for energy transfer from Sm^{3+} to Eu^{3+} was dipole-dipole in nature, which was confirmed by Dexter energy transfer formula and Reisfeld's theory on emission spectra and Inokuti Hirayama (I-H) model on decay curves. The Sm^{3+}/Eu^{3+} co-doped ZPBT glasses reveal the capability to down-convert the n-UV and blue wavelength photons located in the weakest absorption of copper phthalocyanine (CuPc), to red-emitting photons in the optimal absorption of CuPc. The evaluated CIE chromaticity coordinates for the glasses move towards the red region with the increase in Eu^{3+} concentration under n-UV excitation wavelength. The above-mentioned results imply that the Sm^{3+}/Eu^{3+} co-doped ZPBT glasses are the potential candidate for applications in CuPc based solar cells and w-LEDs.

Keywords: Optical Glass, Photoluminescence; Energy transfer; Lifetime

Corresponding author e-mail: jayaphysics@yahoo.com

Accepted manuscript

ACCEPTED MANUSCRIPT

1. Introduction:

In recent years, white light emitting diodes (w-LEDs) have received enormous attention as solid state light sources as they offer characteristics like high brightness, low power consumption and are environment-friendly. At present, w-LEDs are fabricated using single/multitude phosphor with n-UV/blue excitation sources. The approach for w-LEDs fabrication with the combination of RGB (red, green, and blue) phosphors and n-UV LED chips are seeking attention as they offer better CRI, CCT and free from halo effect in comparison to yellow phosphor with the blue LED chip. However, the red phosphor prepared from nitride and sulfide suffers from low chemical stability, low luminous efficiency, and the red phosphor Y_2O_3:Eu^{3+} has intense excitation at 248 nm. Moreover, the quantum efficiency of InGaN LED chip has the maximum value at 400 nm, and "Droop" (where current density drops off) is also absent [1–4]. Therefore, there is an urgent need for red photoluminescent component excitable by n-UV LED chips. Among various activators, the trivalent europium (Eu^{3+}) has gained significant attention due to its emission in the red region upon excitation with the n-UV/blue wavelengths [5,6]. The addition of sensitizer to an activator could extend the excitation region and enhance the emission intensity of activator. Many researchers have successfully expanded the Eu^{3+} excitation by use of suitable sensitizers. Among various sensitizers, Sm^{3+} was found to be the most appropriate sensitizer. The incorporation of Sm^{3+} as the sensitizer enhanced the Eu^{3+} emission in different host matrices. Kang et al. increased the emission intensity by 35% under 410 nm in the $Na_2Y_2Ti_3O_{10}$ host, while Fang et al. revealed the increment in Eu^{3+} emission under 403 nm in $CaLa_2(MoO_4)_4$ host lattice [4,7]. Biju et al. showed the enhancement in Eu^{3+} emission under 402 nm in zinc phosphate glasses [8]. Lin et al. revealed the emission improvement under 482 nm in borate glasses owing to energy transfer from Sm^{3+} to Eu^{3+} [9]. Moreover, the process of energy

Accepted manuscript

ACCEPTED MANUSCRIPT

transfer can be used as a strategy to down convert unused photons of the solar spectrum to red emitting photons, which lie in the absorption region of the organic absorber material copper phthalocyanine (CuPC) [10,11]. The phosphor mentioned above is encapsulated in the organic resin made of polymer. The organic resin gets deteriorated at high temperatures, high power and/or high energy excitations light sources. Therefore, glasses doped with rare earth are preferred over phosphor as they have simpler manufacturing technique, lower production cost, highly durable, excellent thermal and mechanical stability [12–14]. Along with this, glasses serves the purpose of both the encapsulant and wavelength converter and is free from the organic resin.

Among various inorganic glasses, phosphate glasses have been extensively studied as they offer unique characteristics like transparency in the wide spectral region, low melting and softening temperature, and high mechanical and thermal stability. Phosphate glasses provide 1000 times greater rare earth ion solubility than in borate and silicate glasses which make them as an appropriate candidate as a host material for luminescence applications. However, the poor chemical durability and the hygroscopic nature of these glasses are a major limitation for practical applicability in devices. Zinc oxide (ZnO) offers unique properties like low toxicity, non-hygroscopic, direct band gap, low cost, intrinsic emitting property and large exciton binding and makes phosphate glasses moisture resistant due to the formation of P-O-Zn bonds. The addition of BaO to phosphate structure lowers the melting temperature as well as leads to disruption of the glass network. The heavy metal oxide like TiO_2 incorporation to the phosphate glasses significantly improves chemical durability and stabilization of the glass structure [12,14].

Therefore, in the present investigation Sm^{3+}/Eu^{3+} co-doped ZPBT glasses were synthesized for the first time via melt quenching technique and the energy transfer mechanisms were

Accepted manuscript

ACCEPTED MANUSCRIPT

discussed in detail. Furthermore, the efficiency and probability of energy transfer and CIE Chromaticity coordinates were calculated. The aim is to investigate these glasses for applications in the field of optoelectronics.

2. Experimental:

The Glasses were prepared with conventional melt-quenching technique with molar composition as mentioned below:

(1) $39ZnO\text{-}35P_2O_5\text{-}20BaO\text{-}5TiO_2\text{-}XSm_2O_3$ (X=0.1, 0.5, 1.0, 1.5, and 2.0) (Sample name with X= 1 was named as SM01)

(2) $39ZnO\text{-}35P_2O_5\text{-}20BaO\text{-}5TiO_2\text{-}1Eu_2O_3$ (Sample name = EU01)

Along with these two glass samples, a series of glasses doped with Sm_2O_3 and Eu_2O_3 were prepared in the molar composition as follows:

(3) $(39\text{-}X)ZnO\text{-}35P_2O_5\text{-}20BaO\text{-}5TiO_2\text{-}1Sm_2O_3\text{-}XEu_2O_3$

The values for X were 0.50, 1.0, 1.5 and 2.0 and the glasses were named as SE01, SE02, SE03, and SE04, respectively. The starting materials were Analytical Reagent (A.R) grade ZnO, TiO_2, $BaCO_3$, $NH_4H_2PO_4$, high purity Sm_2O_3, and Eu_2O_3. The chemicals were ground in an agate mortar for 1 hour using acetone as the wetting medium. The mixture was then placed in the muffle furnace at 1150 °C for 1 hour, and the melt was then poured on the preheated brass plate and annealed at 400 °C for 3 hours to remove mechanical and thermal stress. Finally, colorless and transparent glasses were obtained. The photoluminescence (PL) properties were measured using Shimadzu RF-5301PC spectrofluorophotometer fitted with xenon flash lamp. The decay analysis was performed using an Edinburgh FLS920, where xenon lamp was excitation source.

Accepted manuscript

ACCEPTED MANUSCRIPT

3. Results and discussion:

3.1 *Photoluminescence properties of Sm^{3+} doped ZPBT glasses*

Fig. 1 represents the excitation and emission spectrum Sm^{3+} doped ZPBT glasses. The excitation spectrum was recorded by monitoring emission at 599 nm. The excitation spectrum reveals several peaks originating from the $^6H_{5/2}$ ground level to different excited levels at 343, 359, 372, 399, 418, 437 and 467 nm corresponding to the $^4H_{9/2}$, $^4D_{3/2}$, $^6P_{7/2}$, $^4F_{7/2}$, $^6P_{5/2}$, $^4G_{9/2}$, and $^4I_{11/2}$ +$^4I_{13/2}$+$^4M_{15/2}$ transitions of Sm^{3+} ions, respectively. The emission spectra under different excitations (λ_{ex} = 399 and 467 nm) revealed three emission bands centered at 563, 599 and 645 nm corresponding to $^4G_{5/2}\rightarrow{}^6H_{5/2}$, $^4G_{5/2}\rightarrow{}^6H_{7/2}$, and $^4G_{5/2}\rightarrow{}^6H_{9/2}$ transitions, respectively. The $^4G_{5/2}\rightarrow{}^6H_{5/2}$ is magnetic dipole (MD) transition in nature following the selection rules ($\Delta J=0, \pm1$; J is angular momentum), whereas $^4G_{5/2}\rightarrow{}^6H_{9/2}$ is attributed to forced electric dipole (ED) transition following the selection rule ($\Delta J\leq6$; J or J´=0, when J=2, 4, and 6). The MD transition is insensitive to the crystal environment whereas forced ED transition is hypersensitive in nature, and the emission intensity of this transition gets strongly affected by the crystal field of the ligand atoms. The $^4G_{5/2}\rightarrow{}^6H_{7/2}$ transition arose due to both the MD and forced ED transition [15,16]. The intensity ratio of forced ED to MD transition indicate about the symmetry of environment around the rare earth. In the present case, the MD transition is more intense than ED transition which suggests that there is no deviation from the inversion symmetry. The emission intensity of the Sm^{3+} doped ZPBT glasses increased up to 1 mol % and decreased after that as shown in the inset of Fig. 1. The decrease in the emission intensity arises due to the concentration quenching phenomenon [17].

3.2 Photoluminescence properties of Sm^{3+}/Eu^{3+} co-doped ZPBT glasses:

Accepted manuscript

ACCEPTED MANUSCRIPT

Fig. 2 compares the excitation spectrum of EU01 and SE04 (1 mol% of Eu^{3+} and 2 mol% Sm^{3+}/Eu^{3+} co-doped ZPBT glasses) by monitoring emission at 613 nm. The emission at 613 nm is due to Eu^{3+}, but the excitation spectrum for the Sm^{3+}/Eu^{3+} co-doped ZPBT glass revealed peaks of Sm^{3+} also in addition to that of Eu^{3+}. The peaks at 343, 399, 437 and 473 nm are associated with Sm^{3+} as discussed previously, and the peaks at 360, 381, 392, 412, and 462 nm are attributed to $^7F_0 \rightarrow {}^5D_4$, $^7F_0 \rightarrow {}^5L_7$, $^7F_0 \rightarrow {}^5L_6$, $^7F_0 \rightarrow {}^5D_3$, and $^7F_0 \rightarrow {}^5D_2$ transitions, respectively of Eu^{3+} [18]. A few reports on the Sm^{3+} doped and Eu^{3+} doped glasses have been examined and revealed the excitation peaks of either Sm^{3+} or Eu^{3+} ions [19–24]. However, in the present case, the excitation spectrum of Eu^{3+} is extended and also enhanced the emission intensity by co-doping Sm^{3+}. Therefore, the introduction of Sm^{3+} has revealed the sensitization effect on Eu^{3+} in the Sm^{3+}/Eu^{3+} co-doped ZPBT glasses. The emission spectra of the co-doped ZPBT glasses i.e. Sm^{3+} (1 mol%) and Eu^{3+} (0.0, 0.5, 1.0, 1.5 and 2.0 mol%) under 399 nm are represented in Fig. 3. For 1 mol% Sm^{3+} doped ZPBT glasses under 399 nm, which matches well with excitation the n-UV LED chips, emission peaks due to only Sm^{3+} was observed at 563, 599 and 645 nm as discussed previously. When Eu^{3+} is co-doped with Sm^{3+}, in addition to Sm^{3+} peaks, Eu^{3+} emission peaks were also observed at 577, 591, 613, 655, and 701 nm corresponding to the transition arising from $^5D_0 \rightarrow {}^7F_0$, $^5D_0 \rightarrow {}^7F_1$, $^5D_0 \rightarrow {}^7F_2$, $^5D_0 \rightarrow {}^7F_3$, and $^5D_0 \rightarrow {}^7F_4$, respectively. The $^5D_0 \rightarrow {}^7F_2$ is forced ED transition which is hypersensitive in nature, and the emission intensity of this transition is strongly affected by the crystal field of ligand atoms. While the $^5D_0 \rightarrow {}^7F_1$ is MD transition which is insensitive to the crystal environment. The peak due to Sm^{3+} and Eu^{3+} at 645 and 655 nm are merged into one and hence not distinguishable. As the concentration of the Eu^{3+} is increased, the intensity of peaks due to Eu^{3+} is enhanced while that of Sm^{3+} are diminished. The decrease in the Sm^{3+} emission intensity with increase in Eu^{3+} concentration may be due to

Accepted manuscript

ACCEPTED MANUSCRIPT

the energy transfer from Sm^{3+} to Eu^{3+} [25,26]. The inset of Fig. 3 represents the comparison between the emission observed for SE04 (1 mol% Sm^{3+} and 2 mol % Eu^{3+} co-doped ZPBT glass) under both n-UV (399 nm) and blue (467 nm) excitation wavelengths. The emission spectra revealed all the peaks under both the excitations at the same position with variation in intensity. The intense excitation peaks (399 and 467 nm) for Sm^{3+}/Eu^{3+} co-doped ZPBT glasses lies in the weakest absorption of the region of CuPc solar cells. The above mentioned results indicate that Sm^{3+}/Eu^{3+} co-doped glasses has the capability to down-convert the photons in the n-UV and blue regions of the spectrum to red and orange region which is the strongest absorption region for CuPc based solar cells [11,27]. Hence, Sm^{3+}/Eu^{3+} co-doped ZPBT glasses can be placed on top of the CuPc based organic solar cells to down-convert the n-UV/blue and can lead to enhance the efficiency of the CuPc solar cells.

The energy transfer between rare-earth ions may take place by two interaction mechanisms: multipolar interaction and exchange interaction. Exchange interaction occurs only when the sensitizer/donor and the activator/acceptor are suited at the nearest neighbour positions. The interaction in Sm^{3+}/Eu^{3+} doped ZPBT glasses focuses on the mechanism of the multipolar interaction. To investigate the type of multipolar interaction, Dexter's energy transfer formula for multipolar interaction and Reisfeld's approximation was applied, as per the following equation [28]:

$$\frac{\eta_0}{\eta} \propto C^{n/3} \quad (1)$$

where η_0 and η are the luminescent quantum efficiency of the Sm^{3+} in the absence and presence of the Eu^{3+}, C is the sum of the mole percent of Sm^{3+} and Tb^{3+}, and the value of n is 6, 8 and 10 corresponding to dipole-dipole, dipole-quadrupole and quadrupole-quadrupole interaction,

Accepted manuscript

ACCEPTED MANUSCRIPT

respectively. The η_0/η value can be approximately estimated by the ratio of related luminescence intensities as:

$$\frac{I_{s0}}{I_s} \propto C^{n/3} \quad (2)$$

where I_{s0} is the intrinsic emission intensity of Sm^{3+} and I_s is the emission intensity of Sm^{3+} in the presence of Eu^{3+}. The graph was plotted between I_{s0}/I_s versus $C^{n/3}$ and the best fit was obtained for n=6 under 399 nm excitation as represented in Fig. 4. The value of n=6 suggests that the energy is transferred from the Sm^{3+} to Eu^{3+} due to the non-radiative dipole-dipole interaction.

The phenomenon of energy transfer process was studied on the basis of energy level diagram as presented in Fig. 5. In case of SM01 and EU01 glass samples, the excitation energy is absorbed by the rare earth ions (Sm^{3+} and Eu^{3+}), which in turns excites the electron from the ground state to the higher excited state. The excited electrons then rapidly falls to the lower energy states (Sm^{3+}:$^4G_{5/2}$ and Eu^{3+}:$^5D_0$) by non-radiative relaxation, and then relaxes to the lower states (Sm^{3+}:^6H_J (J=5/2, 7/2 and 9/2) and Eu^{3+}:^7F_J (J= 0 to 4)) liberating energy in the form of visible emission. The $^4G_{5/2}$ energy level of Sm^{3+} is 638 cm^{-1} higher than the $^5D_0$ energy level of Eu^{3+}. Therefore, it is possible that a part of the energy from Sm^{3+} is non-radiatively transferred to the Eu^{3+}, which results in decrement of Sm^{3+} emission as indicated in Fig. 3. The smaller energy difference between the $^4G_{5/2}$ and $^5D_0$ makes the energy transfer possible via phonon assisted non-radiative transition, which suggests that Sm^{3+} act as efficient sensitizer/donor for the Eu^{3+}.

3.3 Decay analysis and energy transfer efficiency/probability:

The decay profiles for different glasses (SM01, SE01, SE02, SE03 and SE04) were recorded by monitoring emission at 599 nm corresponding to $^4G_{5/2} \rightarrow {}^6H_{7/2}$ transition under the excitation of 399 nm as represented in Fig. 6. The decay curves were fitted with different

Accepted manuscript

ACCEPTED MANUSCRIPT

exponential equations and the best fit was obtained for bi-exponential equation as represented below [14]:

$$I = I_0 + A_1 exp\left(-\frac{t}{\tau_1}\right) + A_2\, exp\left(-\frac{t}{\tau_2}\right) \quad (4)$$

where I and I_0 are the luminescence intensities at time t and 0, τ_1 and τ_2 are the components of the lifetime, corresponding to the fast and slow lifetimes, respectively; A_1 and A_2 are the fitting constant, and t is the time. The average value of lifetime can be calculated for the bi-exponential as given by equation:

$$\tau_{avg} = \frac{A_1\tau_1^2 + A_2\tau_2^2}{A_1\tau_1 + A_2\tau_2} \quad (5)$$

The average lifetime values for SM01, SE01, SE02, SE03 and SE04 are represented in Table 1. A deeper insight on the process of energy transfer can be estimated from the lifetime values. It can be observed from Table 1, that the value of lifetime decreases with an increase in the Eu^{3+} concentration, which is a strong evidence of energy transfer from Sm^{3+} to Eu^{3+}. The energy transfer efficiency (η_T) value can be calculated from the equation as mentioned below [29]:

$$\eta_{T(Tb\rightarrow Sm)} = 1 - \left(\frac{\tau_d}{\tau_{d0}}\right) \quad (6)$$

The energy transfer probability rate in terms of lifetime can be expressed by the equation:

$$P_{T(Tb\rightarrow Sm)} = \frac{1}{\tau_d} - \frac{1}{\tau_{d0}} \quad (7)$$

where, τ_{d0} and τ_d are the decay time of the Sm^{3+} in the absence of the Eu^{3+} and in the presence of the Eu^{3+}, respectively. The values of the energy transfer efficiencies (η_T) and energy transfer probabilities (P_T) are represented in the Table 1. A graph showing variation in lifetime values and energy transfer efficiencies with increasing Eu^{3+} concentration is presented in Fig. 7. The

Accepted manuscript

ACCEPTED MANUSCRIPT

value of both η_T and P_T increase with an increase in the Eu^{3+} concentration, indicating that with the increase in Eu^{3+} concentration more energy is transferred from Sm^{3+} to Eu^{3+}.

The type of multipolar interaction can be obtained from decay curves by applying Inokuti-Hirayama (I-H) model. It gives a deeper insight on the type of interaction involved in the energy transfer process from the donor to acceptor. The decay of the luminescence given by equation [17,30]:

$$I_t = I_0 \exp\left\{\frac{-t}{\tau_0} - Q\left(\frac{t}{\tau_0}\right)^{\frac{3}{s}}\right\} \quad (8)$$

where, I_o the luminescence intensity at time t=0, I_t is the luminescence intensity at time t, t is time after excitation, Q is the energy transfer parameter, τ_0 is the intrinsic donor decay time in the absence of the acceptor. S is the multipole effect and takes the value 6, 8 and 10 for dipole-dipole, dipole-quadrupole and quadrupole-quadrupole interaction, respectively.

$$Q = \frac{4\pi}{3}\Gamma\left(1 - \frac{3}{s}\right).N_0.R_0^3 \quad (9)$$

where, Γ is gamma function, N_0 is the acceptor ion concentration and R_0 is the critical transfer distance, which is defined as the donor–acceptor separation when rate of energy transfer between a donor and acceptor ion is equal to the rate of intrinsic decay rate (τ_0^{-1}). The type of multipolar interaction was identified by fitting the decay curve for SE04 glass sample for different values of S=6, 8 and 10 and the best fit was obtained for S=6 as shown in Fig. 8 (a) and (b) represents the decay curve for SM01, SE01, SE02, SE03 and SE04 glass samples fitted with S=6. The results of the I-H model indicates that the interaction is dipole-dipole in nature and is in accordance with the Dexter energy transfer formula and Reisfeld's approximation. The donor–acceptor interaction parameter C_{DA} is calculated by the using the expression as mentioned below:

Accepted manuscript

ACCEPTED MANUSCRIPT

$$C_{DA} = R_0.\tau_0^{-1} \quad (10)$$

where, R_0 is critical energy transfer distance. The values of Q, R_0 and C_{DA} are given in Table 1. It can be observed that the Q value increases from 0.448 to 1.287, indicating that the dipole-dipole interaction becomes more dominant with increasing Eu^{3+} concentration. The values of C_{DA} and R_0 also increases with increasing concentration of Eu^{3+} concentration [31,32].

The CIE chromaticity coordinates calculated from emission spectra for SM01, SE01, SE02, SE03 and SE04 glass sample under 399 nm excitation are presented in Fig. 9, respectively and tabulated in Table 1. Under the excitation of 399 nm, it is observed that with increase in concentration of Eu^{3+}, the chromaticity coordinates shift towards the red region, which is due to the enhancement in the emission peak of Eu^{3+} due to efficient energy transfer from Sm^{3+} to Eu^{3+}. The CIE chromaticity coordinates for SE04 are (0.614, 0.384) under n-UV excitation and is close to the commercial available $Y_2O_2S:Eu^{3+}$ (0.647, 0.343) [12]. The CIE chromaticity coordinates values suggest the utility of Sm^{3+}/Eu^{3+} co-doped ZPBT glasses as the red fluorescent component for w-LEDs.

4. Conclusions:

A series of Sm^{3+}/Eu^{3+} co-doped transparent ZPBT glasses have been successfully prepared via melt quenching technique. The Sm^{3+} doped glasses show dominant emission at 599 nm corresponding to $^4G_{5/2} \rightarrow {}^6H_{7/2}$ transition, while Eu^{3+} doped glasses revealed strongest emission at 613 nm corresponding to $^5D_0 \rightarrow {}^7F_2$ transition. The energy transfer mechanism from Sm^{3+} to Eu^{3+} was dipole-dipole in nature, which was confirmed by applying Dexter energy transfer formula and Reisfeld's theory on emission spectra and I-H model on decay curves. The excitation spectrum for Sm^{3+}/Eu^{3+} co-doped ZPBT glasses of Eu^{3+} was expanded by addition of Sm^{3+} as a

Accepted manuscript

ACCEPTED MANUSCRIPT

sensitizer. The emission spectra of Sm^{3+}/Eu^{3+} co-doped ZPBT glasses revealed the down-conversion capability of the n-UV and blue wavelength photons located in the weakest absorption of copper phthalocyanine (CuPc) to red-emitting photons lying in the optimal absorption of CuPc. The calculated CIE chromaticity coordinates under n-UV excitation moves towards red region with increase in the Eu^{3+} concentration. These results strongly suggests the effective applicability of Sm^{3+}/Eu^{3+} co-doped ZPBT glasses as a potential candidate for CuPc based solar cells and n-UV/blue LED chips based w-LEDs.

Acknowledgements

Kaushal Jha is grateful to the University Grants Commission (UGC) for providing financial support in the form of senior Research Fellowship (SRF). The author (M. Jayasimhadri) is grateful to DST-SERB, Govt. of India for the sanction of a research project (No. SB/FTP/PS-082/2014, dt. 02/03/2015).

References:

[1] R. Xie, N. Hirosaki, M. Mitomo, K. Takahashi, K. Sakuma, R. Xie, N. Hirosaki, M. Mitomo, Highly efficient white-light-emitting diodes fabricated with short-wavelength yellow oxynitride phosphors, 101104 (2011) 2004–2007.

[2] J.S. Kim, P.E. Jeonny, J.C. Choi, H.L. Park, S.I. Mho, G.C. Kim, Warm-white-light emitting diode utilizing a single-phase full-color $Ba_3MgSi_2O_8:Eu^{2+}$, Mn^{2+} phosphor, Appl. Phys. Lett. 84 (2004) 2931–2933.

[3] H. Masai, Y. Yamada, Y. Suzuki, K. Teramura, Y. Kanemitsu, T. Yoko, Narrow energy gap between triplet and singlet excited states of Sn^{2+} in borate glass., Sci. Rep. 3 (2013) 3541.

Accepted manuscript

ACCEPTED MANUSCRIPT

[4] D. Kang, H.S. Yoo, S.H. Jung, H. Kim, D.Y. Jeon, Synthesis and Photoluminescence Properties of a Novel Red-Emitting $Na_2Y_2Ti_3O_{10}$:Eu^{3+},Sm^{3+} Phosphor for White-Light-Emitting Diodes, J. Phys. Chem. C. 115 (2011) 24334–24340.

[5] Y. Tian, B. Chen, B. Tian, R. Hua, J. Sun, L. Cheng, H. Zhong, X. Li, J. Zhang, Y. Zheng, T. Yu, L. Huang, Q. Meng, Concentration-dependent luminescence and energy transfer of flower-like $Y_2(MoO_4)_3$:Dy^{3+} phosphor, J. Alloys Compd. 509 (2011) 6096–6101.

[6] Y. Tian, B. Chen, R. Hua, J. Sun, L. Cheng, H. Zhong, X. Li, J. Zhang, Y. Zheng, T. Yu, L. Huang, H. Yu, Optical transition, electron-phonon coupling and fluorescent quenching of $La_2(MoO_4)_3$:Eu^{3+} phosphor, J. Appl. Phys. 109 (2011) 53511.

[7] Y.-C. Fang, S.-Y. Chu, P.-C. Kao, Y.-M. Chuang, Z.-L. Zeng, Energy Transfer and Thermal Quenching Behaviors of $CaLa_2(MoO_4)_4$:Sm^{3+},Eu^{3+} Red Phosphors, J. Electrochem. Soc. 158 (2011) J1.

[8] P.R. Biju, G. Jose, V. Thomas, V.P.N. Nampoori, N.V. Unnikrishnan, Energy transfer in Sm^{3+}:Eu^{3+} system in zinc sodium phosphate glasses, Opt. Mater. 24 (2004) 671–677.

[9] S. Sailaja, C. Nageswara Raju, C. Adinarayana Reddy, B. Deva Prasad Raju, Y.-D. Jho, B. Sudhakar Reddy, Optical properties of Sm^{3+}-doped cadmium bismuth borate glasses, J. Mol. Struct. 1038 (2013) 29–34.

[10] A.N. Meza-Rocha, A. Speghini, M. Bettinelli, U. Caldiño, Orange and reddish-orange light emitting phosphors: Sm^{3+} and Sm^{3+}/Eu^{3+} doped zinc phosphate glasses, J. Lumin. 167 (2015) 305–309.

[11] X. Min, Z. Huang, M. Fang, Y.-G. Liu, C. Tang, X. Wu, Energy Transfer from Sm^{3+} to

Accepted manuscript

ACCEPTED MANUSCRIPT

Eu $^{3+}$ in Red-Emitting Phosphor $LaMgAl_{11}O_{19}:Sm^{3+}$, Eu^{3+} for Solar Cells and Near-Ultraviolet White Light-Emitting Diodes, Inorg. Chem. 53 (2014) 6060–6065.

[12] K. Jha, M. Jayasimhadri, Structural and emission properties of Eu^{3+} -doped alkaline earth zinc-phosphate glasses for white LED applications, J. Am. Ceram. Soc. 100 (2017) 1402–1411.

[13] A.K. Vishwakarma, K. Jha, M. Jayasimhadri, A.S. Rao, K. Jang, B. Sivaiah, D. Haranath, Red light emitting $BaNb_2O_6:Eu^{3+}$ phosphor for solid state lighting applications, J. Alloys Compd. 622 (2015) 97–101.

[14] K. Jha, M. Jayasimhadri, Spectroscopic investigation on thermally stable Dy3+ doped zinc phosphate glasses for white light emitting diodes, J. Alloys Compd. 688 (2016) 833–840.

[15] A.K. Vishwakarma, M. Jayasimhadri, Pure orange color emitting Sm^{3+} doped BaNb2O6 phosphor for solid - state lighting applications, J. Lumin. 176 (2016) 112–117.

[16] A. Mohan Babu, B.C. Jamalaiah, T. Sasikala, S.A. Saleem, L. Rama Moorthy, Absorption and emission spectral studies of Sm^{3+}-doped lead tungstate tellurite glasses, J. Alloys Compd. 509 (2011) 4743–4747.

[17] S. N Rasool, L. R Moorthy, C.K. Jayasankar, Spectroscopic Investigation of Sm3+ doped phosphate based glasses for reddish-orange emission, Opt. Commun. 311 (2013) 156–162.

[18] W. Zhang, S. Ouyang, Z. Zhang, Y. Zhang, H. Xia, Luminescent properties of Eu^{3+}-doped glass ceramics containing $BaGdF_5$ nanocrystals under NUV-excitation for W-LEDs, Ceram. Int. 41 (2015) 14035–14040.

[19] F. Zaman, J. Kaewkhao, G. Rooh, N. Srisittipokakun, H.J. Kim, Optical and luminescence

Accepted manuscript

ACCEPTED MANUSCRIPT

properties of Li_2O-Gd_2O_3-MO-B_2O_3-Sm_2O_3 (MO=Bi_2O_3, BaO) glasses, J. Alloys Compd. 676 (2016) 275–285.

[20] N. Wantana, S. Kaewjaeng, S. Kothan, H.J. Kim, J. Kaewkhao, Energy transfer from Gd3+ to Sm3+ and luminescence characteristics of CaO–Gd_2O_3–SiO_2–B_2O_3 scintillating glasses, J. Lumin. 181 (2017) 382–386.

[21] P. Meejitpaisan, S. Insiripong, C. Kedkaew, H.J. Kim, J. Kaewkhao, Radioluminescence and optical studies of gadolinium calcium phosphate oxyfluoride glasses doped with Sm^{3+}, Radiat. Phys. Chem. 137 (2017) 62–67.

[22] J. Rajagukguk, J. Kaewkhao, M. Djamal, R. Hidayat, Suprijadi, Y. Ruangtaweep, Structural and optical characteristics of Eu^{3+} ions in sodium-lead-zinc-lithium-borate glass system, J. Mol. Struct. 1121 (2016) 180–187.

[23] J. Kaewkhao, K. Boonin, P. Yasaka, H.J. Kim, Optical and luminescence characteristics of Eu^{3+} doped zinc bismuth borate (ZBB) glasses for red emitting device, Mater. Res. Bull. 71 (2015) 37–41.

[24] E. Kaewnuam, H.J. Kim, C.K. Jayasankar, N. Chanthima, J. Kaewkhao, The photoluminescence, optical and physical properties of Sm^{3+}-doped lithium yttrium borate glasses, Phys. Chem. Glas. Eur. J. Glas. Sci. Technol. Part B. 57 (2016) 85–89.

[25] Y. Jin, Z. Hao, X. Zhang, Y. Luo, X. Wang, J. Zhang, Dynamical processes of energy transfer in red emitting phosphor $CaMoO_4$:Sm^{3+}, Eu^{3+}, Opt. Mater. 33 (2011) 1591–1594.

[26] Z. Wang, P. Li, Z. Yang, Q. Guo, Luminescence and energy transfer of Sm^{3+} and Eu^{3+} in Ca_2PO_4Cl, J. Lumin. 151 (2014) 170–175.

Accepted manuscript

ACCEPTED MANUSCRIPT

[27] H.-Y. Lin, Y.-C. Fang, S.-Y. Chu, Energy Transfer Sm^{3+}→Eu^{3+} in Potential Red Phosphor (Ca, Ba)$_3$(VO_4)$_2$:Sm^{3+}, Eu^{3+} for Use in Organic Solar Cells and White Light-Emitting Diodes, J. Am. Ceram. Soc. 93 (2010) 3850–3856.

[28] G. Li, D. Geng, M. Shang, C. Peng, Z. Cheng, J. Lin, Tunable luminescence of Ce^{3+}/Mn^{2+}-coactivated $Ca_2Gd_8(SiO_4)_6O_2$ through energy transfer and modulation of excitation: potential single-phase white/yellow-emitting phosphors, J. Mater. Chem. 21 (2011) 13334.

[29] W.J. Yang, L. Luo, T.M. Chen, N.S. Wang, Luminescence and energy transfer of Eu- and Mn-coactivated $CaAl_2Si_2O_8$ as a potential phosphor for white-light UVLED, Chem. Mater. 17 (2005) 3883–3888.

[30] M. Inokuti, F. Hirayama, Influence of Energy Transfer by the Exchange Mechanism on Donor Luminescence, J. Chem. Phys. 43 (1965) 1978.

[31] S. Mahamuda, K. Swapna, M. Venkateswarlu, A. Srinivasa Rao, S. Shakya, G. Vijaya Prakash, Spectral characterisation of Sm^{3+} ions doped Oxy-fluoroborate glasses for visible orange luminescent applications, J. Lumin. 154 (2014) 410–424.

[32] R. Shi, J. Xu, G. Liu, X. Zhang, W. Zhou, F. Pan, Y. Huang, Y. Tao, H. Liang, Spectroscopy and Luminescence Dynamics of Ce^{3+} and Sm^{3}+ in in $LiYSiO_4$, 120 (2016) 4529–4537.

Accepted manuscript

ACCEPTED MANUSCRIPT

Figure Captions:

Fig. 1. Excitation spectrum of SM01 glass by monitoring emission at 599 nm and emission spectrum under 399 excitation. (Inset: Represents variation in emission intensity of 599 nm peak with different Sm^{3+} concentration in ZPBT glasses)

Fig. 2. Excitation Spectra of EU01 and SE04 glasses by monitoring emission at 613 nm.

Fig. 3. Emission spectra of SM01, SE01, SE02, SE03, and SE04 glasses under 399 nm excitation. (Inset: Represents emission spectra of SE04 glass under 399 and 467 nm excitation)

Fig. 4. Dependence of I_{s0}/I_s of Sm^{3+} on $C_{Tb+Sm}^{6/3}$ x 10^4, $C_{Tb+Sm}^{8/3}$ x 10^5, $C_{Tb+Sm}^{10/3}$ x 10^6 of SM01, SE01, SE02, SE03, and SE04 glasses for 399 nm excitation.

Fig. 5. Energy level diagram showing energy transfer involved in Sm^{3+}/ Eu^{3+} co-doped ZPBT glasses.

Fig. 6. Decay profiles of SM01, SE01, SE02, SE03, and SE04 glasses under excitation of 399 nm fitted with bi-exponential equation.

Accepted manuscript

ACCEPTED MANUSCRIPT

Fig. 7. Variation of average decay time, energy transfer efficiency of Sm^{3+}/Eu^{3+} co-doped ZPBT glasses with Eu^{3+} concentration under 399 nm excitation.

Fig. 8. (a) Decay profiles fitted by I-H model (S=6, 8 and 10) for SE04 glasses and (b) Decay profiles fitted with I-H model (S=6) for SM01, SE01, SE02, SE03, and SE04 glasses under 399 nm excitation.

Fig. 9. CIE diagram representing chromaticity coordinates for SM01, SE01, SE02, SE03, and SE04 glasses under 399 nm excitation.

Accepted manuscript

ACCEPTED MANUSCRIPT

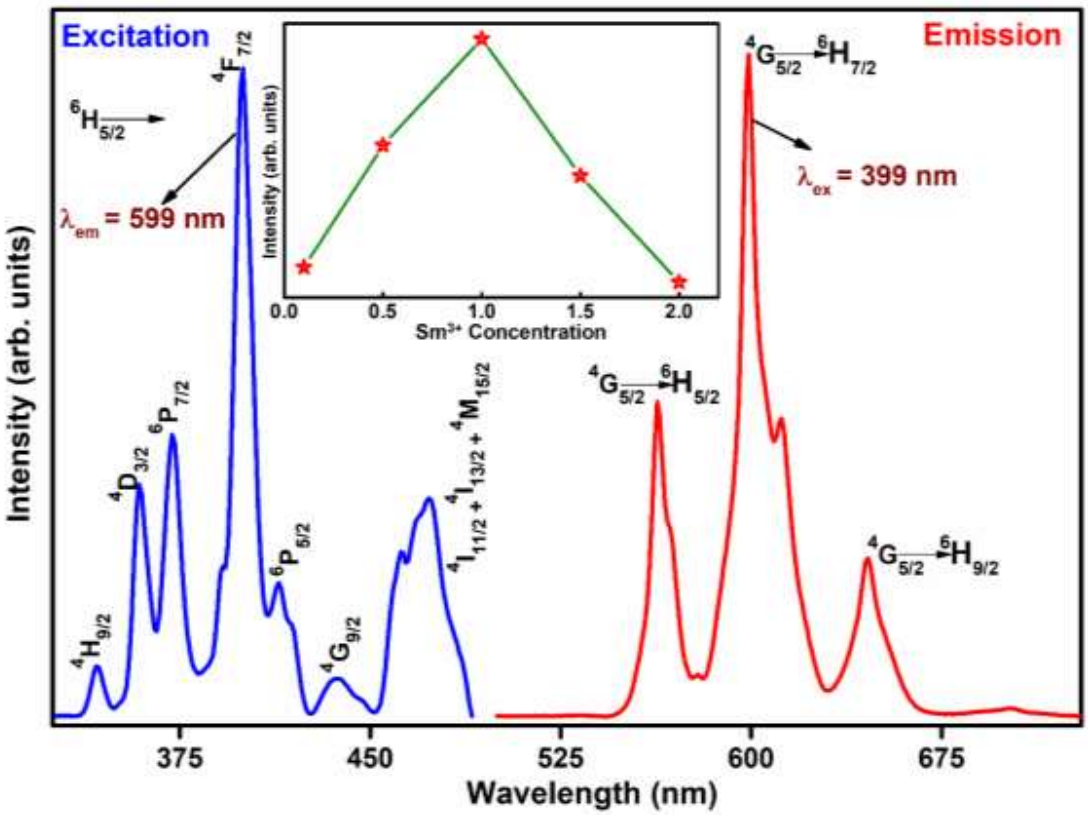
Table 1. Average lifetime (τ_{avg}), Energy transfer efficiency (η_T), Energy transfer probability rate (P_T), energy transfer parameter (Q), critical transfer distance (R_0), donor–acceptor interaction parameter (C_{DA}) and CIE chromaticity coordinates.

Sample name	τ_{avg} **(ms)**	η_T **(%)**	P_T	**Q**	**Ro (Å)**	C_{DA} **(10^{-44} cm^6s^{-1})**	**CIE Chromaticity coordinates**	
							Excitation wavelength	
							399 nm	**467 nm**
SM01	1.97	0.00	0.000	-	-	-	(0.570, 0.428)	(0.594, 0.398)
SE01	1.85	6.22	0.028	0.694	2.023	3.540	(0.578, 0.418)	(0.609, 0.382)
SE02	1.70	12.38	0.072	0.919	2.728	6.314	(0.584, 0.410)	(0.618, 0.372)
SE03	1.52	21.64	0.142	1.023	3.313	12.601	(0.595, 0.402)	(0.629, 0.365)
SE04	1.20	38.14	0.317	1.287	4.292	19.237	(0.614, 0.384)	(0.636, 0.357)

Accepted manuscript

ACCEPTED MANUSCRIPT

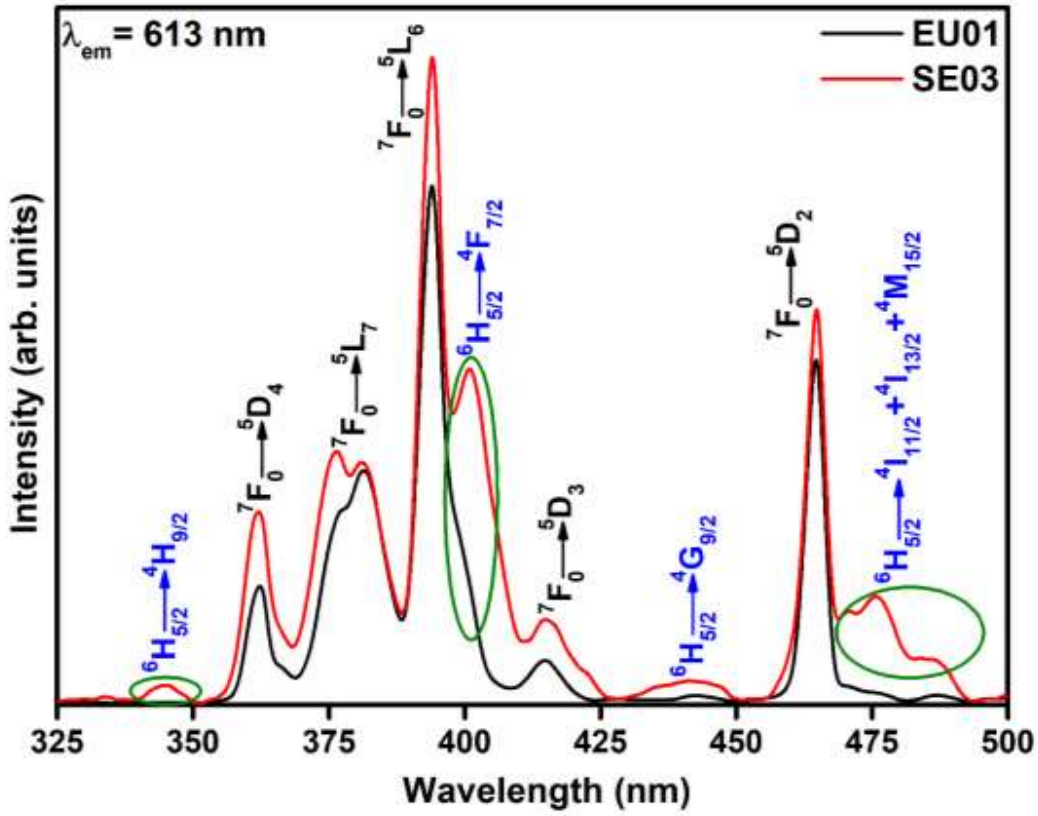
Fig. 1



Accepted

ACCEPTED MANUSCRIPT

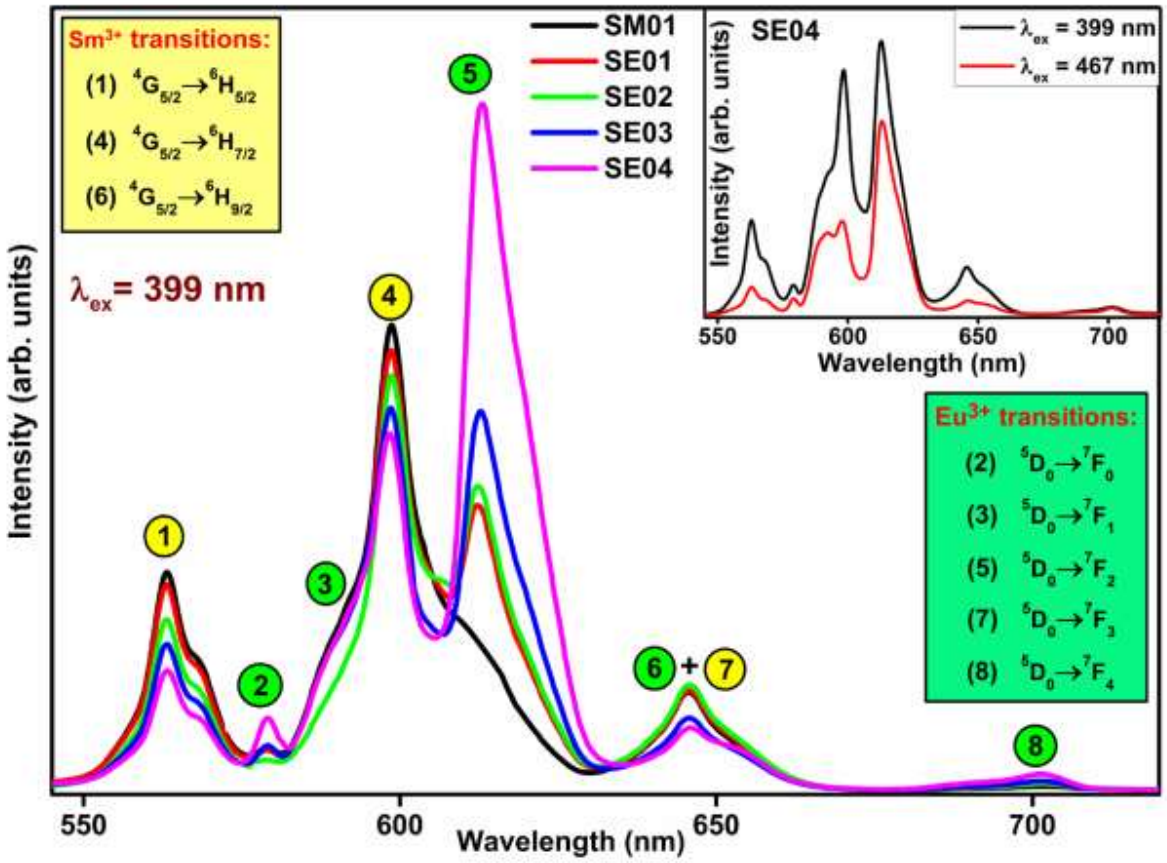
Fig. 2



Accepted

ACCEPTED MANUSCRIPT

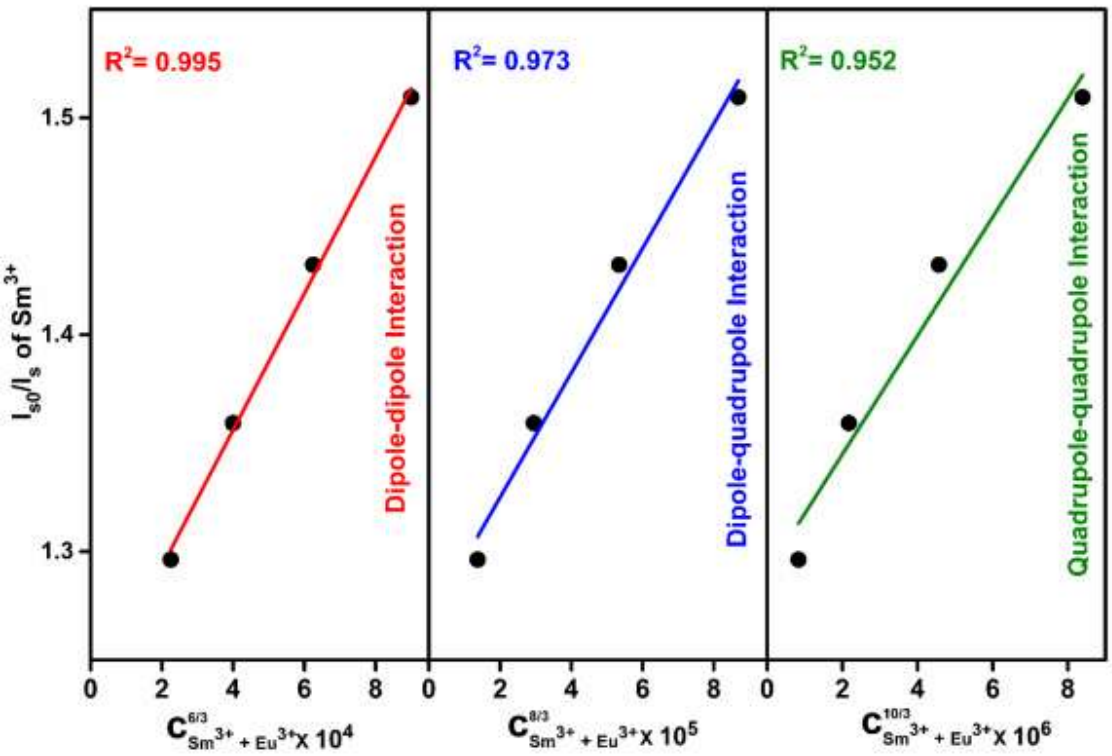
Fig. 3



Accepted

ACCEPTED MANUSCRIPT

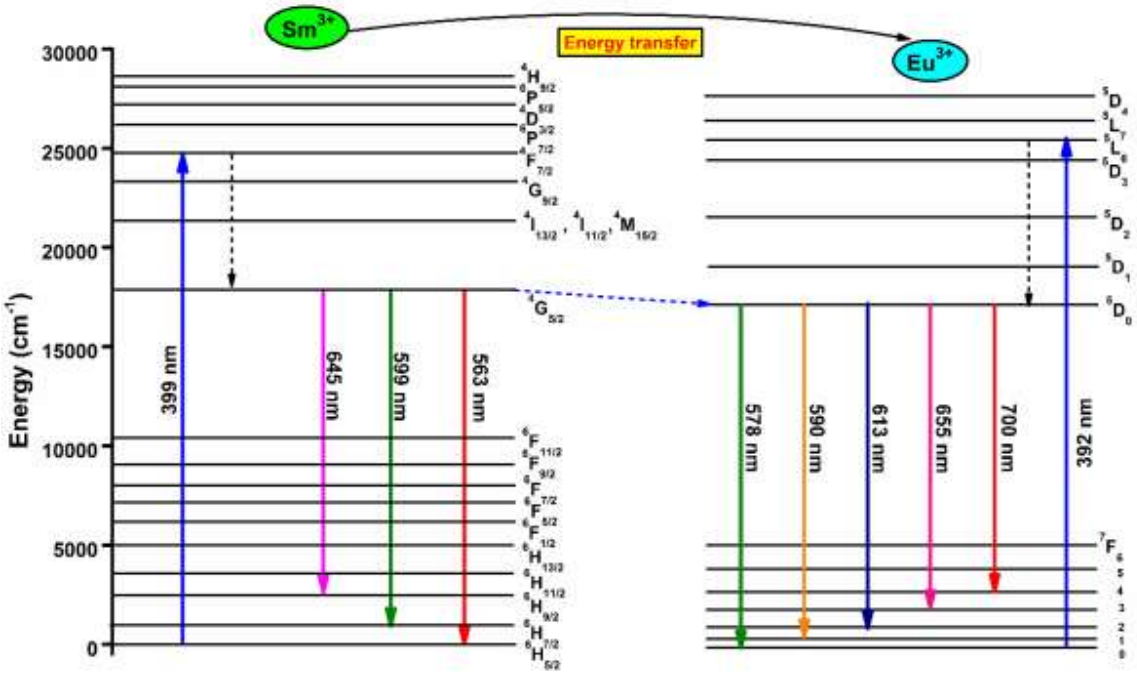
Fig. 4



Accepted M

ACCEPTED MANUSCRIPT

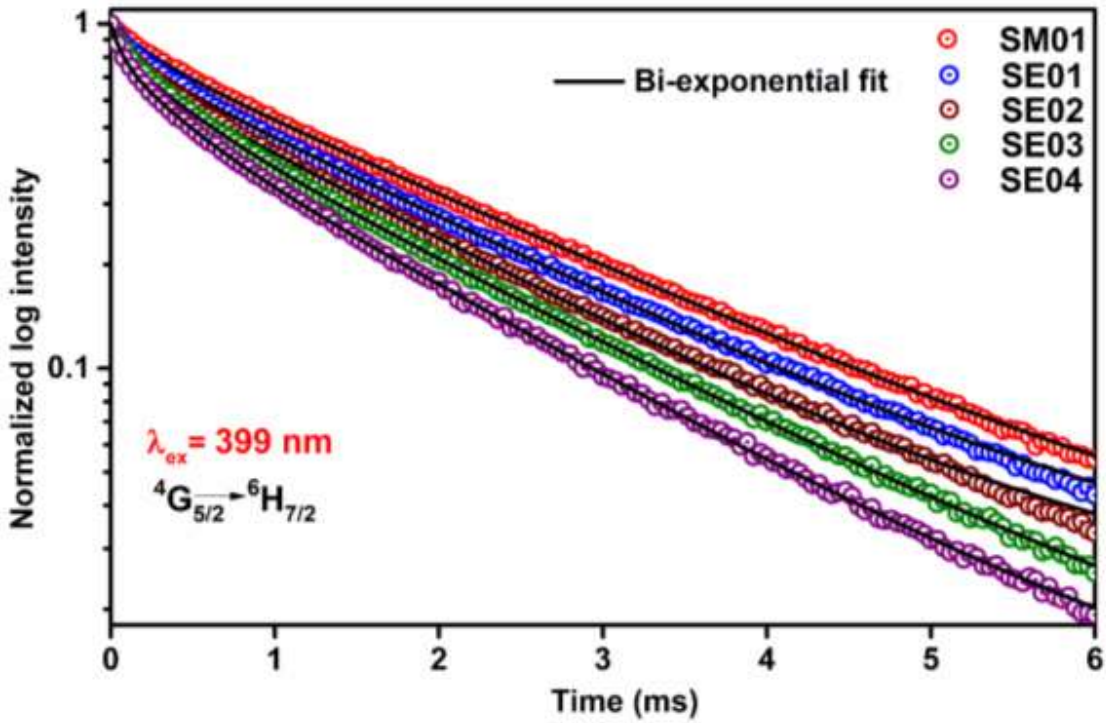
Fig. 5



Accepted manuscript

ACCEPTED MANUSCRIPT

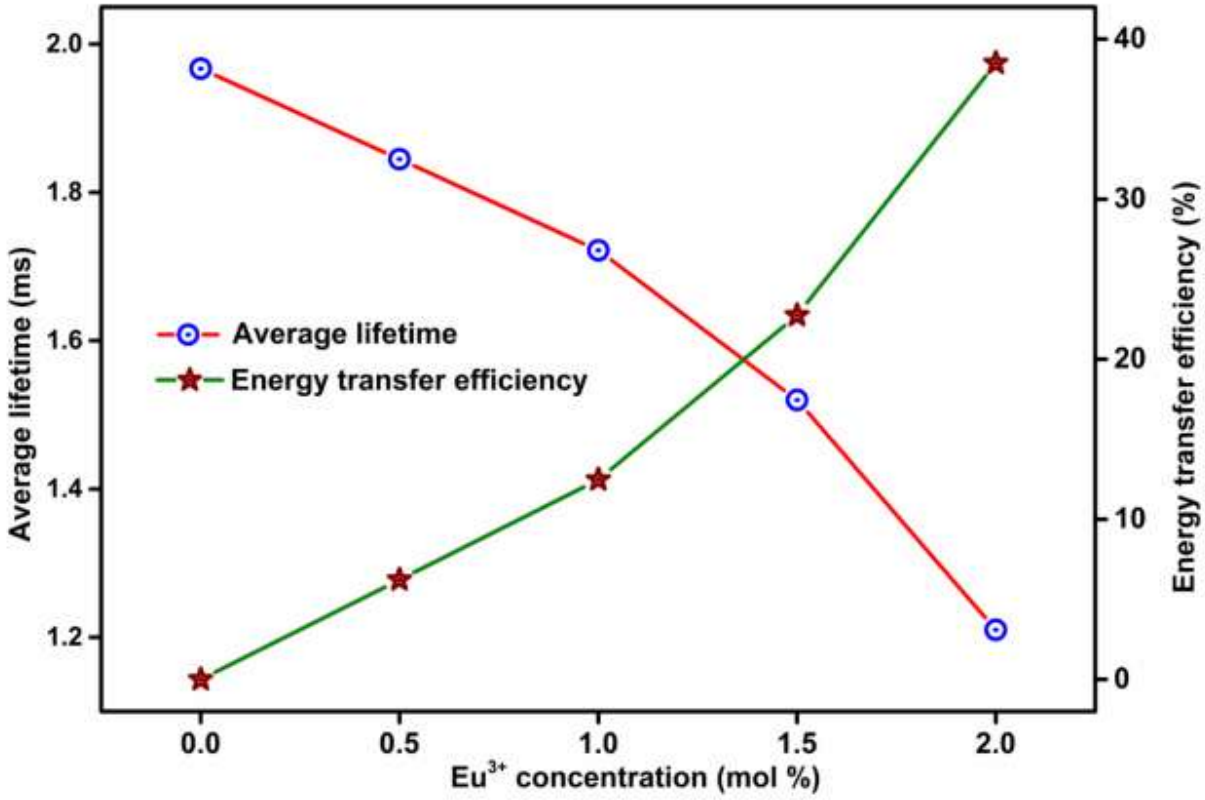
Fig. 6



Accepted

ACCEPTED MANUSCRIPT

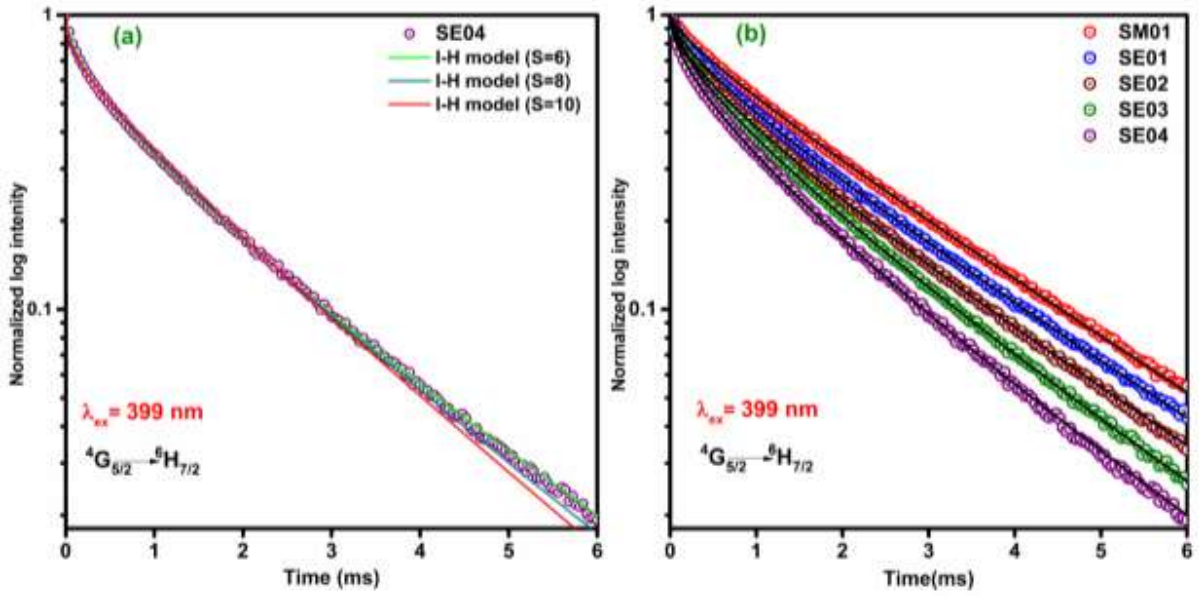
Fig. 7



Accepted

ACCEPTED MANUSCRIPT

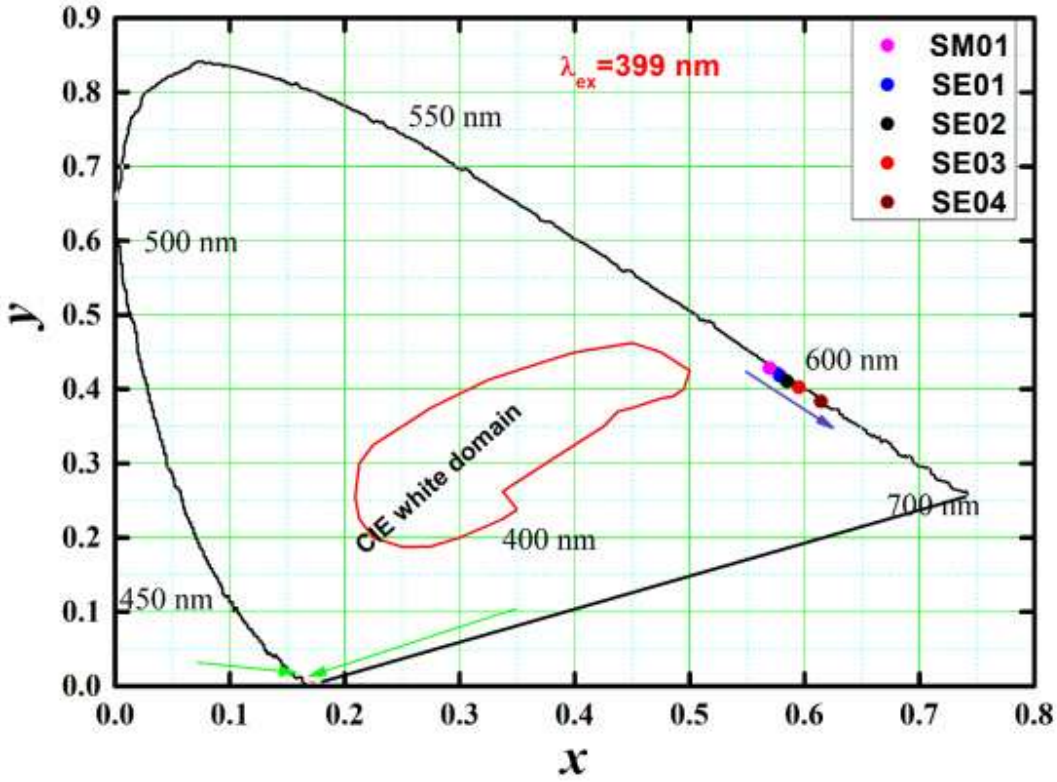
Fig. 8



Accepted manuscript

ACCEPTED MANUSCRIPT

Fig. 9



Accepted

PAPER • **OPEN ACCESS**

Electronically Tunable Fractional Order All Pass Filter

To cite this article: Rakesh Verma *et al* 2017 *IOP Conf. Ser.: Mater. Sci. Eng.* **225** 012229

View the article online for updates and enhancements.

Related content

- Design, simulation and comparative analysis of CNT based cascode operational transconductance amplifiers
M Nizamuddin, Sajad A Loan, Abdul R Alamoud et al.
- A high-performance, low-power ΔΣ ADC for digital audio applications
Luo Hao, Han Yan, Ray C. C. Cheung et al.
- A low-power low-voltage slew-rate enhancement circuit for two-stage operational amplifiers
Shu Chen, Xu Jun, Ye Fan et al.

This content was downloaded from IP address 14.139.251.107 on 17/09/2017 at 06:17

Electronically Tunable Fractional Order All Pass Filter

RakeshVerma[1], Neeta Pandey[2], Rajeshwari Pandey[2]
[1]Ph.D. Scholar, [2]Associate Professor
Department of Electronics and Communication Engineering, Delhi Technological University Delhi, Delhi INDIA
[1]dce.rkverma@gmail.com , [2]n66pandey@rediffmail.com,
rajeshwaripandey@gmail.com

Abstract: In this paper, an electronically tunable fractional order all pass filter (FOAPF) based on operational transconductance amplifier (OTA) is presented. It uses two OTAs and single fractional order capacitor (FC) of non-integer order α to provide FOAPF of α order. Two different values of α, in particular 0.5 and 0.9, for FC are taken for investigation. The functionality of the proposal is verified through SPICE simulations using TSMC 0.18 µm Complementary Metal Oxide Semiconductor (CMOS) process parameters. Simulated and theoretical frequency and time domain responses are found to be in close agreement.

Keywords: All pass filter, fractional order element, fractional order filter, OTA

1. INTRODUCTION

All pass filters (APF) are widely used in phase shifting application for analog signal processing system [1]-[6] where they pass all frequencies over the desired frequency range with a predictable phase shift. Several active first order filter realization based on various active building blocks such as current differencing buffer amplifier (CDBA) [6], [7], current conveyor (CC) [8], universal voltage conveyor (UVC) [9], [10], second generation current conveyor (CCII) [3], [11]-[13], third generation current conveyor (CCIII) [14], second generation current controlled conveyor (CCCII) [15], differential voltage current conveyor (DVCC) [4], [16]-[21], differential difference current conveyor (DDCC) [22], [23], dual-X second generation current conveyor (DXCCII) [24], [25], fully differential CCII [5], [26], [27], current controlled conveyor transconductance amplifier (CCCTA) [28], operational transconductance amplifiers (OTAs) [9], [20], [29], [30], voltage differencing inverting buffered amplifier (VDIBA) [31], voltage differencing transconductance amplifier (VDTA) [32] are available in literature.. It is observed that the active blocks with OTA or in particular having OTA block are useful for achieving electronic tuning of phase response of APF.

Content from this work may be used under the terms of the Creative Commons Attribution 3.0 licence. Any further distribution of this work must maintain attribution to the author(s) and the title of the work, journal citation and DOI.
Published under licence by IOP Publishing Ltd

Research interest in fractional order filters (FOFs) is growing recently due to inherent extra degree of freedom and possibility of embedding concept of scaling effect on frequency which leads to increase design flexibility. Their design equations are generalized from the theory of classical filter. The FOFs make use of fractional order element (FOE) whose behavior is approximated by Oustaloup Recursive approximation [33], Carlson approximation [33], Matsuda approximation [33], Chareff approximation [33], Continued Fraction Expansion (CFE) [33], Modified Oustaloup [34] and El-Khazali reduced order approximations [35]. Based on the finite element approximation of FOE, the implementation of fractional order capacitor (FC) may be obtained by a structure approximating half order FC as presented via semi-infinite RC trees in [36] or by other combinations of RC ladder networks [37] such as cross RC ladder network, domino ladder, tree structure etc. The method outlined in [38] gives structure for approximating FC of any order.

This work presents electronically tunable fractional order all pass filter (FOAPF). Two FOAPFs [39], [40] are available in open literature to the best of authors' knowledge but these lacks in electronic tuning feature. The remaining part of this paper is organized as follows. Section 2 is divided into three subsections which include FOE, OTA and realization of FOAPF. Section 3 deals with theoretical and simulation results and finally conclusion is placed in section 4.

2. PROPOSED CIRCUIT

2.1 Fractional Order Element (FOE)

The impedance function of an FOE (denoted as F) may be expressed as $Z_F(s) = as^{\alpha}$ [41], where α represents non-integer value and is termed as fractional order. The FOE impedance function can be represented in terms of magnitude ($|a\omega^{\alpha}C|$) and phase ($\alpha\pi/2$) functions. It may be noted that though, its magnitude function is frequency dependent but phase is independent of frequency and has a constant value for a given fractional order. Therefore, the FOE is also termed as a constant phase element (CPE). The FOE is not commercially available though, its behavior can be simulated by finding an appropriate rational approximation [42] of its impedance function. The FOE is versatile element and is used to generate various basic structures such as fractional order capacitor (FC), fractional order inductor (FI), differentiator [43], [44], integrator [43], [44] inverted-L type [42] and the derived RC and RL circuits as imaginary impedance [45] in fractional domain and is found in designing of various fractional order analog circuits.

2.2 Operational Transconductance Amplifier (OTA)

The circuit symbol of OTA is given in Fig. 1. It processes differential voltage and provides output current as

$$I_0 = \pm g_m(V_+ - V_-) \tag{1}$$

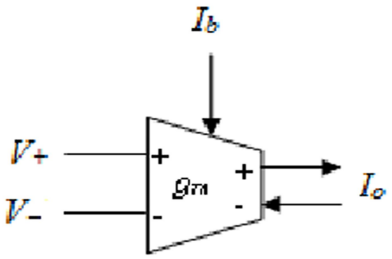


Fig. 1 Circuit Symbol of OTA

Here the transconductance gain g_m of OTA can be characterized by

$$g_m = \sqrt{\left(«_n C_{ox} \frac{W}{L} I_b \right)} \quad (2)$$

Where $«_n$, C_{ox} and W/L are the electron mobility of NMOS, gate oxide capacitance per unit area and transistor aspect ratio respectively. This expression shows that the value of g_m depends on bias current (I_b) which allows electronic tunability of the circuit parameters. Fig. 2 shows MOS circuit realization of OTA [46] for the simulation.

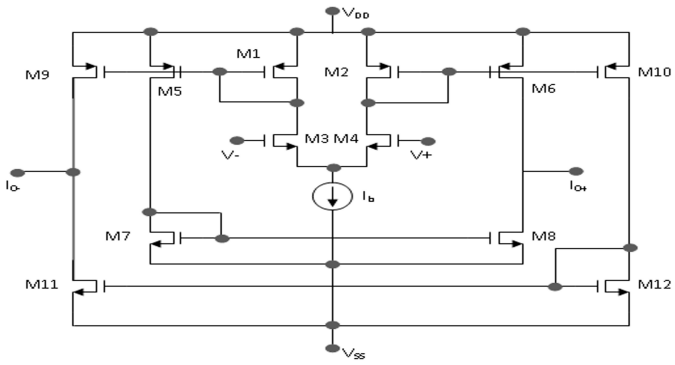
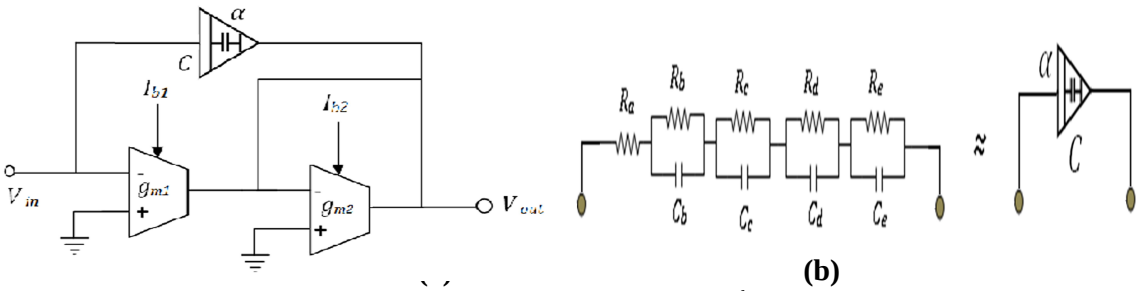


Fig.2 CMOS realization of OTA [46]

2.3 Realization of Fractional Order All Pass Filter (FOAPF)

Fig. 3(a) shows FOAPF based on OTA which is generalized by replacing traditional capacitor with FC in structure [47]. The impedance function of FC gives magnitude as $1/(\mu \tilde{} C)$ and phase as $-\sim ® / 2$.The behavior of FC is approximated by CFE method and then realized with the RC ladder network of Fig. 3(b).



(b)

Fig. 3 Circuit diagram of **(a)** OTA based FOAPF (b) 4th order approximation of FC

A single component of FC having non-integer order α and capacitor value C is chosen for designing of FOAPF. The impedance function of FC gives its magnitude as $1/(\mu^{\sim} C)$ and phase as $-\sim\!\circledR/2$.

Routine analysis of Fig. 3(a) provides following transfer function

$$T(s)_{FAPF}^{\sim} = \frac{s^{\sim} - g_{m1}/C}{s^{\sim} + g_{m2}/C} \tag{3}$$

The pole-zero plot of classical first order filter in complex s-plane allocates zero at $s = \mu_{b1}$ and pole at $s = -\mu_{b2}$.Consequently s-plane transformation into fractional domain (s^{α}) yields zero at $s^{\sim} = \mu_{b1}{}^{\sim}$ and pole at $s^{\sim} = -\mu_{b2}{}^{\sim}$.

Setting $s = \mu e^{j\circledR/2} (= j\mu)$, $\mu_{b1}{}^{\sim} = g_{m1}/C$ and $\mu_{b2}{}^{\sim} = g_{m2}/C$, the frequency response of (3) becomes

$$T(j\mu)_{FAPF}^{\sim} = \frac{\left(\mu e^{j\circledR/2}\right)^{\sim} - (\mu_{b1})^{\sim}}{\left(\mu e^{j\circledR/2}\right)^{\sim} + (\mu_{b2})^{\sim}} \tag{4}$$

The magnitude and phase of FOAPF may be expressed by (5) and (6) respectively

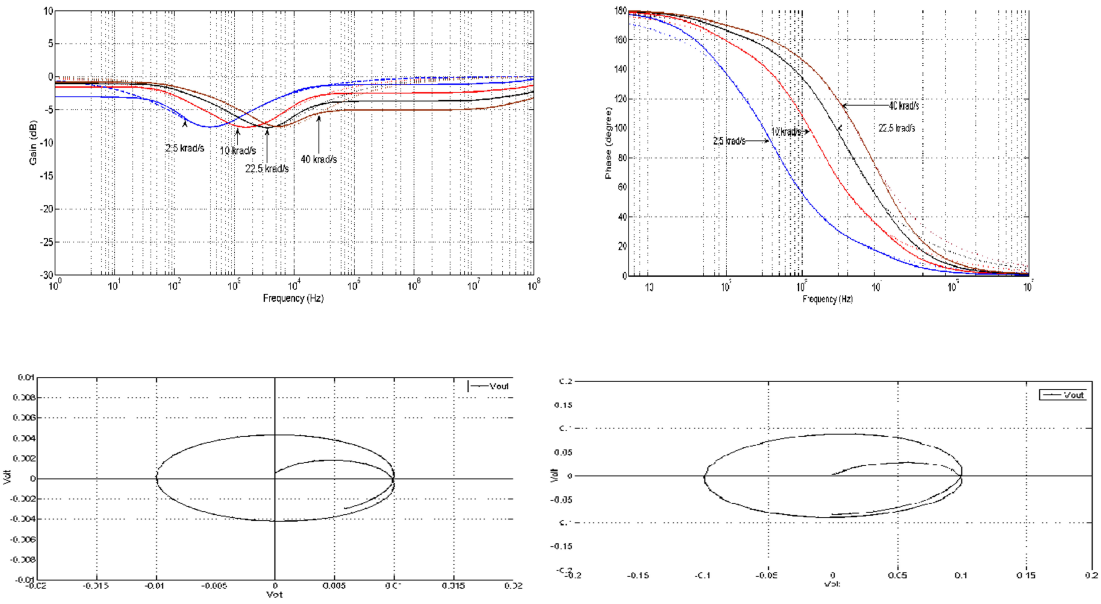
$$\left| T(j\mu) = \sqrt{\left(\frac{\mu^{2\sim} + \mu_{b1}{}^{2\sim} - 2\mu^{\sim}\mu_{b1}{}^{\sim}\cos(\sim\!\circledR/2)}{\mu^{2\sim} + \mu_{b2}{}^{2\sim} + 2\mu^{\sim}\mu_{b2}{}^{\sim}\cos(\sim\!\circledR/2)} \right)} \right| \tag{5}$$

$$\angle T(j\mu) = \tan^{-1}\left[\frac{\mu^{\sim}\sin(\sim\!\circledR/2)/\{\mu^{\sim}\cos(\sim\!\circledR/2) - \mu_{b1}{}^{\sim}\}}{\mu^{\sim}\sin(\sim\!\circledR/2)/\{\mu^{\sim}\cos(\sim\!\circledR/2) + \mu_{b2}{}^{\sim}\}} \right] \tag{6}$$

It has been seen [40] that the gain at $\mu = \mu_{rp}$ (at which $\angle T(j\mu) = \pm\circledR/2$) has minima if $\sim < 1$, maxima if $\sim > 1$ and flat if $\sim = 1$. In this work the behavior of FC is emulated through RC ladder network as shown in Fig. 3(b) which is based on 4th order CFE approximation.

3. CIRCUIT SIMULATION

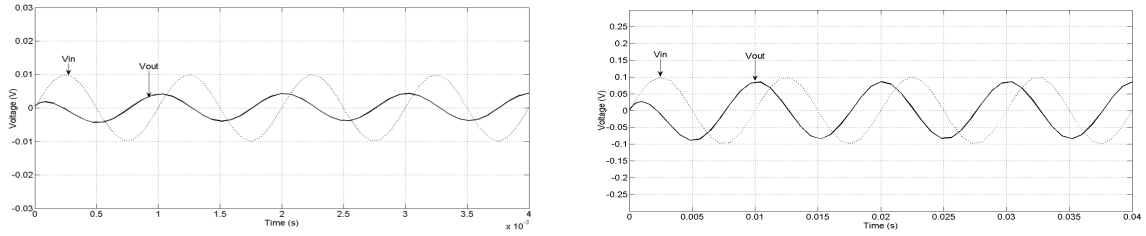
The proposed FOAPF is functionally verified through SPICE simulation wherein CMOS based schematic of OTA [46] is used with 0.18 µm TSMC CMOS process parameters. Simulations are carried out for two different FCs of fractional orders 0.5 and 0.9 respectively. The FCs of 1µF each are designed around a centre frequency of 1 kHz. To obtain electronic tunability of FOAPF parameters the g_m of OTAs is controlled through bias currents (I_{b1} and I_{b2}) variation. The supply voltages are taken as ±1.8 V. The frequency responses of the designed FOAPF, as obtained through SPICE simulation (solid lines) and theoretical (dash lines) results are depicted in Figs. 4 and 5 respectively. The theoretical results are calculated from (5) and (6) and are plotted using MATLAB program. In the responses of Figs. 4 and 5 the pole frequencies ($\mu_{b1} = \mu_{b2}$) of 2.5 krad/s, 10 krad/s, 22.5 krad/s, 40 krad/s are chosen for α = 0.5 whereas for α = 0.9 the pole frequencies are fixed at 500 rad/s, 750 krad/s, 1 krad/s, 1.25 krad/s. It may be observed from various responses that the simulation and theoretical results are quite close for a wide range of frequencies.



(a) **(b)**

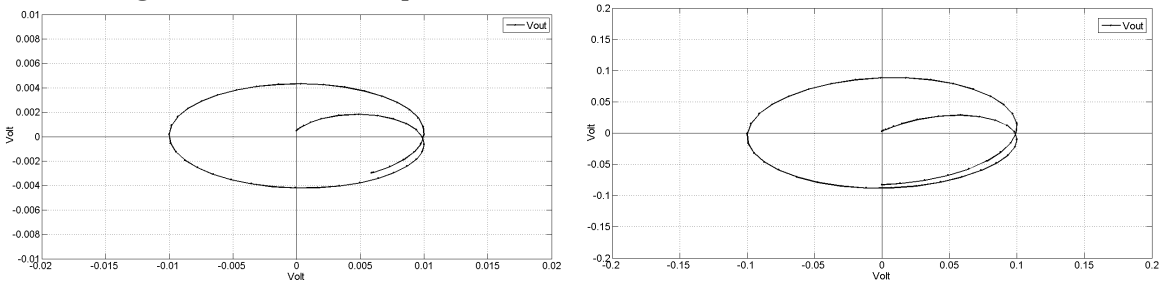
Fig. 5 FOAPF (a) magnitude (b) phase responses for order of FC is α=0.9

The time domain response of proposed filter is shown in Fig. 6 where inputs (i) 10 mV amplitude and 1 kHz frequency sinusoidal signal for order α = 0.5 as shown in Fig. 6(a) and (ii) 100 mV amplitude and 100 Hz frequency sinusoidal signal for order α = 0.9 as shown in Fig. 6(b); are applied to the filter and output is about -90^0 phase shifted. In addition, their X-Y plot (Lissajous pattern) with -90^0 phase shift is also illustrated in Fig. 7 which verifies the circuit as a phase shifter.



(a) **(b)**

Fig. 6: Time domain response of FOAPF having **(a)** α = 0.5 and **(b)** α = 0.9



(a) **(b)**

Fig. 7: (a) and (b) Lissajous (XY) pattern of Fig. 4 (a) and (b)

4 CONCLUSION

This paper proposes an electronically tunable FOAPF by generalizing first order all pass filter into fractional domain where tuning operation is executed through bias currents of OTAs. The phase shift operation is also tuned electronically. It is shown that all pass filter has more flexibility in shaping the filter response when generalizing into fractional domain. The frequency and time domain responses of FOAPF of order 0.5 and 0.9 are depicted which are close to theoretical results.

REFERENCES

[1] R. Schaumann, and M. E. Van Valkenbrg, "Design of analog filters," Oxford University Press, New York, 2001.
[2] D. Comer, and J. McDermid, "Inductorless bandpass characteristics using all-pass networks," IEEE Transactions on Circuit Theory. vol. 15, no. 4, pp. 501–503, 1968.
[3] O. Cicekoglu, H. H. Kuntman, and S. Berk, "All pass filters using a single current conveyor," Proceedings of the 6th International Conference on Optimization of Electrical and Electronic Equipments, Brasov, pp. 649– 654. 1998.
[4] J. W. Horng, "DVCCs based high input impedance voltage-mode first-order allpass, highpass and lowpass filters employing grounded capacitor and resistor," Radioengineering. vol. 19, no. 4, pp. 653–656, 2010.
[5] B. Metin, N. Herencsar, and K. Pal, "Supplementary first-order all-pass filters with two grounded passive elements using FDCCII," Radioengineering, vol. 20, no. 2, pp. 433-437, 2011.
[6] A. Toker, S. Ozoguz, O. Cicekoglu, and C. Acar, "Current-mode all-pass filters using current differencing buffered amplifier and a new high-Q bandpass filter configuration," IEEE Transactions on Circuits and Systems II: Analog and Digital Signal Processing, vol. 47, no. 9, pp. 949-954, 2000.
[7] F. Kacar, Y. Ozcelep, "CDBA based voltage-mode first-order all-pass filter topologies'" Istanbul University-Journal of Electrical & Electronics Engineering, vol. 11, no.1, 2011.
[8] H. P. Chen, and K. H. Wu, "Grounded-capacitor first-order filter using minimum components," IEICE Transactions of Fundamentals, Vol. E89-A, pp. 3730-3731, 2006.
[9] N. Herencsar, J. Koton, and K. Vrba, "A new electronically tunable voltage-mode active-C phase shifter using UVC and OTA," IEICE Electronics Express, vol. 6, no. 17, pp. 1212-1218, 2009.
[10] N. Herencsar, J. Koton, J. Jerabek, K. Vrba, and O. Cicekoglu, "Voltage-mode all-pass filters using universal voltage conveyor and MOSFET-based electronic Resistors," Radioengineering, vol. 20, no. 1, pp. 10-18, 2011.
[11] A. Toker, S. Ozcan, H. Kuntman, and O. Cicekoglu, "Supplementary all-pass sections with reduced number of passive elements using a single current conveyor," International Journal of Electronics, vol. 88, no. 9, pp. 969-976, 2001.
[12] M. A. Ibrahim, H. Kuntman, S. Ozcan, O. Suvak, and O. Cicekoglu, "New first-order inverting-type second-generation current conveyor-based all-pass sections including canonical forms," Electrical Engineering, vol. 86, no. 5, pp. 299-301, 2004.

[13] F. Yucel, and E. Yuce, “CCII based more tunable voltage-mode all-pass filters and their quadrature oscillator applications,” International Journal of Electronics and Communication (AEU), vol. 68, no. 1, pp. 1-9, 2014.
[14] S. Maheshwari, and I. A. Khan, “Novel first order all-pass sections using a single CCIII,” International Journal of Electronics, vol. 88, no. 7, pp. 773-778, 2001.
[15] S. Minaei and O. Cicekoglu, “A resistorless realization of the first-order all-pass filter”, International Journal of Electronics, vol. 93, no. 3, pp. 177-183, 2006.
[16] S. Maheshwari, "High input impedance VM-APSs with grounded passive elements," IET Circuits, Devices and Systems, vol. 1, pp. 1, 72-78, 2007.
[17] S. Maheshwari, "A canonical voltage-controlled VM-APS with a grounded capacitor," Circuits, Systems and Signal Processing, vol. 27, no. 1, pp. 123-132, 2008.
[18] S. Maheshwari, "High input impedance voltage-mode first-order all-pass sections," International Journal of Circuit Theory and Applications, vol. 36, no. 4, pp. 511-522, 2008.
[19] S. Minaei, and E. Yuce, "Novel voltage-mode all-pass filter based on using DVCCs," Circuits, Systems, and Signal Processing, vol. 29, no. 3, pp. 391-402, 2010.
[20] T. Tsukutani, H. Tsunetsugu, Y. Sumi, and N. Yabuki, “Electronically tunable first-order all-pass circuit employing DVCC and OTA,” International Journal of Electronics, vol. 97, no. 3, pp. 285-293, 2010.
[21] S. Maheshwari, J. Mohan, and D. S. Chauhan, “Novel voltage-mode cascadable all-pass sections employing grounded passive components,” Journal of Circuits, Systems, and Computers, vol. 22, 2013.
[22] M. A. Ibrahim, H. Kuntman, and O. Cicekoglu, “First-order all-pass filter canonical in the number of resistors and capacitors employing a single DDCC,” Circuits, Systems, and Signal Processing, vol. 22, no. 5, pp. 525-536, 2003.
[23] J. W. Horng, C. M. Wu, and N. Herencsar, “Fully differential first-order all pass filters using a DDCC,” Indian Journal of Engineering and Materials Sciences, vol. 21, no. 4, pp. 345-350, 2014.
[24] S. Minaei, and E. Yuce, “Unity/variable-gain voltage-mode/current-mode first-order all-pass filters using single dual-X second-generation current conveyor,” IETE Journal of Research, vol. 56, no. 6, pp. 305-312, 2010.
[25] S. Maheshwari, and B. Chaturvedi, “High-input low-output impedance all-pass filters using one active element,” IET Circuits, Devices and Systems, vol. 6, no. 2, pp. 103-110, 2012.
[26] S. Maheshwari, J. Mohan, and D. S. Chauhan, “Voltage-mode cascadable all-pass sections with two grounded passive components and one active element,” IET Circuits, Devices and Systems, vol. 4, no. 2, pp. 113-122, 2010.
[27] J. Mohan, and S. Maheshwari, “Additional high-Input low-output impedance voltage-mode all pass section,” Journal of Circuits, Systems, and Computers, vol. 23, no. 6, pp. 1-14, 2014.
[28] W. Tangsrirat, J. Budboonchu, and T. Pukkalanun, “Resistorless voltage-mode first-order allpass section using single current-controlled conveyor transconductance amplifier,” Indian Journal of Pure & Applied Physics, vol. 53, no. 5, pp. 335-340, 2015.
[29] A. U. Keskin, K. Pal, and E. Hancioglu, "Resistorless first order all-pass filter with electronic tuning," AEU-International Journal of Electronics and Communications, vol. 62, no. 4, pp. 304-306, 2008.

[30] I. A. Khan, and M. T. Ahmed, “Electronically tunable first-order OTA-capacitor filter sections,” International Journal of Electronics, vol. 61, no. 2, pp. 233-237, 1986.
[31] N. Herencsar, S. Minaei, J. Koton, E. Yuce, and K. Vrba, “New resistorless and electronically tunable realization of dual-output VM all-pass filter using VDIBA,” Analog Integrated Circuits and Signal Processing, vol. 74, no. 1, pp. 141-154, 2013.
[32] S. Maneewan, N. Udorn, P. Silapan, D. Duangmalai, and W. Jaikla, "A voltage-mode first order all pass filter based on VDTA," Advances in Electrical and Electronic Engineering, vol. 12, no. 1, 2014.
[33] B. M. Vinagre, I. Podlubny, A. Hernandez, and V. Feliu, "Some approximations of fractional order operators used in control theory and applications," Fractional Calculus & Applied Analysis, vol. 3, no. 3, pp. 945-950, 2000.
[34] D. Y. Xue, C. Zhao, and Y. Q. Chen, "A modified approximation method of fractional order system," IEEE Conference on Mechatronics and Automation, pp. 1043–1048, 2006.
[35] R. El-Khazali, "On the biquadratic approximation of fractional order laplacian operators," Springer-Analog Integrated Circuits and Signal Processing, vol. 82, no. 3, pp. 503-517, 2015.
[36] M. Nakagava, and K. Sorimachi, "Basic characteristics of a fractance device," IEICE Transactions on Fundamentals, vol. E75-A, no. 12, pp. 1814–1818, 1992.
[37] I. Podlubny, I. Petras, B. M. Vinagre, P. O. Leary, and L. Dorcak, "Analogue realizations of fractional order controllers," Springer-Nonlinear Dynamics, vol. 29, no. 4, pp. 281-296, 2012.
[38] M. Sugi, Y. Hirano, Y. F. Miura, and K. Saito, "Simulation of fractal immittance by analog circuits: an approach to the optimized circuits," IEICE Transactions on Fundamentals, vol. E82-A, no. 8, pp. 205-209, 1999.
[39] B. Maundy, A. Elwakil, and S. Gift, "On the realization of multiphase oscillators using fractional-order allpass filters," Circuits, Systems, and Signal Processing, vol. 31, no. 1, pp. 3-17, 2012.
[40] A. G. Radwan, A. M., Soliman, and A. S. Elwakil, “First-Order Filters Generalized to the Fractional Domain, World Scientific-Journal of Circuits, Systems, and Computers,” vol. 17, no.1, pp. 55–66, 2008.
[41] T. J. Freebom, B. Maundy, and A. Elwakil, “Fractional resonance-based $RL_{\alpha}C_{\beta}$ filters,” Hindawi-Mathematical Problems in Engineering, 2013. doi:10.1155/2013/726721.
[42] B.T. Krishna, "Studies on Fractional Order Differentiators and Integrators: A Survey," Elsevier Signal Processing, Vol. 91, Issue 3, pp. 386-426, 2011.
[43] G. Tsirimokou, C. Psychalinos, "Ultra-Low Voltage Fractional Order Differentiator and Integrator Topologies: An Application for Handling Noisy ECGs," Springer-Analog Integrated Circuits and Signal Processing Journal, Vol. 81, Issue 2, pp. 393-405, 2014.
[44] T. Suksang, W. Loedhammacakra, V. Pirajnanchai, "Implement the Fractional Order, Half Integrator and Differentiator on the OTA Based $PI^{\lambda}D^{\mu}$ Controller Circuit," IEEE Conference on ECTICON, pp. 1-4, 2012.
[45] A.G. Radwan, K.N. Salama, "Fractional Order RC and RL Circuits," Springer-Circuits, Systems, and Signal Processing, Vol. 31, Issue 6, pp. 1901-1915, 2012.
[46] Raj Senani, D. R. Bhaskar, M. Gupta, and A. K. Singh, "Canonic OTA-C sinusoidal oscillators: Generation of new grounded-capacitor versions,"American Journal of Electrical and Electronic Engineering, vol. 3, no. 6, pp. 137-146, 2015.

[47] R. L. Geiger, and E. Sanchez-Sinencio, "Active filter design using operational transconductance amplifiers: a tutorial," IEEE Circuits and Devices Magazine, vol. 1, no. 2, pp. 20–32, 1985.



Rakesh Verma received B. Tech degree in Electronics and Communication Engineering (ECE) from Birla Institute of Applied Sciences, Bhimtal and M. Tech degree in Control and Instrumentation Engineering from Delhi Technological University, Delhi. He has served as Assistant Professor in ECE department, National Institute of Technology, Delhi. At present, he is a Ph. D research scholar in ECE department, Delhi Technological University, Delhi. His research interest is focused on fractional order current mode circuits.



Neeta Pandey is currently working as an Associate Professor in Department of Electronics and Communication Engineering, Delhi Technological University. She did her M. E. in Microelectronics from Birla Institute of Technology and Sciences, Pilani and Ph. D. from Guru Gobind Singh Indraprastha University Delhi. She is a life member of ISTE, and senior member of IEEE, IEEE WIE USA. She has published papers in International, National Journals of repute and conferences. Her research interests are in Analog and Digital VLSI Design.



Rajeshwari Pandey is currently working as an Associate Professor in Department of Electronics and Communication Engineering, Delhi Technological University, Delhi, India. She did her M.E (Electronics and Control) from BITS, Pilani, Rajasthan, India and Ph. D. from Faculty of Technology, Delhi University, India. Her research interests include Analog Integrated Circuits, and Microelectronics. She has published papers in International, National Journals of repute and conferences. She is life member of IETE, ISTE and member of IEEE, IEEE WIE for 10 years.

International Journal of Research in Engineering and Innovation (IJREI)
journal home page: http://www.ijrei.com
ISSN (Online): 2456-6934



Exergetic performance and parametric evaluation of simple linde liquefaction system using different gasses

R.S Mishra, Devender Kumar

Department of Mechanical, Production and Automobile Engineering, Delhi Technological University, Delhi, India

Abstract

An abbreviated methodology for exergy destruction estimation in simple Linde cryogenic systems discussed in this paper. Energy-Exergy analysis of every component at each stage is done using computational numerical technique. It helps in find out the losses and loopholes responsible for the reduced efficiency of the system. A thorough study is done to determine pressure ratio effect on the first law, second law, specific heat, NTU of heat exchangers and exergy depletion in each sub-component of Linde system. Different gasses are employed to check the compatibility of the regime with each gas at various pressure ratio. From the study, its summarize that due to various physical properties of gasses, same configure Linde system respond very differently in the process of liquefaction of each gas. From the comparison, graphical data of six gasses its notice that the 60-80 bar pressure ratio is optimum pressure ratio suiting all considered gasses for simple Linde system. It also depicted from research that exergy depletion or destruction in sub-component also depend upon the type of gas using for liquefaction. Various results show that first and second law efficiency of the system is still low providing future challenges of improvement in system and helping in decreasing exergy destruction for better performance of the system.

© 2017 ijrei.com. All rights reserved

Keywords: Second Law Analysis, Super Critical Power Plant, Thermodynamic Analysis, Irreversibility optimization

1. Introduction

Cryogenics has always been an important area of refrigeration because many scientific and engineering types of research are done using low-temperature liquefied gasses. Cryogenics isa branch of physics which deals with theachieving very low temperatures (below the 173 K.) and study their effects on matter Cryogenic study presents broad goals for cryogenic support for various gas liquefaction systems. Due to the industrial revolution, various issues like cost, efficiency and reliability are the challenges factors in the employment of cryogenic support technology. In one of many ways,exergy can also be relatedto the ratio of useful effect and its cost to produce that effect. Standardization technique in cryogenic industry is one way of cost reduction and accessing reliability but other side increase in reliability result decrease in efficiency of the system e.g. using two over one expander in a Brayton Cycle. For improvement in the reliability factor, redundancy must be increased, but it hamper costing factor of the system. Generally, most of the refrigerators unit run approx. at 10 % to 30% of Carnot efficiency and biggest reason behind the low efficiency degradation of exergy in compressors and heat exchangers units. In most of cases largest amount of exergy destruction or irreversibility is take place in compressor of a cryogenic refrigerator Badescu [1] depicted that most exergy destruction in vapour compression heat pump is taken place in compressor and condenserunit, butfrom various research it stated that use of liquid nitrogen (LN)methodologywith estimated cost and reliability help in reduce the irreversibility in compressor [2] whereas irreversibility in heat exchanger could be reduced by proper insulation.Main causes of exergy destruction in the heat exchanger are heat exchange in between the two flows, loss of pressure due

Corresponding author: R.S. Mishra
Email Id: rsmishradtu@gmail.com

to friction between fluid layers and losses due to the environment factors and these three phenomena occurred mutually in heat exchange process. From another minor factor which causes the losses in heat exchangers, streamwise conduction in the walls [3] is most prominent. Ren et al. [4] in research show that regenerative evaporative cooling technique shows highest performance and effectiveness of indirect heat exchanger is an important factor in enhancing the exergy efficiency of the regenerative unit. Whereas Bejan [5] work considered as the basis of exergetic analysis on heat exchangers. To design and evaluation any cryogenic plant, characterizing and understanding the exergetic behavior of a heat exchanger (HX) is very necessary.Numbers of research or studies partially or entirely based on the concept of rational efficiency ($\eta_{rational}$)which generally defined as the exergy received by cold fluid divided by exergy released by hot fluid [4].Irreversibility is the main factor due to which exergy of the cold fluid to the hot fluid are not equal. Exergetic behavior characteristic of an exchanger in term of total exergy loss discuss in the literature [5-6]. However, from various studies its notice that none of exergetic loss or rational efficiency tell exactly about the factors behind irreversibility, so to reduce exergy depletion in a heat exchanger (HX), it very important to find out which dominant factor causes the most destruction. Generally surrounding attached exergetic value of an exchanger is neglected, because of very small (10%)[7].According to Boyle-Mariotte principle, expectation of temperature change during expansion process is nil but in real gas expansion case, for every 1 bar pressure drop temperature drop in valve is approx. 0.25 °C. This indicate that this law not applicable for real gases. J. K. van der Waals (1873)in there research also explain about this effect and notice that compressed gas molecules doesn't interact each other nor freely move which leads to the temperature drop during decompression .Friction and eddy losses take place in the valve which in turn responsible for exergy loss in the valve of the cryogenic unit. Separation unit is very important part of cryogenic system, Joule-Thomson refrigeration effect and countercurrent heat exchange principle are breakthrough for cryogenic air separation leads lots of further research and development in separation unit. Rosen et al. [8] improve analysis of vapour compression system by introducing the concept that it's necessary to do exergy analysis to choose the refrigerant for a system. Major analysis is performed using different hydrocarbon refrigerant. In this paper we studied and discuss about the exergy analysis of simple Linde system. Exergy analysis of Linde system is done before [9] but it is done via using control volume technique. The losses in inner component of system is not dare cuss earlier. Exergy analysis is done at every state of the system to find out the losses in each individual component and they are calculated in term of exergy destruction. Further the effect of pressure ratio on liquefaction and various other performance parameters of system with gases like nitrogen, methane, argon, fluorine, oxygen and air respectively is studied in this paper. The whole parameters studied further help in improving the Linde system of liquefaction for different gas.

2. System Description

Cryogenic industries use various processes for liquefaction of gas in which some are complex with high efficiency, and some are simple with low efficiency. Here we are considered simpleLinde-Hampson cycle shown in Fig:1 The schematic diagram of cycle providing full algorithm about working of the system which in turn also useful in energy and exergy analysis of the system. Initially, compressor compressed the gas by the isothermal process. The temperature of the system is kept constant by rejecting heat of compressor using coolant jacket around it. After increasing the gas pressure in the compressor, it is cooled in counter flow heat exchanger work as regenerative in cryo cycle. The hot pressurized stream from compressor exchange heat with cold stream of uncondensed gas from the previouscycle of cryo system. After rejecting the heat to cold stream, the pressurized flow induced in J-T(Joule-Thomson) valve where it is throttled and two states (liquid-vapour) mixture of gas is obtained. The liquid part is collected using various distillation technique while vapourportionis routed back to the compressor and in the way, after regenerative, the vapour is mixed with the makeup gas for continuous running of cryo plant.

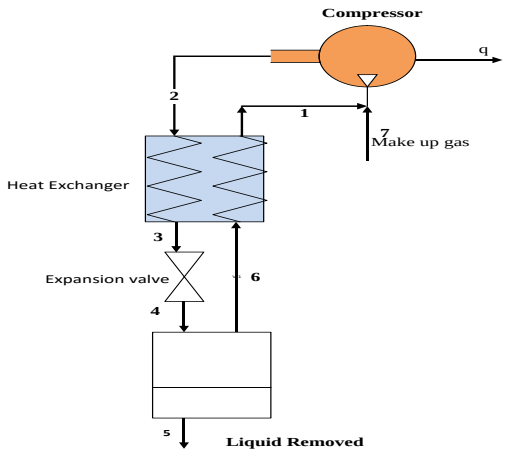


Figure 1: Schematic diagram of Linde-Hampson cycle

3. System Analysis

Various mathematical equations are used for exergy analysis of Linde system. Mathematic analysis of following components is done below

3.1. Compressor

The compressorplaysasignificant role in any liquefaction system and as per literature study above it also causes the highest destruction of energy mean most top exergy destruction take place in the compressor.

$$W_c = \left(m_2 * \left((h_2 - h_1)\right) - T_2 * (s_2 - s_1)\right) \quad (1)$$

Whereas 'W_c'represent the actual work done in the Linde system, h, s, T and m repestively are enthalpy entropy temperature and mass flow rate of gas at state 1 and 2.

$$COP = \frac{h_1 - h_6}{(h_2 - h_1) - (T_1 * (s_2 - s_1))} \quad (2)$$

The coefficient of performance (COP) of system represent the first law efficiency of the system, it is the ratio of refrigeration effect and work done on the system. Refrigeration effect can be defined as the heat removed from the gas state to saturated liquid state.

$$h_f = h_6 \quad (3)$$

whereash_f is enthalpy of saturated liquid state.

$$Ed_{comp} = \begin{pmatrix} m_6 * T_1 * (s_1 - s_2) - \\ \left(Q * \left(\frac{T_0}{T_1}\right)\right) \end{pmatrix} \quad (4)$$

Here Ed denoted the exergy destruction and Ed_{comp}represent the exergy destruction in compressor. Where as Q represent the energy given to the compressor andT_0 is the ambienttemperature. The term $\left(T_1 * (s_1 - s_2)\right)$ in above equation has significant use and represent the irreversibility.Irreversibility account for the exergy destroyed in closed system. Further division of equation $(s_1 - s_2)$represent the entropy generation at state 1 and 2.

3.2. Heat exchanger analysis

Due to their significant temperature difference exchanger is used to exchange thermal heat from hot to cold fluid. The energy and exergy balance equation of heat exchanger is following

$$\mathrm{m_{h_{HX}}} * \left(\mathrm{h_{h,i}} - \mathrm{h_{h,o}}\right) = \mathrm{m_{c_{HX}}} * \left(\mathrm{h_{c,o}} - \mathrm{h_{c,i}}\right) + \mathrm{q} \quad (5)$$

$$\mathrm{Ex_{in_{HX}}} - \mathrm{Ex_{out_{HX}}} - \mathrm{Ed_{HX}} = \mathrm{E_{x_{HX}}} = 0 \Rightarrow \text{steady} \quad (6)$$

$$\mathrm{Ex_{HX}} = \mathrm{m_i} * \begin{pmatrix} (\mathrm{h_{in}} - \mathrm{h_{out}}) - \\ \left(\mathrm{T_0} * (\mathrm{s_{in}} - \mathrm{s_{out}})\right) \end{pmatrix} \quad (7)$$

$$\mathrm{Ed_{HX}} = \left(\left(\mathrm{Ex_{in_{HX}}}\right) - \left(\mathrm{Ex_{out_{HX}}}\right)\right) \quad (8)$$

Here 'HX' term denoted to heat exchanger of the system.

Exergy analysis of simple Linde system is to calculate the losses in the heat exchanger. The losses due to surrounding make an exergytransfer, but heat insulation technique avoided most of the exergy destruction due to environmental effect, so it is neglected. Another factors for the exergy destruction in HX are fluid friction across the wall and loss of the head of flow in pipes. The primary cause of destruction is temperature and pressure loss in pipes.

The specific heat energy rate q can be written as the function of flow rate (m) and difference of temperature of fluid at entry and exit(ΔT), the function can be written as

$$q_{specific} = f(m, \Delta T) \quad (9)$$

Heat transfer rates in exchanger's are found out by below formulations:

$$\mathrm{q_{HX}} = \mathrm{C_{h,HX}} * \left(\mathrm{T_{h_i}} - \mathrm{T_{h_o}}\right) \quad (10)$$

$$\mathrm{q_{HX}} = \mathrm{C_{c,HX}} * \left(\mathrm{T_{c_o}} - \mathrm{T_{c_i}}\right) \quad (11)$$

For maximum heat transfer following condition should be satisfied.

$$\mathrm{T_{h_i}} = \mathrm{T_{c_o}};\ \mathrm{T_{h_o}} = \mathrm{T_{c_i}} \quad (12)$$

Maximum heat transfer rate capacity $q_{\max HX}$which is the maximum heat transfer between cold and hot fluid is formulated as

$$\mathrm{q_{max_{HX}}} = \mathrm{C_{min_{HX}}} * \left(\mathrm{T_{h_i}} - \mathrm{T_{c_i}}\right) \quad (13)$$

The representation of HX effectiveness (epsilon) is:

$$\varepsilon = \mathrm{q_{HX}}/\mathrm{q_{max_{HX}}} \quad (14)$$

$$\varepsilon = ((\text{Actual thermal energy})/ (\text{actual exchange of energy}))/ ((\text{Highest thermal energy possible})/ (\text{Maximum energy transfer}) \quad (15)$$

$$\mathrm{Ntu_{HX}} = (\mathrm{G_{HX}})/\mathrm{C_{min_{HX}}} \quad (16)$$

$$\mathrm{G_{HX}} = \mathrm{U} * \mathrm{A} \quad (17)$$

NTU 'Number of Transfer Unit' is a dimensionless parameter which broadly provides the size of the heat exchanger, 'U' overall heat transfer coefficient whereas 'A' represent area of the heat exchanger. During the exchange of thermal energy in exchangers, the entropy of the hot side decreases. Heat exchangers which are used in refrigeration/ liquefaction units, the main purpose is to amplify the exergy of the high-pressurehigh-temperature fluid so it capable enough to receive heat from the outer load. Based on said condition rational exergetic efficiency

written as:

$$\eta_{HX,Rational} = \left(m_h * \left(Ex_{h,out_{HX}} - Ex_{h,in_{HX}}\right)\right) / (m_c * (Ex_{c,out_{HX}} - Ex_{c,in_{HX}})) \quad (18)$$

In Linde system heat exchanger, change of exergy destruction is written in the following form

$$Ex_{in_{HX}} = m_2 * \begin{pmatrix} (h_2 - h_3) - \\ (T_0 * (s_2 - s_3)) \end{pmatrix} \quad (19)$$

$$Ex_{out_{HX}} = m_g * \begin{pmatrix} (h_6 - h_7) - \\ (T_0 * (s_6 - s_7)) \end{pmatrix} \quad (20)$$

$$Ed_{HX} = abs\left(\left(Ex_{in_{HX}}\right) - \left(Ex_{out_{HX}}\right)\right) \quad (21)$$

3.3. Joule-Thomson Valve

The expansion valve used in the system is J-T valve, which works isenthalpic

$$h_3 = h_4 \quad (22)$$

$$x_4 = \frac{m_f}{m_f + m_g} \quad (23)$$

Where 'x' defined as the dryness fraction after the Joule-Thompson valve effect.

$$Ex_{in_{Val}} = m_2 * \begin{pmatrix} (h_3 - h_0) \\ -\dot{T}_0 * (s_3 - s_0) \end{pmatrix} \quad (24)$$

$$Ex_{out_{Val}} = m_2 * \begin{pmatrix} (h_4 - h_0) \\ -\dot{T}_0 * (s_4 - s_0) \end{pmatrix} \quad (25)$$

$$Ed_{Val} = \left(Ex_{in_{Val}} - Ex_{out_{Val}}\right) \quad (26)$$

3.4. Separator Analysis

$$m_2 * h_4 = m_f * h_5 + m_g * h_6 \quad (27)$$

$$Ed_{sep} = T_0 * \begin{pmatrix} \left(m_g * s_6 - \dot{m}_2 * s_4\right) \\ + \left(\frac{m_g * h_6 - m_f * h_5}{T_0}\right) \end{pmatrix} \quad (28)$$

$$Ed_{Linde\ sys} = Ed_{comp} + Ed_{HX} + Ed_{Val} + Ed_{sep} \quad (29)$$

4. Case study

A Mathematical technique for simple Linde gas liquefaction cycle has been formulated using numerical computational technique with the help of EES (engineering equation solver) commercial. In the thermodynamic analysis of cycle, considered parameters like COP, liquefaction rate, compressor work and exergy destruction are varied with the cyclic pressure ratio, which have a direct relationship with the performance of cycle. Effect of these parameters on the performance of the system is calculated with other gasses to get the optimum performance parameters of the regime for each gas liquefaction. In the process of study compressor (COMP) efficiency and HX effectiveness is considered stable at 85% and 0.85respectively. An illustrative example is presented here for the oxygen liquefaction with simple Linde cycle shown in figure 1 at 40 bar outlet pressure ratios of the compressor. Apart from above constant terms following other assumption are also considered while working on cycle like the compression process is isothermal; expansion process in J-T valve is completely is enthalpic, and there is no heat leakage to the surrounding. Furthermore, the gas is taken is oxygen at the inlet of the compressor is 1 bar at 300 K. With all these assumptions and constant parameters each of system components is studied at every state with other gasses of liquefaction. Various results are being listed in Table 1-2.

Table: 1 Different performance parameters at 40 bar pressure ratio

$COP = 0.6776$	$\varepsilon_{HX} = 0.85$	$NTU_{HX} = 4.092$]
$\eta_{2nd_{\%}} = 19.76$ %	$m_2 = 1$ [Kg/s]	R$=Oxygen
$P_1 = 1$ [bar]	$m_f = 0.08951$[Kg/s]	
$P_2 = 40$ [bar]	$m_g = 0.9105$[Kg/s]	
$W_c = 284.57\ kj/kg$	$m_{HX} = 1$[Kg/s]	

Table:2 System Properties at different stages at 40 bar pressure ratio

Temperature $[K]$	Enthalpy $[kJ/kg]$	Entropy $[kJ/kg-K]$	Specific Heat $[kJ/kg-K]$
$T_0 = 298$	$h_0 = 0.4348$	$s_0 = 0.0012$	$cp_{c_{f_{HX}}} = 0.9158$
$T_1 = 300$	$h_1 = 1.403$	$s_1 = 0.0049$	$cp_{h_{f_{HX}}} = 0.826$
$T_2 = 300$	$h_2 = 8.039$	$s_2 = 0.9757$	
$T_3 = 148.7$	$h_3 = 210.6$	$s_3 = 1.998$	
$T_4 = 90.19$	$h_4 = 210.6$	$s_4 = 1.315$	
$T_5 = 90.19$	$h_5 = 404.7$	$s_5 = 3.467$	
$T_6 = 90.19$	$h_6 = 191.5$	$s_6 = 1.103$	
$T_7 = 268.5$	$h_7 = 27.47$	$s_7 = 0.0096$	

The properties of different gases are obtained using computation software. The analysis is repeated at different pressure ratio and as a part of analysis, exergy destructions of each component is computed and various results of these studies are discussed in Fig 2-11.

5. Results and Discussion

From the figure 2 its notice that every gas show different trend in COP and second law efficiency due to their individual physical properties at various condition (P,T).From graph study, it determined that Methane gas liquefaction process have highest COP and exergyefficiency at 60 bars while best-suited pressure ratio performance wise for the simple Linde system is between 60-80 bar for all other given gasses liquefaction process. Beyond the 80 bar, the system performance starts

decreasing and finally start hampering the output of the system. From figure 3 showing that liquefied mass rate process. Beyond the 80 bar, the system performance starts decreasing and finally start hampering the output of the system. From figure 3 showing that liquefied mass rate. Start dropping after 80 and 100 bars for gasses. In this Methane and Argon show slightly unusual trend because after 200 bar methane liquefaction mass rate again start increasing while a decrease in output of argon is very slow after 100 bars or it shows almost constant line after 120 bar compressor.

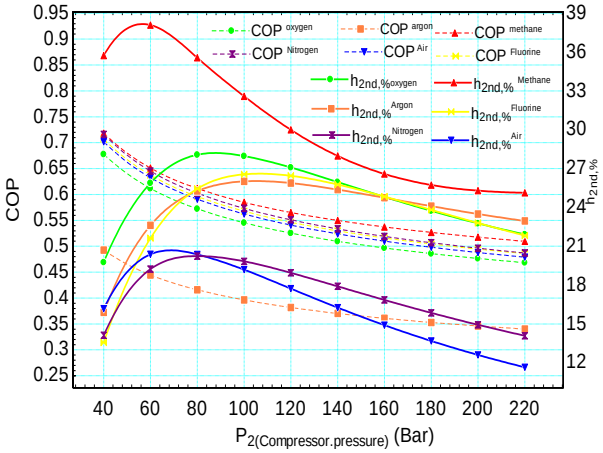


Figure 2: COP and the exergy efficiency versus compressor pressure for various gasses

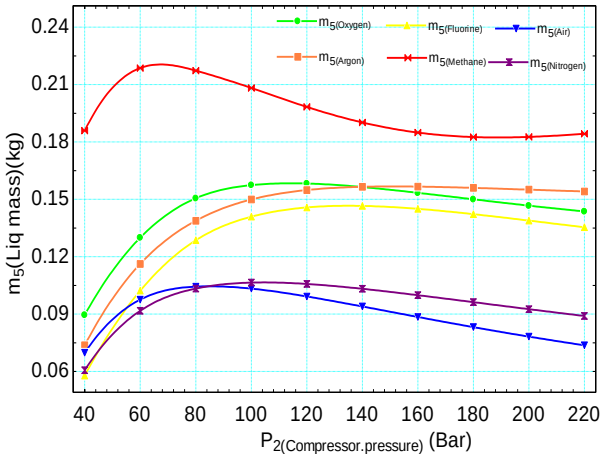


Figure 3: Liquefied mass (m_5) versus compressor pressure for differentgasses

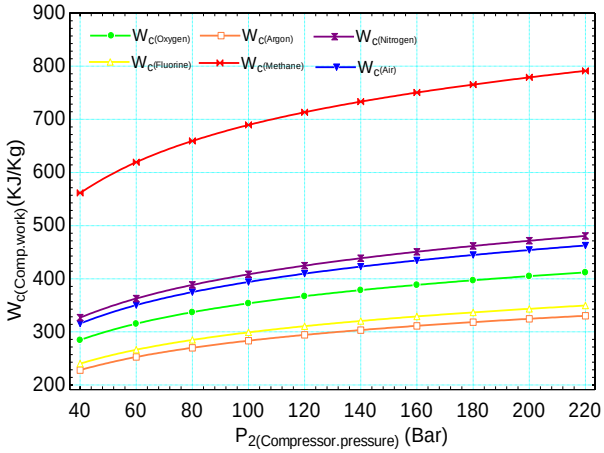


Figure 4: Compressor work input versus compressor pressure for various gases

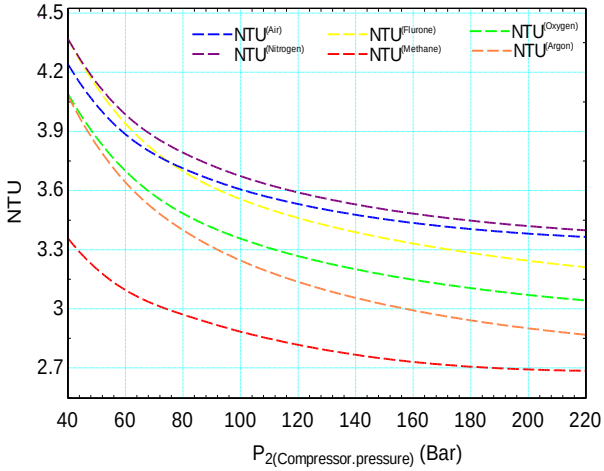


Figure 5: NTU versus compressor pressure for various gases

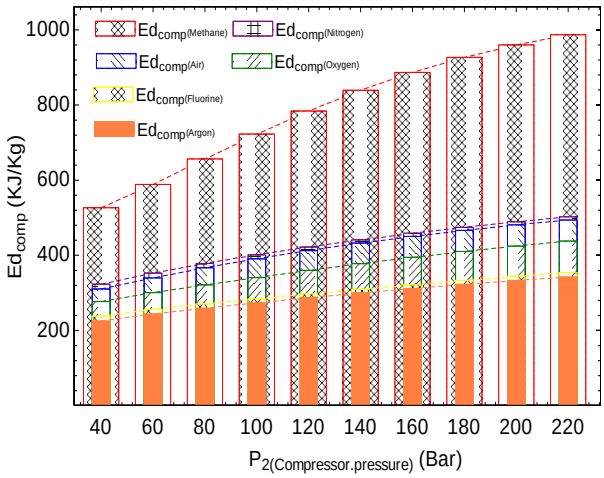


Figure 6: Exergy destruction in compressor versus compressor pressure ratio

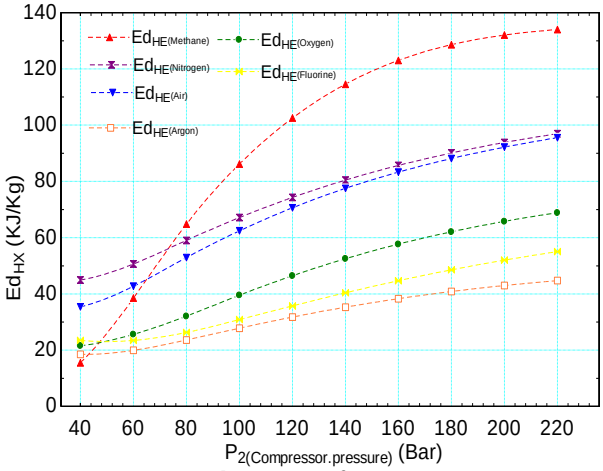


Figure 7: Exergy destruction of HX versus compressor pressure for various gases

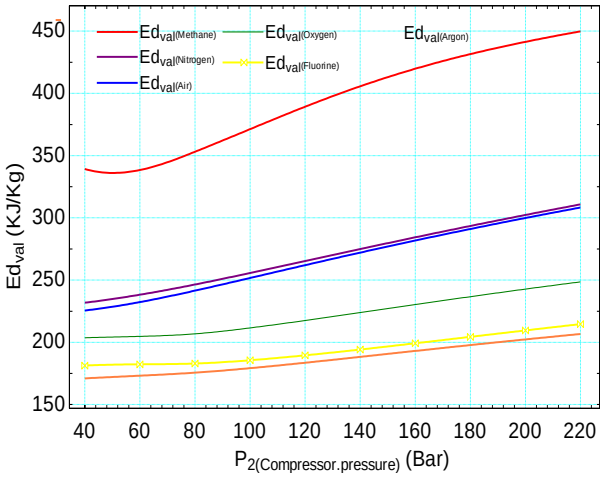


Figure 8: Exergy destruction of J-T valve versus compressor pressure for various gases

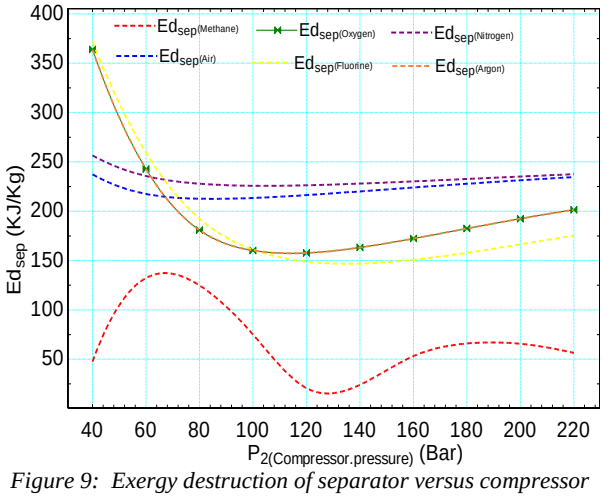


Figure 9: Exergy destruction of separator versus compressor pressure for various gases

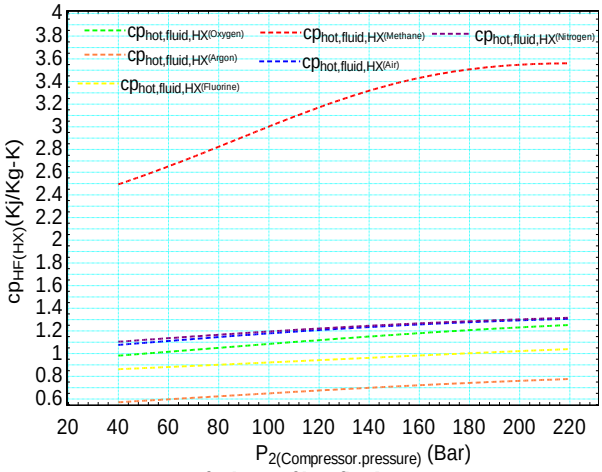


Figure 10: Specific heat of hot fluid versus compressor pressure for differentgasses

For the liquefaction process amount of actual work requirement is gradually increases with increase in pressure ratio or compressor pressure. Figure 4 show amount of real work needed for liquefaction of any given gas. It indicates that Methane gas required highest energy and slope of increment of methane also highest among other given gasses. The requirement of actual work for Methane in optimum pressure ratio range 60-80 bar is in between 600-700 kJ/kg while other gasses requirement is in between 200-400 kJ/kg. Figure 5 determine the dimensionless character NTU of system heat exchanger which help in knowing the area required of the heat exchanger of a liquefied system that very useful in designing the system. In exergy analysis calculating the exergy destructions component wise and whole of the system play a crucial role in the improvisation of the system performance. Figure 6-9 show exergy destructions in an individual component of simple Linde system with different gasses. But the variation in exergy destruction with compressor pressure for differentgasses is different for a differentpart. Figure 6-9 Show the exergy destructions in respectively in compressor heat exchanger-T valve and separator of the system. From the analysis, it notices that working with Methane gas is produces highest exergydamages in the compressor and J-T valve as compared to other gasses while heat exchanger shows highest but after 80 bar pressure ratios before it methane show lowest at 40 bar and highest increasing slope between 40 and 80 bars. The separator of Linde system shows adifferent trend of exergy destructions for each gas. Methane liquefaction shows thesinusoidal distribution of exergy destruction increasing from 40 to 60 bar and after that start decreasing up to the lowest at 124 bars then start increasing again with less slop of increment as previous one. Gasses like oxygen, argon, and Fluorine show the almost same slope of decrement of exergy destruction in separator while Air and Nitrogen

show similar fallout. From figure 9 study, the lowest loss of exergy destruction will result in between 60 to 80 bar for most of the gasses except methane. Valve and separator have to work at extremely low temperature, and they are the cold unit of systems. If the exergy at low temperature is not fully utilized, the irreversibility become too high, and exergyis used it by heat transfer with a secondary fluid, the exergy loss is dependent on the outlet temperature of the cooled secondary fluid [10].Specific heat of fluid in HX highly influence the performance of the system. For HX in the system, the specific heat capacity of the hot fluid is graphically representedas a function of cycle pressure ratio in figure 10-11 using different gasses. From figures its depicted that Fluorine and, Argon has lower Cp_{hf} (specific heat of hot fluid) while Methane has highest Cp_{hf} as estimated to other gasses used in cycle study. With pressure ratio increases, the Cp_{hf} of the gas increases very slowly. Cp_{hf}between pressure range is 60-80 is an average of the Cp_{hf} calculated upto 220 bars. The slope of increment in every individual gas is mostly like each other except Methane which showing the steep slope of increase in Cp_{hf} with increasing compressor pressure.

6. Conclusions

Various performance parameters studied with increasing pressure ratio. Exergy analysis of Linde system and its component with different gasses help in determine the loophole and best performance parameters for each given gas liquefaction process. Following points are concluded from the present investigation

(1) COP and Second law efficiency of system is degrading at high pressure for all gasses
(2) The optimum performance pressure ratio range for system is 60-80 bar
(3) Among all six gases methane gas liquefaction process required more attention.
(4) Gas of the liquefaction is very important factor in determine the most exergy destructions causing component of same Linde system
(5) Well insulated heat exchanger has the lowest exergy destructions among all component for most gases
(6) Specific heat of the gas at every stage play a vital role in designing of system.

References

[1] Badescu, V., First and Second Law Analysis of a Solar Assisted Heat Pump Based Heating System, Energy Conversion and Management, Vol. 43, pp. 2539–52, 2002.

[2] M. J. Gouge, J. A. Demko and B. W. McConnell, ORNL,J. M. Pfotenhauer, University of Wisconsin "Cryogenics Assessment Report" Final version, May 2002.

[3] Kotas, T.J. The Exergy Method of Thermal Plant Analysis; 1995 Ed.; Krieger Publishing Company: London, UK, 1985.

[4] Ren, C., Li, N., Tang, G., Principle of Exergy in HVAC and Evaluation of Evaporative Cooling Schemes. Building and Environment, Vol. 37, pp.1045–55, 2002.

[5] Bejan, A. General Criterion for rating heat-exchanger performance. Int. J. Heat Mass Transf. 1978, 21, 655–658.

[6] Wu, S.T.; Yuan, X.F.; Li, Y.R.; Xiao, L. Exergy transfer effectiveness on heat exchanger for finite pressure drop. Energy 2006, 32, 2110–2120.

[7] Franco, A.; Russo, A. Combined cycle plant efficiency increase based on the optimization of the heat recovery steam generator operating parameters. Int. J. Therm. Sci. 2002, 41, 843–859.

[8] Saidur, R.; Ahamed, J.; Masjuki, H. Energy, exergy and economic analysis of industrial boilers. Energy Policy 2010, 38, 2188–2197.

[9] Ignacio Lopez Paniagua *, Javier Rodrıguez Martın, Celina Gonz´alez Fernandez,AngelJime´nez A lvaro and Rafael Nieto Carlier." A New Simple Method for Estimating Exergy Destruction in Heat Exchangers" Entropy 2013, 15, 474-489; doi:10.3390/e15020474.

[10] Rosen, M.A., Leong, W.H., Le, M.N., Modeling and Analysis of Building Systems that Integrate Cogeneration and District Heating and Cooling, In: Proceedings of eSim Conference. 2001

[11] Mehmet Kanoglu, Ibrahim Dincer and Marc A Rosen, "Performance analysis of gas liquefaction cycles" Int. J. Energy Res. 2008; 32:35–43.

[12] Kim, Youngmin and Favrat, Daniel, "Energy and Exergy Analysis of a Micro Compressed Air Energy Storage and Air Cycle Heating and Cooling System" (2008). International Refrigeration and Air Conditioning Conference. Paper 950.

Nomenclature

T	temperature (K)
h	specific enthalpy (kJ/kg)
s	specific entropy (kJ/kg K)
Cp	specific heat (kJ/kg K)
m	rate of mass flow (kg/s)
Q	rate of heat transfer (kW)
W	work(kJ/s)
C	heat capacity,(kW/K)
CR	heat capacity ratio
Ex	rate of exergy flow (kW)
Edest	rate of exergy destruction (kW)
Sgen	rate of entropy generation (kW/K)
COMP	compressor

Subscripts

c_i	cold stream in
c_o	cold stream out
h_i	hot stream in
h_o	hot stream out
H	hot stream reference state
HX	heat exchanger
J-T Val	Joule Thompson valve

International Journal of Research in Engineering and Innovation (IJREI)
journal home page: http://www.ijrei.com
ISSN (Online): 2456-6934



Exergy analysis of orc integrated combined cycle power plant with single pressure heat recovery steam generator

R.S. Mishra, Yunis Khan

Department of Mechanical Production and Automobiles Engineering, Delhi Technological University Delhi-110042 India

Abstract

There is energy crises in world so increasing demand of power has made the power plants of scientific interest, but most of the power plants are designed by the energetic performance criteria based on first law of thermodynamics only. The real useful energy loss cannot be justified by the fist law of thermodynamics, because it does not differentiate between the quality and quantity of energy. The exergy analysis (second law analysis) is used for providing information about the losses qualitatively as well as quantitatively along with their locations. Exergetic optimization improves the performance of a system by reducing the exergy destruction and increasing exergetic efficiency. This analysis shows exergy loss at each and every point of unit equipment's. Also presents major losses of available energy at combustor, HRSG and gas turbine and organic condenser. The primary objectives of this work are to analyze the system components separately and to identify and quantify the sites having largest exergy losses at different load. Exergy analysis considered real variation ranges of the main operating parameters such as pressure ratio, air fuel ratio. The effects of theses parameters on the system performances are investigated.

© 2017 ijrei.com. All rights reserved

Keywords: combined cycle, organic Rankine cycle, heat recovery steam generator, exergy analysis, gas turbine.

1. Introduction

Energy systems contain an extremely large number and a few types of coordinated efforts with the world outside their physical limitations. Thus, architects must address numerous wide issues, particularly energy, economy and the environment. Combined cycle power plants (CCPPs) have as of late gotten significant consideration because of their nearly high energy efficiencies, low poisonous waste and ozone depleting substance releases, and operational suppleness. A typical combined cycle power plant is the cycle, which is comprised of a gas cycle (topping cycle) and a steam turbine cycle (bottoming cycle) coupled through a heat recovery steam generator (HRSG).But exhaust gas from the gas turbine is not fully utilized by the HRSG. Almost 150^0 C goes to waste from HRSG with exhaust through stack. This low amount heat can be fully utilize with the low temperature heat cycle such as the integration of organic Rankine cycle (bottom left cycle).In this organic Rankine cycle first law analysis is not sufficient for telling about performance of the cycle because some critical components have more exergy destruction in this cycle such as organic condenser, heat recovery boiler (HRB).

To streamline the efficiency, cost viability and ecological effect of such plants, it is critical to decide the areas, sorts and genuine extents of wasteful aspects (irreversibility's). Exergy investigation is a helpful tool for such examinations, and allows measurement of the thermodynamic wasteful aspects of the procedure.

The scope and purpose of this research is to develop effective methodology to achieve exergetic optimizations of CCGT power plants. Therefore, the aim of the work is to improve the performance of the power plant by means of proposing an exergy optimization method. With the help of this method, it would be possible to

(a) Provide information about the exergy destruction and exergy losses along with their location.
(b) Predict the highest exergy destructor components of the system.
(c) Suggest ways of improving the exergetic efficiency.
(d) Find the optimal realistic values of operating parameters, which gives the maximum possible power output and efficiency. Additionally, is would be

Corresponding author: R.S. Mishra
Email Id: rsmishra@dce.ac.in

possible to calculate minimum possible exergy destructions.

2. Literature Review

In order to have an idea of the present methodology development in the area of performance and optimization of combined cycle gas turbine power plant, a brief survey of available literature was made. However, this chapter is concerned with a review of literature on optimization performed on various thermal systems. In general, some authors focus on the gas turbine operating parameters (topping cycle), others optimize the steam plant (bottoming cycle) on the basis of a given gas turbine, whereas others propose appropriate optimization methods for the whole combined cycle power plant. Furthermore, the optimization can be analyzed from a thermodynamic point of view, according to the first and/or second law analysis, or using a thermo economic or environmental-economic strategy Kaviri et al [1], Ahmadi and Dincer [2], Boyano et al [3] and Petrakopoulou et al [4]). From the point of view of optimization methodology, there are many types of analyses. In this work, the review will highlight most common methodology: the exergy destruction method, and the exergo economic method: Ibrahim et al [5], Ameri and Hejazi [6], Boonnasa et al [7] and Hosseini et al [8]. The properties of air entering combustion chamber depend upon the compressor pressure ratio studied by Ibrahim and Rahman [9], and Khaliq and Kaushik [10] performed a parametric thermodynamic analysis of a combined cycle gas turbine. They investigated the effect of operating parameters, compression ratio, gas-turbine peak temperature ratio, isentropic compressor and efficiency and air fuel ratio on the overall plant performance. Their results show that the compression ratios, air to fuel ratio as well as the isentropic efficiencies are strongly influenced by the overall thermal efficiency of the combined cycle gas turbine power plant. The overall thermal efficiency increases with compression ratio as well as isentropic compressor and turbine efficiency. However, the variation of overall thermal efficiency is minor at the lower compression ratio while it is very significant at the higher compression ratio for both isentropic compressor and turbine efficiency. The overall efficiencies for combined cycle gas turbine are much higher than the efficiencies of gas turbine plants power output decreases linearly with the increase temperature. Mohagheghi and Shayegan [11] performed the thermodynamic optimization of design variables and heat exchangers layout in a heat recovery steam generator HRSG for combined cycle gas turbine CCGT using a genetic algorithm. Their method was introduced for modeling the steam cycle in advanced combined cycles by organizing the non-linear equations and their simultaneous used solutions with numerical methods. 8 In addition to the optimization of design variables of the recovery boiler, they performed the distribution of heat exchangers among different sections and optimized their layouts in HRSGs. A standard gas turbine was assumed, and then outlet gas stream conditions (mass flow rate, temperature, and chemical composition of gas stream) were considered as the inlet parameters for the recovery boiler model. From the optimization process maximum output power from a steam cycle for different HRSGs was then analyzed.

Bracco and Silvia [12] studied a combined cycle power plant with a single level heat recovery steam generator HRSG. They developed a mathematical model to determine the optimal steam pressure values in the HRSG according to different objective functions (in the HRSG for a given gas turbine). Their work reports numerical results for the combined cycle power plant considering four different gas turbines. The optimization approach was focused on the study of the heat transfer between the steam and the exhaust gas in the HRSG, based on an exergetic analysis. They present the comparison among different objective functions that refer to the HRSG specifically or to the whole bottoming cycle. In their mathematical model, they considered the presence of specific constraints for the operating parameters of the power plant, the most important constraints that were considered refer to the steam quality at the turbine outlet, the HRSG outlet exhaust gas temperature and the steam turbine blade height. In their work, a parametric analysis was also performed to evaluate the influence of the gas temperature at the HRSG inlet and the pinch point temperature difference on the considered objective functions. Woudstra et al [13] performed the thermodynamic evaluation of combined cycle plants with the same gas turbine and different steam bottoming cycles. The evaluation showed that the increasing the number of pressure levels of steam generation will reduce the losses due to heat transfer in the HRSG, but also the exergy loss due to the exhaust of flue gas to the stack. Among the investigated configurations for bottoming cycle, triple pressure reheat was the best option from exergy point of view. Mansouri et al [14] investigated the effect of pressure levels of steam generation at heat recovery steam generator HRSG on the energetic and exergetic efficiency of HRSG, bottoming cycle and combined cycle power plants, as well as the effect of 9

Xiang and Chen [15] considered a combined cycle with three-pressure HRSG, equipped with the GE PG9351FA gas turbine. They maximized the combined cycle efficiency through the optimization of the HRSG operating parameters by minimizing exergy losses.

From the literature review it is found that the efficiency of the combined cycle is more than the simple individual cycle. Other important conclusion found that the more and more energy going to waste from stack with exhaust flue gases even after passing through HRSG. Almost flue gas around 150 ^{0}C is going to waste from stack. It is concluded that no researcher use the energy at temperature 150^{0}C from the flue gases and also not done exergy analysis of this model. The integration of the ORC (organic Rankine cycle) in the pre-existing cycle is done for recovery of the low temperature heat from the exhaust gases which are coming from the HRSG after generation of the steam for

simple Rankine cycle and exergy analysis is carried out for whole system. It is proposed to examine the effect of the various parameters on the performance of the combined cycle with ORC. These parameters are following

- Effect of the pressure ratio
- Effect of the air fuel(A/F) ratio

3. Exergy Analysis

For thermodynamic analysis (exergetic and energetic) a model is proposed in this model there are following components-compressor, combustor, gas turbine ,steam turbine, HRSG, condenser, heat recovery boiler, organic turbine, pumps Which are shown in figure 1.

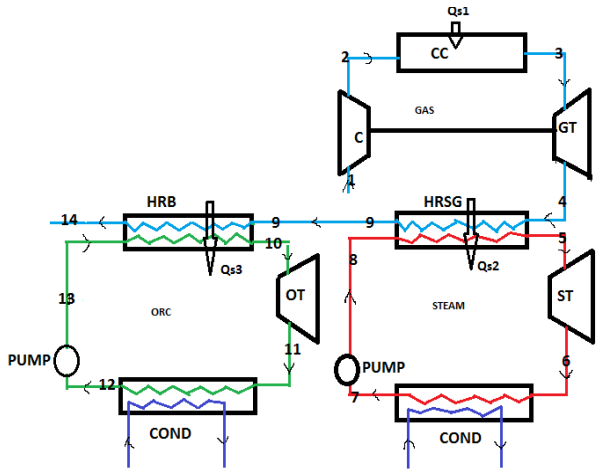


Figure 1: Thermodynamic model of combined cycle with ORC

3.1 System Description

Systems have the different components which are described above following ways it is works through following points

At stage 1 there is ambient conditions are defined this is the entry of the compressor and point 2 is the entry of the combustion chamber where heat is given and then combustion of fuel takes place. After the combustion is over the hot flue gases goes to the gas turbine at stage 3 where work is taken by rotation of the shaft .After expansion flue gases goes to the HRSG at stage 4 at pressure above the slightly above the atmospheric pressure where heat is given to the water for generation of the steam and remaining hot gases from stack goes to the heat recovery boiler at stage 9.stage 5 is entry to steam turbine and stage 6 exit to the steam turbine and entry to the surface condenser. In heat recovery boiler the heat is given to the organic fluid (R410A) which is circulates in ORC plant. At stage 10 organic fluid vapours goes to the organic expander where small amount of work is recovered. At stage 14 the remaining gases goes to atmosphere almost at atmospheric temperature and pressure. Then there is no potential remains. This is shown in figure 1.

Following assumptions are made in the study of this model:

1. All components are in steady state.
2. No pressure loss in any component.
3. There is no heat and pressure loss in pipes connecting in each components.
4. After steam turbine and organic expander fluids are saturated vapour.
5. No pressure loss in HRSG and heat recovery boiler

3.2 Exergy Analysis

Exergy destruction or loss is given by

$$\dot{E}D_i = \sum(\dot{m}e)_{in} - \sum(\dot{m}e)_{out} + \left[\sum\left(\dot{Q}(1-\frac{T_o}{T})\right)_{in} + \sum\left(\dot{Q}(1-\frac{T_o}{T})\right)_{out}\right] \pm \sum\dot{W}$$

Exergy destruction rate in compressor given

$ED_c = m_a * T_0 * (s_2 - s_1)$

Exergy destruction rate in combustion chamber given as

$ED_{cc} = (m_f + m_a) * T_0 * (s_3 - s_2) - Qs_1 * (1 - T_0/Tc)$

Exergy transfer in combustion chamber from fuel is given as

$ET = Q_{S1} * [1 - T_0/T_C]$

Exegy destruction rate in gas turbine given as

$ED_{gt} = (m_f + m_a) * T_0 * (s_4 - s_3)$

Exergy destruction rate in HRSG given as

$ED_{HRSG} = m_a * [(h_4 - h_9) - T_0 * (s_4 - s_9)] + m_s * [(h_8 - h_5) - T_0 * (s_8 - s_5)]$

Exergy destruction rate in steam turbine given as

$ED_{st} = m_s * T_0 * (s_6 - s_5)$

Exergy destruction rate in steam condenser given as

$ED_{cond} = m_s * [(h_6 - h_7) + T_0 * (s_6 - s_7)]$

Exergy destruction rate in HRB given as

$ED_{HRB} = (ma + mf) * [(h_9 - h_{14}) - T_0 * (s_9 - s_{14})] + m_{of} * [(h_{13} - h_{10}) - T0 * (s_{13} - s_{10})]$

Exergy Destruction rate in organic turbine given as

$ED_{ot} = m_{of} * T_0 * (s_{11} - s_{10})$

Exergy destruction rate in organic condenser given as

$ED_{ocond} = m_{of} * [(h_{11} - h_{12}) + T_0 * (s_{11} - s_{12})]$

Overall exergetic efficiency of plant with ORC

$\dot{\eta}_{exergetic\ with\ ORC} = (W_{GT} + W_{ST} + W_{OT} - W_C - W_P - W_{OP}) / ET$

4. Results and Discussions

The study of different cycles on which the thermal power plant work with respect to exergy. The exergy destruction shows a loss that can be recovered by using the suitable design of the various portions of the system and also it confirms the best possible process of the power plant according to second law of Thermodynamics. As the exergy and cost of energy are complimentary to each other exergy destruction shows a loss, which can be quantify by analysis the system in mathematically. In the present work the analysis is done in the combined cycle power plant. Fig.2 shows exergy destruction of air compressor as a function of air fuel ratio at various pressure ratios. Pressure ratio was varied from 5 to 20 while air fuel ratio was varied from 60 to 130. With the increase in air fuel ratio, exergy destruction rate of air compressor increases. Here, the mass of fuel remains constant as 1Kg and mass of air increases so air fuel ratio. To compress more air, compressor has to work more and it results in increased exergy destruction rate. At a particular ratio, as pressure ratio increases exergy destruction rate increases too. This is because more work required by compressor and work done required by compressor is directly proportional to the pressure ratio. Fig 3 demonstrates the variation of Exergy destruction rate of combustion chamber as a function of air fuel ratio at various pressure ratios. Air fuel ratio was varied from 60 to 130. Pressure ratio was varied from 5 to 20 in a step of 5. With the increase in air fuel ratio, the exergy destruction rate increases. This is due to the increased amount of heat addition in combustion chamber and it results in increment of exergy destruction rate. At a particular air fuel ratio, as pressure ratio increases the exergy destruction rate decreases. This happens because due to increased pressure ratio, combustion chamber receives the air with high temperature so it requires less chemical energy addition.

Fig 5 illustrates the variation of Exergy destruction rate of HRSG as a function of air fuel ratio at various pressure ratios. As air fuel ratios increasing, exergy destruction rate is increases very rapidly because at lower air fuel ratio, the inflow temperature is high and decreasing with increase in AFR those results increases destruction rate. At a particular inlet temperature, with increase in air fuel ratio the exergy destruction rate increases. This is due to the increased amount of heat addition in combustion chamber and it results in increment of exergy destruction rate. At a particular inlet temperature, as air fuel ratio increases, marginal exergy destruction rate decreases.

Fig 6 displays the Exergy Destruction Rate of steam turbine at Various Pressure Ratios versus Air Fuel Ratio. On increasing the pressure ratio, the temperatures increased is very much high as compared to temperature decreased by increasing air fuel ratio that's why exergy destruction rate continuously increases on increasing air fuel ratio and at higher pressure ratio.

Fig 7 indicates the Exergy Destruction Rate of condenser at Various Pressure Ratios versus Air Fuel Ratio. This shows the same pattern as of steam turbine and reason is same too.

Fig 8 displays exergy destruction in HRB with air fuel ratio at different pressure ratio. On increasing air fuel ratio exergy destruction increases because increases air fuel ratio more heat required in combustion chamber as discussed above so more inlet temperature in HRB.

Fig 9 shows the variation in exergy destruction with air fuel ratio in organic turbine. In this fig same reason as fig 9 for increasing exergy destruction. No effects on exergy destruction on pressure ratio because HRB inlet and outlet temperatures are fixed but it varies based on design of HRB. Also same reason and effects of air fuel ratio and pressure ratio on other component of ORC system. Input parameters taken for study are given below these parameters are taken from different running power plants. These are shown in Table-1

Table-1: Input parameters of Gas turbine power plant with ORC

S.No	Parameters	Symbol	Value
1	Ambient temperature	T_0	298K
2	Flue gases temperature from Flue gases temperature from HRSG.	T_9	423K
3	Constant pressure in HRSG	P_5	10 bar
4	Temperature inlet to steam turbine	T_5	813K
5	Temperature inlet to organic turbine	T_{10}	403K
6	Pressure inlet to organic turbine	P_{10}	25bar
7	Pressure outlet to organic turbine	P_{11}	2bar
8	Pressure outlet to steam turbine	P_6	0.07bar
9	Outlet temperature of gases from HRB	T_{14}	300K
10	Organic fluid for ORC	R410A	-

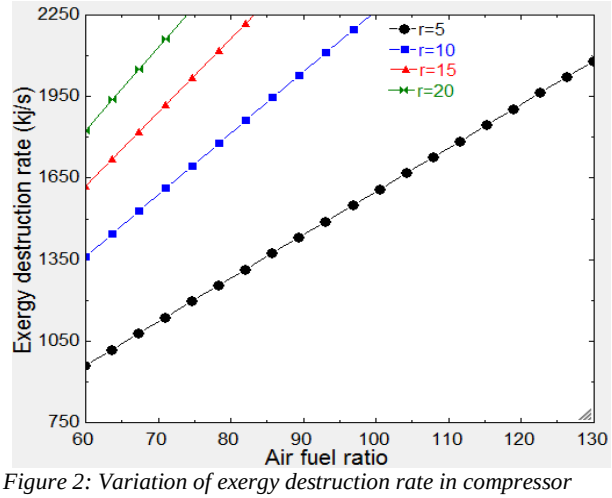


Figure 2: Variation of exergy destruction rate in compressor with air fuel ratio at different pressure ratio

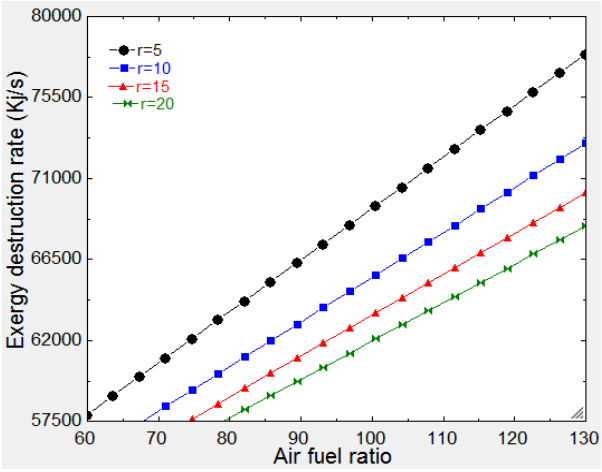


Figure 3: Variation of exergy destruction rate in combustion chamber with air fuel ratio at different pressure ratio

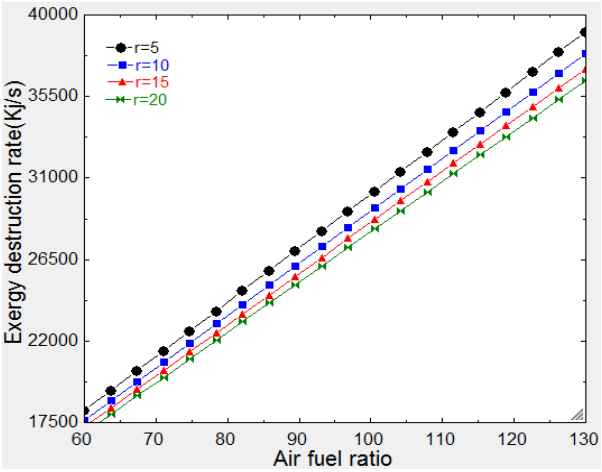


Figure 4: Variation of exergy destruction rate in gas turbine with air fuel ratio at different pressure ratio

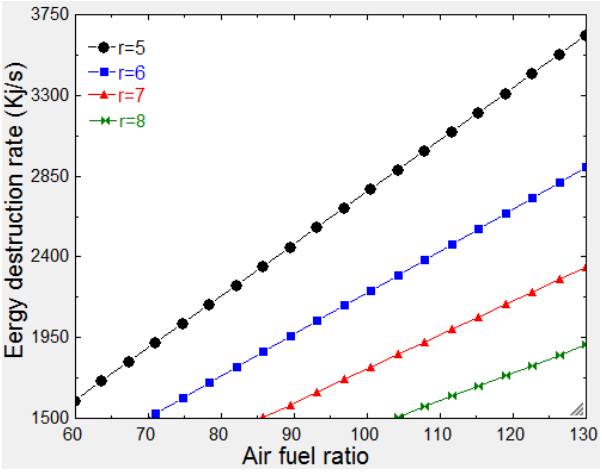


Figure 5: Variation in exergy destruction rate in HRSG with air fuel ratio at different pressure ratio

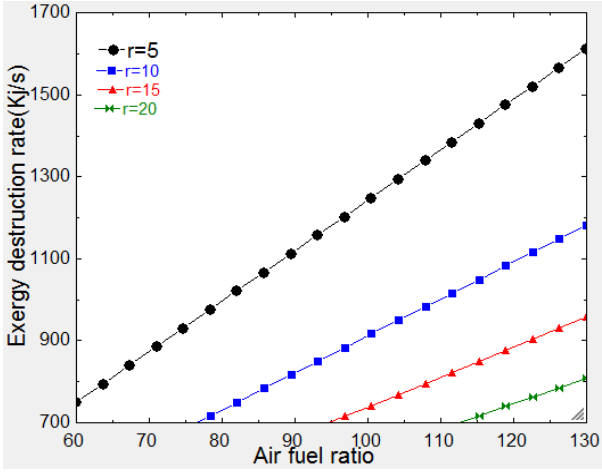


Figure 6: Variation in exergy destruction rate in steam turbine with air fuel ratio at different pressure ratio

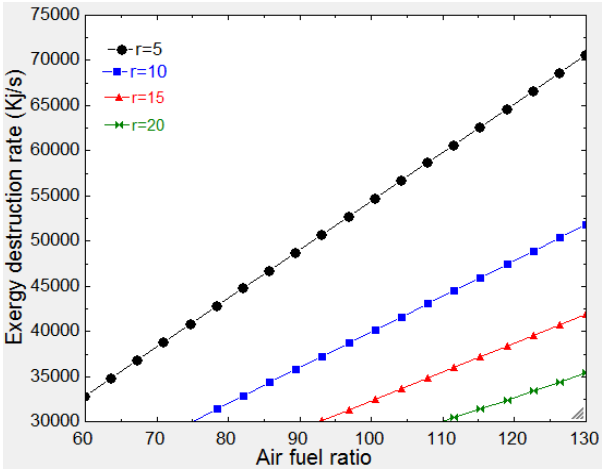


Fig 7: Variation in exergy destruction rate in steam condenser with air fuel ratio at different pressure ratio

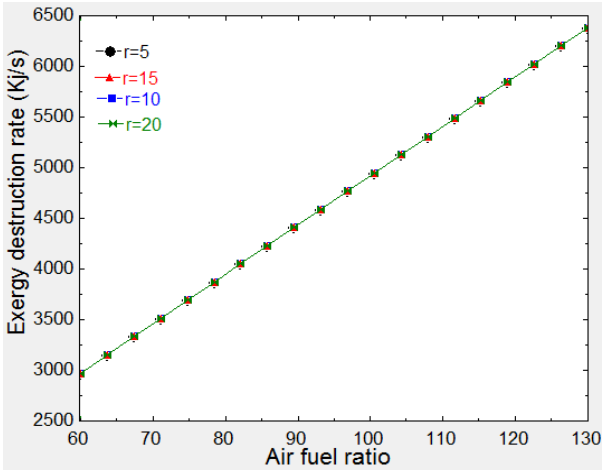


Figure 8: Variation in exergy destruction rate with HRB with air fuel ratio at different pressure ratio

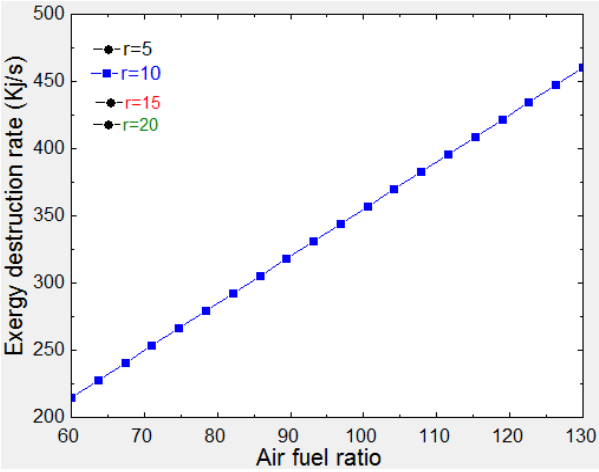


Figure 9: Variation in exergy destruction rate in organic turbine with air fuel ratio at different pressure ratio

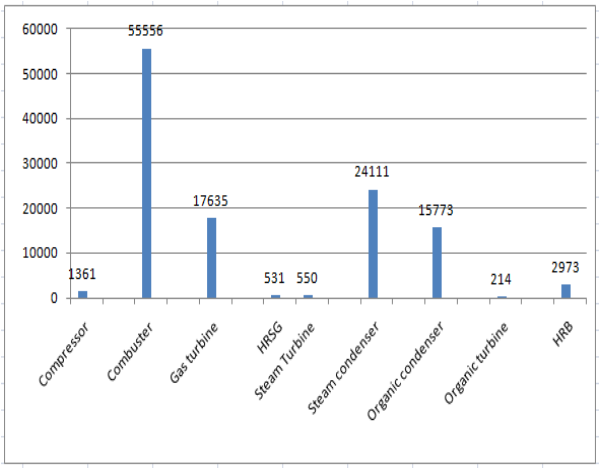


Figure 10: Exergy destruction rate (kj/s) for each component of system

The variation of thermodynamic performance parameter in terms of exergetic efficiency with pressure ratio are shown in fig. (11) and second law efficiency in terms of exergetic efficiency with air fuel ratio is shown in fig.(12). It is shown that exergetic efficiency is increasing continuously with pressure ratio but decreasing with air fuel ratio. This is because increasing pressure ratio compressor outlet temperature is increase responding exergy transfer decrease having same work output and hence exergetic efficiency increases. On other hand decrease in exergetic efficiency with increase in air fuel ratio, because increase in air fuel ratio decreases the inlet temperature of the gas turbine and also flue gases .so exergy transfer in combustor have to be increase.

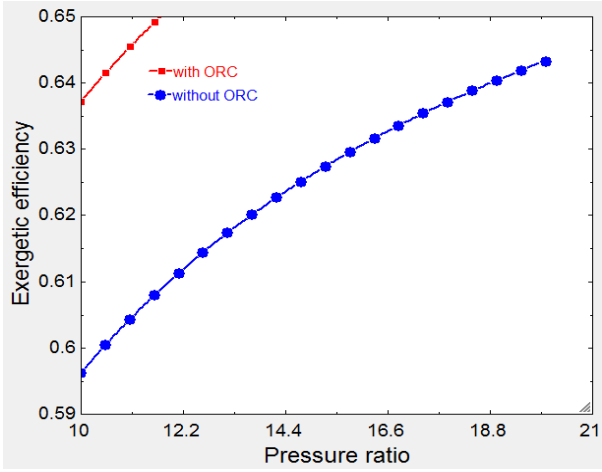


Figure 11: Variation of Exergetic efficiency with pressure ratio

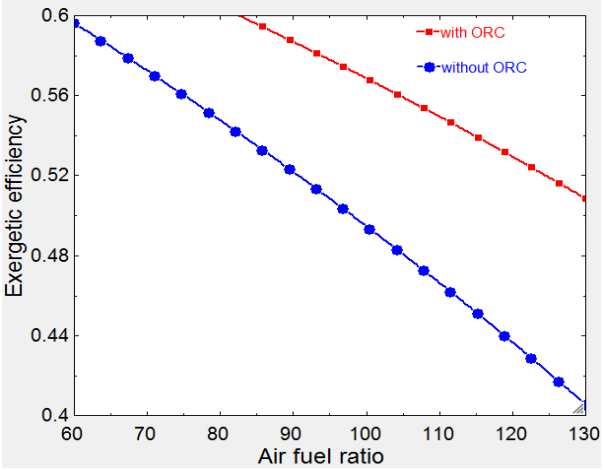


Figure 12: Variation of Exergetic efficiency with air fuel ratio

The variation of thermal efficiency (first law efficiency in terms of energy efficiency with respect to the pressure ratio of Combined cycle Gas turbine power plant with ORC and first law efficiency (thermal efficiency in terms of energy efficiency) with air fuel ratio respectively and compared efficiency with and without ORC shown in Fig-13 and Fig-14 respectively. .Same effects are calculated as well as exergetic efficiency without ORC. Here also same reason for increase and decrease of thermal efficiency (first law efficiency in terms of Energy Efficiency and second law efficiency in terms of exergetic efficiency with pressure ratio and air fuel ratio shown in Fig-13 & Fig-14 respectively .

.

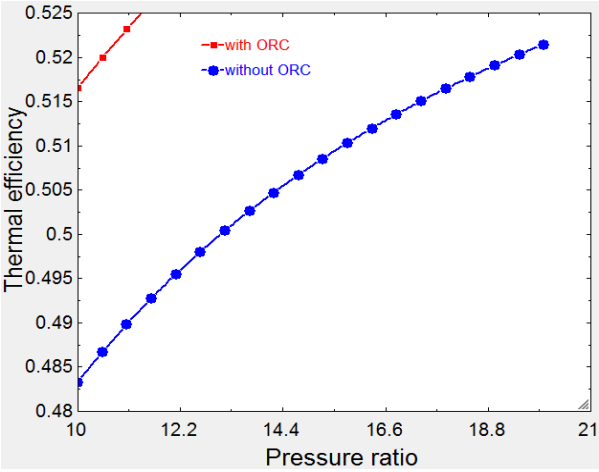


Figure 13: Figure 5: Thermal efficiency vs air fuel ratio pressure ratio

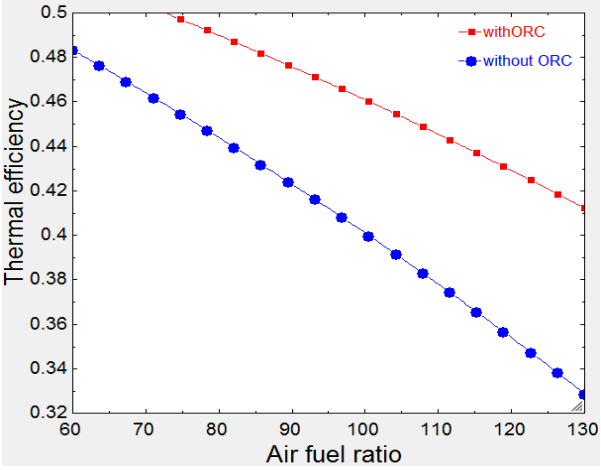


Figure 14: Variation of first law efficiency in terms of Thermal efficiency (Energy Efficiency) with air fuel ratio

5. Conclusions

Following conclusions have been made

1. Maximum exergy destruction components are combustor, gas turbine and steam condenser.
2. In organic Rankine cycle organic condenser and HRB have more exergy destruction.
3. More sensitive components are HRSG and HRB. So design of these required carefully.
4. Exergy destruction in each component in ORC with pressure ratio depends on design of HRB.
5. Combined cycle Gas turbine power plant with ORC, the second law efficiency in terms of exergetic efficiency is more than combined cycle Gas turbine power plant without ORC.
6. Combined cycle Gas turbine power plant With ORC, the thermal efficiency (in terms of first law efficiency) defined as energy efficiency is more than combined cycle Gas turbine power plant without ORC.
7. The integration of ORC with the existing combined cycle is effective and heat from the exhaust gases is fully utilized by integration of ORC.

References

[1] Kaviri A. G., Jaafar M. N., Lazim T. M., ikoij\Barzegaravval, H., Exergy environmental optimization of Heat Recovery Steam Generators in combined cycle power plant through energy and exergy analysis. Energy Conversion and Management, 6(2013), pp.27–33.

[2] Ahmadi P., Dincer I., Exergo environmental Analysis and Optimization of a Cogeneration Plant System using Multimodal Genetic Algorithm (MGA). Energy, 35(2010), pp. 5161-72.

[3] Boyano A., Blanco-Marigorta A. M., Morosuk T., Tsatsaronis G., Exergoenvironmental Analysis of a Steam Methane Reforming Process for Hydrogen Production. Energy, 36(2011), pp. 2202-2214.

[4] Petrakopoulou F., Boyano A., Cabrera M., Tsatsaronis G., Exergo economic and Exergo environmental Analyses of a Combined Cycle Power Plant with Chemical Looping Technology. International Journal of Greenhouse Gas Control, 5(2011), pp. 475-482.

[5] Ibrahim K. T., Rahman M. M., Abdalla N. A., Optimum Gas Turbine Configuration for Improving the Performance of Combined Cycle Power Plant. Procedia Engineering,15 (2011), pp.4216-4223.

[6] Ameri M., Hejazi H. S., The Study of Capacity Enhancement of the Chabahar Gas Turbine Installation using an Absorption Chiller. Applied Thermal Engineering, 24(2004), pp.59–68.

[7] Boonnasa S., Namprakai P., Muangnapoh T., Performance Improvement of the Combined Cycle Power Plant by Intake Air Cooling using an Absorption Chiller, Energy,31(2006), pp. 2036–2046.

[8] Hosseini R., BeshkanI. A., Soltani M., Performance Improvement of Gas Turbines of Fars (Iran) Combined Cycle Power Plant by Intake Air Cooling using a Media Evaporative Cooler. Energy Conversion and Management, 48(2007), pp. 1055–1064.

[9] Ibrahim T. K., Rahman M. M., Effect of Compression Ratio on Performance of Combined Cycle Gas Turbine. International Journal of Energy Engineering, 2 (2012)1, pp. 9-14.63

[10] Khaliq A., Kaushik S., Thermodynamic Performance Evaluation of Combustion Gas Turbine Cogeneration System with Reheat. Applied Thermal Engineering, 24(2004), pp. 1785–1795.

[11] Mohagheghi M., Shayegan J., Thermodynamic Optimization of Design Variables and Heat Exchangers Layout in HRSGs for CCGT, using Genetic Algorithm. Applied Thermal Engineering, 29 (2009), pp. 290–299.

[12] Bracco S., Silvia S., Exergetic Optimization of Single Level Combined Gas Steam Power Plants Considering Different Objective Functions. Energy, 35(2010), pp. 5365-5373.
[13] Woudstra N., Woudstra T., Pirone A., Van der Stelt T., Thermodynamic Evaluation of Combined Cycle Plants. Energy Conversion and Management, 51(2010)5, pp. 1099–1110.
[14] Mansouri M. T., Ahmadi P., Kaviri A. G., Exergetic and Economic Evaluation of the Effect of HRSG configurations on the Performance of Combined Cycle Power Plants. Energy Conversion and Management, 58(2012), pp. 47–58.
[15] Xiang W., Chen Y., Performance Improvement of Combined Cycle Power Plant Based on the Optimization of the Bottom Cycle and Heat, Recuperation, Thermal science,16(2007), pp. 84-89.

Nomenclature

Symbols/Subscript

ED	Exergy destruction
Qs1	Heat addition to combustion chamber
Qs2	Heat addition to HRSG
Qs3	Heat transfer to HRB
HRB	Heat recovery boiler
GT	Gas turbine
ST	Steam turbine
OT	Organic turbine
W	work
C	compressor
P	pump
m	mass flow rate
CC	combustion chamber
HRSG	Heat recovery steam generator
ORC	Organic Rankine cycle
a	Air
COND	Condenser
ṅ	Efficiency

International Journal of Research in Engineering and Innovation (IJREI)
journal home page: http://www.ijrei.com
ISSN (Online): 2456-6934



Friction stir welding/processing studies of aluminum alloy & titanium 64

R.S. Mishra & Preeti Rani

Department of Mechanical Production and Automobiles Engineering, Delhi Technological University Delhi-110042 India

Abstract

The main objective of this research paper is to consider and show a detailed study of friction stir welding/processing conducted by most of the researchers on aluminum alloy & titanium 64. The study is consist of influence of process parameters on response parameters, material flow during welding, and effect of reinforcement on the weld joint by friction stir welding, microstructure study to define the effect of different parameters on the grain structure of aluminum alloy. And the study showed that the effect of welding parameters like tool rotation speed, welding speed, tool pin diameter, shoulder diameter and tool pin profile have a significant effect on the tensile strength, micro hardness, yield strength and strain rate of FSW/FSPed aluminum alloy & titanium 64.
©2017 ijrei.com. All rights reserved
Key words: Friction stir welding, Aluminum alloy, Titanium 64

1. Introduction

Friction Stir Welding is a solid-state process, which means that the Parent materials are to be joined without melting during the welding process due to which the original characteristics of parent material remains unchanged after welding as much as possible. Friction stir welding is conducted with the help of a designed cylindrical tool consisting of a cylindrical shouldered and a profiled pin that rotates and plunged into the interface between two plate materials those are need to join. When tool pin and work-piece comes in contact friction takes which generates heat for the welding that causes softening of work-piece without melting and allows traversing of the tool along the weld line under pressure. Due to rotation of tool intermixing of work-piece material takes place and work-piece plates joined together. Friction stir processing is a local thermo-mechanical metal working process used to modify microstructure of metallic materials based on the principle of friction stir welding and it also used to increase ductility, improve corrosion resistance properties and helps to produce super-plastic materials by microstructure refinement.

2. Literature Review of Aluminium Alloy &Titanium 64 Metals

A comprehensive review of various research data which shows the effect of different process parameters on friction stir welded / processed of dis-similar metals has been discussed. This review consist of published papers of dis-similar metals has been presented in tabular form. The review table given below explains the details of parameters considered by earlier authors.

Corresponding author: R.S. Mishra
Email Id: rsmishra@dce.ac.in

S.No	Author	Title of Paper	Material	Tool and Groove size	Input Parameter	Output Parameter	Conclusion
1	Bahrami.M , et al (2014)	A novel approach to develop Al matrix nano composite employing FSW technique	7075-O Al plate thickness 6 mm	H13 hot working steel	➢ Tool shoulder diameter 16 mm. ➢ Threaded taper pin profile height - 5.7 mm. ➢ Tool Rotational speed - 800, 1000, and 1250 rpm 4) Traverse speed -30.5, 40, and 50 mm/min	➢ Microstructural observation ➢ Mechanical properties	(1) 7075 Aluminum matrix nano-composite reinforced with SiC particles was developed in the stir zone. (2) At high rotational speed (1250 rpm) powder dispersion improved due to effective stirring action of the pin. (3) UTS of specimen FSWed with powder at 1250 rpm and 40 mm/min was 31% superior to that of the specimen FSWed without powder. (4) The addition of SiC particles led to 76.1% enhancement of elongation.
2	Chen, Y. (2015).	Interface characteristic of friction stir welding lap joints of Ti/Al dissimilar alloys	TC1 Ti alloy and LF6 Al alloy plates thickness 2 mm 250 mm×100 mm	Lap joint	➢ Tool concaved shoulder diameter - 15mm. ➢ Cone-threaded pin diameter 4 mm. ➢ Tool Rotational speed 600, 950 and 1500 rpm ➢ Traverse speed 60, 95, 118 & 150 mm/min. ➢ Tilt angle - 2 ^{0}	➢ Interface macrograph of lap joints with different parameters. ➢ Failure loads of lap joints ➢ Microstructure and element distribution on interface. ➢ Micro hardness distribution	(1) At the welding speed of 60 mm/min and the tool rotation rate of 1500 r/min, the interfacial zone of lap joint can be divided into three kinds of layers. When the welding speed increases to 150 mm/min, groove-like crack occurs on the interface. (2) The failure loads of the lap joints decrease with the increase of welding speed. (3) The micro hardness of the lap joint presents an uneven distribution, the maximum value of hardness reaches HV 502 in the middle of the stir zone.
3	Aonuma.M ., et al (2010)	Dissimilar Metal Joining of 2024 and 7075 Al- Alloys to Ti-Alloys by Friction Stir Welding	Al Alloy - 2024-T3 & 7075-T651 Titanium Ti-6Al-4V	Tool Material - SKD61	➢ Tool shoulder diameter (mm) 15. ➢ Pin diameter (mm) – 6. ➢ Tool pin length (mm) - 1.9. ➢ Tool rotating speed (rpm) - 850 ➢ Welding Feeds (mm/min) - 100, 200, 300. ➢ Tilt angle - 3 ^{0}	➢ Macrostructures ➢ Microstructures ➢ Tensile strength ➢ Hardness	(1) In joining Ti and Al alloys by friction stir welding, the weldability of the Ti and 2024 Al alloy was better than of the Ti and 7075 alloy, and the tensile strengths of the Ti/2024 joints were higher than the other joints under the same joining conditions in this study. (2) Increasing the travel speed tends to increase the tensile strength of the Ti and Al alloy joint. The tensile strength of the Ti-6Al-4V and Al alloy joint is lower than the Ti and Al alloy joint.

4	Wang.J., et al (2014)	Tool wear mechanisms in friction stir welding of Ti–6Al–4V alloy	Ti–6Al–4V sheets Thickness - 2.5mm	Tool Material - W–La, CY16 and WC411	➢ Tool of a cylindrical pin with an increased pin tip diameter - 6.3mm. ➢ Tool rotating speed (rpm) 900, 1000, 1100. ➢ Welding Feeds (mm/min) - 25, 50	➢ Microscope images	(1) Friction stir welding (FSW) of titanium alloy Ti–6Al–4V was performed using three types of tools made of W–1.1%La2O3 and two different grades of WC–Co based materials. (2) Deformation was reduced by introducing a larger cylindrical pin designing the W–1.1%La2O3 tool. Among the cermets tools, fracture was observed in CY 16 grade WC–Co tool with 8wt %Co but was not found in WC411 grade WC–Co tool with 11wt%Co. Adhesive wear mechanism was related to the result of chemical affinity between WC–Co andTi–6Al–4V alloy.
5	Bang.H., et al (2013)	Joint properties of dissimilar Al6061-T6 aluminum alloy /Ti-6%Al-4%V titanium alloy by gas tungsten arc welding assisted hybrid friction stir welding	Al6061-T6 aluminum alloy and Ti-6%Al-4%V titanium alloy Thickness - 3.5 millimeters	Tool Material - WC-12% CO BUTT JOINT	➢ Tool shoulder diameter (mm) – 18. ➢ Pin diameter (mm) – 5. ➢ Tool pin length (mm) - 3.3. ➢ Tool rotating speed (rpm) - 300~450. ➢ Welding Feeds (mm/min) - 1.0~1.4 mm/sec. ➢ Tilt angle - 3 ^{0}	➢ Surface and cross-section characteristics in FSW and of HFSW welds. ➢ Mechanical characteristics in FSW and of HFSW welds. ➢ Microstructure in FSW and of HFSW welds. ➢ Thermal history in FSW and of HFSW welds	(1) The ultimate tensile strength was approximately 91% in HFSW welds by that of the Al alloy base metal, which was 24% higher than that of FSW welds without GTAW under same welding condition. (2) Elongation in HFSW welds increased significantly compared with that of FSW welds, which resulted in improved joint strength. (3) The ductile fracture was the main fracture mode in tensile test of HFSW welds.
6	Squillace.A., et al (2011)	Effect of welding parameters on morphology and mechanical properties of Ti–6Al–4V laser beam welded butt joints	Ti–6Al–4V (ASTM B265 Grade5) Thickness - 1.6 mm	butt configuration using a Nd-YAG laser was studied.	➢ Tool shoulder diameter (mm) 18. ➢ Pin diameter (mm) – 5. ➢ Tool pin length (mm) - 3.3. ➢ Laser power 0.8,1.0,1.2 KW ➢ Welding Feeds - 17, 25, 34, 42, 50 and 58 mm/s ➢ Tilt angle - 3 ^{0}	➢ Morphology of the welds. ➢ Microstructures ➢ Micro hardness ➢ Tensile test ➢ Fatigue tests	(1) The interface between Al and filler metal became curved in shape with increasing bonding time due to capillary force at grain boundaries. The bonding at the interface between Ti and filler metal proceeds by the formation of two different intermetallic compound layers.

7	Ji.Y., et al (2016)	Microstructure and Mechanical Properties of Friction Welding Joints with Dissimilar Titanium Alloys	LFW joint with Ti-6Al-4V (Ti64) and Ti-5Al-2Sn-2Zr-4Mo-4Cr (Ti17) 130*75 * 20 mm			➢ Macro and Microstructure ➢ Compositional Analysis ➢ Microhardness ➢ Tensile Properties	(1) The microstructure across the linear friction welding dissimilar joints with titanium alloys displayed marked change, mainly consisting of a re-crystallized grain zone in the weld center, deformed grains and partial re-crystallization in the thermo-mechanical affected zones. (2) The maximum hardness is located in the weld metal, which may result from the fine grains arising from the rapid cooling during the welding process. (3) The linear friction welding dissimilar joints obtained higher tensile strength than base metal Ti64 with lower strength. The failure located in the Ti64 side approximately 1.2 mm away from the welding interface.
8	Sohn.w., et al (2014)	Microstructure and bonding mechanism of Al/Ti bonded joint using Al /10Si /1Mg filler metal	1050 Al alloy and cp-Ti alloy using filler metal(Al /10Si /1Mg) with a thickness of 100 mm Thickness 3 mm			➢ Characterization of micro structures at Al/filler metal interface during diffusion bonding. ➢ Characterization of microstructures at filler metal/Ti interface during diffusion bonding ➢ Characterization of interfacial bond strength at Al/Ti diffusion bonded joint	(1) The results show that the bonding at the interface between Al and filler metal proceeds by wetting the Al with molten filler metal, and followed by removal of oxide layer on surface of Al. (2) The interface between Al and filler metal moved during the isothermal solidification of filler metal by the diffusion of Si from filler metal into Al layer. (3) The interface between Al and filler metal became curved in shape with increasing bonding time due to capillary force at grain boundaries. The bonding at the interface between Ti and filler metal proceeds by the formation of two different intermetallic compound layers.
9	Aonuma.M., et al (2012)	Dissimilar metal joining of ZK60 magnesium alloy and titanium by friction stir welding	Titanium and Mg–Zn–Zr alloy Thickness - 2.0 mm	Tool Material - SKD61 alloy steel Butt joint	➢ Tool shoulder diameter (mm) – 15. ➢ Pin diameter (mm) - 6. ➢ Tool pin length (mm) - 1.9 ➢ Tool rotational speed - 850 rpm ➢ Tool traverse speed - 50, 100 mm/min ➢ Tilt angle - 3^{0} ➢ Probe offsets of 1.0 and 1.5 mm	➢ SEM image ➢ Fractured surface of Mg and Ti joint	(1) Alloying elements of ZK60 Mg–Zn–Zr alloy on the microstructure of the dissimilar joint interface with titanium and the joint strength in comparison with pure magnesium and titanium has been investigated. (2) The fracture of the joint by tensile test occurred mainly in the stir zone of Mg–Zn–Zr alloy and partly at the joint interface. The tensile strength of the Mg–Zn–Zr alloy and titanium joint was higher than that of the pure magnesium and titanium .

10	Chen.Y.C., et al (2009)	Microstructural characterization and mechanical properties in friction stir welding of aluminum and titanium dissimilar alloys	ADC12 cast aluminum alloy sheet& Pure titanium sheet	Tool Material - (made of WC–Co)	➢ Tool shoulder diameter (mm) 15. ➢ Pin diameter (mm) - 5 mm. ➢ Tool pin length (mm) - 3.9. ➢ Tool rotational speed - 850 rpm. ➢ Tool traverse speed - 50, 100 mm/min. ➢ Tilt angle - 3 ^{0}	➢ Failure loads and fracture locations of joints. ➢ Qualitative EDS map analysis of mixture structure. ➢ XRD spectrums from different fracture surfaces	(1) ADC12 Al alloy and pure Ti can be successfully lap welded using friction stir welding technology. (2) The maximum failure load of lap joints can reach 62% that of ADC12 Al alloy base metal. The transient phase TiAl3 forms at the joining interface by Al–Ti diffusion reaction. (3) The formation of TiAl3 is strongly dependant on welding speeds (heat inputs) during FSW and thus affects the mechanical properties of joints.
11	Liu.H.J.,et al (2010)	Microstructural characteristics and mechanical properties of friction stir welded joints of Ti–6Al–4V titanium alloy	Ti–6Al– 4V plates Thickness - 2 mm	Tool Material - Tungsten–rhenium	➢ Tool rotational speed - 400 rpm. ➢ Tool traverse speed - 25, 50 and 100 mm/min. ➢ Tilt angle - 2.5 . ➢ Plunge depth - 0.2 mm	➢ Features of the microstructural zones. ➢ Effect of welding speed on the SZ microstructure. ➢ Hardness profile. ➢ Transverse tensile test	(1) Defect-free welds were successfully obtained with welding speeds ranging from 25 to 100 mm/min. (2) A bimodal microstructure was developed in the stir zone during friction stir welding, while microstructure in the heat affected zone was almost not changed compared with that in the base material.
12	Bang.H., et al (2013)	Joint properties of dissimilar Al6061-T6 aluminum alloy/Ti–6%Al–4%V titanium alloy by gas tungsten arc welding assisted hybrid friction stir welding	Al6061-T6 aluminum alloy and Ti–6%Al–4%V titanium alloy Thickness - 3.5 mm	Tool Material - F113 WC-12% CO	➢ Tool shoulder diameter (mm) 18. ➢ Pin diameter (mm) – 5. ➢ Tool pin length (mm) - 3.3. ➢ Tool rotational speed - 850 rpm. ➢ Tool traverse speed - 50, 100 mm/min. ➢ Tilt angle - 3^0 ➢ Probe off sets of 2 mm	➢ Surface and cross-section characteristics in FSW and of HFSW welds. ➢ Mechanical characteristics in FSW and of HFSW welds. ➢ Microstructure in FSW and of HFSW welds. ➢ Thermal history in FSW and of HFSW welds	(1) The ultimate tensile strength was approximately 91% in HFSW welds by that of the Al alloy base metal, which was 24% higher than that of FSW welds without GTAW under same welding condition. (2) Notably, it was found that elongation in HFSW welds increased significantly compared with that of FSW welds, which resulted in improved joint strength. The ductile fracture was the main fracture mode in tensile test of HFSW welds.

13	Xie.G.M., et al (2008)	Effect of microstructural evolution on mechanical properties of friction stir welded ZK60 alloy	ZK60 alloy Thickness - 8mm		➢ Tool shoulder diameter (mm) – 20. ➢ Pin diameter (mm) -6 . ➢ Tool pin length (mm) - 5.7. ➢ Tool rotational speed - 800 rpm. ➢ Tool traverse speed - 100 mm/min. ➢ Tilt angle -2.5 ^{0}	➢ XRD patterns obtained. ➢ Microstructure ➢ SEM images of ZK60 Mg-alloy	(1) Under a rotation rate of 800 rpm and a traverse speed of 100 mm/min, 6mm thick extruded ZK60 magnesium alloy plate was successfully friction stir welded and defect-freenweld was obtained. (2) The UTS, YS and elongation of the FSW joint reached 87%, 77%, and 65% of the PM, respectively. After aging treatment, UTS, YS and elongation were increased to 94%, 92%, and 77% of the PM, respectively. 3) During FSW, fine and equiaxed recrystallized grains of 5.3 m were generated and MgZn2 particles were broken up and dispersed with most of them being dissolved into the magnesium matrix.
14	Dressler.U. , et al (2009)	Friction stir welding of titanium alloy TiAl6V4 to aluminium alloy AA2024-T3	TiAl6V4 and Al-alloy 2024-T3 Thickness 2 mm	Tool material - Standard tool steel butt joints	➢ Tool concave shoulder diameter (mm) – 18. ➢ Pin threaded and tapered diameter (mm) -6 ➢ Tool pin length (mm) - 5.7. ➢ Tool rotational speed - 800 rpm. ➢ Tool traverse speed - 100 mm/min 6) Tilt angle -2.5 ^{0}	➢ Microstructure ➢ Hardness profile ➢ Stress–strain curves	(1) Titanium alloy TiAl6V4 and aluminium alloy 2024-T3 were successfully joined by friction stir welding. (2) Hardness and tensile strength of the butt joint were investigated. (3) The weld nugget exhibits a mixture of fine recrystallized grains of aluminium alloy and titanium particles. (4) Hardness profile reveals a sharp decrease at titanium/aluminium interface and evidence of microstructural changes due to welding on the aluminium side. The ultimate tensile strength of the joint reached 73% of A2024-T3 base material strength.
15	Zhang.Yu , et al (2008)	Microstructural characteristics and mechanical properties of Ti–6Al–4V friction stir welds	Ti–6Al–4V plate thickness-3 mm.	Tool material - Mo-based alloy tool	➢ Tool convex shoulder diameter (mm) -15. ➢ Pin threaded and tapered diameter (mm) -5.1. ➢ Tool tapered pin length (mm) -3. ➢ Tool rotational speed - 300 and 600 rpm. ➢ Tool traverse speed - 2mm and 1 mm/s	➢ Microstructural features of welds ➢ Microstructural evolution in the 400 rpm weld. ➢ Heat affected zone (HAZ). ➢ Effect of rotational speed on the SZ microstructure. ➢ Vickers hardness profile of weld. ➢ Transverse tensile test	(1) The microstructural evolution of these regions during FSW can be reasonably explained by taking into account solid-state transformation and the annealing effect of the microstructure. (2) Mechanical properties were heterogeneously distributed in the weld, which were directly related with the heterogeneous distribution of microstructure. (3) The SZ exhibited much higher mechanical properties than the base material, while the HAZ was the weakest in the weld, and its properties were representative of the transverse tensile properties of the weld.

16	Aonuma.M ., et al (2009)	Effect of alloying elements on interface micro structure of Mg–Al–Zn magnesium alloys and titanium joint by friction stir welding	Mg–Al–Zn alloy plates of AZ31B, AZ61A and AZ91D, and a Ti plate Thickness-2.0 mm	Tool Material - SKD61 alloy tool steel. Square butt joints	➢ Tool shoulder diameter (mm) – 15. ➢ Tool screw-type Pin diameter (mm) -5.0. ➢ Tool screw-type pin length (mm) - 1.9. ➢ Tool rotational speed - 850 rpm ➢ Tool traverse speed - 50 mm/min ➢ Tilt angle - 3 ^{0}	➢ Microstructure in stir zone of Mg–Al–Zn alloy. ➢ Effect of aluminum on joint interfacial microstructure and tensile strength	(1) An Al-rich layer was formed at the joint interface. Increasing the aluminum content of the Mg–Al–Zn alloy, Ti–Al intermetallic compound layer was observed clearly on the joint interface. (2) The joint fractured in the intermetallic compound layer in the tensile test. The intermetallic compound plays an important role in making a Ti/Mg joint, but the increased thickness of this compound tends to reduce the tensile strength.
17	Ragu Nathan.S.., et al (2017)	Failure analysis of tungsten based tool materials used in friction stir welding of high strength low alloy steels	High strength low alloy (HSLA) steel Thickness- 5 mm thick	Tool Material – 3 different grades of tungsten based alloy W90, W95 and W99	➢ Tool rotational speed - 600 rpm. ➢ Tool traverse speed - 30 mm/min	➢ Thermo-mechanical analysis. ➢ Microscopic observations. ➢ EBSD analysis. ➢ Evaluation of transfer layer	(1) Three tungsten base tool materials used in this investigation, W99 (W–1%La2O3) tool exhibited better microstructural stability without undergoing physical (dimensional) changes in tool configuration. (2) The W/matrix de-cohesion, matrix tearing and W-cleavage in the W90 and W95 tools are mainly due to formation of Fe–Co– Ni phase (softer phase) in the matrix. (3) It was found that the tool made of 99% W and 1% La2O3 withstood high strain rate, temperature and flow stresses generated during FSW of HSLA steel. This is mainly due to the microstructural stability of the tool materials and formation of protective transfer layer during FSW of HSLA steel.
18	Husain Mehdi et al (2016)	Mechanical properties and microstructure studies in Friction Stir Welding (FSW) joints of dissimilar alloy – a review	7050-T651, Al-4Mg-1Zr, Al- Alloy F357	CY16, W-La, WC-411 tool	➢ 350 rpm and 15 mm/min ➢ 2236 rpm to 1500 rpm	➢ Mechanical Properties ➢ Wear Property ➢ Microstructure ➢ Macrostructure	Welding parameter such as tool rotation, transverse speed and axial force have a significant effect on the amount of heat generated and strength of FSW joints. Microstructure evaluation of FSW joints clearly shows the formation of new fine grains and refinement of reinforcement particles in the weld zone with different amount of heat input by controlling the welding parameter

19	Husain Mehdi et al (2017)	Influences of Process Parameter and Microstructural Studies in Friction Stir Welding of Different Alloys: A Review	7475 Al 7050-T65 cast A356 aluminum Al-4Mg-1Zr	CY16, W-La, WC-411 tool	➢ 2236 rpm and travel speed of 2.33 mm/s ➢ 700 rpm and a traverse speed of 203 mm/min ➢ Tool rotation rate of 300,700, 900 and 1100 rpm and a traverse speed 2 and 8 ipm	➢ Mechanical Properties ➢ Microstructure ➢ Macrostructure ➢ Wear Properties	The mechanical properties of welded joint by friction stir welding are largely dependent on the combined effect of both the composition of alloying element and processing parameter.
20	Mironov.S. , et al (2009)	Development of grain structure during friction stir welding of pure titanium	Purity a-titanium (ASTM Grade, Thickness- 3 mm thick Butt-welded Joint	Tool Material - Mo-based alloy	➢ Tool convex shoulder diameter (mm) – 15. ➢ Pin threaded and tapered diameter (mm) -5.1 ➢ Tool tapered pin length (mm) -3 ➢ Tool rotational speed - 200 rpm ➢ Tool traverse speed -	➢ Base material ➢ Low-magnification overview ➢ TMAZ ➢ Stir zone	(1) The global straining state during the process was deduced to be close to the simple shear with the shear surface being nearly along the truncated cone having a diameter close to that of the tool shoulder in the top part of the SZ and the pin diameter in the bottom part of the SZ. (2) The material flow was shown to arise mainly from the prism slip, giving rise to the pronounced P-fiber fhk i lgh11 20i simple shear texture in the SZ. (3) The grain structure evolution was shown to be a complex process driven mainly by the texture-induced grain convergence, but also involving the geometrical effects of strain and limited discontinuous recrystallization.
21	Buffa.G., et al (2012)	On the Choice of Tool Material in FSW of Titanium Alloys	Ti–6Al–4V titanium alloy sheets 100 mm x 200 mm Thickness- 3 mm thick	Tool Material – 3 different Tool (two WC based materials) K10-K30 and W25Re.	➢ Tool shoulder diameter (mm) - 16 mm. ➢ Tool conical Pin diameter (mm) -5 ➢ Tool conical pin length (mm) -2.6 ➢ Tool rotational speed - 300, 700 and 1000 rpm ➢ Tool traverse speed - 35 mm/min	Numerical Model	(1) All the tools failures were observed between the end of the sinking stage and the first few mm of welding. According to the numerical results, (2) Although characterized by a large hardness value, the K10 material revealed as inadequate for FSW of titanium alloys as brittle fractures occur. No weld could be obtained with the low rotational speed and unsatisfying tool life values were observed at the increasing of the tool rotation.

3. Conclusions & Recommendations

- It was difficult to weld aluminum alloy & titanium 64 because of high strength and large difference of melting point.
- Improve the strength of weld joint reinforcements is going to add in the weld joint to enhance the weld quality and to check the effect of reinforcement on the microstructure and mechanical properties of weld joint .

References

[1] Bahrami, M., Kazem, M., Givi, B., Dehghani, K., & Parvin, N. (2014). On the role of pin geometry in microstructure and mechanical properties of AA7075 / SiC nano-composite fabricated by friction stir welding technique. Journal of Materials & Design, 53, 519–527.

[2] Chen, Y. (2015). Interface characteristic of friction stir welding lap joints of Ti / Al dissimilar alloys, 632 6 (February 2015).

[3] Aonuma, M., & Nakata, K. (2011). Dissimilar Metal Joining of 2024 and 7075 Aluminium Alloys to Titanium Alloys by Friction Stir Welding *, 52(5), 948–952.
[4] Wang, J., Su, J., Mishra, R. S., Xu, R., & Baumann, J. A. (2014). Tool wear mechanisms in friction stir welding of Ti – 6Al – 4V alloy. Wear, 321, 25–32.
[5] Bang, H., Bang, H., Song, H., & Joo, S. (2013). Joint properties of dissimilar Al6061-T6 aluminum alloy / Ti-6%Al-4%V titanium alloy by gas tungsten arc welding assisted hybrid friction stir welding. JOURNAL OF MATERIALS&DESIGN.
[6] Squillace, A., & Prisco, U. (2012). Effect of Welding Parameters on Morphology and Mechanical Properties of Ti-6Al-4 V Laser Beam Welded Butt Joints. Journal of Materials Processing Tech., 212(2), 427–436.
[7] Ji, Y., Wu, S., & Zhao, D. (2016). Microstructure and Mechanical Properties of Friction, 1–11.
[8] Sohn.w. (2014). Microstructure and bonding mechanism of Al / Ti bonded joint using Al – 10Si – 1Mg filler metal Microstructure and bonding mechanism of Al / Ti bonded joint using, (August 2003).
[9] Aonuma, M., & Nakata, K. (2012). Dissimilar metal joining of ZK60 magnesium alloy and titanium by friction stir welding. Materials Science & Engineering B, 177(7), 543–548.
[10] Chen, Y. C., & Nakata, K. (2009). Microstructural characterization and mechanical properties in friction stir welding of aluminum and titanium dissimilar alloys. Materials and Design, 30(3), 469–474.
[11] Liu, H. J., Zhou, L., & Liu, Q. W. (2010). Microstructural characteristics and mechanical properties of friction stir welded joints of Ti – 6Al – 4V titanium alloy. Materials and Design, 31(3), 1650–1655.
[12] Bang, H., Bang, H., Song, H., & Joo, S. (2013). Joint properties of dissimilar Al6061-T6 aluminum alloy / Ti – 6 % Al – 4 % V titanium alloy by gas tungsten arc welding assisted hybrid friction stir welding. Materials and Design, 51, 544–551.
[13] Xie, G. M., Ma, Z. Y., & Geng, L. (2008). Effect of microstructural evolution on mechanical properties of friction stir welded ZK60 alloy, 486, 49–55. https://doi.org/10.1016/j.msea.2007.08.043.
[14] Dressler, U., Biallas, G., & Mercado, U. A. (2009). Friction stir welding of titanium alloy TiAl6V4 to aluminium alloy AA2024-T3, 526, 113–117.
[15] Zhang, Y., Sato, Y. S., Kokawa, H., Hwan, S., Park, C., & Hirano, S. (2008). Microstructural characteristics and mechanical properties of Ti – 6Al – 4V friction stir welds, 485, 448–455.
[16] Aonuma, M., & Nakata, K. (2009). Effect of alloying elements on interface microstructure of Mg – Al – Zn magnesium alloys and titanium joint by friction stir welding, 161, 46–49.
[17] Nathan, S. R., Malarvizhi, S., Balasubramanian, V., & Rao, A. G. (2016). Failure analysis of tungsten based tool materials used in friction stir welding of high strength low alloy steels. EFA, 66, 88–98.
[18] Husain Mehdi, R.S. Mishra, Mechanical properties and microstructure studies in Friction Stir Welding (FSW) joints of dissimilar alloy- A Review, Journal of Achievements in Materials and Manufacturing Engineering 77/1 (2016) 31-40.
[19] Husain Mehdi, R.S. Mishra, Influences of Process Parameter and Microstructural Studies in Friction Stir Weldingof Different Alloys: A Review, International Journal of Advanced Production and Industrial Engineering, IJAPIE-SI-MM 509 (2017) 55–62.
[20] Mironov, S., Sato, Y. S., & Kokawa, H. (2009). Development of grain structure during friction stir welding of pure titanium. Acta Materialia, 57(15), 4519–4528.
[21] Buffa, G., Fratini, L., Micari, F., & Settineri, L. (2012). Politecnico di Torino Porto Institutional Repository on the Choice of Tool Material in Friction Stir Welding of Titanium Alloys.

Available online at www.ijapie.org

INTERNATIONAL JOURNAL OF ADVANCED PRODUCTION AND INDUSTRIAL ENGINEERING

IJAPIE-2017-07-319, Vol 2 (3), 82-88

IJAPIE
Connecting Science & Technology withManagement.
A Journal for all Products &Processes.

Harmonic Reduction in Power Distribution Network using UPQC

J.N.Rai*, Ram Bhagat
(Department of Electrical Engineering, Delhi Technological University, Delhi, India)
**Email: jnrai.phd@gmail.com*

Abstract : Unified Power Quality Conditioner (UPQC) is a versatile custom power device. It consists of two VSCs connected back-to-back to compensate for both distorted Point at Common Coupling (PCC) voltage and supply current imperfections. UPQC is designed to prevent the harmonics injected by the non-linear load from entering the source terminal. Regulation of voltage at the point of common coupling is carried out by series connected converter. SRF based current control method is used for current compensation by the shunt device. Hysteresis voltage control technique is used for shunt compensation by the series device which simultaneously acts as shunt and series active power filters. Maintaining a constant value for dc link voltage is essential for UPQC to perform normally which is carried out by shunt connected VSC. MATLAB based simulation is carried out to demonstrate the effectiveness of the proposed control scheme.

Keywords : UPQC, Non-Liner RL Load, Harmonics, synchronous reference frame (SRF), Hysteresis Voltage, Control Point at Common Coupling (PCC).

I. INTRODUCTION

Use of non–linear and time varying loads has led to distortion of voltage and current waveforms and increased reactive power demand in AC mains. Distortion due to harmonics is known to be the source of several problems, such as increased power losses, excess heating in rotating machinery, flicker and audible noise, significant interference with communication circuits, and incorrect operation of sensitive loads[1].Power electronics based equipment which includes adjustable–speed motor drives, DC motor drives, electronic power supplies, electronic ballasts, battery chargers are responsible for the rise in power quality related problems. Power quality is affected by harmonic distortion, temporary interruptions, voltage sag, voltage swell, under voltages, voltage spikes and noise [2]. Non-linear loads appear to be prime sources of harmonic distortion in a power distribution system. As the harmonic currents pass through the line impedance of the system, harmonic voltages appear, causing distortion at the coupling point. Harmonics have a number of undesirable effects on the distribution system. There are two basic categories: short term and long term. Short–term effects are usually the most noticeable and are related to excessive voltage distortion. Long–term effects often go undetected and are usually related to increased resistive losses or voltage stress [3]. In addition, harmonic currents produced by nonlinear loads can interact adversely with a wide range of power system equipment, most notably capacitors, transformers and motors, causing additional losses, overheating and overloading. As the presence of harmonics in distribution system is harmful, there is a need to define a framework to suppress it. To mitigate these identified power quality problems efforts are going on in the field of filters. Present day power quality renders these efforts futile. New technology known as custom power devices(CPD) has been developed for such distribution systems. These devices are applicable to distribution systems for enhancing the reliability and quality of the power supply. CPDs include DSTATCOM, DVR[6] and UPQC.

The Unified Power Quality Conditioner (UPQC) (figure 1) is one of the versatile custom power device, which can compensate both current and voltage related problems, simultaneously. The series Active Power Filter (APF) compensates voltage-based distortions, while the shunt APF cancels current-based distortions such as harmonics, reactive power and negative sequence current etc.

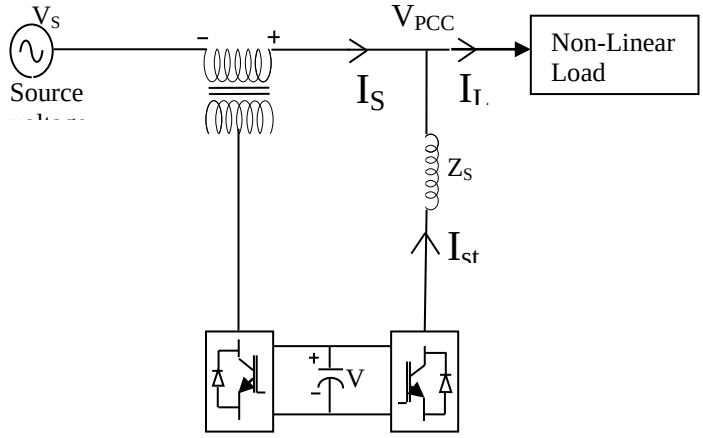


Fig.1. UPQC Block Diagram

The investigator has gone through a number of literatures in this regard. Some of them are:(a) the indirect current control approach, in terms of its simplicity and effectiveness, for the operation of a series APF[4].(b)Simulation of instantaneous

active and reactive theory based shunt active filter with MATLAB/ Simulink, a better solution for reduction of the harmonics[5].(c)A series active harmonic compensator which compensates the harmonic contents present in load voltage at PCC[7].

In this paper UPQC is designed to remove the harmonic injected by the non-linear load from entering into the source terminal. Regulation of voltage at the point of common is carried out by series connected converter. SRF based current control method is used for current compensation by the shunt device and Hysteresis voltage control technique is used for series device which simultaneously act as shunt and series active power filters.

II. SYSTEM DESCRIPTION

The system under consideration is shown in Fig.2.The UPQC is connected before the load to protect a sensitive load from any voltage based distortions and simultaneously making the source currents sinusoidal. The UPQC is realized by using two voltage source inverters (VSIs) connected back to back with a common DC link Voltage. One VSI is acting as a shunt APF, while the other as series APF. The series APF[8] is connected between the source and the load with the help of three single phase injection transformer. Injection transformer is used to inject voltage in the line by the series APF. While, shunt APF is connected at point of common coupling (PCC). Each APF is realized by using six Insulated Gate Bipolar Transistors (IGBT) switches[10]. The load under consideration is a non-linear load. A three-phase diode bridge rectifier with a RL load is considered as a non-linear load. The values of the circuit parameters and load under consideration are given in Appendix.

III. CONTROL SCHEME

The series active filters control has been carried out by means of following compensation strategy-

Control strategy which measures the load voltage to make that the APF generates a voltage with that same harmonic content and the opposite sign [9].

$$V_{ch} = K_v \cdot V_{lh} \qquad (1)$$

The measurement of the load voltage harmonic generally depends on the instrumentation sensibility k_v. The voltage supplied by the APF is expressed as follows:

$$V_{ch} = K_v \cdot V_{lh} \qquad (2)$$

From equation 2, the voltage in the point of common coupling is, for a specific harmonic :

$$V_{cch} = V_{lh}\left(1 - K_v\right) \qquad (3)$$

REFERENCE SIGNAL GENERATION

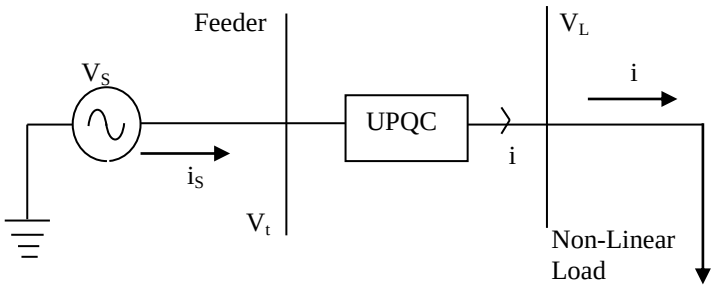


Fig.2 System Under Consideration

The Reference signal generation is done by using UTT theory[11]. The equations showing the generation of the reference signals are given below-

A. Series Active filter

The extraction of three-phase voltage reference signal for series APF is based on Unit Vector Template Generation, achieved with the help of PLL. These Unit Vector Templates are multiplied with the desirable peak amplitude (V_{tmn}) of load voltage to obtained reference load voltages denoted by V_{lar}, V_{lbr} and V_{lcr} for phase a, b and c respectively and are given by-

$$V'_{lar} = V_{tmn} \cdot u_a \qquad (4)$$

$$V'_{lbr} = V_{tmn} \cdot u_b \qquad (5)$$

$$V'_{lcr} = V_{tmn} \cdot u_c \qquad (6)$$

where u_a, u_b and u_c are unit vector templates which are in phase with supply voltage and are given by-

$$u_a = sin(\omega t) \qquad (7)$$

$$u_b = sin(\omega t + 120) \qquad (8)$$

$$u_c = sin(\omega t - 120) \qquad (9)$$

B. Shunt Active Filter

Unit vector template generation theory is again used here. These Unit Vector Templates are multiplied with the desirable peak amplitude I_{tmn} to obtain the reference currents denoted by I_{lar}, I_{lbr} and I_{lcr} for phase a, b and c respectively and are given by-

$$I'_{lar} = I_{tmn} \cdot i_a \qquad (10)$$

$$I'_{lbr} = I_{tmn} \cdot i_b \qquad (11)$$

$$I'_{lcr} = I_{tmn} \cdot i_c \qquad (12)$$

Where i_a, i_b and i_c are unit vector templates which are in phase with supply current and are given by-

$$i_a = sin(\omega t) \qquad (13)$$

$$i_b = sin(\omega t + 120) \qquad (14)$$

$$i_c = sin(\omega t - 120) \qquad (15)$$

HYSTERSIS CURRENT CONTROL METHOD

In this method, the actual current continually tracks the command current within a hysteresis-band. Pre-set upper and lower tolerance limits are compared to the extracted error signal. As long as the error is within the tolerance band, no switching action takes place. Switching occurs whenever the error leaves the tolerance band. The hysteresis current control is the fastest method with minimum hardware and software. In this article the hysteresis current control method is used, because of its simplicity of implementation and robustness. This strategy provides satisfactory control of current without requiring extensive knowledge of control system model or its parameters.

SIMULATION WITHOUT UPQC: The simulation waveforms are given as figure 3 for load voltage and current source ,figure 4 shows THD in source current and whereas figure 5 shows THD in load voltage without UPQC

The simulation Circuits and waveforms are given below

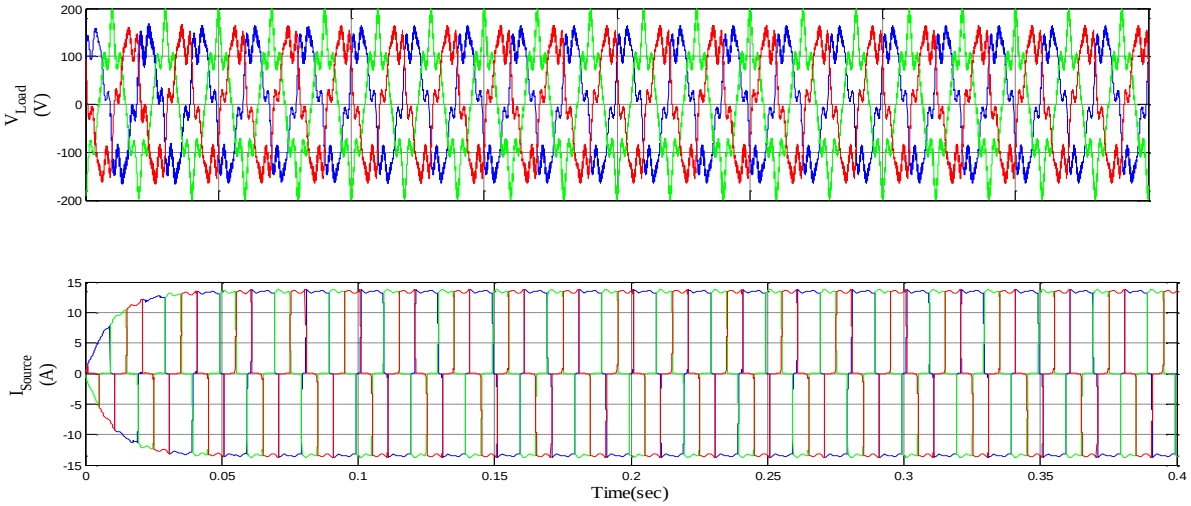


Fig.3. Load Voltage and Source Current without UPQC

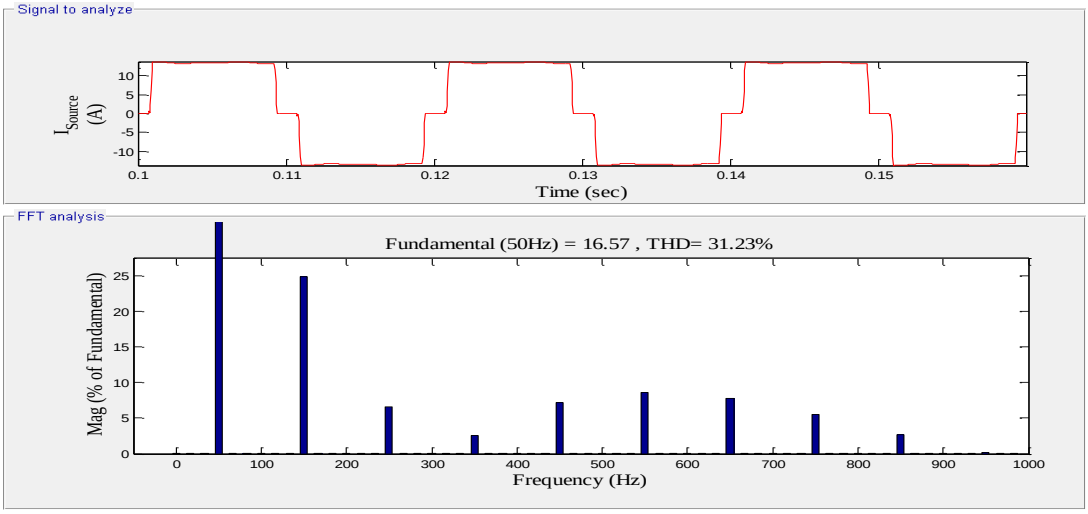


Fig.4. THD in source current without UPQC.

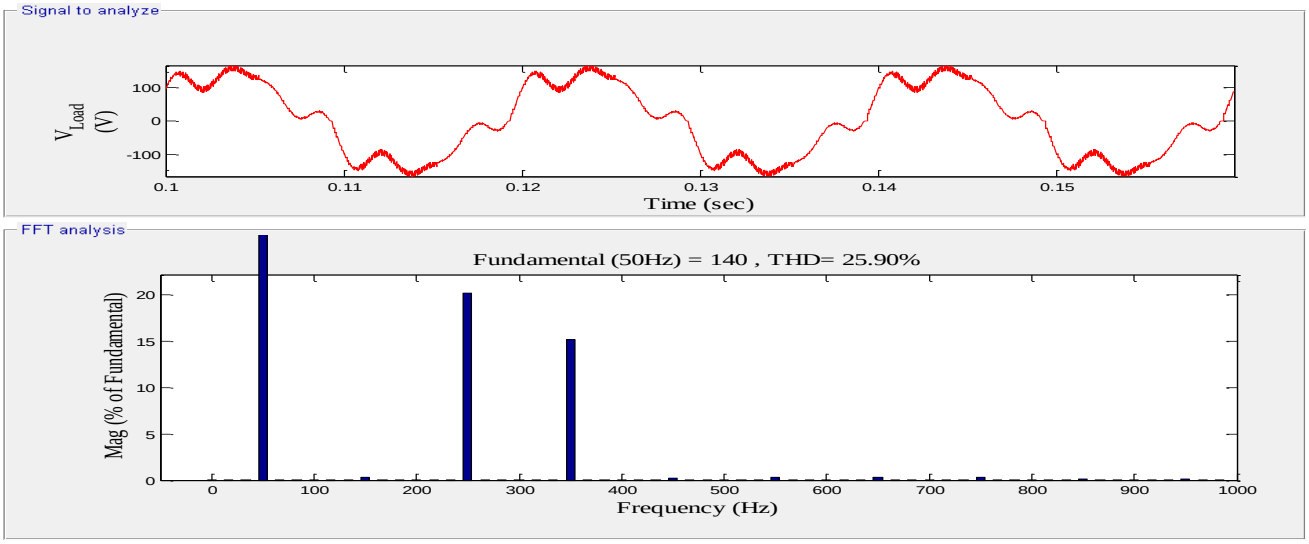


Fig.5. THD in Load Voltage without UPQC

IV. SIMULATION RESULTS AND DISCUSSION

The objectives of work carried out can be summarized as follows:

1. Reduction in the harmonics in the voltage at PCC.
2. Reduction in the harmonics in the source current.

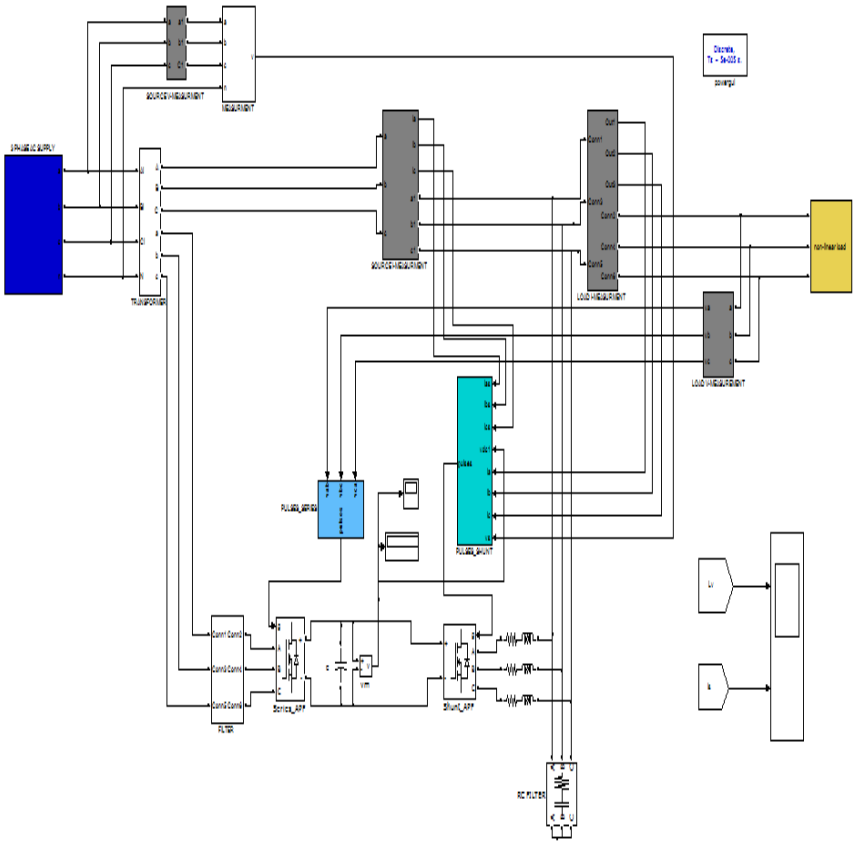


Fig 6 : Simulation model of circuit with rectifier fed RL Load using UPQC.

SIMULATION WITH UPQC

Simulation model of circuit using unified power quality conditioner is given figure 6 below along with their corresponding waveforms of voltage at PCC and source current shown in figure 7. In the present study, hysteresis band gap controllers and Unit Vector Template Technique(UTT) generation theory are used for both series and shunt active power filters. To show the clear operation of UPQC, both Series active power filter and shunt active power filter are put in operation at t = 0.1s so that the distorted current and voltage waveform can be shown in a single diagram along with compensated voltage and current waveforms. To show the improvement in power quality improvement in distribution network as shown in table .The response of UPQC for THD in load voltage and THD in source voltage shown in figure 8 & 9.

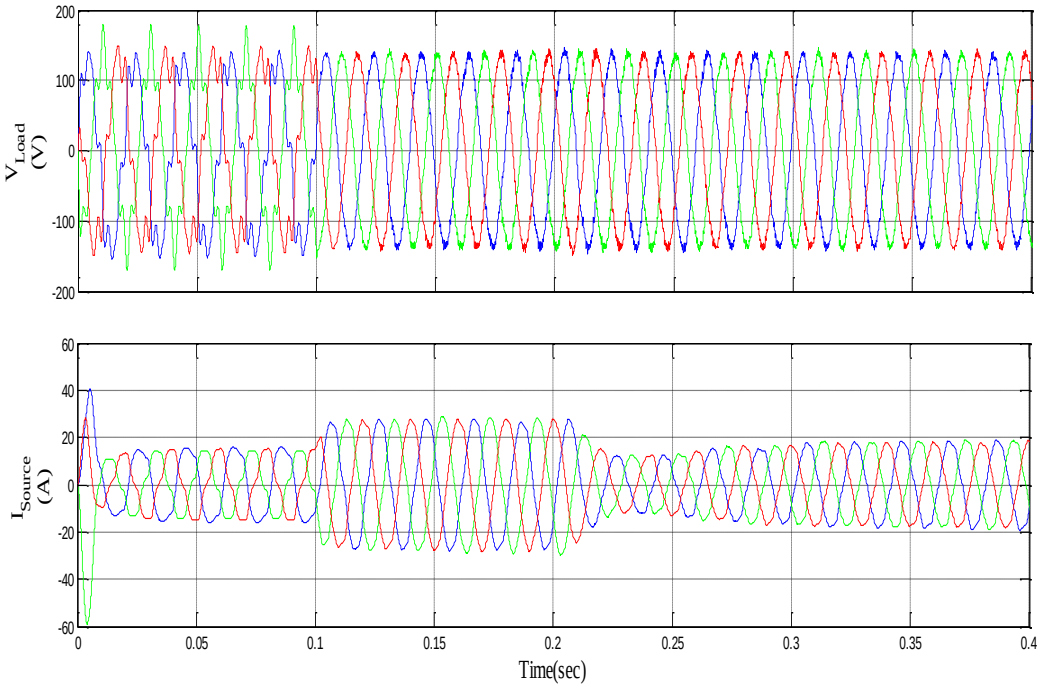


Fig.7. Load Voltage and Source Current with UPQC

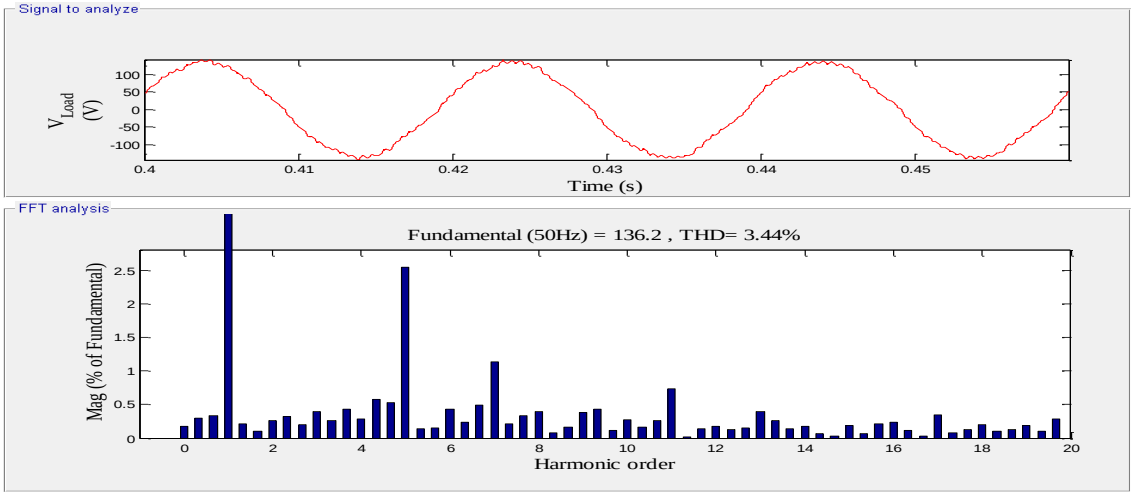


Fig.8. THD in Load Voltage using UPQC.

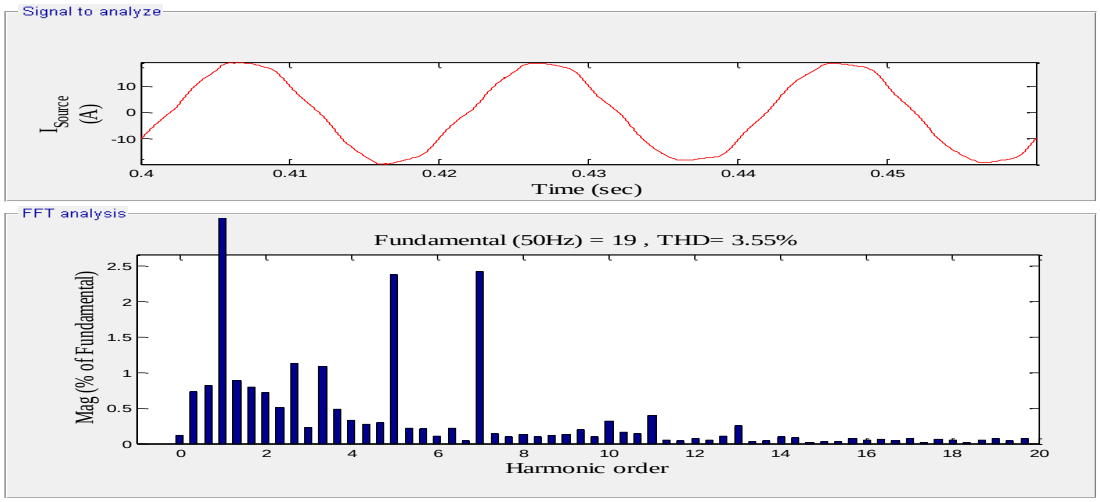


Fig.9. THD in Source Voltage using UPQC.

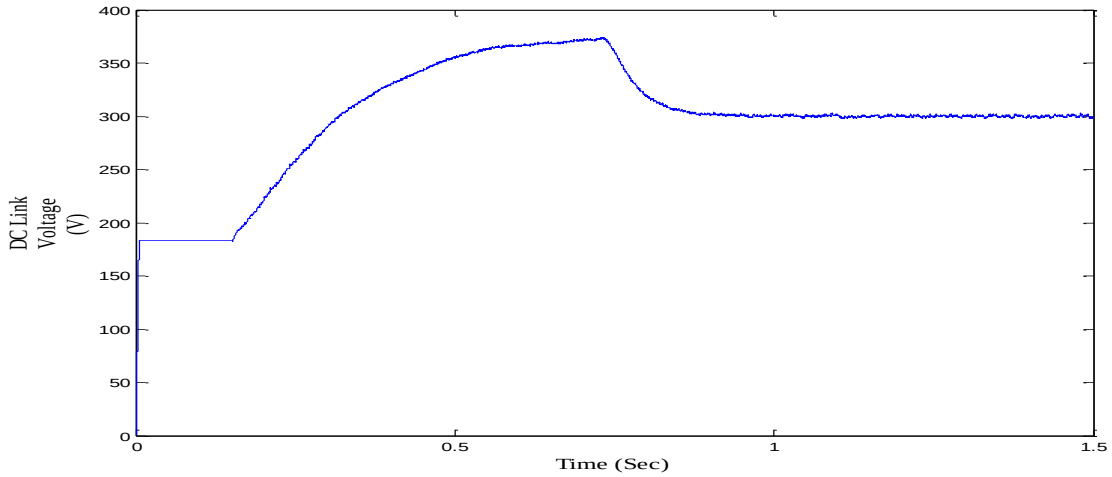


Fig 10 : DC Link Voltage

V. Result & Discussion

The THD in voltage and current is calculated using Fast Fourier Transform and is given by:

$$THD = \frac{\sqrt{\sum_{n}^{\infty} V_n^2}}{V_1} \qquad (1)$$

Where V_n denotes the magnitude of the n harmonic voltage and V_1 is the magnitude of the fundamental voltage. Similar expressions can also be written for current harmonics. The response of DC link voltage corresponding to time shown in figure 10.

Table 1: Simulation Results

Sr No	Without UPQC	With UPQC
1	THD in source current 31.23 %	THD in source current 3.55 %
2	THD in voltage at PCC 25.90 %	THD in voltage at PCC 3.44 %

From Table -1 it can be elucidated that the use of UPQC has considerably reduced the THD in source current from more than 30% to only about 3.55% which is well within the IEEE tolerance limits of 5.0%. The THD in voltage waveform has also reduced from about 25% to about 3.44% which also is within the IEEE tolerance limits.

Thus, the overall quality of the power has considerably improved by employing UPQC.

VI. CONCLUSIONS

The UPQC has become the most important technique for improvement of power in electrical power distribution systems. In this paper, a model for 3-phase UPQC for non-linear loads connected at PCC is simulated using MATLAB/ Simulink for the reduction of harmonics in voltage at PCC. The simulation studies demonstrate the Performance of UPQC

The performance of UPQC is verified with simulation results. From the results, it is clear that the harmonics have reduced by

nearly 7-8 times .The THD in voltage at PCC without using UPQC was about 25.90%.The THD in voltage at PCC reduced to about 3.55% after using the UPQC.THD in source current reduced to about 3.44% from more than

30%.Harmonics levels are maintained below IEEE-519 standards.

APPENDIX

The system parameters are used as follows:
Source voltage: 110(ph-ph), 50Hz
Transformer: 1000VA, 240/24, 50Hz
Filter: R=16Ω, 200μF
Load: a three-phase diode bridge
rectifier with R=20Ω and L=100mH on DC side.

REFERENCES

[1] Srinivas Bhaskar Karanki, Nagesh Geddada, Mahesh K. Mishra and B. Kalyan Kumar,"Modified Three-Phase Four-Wire UPQC Topology with Reduced DC-Link Voltage Rating," *IEEE Trans. Industrial Electronics*, vol.60, no.9, Sept.2012.
[2] B.Singh and V.Verma, "A New Control Scheme of Series Active Filter for Varying Rectifier Loads," *IEEE Conf. Power Electron.* , vol.1, pp. 612-620, 1997.
[3] Metin Kesler and Engin Ozdemir, "Synchronous-Reference-Frame-Based Control Method for UPQC Under Unbalanced and Distorted Load Conditions*," IEEE Trans. Industrial Electronics*,vol.58, no.9, Sept.2011.
[4] Norman Mariun, AhsanulAlam, SenamMehmod and HashimHisram, "Review of control strategy for power quality conditioner", *In Proc. National Power & Energy Conference (PECon)*, pp. 109-115, Malaysia. Nov 2004.
[5] Naresh K. Kummari, Asheesh K. Singh, "Comparative Evaluation of DSTATCOM Control Algorithms for Load Compensation," *IEEE Conf. Industrial Harmonics and Quality of Power*, pp. 299-306, 2012.
[6] Yash Pal and A. Swaroop, "Performance of UPQC for power quality improvement," *IEEE PEDES. Joint Internatinal conf.* , pp.1-7, 2010.
[7] L. H. Tey, andP. L. So, "System Harmonics Compensation using PWM Voltage Source Inverter-Based Active Filters", *In Proc. IEEE Power Tech Conference* vol.1, Portugal ,Sept. 2001.
[8] Vinod Khadkikar, "Enhancing Electric Power Quality Using UPQC: A Comprehensive Overview," *IEEE Trans. Power Electron.*, vol. 27, pp.2284-2297, 2012.
[9] Enio R. Ribeiro and Ivo Barbi, "Harmonic Voltage Reduction Using a Series Active Filter Under Different Load Conditions", *IEEE Trans. Power Electronics*, Vol. 21, No. 5, Sept. 2006.
[10] P. Salmeron and S. P. Litran, "Improvement of the Electric Power Quality Using Series Active and Shunt Passive Filters", *IEEE Trans. Power Delivery*, Vol. 25, No. 2, April 2010.
[11] S.P. Litan, P. Salmeron, R.S.Herrera, J.R. Vazquez, "Control of Series Active Filter by state feedback," *Comision IEE Proc.Electr.Power Appl.*, vol, 151,no.3, pp. 276-282, May 2004.



J.N Rai, received the Ph.D degree in Electrical Engineering in 2016 from Jamia Millia Islamia (Central University). His research interest are in Power generation, Power system modeling , Power system Operation & Control and Advanced Modeling and Control Techniques applied to Power Plant. He is currently working as a Professor in Department of Electrical Engineering, Delhi Technological University (formerly Delhi College of Engineering), India.



Ram Bhagat, received the B.TechM.E. degree in Electrical Engineering in 1997and 2004 respectively. His research interest are in Analog Signal Processing, Control System and Automation. He is currently working as an Assistant Professor in Delhi Technological University (formerly Delhi College of Engineering), India.

International Journal of Research in Engineering and Innovation (IJREI)
journal home page: http://www.ijrei.com
ISSN (Online): 2456-6934

Methods for improving thermal performances of vapour absorption system using heat pipes

R.S. Mishra, Ankit Dwivedi

Department Mechanical, Production and Automobile Engineering, Delhi Technological University, Delhi India

Abstract

Several types of types of VAR systems such as single effect, double effect, triple effect etc. Energy-exergy analysis have been performed in the literature so far. The heat pipes can be made an integral part of the system and these valuable thermodynamic analyses can be executed for improving its thermal performances. In terms of energy efficiency (COP) and exergetic efficiency. Another problems is the waste heat going to the environment from condenser has never been used, which can be supplied back to the generator is required low grade energy for its operation can be used for improving its thermal performances.

The VAR system can be coupled with other systems may be refrigerating or power generating in which heat is released in the loop heat pipes will make the system compact, and that effect must be studied to optimize the performance of the VAR systems. It was observed that intra-Cycle heat exchange in the VAR system reduces heat input thus improved in the thermal performance in terms of first law efficiency(Energy-Efficiency) and second law efficiency (Exergetic efficiency) of the VAR system and highly effective heat exchange through the heat pipe due to removal of condenser exergetic losses improved second law performances. Similarly the gas power plant coupled with modified vapour absorption refrigeration improves the first law efficiency in terms energy-efficiency (COP) and second law efficiency in terms of exergetic efficiency with reduction in system exergy destruction ratio.
© 2017 ijrei.com. All rights reserved

Keywords: Thermodynamic analysis, Heat Pipes, Vapour Absorption Refrigeration Systems, Exergy-Energy Analysis

1. Introduction

Vapour Absorption Refrigeration Systems (VARS) belong to the class of vapour cycles similar to vapour compression refrigeration systems. However, unlike vapour compression refrigeration systems, the required input to absorption systems is in the form of heat. Hence these systems are also called as heat operated or thermal energy driven systems. Since conventional absorption systems use liquids for absorption of refrigerant, these are also sometimes called as wet absorption systems. Similar to vapour compression refrigeration systems, vapour absorption refrigeration systems have also been commercialized and are widely used in various refrigeration and air conditioning applications. Since these systems run on low-grade thermal energy, they are preferred when low-grade energy such as waste heat or solar energy is available. Since conventional absorption systems use natural refrigerants such as water or ammonia they are environment friendly.

Condenser

Just like in the traditional condenser of the vapor compression cycle, the refrigerant enters the condenser at high pressure and temperature and gets condensed. The condenser is of water cooled type.

Expansion valve or restriction

When the refrigerant passes through the expansion valve, its pressure and temperature reduces suddenly. This

Corresponding author: R.S.Mishra
Email Id: rsmishradtu@gmail.com

refrigerant (ammonia in this case) then enters the evaporator.

Evaporator

The refrigerant at very low pressure and temperature enters the evaporator and produces the cooling effect. In the vapor compression cycle this refrigerant is sucked by the compressor, but in the vapor absorption cycle, this refrigerant flows to the absorber that acts as the suction part of the refrigeration cycle.

Absorber

The absorber is a sort of vessel consisting of water that acts as the absorbent, and the previous absorbed refrigerant. Thus the absorber consists of the weak solution of the refrigerant (ammonia in this case) and absorbent (water in this case).
When ammonia from the evaporator enters the absorber, it is absorbed by the absorbent due to which the pressure inside the absorber reduces further leading to more flow of the refrigerant from the evaporator to the absorber. At high temperature water absorbs lesser ammonia, hence it is cooled by the external coolant to increase it ammonia absorption capacity.

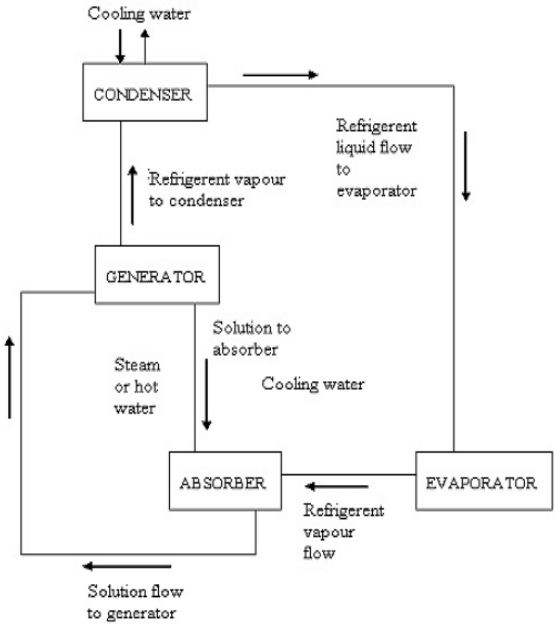


Figure.1: Vapor Absorption Refrigeration System

The absorption refrigeration system comprises of condenser, expansion valve, evaporator, absorber, pump and generator. The refrigerant leaving the evaporator enter the absorber, where it is absorbed by the absorbent. The strong solution of refrigerant-absorber enters the generator with the help of the pump. The refrigerant then enters the condenser while the remaining weak solution enters back to the absorber and the cycle is repeated.
The initial flow of the refrigerant from the evaporator to the absorber occurs because the vapor pressure of the refrigerant-absorbent in the absorber is lower than the vapor pressure of the refrigerant in the evaporator. The vapor pressure of the refrigerant-absorbent inside the absorbent determines the pressure on low-pressure side of the system and also the vaporizing temperature of the refrigerant inside the evaporator. The vapor pressure of the refrigerant-absorbent solution depends on the nature of the absorbent, its temperature and concentration.
When the refrigerant entering in the absorber is absorbed by the absorbent its volume decreases, thus the compression of the refrigerant occurs. Thus absorber acts as the suction part of the compressor. The heat of absorption is also released in the absorber, which is removed by the external coolant.

Pump

When the absorbent absorbs the refrigerant strong solution of refrigerant absorbent (ammonia-water) is formed. This solution is pumped by the pump at high pressure to the generator. Thus pump increases the pressure of the solution to about 10bar.

Generator

The refrigerant-ammonia solution in the generator is heated by the external source of heat. This is can be steam, hot water or any other suitable source. Due to heating the temperature of the solution increases. The refrigerant in the solution gets vaporized and it leaves the solution at high pressure. The high pressure and the high temperature refrigerant then enters the condenser, where it is cooled by the coolant, and it then enters the expansion valve and then finally into the evaporator where it produces the cooling effect. This refrigerant is then again absorbed by the weak solution in the absorber.
When the vaporized refrigerant leaves the generator weak solution is left in it. This solution enters the pressure reducing valve and then back to the absorber, where it is ready to absorb fresh refrigerant. In this way, the refrigerant keeps on repeating the cycle.
The pressure of the refrigerant is increased in the generator, hence it is considered to be equivalent to the compression part of the compressor.

1.1 Loop Heat Pipe

Loop heat pipes (LHPs) are two-phase heat transfer devices. It uses the evaporation and condensation of a working fluid to transfer the heat from one point to other. Capillary forces are developed in the fine porous wicks which helps to circulate the fluid. It does not require

electrical power because they have no moving mechanical parts.

The pressure loss at the wick in the Loop Heat Pipes can be kept lower than in the conventional HPs. The wick is made of copper instead of PTFE (polytetrafluoroethylene) and has pores of size 0.3mm. Loop Heat Pipes are similar to heat pipes but have the advantage of being able to provide reliable operation over long distance. They can transport a large heat load over a long distance with a small temperature difference.

Different designs of Loop Heat Pipes ranging from powerful, large size LHPs to miniature LHPs (micro loop heat pipe) have also been developed and successfully employed in a wide sphere of applications both ground based as well as space applications. Compared with conventional Heat Pipes (HPs), which also use capillary forces to circulate the working fluid, the LHPs can transport heat over longer distances.

In the conventional Heat pipes, vapour flows through the center of the pipe from an evaporation area to a condensation area, while liquid flows through the wick, which is located in the inner surface of the entire pipe, from the condensation area back to the evaporation area. Therefore, if the distance needed for heat transport becomes longer, the length of the wick and the entire pipe also become longer.

In contrast, in the LHPs, the wick is located only in the evaporator. Therefore, if the distance needed for the heat transport becomes longer, the length of the wick does not change. Because of this difference, the pressure loss at the wick in the LHPs can be kept lower than in the conventional HPs.

The wicks in the LHPs develop high capillary pressures that are used to operate against gravity and can also be used to increase the horizontal distance for heat transport. The heat losses from vapor and liquid lines to ambient air and due to the pressure losses in the single-and two-phase fluids in the vapor and liquid lines. Figure shows the layout of loop heat pipe.

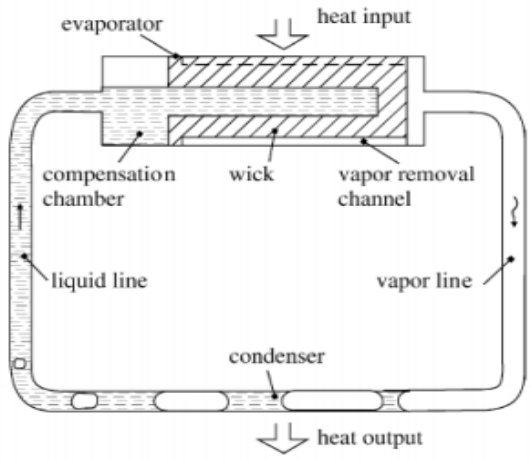


Figure.2: Loop Heat pipe [20]

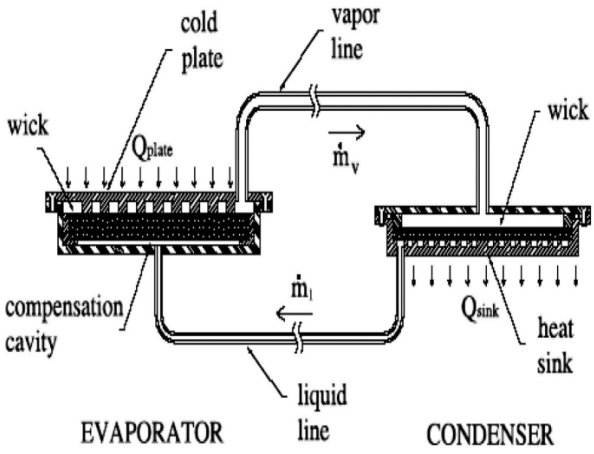


Figure 3: Loop Heat pipe [20]

Qualities of LHP

- High heat flux capability
- Capability to transport energy over long distances without restriction on therouting of the liquid and vapour lines
- Ability to operate over a range of 'g' environments.
- No wick within the transport lines
- Vapour and liquid flows separated, therefore no entrainment
- May be adapted to allow temperature control.

1.2 Use of exergy method for finding irreversibility in the system

Whole part of heat energy can never be converted completely into work, there some part of energy which used and second which get waste, the useful part of energy that is able to convert into heat is called available energy or exergy and unavailable part which get destroyed is called unavailable energy. As the first law of thermodynamics state that the energy is always conserved but the content of that energy wihic is capable of producing useful work is not constant that is exergy. The maximum useful work or exergy at a particular state is a composite property depending upon the state of system and surrounding. A dead state having Zero exergy that is equilibrium state.

1.3 Literature Review

Da-Wen Sun [1] (1996) performed a detailed thermodynamic analysis of the properties of these binary fluids and expressed in polynomial equations. The performances of three cycles were compared. It was found that ammonia-lithium nitrate and ammonia-sodium thiocyanate cycles are suitable alternatives to ammonia-water absorption systems. The performance of the

ammonia-sodium thiocyanate cycle is slightly better than that of the ammonia-lithium nitrate cycle.

M.M. Talbiet et al.[2] (2000)carried out an exergy analysis on a single-effect absorption refrigeration cycle with lithium-bromide±water as the working Fuid pair. A design procedure has been applied to a lithium-bromide absorption cycle and an optimisation procedure that consists of determining the enthalpy, entropy, temperature, mass Fow rate, heat rate in each component, and coefficient of performance has been performed.

E. Kuremet et al [3] (2001)analyzed the Absorption Heat Pump (AHP) and Absorption Heat Transformers (AHT) using ammonia-water and water-lithium bromide solutions. A fundamental AHP and AHT systems was described and explained the operating sequence. Since the AHT systems widely uses ammonia-water solution with ammonia as the refrigerant and water-lithium bromide solution with water as the refrigerant, the comparison of the two was presented in respect of the coefficient of performance (COP), the flow ratio (FR) and the maximum system pressure. They concluded that the AHT system using water-lithium bromide solution provided better performance than the system using ammonia-water.

R.D. Misraet et al [4] (2002) applied the thermo-economic theory is to the economic optimization of a single effect water/LiBr vapour absorption refrigeration system for air-conditioning application. They applied a simplified cost minimization methodology to evaluate the economic costs of all the internal flows and products of the system by formulating exerg-o-economic cost equations. Having determined these costs, they evaluated the system therm-o-economically to identify the effects of design variables on costs and enabled to suggest values of design variables that made the overall system cost effective. An approximate optimum design configuration was obtained by means of sequential local optimization of the system, carried out unit by unit.

S.A. Adewusi et al [5](2004). studied the performance of single-stage and two-stage ammonia–water absorption refrigeration systems (ARSs).They calculated entropy generation of each component and the total entropy generation of all the system components as well as COP of the ARSs .The results showed that the two stage system had a higher S_ tot and COP, while the single-stage system has a lower S_ tot and COP. They investigated trend in COP and S_ tot with the change in heat exchangers effectiveness, absorbers temperatures and condenser and evaporator temperatures for both systems and found that an increase in COP corresponds to a decrease in S_ tot.

S. Arivazhagan et al. [6] (2006) investigated experimentally on the performance of a two-stage half effect vapour absorption cooling system .The prototype is designed for 1 kW cooling capacity using HFC based working fluids (R134a as refrigerant and DMAC as absorbent). The performance of the system in terms of degassing range, coefficient of performance and second law efficiency had been obtained. The system was capable of producing evaporating temperature as low as 7°C with generator temperatures ranging from 55 to 75 °C. The degassing range is 40% more in high absorber than in low absorber as the high absorber is operated at optimum intermediate pressure. The optimum generator temperature is found to be in the range of 65–70 °C at which the coefficient of performance is 0.36.

Rabah Gomri et al [7] (2008) performed exergy analysis of double effect lithium bromide/water absorption refrigeration system. The system consisted of a second effect generator between the generator and condenser of the single effect absorption refrigeration system, including two solution heat exchangers between the absorber and the two generators. They used a new set of computationally efficient formulations of thermodynamic properties of lithium bromide/water solution. In addition to the coefficient of performance and the exergetic efficiency of the system, the number of exergy of each component of the system is also estimated. The results showed that the performance of the system increased with increasing low pressure generator (LPG) temperature, but decreased with increasing high pressure generator (HPG) temperature. The highest exergy loss occurred in the absorber and in the HPG, which therefore makes the absorber and HPG the most important components of the double effect refrigeration system. In another comparative study between single effect and double effect absorption refrigeration systems with identical cold output was carried out. Results were used to study the influence of the various operating parameters on the performance coefficient, the thermal loads of the components, exergetic efficiency (rational efficiency) and the total change in exergy of the two systems. They concluded that the COP of double effect system was approximately twice the COP of single effect system but the exergetic efficiency of double effect system increased slightly compared to the exergetic efficiency of single effect system. They recorded that for each condenser and evaporator temperature, there was an optimum generator temperature where the total change in exergy of the single effect and double effect absorption refrigeration systems was minimum. At this point the COP and exergetic efficiency of the systems become maximum.

S.C. Kaushiket al [8] (2009) presented the energy and exergy analysis of single effect and series flow double effect water–lithium bromide absorption systems. They developed a computational model for the parametric investigation of the systems. Newly developed computationally efficient property equations of water–lithium bromide solution have been used in the computer code. The analysis involves the determination of effects temperatures and pressure drop on the energetic and exegetic performance of these systems. The performance parameters are computed. The results indicated that coefficient of performance of the single effect system lies in range of 0.6–0.75 and the coefficient of performance for the series flow double effect system lies in the range of 1–1.28. Irreversibility is highest in the absorber in both systems when compared to other system components.

Saeed. Sedigh et al.[9](2011)analyzedthe performancesof

half-effect, single-effect and double-effect H2O/LiBr absorption cycles and it was found that there is an obvious blank for generation temperature between the maximum generation temperature of the single-effect cycle and the minimum generation temperature of the double-effect cycle. It was proposed that the one and a half-effect cycle can fill up the blank perfectly. In this paper, the energy analysis of single effect and half effect water– lithium bromide absorption systems is presented. A computational model has been developed for the parametric investigation of these systems. The effect of various parameters has been presented. It is shown that an increase in the generator temperature increases the COP in both single and half effect systems up to an optimum generator temperature. It is also shown that increasing the absorber temperature reduces the system performance influentially as compared to increasing the condenser temperature.

Gulshan Sachdeva et al [10] (2014) performed the exergy analysis of vapor absorption refrigeration system using LiBr-H2O as working fluid with the modified Gouy-Stodola approach rather than the classical Gouy-Stodola equation. Mathematical expressions for effective temperature had been formulated and calculated for each component of the system. The main aim of this analysis had been to determine the performance of the system and the components having major irreversible loss. Results showed that exergy destruction rate is considerable in absorber and generator followed by evaporator and condenser. The value of exergy determined by the modified Gouy-Stodola equation deviates maximum i.e. 26% in the generator as compared to the exergy calculated by the classical Gouy-Stodola method.

Yu.F. Maydanik [11] (2004) in a review stated that Loop heat pipes (LHPs) are two-phase heat-transfer devices with capillary pumping of a working fluid. They possess all the main advantages of conventional heat pipes, but owing to the original design and special properties of the capillary structure are capable of transferring heat efficiency for distances up to several meters at any orientation in the gravity field, or to several tens of meters in a horizontal position. Besides, the LHP conception allows a wide variety of different design embodiments, which essentially extends the sphere of functional possibilities and practical application of these devices. The paper is a review of developments, results of theoretical analysis and tests of LHPs performed at the Institute of Thermal Physics and some other organizations. It gives examples of successful application of these highly efficient devices in space technology and electronics. Randeep Singh et al [12] (2007) addressed the thermal characteristics of the miniature Loop Heat Pipe (mLHP) with the flat disk shaped evaporator, 10 mm thick and 30 mm in diameter, for the thermal control of the compact electronic equipment. The loop was made of copper with nickel wick and water as the working fluid. It was found that the device was able to start-up at input power as low as 5 W, however the start-up time was very high at such heat loads. During the testing, the thermal response presented by the loop to achieve steady state was very short. Overall, the effect of these oscillations on the thermal performance of the mLHP was not very significant. In the horizontal orientation, the device was able to transfer maximum heat load of 70 W with evaporator temperature below 100 ± 5 ◦C limit. The thermal resistance (RmLHP) of the mLHP lies between 0.17 to 5.66 ◦C/W.

T.X. Li et al [13] (2007) designed an innovative dual-mode multifunction heat pipe type chemisorption ice maker was, in which the compound adsorbent of activated carbon–CaCl2 was used to improve the mass and heat transfer performance of adsorbent. The heating, cooling and heat recovery processes between two adsorbent beds were performed by multifunction heat pipes without additional power consumption. The first operation mode was a highly efficient mass and heat recovery sorption cycle where driving heat source temperature was about 145 °C. The second operation mode was a two-stage heat recovery sorption cycle in which available driving heat source temperature was about 103 °C. The results showed that the first operation mode cycle can increase the coefficient of performance (COP) by 69% when compared with basic cycle. The second operation mode cycle could operate effectively with relatively low-grade generation temperature, and the performance of the two-stage heat recovery cycle was improved by more than 23% when compared with conventional two stage cycle under the same generation temperature of 103 °C and cooling water temperature of 30 °C.

Behrooz M. Ziapour et. al [14] (2010) analysed a diffusion absorption refrigeration heat pipe (DARHP) cycle for an ammonia-water DARHP cycle with helium .In order to obtain characteristics of the DARHP system. The second law efficiency was examined parametrically by the computer simulation. They validated the model by comparing it with previously published experimental data for DARHP system. The cycle performance results under different conditions indicated that the best performance was obtained for the concentration rich solution of 0.35 ammonia mass fraction and the concentration of weak solution about 0.1. It showed that the exergy losses in the evaporator, condenser and dephlegmator were small. Also the second law efficiency increases with increasing evaporator temperature; and decreases with increasing thermosyphon temperature.

Z.S. Lu et al [15] (2011) proposed and investigated a heat pipe type adsorption refrigerator system which can be powered by solar energy or waste heat of engine. They studied the performance of compound adsorbent (CaCl2 and activated carbon)–ammonia adsorption refrigeration cycle with different orifice sets and different mass and heat recovery processes by experimental prototype machine. Specific cooling power (SCP) and coefficient of performance (COP) were calculated with experimental data to analyze the influences of operating condition. The results showed that the jaw opening of the hand needle nozzle can influence the adsorption performance obviously and the thermostatic expansion valve (TEV) is effective in

the intermediate cycle time in the adsorption refrigeration system. The SCP of the cycle with the mass-heat recovery together (combined recovery process) is superior to that of the conventional cycles with mass recovery or heat recovery independently.

Basant K. Agrawal et al [16] (2011), proposed a triple effect refrigeration cycle, a natural refrigerant based N2O compression cycle employed to the combined absorption cycle with an ejector refrigeration cycle. This triple effect cycle combines the advantages of absorption cycle, ejector cycle and low temperature N2O refrigerant based compression cycle. This combined cycle can produce refrigeration output of different magnitude at different temperature simultaneously and can be driven by the waste heat which is available abundantly in different form. System performance and exergy destruction on each component of combined cycle are evaluated based on parametric, energetic and exergetic analysis. The results showed that the waste flue gas temperature, turbine inlet pressure, turbine outlet pressure, ejector evaporator temperature and compressor discharge pressure have significant effects on the refrigeration outputs, exergy efficiency and thermal efficiency.

L. Garousi Farshiet al [17] (2013) compared Ammonia /$LiNO_3$ and ammonia/NaSCN absorption refrigeration cycles as alternatives to ammonia/water cycles for refrigeration applications at temperatures below 0 °C. They are found to have higher coefficient of performance (COP) and purification of the refrigerant vapour is not required. Entropy data for such solutions are calculated using their most recently published thermophysical property data. They used simulation results to examine the influence of various operating parameters on performance and the possibility of crystallization. For low generator temperatures, ammonia/LiNO3 cycles have better performance and at high generator temperatures, ammonia/NaSCN cycles are with better performance, but the range of allowable generator temperatures is quite limited for this mixture

Yuan-Ching Chiang et al. [18](2014)thoroughly investigated the composition factors influencing thermal performance, such as wick structures, working fluids, the modulation fields of working fluids, and combinations of these factors, were. The evaluated materials comprised micro grooved, sintered, and wickless heat pipes; magnetic nano fluids exhibiting volumetric fractions (vol.) of 0.16%e3.20%; and de-ionized water. A strong magnetic field of 200 Oe was applied. The results indicated that combining grooved heat pipes and a 0.80% vol. of magnetic nano fluids or sintered heat pipes and a 0.16%vol. of magnetic nano-fluids yielded the optimal promotions: the thermal resistance was reduced by approximately 80%and the critical heat flux was enhanced 2.7-fold compared with general wickless heat pipes filled with de-ionized water.

T.S. Jadhav et al [19] (2015) in their literature review indicated that very limited information is available on annual energy saving analysis of air conditioning system with HPHX for Indian climatic zones. The possible energy savings using HPHX for heat recovery in air conditioning system for Indian climatic zones was studied. The analysis is carried out for total 25 Indian cities representing different climatic zones. The annual energy savings with HPHX for a particular city is calculated for number of hours when outdoor air dry bulb temperature exceeds 25 °C. The maximum energy saving potential is revealed for hot and dry, warm and humid and composite Indian climatic zones.

Chengchu Yan et al.[20] (2015) presented a seasonal cold storage system that uses separate type heat pipes to charge the cold energy from ambient air in winter automatically, without consuming any energy. The charged cold energy is stored in the form of ice in an insulated tank and is extracted as chilled water for cooling supply in summer, which help to reduce the chiller running time and reduce the associated electricity consumption and greenhouse gas emission significantly. They developed a quasi-steady two-dimensional mathematical model of the system for characterizing the dynamic performance of ice growth. The model was validated using the field measurement data from an ice charging experiment conducted in Beijing.

Fabian Korn et al [21] [2012]performed several vital experiments on heat pipes to establish it to be one of the most effective procedures to transport thermal energy from one point to another, mostly used for cooling. It is based on a combination of conduction and convective heat transfer, what makes it to a complex heat transfer problem. In this report the main working principal and most important possibilities to calculate a heat pipe will be shown. All in all it is necessary to understand all the basic theories of heat and mass transfer to understand the working principle of a heat pipe. On a first look a heat pipe seemed to be a very easy tool to transport energy, but if one looks closer, it is a very complex heat and mass transfer process which takes place in a heat pipe. First of all one has convective heat transfer in the adiabatic transport range, and one has convection through porous materials also. The second major point is mass transfer due to vaporization and condensation, also through porous media. Furthermore there are capillary effects, pressure effects and heat conduction effects involved, which creates a complex structure of heat transfer, where a lot of knowledge is involved. And all of these points can be treated as one problem, from this follows that a complete understanding of all involved processes needs more time and space than it is available for this project report.

R. Rajashree et al.[22] [1990] went through a numerical analysis of an unsteady, viscous, laminar, incompressible, two dimensional heat and mass transfer, in the vapour gas region of gas loaded circular heat pipe . The governing equations of motion were solved using Dufort-Frankel finite difference scheme with appropriate initial and boundary conditions. Successive over relaxation technique has been adopted to solve Poisson equation. The analysis is restricted to the vapour space of the cylindrical heat pipe with evaporator, adiabatic and condenser sections and the

qualitative behaviors of the start-up transient in the vapour gas region has been presented with sodium as vapour for different Reynolds Number. The study demonstrated the qualitative behavior of heat and mass transfer can be studied with the above method with precision.

2. Research gaps identified

Loop heat pipes are being used in Solar Plants, Cooling of Electronic devices, Cooling of Space Shuttles etc. In several researches performed they are being used directly to maintain temperature of several cold storages around the world. It has high heat flux capacity. After reading available research papers following gaps can be identified:

- There are types of VAR systems such as Single Effect, Double Effect, and Triple Effect etc. of which First Law, Second Law and Economic Analysis have been performed. But Heat Pipes can be made an integral part of the system and these valuable analyses can be executed on this new system and results can be studied deeply.
- Waste heat going to the environment from condenser has never been used, which can be supplied back to the generator which requires low grade energy for its operation.
- Also the VAR system can be coupled with other systems may be refrigerating or power generating in which heat is released.
- The Loop Heat Pipes will make the system compact, and that effect must be studied to optimize the performance of the VAR systems.

Studying the literature available on the selected field the main research work has to be done on followings.

1. Intra-cycle heat utilization in the VAR system with help of LHP.
2. Thermodynamic and Thermo-Economic analysis of different types VAR system with LHP for intra-cycle heat transfer e.g. single effect, half effect etc.
3. Study of suitability of Heat Pipes for connecting different heat sources with VAR systems.
4. Study of different fluids in the heat pipe working as a part of the VAR system.

3. Methodology

Compressor in the Vapour Absorption System is replaced by three devices namely Generator, Absorber and Pump and it produces refrigeration using Low Grade energy. In this research it is aimed to remove the condenser also and to use a flow condensation instead. The heat released during the condensation of the rich refrigerant is to be used to evaporate the working fluid in the LHP. The condenser of the LHP will be in contact with the solution leaving the absorber. Thus utilization of the waste heat in the condenser can be done. Other systems can also be connected with each other to have a combined effect. Through the various parametric studies with the help of EES, the optimization of this system can be executed. The primitive system can be explained in the term of the figure.

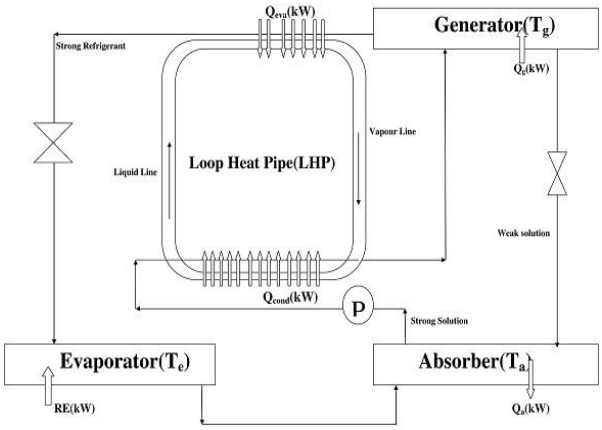


Figure 4: Modified VARS with a LHP

4. Results and Discussions

The VAR system uses low grade energy for its operation, which can be obtained from several cheaply available sources (solar, waste heat etc). The COP is low and irreversibilities related to heat transfer in the cycle are associated. With the use of a Loop Heat Pipe external heat sources can be connected which will increase the COP of the system. For optimizing a VAR system a LHP can be used to utilize the waste heat for intra-cycle heat exchange. Which will eventually increase the First Law COP, Second Law COP and will reduce the irreversibilities connected with the operation of a VAR system. The temperature variation can also be controlled by the use of heat pipe which will result in reduction of energy. The coupling of different cycles will not require complex heat exchangers but Simple LHPs which are available in different heat flux capacities. Thermal modelling of the VAR systems including a LHP for improving of First Law efficiency in terms of COP. And Thermal modelling of the VAR systems including a LHP for improving of Second Law in terms of exergetic efficiency by reducing irreversibilities in the system.

5. Conclusions & Recommendations

The Second Law analysis of the several systems which is possible in order to recover the waste heat is proposed in this paper. During which some combinations of parameter will be varied and following conclusions were made as follows:

1. Intra-Cycle heat exchange in the VAR system reduces heat input thus improved in the thermal performance in terms of first law efficiency (Energy-Efficiency) and second law efficiency (Exergetic efficiency) of the VAR system.

2. Highly effective heat exchange through the heat pipe due to removal of condenser exergetic losses improved second law performances
3. Gas power plant coupled with modified VAR improved first law efficiency(Energy-Efficiency) and second law efficiency(Exergetic efficiency)

References

[1] Da-Wen Sun," Comparison of the performances andNH3-H20, NH3-LiNO3 and NH3-NaSCN Vapor Absorption Refrigeration Systems" Energy Convers. MgmtVol. 39, No. 5/6, pp. 357-368, 1998.

[2] M.M. Talbi, B. Agnew," Exergy analysis: an absorption refrigerator using lithium bromide and water as the working Fuids" Applied Thermal EngineeringVol. 20 (2000) 619-630.

[3] E. Kurem,"A comparison betweenAmmonia-waterand Water-Lithium Bromidesolutionsin vapour absorption heat transformers "In. Comm. Heat Mass Transfer, Vol-28, No-3, pp-421-438 , (2001).

[4] R.D.Misra, P.K. Sahoo, S. Sahoo, A. Gupta,"Thermoeconomic optimization of a single effect water/LiBr vapour absorption refrigeration system" International Journal of Refrigeration Vol.26 (2003) 158–169.

[5] S.A. Adewusi, Syed M. Zubair," Second law based thermodynamic analysis of ammonia–water absorption systems" Energy Conversion and Management Vol. 45 (2004) 2355–2369.

[6] S. Arivazhagan , R. Saravanan , S. Renganarayanan ," Experimental studies on HFC based two-stagehalf effect vapour absorption cooling system" Applied Thermal EngineeringVol. 26 (2006) 1455–1462.

[7] RabahGomri ,RiadHakimi," Second law analysis of double effect vapour absorption cooler system" Energy Conversion and Management Vol.49 (2008) 3343–3348.

[8] S.C. Kaushika, Akhilesh Arora," Energy and exergy analysis of single effect and series flow double effect water–lithium bromide absorption refrigeration systems" internationaljournal of refrigeration Vol.32 (2009) 1247 – 1258.

[9] RabahGomri," Second law comparison of single effect and double effect vapour absorption refrigeration systems" Energy Conversion and Management Vol. 50 (2009) 1279–1287. refrigeration system" Int. J. Energy Res. 2008; Vol.32:161–174.

[10] M. Belghazi, A. Bontemps, C. Marvillet," Experimental study and modelling of heat transfer during condensation of pure fluid and binary mixture on a bundle of horizontal finned tubes" International Journal of Refrigeration Vol.26 (2003) 214–220.

[11] Yu.F. Maydanik," Review Loop heat pipes" Applied Thermal Engineering Vol.25 (2005) 635–657.

[12] Randeep Singh, AliakbarAkbarzadeh ,MasatakaMochizuk," Operational characteristics of a miniature loop heat pipe with flat evaporator" International Journal of Thermal Sciences Vol.47 (2008) 1504–1515.

[13] T.X. Li, R.Z. Wang , L.W. Wang, Z.S. Lu, C.J. Chen," Performance study of a high efficient multifunction heat pipe type adsorption ice making system with novel mass and heat recovery processes" International Journal of Thermal SciencesVol.46 (2007) 1267–1274.

[14] Behrooz M. Ziapour*, Mohsen Tavakoli," Performance study on a diffusion absorption refrigeration heat pipe cycle" International Journal of Thermal Sciences 50 (2011) 592-598.

[15] Z.S. Lu , L.W. Wang, R.Z. Wang," Experimental analysis of an adsorption refrigerator with mass and heat-pipe heat recovery process" Energy Conversion and ManagementVol. 53 (2012) 291–297.

[16] Basant K. Agrawal*, Munawar N. Karimi," Thermodynamic performance assessment of a novel waste heat based triple effect refrigeration cycle" International Journal of RefrigerationVol. 3 5 (2 0 1 2) 1 6 4 7-1 6 5 6.

[17] L. GarousiFarshia,*, C.A. Infante Ferreira b, S.M.S. Mahmoudi a, M.A. Rosen," First and second law analysis of ammonia/salt absorption refrigeration systems" International Journal of Refrigeration Vol. 4 0 (2 0 1 4) 1 1 1-1 2 1.

[18] T.X. Li, R.Z. Wang, L.W. Wang, Z.S. Lu," Experimental investigation of an innovative dual-mode chemisorption refrigeration system based on multifunction heat pipes" International Journal of Refrigeration 3 1 (2 0 0 8) 1 1 0 4 – 1 1 1 2.

[19] T.S. Jadhav , M.M. Lele," Theoretical energy saving analysis of air conditioning system using heat pipe heat exchanger for Indian climatic zones" Engineering Science and Technology, an International JournalVol. 18 (2015) 669-673.

[20] ChengchuYan ,Wenxing Shi , Xianting Li , Shengwei Wang," A seasonal cold storage system based on separate type heat pipe for sustainable building cooling" Renewable Energy Vol.85 (2016) 880-889.

[21] Korn, F., "Heat Pipes and its Applications" Project Report 2008 MVK160 Heat and Mass Transport May 07, 2008, Lund, Sweden.

[22] Rajashree, R., Rao, K.S., "**A** Numerical Study of the Performance of Heat Pipe" Indian Journal of Pure and Applied Mathematics, 21 (1): 95-108, January 1990.

ACS APPLIED MATERIALS & INTERFACES

Subscriber access provided by DELHI TECH UNIV

Article

Microporous Nanocomposite Enabled Microfluidic Biochip for Cardiac Biomarker Detection

Nawab Singh, Md. Azahar Ali, Prabhakar Rai, Ashutosh Sharma, Bansi Dhar Malhotra, and Renu John

ACS Appl. Mater. Interfaces, **Just Accepted Manuscript** • DOI: 10.1021/acsami.7b07590 • Publication Date (Web): 11 Sep 2017

Downloaded from http://pubs.acs.org on September 17, 2017

Just Accepted

"Just Accepted" manuscripts have been peer-reviewed and accepted for publication. They are posted online prior to technical editing, formatting for publication and author proofing. The American Chemical Society provides "Just Accepted" as a free service to the research community to expedite the dissemination of scientific material as soon as possible after acceptance. "Just Accepted" manuscripts appear in full in PDF format accompanied by an HTML abstract. "Just Accepted" manuscripts have been fully peer reviewed, but should not be considered the official version of record. They are accessible to all readers and citable by the Digital Object Identifier (DOI®). "Just Accepted" is an optional service offered to authors. Therefore, the "Just Accepted" Web site may not include all articles that will be published in the journal. After a manuscript is technically edited and formatted, it will be removed from the "Just Accepted" Web site and published as an ASAP article. Note that technical editing may introduce minor changes to the manuscript text and/or graphics which could affect content, and all legal disclaimers and ethical guidelines that apply to the journal pertain. ACS cannot be held responsible for errors or consequences arising from the use of information contained in these "Just Accepted" manuscripts.

ACS Publications

ACS Applied Materials & Interfaces is published by the American Chemical Society.
1155 Sixteenth Street N.W., Washington, DC 20036

Published by American Chemical Society. Copyright © American Chemical Society. However, no copyright claim is made to original U.S. Government works, or works produced by employees of any Commonwealth realm Crown government in the course of their duties.

Microporous Nanocomposite Enabled Microfluidic Biochip for Cardiac Biomarker Detection

Nawab Singh[a], Md. Azahar Ali[b], Prabhakar Rai[c], Ashutosh Sharma[c], B. D. Malhotra[d]*, and Renu John[a]*

[a]Department of Biomedical Engineering, Indian Institute of Technology Hyderabad Kandi, Sangareddy-502285 Telangana, India.
[b]Department of Electrical and Computer Engineering, Iowa State University, Ames, Iowa-50011, USA.
[c]Department of Chemical Engineering, Indian Institute of Technology Kanpur, Kanpur, 208016, India.
[d]Department of Biotechnology, Delhi Technological University, Shahbad Daulatpur, Main Bawana Road, Delhi-110042, India.

ABSTRACT

This paper demonstrates an ultrasensitive microfluidic biochip nanoengineered with microporous manganese-reduced graphene oxide nanocomposite for detection of cardiac biomarker, namely human cardiac troponin I. In this device, the troponin sensitive microfluidic electrode consisted of a thin layer of manganese-reduced graphene oxide (Mn_3O_4-RGO) nanocomposite material. This nanocomposite thin layer was formed on surface of a patterned indium tin oxide (ITO) substrate after modification with 3-aminopropyletriethoxysilane (APTES) and was assembled with a polydimethylsiloxane-based microfluidic system. The nanoengineered microelectrode was functionalized with antibodies specific to cardiac troponin I. The uniformly distributed flower-shaped nanostructured manganese oxide (nMn_3O_4) onto RGO nanosheets offered large surface area for enhanced loading of antibody molecules and improved electrochemical reaction at the sensor surface. This microfluidic device showed an excellent sensitivity of log [87.58] kΩ/(ng mL^{-1})/cm^2 for quantification of human cardiac troponin I (cTnI) molecules in a wide detection range of 0.008–20 ng/mL. This device was found to have high stability, high reproducibility and minimal interference with other biomarkers cardiac troponin C and T, myoglobin and B-type natriuretic peptide. These advantageous features of the Mn_3O_4-RGO nanocomposite, in conjunction with microfluidic integration, enabled a promising microfluidic biochip platform for point-of-care detection of cardiac troponin.

Keywords: Microporous nanocomposite; Nanostructured Mn_3O_4; RGO Nanosheets; Microfluidic Biochip; Cardiac Biomarker; Troponin I; Electrochemical impedance spectroscopy

***Corresponding Authors:** renujohn@iith.ac.in*, Ph: +91-40-23016097, bansi.malhotra@gmail.com*

1. INTRODUCTION

Coronary heart diseases resulting from the blockage of the heart arteries are major cause of causalities worldwide. Complications such as angina pectoris, acute myocardial infarction (AMI) or a total heart failure results from interruption in blood supply to the heart muscles. Cardiac troponins have been known to be tissue-specific biomarkers that are expressed in heart muscle during above said episodes and hence play an important role towards the management of acute coronary syndromes. There are three main isoforms of cardiac troponins (cTnC, cTnT and cTnI) in blood circulation that are known to indicate the onset of AMI. According to the American College of Cardiology and European Society of Cardiology, the cardiac troponin is central to the definition of AMI. Cardiac troponins are considered as biomarkers of choice for detection of cardiac cellular injury and may show high selectivity and sensitivity for the myocardial damage. In particular, cardiac troponin I (cTnI) is a normal protein released from myocytes when myocardium injury take place and is extremely specific to cardiac tissue and precisely diagnoses myocardial infarction[1–3]. Therefore, the quantification of cTnI has high demand for development of reliable, easy-to-use and low cost point-of-care (POC) devices to meet the unmet challenges in cardiovascular disease (CVD) management[4,5]. For example, enzyme-linked immunosorbent assays, radio immunoassays and chemiluminescent immunoassays are the conventional techniques, that can be employed for detection of cTns[6,7]. The issues with these techniques relate to the sensitivity, several steps for processing of samples, time consumption and the high test cost. Poor sensitivities of the assay-based techniques results in false negative due to the low serum concentrations of cTns at the early onset of ischemia.[4,5] Better accuracy, high sensitivity, and selectivity are some of the advantages of nano-scale biosensors based on composite materials for improving detection capabilities of biomoleucles compared to traditional technologies.

Microfluidic biosensors offer several benefits such as portability, low consumption of reagents, high sensitivity, fast response, and massive parallelization[8,9]. Significant efforts have been made for the integration of composite nanomaterials with the microfluidic POC biosensors. Incorporation of functional nanocomposites into microfluidic biosensors has led to increased surface area and high characteristic ratio of the devices. Nanotubes of titanium dioxide[4], zinc oxide nanowires for environmental pH conditions and carbon nanotubes (CNTs) for detection of dopamine and catechol can be integrated into microfluidic sensing platforms to obtain enhanced electrochemical reactivity and bio/chemical sensing capabilities resulting in higher sensitivity, fast response time and stability[10,11]. A high sensing performance bio-interface developed using graphene foam-titanium nitride integrated microfluidic structures and exploited to construct soil nutrient sensors was found to result in improved loading capacity of the bio-receptor resulting in high

sensitivity[12]. In spite of these interesting developments, it is challenging to integrate nanocomposites into microfluidic channels and even create bio-interface platforms by immobilizing specific biomolecules.

The enhanced surface area of the reduced graphene oxide (RGO) and the presence of functional groups on its surface can be convenient for increased loading of the organic and biomolecules[13,14]. In RGO, some of the remaining oxygen bonded using about 25% sp^3 hybridized carbon atoms may facilitate covalent coupling with biological molecule[15–18]. Reduced graphene oxide (RGO) sheets is associated with the surface and electrical properties such as surface adsorption, electrochemical reactivity and motion of electrons due to enhanced sp^2 segment that may yield improved reaction time and sensitivity of a biosensor[16–18]. The RGO can thus be employed for development of electrochemical biosensors to monitor glucose[19], hydrogen peroxide[20] and other chem/bio species. However, the functional groups are known to be responsible for biomolecules conjugation on the RGO surface, the electrical conductivity has been found to be play an important role to obtain efficient biosensors[21]. In this context, RGO may perhaps be decorated by nanostructured metal oxides to improve the electrochemical reactivity[22–25] and this nanocomposite structure may offer greater electrical conductivity, and electro-catalytic activity of RGO[22,26–28]. Ali et al. fabricated a mesoporous graphene and nickel oxide nanocomposite platform for affinity biosensing application[15]. Besides this, CuO-graphene, TiO_2-graphene was used for biosensing[29–31].

Many metal oxides such as RuO_2, Co_3O_4, NiO, IrO_2, Mn_3O_4, etc. have been used for electrochemical biosensing applications. Among them, Mn_3O_4 is an interesting biosensing transducer material owing to its excellent electrochemical properties, high carrier mobility, good electrochemical catalytic activity, chemical stability and good biocompatibility and can reduce agglomeration of RGO nanosheets. Nanostructured manganese oxide (nMn_3O_4) in different shapes (hollow spheres, nanorods and nanoparticles) were recently employed for electrochemical biosensing and energy storage[32–35]. The nanostructured 3D flower-shaped Mn_3O_4 has been reported to be an interesting material due to its biocompatibility[32,33]. Incorporation of nMn_3O_4 using RGO sheets may perhaps offer improved bio-interface for increased conveyor transport. In addition, microporous characteristics of nMn_3O_4 deposited onto RGO sheets may allow larger pore size to hold increased number of antibody molecules on its surface resulting in enhanced limit-of-detection, higher sensitivity and stability. Also the nMn_3O_4-RGO composite may provide increased mobility for improved biomolecules sensing[36]. With these functional properties combined with its microporous feature, nMn_3O_4-RGO nanocomposite material should be an interesting candidate for integration with microfluidic POC biosensor to monitor cTnI in human serum samples.

We explored the possibility of developing a microfluidic POC biosensor chip for immunodiagnosis of cardiac troponin I biomarker via electrochemical impedance technique. We fabricated a unique immunoelectrode-based sensor consisting of a microporous nMn_3O_4-RGO composite structure modified with 3-aminopropyl-triethoxysilane (APTES) and specific antibodies of cTnI (anti-cTnI). This cTnI sensitive electrode acted as a working electrode of the microfluidic device and the other two electrodes acted as reference and counter electrodes (Figure 1). The characteristics of this sensor such as sensitivity, detection range, reproducibility, and operational stability were determined.

2. EXPERIMENTAL SECTION

2.1 Chemical and Reagents: The SU8-2050 negative and Shipley 1818 positive photoresists for polydimethylsiloxane (PDMS) microchannels and ITO electrode fabrication, respectively, were procured from Microchem (Newton, MA). Graphite powder flakes (45 µm, >99.99, wt%), manganese chloride, sodium hydroxide, cetyltrimethylammonium bromide (CTAB), 1-hydroxy-2,5-pyrrolidinedione (NHS), and 1-(3-(dimethyl amino)-propyl)-3-ethylcarbodiimide hydrochloride (EDC) were procured from Merck, USA. 3-Aminopropyltriethoxysilane (APTES) was purchased from Alfa-aesar-Thermo Fisher Scientific. Antibodies of cardiac troponin I (Ab) mouse monoclonal and human cardiac troponin I (cTnI) protein were purchased from abcam USA. The phosphate buffer saline (PBS) pH 7.4 was utilized for the various studies conducted using this sensor.

2.2 Synthesis of Nanostructured Mn_3O_4: Flower-shaped Mn_3O_4 nanostructures were synthesized following previously reported method[32,37]. 0.8 M of manganese chloride tetrahydrate ($MnCl_2.4H_2O$) was dissolved in 200 mL ethanol and stirred after which 0.5 mM cetyltrimethylammonium bromide (CTAB) was added in strong stirring until it dissolved completely. After that, the mixture contained in a 250 mL flask was heated at 90 ^oC for 24 h. Afterwards, the solution was cooled at 25 ^oC, and 0.3 M of sodium hydroxide (NaOH) was added to the solution at 800 rpm, and 10 mL 30% H_2O_2 was slowly added drop wise. Later, the solution was kept for 24 h to obtain the precipitate. After separation, the precipitate was washed with deionized water and ethanol for 5 times, and dried at 90 °C for 24 h under vacuum. After that the precipitate was placed into a muffle furnace at 350 ^oC around 5 h with increasing temperature speed at a rate of 15 $^oC\ min^{-1}$ in air resulting in the formation of nanostructured Mn_3O_4.

A sequence of experiments was carried out to study the effect of reaction time and temperature on the morphological structure of Mn_3O_4. The effect of the reaction temperature on the hydrothermal reaction was examined wherein at a lower temperature (60 ^oC), the amorphous Mn_3O_4 was formed. With a temperature of 75^oC, the Mn_3O_4 nanosheets started to form flower-like

structures. At a temperature of 90 ^{o}C and with reaction time of 12 h, three-dimensional (3D) structured Mn_3O_4 was formed. This result showed that the reaction temperature and the reaction time have significant effect on the structure formation of Mn_3O_4 material.

2.3 Synthesis of RGO: Graphene oxide (GO) was synthesized using improved modified Hummer's method[38,39] with a small modification. Briefly, we took 2.5 g of graphite powder by using a combination of 50 mL of 98% H_2SO_4, 6 g $K_2S_2O_8$ and 6 g of P_2O_5 for 5 h at 85 ^{o}C. The resulting suspension, after washing with deionized water for seven times was dried under vacuum at 60 ^{o}C. A mixture of H_2SO_4:H_3PO_4 (130:13) was used for oxidation of the graphite by continuous stirring. After 15 min, 10 g of $KMnO_4$ was included in the mixture under vigorous stirring for 18 h at 55 ^{o}C. After 18 h the reaction was stopped and cooled at 25 ^{o}C after which 250 mL of ice was added into the mixture followed by 2 mL of H_2O_2 (30%) and filtered by porous mesh. Then, the filtrate was placed in centrifuge at 6000 rpm around 2 h and the residue was washed many times using deionized water, 30% hydrochloric acid and ethyl alcohol followed by centrifugation separation. The last residue was suspended in 150 mL of ether and filtered by 0.45 µm pore size polytetrafluoroethylene (PTFE) membrane. The obtained semi-solid material was dried out under vacuum for 12 h to obtain GO powder.

The reduction of GO was accomplished with a slight modification[40]. Some drops of 10% NaOH were added to well-dispersed GO in deionized water to make basic condition wherein the pH of the solution was raised to 10.0. Basic pH helped to increase the stability of colloidal solution of GO by electrostatic repulsion. 1.0 g of sodium borohydride ($NaBH_4$) was directly added to 300 mL of GO suspended solution (2 mg mL^{-1}) with magnetic mixer, and the mixture was retained at 80 ^{o}C for 80 min by continuous stirring. The solution turned to black from brown and was washed with ethyl alcohol. The washed solution centrifuged at 6000 rpm for 10 min was re-dispersed in H_2SO_4 at 170 ^{o}C for 4 h. This solution was filtered again through Durapore membrane (0.22 µm) to produce reduced graphene oxide (RGO) and dried at 90 ^{o}C for 4 h under vacuum. This RGO had a significant volume of carboxylic groups that could be utilized for immobilization of biomolecules.

2.4 Nanocomposite Formation: Nanocomposite of manganese and reduced graphene oxide (Mn_3O_4-RGO) was synthesized *via* low temperature hydrothermal process. Effectively-dispersed colloidal suspension of Mn_3O_4 (0.8 mg/mL) and RGO (0.2 mg/mL) was prepared separately in isopropanol solution at constant stirring (800 rpm) for 12h followed by ultrasonication for about 6h. Then, mixture of both colloidal suspensions was stirred at 500 rpm by addition of a few drops of ethanol amine, and NaOH, and kept overnight at 60 ^{o}C. This solution was transferred to teflon vessel containing hydrothermal pressure tank and was kept for 160 ^{o}C for 12h. The resulting product was

cooled and centrifuged at 10000 rpm for 30 min followed by washing with DI water. In this protocol, the positively charged nMn_3O_4 was attached to oppositely charged RGO sheets *through* electrostatic interactions. We examined zeta potential of the nMn_3O_4, RGO and nMn_3O_4-RGO composite, respectively. The value of zeta potential was found to be positively charged (+27.24 mV) for nMn_3O_4 (Figure S1 a). For RGO we observed negatively charged zeta potential (−37.20 mV) which provided sturdy electrostatic interfaces with nMn_3O_4 (Figure S1, b). The increased zeta potential to −55.38 mV in case of the nMn_3O_4-RGO composite (Figure S1, c) revealing the formation of highly stable composite material. After this, 3-aminopropyletriethoxysilane (APTES) was used for the functionalization of synthesised nMn_3O_4-RGO nanocomposite. Subsequently a solution of nMn_3O_4-RGO composite prepared in 100 mL of isopropanol was maintained at 60˚C with constant stirring. After dispersion of the nanocomposite, 1000 µL of 98% APTES was added and further stirred at 400 rpm for 48h at 27 ^{o}C in a closed vessel. The final product was washed with DI water, dried at 60 ˚C and stored in dry place.

2.5 Microfluidic Device Fabrication: The microfluidic channel was fabricated using photolithography for detection of cTnI. The fabrication steps included pattering of indium tin oxide (ITO) on glass, selective deposition of nMn_3O_4-RGO composite for antibody immobilization, and assembly of PDMS microfluidic channels.

First, the ITO coated glass substrate properly cleaned through bath sonication with methanol and acetone was used to fabricate patterned microelectrode of size of 3mm × 3mm using photolithographic technique followed chemical etching. For this purpose, a small amount of positive photoresist (Shipley 1818) was coated onto ITO using spin coating at 3000 rpm for 30 s. The photoresist/ITO was soft baked onto hot plate at 115 ^{o}C for 60 s for evaporating off the solvent. This photosensitive substrate was exposed to UV radiation with an intensity of 25 mW/cm^2 for 3 min through an optical mask. The substrate was then immersed in a solution for 2 min. Further, the developed substrate was dipped into the benzene and shacked vigorously and baked at 120 ^{o}C for 5 min. Following this, selective etching of the exposed ITO regions were carried out by immersing the substrate into ITO etchant solution (15% HCL solution+ zinc dust). Finally, the unexposed photoresist remains on ITO substrate was washed away with acetone. The patterned ITO electrodes were then hydrolysed by a mixture of H_2O_2:NH_3:H_20 (1:1:5) solution at 75 °C for 1 h. The fabrication steps for ITO microelectrodes are shown in Scheme S1.

The dispersed gel-like solution of APTES-nMn_3O_4-RGO was uniformly deposited onto the fabricated hydrolysed ITO electrode via dip coating technique and kept in closed chamber for 12 h at 27 ^{o}C, followed by washing with DI water. Silane groups of APTES are known to have a strong affinity

to interact with hydroxylated ITO (IT–O–H) to create IT–O–Si bond on the surface of electrode. For reference electrode we used Ag/AgCl electrode. In this step, Ag layer of 500 nm-thickness was deposited onto the fabricated ITO electrode by direct current (DC) magnetron sputter coater. The Ag electrodes were treated with 0.2 M KCl for 90 s to form the Ag/AgCl reference electrode while bare ITO worked as the counter electrode.

The polydimethylsiloxane (PDMS) microchannels were fabricated using soft lithography technique. For this purpose, SU-8 negative photoresist was spin coated (~200 µm thick) on a pre-cleaned glass substrate. The glass substrate was then heated on a hot plate at 95 ^{o}C for 30 min to evaporate solvent and exposed to UV rays through an optical mask. And this was heated again for 10 min (post exposure bake) at 100 ^{o}C. The unexposed part was removed via developer solution in order to form the master. The developed master was washed for approximately 20 s using isopropyl alcohol and dried using nitrogen. A mixture of pre-polymer and silicon elastomer (Sylgard 184, Dow Corning, curing agent of PDMS) in a volume ratio of 10:1, was transferred on top of the master, degassed in vacuum and preserved at 80 ^{o}C for around 60 min. The PDMS slab was first peeled off from the master. Both the height and width of the microchannel were 200 µm. A 1 mm radius of circle was designed in the middle which linked to the inlet and outlet of device via microchannel. The inlet and outlet were made by holes punching machine. The step-wise demonstration for microchannel fabrication was shown in Scheme S2.

The patterned APTES-nMn_3O_4-RGO electrode on ITO glass was dried at 37 °C for about 2 h and sealed with PDMS microchannel via oxygen plasma treatment. Prior to Ab immobilization, the APTES-nMn_3O_4-RGO/ITO surface was treated with EDC and NHS solution to activate the functional groups at APTES-nMn_3O_4-RGO. Then, 15 µL of Ab solution was injected into device via syringe pump. The carboxylic (−COOH) groups at edges of RGO sheets in APTES-nMn_3O_4-RGO composite reacted with −NH_2 groups of the antibody (Ab) via amid bond formation. It is found that the –COOH groups were more reactive than hydroxyl groups (–OH) and –O– provided the nucleophilic substitution reaction with −NH_2 groups of the Ab. Also, the surface of RGO was covered with nMn_3O_4 to form Mn_3O_4-RGO nanocomposite and the silane moieties were attached onto nMn_3O_4-RGO composite after 3-aminopropyletriethoxysilane (APTES) functionalization. Thus, the –OH and –O– groups on RGO surface could not perhaps react with −NH_2 groups of the antibodies (Ab). The antibody molecules formed the strong covalent (C−N) bond between −COOH group of APTES-nMn_3O_4-RGO and −NH_2 group of Ab. BSA molecules were used to block the non-specific sites of Ab functionalized APTES-nMn_3O_4-RGO surface. The flow rate (10 µL/min) was controlled by a syringe pump to transport PBS and cTnI solution through this chip. The fabricated microfluidic device was placed in a storage at 4 ^{o}C .

2.6 Instrumentation: The synthesized nMn_3O_4, RGO, nMn_3O_4-RGO nanocomposite and functionalized APTES-nMn_3O_4-RGO were characterized using transmission electron microscopy (TEM, FEI Titan G2 60-300), field emission-scanning electron microscopy (FE-SEM, ZEISS Supra 40VP Germany) with EDX mapping, Brunauer–Emmett–Teller analysis (BET, AUTOSORB-iQ-XR-2), X-ray diffraction (XRD, Rikagu) and Raman spectroscopy. We used Fourier transform infrared spectrometer (FT-IR, PerkinElmer, model 2000) to investigate the protein (Ab) functionalization on the APTES-nMn_3O_4-RGO film. The electrochemical measurements on this microfluidic chip for cTnI detection were conducted using an Autolab Potentiostat/Galvanostat (Model AUT-86000) in presence of 50 mM phosphate buffer saline (pH 7.4) having 5 mM potassium ferro-ferricyanide solution.

3. RESULTS AND DISCUSSION

3.1 X-Ray Diffraction Analyses: The results of XRD analysis (Figure 2a) confirmed the crystalline behaviour of Mn_3O_4, RGO, and Mn_3O_4-RGO. The x-ray diffraction peaks for Mn_3O_4 were found at 2θ = 28.77, 32.20, 36.08, 44.23, 50.77, 58.37, 60.0, and 64.46 pertaining to (112), (103), (211), (220), (105), (321), (224), and (400) reflection planes, respectively, that corresponded to the tetragonal spinel structure of Mn_3O_4 (JCPDS file,24-0734). The mean crystal size of nMn_3O_4 was found to be as ~25 nm for (211) plane.[32]. A wide peak was obtained at 2θ site of 25.8° for (002) mirror image plane of RGO due to its graphitic nature [Figure 2a]. About ~0.97 nm interlayer spaces of RGO was calculated by full width at half maximum (FWHM=16.1°) for (002) plane by Eq.1

$$d_{002}=\frac{0.9\lambda}{\beta_{002}\cos\theta_{002}} \quad (1)$$

where d_{002} is the distance between two sheets and β_{002} is the FWHM. For nMn_3O_4-RGO, the various crystallographic planes such as (002), (112), (103), (211) and (224) confirmed the formation of nMn_3O_4-RGO composite.

3.2 Raman Spectroscopic Analyses: The Raman analysis were accompanied for nMn_3O_4, nMn_3O_4-RGO composite with and without modification of APTES [Figure 2b]. The peak found at 644 cm^{-1} of nMn_3O_4 was assigned in the direction of A_{1g} mode corresponding to the Mn–O vibration of Mn^{2+} ions in a tetrahedral coordination. With tetragonal Hausmannite structure, the spectra for nMn_3O_4 indicated the existence of other two minor peaks at 497, and 348 cm^{-1} [41]. In nMn_3O_4-RGO spectra, two peaks found at 1368 cm^{-1} and 1583 cm^{-1} were owing to D and G bands, respectively. The band 1368 cm^{-1} was related with deformation and imperfection in the graphite layers pertained to the sp^3 bond in RGO whereas 1583 cm^{-1} represented the in-plane vibration of sp^2-hybridized C=C bond arising owing to E_{2g} phonons[23,42]. The intensity ratio (I_D/I_G) of the nMn_3O_4-RGO composite (0.94)

offered a complex unit of the distortions and crystallite size of the graphite layers. The average crystallite size is determined to be 22.24 nm of nMn_3O_4-RGO composite using Eq.2.

$$La(nm) = (2.4 \times 10^{-10})\lambda_1^4 \left(\frac{I_D}{I_G}\right)^{-1} \quad (2)$$

Where I_D and I_G are the peak intensities whereas λ_l is the wavelength of laser in nm,[36]. The peak 1583 cm^{-1} in spectra be able to interconnected with the RGO layers using the relation[43]

$$\omega G = 1581.6 + 11/(1 + n^{1.6}) \quad (3)$$

Where, n represents the layers in the material and ω_G represent the position of peak in wavenumber. The prepared RGO had about three layers. In addition, the decrease in the peak intensity indicated functionalization of APTES-nMn_3O_4-RGO. Also, the band present at 1077 cm^{-1} is consistent with the Si–O–C band revealing the presence of APTES in the APTES-nMn_3O_4-RGO sample[44].

3.3 Fourier transform infrared (FTIR) Analyses: The FTIR was conducted to prove the conjugation of protein on the electrode surface (Figure 2c). The absorption peaks were observed in the 500–650 cm^{-1} range. The 628 cm^{-1} absorption band was due to Mn–O stretching in tetrahedral site of Mn_3O_4, the band seen at 526 cm^{-1} was ascribed to Mn–O vibration in octahedral site[32]. For nMn_3O_4-RGO, the absorption peaks found at 1028, 1250–1402, 1450–1641 and 1745 cm^{-1} pertained to the =C–H bending, –C–H bending, aromatic C=C stretching and C=O stretching at RGO, respectively. The peaks at 2861 and 2929 cm^{-1} were due to $–CH_2$ stretching and the obtained at 3446 cm^{-1} was allocated to O–H vibration. The bands at 807 and 1098 cm^{-1} were perhaps responsible for C–O–C vibration of epoxy groups at nMn_3O_4-RGO[45]. For APTES-nMn_3O_4-RGO, the peaks at 2851 cm^{-1} and 2916 cm^{-1} related to symmetric v_sCH_2 and asymmetric $v_{as}CH_2$ of the alkyl chains of the silane moieties of APTES. The peaks seen at 1038 and 1129 cm^{-1} can be due to vSi–O–C and vSi–O–Si revealed successful APTES functionalization of nMn_3O_4-RGO composite. Thus, the silane moieties were grafted onto nMn_3O_4-RGO composite *via* the SN^2 nucleophilic substitution by reacting epoxy groups of RGO and amino moieties of APTES[45–47]. The peaks found at 1268 and 1377 cm^{-1} were owing to C–N (amine) vibration but the found peaks at 1572 and 1646 cm^{-1} were owing to N–H bending and C=O stretching vibration, respectively, confirming the formation of amide bond between the antibody and APTES-Mn_3O_4-RGO.

3.4 X-ray photoelectron spectroscopy analyses: The X-ray photoelectron spectroscopy (XPS) studies were conducted onto APTES-nMn_3O_4-RGO. Figure 3a shows various peaks in its wide scan spectra due to existence of trace elements C, O, N, Si and Mn that are available in APTES-nMn_3O_4-RGO composite. Figure 3b shows peaks at 652.9 and 641.4 eV due to the Mn $2p_{1/2}$ and Mn $2p_{3/2}$ spin-orbit

states confirming the presence of Mn^{4+} species in APTES-nMn_3O_4-RGO. Figure S7 (a) exhibited Mn 2p spectrum for Mn_3O_4 film whereas the peaks for Mn $2p_{1/2}$ and Mn $2p_{3/2}$ states were found at the binding energies of 640 eV and 645 eV with energy separation of 5 eV. However, after the nanocomposite formation with APTES and RGO, this energy was shifted to 6.5 eV. Figure 3c shows the deconvoluted C 1s spectra of APTES-nMn_3O_4-RGO nanocomposite. The peaks found at binding energies of 284.3, 285.2, and 286.6 eV were assigned to C–C bonds (graphitic carbon) and C–O (epoxy and alkoxy) groups, respectively, of RGO in nanocomposite. Other peaks at 287.8 and 298.1 eV attributed to C=O, and O–C=O, respectively indicating the presence of RGO in nanocomposite. It appeared that O–C=O groups mainly interacted with $–NH_2$ groups of antibodies for immobilization via amidation reaction. Figure S7 (b) shows the O 1s spectra for Mn_3O_4 film and appeared XPS peak at 530.5, 532 and 533.2 eV due to formation of Mn−O−C, Mn−O−Mn and Mn−OH, respectively. On incorporation of RGO in nanocomposite, an additional peak at a binding energy of 529 eV and other peaks observed in case of Mn_3O_4 film were found to slightly shift to higher energies (Figure 3d). For N 1s spectra of APTES-nMn_3O_4-RGO nanocomposite (Figure 3e) displays two distinct peaks at 398.5 and 400.4 eV due to neutral nitrogen amino groups ($-NH_2$) and $-NH_3^+$ ions in APTES of synthesized nanocomposite. Si 2p spectrum of nanocomposite film further confirmed the existence of APTES. Figure 3f shows resolution peaks found in Si 2p spectrum for nanocomposite wherein peaks at 101.4 and 103.6 eV were due to existence of $(Si–O)_1$ and $(Si–O)_4$ saline groups of APTES which helped to bind with hydroxylated ITO by forming IT−O−Si bond.

3.5 UV-visible Spectroscopic Analyses: The UV-visible studies were carried out, on the RGO, nMn_3O_4 and nMn_3O_4-RGO nanocomposite (Figure S2, Supporting Information). The absorption spectra of nMn_3O_4 showed two distinct regions (270 to 400 nm and 400 to 530 nm region) (S2, a). The first region was due to the allowed $O^{2-} \rightarrow Mn^{2+}$ and $O^{2-} \rightarrow Mn^{3+}$ ligand to metal charge transfer transition, and the second region was attributed to d–d crystal field transition[35]. The absorption found at 271 nm was because of unsaturated carbon chain of RGO (S2, b)[39]. The spectra of the nMn_3O_4-RGO composite (S2, c) showed two peaks at 294 and 260 nm wherein the absorption peak at 320 nm was shifted to 294 nm due to the attachment of nMn_3O_4 on the surface of RGG sheets. The peak shift from 271 to 260 nm indicated the formation of nMn_3O_4-RGO composite resulting in excellent electron transfer and increased transition energy[15,48].

3.6 Brunauer–Emmett–Teller Analyses: To quantify the specific surface area and the porosity for nMn_3O_4-RGO and APTES-nMn_3O_4-RGO matrix, the Brunauer–Emmett–Teller (BET) studies were conducted. The adsorption and desorption isotherms were observed for nMn_3O_4-RGO and APTES-nMn_3O_4-RGO (Figure 4a and 4b). The nMn_3O_4-RGO composite showed a specific surface area of 90.385 m^2/g. The results of BET studies revealed the total pore volume of micropores about 0.750

cc/g. The pore size distribution curve (Figure 4a) indicated that the nMn_3O_4-RGO was dominated by micropores with a minor fraction of mesopores. The mean pore diameter was found to be 1.96 nm for nMn_3O_4-RGO. After modification of nMn_3O_4-RGO with APTES, the specific surface area was found to be 40.088 m^2/g. The BET analysis for APTES-nMn_3O_4-RGO showed a total pore volume of micropores about 0.317 cc/g, dominated with micropores and a minor fraction of mesopores. The mean pore diameter of APTES-nMn_3O_4-RGO (Figure 4b) was about 1.95 nm which was less than the nMn_3O_4-RGO (1.96 nm). The highly microporous structure and pore size helped towards effective attachment of the antibodies on to the microfluidic sensor electrode surface.

3.7 Microscopic Analyses: To characterize the structure and size of the nMn_3O_4, RGO sheets, and their composites, we carried out TEM. Hexagonal shaped nMn_3O_4 had a uniform sized distribution of 20–26 nm with fine granules (Figure 5a-b). Figure 5(c) shows a high magnification image and the inset shows an electron diffraction pattern of nMn_3O_4 with two diffraction rings of different radii corresponding to (211) and (103) planes. Atomic scale image of nMn_3O_4 shows clear lattice fringes assigned to (211) and (103) reflection planes with an interplanar spacing of 0.248 and 0.276 nm, respectively. Thus, the anisotropic growth of the nMn_3O_4 was mostly along the (211) and (103) directions. The dense network of RGO nanosheets and twisted into wrapped wrinkles, and also compact and tinny layers of RGO nanosheets were shown in Figure 5(d-e). Edges and basal planes of RGO sheets (Figure 5d) were perhaps due to the interaction of oxygen (O−) containing bonds between the adjacent layers. SAED pattern of RGO (inset of Figure 5e) shows two (002) and (004) reflection planes indicating high crystallinity that was consistent with the results of XRD studies. The homogeneous nMn_3O_4 could be selectively deposited on the surface of a RGO nanosheets as depicted in Figure 5(f-g). Oxygen (O^-) containing hydroxyl, epoxy functional groups and wrapped wrinkles RGO structure played a significant role in the integration of nMn_3O_4 on the surface of RGO[35]. Figure 5(h) shows lattice fringes of the nMn_3O_4-RGO composite and its mapping of layer distributions. With APTES functionalization, the nMn_3O_4 on RGO sheets perhaps agglomerated Figure (5i).

The morphological shape of nanostructures Mn_3O_4 and RGO sheets, and their composites with biomolecules were investigated (Figure 6) using FE-SEM. Figure 6(a, b, c and d) exhibits FE-SEM images of as-prepared Mn_3O_4 under different hydrothermal reaction conditions such as 60 ^oC, 24 h (a), 75 ^oC, 24 h (b), 90 ^oC, 12 h (c) and 90 ^oC, 24 h (d). With high temperature treatment, the Mn_3O_4 appeared to become spherical, flower-shaped and somewhat elongated (Figure 6d). At high magnification, the spherical particles showed 3D flower-shaped structure of 2D Mn_3O_4 with globular nanosphere morphology (Figure 6e, f). The multilayer RGO sheets were found to be folded, wrinkled and agglomerated (Figure 6g, h). The RGO sheets stacked to form thicker sheets due to π-π

interfaces between the separate sheets through adjacent dimensions varying from nano to micrometers. Figure 6(i, j) showed uniform distribution of the flower-shaped Mn_3O_4 nanosphere on RGO sheets. The RGO sheets wrapped by flower-shaped Mn_3O_4 nanospheres were perhaps oppositely charged such as was apparent from the zeta potential studies (Figure S1) resulting in highly stable microporous composite. After APTES functionalization, a morphological change was observed due to the displacement of epoxy (C–O–C) groups of RGO via $–NH_2$ groups of APTES. As a result of nanocomposite structure, aggregation of nMn_3O_4-RGO with APTES chain was visible (Figure 6k). Immobilization of anti-cardiac troponin I antibody (Ab) on APTES-nMn_3O_4-RGO surface (Figure 6l) resulted in uniform distribution of Ab due to the formation of amide bond as was evident by FT-IR studies (Figure 2c).

The elemental content of nMn_3O_4, RGO, and nMn_3O_4-RGO, APTES-nMn_3O_4-RGO were confirmed by energy-dispersive X-ray (EDX) analysis and EDX mapping (Figure S3, S4, S5 and S6). The quantitative results of EDX analysis provided the existence of Mn and O elements in nMn_3O_4 film (Figure S3). The weight and atomic % of Mn and O were found to be about 73.40%, 26.60% and 44.56%, 55.44%, respectively, inset of (Figure S3, c). The EDX mapping confirmed the presence of Mn (a) and oxygen elements (b) in nMn_3O_4 film. In RGO, the weight and atomic percentage of C and O were found to be as 73.51%, 26.49% and 78.71%, 21.29%, respectively, inset of (Figure S4, c). The EDX mapping confirmed the presence of C (Figure S4, a) and O elements (b) in RGO. The nMn_3O_4-RGO composite film showed additional peaks for C element due to presence of carbon chain and organic groups. The weight and atomic % of Mn, O and C in nMn_3O_4-RGO film were obtained as 39.43%, 25.85%, and 34.72% and 18.74%, 30.93%, and 50.33%, respectively, inset of (Figure S5, d). Also, EDX mapping revealed the presence of C (Figure S5, a), O (b) and Mn elements (c) in nMn_3O_4-RGO film. APTES-nMn_3O_4-RGO nanocomposite showed the additional peaks for nitrogen (N) and silicon (Si) due to the presence $–NH_2$ and silane groups (Figure S6). The weight and atomic % of C, N, O, Si and Mn in APTES-nMn_3O_4-RGO was found to be about 27.16%, 3.28%, 34.69, 7.43 and 27.45% and 41.66%, 4.32%, 30.95, 4.87 and 18.2%, respectively, inset of (Figure S6, g). Also, EDX mapping indicated the presence of C (Figure S6, a), N (b), O (c), Si (d) and Mn elements (e) in the APTES-nMn_3O_4-RGO nanocomposite. The repeatability of nanocomposite formation was good as was evident by its low relative standard deviation (±4.7) obtained for the concentration of various elements found in nanocomposite.

4. ELECTROCHEMICAL CHARACTERIZATION

Cyclic voltammetry (CV) studies were carried out for all electrodes using 5 mM potassium ferro-ferricyanide solution for redox reaction to investigate electrochemical redox properties, (Figure 7i). On incorporation of nMn_3O_4 onto RGO sheets, the electrochemical current increased to 145.21 µA (curve a) from RGO, 96.3 µA (curve b). It was reported that nanostructured metal oxides such as nickel oxide and zirconium oxide were incorporated onto RGO to obtain enhanced the electrochemical reactivity[15,49]. After APTES modification on the surface of nMn_3O_4-RGO, the current decreased to 82.93 µA (curve c) due to aminopropyl-functional resins things of APTES[47]. This microporous structure of nMn_3O_4-RGO surface play a vital role in loading of APTES. On adding of antibody-BSA, the oxidation current of Ab/APTES-nMn_3O_4-RGO further decreased to 46.41 µA (curve d) because of non-conducting nature of antibody-BSA molecules.

The electrochemical impedance spectroscopy (EIS) measurements of the fabricated biosensor electrodes were carried out. The Nyquist plot was utilized to calculate the virtual change in charge transfer resistance (R_{ct}), wherein R_{ct} and double layer capacitance (C_{dl}) be able to obtained from real (Z') and imaginary (Z'') modules that mostly originated from the resistance and capacitance. The R_{ct} and C_{dl} can be correlate with frequency using Eq.4

$$R_{ct}C_{dl} = \frac{1}{2\pi f_{max}} = \tau \qquad (4)$$

where, f_{max} is the maximum frequency and τ is the time constant. The impedance spectra of several sensor electrodes are shown Figure 7, ii with frequency ($0.01–10^5$ Hz) at a function of potential (0.01V). The R_{ct} value for RGO sensor electrode was found to be as 776.44 Ω (curve a) as compared to nMn_3O_4-RGO electrode 412.33 Ω (curve b). The higher impedance could be correlated with the presented oxygen and carbonic groups on RGO surface that hinder the electron transport for the period of redox reaction. Alternately, the formation of nMn_3O_4-RGO composite was found to be enhanced due to electron conduction from electrolyte solution resulting in low impedance signal. Further, APTES modification on nMn_3O_4-RGO yielded a value of R_{ct} as high 1.05 kΩ (curve c) due to addition of amino silane moieties on nMn_3O_4-RGO surface. After immobilization of antibodies (Ab) and BSA on APTES-nMn_3O_4-RGO, the R_{ct} increased to 3.02 kΩ (curve d) due to formation of protein layers that hindered the electrons transfer in the electrolyte solution.

4.1 Detection of Cardiac Troponin I: The electrochemical impedance spectroscopy (EIS) is a sensitive detection tool and there is no need for any labelling chemicals. We conducted the EIS measurements while allowing antigen-antibody interactions on the surface to detect cardiac troponin (cTnI). The impedance signal at the sensor electrode/electrolyte interface changes when target antigens are

captured on the sensor surface. The impedimetric response of this microfluidic chip was measured as a function of cTnI concentration (0.008–20 ng/mL) with incubation time of about 3 min (Figure 8, i). During the impedance measurements, the various concentrations of cTnI were flowed on to the sensor surface through the inlet of the microchannel with the help of syringe pump. The electrochemical impedance cell circuit was shown in Figure 7, ii (inset). The R_{ct} values of this sensor chip were found to increase linearly with cTnI concentration (Figure 8, i). The variation of R_{ct} of the sensor occurred due to interactions of cTnI antigen and antibody at electrode/electrolyte interface. The captured cTnI molecules on the Ab/APTES-nMn_3O_4-RGO immunoelectrode surface due to their specific binding perhaps inhibited the electrons generated from redox conversation to the sensor electrode resulting in increased impedance. The flow rate of cTnI solution was kept at 10 µL/min via microchannel to facilitate incubation with the biochip surface. After detection, the solution was discarded and the channels were washed with 10 mM sodium acetate buffer (pH 7.4). 4.0 mM HCl solution was exposed to the sensor surface for 2 min in order to regenerate the sensor chip. Sensor calibration plot between R_{ct} values and cTnI concentrations was shown in (Figure 8, ii). The regression equation for this sensor was found to by following equation with a linear regression coefficient of 0.992.

$$R_{ct}\ (\Omega) = \log [8.65]\ k\Omega - \log [2.75]\ k\Omega\ ng^{-1}\ mL \times \log [cTnI\ (ng/mL)] \quad \text{Eq.5}$$

The sensitivity of the fabricated microfluidic sensor was found to be log [87.58] kΩ/(ng mL^{-1})/cm^2. This could be assigned to the incorporation of the microporous nMn_3O_4-RGO composite into the microfluidic device. The detection limit of this microfluidic sensor for detection of cTnI biomolecules was found to be 8.0 pg/mL [Table S1]. Microporous feature of nMn_3O_4-RGO and its flower like 3D nanostructures may result in enhanced loading capacity of covalently functionalized antibodies resulting in high sensitive device for detection of low concentrated cTnl molecules.

The association and dissociation constant of this biosensor (determined to be 0.32 M^{-1} s^{-1} and 3.15 s^{-1} respectively) revealed that cTnI molecules had higher affinity towards sensor. This could be due to the microporous composite formation that allowed strong bonding of the antibodies for cTnI detection. A transient plot of impedance showed that this sensor had detection time of 100 s and the detection limit was 0.03 ng/mL of cTnI (Figure S9).

The response of the fabricated sensor was validated with real serum samples containing different concentrations of cTnl. The serum samples containing different trace levels of cTnI were collected from hospital as per biosafety and ethics protocols. These samples were injected onto the sensor chip to expose the sensor surface and EIS spectra was recorded (Figure 8, iii). The EIS signals were obtained using standard solution of cTnI with increasing concentration from 0.8 to 20 ng/mL.

We also conducted the experiments with various concentration of cTnI in human serum sample. Specific immuno-interaction between the antibody on the electrode surface and the biomarker (cTnI) present in the serum sample resulted in enhanced surface density of cTnI on the electrode surface. As the concentration of cTnI increased, the value of impedance was found to increase due to the increased interaction of cTnI serum and antibodies at electrode/electrolyte interface and the captured cTnI molecules at the Ab/APTES-nMn_3O_4-RGO immunoelectrode surface (Figure 8, iv).The average relative standard deviation (RSD) for the output impedance (Table S2) was less than ±5% and ±3% for the serum samples with cTnI concentrations of 0.8, 5 and 2, 15 ng/mL, respectively. However, the RSD value showed a decrease to even less than ±1% for 10 and 20 ng/mL concentrations (Figure 8, iv). Thus, this microfluidic sensor chip could be used to quantify cTnI concentrations in the serum samples, as low as 0.8 ng/mL.

The reproducibility, selectivity and stability studies of this microfluidic sensor were systematically conducted. Four sets of immunoelectrodes were fabricated on microfluidic platforms to conduct reproducibility test. The reproducibility studies were conducted keeping similar conditions for buffer concentration, temperature, flow rate, and cTnI concentration of 0.8 ng/mL. These microfluidic immuno sensors showed an average standard deviation of about 0.48 (Figure 7, iii and iv) confirming a good reproducibility.

A control study of this sensor was carried out for detection of cTnI to avoid false signal (Figure 9, i). For this purpose, the working electrode of microfluidic device was constructed using APTES-nMn_3O_4-RGO without immobilizing antibody (Ab) on its surface. The observed R_{ct} values in the presence of cTnI concentration were not significant as shown in [Figure 9, i (curve a)]. This could be due to non-specific interactions of cTnI molecules and APTES-nMn_3O_4-RGO. Thus, Ab immobilized APTES-nMn_3O_4-RGO immunoelectrode was highly specific [Figure 9, i (curve b)]. For the activity test for cardiac biomarker, three sets of microfluidic immunoelectrodes platforms were fabricated to conduct the activity and correctness of cardiac biomarker after captured by functioned microfluidic biochip. We immobilized different amounts of cTnI antibody solution onto surface of microfluidic electrodes and the activity of electrodes after captured cTnI were conducted under similar condition for buffer concentration, pH 7.4, temperature, flow rate, and cTnI concentration of 0.8 ng/mL. The impedimetric responses of the three microfluidic electrodes was investigated as a function of antibody concentration 10, 15 and 20 µL. The R_{ct} values of three sensor chips were found to be increased with increasing the loading amounts of cTnI antibody (10–20 µL) (Figure S8, i) after which R_{ct} value was found to be saturated. But the observed R_{ct} values of electrode 2 and electrode 3 is not significant (Figure S8, ii). This could be due to limited reactions of sensor surface. However, with 20 µL concentration of antibodies, the sensor showed the maximum activity, which was almost same

activity as 15 µL. Thus sensing of cardiac biomarker was conducted by immobilizing 15 µL concentration.

The selectivity of this sensor was determined in presence of cTnI (0.4 ng/mL) concentration with 0.4 ng/mL concentration of all interferents such myoglobin (Mb), cardiac troponin C (cTnC), cardiac troponin T (cTnT) and B-type natriuretic peptide (BNP) using EIS technique (Figure 9, ii). The impedance response of the microfluidic sensor was not considerably affected in presence of interferents in the course of cTnI detection. The cTnI showed the high R_{ct} value related to all interferents, indicating the absorption of cTnI molecules on the sensor surface. Though, a slight variation was found in case of BNP biomolecules indicating good selectivity of this biosensor. Also, this sensor exhibited good stability within 30 days while stored in 4^0C.

5. CONCLUSIONS

A microfluidic sensor chip has been fabricated and used for detection of cardiac troponin I. This sensor is label-free, highly sensitive, and highly reproducible, with low detection limits for detection of cTnl. In this device, an nMn_3O_4-RGO microporous composite has been integrated with a microfluidic setting. The unique features of nMn_3O_4-RGO composite such as its microporosity, surface modifications, and excellent redox behaviour have not only facilitated antibody immobilization but have also resulted in improved sensing performance such as high sensitivity, and high selectivity. In this microfluidic device, the flower like-3D structure of nMn_3O_4-RGO composite has provided a microenvironment for controlled antigen-antibody reactivity. The results of binding kinetics studies conducted on this sensor show higher affinity of the sensor towards specific cardiac troponin I. In addition, the large surface area and high electrochemical reactivity of this sensor offer fast electron transfer rate. The nMn_3O_4-RGO microporous composite-based microfluidic sensor could serve as an ideal platform for detection of other biomolecules as well with appropriate modification.

ASSOCIATED CONTENT

Supporting Information

Detailed fabrication route for microelectrode and microfluidic channels using photolithographic technique, Zeta potential studies, UV-visible studies, EDX mapping, XPS analysis of Mn_3O_4, Activity test for antibody, detection time, and tables.

FIGURE CAPTIONS

Schematic: Graphical abstract.

Figure 1 Schematic representation of the fabrication of microfluidic biochip for detection of Cardiac Biomarker. (a) Photograph of a microfluidic biochip for detection of cardiac biomarker. (b) Schematic representation of the sensor using embedded APTES-Mn_3O_4-RGO as a working electrode. (c) FESEM image of embedded microporous nanocomposite on to the fabricated microelectrode. (d) The

APTES-Mn_3O_4-RGO are functionalized with antibody of cTnI molecules to recognize specific detection of cardiac troponin I.

Figure 2 (a) X-ray diffraction pattern of nanostructured Mn_3O_4, RGO and Mn_3O_4-RGO nanocomposite. (b) Raman spectra of Mn_3O_4, Mn_3O_4-RGO and APTES-Mn_3O_4-RGO. (c) FTIR spectra of Mn_3O_4-RGO, APTES-Mn_3O_4-RGO and Ab/APTES-Mn_3O_4-RGO bioelectrode.

Figure 3 X-ray photoelectron spectroscopy analysis for APTES-nMn_3O_4-RGO composite. (a) Wide-scan spectra, (b) Mn 2p spectra, (c) C 1s spectra after deconvolution, (d) O 1s spectra, (e) N 1s spectra and (f) Si 2p spectra for APTES-nMn_3O_4-RGO composite.

Figure 4 (a) Nitrogen adsorption-desorption isotherms of Mn_3O_4-RGO. Inset: pore size distribution pattern. (b) Nitrogen adsorption-desorption isotherms of APTES-Mn_3O_4-RGO. Inset: pore size distribution pattern.

Figure 5. Transmission electron microscopy characterization of the nanoengineered APTES-Mn_3O_4-RGO electrode. (a and b) TEM images of Mn_3O_4 nanostructure. (c) Atomic scale image of Mn_3O_4 nanostructure. Inset: electron diffraction pattern. (d and e)TEM images of RGO sheets. Inset: electron diffraction pattern. (f and g) Mn_3O_4-RGO composite. (h) Atomic scale image of Mn_3O_4-RGO composite. Inset: electron diffraction pattern. (i) TEM image of APTES-Mn_3O_4-RGO.

Figure 6. Scanning electron microscopy characterization of the nanoengineered Ab/APTES-Mn_3O_4-RGO electrode. (a, b, c and d) FESEM images of as-prepared Mn_3O_4 under different hydrothermal reaction conditions such as 60 ^oC, 24 h, 75 ^oC, 24 h, 90 ^oC, 12 h and 90 ^oC, 24 h, respectively. (e and f) Spherical flower-shaped images at optimization condition at 90 ^oC, 24 h, and inset of (f) showing high resolution image of Mn_3O_4. (g and h) FESEM image of RGO sheets. (i and j) Mn_3O_4-RGO composite. (k) APTES modified Mn_3O_4-RGO composite. (l) FESEM image of Ab/APTES-Mn_3O_4-RGO after Ab immobilization.

Figure 7 (i) CV responses of the sensor using the RGO, Mn_3O_4-RGO, APTES-Mn_3O_4-RGO electrode and Ab/APTES-Mn_3O_4-RGO bioelectrode at a scan rate of 40 mV s^{-1} in the presence of PBS (50 mM, pH 7.4) having an equal molar concentration (5 mM) of potassium ferro-ferricyanide solution. (ii) Shows the impedance spectra of several sensor electrodes with frequency (0.01–10^5 Hz) at afunction of potential (0.01V). (iii) Reproducibility test conducted at 0.8 ng/mL cTnI concentration for four sensors. (iv) Reproducibility histogram plot for the impedance outputs of the sensors.

Figure 8 (i) EIS response of the sensor with the Ab/APTES-Mn_3O_4-RGO bioelectrode as a function of cTnI concentration (0.008–20 ng/mL) at 0.01 V. (ii) Sensor calibration plot showing the output impedance versus cTnI concentration. The inset shows the relationship between the logarithm of cTnI concentration and output impedance. (iii) EIS responses of the sensor to serum samples. (iv) Comparison plots for EIS signals of the sensor responding to synthetic and serum samples. The error bars were obtained by calculating the standard deviation of three consecutive measurements for each concentration.

Figure 9 (i) Control study of Ab/APTES-Mn_3O_4-RGO bioelectrode. (ii) The selectivity of Ab/APTES-Mn_3O_4-RGO bioelectrode.

REFERENCES

(1) Horak, J.; Dincer, C.; Qelibari, E.; Bakirci, H.; Urban, G. Polymer-Modified Microfluidic Immunochip for Enhanced Electrochemical Detection of Troponin I. *Sens. Actuators B Chem.* **2015**, *209*, 478–485.
(2) Periyakaruppan, A.; Gandhiraman, R. P.; Meyyappan, M.; Koehne, J. E. Label-Free Detection of Cardiac Troponin-I Using Carbon Nanofiber Based Nanoelectrode Arrays. *Anal. Chem.* **2013**, *85* (8), 3858–3863.
(3) Kim, K.; Park, C.; Kwon, D.; Kim, D.; Meyyappan, M.; Jeon, S.; Lee, J.-S. Silicon Nanowire Biosensors for Detection of Cardiac Troponin I (cTnI) with High Sensitivity. *Biosens. Bioelectron.* **2016**, *77*, 695–701.
(4) Kar, P.; Pandey, A.; J. Greer, J.; Shankar, K. Ultrahigh Sensitivity Assays for Human Cardiac Troponin I Using TiO_2 Nanotube Arrays. *Lab. Chip* **2012**, *12* (4), 821–828.
(5) Thygesen, K.; Mair, J.; Katus, H.; Plebani, M.; Venge, P.; Collinson, P.; Lindahl, B.; Giannitsis, E.; Hasin, Y.; Galvani, M.; Tubaro, M.; Alpert, J. S.; Biasucci, L. M.; Koenig, W.; Mueller, C.; Huber, K.; Hamm, C.; Jaffe, A. S. Recommendations for the Use of Cardiac Troponin Measurement in Acute Cardiac Care. *Eur. Heart J.* **2010**, *31* (18), 2197–2204.
(6) Wang, J.; Ibáñez, A.; Chatrathi, M. P.; Escarpa, A. Electrochemical Enzyme Immunoassays on Microchip Platforms. *Anal. Chem.* **2001**, *73* (21), 5323–5327.
(7) Apple, F. S.; Falahati, A.; Paulsen, P. R.; Miller, E. A.; Sharkey, S. W. Improved Detection of Minor Ischemic Myocardial Injury with Measurement of Serum Cardiac Troponin I. *Clin. Chem.* **1997**, *43* (11), 2047–2051.
(8) Sackmann, E. K.; Fulton, A. L.; Beebe, D. J. The Present and Future Role of Microfluidics in Biomedical Research. *Nature* **2014**, *507* (7491), 181–189.
(9) Whitesides, G. M. The Origins and the Future of Microfluidics. *Nature* **2006**, *442* (7101), 368–373.
(10) Kim, J.; Li, Z.; Park, I. Direct Synthesis and Integration of Functional Nanostructures in Microfluidic Devices. *Lab. Chip* **2011**, *11* (11), 1946–1951.
(11) Vilela, D.; Garoz, J.; Colina, Á.; González, M. C.; Escarpa, A. Carbon Nanotubes Press-Transferred on PMMA Substrates as Exclusive Transducers for Electrochemical Microfluidic Sensing. *Anal. Chem.* **2012**, *84* (24), 10838–10844.
(12) Ali, M. A.; Mondal, K.; Wang, Y.; Jiang, H.; Mahal, N. K.; Castellano, M. J.; Sharma, A.; Dong, L. In Situ Integration of Graphene Foam–titanium Nitride Based Bio-Scaffolds and Microfluidic Structures for Soil Nutrient Sensors. *Lab. Chip* **2017**, *17* (2), 274–285.
(13) Liu, S.; Guo, X. Carbon Nanomaterials Field-Effect-Transistor-Based Biosensors. *NPG Asia Mater.* **2012**, *4* (8), e23.
(14) Yang, K.; Feng, L.; Shi, X.; Liu, Z. Nano-Graphene in Biomedicine: Theranostic Applications. *Chem. Soc. Rev.* **2012**, *42* (2), 530–547.
(15) Ali, M. A.; Singh, C.; Mondal, K.; Srivastava, S.; Sharma, A.; Malhotra, B. D. Mesoporous Few-Layer Graphene Platform for Affinity Biosensing Application. *ACS Appl. Mater. Interfaces* **2016**, *8* (12), 7646–7656.
(16) Cui, S.; Pu, H.; Mattson, E. C.; Wen, Z.; Chang, J.; Hou, Y.; Hirschmugl, C. J.; Chen, J. Ultrasensitive Chemical Sensing through Facile Tuning Defects and Functional Groups in Reduced Graphene Oxide. *Anal. Chem.* **2014**, *86* (15), 7516–7522.
(17) Wei, J.; Qiu, J.; Li, L.; Ren, L.; Zhang, X.; Chaudhuri, J.; Wang, S. A Reduced Graphene Oxide Based Electrochemical Biosensor for Tyrosine Detection. *Nanotechnology* **2012**, *23* (33), 335707.
(18) Pumera, M.; Ambrosi, A.; Bonanni, A.; Chng, E. L. K.; Poh, H. L. Graphene for Electrochemical Sensing and Biosensing. *TrAC Trends Anal. Chem.* **2010**, *29* (9), 954–965.
(19) Bai, X.; Chen, G.; Shiu, K.-K. Electrochemical Biosensor Based on Reduced Graphene Oxide Modified Electrode with Prussian Blue and Poly(toluidine Blue O) Coating. *Electrochimica Acta* **2013**, *89*, 454–460.

(20) Zhou, M.; Zhai, Y.; Dong, S. Electrochemical Sensing and Biosensing Platform Based on Chemically Reduced Graphene Oxide. *Anal. Chem.* **2009**, *81* (14), 5603–5613.
(21) Kim, Y.; Shanmugam, S. Polyoxometalate–Reduced Graphene Oxide Hybrid Catalyst: Synthesis, Structure, and Electrochemical Properties. *ACS Appl. Mater. Interfaces* **2013**, *5* (22), 12197–12204.
(22) Zhang, W.; Liu, F.; Li, Q.; Shou, Q.; Cheng, J.; Zhang, L.; Nelson, B. J.; Zhang, X. Transition Metal Oxide and Graphene Nanocomposites for High-Performance Electrochemical Capacitors. *Phys. Chem. Chem. Phys.* **2012**, *14* (47), 16331–16337.
(23) Williams, G.; Seger, B.; Kamat, P. V. TiO_2-Graphene Nanocomposites. UV-Assisted Photocatalytic Reduction of Graphene Oxide. *ACS Nano* **2008**, *2* (7), 1487–1491.
(24) Chen, S.; Zhu, J.; Wu, X.; Han, Q.; Wang, X. Graphene Oxide−MnO_2 Nanocomposites for Supercapacitors. *ACS Nano* **2010**, *4* (5), 2822–2830.
(25) Stankovich, S.; Dikin, D. A.; Dommett, G. H. B.; Kohlhaas, K. M.; Zimney, E. J.; Stach, E. A.; Piner, R. D.; Nguyen, S. T.; Ruoff, R. S. Graphene-Based Composite Materials. *Nature* **2006**, *442* (7100), 282–286.
(26) Zhu, J.; Zhu, T.; Zhou, X.; Zhang, Y.; Lou, X. W.; Chen, X.; Zhang, H.; Hng, H. H.; Yan, Q. Facile Synthesis of Metal Oxide/reduced Graphene Oxide Hybrids with High Lithium Storage Capacity and Stable Cyclability. *Nanoscale* **2011**, *3* (3), 1084–1089.
(27) Kamat, P. V. Graphene-Based Nanoarchitectures. Anchoring Semiconductor and Metal Nanoparticles on a Two-Dimensional Carbon Support. *J. Phys. Chem. Lett.* **2010**, *1* (2), 520–527.
(28) Lang, X.; Hirata, A.; Fujita, T.; Chen, M. Nanoporous Metal/oxide Hybrid Electrodes for Electrochemical Supercapacitors. *Nat. Nanotechnol.* **2011**, *6* (4), 232–236.
(29) Song, J.; Xu, L.; Zhou, C.; Xing, R.; Dai, Q.; Liu, D.; Song, H. Synthesis of Graphene Oxide Based CuO Nanoparticles Composite Electrode for Highly Enhanced Nonenzymatic Glucose Detection. *ACS Appl. Mater. Interfaces* **2013**, *5* (24), 12928–12934.
(30) Jang, H. D.; Kim, S. K.; Chang, H.; Roh, K.-M.; Choi, J.-W.; Huang, J. A Glucose Biosensor Based on TiO_2–Graphene Composite. *Biosens. Bioelectron.* **2012**, *38* (1), 184–188.
(31) Wang, K.; Li, H.-N.; Wu, J.; Ju, C.; Yan, J.-J.; Liu, Q.; Qiu, B. TiO_2-Decorated Graphene Nanohybrids for Fabricating an Amperometric Acetylcholinesterase Biosensor. *Analyst* **2011**, *136* (16), 3349–3354.
(32) Singh, N.; Ali, M. A.; Suresh, K.; Agrawal, V. V.; Rai, P.; Sharma, A.; Malhotra, B. D.; John, R. In-Situ Electrosynthesized Nanostructured Mn_3O_4-Polyaniline Nanofibers- Biointerface for Endocrine Disrupting Chemical Detection. *Sens. Actuators B Chem.* **2016**, *236*, 781–793.
(33) Kamil Reza, K.; Singh, N.; Yadav, S. K.; Singh, M. K.; Biradar, A. M. Pearl Shaped Highly Sensitive Mn_3O_4 Nanocomposite Interface for Biosensor Applications. *Biosens. Bioelectron.* **2014**, *62*, 47–51.
(34) Yue, J.; Gu, X.; Chen, L.; Wang, N.; Jiang, X.; Xu, H.; Yang, J.; Qian, Y. General Synthesis of Hollow MnO_2, Mn_3O_4 and MnO Nanospheres as Superior Anode Materials for Lithium Ion Batteries. *J. Mater. Chem. A* **2014**, *2* (41), 17421–17426.
(35) Wang, L.; Li, Y.; Han, Z.; Chen, L.; Qian, B.; Jiang, X.; Pinto, J.; Yang, G. Composite Structure and Properties of Mn_3O_4/graphene Oxide and Mn_3O_4/graphene. *J. Mater. Chem. A* **2013**, *1* (29), 8385–8397.
(36) Jayawardena, K. D. G. I.; Rhodes, R.; Gandhi, K. K.; Prabhath, M. R. R.; Dabera, G. D. M. R.; Beliatis, M. J.; Rozanski, L. J.; Henley, S. J.; Silva, S. R. P. Solution Processed Reduced Graphene Oxide/metal Oxide Hybrid Electron Transport Layers for Highly Efficient Polymer Solar Cells. *J. Mater. Chem. A* **2013**, *1* (34), 9922–9927.
(37) Wang, Y.; Zhu, L.; Yang, X.; Shao, E.; Deng, X.; Liu, N.; Wu, M. Facile Synthesis of Three-Dimensional Mn_3O_4 Hierarchical Microstructures and Their Application in the Degradation of Methylene Blue. *J. Mater. Chem. A* **2015**, *3* (6), 2934–2941.
(38) Marcano, D. C.; Kosynkin, D. V.; Berlin, J. M.; Sinitskii, A.; Sun, Z.; Slesarev, A.; Alemany, L. B.; Lu, W.; Tour, J. M. Improved Synthesis of Graphene Oxide. *ACS Nano* **2010**, *4* (8), 4806–4814.

(39) Srivastava, S.; Kumar, V.; Ali, M. A.; Solanki, P. R.; Srivastava, A.; Sumana, G.; Saxena, P. S.; Joshi, A. G.; Malhotra, B. D. Electrophoretically Deposited Reduced Graphene Oxide Platform for Food Toxin Detection. *Nanoscale* **2013**, *5* (7), 3043–3051.
(40) Gao, W.; Alemany, L. B.; Ci, L.; Ajayan, P. M. New Insights into the Structure and Reduction of Graphite Oxide. *Nat. Chem.* **2009**, *1* (5), 403–408.
(41) Bussamara, R.; Melo, W. W. M.; Scholten, J. D.; Migowski, P.; Marin, G.; Zapata, M. J. M.; Machado, G.; Teixeira, S. R.; Novak, M. A.; Dupont, J. Controlled Synthesis of Mn_3O_4 Nanoparticles in Ionic Liquids. *Dalton Trans.* **2013**, *42* (40), 14473–14479.
(42) Mondal, K.; Kumar, J.; Sharma, A. Self-Organized Macroporous Thin Carbon Films for Supported Metal Catalysis. *Colloids Surf. Physicochem. Eng. Asp.* **2013**, *427*, 83–94.
(43) Wang, H.; Wang, Y.; Cao, X.; Feng, M.; Lan, G. Vibrational Properties of Graphene and Graphene Layers. *J. Raman Spectrosc.* **2009**, *40* (12), 1791–1796.
(44) Gui, M. M.; Yap, Y. X.; Chai, S.-P.; Mohamed, A. R. Multi-Walled Carbon Nanotubes Modified with (3-Aminopropyl)triethoxysilane for Effective Carbon Dioxide Adsorption. *Int. J. Greenh. Gas Control* **2013**, *14*, 65–73.
(45) Yang, H.; Li, F.; Shan, C.; Han, D.; Zhang, Q.; Niu, L.; Ivaska, A. Covalent Functionalization of Chemically Converted Graphene Sheets via Silane and Its Reinforcement. *J. Mater. Chem.* **2009**, *19* (26), 4632–4638.
(46) Zhang, Y.; Shen, Y.; Han, D.; Wang, Z.; Song, J.; Niu, L. Reinforcement of Silica with Single-Walled Carbon Nanotubes through Covalent Functionalization. *J. Mater. Chem.* **2006**, *16* (47), 4592–4597.
(47) Singh, N.; Reza, K. K.; Ali, M. A.; Agrawal, V. V.; Biradar, A. M. Self Assembled DC Sputtered Nanostructured Rutile TiO_2 Platform for Bisphenol A Detection. *Biosens. Bioelectron.* **2015**, *68*, 633–641.
(48) Zhong, L.; Yun, K. Graphene Oxide-Modified ZnO Particles: Synthesis, Characterization, and Antibacterial Properties. *Int. J. Nanomedicine* **2015**, *10* (Spec Iss), 79–92.
(49) Liu, J.; Meng, X.; Hu, Y.; Geng, D.; Banis, M. N.; Cai, M.; Li, R.; Sun, X. Controlled Synthesis of Zirconium Oxide on Graphene Nanosheets by Atomic Layer Deposition and Its Growth Mechanism. *Carbon* **2013**, *52*, 74–82.

Figures

Figure 1

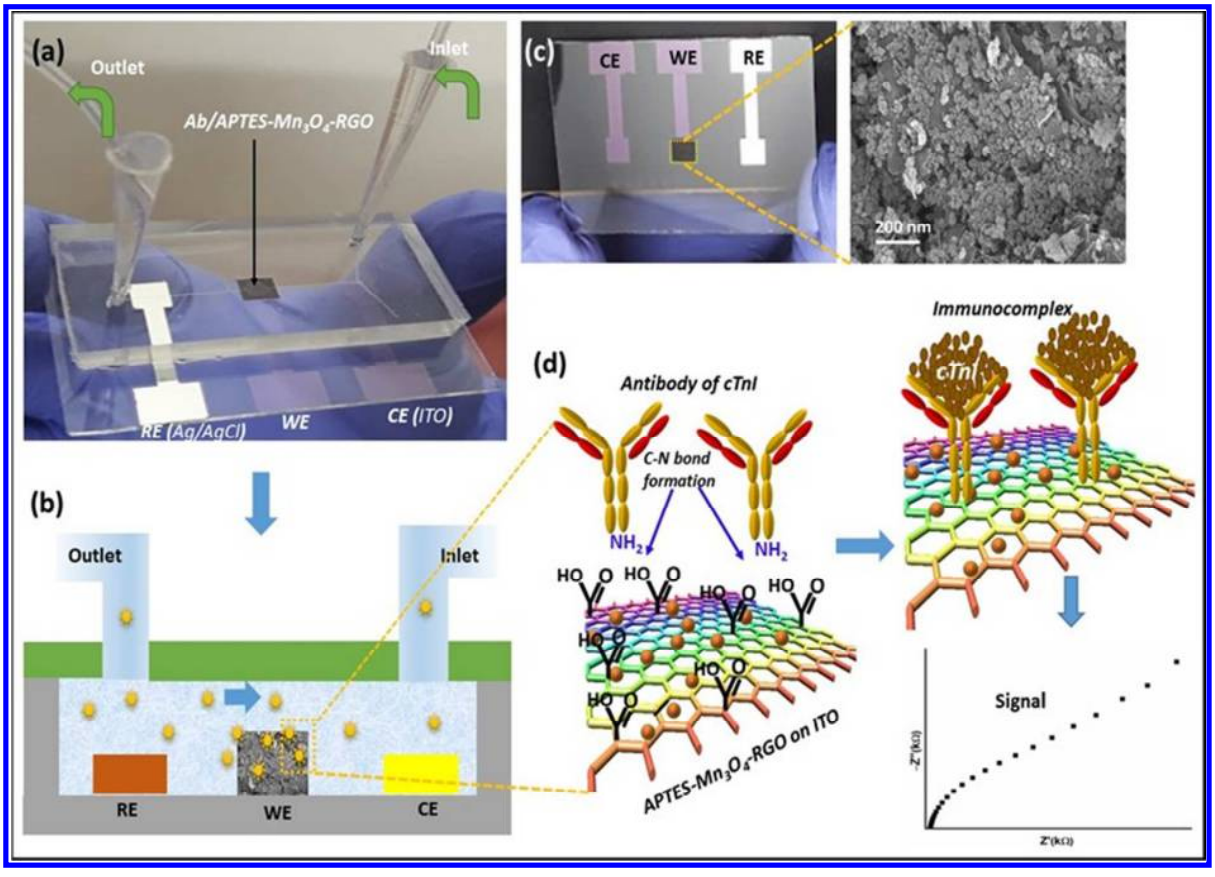


Figure 2

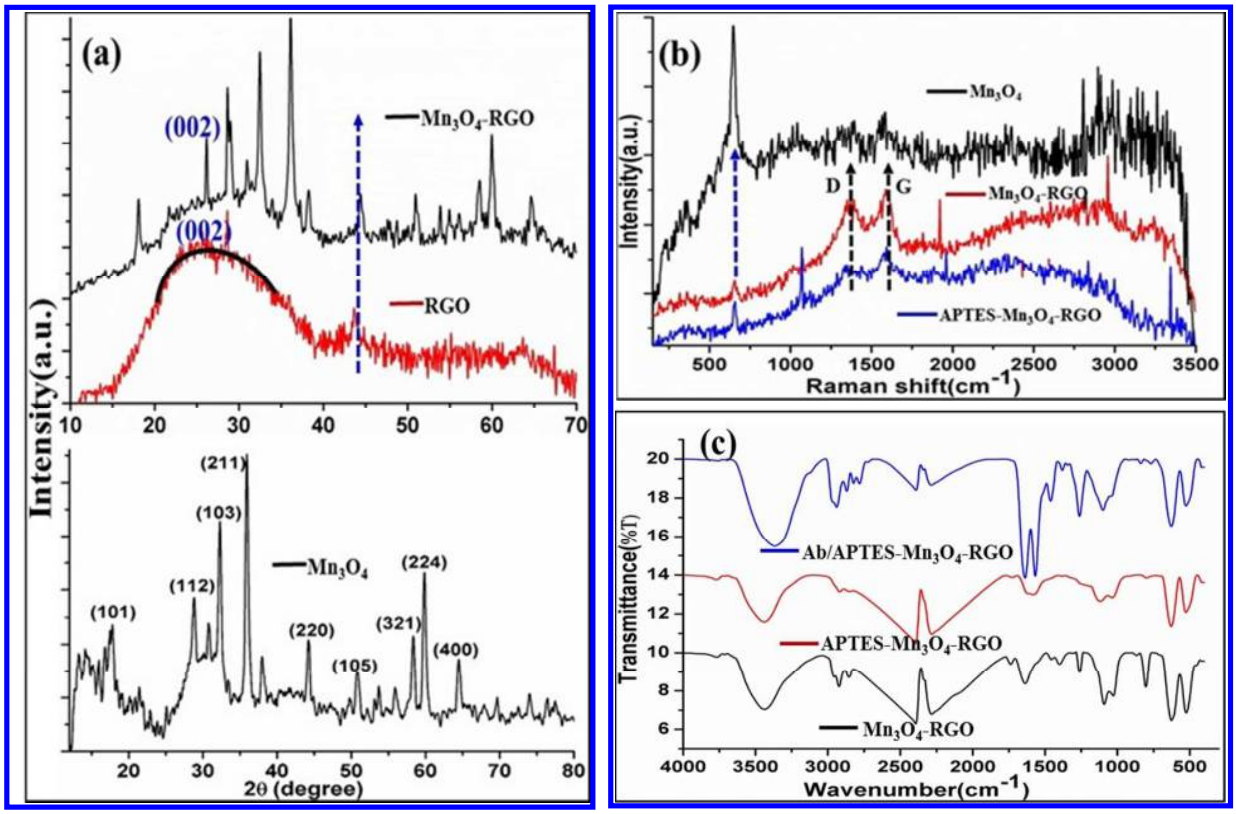

(a)
(002)
(002)
Mn3O4-RGO
RGO
Intensity(a.u.)
(211)
(103)
(112)
(101)
(220)
(105)
(321)
(224)
(400)
Mn3O4
2θ (degree)
(b)
Mn3O4
D
G
Mn3O4-RGO
APTES-Mn3O4-RGO
Intensity(a.u.)
Raman shift(cm-1)
(c)
Ab/APTES-Mn3O4-RGO
APTES-Mn3O4-RGO
Mn3O4-RGO
Transmittance(%T)
Wavenumber(cm-1)

Figure 3

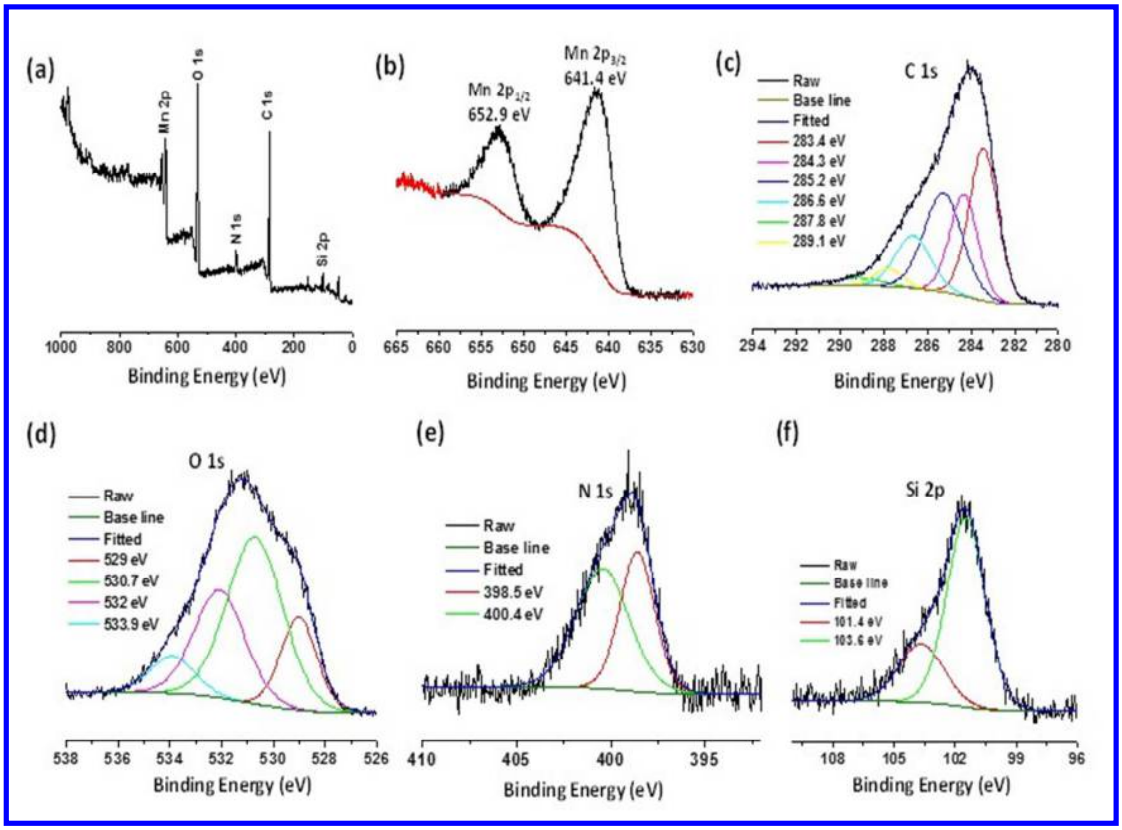

(a)
Mn 2p
O 1s
C 1s
N 1s
Si 2p
1000 800 600 400 200 0
Binding Energy (eV)
(b)
Mn 2p1/2
652.9 eV
Mn 2p3/2
641.4 eV
665 660 655 650 645 640 635 630
Binding Energy (eV)
(c)
C 1s
Raw
Base line
Fitted
283.4 eV
284.3 eV
285.2 eV
286.6 eV
287.8 eV
289.1 eV
294 292 290 288 286 284 282 280
Binding Energy (eV)
(d)
O 1s
Raw
Base line
Fitted
529 eV
530.7 eV
532 eV
533.9 eV
538 536 534 532 530 528 526
Binding Energy (eV)
(e)
N 1s
Raw
Base line
Fitted
398.5 eV
400.4 eV
410 405 400 395
Binding Energy (eV)
(f)
Si 2p
Raw
Base line
Fitted
101.4 eV
103.6 eV
108 105 102 99 96
Binding Energy (eV)

Figure 4

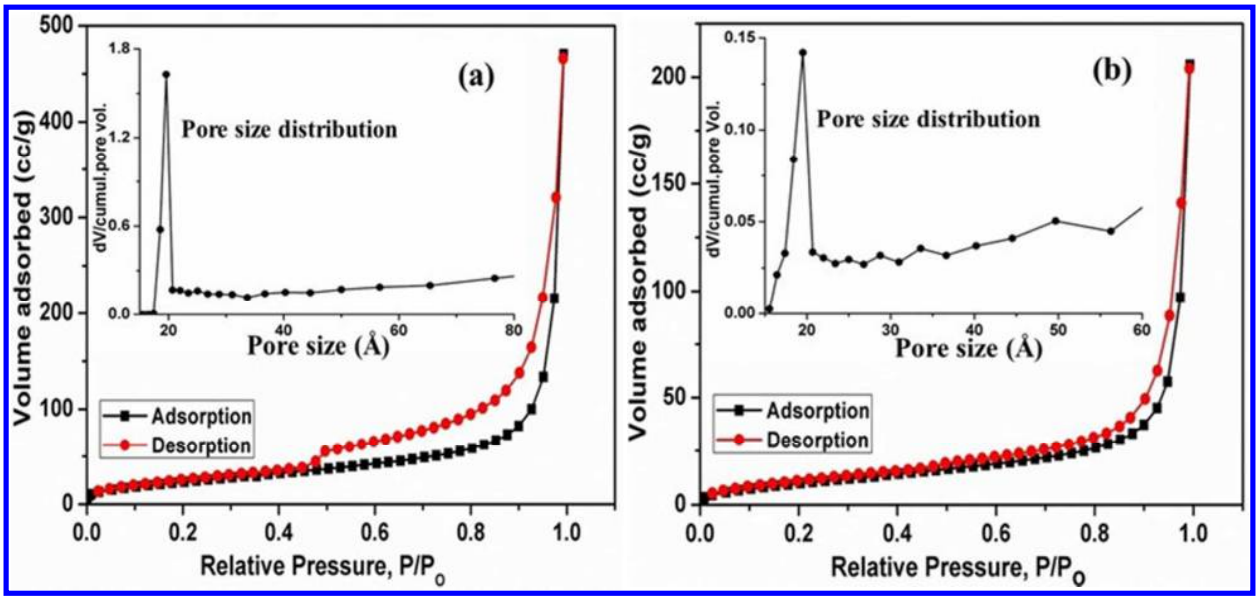

(a)
Pore size distribution
dV/cumul.pore vol.
Pore size (Å)
Adsorption
Desorption
Volume adsorbed (cc/g)
Relative Pressure, P/P0
(b)
Pore size distribution
dV/cumul.pore Vol.
Pore size (Å)
Adsorption
Desorption
Volume adsorbed (cc/g)
Relative Pressure, P/P0

Figure 5

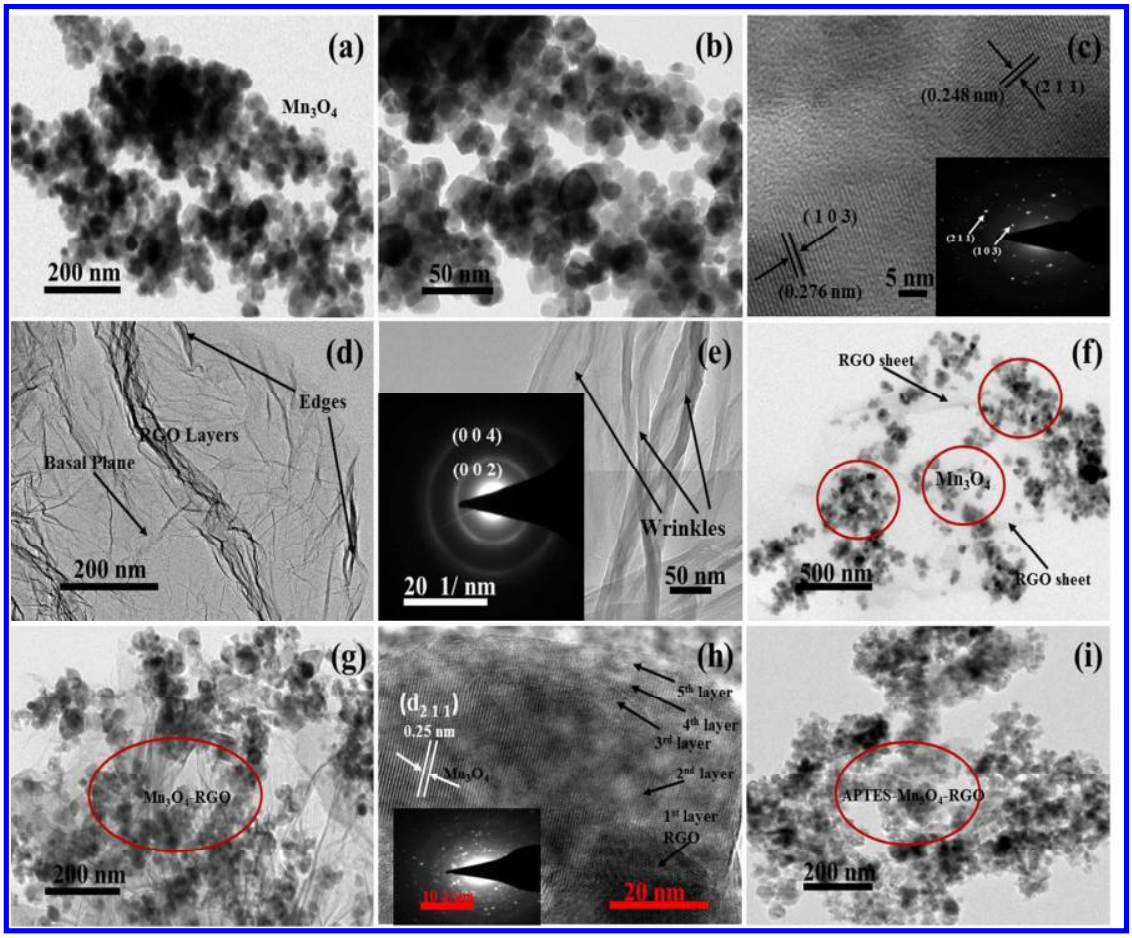

(a)
Mn_3O_4
200 nm
(b)
50 nm
(c)
(0.248 nm)
(2 1 1)
(1 0 3)
(0.276 nm)
5 nm
(d)
Edges
RGO Layers
Basal Plane
200 nm
(e)
(0 0 4)
(0 0 2)
20 1/ nm
Wrinkles
50 nm
(f)
RGO sheet
Mn_3O_4
500 nm
RGO sheet
(g)
Mn_3O_4-RGO
200 nm
(h)
$(d_{2\,1\,1})$
0.25 nm
Mn_3O_4
5th layer
4th layer
3rd layer
2nd layer
1st layer
RGO
20 nm
(i)
APTES-Mn_3O_4-RGO
200 nm

Figure 6

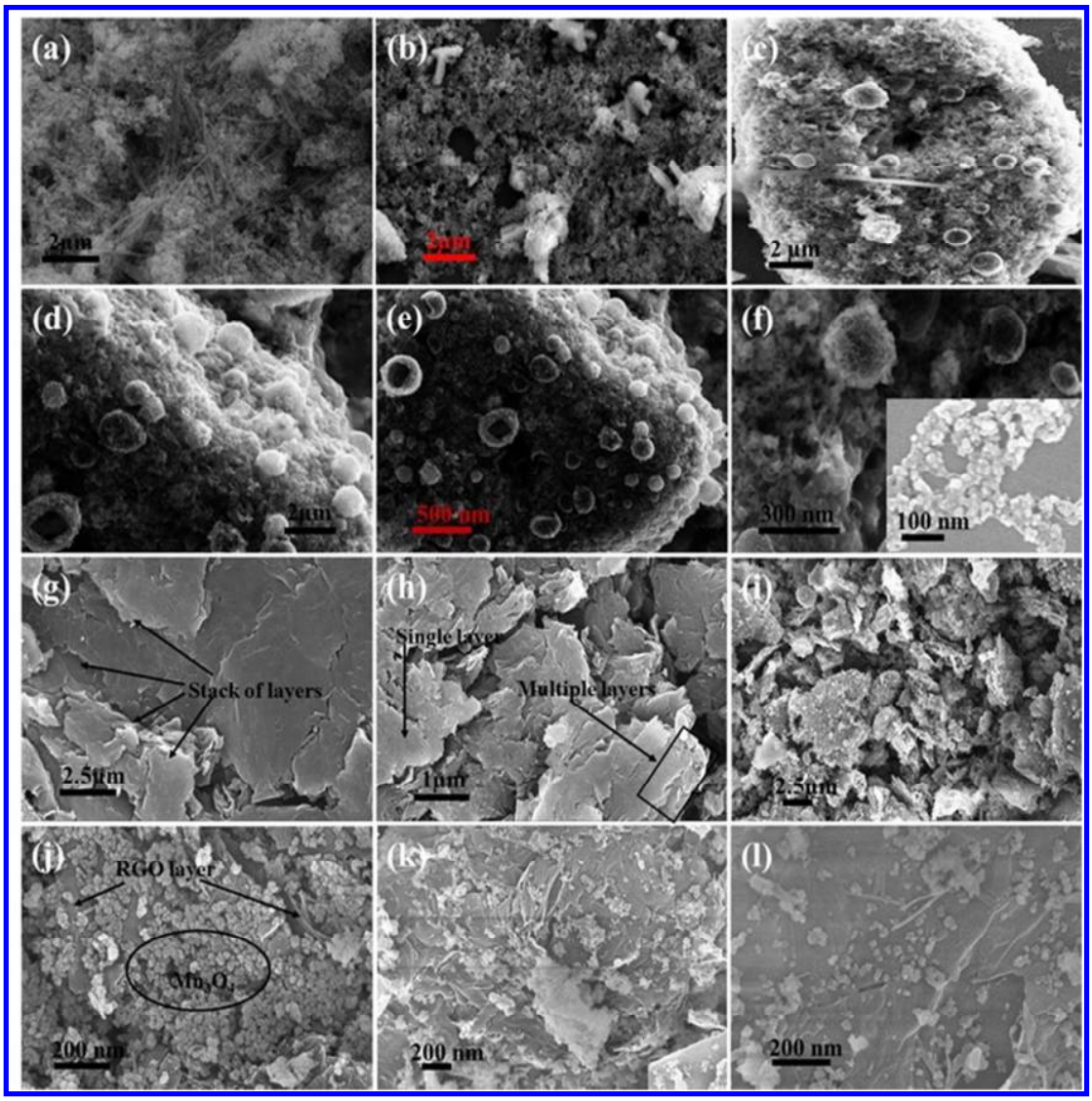

(a)
2μm
(b)
5μm
(c)
2 μm
(d)
2μm
(e)
500 nm
(f)
300 nm
100 nm
(g)
Stack of layers
2.5μm
(h)
Single layer
Multiple layers
1μm
(i)
2.5μm
(j)
RGO layer
Mn_3O_4
200 nm
(k)
200 nm
(l)
200 nm

Figure 7

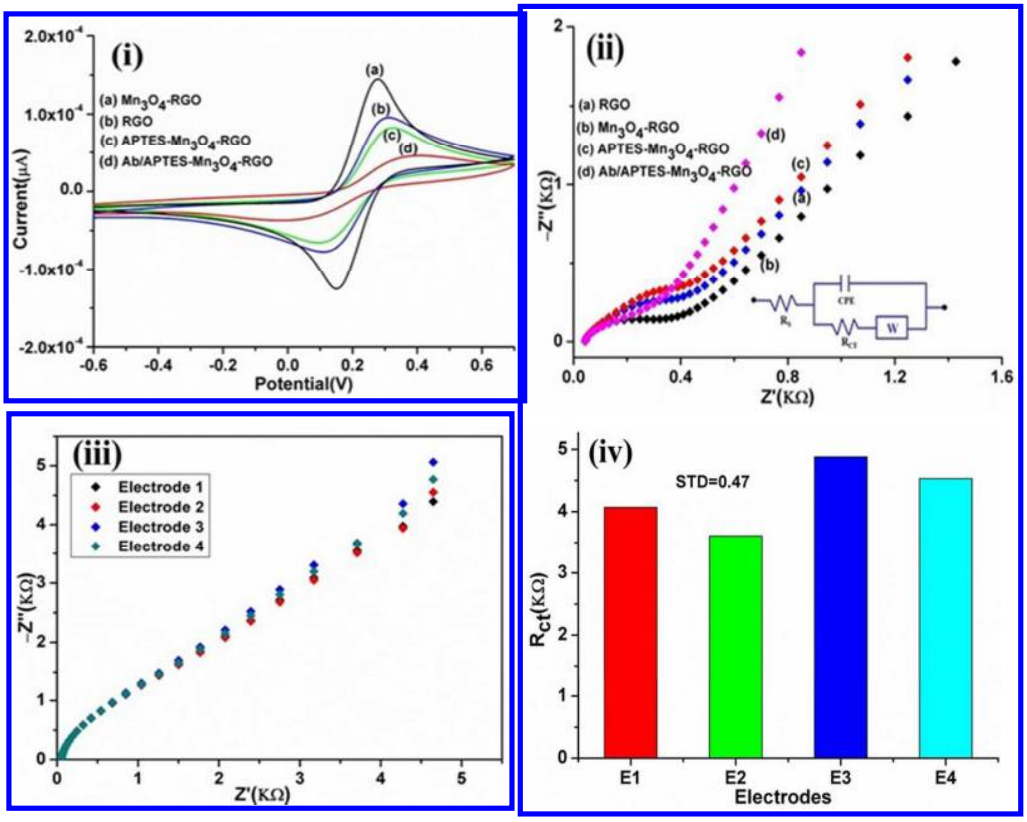

(i)
(a) Mn_3O_4-RGO
(b) RGO
(c) APTES-Mn_3O_4-RGO
(d) Ab/APTES-Mn_3O_4-RGO
Current(μA)
Potential(V)
(ii)
(a) RGO
(b) Mn_3O_4-RGO
(c) APTES-Mn_3O_4-RGO
(d) Ab/APTES-Mn_3O_4-RGO
-Z''(KΩ)
Z'(KΩ)
CPE
W
(iii)
Electrode 1
Electrode 2
Electrode 3
Electrode 4
-Z''(KΩ)
Z'(KΩ)
(iv)
STD=0.47
R_{ct}(KΩ)
E1
E2
E3
E4
Electrodes

Figure 8

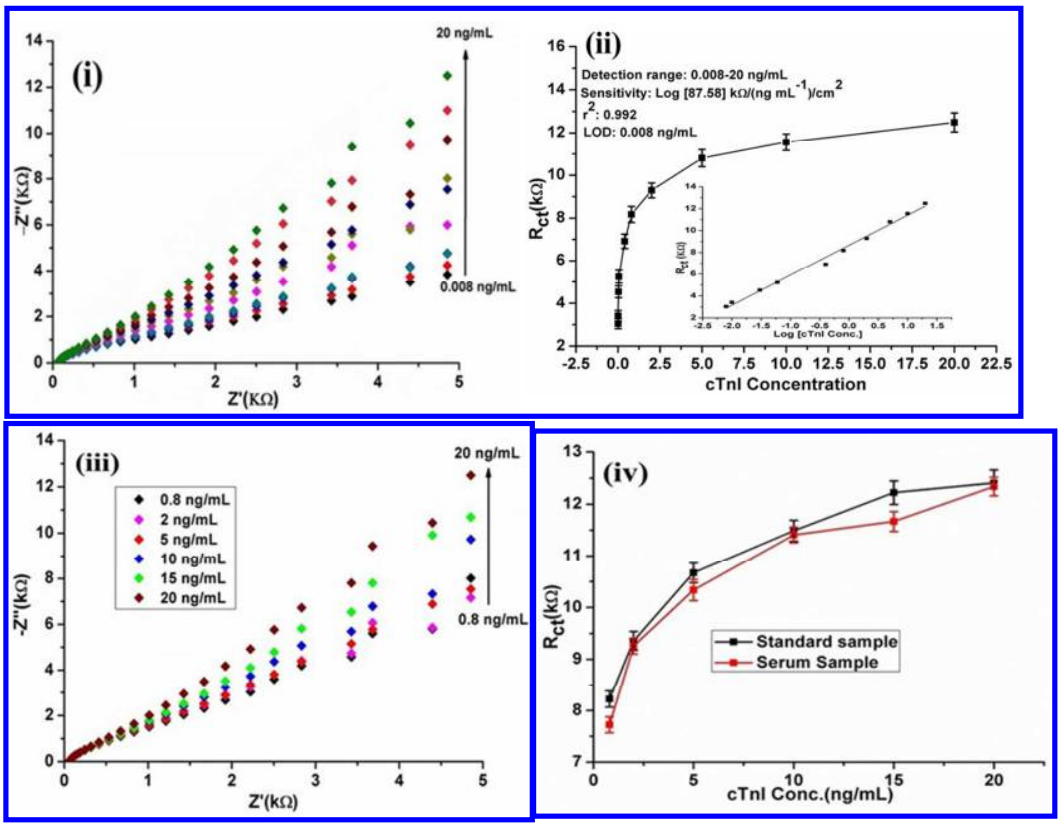
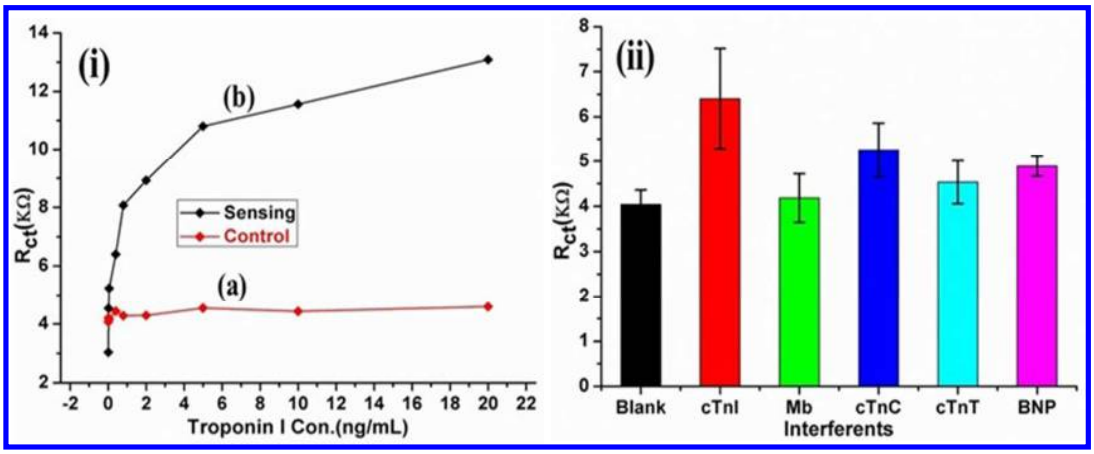
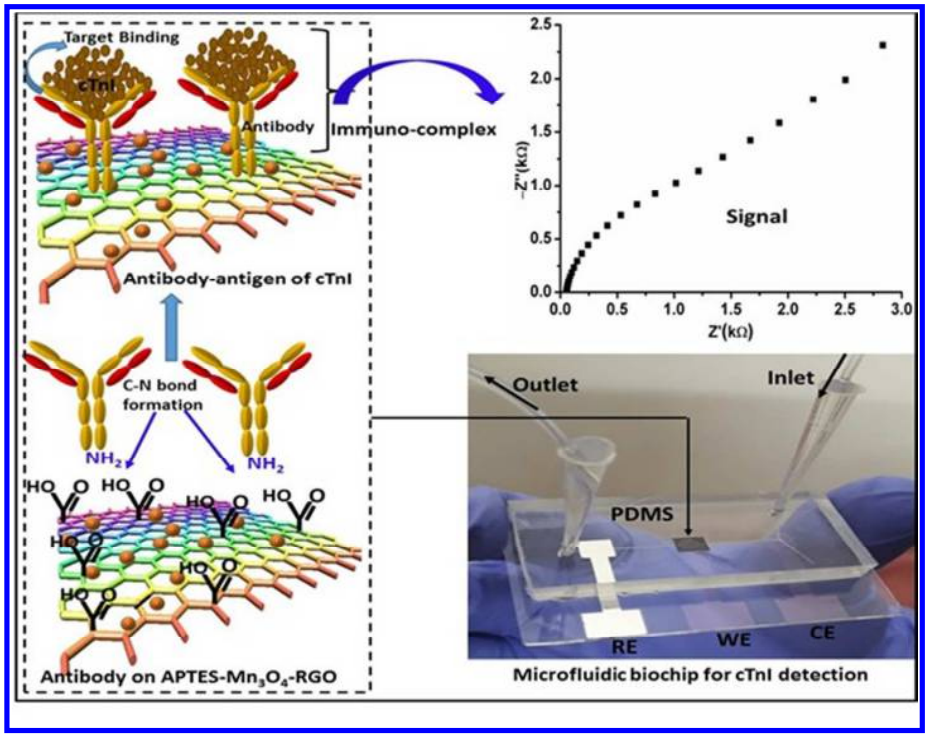

(i)
20 ng/mL
0.008 ng/mL
-Z''(KΩ)
Z'(KΩ)
(ii)
Detection range: 0.008-20 ng/mL
Sensitivity: Log [87.58] kΩ/(ng mL-1)/cm2
r2: 0.992
LOD: 0.008 ng/mL
Rct(kΩ)
cTnI Concentration
Log [cTnI Conc.]
(iii)
0.8 ng/mL
2 ng/mL
5 ng/mL
10 ng/mL
15 ng/mL
20 ng/mL
-Z''(kΩ)
Z'(kΩ)
(iv)
Standard sample
Serum Sample
Rct(kΩ)
cTnI Conc.(ng/mL)

Figure 9


(i)
(b)
(a)
Sensing
Control
R_{ct}(KΩ)
Troponin I Con.(ng/mL)
(ii)
R_{ct}(KΩ)
Blank
cTnI
Mb
cTnC
cTnT
BNP
Interferents

Graphical Abstract



Journal of Thermal Engineering, Vol. 3, No. 5, pp. 1453-1465, October, 2017
Yildiz Technical University Press, Istanbul, Turkey

NUMERICAL STUDY OF PRESSURE DROP AND HEAT TRANSFER IN A STRAIGHT RECTANGULAR AND SEMI CYLINDRICAL PROJECTIONS MICROCHANNEL HEAT SINK

M. Zunaid[1,*], A. Jindal[1], D. Gakhar[1], A. Sinha[1]

ABSTRACT

The heat transfer and pressure drop characteristics of a straight rectangular and semi cylindrical projections microchannel heat sink were investigated. The heat sinks, made of copper, were aligned in row as a cluster of 21 microchannels, 231 μm wide and 713 μm deep. Water was used as cooling fluid and was made to flow through the channels. A three dimensional analysis was done for Reynolds number ranging between 200 to 1000 with constant heat flux of 10^6 W/m^2 defined relative to the platform area of the heat sink. The temperature rise and pressure drop of the fluid in straight microchannel heat sink was evaluated using ANSYS-CFX package and was validated using experimental data. Similar analysis was done for semi cylindrical projections microchannel heat sink by solving the conjugate heat transfer problem. A comparison of heat transfer and pressure drop between rectangular and semi cylindrical projections microchannel was done and the results were laid out. Results shows that heat transfer increases with the use of semi cylindrical projections microchannel heat sink.

Keywords: *Heat Sink, Microchannel, Heat Transfer, Reynolds Number, Conjugate Heat Transfer, Semi Cylindrical Projections*

INTRODUCTION

Microchannel heat sinks provide a cutting edge technology for removal of large amount of heat from a very small surface area. These are starting to challenge the use of traditional coil technology for heat exchange in many industries. Since the most recent decade, smaller scale machining technology is utilized at an expanded rate for the improvement of exceptionally productive cooling gadgets known as micro-channel heat sinks due to its greater advantages, for example, less coolant requirement and small size. Thus, the investigation of heat transfer and fluid flow in smaller scale channels which are two important parts of such gadgets, have pulled in additional considerations with expansive applications in both designing and performance issues. The construction of the heat sink is done from a material with high thermal conductivity, for example, copper or silicon. Smaller scale channels are created into its surface either by exact machining or miniaturized scale fabrication technology. These small scale channels have trademark measurements going from 10 to 1000 μm, and serve as flow entries for the cooling fluid. These micro-channels possess advantage of very small volume to surface area, small mass, large convective heat transfer coefficient. Miniaturization of electronic gadgets has become necessity of today. The reduced size of the microchips has led to an increase in the heat flux density, which causes overheating of gadgets and makes the general prosperity and working of these gadgets a major test for scientists. So there is a need to move onto profoundly proficient cooling innovation and heat dissipation strategies to meet the safety standards. The cross-sectional area of the heat sink serves as a course to transport liquid to and far from the wall of the channel. The study on single phase micro-channel heat sink has a very extensive coverage since the last two decades. Since the last two decades, micro-channel coolers having different dimensions and different substrate materials have been fabricated and tested with numerous coolants.

The micro-scale cooling and heat transfer was first studied by Tuckerman and Pease [1]. They fabricated a 1×1 cm^2 rectangular silicon wafer microchannel of depth 302 μm and width 50 μm with water as the cooling fluid. The heat sink was capable of dissipating 790 W/cm^2 with a pressure drop of 2.2 bar and maximum substrate temperature of 71˚C. This study demonstrated that electronic circuits can be effectively cooled by microchannels and supported further investigations. Peng and Peterson [2] experimentally investigated the single-phase forced convective heat transfer in micro-channel structures with small rectangular channels having hydraulic diameters of 0.133–0.367 mm for different types of geometric configurations. The results show that the laminar heat transfer is dependent upon the aspect ratio i.e. the ratio of hydraulic diameter to the center-to-center

This paper was recommended for publication in revised form by Kwok-wing Chau
[1]Department of Mechanical Engineering, Delhi Technological University, Bawana Road, Delhi, INDIA
**E-mail address: mzunaid3k@gmail.com*
Manuscript Received 30 May 2016, Accepted 23 August 2016

distance of micro-channels. Further investigations led by Fedorov and Viskanta [3] indicated that the average channel wall temperature along the flow direction was nearly uniform except in the region close to the channel inlet, where very large temperature gradients were observed. This allowed them to conclude that the thermo–properties are temperature dependent. Qu and Mudawar [4] performed experimental and numerical analysis of pressure drop and heat transfer in a single-phase microchannel (0.231 mm x 0.713 mm) at two heat flux levels. Deionized water was employed as the cooling liquid. Good agreement was found between the measurements and numerical predictions, validating the use of conventional Navier–Stokes equations for micro channels. The main objective of these studies is to develop heat transfer modeling tools that are essential to design and optimize heat sink geometry. To develop such optimized geometry, description of flow process in heat sink is essential. Heat transfer in micro-channel involves conduction of heat in the solid heat sink and convection to the coolant fluid. Numerical simulation methods are thus used to provide more accurate description of fluid flow and heat transfer through the microchannel. Using numerical simulation methods, Liu and Garimella [5] studied fluid flow and heat transfer in micro channels and confirmed that, the behavior of micro channels is quite similar to that of conventional channels. Their analysis showed that conventional correlations offer reliable predictions for the laminar flow characteristics in rectangular micro channels over a hydraulic diameter in the range of 244–974 μm. Sabbah et al. [6] observed that the prediction of heat transfer in micro-channels becomes difficult with increase in complicacy of the geometry of the micro-channels, requiring three dimensional analysis of heat transfer in both solid and liquid phases. Despite the small width of the channels, the conventional Navier Stokes and energy conservation equations still apply to the flow (as also observed by Qu and Mudawar [4]) due to the continuum of the working fluid where the channel width is many times larger than the mean free path of liquid molecules (water). Similar results were shown by Mokrani et al. [7] which showed that the conventional laws and correlations describing the flow and convective heat transfer in ducts of large dimension are directly applicable to the micro channels of heights between 500 and 50 microns. The effects of geometric parameters on the Nusselt number were illustrated by P. Mohajeri Khameneh [8] in a single-phase laminar flow and forced convective heat transfer of water in microchannels with the aim to obtain computational Nusselt number in laminar flow. This study showed that the average Nusselt number is enhanced by increasing the width or decreasing the height. Rebrov et al. [9] have reviewed the experimental and numerical results on fluid flow distribution and heat transfer. They found that the experiments with single channels are in good agreement with predictions using the published correlations. The review consists of two parts. In the first, the main methods to control flow distribution were reviewed. Several different designs of inlet/outlet chambers were presented together with corresponding models used for optimization of flow distribution. Nanofluids, which are fluids containing nanometer-sized particles, have emerged as one of the most effective coolants in microchannels. They exhibit enhanced thermal conductivity and the convective heat transfer coefficient compared to the base fluid. Roy et al. [10] studied heat transfer using nanofluids as a coolant inside a radial channel between two coaxial and parallel discs. The non-dimensional governing equations of mass, momentum and energy were solved using computational fluid dynamics. Results have shown that the inclusion of nanoparticles in a traditional coolant can provide considerable improvement in heat transfer rates, even at small particle volume fractions.

Chai, Xia and Wang [11] studied the laminar flow and heat transfer characteristics in the interrupted microchannel heat sink with ribs in the transverse microchambers. In the study they examined the effect of such ribs on velocity contour, pressure distribution and temperature distribution. They also studied the local pressure drop and heat transfer characteristics in such microchannel heat sinks. Results showed that the ribs in the transverse microchambers could effectively prevent the decline of local heat transfer coefficient along the flow direction. A wavy channel structure was studied by Sakanova, Keian, Zhao [12] with the application of nanofluids. The effects of wavy amplitude, wavelength, volumetric flow rate and volume fraction of different types of nanofluids were studied. They found that with pure water as coolant the heat transfer performance of the wavy channel structure is improved, while the replacement of the pure water by nanofluids makes the effect of wavy wall unnoticeable. Xu et al. [13] numerically investigated the flow characteristics and heat transfer in microchannel with dimples. Different geometric parameters of dimpled channel were independently studied under constant Reynolds Number of 500 and a constant heat flux 1 W/mm2. It was found that in comparison to straight channels, dimpled surface reduced the local flow resistance and also improved thermal performance of microchannel heat sink.

Numerical simulations to investigate the influence of geometric parameters on the flow and heat transfer characteristics of rectangular, trapezoidal and triangular shaped microchannel heat sinks was carried out by

Wang et al. [14]. They found that among three kinds of microchannels, the microchannel with rectangular cross-section has the lowest thermal resistance, followed by trapezoidal and triangular cross-sections microchannels. Dang et al. [15], investigated the effect of heat transfer and pressure drop of water in five rectangular-shaped microchannel heat sinks with different configurations (S-type & I-type), in order to optimize performance and design. They showed that when inlet temperature and mass flow rate is kept constant, the performance index of counter flow is always higher than parallel flow. Further, the effect of hydraulic diameter on performance index was found to be more than that of substrate thickness (1.2 & 2mm).

Heat exchangers have often been subjected to thermodynamic optimization or entropy generation minimization like parallel flow, counter flow, cross-flow and phase change heat exchanger optimization. M.M. Awad & Y.S. Muzychka [16] have provided comprehensive review of the progress made in entropy generation minimization (EGM) in order to use it in internal and external structure heat exchanger. EGM combines basic concepts of heat transfer, fluid dynamics and thermodynamics with simple models like microchannel heat exchangers. These models are then used in practical devices and process optimization. Mohamed M Awad [17] has chronologically reviewed the research progress made on EGM (Entropy generation minimization). Entropy generation analysis as the evaluation parameter was used in many studies of the review. Different types of working fluids like water, engine oil, aniline, nanofluids and non-Newtonian were used in the studies. He has also made recommendations of future work for thermodynamic optimization of microchannels using entropy generation analysis. Dongmei Zhou and Timothy Rau [23] correlated numerical simulations and hand results with experimentally obtained results. They designed a methodology to improve the accuracy of the simulations.

In the present work, the pressure drop and heat transfer characteristics of a single-phase rectangular micro-channel with semi cylindrical projections are investigated numerically. It is evident from the above given literature review and to best knowledge of various studies that the numerical analysis of such geometry have not been done before. To ensure the accuracy and reliability of the model, the simulation results of straight microchannel heat sink have been benchmarked with Qu and Mudawar's experimental work [4]. It shows that the numerical data is in good agreement with the experimental data. Heat transfer and pressure drop characteristics for single phase rectangular microchannel with semi cylindrical projections are computed for various Reynolds number in the laminar flow. These are then compared with results of the single phase rectangular microchannel heat sink. An increase in heat transfer and pressure drop is seen for all Reynolds number in the laminar flow. The results are used to assess the suitability of macro transport models in depicting the transport characteristics of micro-channel heat sinks. A detailed description of the heat transfer characteristics is presented and discussed.

MODEL DESCRIPTIONS

Computational and Geometric Configurations

The geometrical configurations of both rectangular and semi cylindrical projections microchannel have been given.

Straight Rectangular Microchannel

A three dimensional CFD analysis for the heat transfer and pressure drop in a rectangular micro-channel is done.

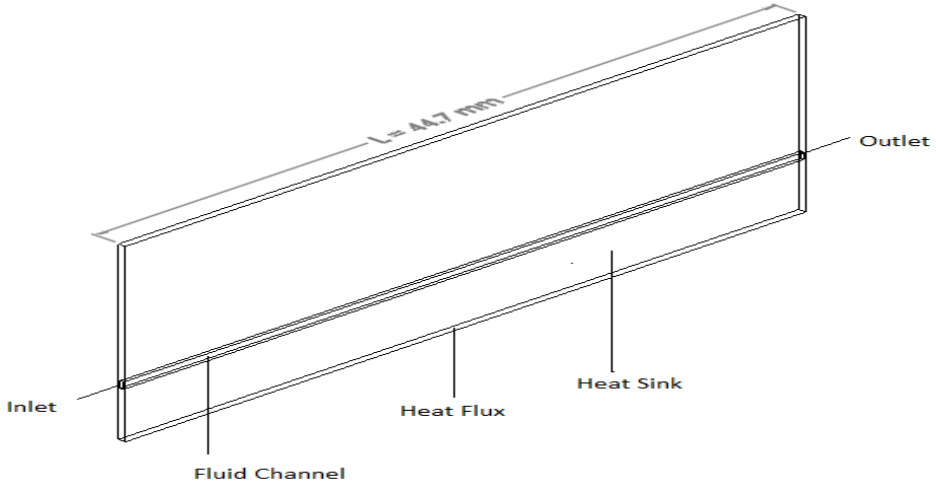
In order to validate this numerical study a reliable experimental study by Qu and Mudawar [4] is necessitated.

The experimental work done by Qu and Mudawar [4], on the test apparatus is modeled and simulated in the present study. In the test apparatus, the heat sink was fabricated from oxygen free copper. Water was moved through straight rectangular channels implanted in a test module. 21 rectangular smaller scale openings were machined into micro- channel surface by an accurate machining procedure (there are 21 parallel rectangular small scale directs in the module). The miniaturized scale openings were equidistantly divided inside the 1 cm heat sink width and had the cross-sectional measurements of 231 μm (width) by 712 μm (height).

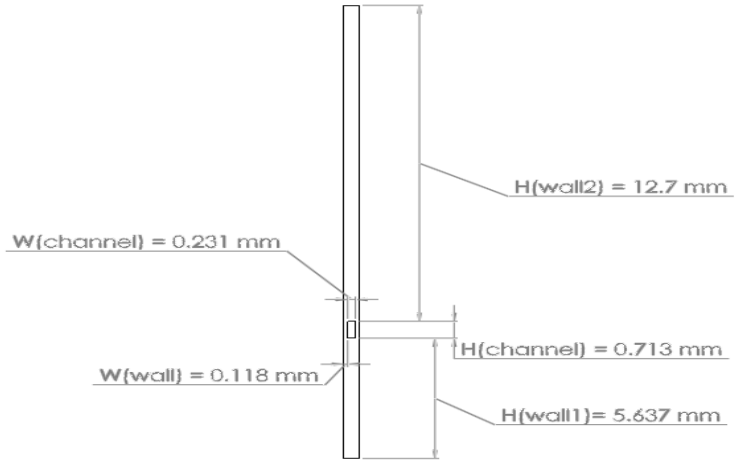
Since symmetry allows the results to be extended to the entire microchannel, a single microchannel with surrounding solid is used for numerical analysis. A schematic and cross section of the modeled microchannel structure used in this study is shown in Figure 1. Meanwhile, geometrical parameters of this model are presented in Table 1.

Table 1. Dimensions of the unit cell used for simulation

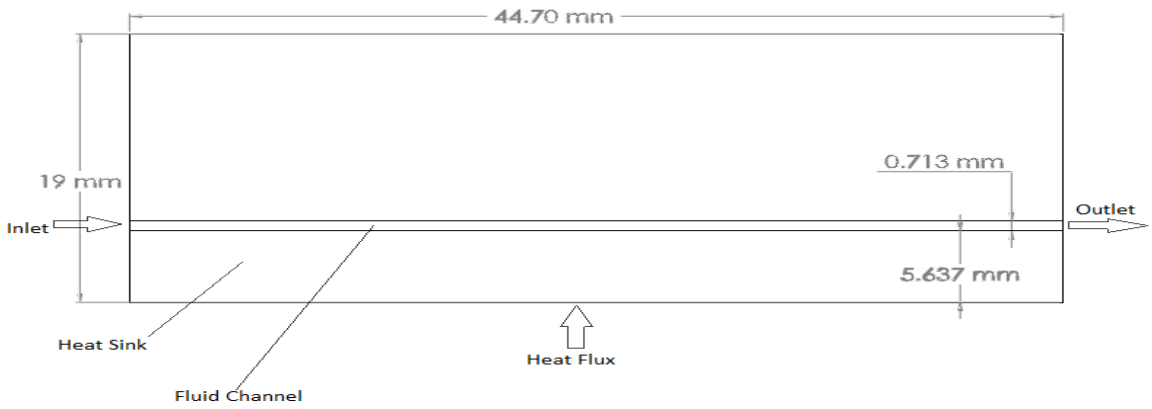
W_{wall}(µm)	$W_{channel}$(µm)	H_{wall2}(µm)	$H_{channel}$(µm)	H_{wall1}(µm)	L(mm)
118	231	12700	713	5637	44.7



(a)



(b)



(c)

Figure 1. Geometrical construction of the unit cell of straight microchannel heat sink used for simulation: - a) Isometric view, b) Side view, c) Front view

In order to increase the calculative capability, fine grids were applied to the microchannel volume and coarse grids to the rest of the heat sink.

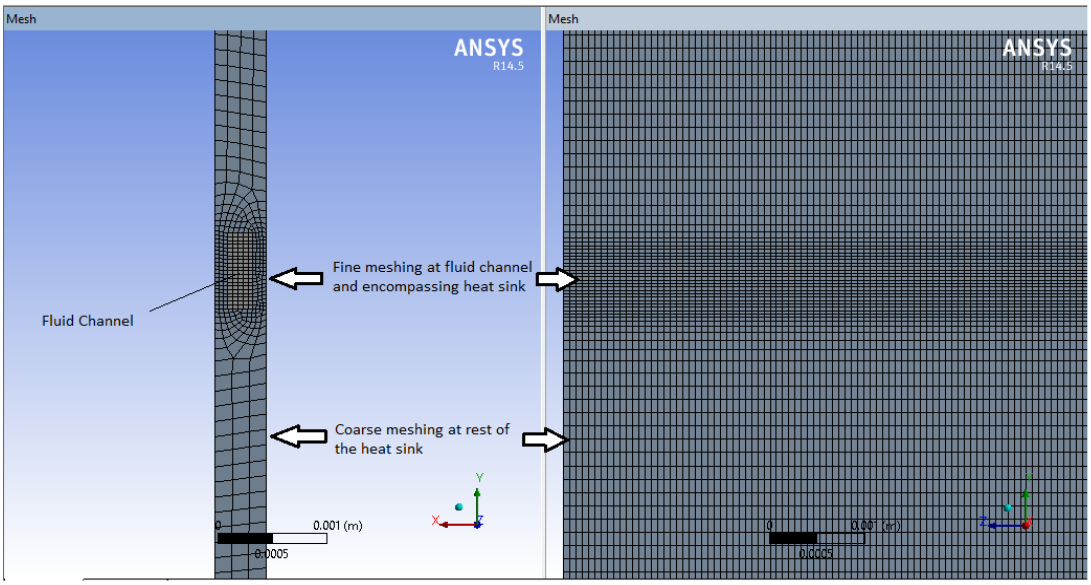


Figure 2. Sectional geometry and meshing grids of straight rectangular microchannel

Semi cylindrical Projections Microchannel

A schematic and cross section of the modeled microchannel structure used in this study is shown in Figure 3. The geometry has same external dimensions as that of the straight microchannel.

Modifications are made in the fluid channel. In the rectangular channel used for the fluid flow in straight microchannel, semi cylindrical projections were added, made of the same material as that of heat sink, placed alternatively on the upper and lower wall of the rectangular slot with its axis perpendicular to the direction of flow of fluid. The radius of the semi cylinder projections used, was taken as R=0.18 mm and length of the projections in same as the width of the rectangular channel. Meanwhile, geometrical parameters of this model are presented in Table 2.

Table 2 Dimensions of the semi cylindrical projections microchannel used for simulation

W_{wall}(µm)	$W_{channel}$(µm)	H_{wall2}(µm)	$H_{channel}$(µm)	H_{wall1}(µm)	L(mm)	R(mm)
118	231	12700	713	5637	44.7	0.18

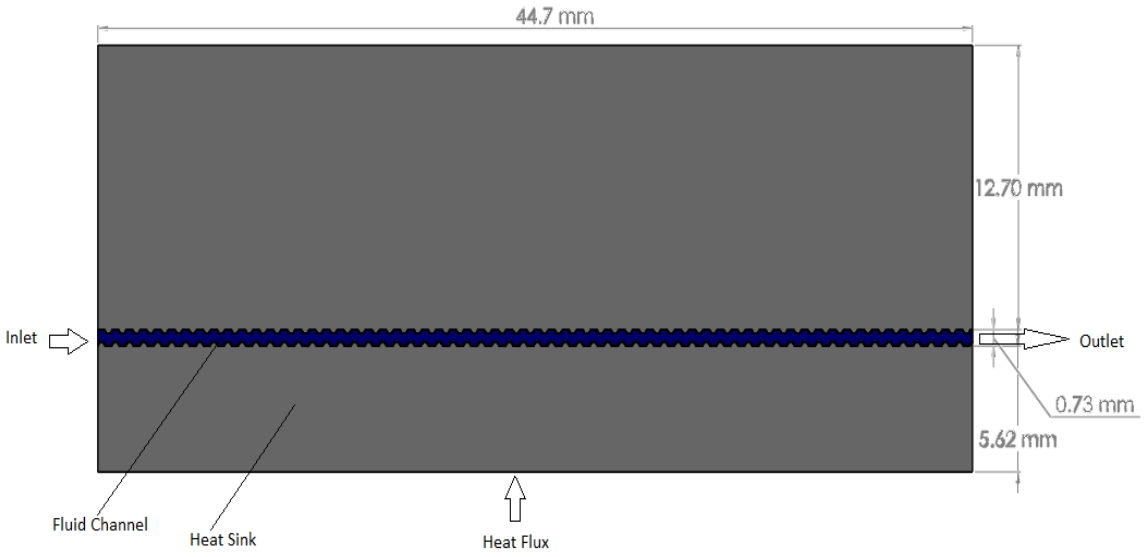
Governing Equations and Boundary Conditions

Several assumptions were considered before arriving on the governing equations and boundary conditions: -

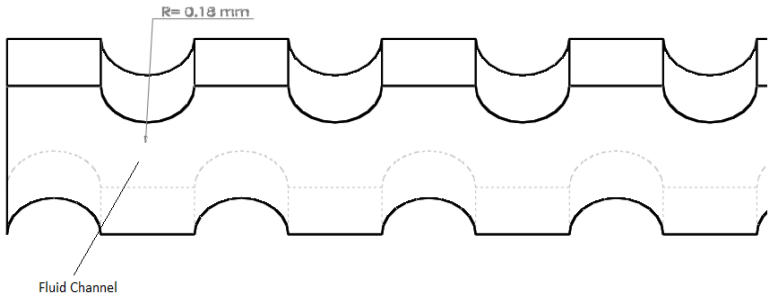
1. The process is steady and the fluid is incompressible.
2. The flow is laminar.
3. The body forces are neglected.
4. The side walls and the top wall of the microchannel structure are adiabatic.
5. Radiation heat transfer and natural convective heat transfer (due to air trapped in heat sink slots) are neglected.

Heat transfer in microchannels is a conjugate one, involving conduction in heat sink and convection to the coolant. One method to solve this conjugate heat transfer problem is to assume a combined computational domain (fluid and solid), [18], [19].

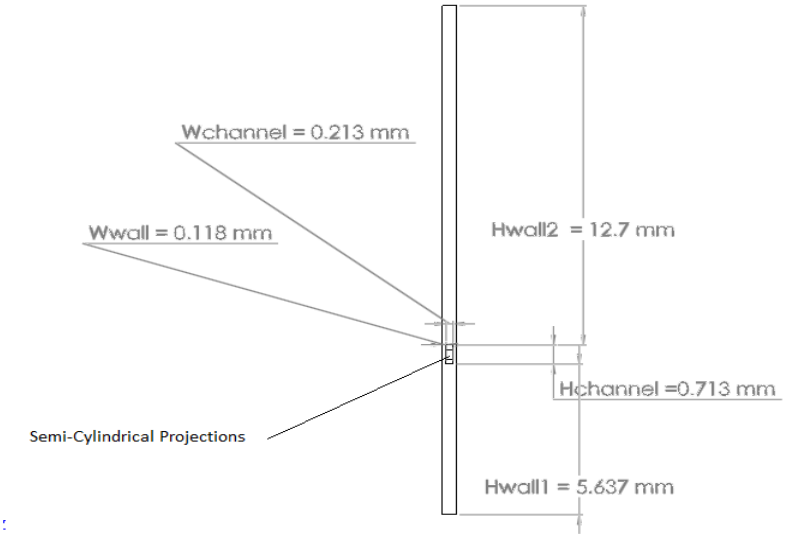
Based on the given assumptions following governing equations are used to describe the fluid flow characteristics and heat transfer.



(a)



(b)



(c)

Figure 3. Geometrical construction of the unit cell of semi cylindrical projections microchannel heat sink used for simulation: - a) Front View, b) Fluid Channel, c) Side View

The equation for conservation of mass, or continuity equation, can be written as follows:

$$\frac{\partial \rho}{\partial t} + \nabla . (\rho \vec{v}) = S_m \tag{1}$$

The equation written above is a general equation for conservation of mass. Here Sm ¬ is the mass added from any user defined sources.

Momentum conservation in a reference frame which is non accelerating can be written as: -

$$\frac{\partial}{\partial t}(\rho\vec{v}) + \nabla.(\rho\vec{v}\vec{v}) = -\nabla p + \nabla.(\bar{\bar{\tau}}) + \rho g + \vec{F} \quad (2)$$

Where, p is the static pressure, τ is the stress tensor, F and ρg are the external forces on body and gravitational force on body.

The energy conservation equation is given as: -

$$\frac{\partial}{\partial t}(\rho E) + \nabla.(\vec{v}\,(\rho E + p)\,) = \nabla.\left(k_{eff}\nabla T + \sum_{J} h_j\overrightarrow{J_J} + \overline{\overline{\tau_{eff}}}.\vec{v}\right) + S_h \quad (3)$$

where, k_{eff} is the effective conductivity ($k+k_t$), where $_{kt}$ is the turbulent thermal conductivity, defined on the basis of turbulence model being used, and J j is the diffusion flux of species J. On the right-hand side of the equation the first three terms represent energy transfer due to species diffusion, conduction, and viscous dissipation, respectively, S_h denotes the chemical reaction heat, and some other sources of heat.

As, we have assumed a unitary computational domain, we only need to specify boundary conditions for the unit cell, which are given as: -

Hydraulic Boundary Conditions

1. Uniform velocity at the inlet of the channel.
2. At channel outlet, mass flow rate boundary condition is applied.
3. Zero velocity at all other solid boundaries.
4. No slip at the surface.

Thermal Boundary Conditions

1. A uniform heat flux of 10^6 W/m^2 at the bottom wall of the heat sink.

Table 3 Zone Specification for straight rectangular microchannel

Heat sink front wall	Wall
Heat sink top wall	Wall
Heat sink back wall	Wall
Heat sink bottom wall	Heat flux
Heat sink right wall	Wall
Heat sink left wall	Wall
Channel entry	Static pressure
Channel outlet	Mass flow outlet
Default Interface	Wall

Data Reduction

The relation between the hydraulic diameter and Reynolds number in a channel is given by

$$Re=\rho v D_h/\mu \quad (4)$$

where, ρ is density, v is average velocity ,μ is dynamic viscocity, D_h is hydraulic diameter of channel, [20], [21].

Mass flow rate is calculated as

$$\dot{m} = \frac{Re.A.\mu}{D_h} \quad (5)$$

Where hydraulic diameter is given as,

$$D_{h=}\frac{4A}{P} \quad (6)$$

where, A=area of cross section of microchannel [$W_{channel}$ x $H_{channel}$] and

P= wetted perimeter[2 x ($W_{channel}$ +$H_{channel}$)]

RESULTS AND DISCUSSIONS

Model Validation

To ensure the accuracy and reliability of the model, the simulation results of straight microchannel heat sink have been benchmarked with Qu and Mudawar's experimental work [4].

Pressure Drop

For the validation of the pressure drop, the experimental pressure drop along the channel is compared with the computational pressure drop.

Figure 3 shows the comparison of experimental and numerical pressure drop results for varying Reynolds numbers. The computational values are found to be in good agreement with the experimental values.

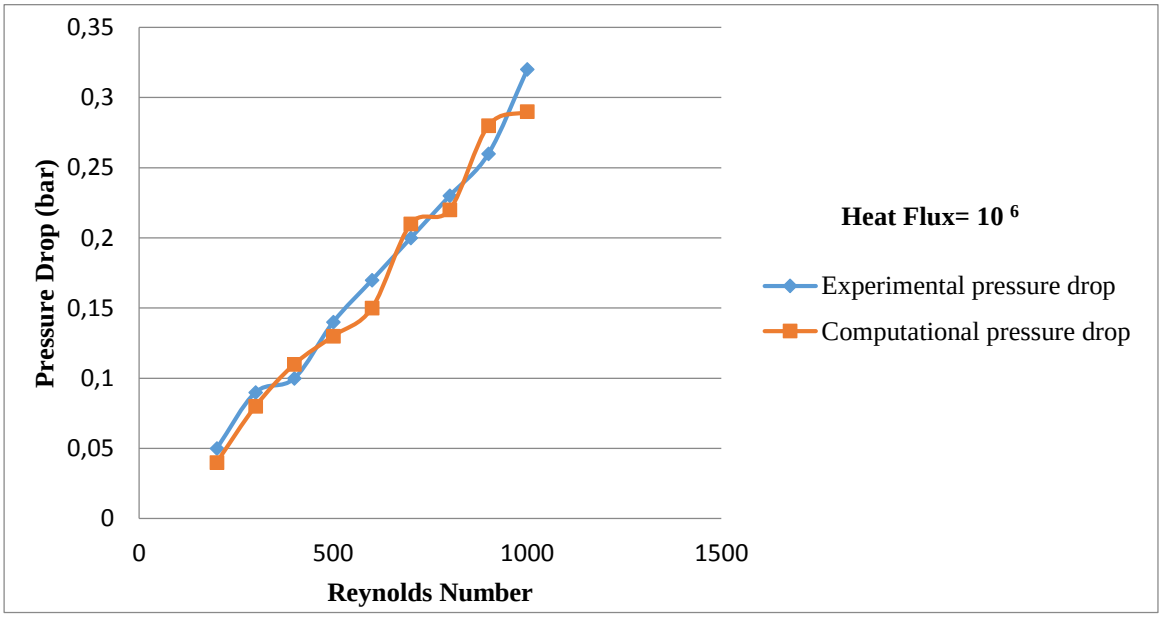


Figure 4. Pressure drop vs Reynolds number for straight rectangular geometry.

A linear relationship is expected between pressure drop and Reynolds number owing to the constant fluid properties. The reason for slope change can be attributed to the temperature dependency of viscosity. For a constant inlet water temperature, the outlet temperature decreases with increase in the Reynold number (Figure 5), which increases water viscosity and hence results in a greater pressure drop.

The trend of graph changes after 600 Reynolds number. This can be attributed to the conversion from the laminar to transition region at 600 Reynolds number, as suggested by Peng and Peterson, [2].

Temperature rise

For further validation the experimental temperature rise is compared with the computational temperature rise. Figure 5 shows the comparison of experimental and numerical temperature rise results for

varying Reynolds numbers. The computational values are found to be in good agreement with the experimental values.

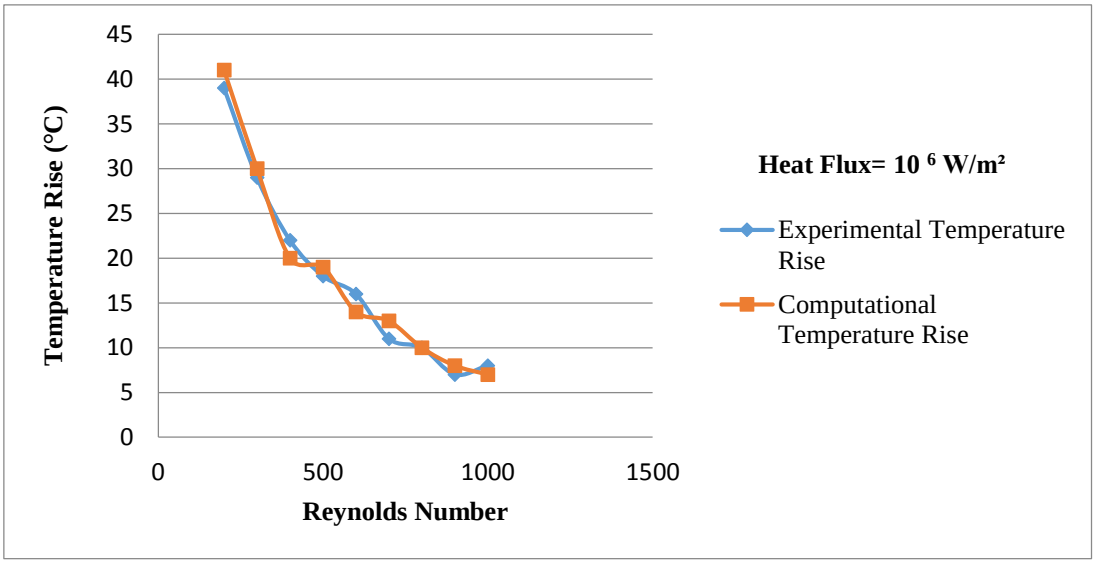


Figure 5. Temperature Rise Vs Reynolds Number for straight rectangular geometry

As expected the heat transfer rate decreases with increase in Reynolds number. But it can be clearly seen that the amount of decrease, falls drastically by increasing the velocity or the Reynolds number. The temperature rise can be given by the following function, [22]: -

$$\text{Temperature rise}: \quad 265.67\ v^{-0.4997} \tag{7}$$

Comparison of Pressure Drop in Two Geometries

Pressure drop across the fluid channel in semi cylindrical projections microchannel heat sink is evaluated using ANSYS CFX package. A comparison is made between the pressure drop in straight micro-channel and semi cylindrical projections micro-channel.

Clearly, as seen from the graph, the pressure drop of water across the fluid channel is found to be greater than that of straight micro-channel for every Reynolds number (200-1000) for constant heat flux of 10^6 W/m^2. The increase in pressure drop is obvious due to the presence of semi cylindrical projections. These projections hinder the fluid flow in the microchannel and hence increase the friction factor. These hindrances lead to a higher pressure loss. The reason for slope change can be attributed to the temperature dependency of viscosity. For a constant inlet water temperature, the outlet temperature decreases with increase in the Reynolds number (Figure 5), which increases water viscosity and hence results in a greater pressure drop. A trend change at Reynolds number 600 can be attributed to the conversion from laminar to transition region, [2].

Comparison of Temperature Rise in Two Geometries

The major goal in this section is to evaluate the temperature rise of water from inlet to outlet in the semi cylindrical projections micro-channel using CFD simulations. Then, an exact comparison is made between the temperature rise in straight micro-channel and semi cylindrical projections micro-channel.

Clearly, as seen from the graph, the temperature rise of water from inlet to outlet in semi cylindrical projections micro-channel is found out to be greater than that of straight micro-channel for every Reynolds number (200-1000) for constant heat flux of 106 W/m2.

The reasons for this behavior are as follows

- The structure analyzed increases the convection heat transfer area.
- This structure interrupts thermal boundary at a regular interval along the flow direction and hence increase the heat transfer.
- Increment in heat transfer can also be attributed to increase in fluid mixing with the help of proposed microchannel structure (semi cylindrical projections).

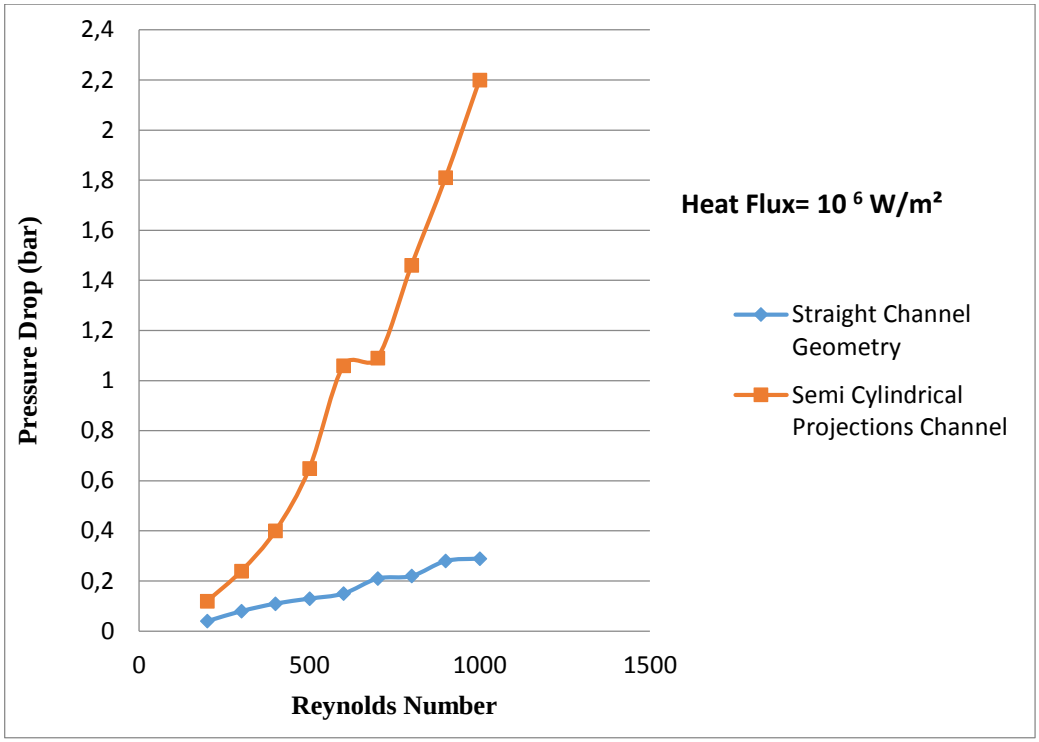


Figure 6. Pressure drop vs Reynolds number comparison of straight and semi cylindrical projections microchannel heat sink

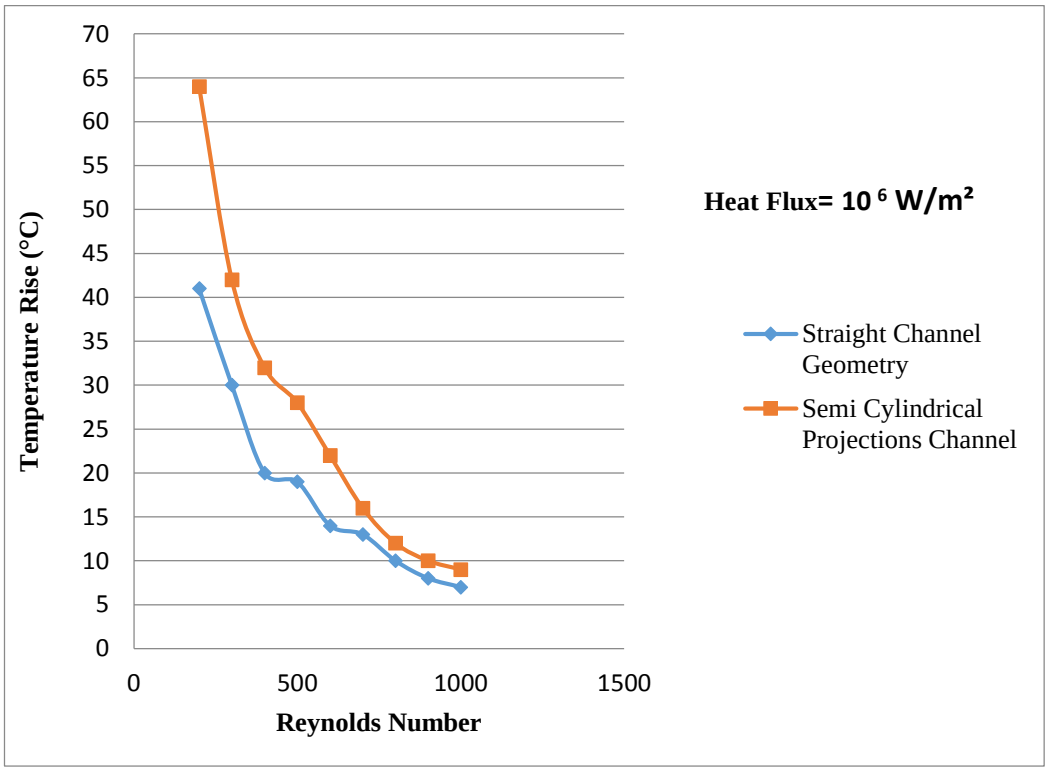


Figure 7. Temperature rise vs Reynolds number comparison of straight and semi cylindrical projections microchannel heat sink

CONCLUSIONS

In this paper, we have investigated, by numerical simulation the conjugate heat transfer problem in a totally new microchannel geometry (semi cylindrical projections) with the assumption of single phase flow. Numerical

analysis of flow properties and heat transfer is conducted and results are laid out. These results are compared with that of a rectangular microchannel heat sink to assess the design of the new geometry. Based on the results following conclusions can be made-

- The heat transfer in semi cylindrical projections microchannel heat sink is greater than that of rectangular microchannel heat sink. This structure increases the convection heat transfer area. It also interrupts thermal boundary layer periodically in the flow direction and hence increases the heat transfer.
- Increment in heat transfer can also be attributed to increase in fluid mixing with the help of proposed microchannel structure (semi cylindrical projections).
- The effect of semi cylindrical projections on pressure drop is obvious and pressure drop increases with increase in Reynolds number. These projections hinder the fluid flow in the microchannel and hence increase the friction factor. These hindrances lead to a higher pressure loss compared to rectangular microchannel heat sink.
- The computational values for heat transfer and pressure drop are found to be in good agreement with that of the experimental values and hence proves that the energy equations can predict the flow and heat transfer characteristics of a microchannel.
- The heat transfer in straight rectangular microchannel heat sink decreases with increase in Reynolds number as the flow velocity increases. The amount of decrease, falls drastically by increasing the velocity.
- The pressure drop in straight rectangular microchannel heat sink increase with increase in Reynolds number. The change in slope can be attributed to the temperature dependency of viscosity of water.

NOMENCLATURE

D_h	Hydraulic Diameter of Channel, [mm]
F	Force, [N]
g	Gravitational Acceleration, [m^2/s]
H	Coefficient of Convective Heat Transfer, [$W/(m^2 K)$]
$H_{channel}$	Height of Channel, [μm]
H_{wall1}	Height of Wall 1, [μm]
H_{wall2}	Height of Wall 2, [μm]
J_j	Diffusion Flux of Species J, [$m^{-2}s^{-1}$]
k_{eff}	Effective Thermal Conductivity, [W/(m K)]
k_t	Turbulent Thermal Conductivity, [W/(m K)]
M	Mass Flow Rate across Channel, [kg/s]
P	Static Pressure, [bar]
Re	Reynolds Number
S_h	Chemical Reaction Heat, [J]
S_m	Mass Added from any user Defined Sources, [kg]
T	Time,[s]
T	Temperature,[K]
V	Average Velocity,[m/s]
$\vec{v}$	Velocity Vector, [m/s]
$W_{channel}$	Width of Channel, [μm]
W_{wall}	Width of Wall, [μm]

Greek Symbols

ρ	Density, [kg/m^3]
μ	Dynamic Viscosity, [kg/(m s)]
τ	Stress Tensor, [N/m^2]

REFERENCES

[1] D.B. Tuckerman, R.F.W. Pease, "High-performance heat sinking for VLSI", IEEE Electron. Dev. Lett. EDL-2 (1981) 126–129.

[2] X.F. Peng, G.P. Peterson, "Convective heat transfer and flow friction for water flow in microchannel structures", Int. J. Heat Mass Transfer 39 (1996) 2599–2608.

[3] A.G. Fedorov, R. Viskanta, "Three-dimensional conjugate heat transfer in the microchannel heat sink for electronic packaging", Int. J. Heat Mass Transfer 43 (2000) 399–415.

[4] I. Mudawar, W. Qu, "Experimental and numerical study of pressure drop and heat transfer in a single-phase micro-channel heat sink", Int. J. Heat and Mass Transfer 45(2002) 2549-2565.

[5] Dong Liu and Suresh V. Garimella, Investigation of Liquid Flow in Microchannels, Journal of Thermophysics and Heat Transfer, 18(2004) pp.65-72.

[6] Sabbah, R., Yagoobi, J., & Hallaj, S. A., Experimental and numerical investigation of heat transfer characteristics of liquid flow with micro-encapsulated phase change material, *ASME Summer Heat Transfer Conference*, 2 (2008) 495-501.

[7] Omar Mokrani, Brahim Bourouga, Cathy Castelain, Hassan Peerhossaini, Fluid flow and convective heat transfer in flat microchannels, Int. J. Heat Mass Transfer 52 (2009) 1337–1352

[8] P. Mohajeri Khameneh et al. A numerical study of single-phase forced convective heat transfer with flow friction in microchannels, International Journal of Engineering 25 (2012) 79-88.

[9] Evgeny V. Rebrov, , Jaap C. Schouten, Mart H.J.M. de Croon Single-phase fluid flow distribution and heat transfer in microstructured reactors, Chemical Engineering Science66(2011)1374-1393.

[10] Gilles Roy, Cong Tam Nguyen, Paul-René Lajoie, Numerical investigation of laminar flow and heat transfer in a radial flow cooling system with the use of nanofluids, Superlattices and Microstructures 35 (2004) 497–511.

[11] Lei Chai, Guo Dong Xia, Hua Sheng Wang, Laminar flow and heat transfer characteristics of interrupted microchannel heat sink with ribs in the transverse microchambers, International Journal of Thermal Sciences 110 (2016) 1-11.

[12] Assel Sakanova, Chan Chun Keian, Jiyun Zhao, Performance improvements of microchannel heat sink using wavy channel and nanofluids, International Journal of Heat and Mass Transfer 89 (2015) 59–74.

[13] Minghai Xu, Hui Lu, Liang Gong, John C. Chai, Xinyue Duan, Parametric numerical study of the flow and heat transfer in microchannel with dimples, International Communications in Heat and Mass Transfer 76 (2016) 348–357 .

[14] Hongtao Wang, Zhihua Chen, Jianguo Gao, Influence of geometric parameters on flow and heat transfer performance of micro-channel heat sinks, Applied Thermal Engineering 107 (2016) 870–879

[15] Thanhtrung Dang, Jyh-tong Teng, Jiann-cherng Chu, Tingting Xu, Suyi Huang, Shiping Jin and Jieqing Zheng (2012). Single-Phase Heat Transfer and Fluid Flow Phenomena of Microchannel Heat Exchangers, Heat Exchangers - Basics Design Applications, Dr. Jovan Mitrovic (Ed.), InTech, DOI: 10.5772/32989.

[16] M.M. Awad, Y.S. Muzychka, Thermodynamic optimization, heat exchangers – basics design applications, in: J. Mitrovic (Ed.), Heat Exchangers – Basics Design Applications, vol. 1, ch. 1, InTech, Rijeka, pp. 3-52, InTech, ISBN 978-953-51-0278-6, 2012.

[17] Mohamed M Awad, A review of entropy generation in microchannels, Advances in Mechanical Engineering 2015, Vol. 7(12) 1–32

[18] S.V. Patankar, A numerical method for conduction in composite materials, flow in irregular geometries and conjugate heat transfer, in: Proceedings of 6th International Heat Transfer Conference, vol. 3, 1978, pp. 297–302.

[19] S.V. Patankar, Numerical Heat Transfer and Fluid Flow, Hemisphere, Washington, DC, 1980.

[20] Yunus A.Cengel, John M.Cimbala, Fluid Mechanics, Third edition, McGraw Hill Education, New York(2013)

[21] Frank M. White, Fluid Mechanics, Seventh edition, McGraw Hill Education (2011)

[22] N. Amanifard, M. Fakhrai, A. Arzpeyma, Y. Mojib and M. Abazare, Numerical Analysis Of Fluid Flow And Heat Transfer In Microchannels, Journal of Applied Mathematics Islamic Azad University Lahijan, Autumn 2004, Page 58-70.

[23] Dongmei Zhou, Timothy Rau, Thermal Design Methodology and Prediction of Heat Sink Performance,

Journal of Thermal Engineering, Yildiz Technical University Press, Istanbul, Turkey Vol. 2, Special Issue 4, No. 4, pp. 826-836, July, 2016.

[24] Erdal Çetkin, Inverted Fins for Cooling of a Non-Uniformly Heated Domain , Journal of Thermal Engineering, Yildiz Technical University Press, Istanbul, Turkey Vol. 1, Issue No. 1, pp. 1-9, January, 2015.

DOI: http://dx.doi.org/10.26483/ijarcs.v8i7.4539

ISSN No. 0976-5697

Volume 8, No. 7, July – August 2017

International Journal of Advanced Research in Computer Science

RESEARCH PAPER

Available Online at www.ijarcs.info

PERFORMANCE EVALUATION OF MLP AND RBF CLASSIFIERS FOR HANDWRITTEN CHARACTER RECOGNITION USING HYBRID FEATURES

Amit Choudhary
Department of Computer Science
Maharaja Surajmal Institute
New Delhi, India

Vinod Kumar
Department of Computer Science and Engineering
Delhi Technological University
Delhi, India

Abstract: For evaluating the accuracy and capability of MLP (Multi Layer Perceptron) and RBF (Radial Basis Function) classifier algorithms; projection profile features for the character images are extracted and are merged with the binarization features after pre-processing every character image, and the combined features thus obtained are used to train both the classifiers (MLP and RBF Network) selected for performing character recognition task. Simulation studies are examined extensively and the proposed hybrid features are found to deliver the recognition accuracy of 93.46% when used with RBF Network as a classifier which is better than the 88.76% accuracy obtained when used with MLP Network as a classifier.

Keywords: OCR, MLP, RBF, Feature Extraction, Projection Profile Features, Hybrid Features

I. INTRODUCTION

In the domain of off-line handwriting recognition, an (ANN) Artificial Neural Network became very popular in the late 70s and emerged as fast and most reliable classifier tool resulting in excellent recognition accuracy. The accuracy of the OCR System in recognizing the off-line handwritten character mainly depends on the selection of feature extraction technique and the classification algorithm employed. The motive behind this work is to compare the handwritten character recognition accuracy of the Multi-layered Perceptron (MLP) and Radial Basis Function Neural Network (RBFNN) classifiers trained with Hybrid Features (Fusion of Binarization and Projection Profile) extracted from the input character samples [1].

Both Multi-layered Perceptron (MLP) and Radial Basis Function (RBF) networks are basically non-linear layered feed forward networks. These networks work as universal approximators. RBF Neural Network is also a type of MLP but with Radial Basis as the activation function in the hidden layer neurons. It is therefore not surprising to find that there always exists an RBF network capable of accurately mimicking a specified MLP or vice versa [1, 2].

MLP may require a smaller number of parameters than the RBF network for the same degree of accuracy. But RBF Network is capable of implementing arbitrary non-linear transformations of the input space as illustrated by the XOR problem, which cannot be solved by any linear perceptron but can be solved by the RBF Network. Hence, the choice of the classifier lies in the problem domain. For different types of pattern classification activities, one neural network as a classifier may be proved to be superior to the other. In this paper, the superiority of the two classifiers is judged for the task of handwritten character recognition.

II. FEATURE EXTRACTION USING BINARIZATION TECHNIQUE

Feature extraction is a process of studying and deriving useful information from the filtered input patterns. The derived information can be general features, which are evaluated to ease further processing. The selection of features is very important because there might be only one-two values, which are significant to recognize a particular character. The performance of the recognition system relies much on the quality of the features extracted as well as on the selected classifier itself [2,3].

The network is trained with 50 samples of handwritten characters where each sample has 26 characters (a-z). In the proposed experiment, 1300 (50×26=1300) handwritten characters have been involved.

After preprocessing of the handwritten character images, the features are extracted by using binarization technique for each character image from the local database of handwritten characters. As all the handwritten character images are resized to 15 × 12 (in order to make all the character images of uniform size), the feature vector of a single character is a column vector of size 180 × 1.

The binary image of character ‘c’, the resized image, Matrix representation of character ‘c’ and the feature vector of character ‘c’ are shown in Fig.1. As there are 26 characters, all the 26 feature vectors are combined to form a sample which is a binary matrix of size 180 × 26 as shown in Fig.2.

© 2015-19, IJARCS All Rights Reserved

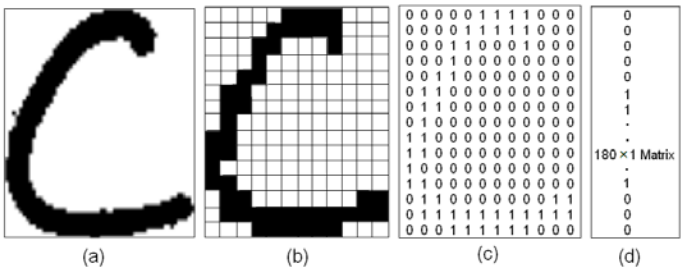


Figure 1. (a) Binary Image of Character 'c' (b) Resized Binary Image of Character 'c'; (c) Binary Matrix representation and (d) Reshaped Binary Matrix or Feature Vector of Character 'c'.

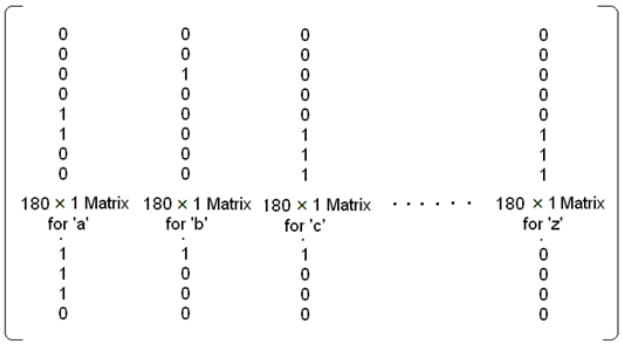


Figure 2. Matrix representation of Input Sample

The number of neurons in the input and output layers are fixed at 180 and 26 respectively. The 180 input neurons are equivalent to the input character's size as every character is resized into a binary matrix of size 15 × 12 and then reshaped to a matrix of size 180 × 1. The number of neurons in the output layer is 26 because there are 26 English alphabets. The number of neurons for the MLP classifier is kept 80, by trial and error method, for optimal result.

III. FEATURE EXTRACTION USING PROJECTION PROFILE

Projection profile features in vertical, horizontal, left diagonal and right diagonal orientations to represent a character 'c' are shown in Fig.3. Projection features in the vertical direction is computed by tracing the character image column wise along the y-axis and counting the number of black pixels in each column. As the entire digit images are resized into 15×12 pixels, there are 12 columns and 15 rows [3].

Hence, the vertical projection profile will contain 12 values, each value representing the sum of number of all black pixels present in that particular column as shown in Fig.3(a). Similarly, for horizontal projection profile, character image is traced horizontally along the x-axis. The row wise sum of number of black pixels present in each row will constitute the 15 values of horizontal projection profile as shown in Fig.3(b). Left diagonal projection profile is computed by traversing the character image along the left diagonal as shown in Fig.3(c). The black pixels are counted in left diagonal direction and the sum of the number of black pixels for each left diagonal line of traversing generates 26 values representing the left diagonal projection profile. In the same way, 26 values representing the right diagonal projection profile are obtained by adding the number of black pixels in each right diagonal line of traversing as shown in Fig.3 (d).

Projection profile values obtained in all the four orientations are combined to form a single feature vector [2,4]. The length of this feature vector is 79 (12+15+26+26=79). As explained in Fig.3, a feature vector representing the character 'c' is obtained by concatenation of these four set of features and can be shown as:

{4 8 5 5 4 4 4 4 5 1 2 2
4 5 3 1 2 2 2 1 2 2 1 2 4 11 6
0 0 0 0 0 3 6 5 5 3 3 1 1 1 2 1 1 2 2 2 2 2 3 2 1 0
0 0 0 1 2 3 2 1 1 1 1 1 2 3 2 3 2 3 3 4 3 5 4 1 1 0}

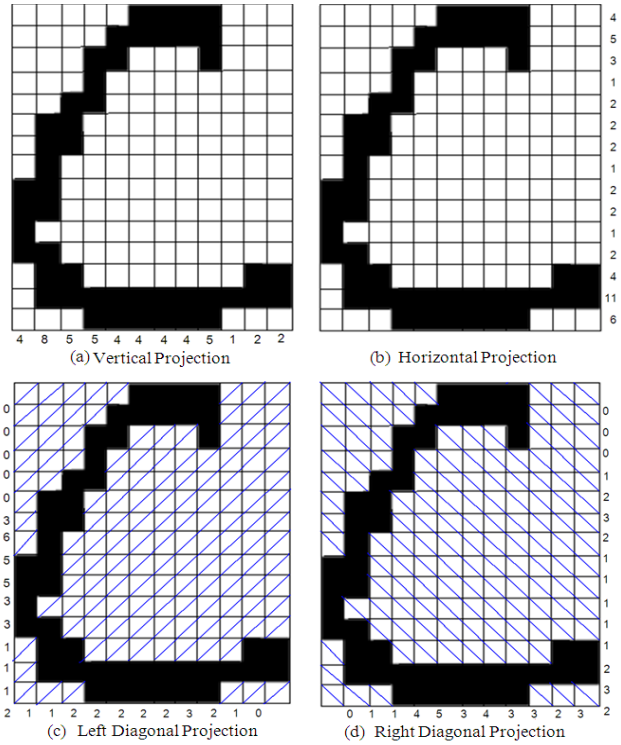


Figure 3. Projection Features of character 'c' in vertical, horizontal, left diagonal and right diagonal Orientations.

This projection profile feature vector of character 'c' can be represented in the form of a column matrix as shown in Fig.4.

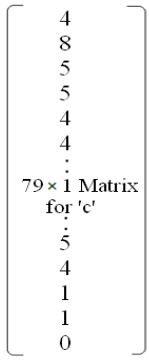


Figure 4. The Projection Feature Vector of Character 'c'.

The projection feature vectors of all the 26 characters (a-z) are created in the form of column matrix of size 79×1 each [3]. All these 26 feature vectors are combined to form a sample which is a binary matrix of size 79×26.

© 2015-19, IJARCS All Rights Reserved

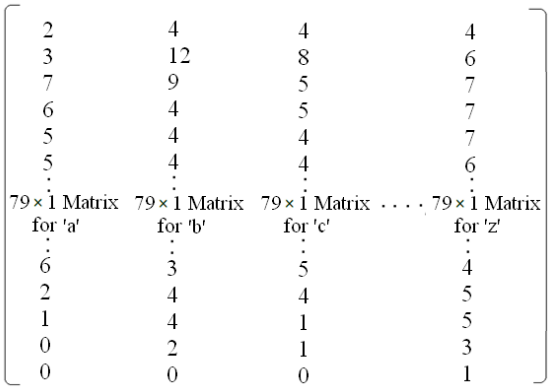


Figure 5. Matrix Representation of Input Training Sample of Size 79×26.

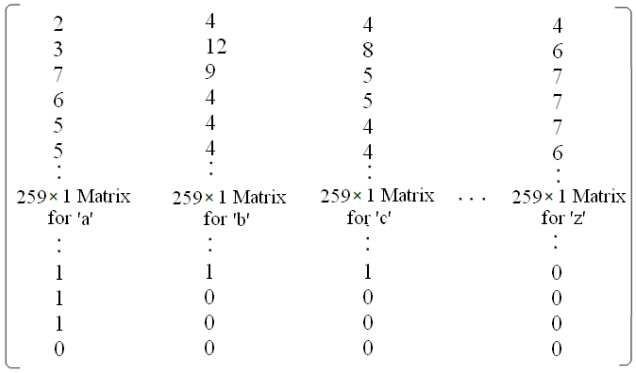


Figure 7. Input Sample Created by Fusion of Binarization and Projection Features.

IV. SAMPLE PREPARATION USING HYBRID FEATURES EXTRACTION

The feature vectors of each individual character using binarization and projection profile are combined. The process of combining involves the concatenation of the two feature vectors in such a way that the projection feature vector is appended at the end of the binarization feature vector. The combined feature vector is termed as "Hybrid Feature Vector" [4, 5]. The process is repeated for all the characters in the character database. The hybrid feature vector for character 'c' obtained by fusion of binarization and projection feature vectors is shown in Fig.6.

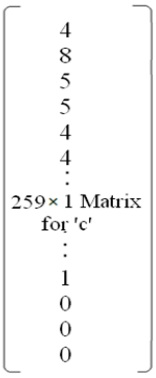


Figure 6. Hybrid Feature Vector of Character 'c'.

It can be observed that the length of the hybrid feature vector is 259 as the projection feature vector of length 79 is appended at the end of the binarization feature vector of length 180 [3].

The hybrid feature vectors of all the 26 characters (a-z) are created in the form of column matrix of size 259×1 each [8]. All these 26 feature vectors are combined to form a sample which is a binary matrix of size 259×26 as shown in Fig.7.

V. IMPLEMENTATION AND DISCUSSION OF RESULTS

MLP neural network classifier has been trained with 50 sets of each character i.e. 1300 (50×26=1300) character image samples from the database has been involved in the training. Each character at the input will put a '1' at that neuron in the output layer in which the maximum trust is shown and rest neuron's result into '0' status. The output of both the network classifiers is binary matrix of size 26×26 each because there are 26 characters and every character has 26×1 output vector. The first 26×1 column stores the first character's recognition output; the following column will be for next character and so on for the whole sample [3].

During recognition, the confusion among the different characters is explained in Fig.8. Character 'a' is presented 50 times to the neural network and is classified 46 times correctly. It is miss-classified four times as 'o'. Character 'b' is classified 50 times correctly. Character 'c' is misclassified as 'e' two times and one time each as 'o' and 'u' and is classified correctly 46 times. The average recognition accuracy of 88.76% is quiet good for this handwritten character recognition experiment using MLP as a classifier [3, 6, 7].

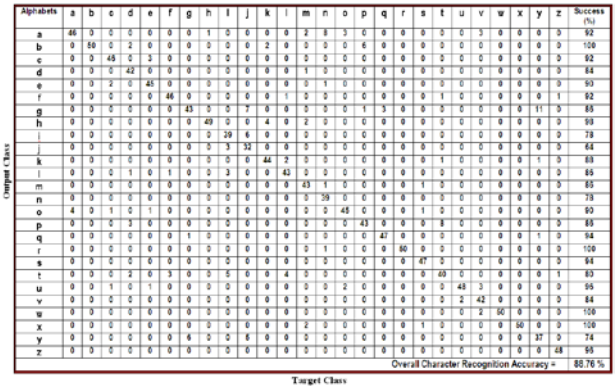


Figure 8. Confusion Matrix representing the MLP Classifier Performance using Hybrid Features.

© 2015-19, IJARCS All Rights Reserved

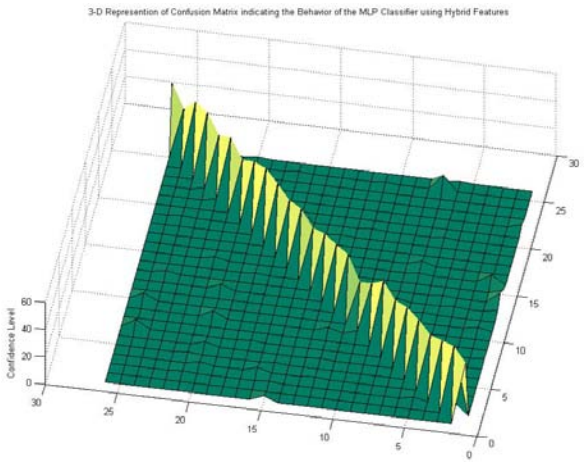


Figure 9. Three-Dimensional Plot of Confusion Matrix representing the MLP Behavior.

The RBF neural network has also been trained with 50 sets of each character i.e. 1300 (50× 26=1300) character image samples from the database. Character 'a' is presented 50 times to the neural network and is classified 49 times correctly. It is miss-classified one times as 'o'. Character 'j' is classified 42 times correctly and misidentified as character 'i' four times and two times each as character 'g' and 'y' out of a total of fifty trials. Recognition accuracy for each character (a-z) as well as overall recognition accuracy is displayed in Fig.10. The average recognition accuracy of 93.46 % is excellent for this handwritten character recognition experiment using RBF as a classifier.

The recognition results obtained when MLP and RBF network classifiers are used to recognize the handwritten characters using Hybrid Features (features extracted from fusion of binarization and projection features) are shown in the form of confusion matrices as shown in Fig.8 and Fig.10 respectively. The confusion matrix shows the confusion among the recognized characters while testing the neural network's recognition accuracy [6, 7]. The respective equivalent 3-D plots drawn in the 'MATLAB Environment' are also shown in Fig.9 and Fig.11 respectively.

Alphabets	a	b	c	d	e	f	g	h	i	j	k	l	m	n	o	p	q	r	s	t	u	v	w	x	y	z	Success (%)
a	49	0	0	0	0	0	0	1	0	0	0	0	0	2	1	0	0	0	0	0	0	3	0	0	0	0	98
b	0	50	0	1	0	0	0	0	0	0	1	0	0	0	0	4	0	0	0	0	0	0	0	0	0	0	100
c	0	0	48	0	0	0	0	0	0	0	0	0	0	0	0	0	0	0	0	0	0	0	0	0	0	0	96
d	0	0	0	47	0	0	0	0	0	0	0	0	0	0	0	0	0	0	0	0	0	0	0	0	0	0	94
e	0	0	0	0	48	0	0	0	0	0	0	0	1	0	0	0	0	0	0	0	0	0	0	0	0	0	96
f	0	0	0	0	0	46	0	0	0	0	0	1	0	0	0	0	0	0	0	1	0	0	0	0	0	0	92
g	0	0	0	0	0	0	48	0	0	2	0	0	0	0	0	1	0	0	0	0	0	0	0	0	0	0	96
h	0	0	0	0	0	0	0	49	0	0	1	0	0	2	0	0	0	0	0	0	0	0	0	0	0	0	98
i	0	0	0	0	0	0	0	0	43	4	0	0	0	0	0	0	0	0	0	0	0	0	0	0	0	0	86
j	0	0	0	0	0	0	0	0	3	42	0	0	0	0	0	0	0	0	0	0	0	0	0	0	0	0	84
k	0	0	0	0	0	0	0	0	0	0	48	0	0	0	0	0	0	0	0	1	0	0	0	0	1	0	96
l	0	0	0	1	0	1	0	0	3	0	0	47	0	0	0	0	0	0	0	0	0	0	0	0	0	0	94
m	0	0	0	0	0	0	0	0	0	0	0	0	46	1	0	0	0	1	0	0	0	0	0	0	0	0	92
n	0	0	0	0	0	0	0	0	0	0	0	0	0	48	0	0	0	0	0	0	0	0	0	0	0	0	96
o	1	0	1	0	1	0	0	0	0	0	0	0	0	0	47	0	0	1	0	0	0	0	0	0	0	0	94
p	0	0	0	0	0	0	0	0	0	0	0	0	0	0	0	48	0	0	0	0	0	0	0	0	0	0	96
q	0	0	0	0	0	0	1	0	0	0	0	0	0	0	0	0	47	0	0	0	0	0	0	0	1	0	94
r	0	0	0	0	0	0	0	0	0	0	0	0	1	0	0	0	0	50	0	0	0	0	0	0	0	0	100
s	0	0	0	0	0	0	0	0	0	0	0	0	0	0	0	0	0	0	47	0	0	0	0	0	0	0	94
t	0	0	0	1	0	2	0	0	1	0	0	2	0	0	0	0	0	0	0	43	0	0	0	0	0	1	86
u	0	0	1	0	1	0	0	0	0	0	0	0	0	0	2	0	0	0	0	0	48	0	0	0	0	0	96
v	0	0	0	0	0	0	0	0	0	0	0	0	0	0	0	0	0	0	0	0	0	42	0	0	0	0	84
w	0	0	0	0	0	0	0	0	0	0	0	0	0	0	0	0	0	0	0	0	0	0	50	0	0	0	100
x	0	0	0	0	0	0	0	0	0	0	0	0	2	0	0	0	0	1	0	0	0	0	0	50	0	0	100
y	0	0	0	0	0	0	4	0	0	2	0	0	0	0	0	0	0	0	0	0	0	0	0	0	44	0	88
z	0	0	0	0	0	0	0	0	0	0	0	0	0	0	0	0	0	0	0	0	0	0	0	0	0	49	98
																											Overall Character Recognition Accuracy = 93.46 %

Output Class

Target Class

Figure 10. Confusion Matrix representing the RBF Network Performance using Hybrid Features.

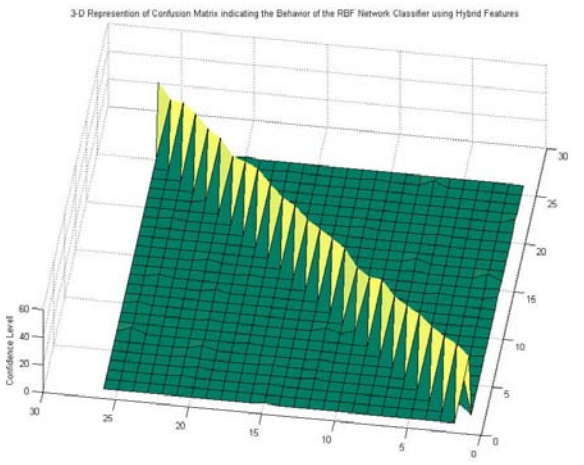


Figure 11. Three-Dimensional Plot of Confusion Matrix representing the RBF Network Behavior.

VI. CONCLUSION

The recognition accuracy of a classifier system mainly depends on the quality of training samples, the techniques employed to extract features and the type of the classifier involved. The proposed method of fusion of character features obtained from binarization and projection profile techniques showed the remarkable enhancement in the performance for the handwritten character recognition using the MLP and RBF network classifiers. By using Hybrid features, the excellent character recognition accuracy of 88.76% and 93.46% is achieved for MLP and RBF classifier respectively.

VII. REFERENCES

[1] S. N. Sivanandam, S. N. Deepa," Principals of Soft Computing", pp. 71–83. Wiley-India,

[2] A. Choudhary, R. Rishi, S. Ahlawat, "Unconstrained Handwritten Digit OCR Using Projection Profile and Neural Network Approach". In: Proceedings of the InConINDIA 2012. AISC, vol. 132, pp. 119–126. Springer, Heidelberg, 2012.

[3] A. Choudhary, R. Rishi, "A Fused Feature extraction approach to OCR : MLP vs. RBF" in: ICT and Critical Infrastructure - Proceedings of the 48th Annual Convention of CSI, CSI-2013 Vol.1 pp. 159-166, 2013

[4] A. Choudhary, R. Rishi, S. Ahlawat, "A New Character Segmentation Approach for Off-Line Cursive Handwritten Words". Elsevier Procedia Computer Science 17, pp. 434–440, 2013.

[5] U. Bhattacharya, B. B. Chaudhuri, "A Majrity voting scheme for multiresolution recognition of handprinted numerals". in Seventh International Conference on Document Analysis and Recognition (ICDAR), vol. 1, p. 16, 2003.

[6] A. Choudhary, R. Rishi, "Improving the Character Recognition Efficiency of Feed Forward BP Neural Network". International Journal of Computer Science and Information Technology (IJCSIT), vol. 3(1), pp. 85–96, 2011.

[7] A. Choudhary, R. Rishi, S. Ahlawat, "Handwritten Numeral Recognition Using Modified BP ANN Structure". in: CCSIT 2011, Part III. CCIS, vol. 133, pp. 56–65, 2011.

[8] A. A. Desai, "Gujarati Handwritten Numeral Optical Character Recognition through Neural Network". Pattern Recognition, vol. 43(7), pp. 2582–2589, 2010.

© 2015-19, IJARCS All Rights Reserved

AIChE

Performance Evaluation of the Supercritical Organic Rankine Cycle (SORC) Integrated with Large Scale Solar Parabolic Trough Collector (SPTC) System: An Exergy Energy Analysis

Harwinder Singh and R.S. Mishra

Department of Mechanical, Production and Industrial, Automobile engineering, Delhi Technological University, Bwana Road, New Delhi, 110042, India; harrymehrok14@gmail.com (for correspondence)

Published online 00 Month 2017 in Wiley Online Library (wileyonlinelibrary.com). DOI 10.1002/ep.12735

In this article, exergy and energy analysis of supercritical organic Rankine cycle integrated with solar parabolic trough collector (SPTC) is presented. Proposed working fluids are R600a, Toluene, R152a, isobutene, and cyclohexane for the supercritical ORC. Performance parameters including exergy efficiency, rate of exergy destruction, improvement potential, fuel depletion ratio, irreversibility ratio and expansion ratio were also examined in this study. The results of the study demonstrate that exergy efficiency increases continuously as both the solar irradiation intensity and inlet pressure of turbine increases, and R600a gives the maximum exergy efficiency among the others, i.e. around 96.09% at $G_B = 0.95$ kW/m^2 and 94.37% at 17 MPa. In addition, the exergy destruction rate decreases continuously with the increase in solar irradiation intensity as well as inlet pressure of the turbine, and it has been observed that the maximum exergy destruction rate occurs in the solar collector, which is around 80% of the total exergy destruction rate of combined SPTC-SORC. Nonetheless, R600a has the minimum value of the exergy destruction rate, i.e., 1527 kW at $G_B = 0.5$ kW/m^2. Alternatively, cyclohexane shows a maximum exergy destruction rate, which is around 3794 kW at $G_B = 0.5$ kW/m^2. Also, SORC turbine and recuperator have a countable value of the exergy destruction rate. Finally, this study revealed that exergetic parameters like improvement potential, fuel depletion ratio and irreversibility ratio are found to be 11,859 kW, 0.579, and 0.9296 for the parabolic trough collector in the combined R600a based SPTC-SORC system. © 2017 American Institute of Chemical Engineers Environ Prog, 00: 000–000, 2017

Keywords: supercritical ORC, SPTC, exergy efficiency, exergy destruction rate, organic fluids

INTRODUCTION

Utilization of renewable energy has become pivotal and it enhances significantly day by day. Consequently, the requirement to improve the performance of renewable energy based power plants also increases. In this direction, among the available other renewable power technologies, the solar parabolic trough collector (SPTC) is the most prominent and promising way to meet the electricity demand because of its high commercial performance and reliability characteristics. In this study, SPTC system is used because it is highly efficient and acceptable according to the Indian sunny climate, i.e., available solar energy potential in the country is 20 MW/km^2 and the incoming solar intensity is 6 kwh/m^2/day [1]. In addition, SPTC based electricity generation systems are well established and commercialized all over the earth in the past twenty years [2]. Gao et al. [3] analyzed the performance of solar based organic Rankine cycle through the various working conditions like inlet pressure and temperature of the turbine. They concluded that with an increase in the inlet temperature, the efficiency also increases and at above the critical temperature, thermal efficiency increases with the increase in inlet pressure. Finally, their findings demonstrate that MM (hexamethyldisiloxane, $C_6H_{18}OSi_2$) working fluid can retain its thermal stability at 300°C and on the basis of thermal efficiency; MM working fluid is the optimal choice among the other working fluids. Bamgbopa and Uzgoren [4] developed a transient model for a simple ORC using R245fa as the working fluid, and they analyze that the critical part of the model is a heat exchanger. In another study, Mazurek et al. [5] analyzed the performance of R245fa based ORC powered by solar energy, and they concluded that the maximum thermodynamic efficiency comes out to be 97% with heat regenerator. Conversely, Gang Pei et al. [6] examined the performance of ORC incorporated with solar thermal device, and they found that the overall electrical efficiency is around 8.6% with solar irradiation of 750 W/m^2.

Furthermore, some studies in the area of cogeneration or trigeneration process with the help of solar integrated ORC also introduced in the recent years. Delgado-Torres et al. [7] analyzed the performance of ORC connected with SPTC and an RO unit for the production of both pure water and electricity, and this study further extended to examine the effect of different organic fluids on an aperture area of the collector. In another study, Al-Sulaiman et al. [8] conducted a thermodynamic analysis of the SPTC integrated with ORC, in which waste heat from the ORC was utilized for the cogeneration process. Finally, they found the improvement in

© 2017 American Institute of Chemical Engineers

energy efficiency, i.e., increases from 15% to 94% during trigeneration. In addition, Tunc et al. [9] performed an exergetic analysis of ORC driven by a single flash geothermal power plant. They selected four different working fluids like isobutane, HCFC123, R134a, and R12 are used to compare the thermal efficiency of the ORC, and finally they conclude that isobutane gives the maximum thermal efficiency and electric power, i.e., around 30% and 6626 kWe.

Other applications of the ORC, Wang and Dai [10] utilized the waste heat recovered by organic Rankine cycle (ORC) integrated from recompression supercritical CO_2 Brayton cycle to generate electric power, and they also performed an exergy-economic analysis by using R123, R245fa, Toluene, isobutane, isopentane, and cyclohexane as a working fluid for the ORC. Finally, they concluded that the total product unit cost of the SCO_2/ORC combined cycle is very less. Kalra et al. [11] analyzed that the working fluid in SORC lies under and above its critical pressure, and they mentioned that supercritical ORC (SORC) has many advantages over the subcritical ORC because in SORC, the cooling curve of heat source match with a heating curve of the working fluid. Furthermore, Chen et al. [12] formulated that the heating process of a SORC does not pass through the different two-phase region like in subcritical ORC, which results in a better thermal match in the evaporator and less irreversibilities occur in the SORC. In different study, Pan et al. [13] found that supercritical ORC (SORC) oftenly selected when critical temperature of the working fluid is extremely lower than the heat source temperature and Also, they mentioned that both supercritical and subcritical ORC are feasible when critical temperature of the working fluid is slightly lower than the heat source temperature. Furthermore, Quan et al. [14] performed an exergetic performance analysis of the direct vapor generation (DVG) SORC system, which is driven by a linear Fresnel reflector (LFR) concentrator and finally, their results demonstrate that the integrated SORC and DVG technology decreases both the irreversibility at evaporator and heat losses along with the cost of system, and thus, enhances the overall efficiency of SORC. Cheng Zhou [15] analyzed that the thermodynamic performance of a hybrid plant using a SORC exceeds than the hybrid plant using a subcritical ORC in term of electricity production. Yağlı et al. [16] compared the exergetic and thermal performance of a R245fa based subcritical and supercritical ORC for the recovery of exhaust waste gas heat of the combined heat and power engine, which is fuelled by biogas. Their results revealed that supercritical ORC has the best performance in the terms of exergy efficiency, thermal efficiency and net power, which is around 27.76%, 15.93%, and 81.52 kW as compared to 27.20%, 15.51%, and 79.23 kW for the subcritical ORC.

Additionally, few studies consider the different optimization methods to enhance the performance of ORC. In this way, Rashidi et al. [17] performed a parametric study and optimization of the ORC with two feed water heater by using artificial neural network (ANN) and artificial bees colony (ABC). Finally, they optimized the selected objective functions such as thermal efficiency, exergy efficiency, and specific work of R717 based ORC. In a different study, they optimized the same objective functions for the four different working fluids based transcritical power cycle with the help of ANN and genetic algorithms (GAs), and they found that R125 has the best thermal efficiency and R32 shows the greatest net work output among the others [18]. In another study, they proposed a procedure based on ANN and particle swarm optimization (PSO) algorithm for the reduction in entropy generation value. Also, they utilized the optimal homotopy analysis method (HAM) and differential transform method (DTM) to study the laminar viscous flow of a conducting fluid in a semi porous channel [19,20].

After reviewing a lot of literature work related to the field of ORC, it was observed that there is no detailed exergetic analysis has been conducted on the large scale solar parabolic trough collectors integrated with SORC. Therefore, the current study is original and the objective of the current study is to examine the exergetic performance of the SORC driven by large-scale solar parabolic trough collectors (SPTCs) along with the exergetic performance parameters such as exergetic efficiency, rate of exergy destruction, improvement potential, fuel depletion ratio, irreversibility ratio as well as expansion ratio. The proposed working fluids for the SORC are R600a, Toluene, R152a, isobutene, and Cyclohexane, respectively.

SYSTEM DESCRIPTION

Organic Rankine cycle (ORC) has an uncomplicated structure with small cost, and also a promising technology for the utilization of low-temperature heat sources including geothermal, solar thermal like CSP and waste heat. The benefit of such expertise is that with the critical condition of organic working fluid, the system can be easily operated at the lower pressure and temperature. The supercritical organic Rankine cycle also has many advantages like simple configuration, higher efficiency and excellent thermal match with a heating source, etc. In SORC system, radial inward flow turbine is the prominence option and lower flow ratio with large pressure ratio in the turbine makes them attractive [21]. The basic concept of the SORC incorporated with solar parabolic trough collectors as shown in the Figure 1. Few hundred collector rows with each of ten modules are included in the field of solar parabolic trough collectors. The geometrical features of the selected solar collector (LS-3) as described in Table 1. The maximum exit temperature of the solar collector is 663 K and the selected working fluid is TherminolVP-1 due to its better thermo-physical properties [22,23]. Selected mass flow rate of the heat transfer fluid is 0.575 kg/s and the selected pinch point temperature of the evaporator is 10 K [24].

MATHEMATICAL MODELLING FOR THE SYSTEM

The modelling of the SPTC integrated SORC system present in this section. First, the exergy modelling of SPTC and then the modelling of SORC system presented below. Exergy analysis of the SPTC system along with important exergetic parameter's equations for exergy balance of component, physical exergy, exergy destruction rate, exergy efficiency, fuel depletion ratio, irreversibility ratio and improvement potential are derived from the previous research or literature [24–27]. For the analysis, exergy inlet is a crucial term and the calculated value for the total exergy inlet from the overall solar collector field is around 20,560 kW. Some assumptions in the study are also made that change in the pressure is negligible except in the case of pump and turbine.

Rate of useful energy gain by SPTC per unit time is described as below:

$$\dot{Q}_u = \dot{m}_r \mathrm{Cp}_r (T_{ro} - T_{ri}) \tag{1}$$

Where $\dot{m}_r$ is the mass flow rate of working fluid in the receiver tube, Cp is the specific heat, subscripts ro and ri refers to the outlet and inlet of the receiver tube. Further another relation for useful heat gain is shown as below i.e.,

$$\dot{Q}_u = A_{ap} F_R \left(S - \frac{A_r}{A_{ap}} \mathrm{Ul}(T_{ri} - T_o) \right) \tag{2}$$

$$A_{ap} = (W - D_{co}) * L \tag{3}$$

$$S = \rho_r \alpha \gamma \tau K_m \mathrm{GB} \tag{4}$$

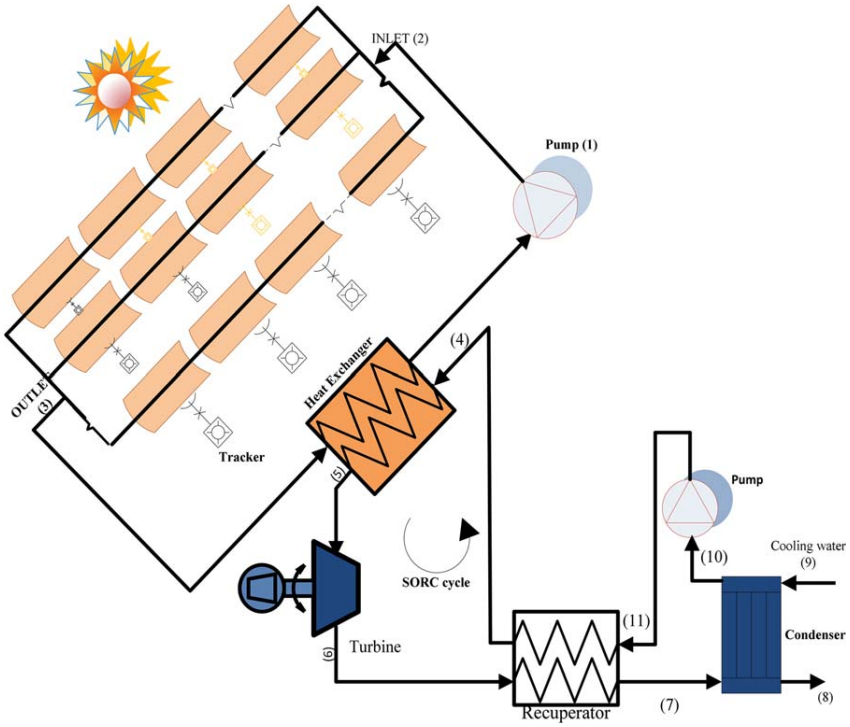


Figure 1. Schematic of the solar parabolic trough collectors integrated with SORC. [Color figure can be viewed at **wileyonlinelibrary.com**]

Where $A_r = \pi D_O L$, F_R is the collector heat removal factor, U_l is the overall heat loss coefficient, A_{ap} is the area of aperture, S is total solar flux absorbed by receiver, T_o is the ambient temperature, W is width of collector, D_{co} is the outer diameter of cover, L is the length of collector, ρ_r is reflectance of the mirrors, α is absorbance of tube, γ is intercept factor, τ is transmittance of glass cover, K_m is incident angle modifier, and G_B is the direct solar irradiation intensity. All the necessary data related to these parameters are listed in Table 1. Further, heat removal factor and collector efficiency factor are defined as under:

$$F_R = \frac{\dot{m}_r C_{Pr}}{\pi D_{r,o} L U_l}\left(1-\exp\left(-\frac{F\pi D_{r,o} U_l L}{\dot{m}_r C_{Pr}}\right)\right) \tag{5}$$

$$F = \frac{U_o}{U_l} \tag{6}$$

Where U_o is the overall heat loss coefficient between ambient and the fluid flowing through receiver and U_l is the heat loss coefficient of solar collector between ambient and receiver tube of the SPTC is defined as under:

$$U_o = \left[\frac{1}{U_l} + \frac{D_{r,o}}{h_{cr,i} D_{r,i}} + \left(\frac{D_{r,o}}{2K_r}\ln\left(\frac{D_{r,o}}{D_{r,i}}\right)\right)\right]^{-1} \tag{7}$$

$$h_{cr,i} = \frac{Nu_r k_r}{D_{r,i}} \tag{8}$$

$$U_l = \left[\frac{A_r}{(h_{con,amc}+h_{rad,amc})A_c} + \frac{1}{h_{rad,cr}}\right]^{-1} \tag{9}$$

$$h_{con,amc} = \frac{\mathrm{Nu} * K_{air}}{D_c} \tag{10}$$

$$h_{rad,amc} = {}_c\sigma\left(T_c^2 + T_o^2\right)T_{co} + T_o) \tag{11}$$

$$h_{rad,cr} = \frac{\sigma\left(T_c + T_{r,avg}\right)\left(T_c^2 + T_{r,avg}^2\right)}{\frac{1}{{}_r} + \frac{A_r}{A_c}\left(\frac{1}{{}_c} - 1\right)} \tag{12}$$

Where subscripts "r", "o", "avg," and "c" refers to the receiver, ambient, average and cover, $h_{cr,i}$ is the heat loss coefficient between receiver and glass cover, $h_{con,amc}$ is the convective heat loss coefficient between ambient and glass cover, $h_{rad,amc}$ is the radiation heat loss coefficient and $h_{rad,cr}$ is the radiation heat loss coefficient between receiver and glass cover, K_{air} is thermal conductivity of air, Nu is nusselt number, σ is Stefan–Boltzmann constant, ${}_c$ is emittance of the glass cover, and ${}_r$ is emittance of the receiver. Now, the temperature of the glass cover and total amount of solar flux or total heat available for the SORC system can be calculated by using the equation as shown below:

$$T_c = \frac{h_{rad,cr} T_r + \frac{A_c}{A_r}\left(h_{con,amc}+h_{rad,amc}\right)T_o}{h_{rad,cr} + \frac{A_c}{A_r}\left(h_{con,amc}+h_{rad,amc}\right)} \tag{13}$$

$$\dot{Q}_{solar} = F_R \mathrm{SCo_s Co_p} \tag{14}$$

$$\eta_{SPTC} = \left(\frac{\dot{Q}u}{G_B \mathrm{WL}}\right) \tag{15}$$

Where $\mathrm{Co_s and Co_p}$ is the total number of collectors per row in series as well as in parallel combination, η_{SPTC} is the efficiency of solar collector, W is the width of mirror, and L is the length of SPTC mirrors field.

In this article, the performance of SORC integrated with SPTC is studied and the configuration of a cycle as shown in Figure 1. In the SORC, working fluid at high critical pressure

and critical temperature is expanded in the radial inward flow turbine up to low temperature, and then stream goes to the condenser, feed pump and heat exchanger (evaporator) unit.

The term exergy is defined as the maximum theoretical useful works that can be obtained from the system as it interacts to the surrounding. Therefore, the steady state exergy balance of the control volume of each component in SORC is defined as under.

Table 1. Input data adapted for the system [24,33].

Solar parabolic collectors
Collector row length 500 m
Collector type LS-3
Collector width 5.76 m
Collector length (single) 12.27 m
Inner diameter of absorber tube 0.06 m
Outer diameter of absorber tube 0.07 m
Inner diameter of cover 0.115 m
Outer diameter of cover 0.121 m
Emittance of the cover 0.86
Emittance of the absorber tube 0.15
Reflectance of mirror 0.94
Intercept factor 0.93
Transmittance of glass cover 0.96
Absorbance of absorber tube 0.96
Intensity of direct irradiation 0.5–0.9 kW/m^2
Incidence angle modifier 1
Maximum outlet temperature 663K
Ambient conditions
Ambient temperature 298.15K
Ambient pressure 101.3 kPa
SORC cycle configuration
SORC pump efficiency 85%
SORC turbine efficiency 87%
Mass flow rate of SORC cycle 0.1 Kg/s
Minimum pinch point temperature 5^{0}C
SORC cycle high pressure 25 MPa
Recuperator effectiveness 95%
Min. Temperature of SORC 55^{0}C
Heat exchanger effectiveness 95%

$$\sum_{R}\left(1-\frac{T_o}{T_R}\right)\dot{Q}_R-\dot{w}_{c.v.}-\sum_{i}\dot{m}_i ex_i-\sum_{e}\dot{m}_e ex_e-\dot{Ex}_d=0 \quad (16)$$

Where subscripts "O" and "R" refers to the value of physical property at surrounding and particular state, $\dot{E}x_d$ is the rate of exergy destruction, "ex" is the exergy per unit mass flow rate, and subscripts "e" and "i" refers to the exit and inlet state, respectively. Now, physical exergy per unit mass flow rate (ex^{ph}) after neglecting the change in both velocity and datum head is mentioned as below.

$$ex^{ph}=(h-h_o)-T_o(s-s_o) \quad (17)$$

Where "h" and "s" is specific enthalpy and specific entropy, Exergy at inlet to the system (Ex_{inlet}) is defined as the maximum useful work available from solar radiation, which is calculated by petela's formula as defined below [28].

$$Ex_{inlet}=A_{ap}G_b\left[1+\frac{1}{3}\left(\frac{T_o}{T_s}\right)^4-\frac{4}{3}\left(\frac{T_o}{T_s}\right)\right] \quad (18)$$

Where $T_s = 5800$K is the temperature of an outer surface of the sun by assuming it as a black body. In addition, the overall exergy efficiency η_{ex} is defined as the ratio of net work output to the input exergy for SORC is defined as under:

$$\eta_{ex}=\frac{\dot{W}_{net,SORC}}{Ex_{inlet}} \quad (19)$$

The thermal efficiency and overall efficiency of the SORC cycle can be expressed as:

$$\eta_{thermal}=\frac{W_{net,SORC}}{\dot{Q}solar} \quad (20)$$

$$\eta_{overall}=(\eta_{thermal})*(\eta_{SPTC}) \quad (21)$$

Now, performance parameters like fuel depletion ratio (Y_{DEP}), irreversibity ratio (Y_{IR}), improvement potential (IP) and expansion ratio for a definite state "R" is defined as below:

$$Y_{DEP(R)}=\frac{Ex_{DES(StateR)}}{Ex_{inlet}} \quad (22)$$

Table 2. Physical, environmental properties and security data of the selected working fluids for SORC cycle adapted from [30–32].

Working substance	**Physical properties data**			**Security Group**	**Environmental properties**		
	Type*	T_c** (K)	P_c^c (MPa)		**Lifetime (years)**	**ODP†**	**GWP††**
R600a	D	408.1	3.64	A3	0.019	0	20
Toluene	D	591.7	4.12	n.a.	n.a.	n.a	n.a
R152a	W	386.4	4.52	A2	1.4	0	124
Isobutane	W	407.8	3.64	A3	<1	0	3
Cyclohexane	D	553.6	4.07	A1	n.a.	n.a	n.a

*W = Wet, D = Dry.
**T_c = critical temperature.
P_c = critical pressure.
†ODP = potential of ozone depletion relative to R11.
††GWP = potential of global warming relative to CO_2.

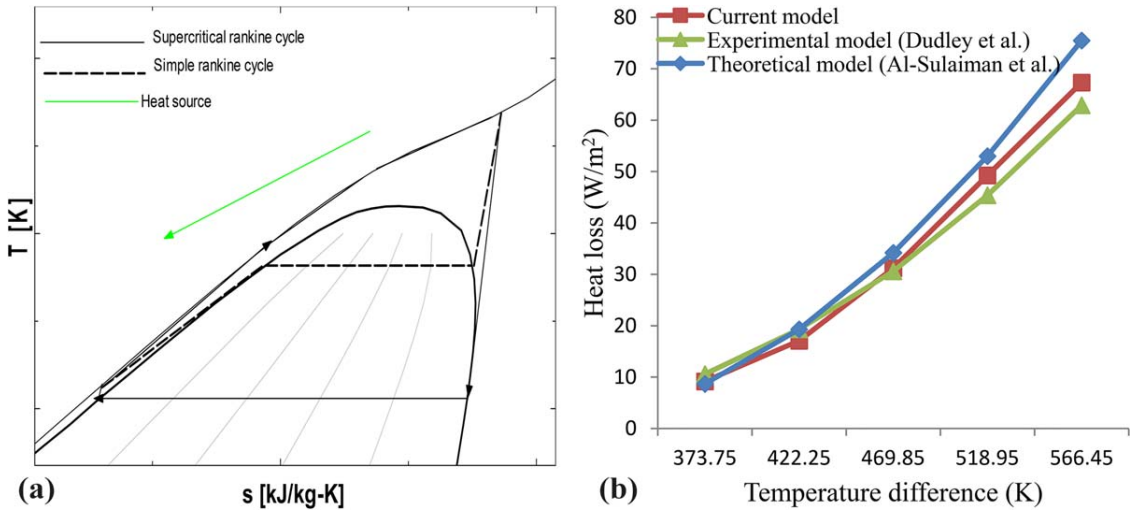


Figure 2. T-S diagram of supercritical organic rankine cycle (SORC). (b) Validation of the considered SPTC system. [Color figure can be viewed at **wileyonlinelibrary.com**]

$$Y_{IR(StateR)} = \frac{Ex_{DES(StateR)}}{Ex_{DESTotal}} \quad (23)$$

$$IP_{(StateR)} = \left(1 - \frac{\eta_{ex}}{100}\right) Ex_{DES(StateR)} \quad (24)$$

$$\varphi = \frac{V_6}{V_5} \quad (25)$$

Validation of Model

This model is validated against the theoretical study of Al-Sulaiman et al. [24] as well as experimental study conducted by the Dudley et al. [29]. In this current model, the change in heat losses with the average temperature of the fluid inside the absorber above the ambient was examined as shown in Figure 2b. Results of the validation process revealed that model is in good agreement with the experimental, which means that there is a marginal difference in the value of heat losses for all the value of temperature difference.

RESULTS AND DISCUSSIONS

In this section, exergy and energy performance of the SORC integrated by large SPTC was examined with respect to the solar irradiation intensity and turbine inlet pressure. Presently, this system assumed to be working on an average value of 0.85 kW/m^2 solar irradiation intensity, in which SORC thermal cycle is operating.

Variations in System Performance with the Solar Irradiation Intensity

The intensity of solar irradiation directly affects to exergy performance of the SORC as demonstrated in Figure 3. From the results, it has been concluded that the exergy efficiency of SORC increases continuously with the increase in solar irradiation intensity. As observed that it gives better and effective utilization of overall solar collector field with respect to increasing solar irradiation intensity directed upon the solar collector rows. Among all the refrigerants selected for the supercritical organic Rankine cycle (SORC), R600a gives the maximum exergetic performance, which is followed by the R152a, Toluene, Isobutane, and Cyclohexane, respectively.

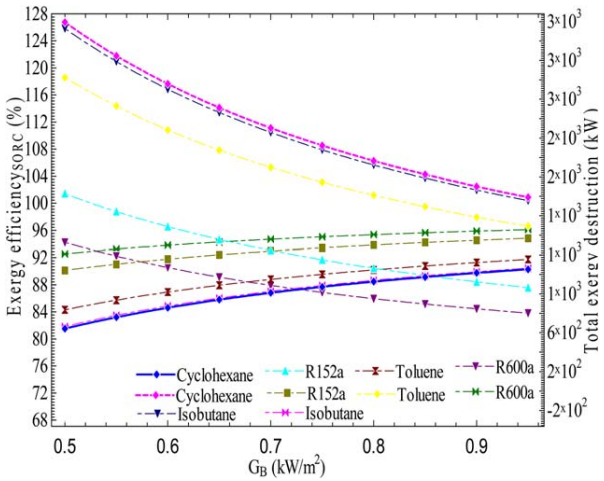


Figure 3. Variations in exergy efficiency and exergy destruction rate of SORC with solar irradiation intensity (G_B). [Color figure can be viewed at **wileyonlinelibrary.com**]

Figure 3 demonstrated that exergy efficiency of R600a based SORC increases from 92.55% at 0.5 kW/m^2 to 96.09% at 0.95 kW/m^2. Also, the change in the rate of exergy destruction of SORC with the intensity of solar irradiation as illustrated in Figure 3. Figure 3 shows that rate of exergy destruction in SORC decreases continuously with the increase in solar irradiation intensity, and it shows an inverse behavior from the exergy efficiency graph. Therefore, Figure 3 clearly demonstrated that R600a has a minimum exergy destruction rate among all the fluids, and its value decreasing from 1527kW at 0.5 kW/m^2 to 807 kW at 0.95 kW/m^2. On the contrary side, cyclohexane having the highest value of the exergy destruction rate, which is decreasing from 3794 kW at 0.5 kW/m^2 to 1990 kW at 0.95 kW/m^2 with the increase in solar irradiation intensity from 0.5 kW/m^2 to 0.95 kW/m^2 as illustrated in Figure 3. Furthermore, it has been observed from the Figure 4 that the maximum value of the exergy destruction rate in the combined SPTC based SORC occurred in the solar collector part, which is due to the great

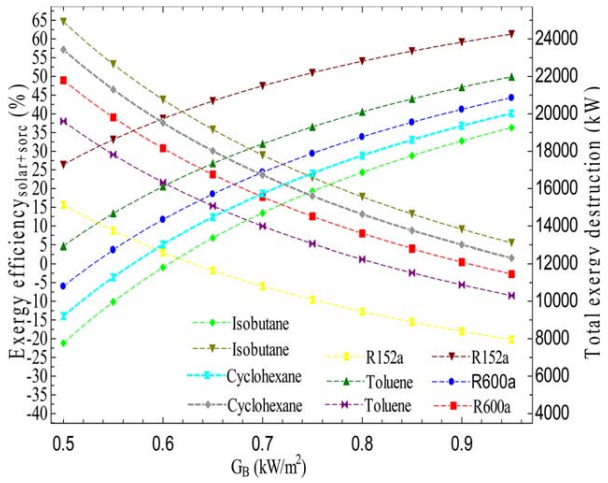


Figure 4. Variations in exergy efficiency and exergy destruction rate of Solar + SORC with solar irradiation intensity (G_B). [Color figure can be viewed at **wileyonlinelibrary.com**]

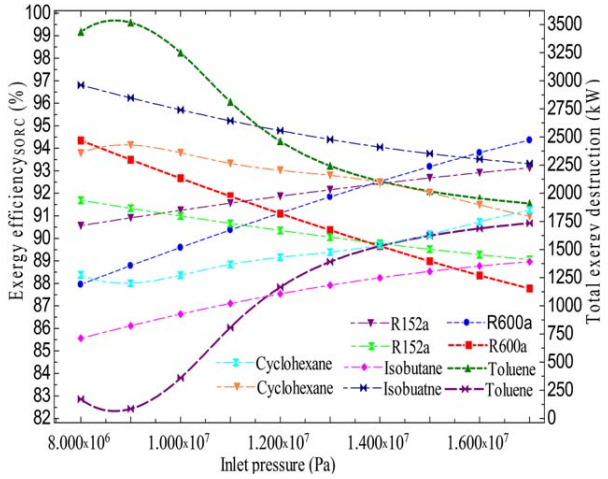


Figure 5. Variations in exergy efficiency and exergy destruction rate of SORC with inlet pressure of SORC turbine. [Color figure can be viewed at **wileyonlinelibrary.com**]

loss of exergy value in the solar collector field. It is clearly understood from the Figure 4 that the total exergy destruction rate of solar combined SORC shows a decreasing trend with an increase in the solar irradiation intensity, which is due to the efficient exploitation of the overall SPTC field and also, the large amount of solar irradiation intensity available for the fewer number of solar collector rows, which are arranged in the series and parallel arrangement can diminishes the total exergy destruction rate in the considered SEGS plant. Finally, it has been concluded that R152a based combined SPTC-SORC having the minimum value of total exergy destruction rate followed by toluene, R600a, cyclohexane, and isobutene having the highest value of exergy destruction rate as illustrated in Figure 4.

Variations in System Performance with Inlet Pressure of SORC Turbine

To design and evaluate the performance of SORC, the inlet pressure is an important parameter to examine the

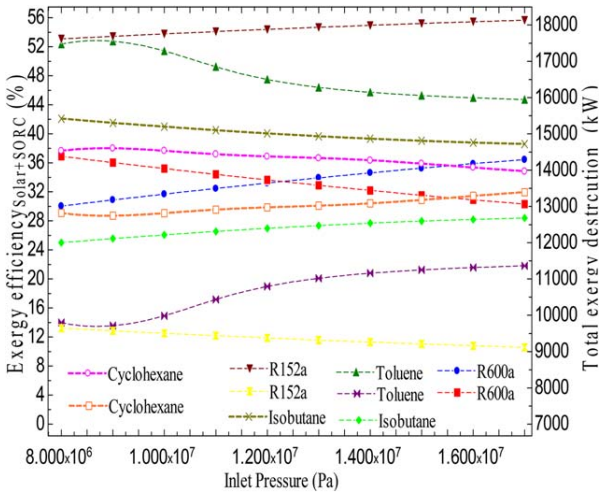


Figure 6. Variations in exergy efficiency and exergy destruction rate of Solar + SORC with inlet pressure of SORC turbine. [Color figure can be viewed at **wileyonlinelibrary.com**]

variations in exergy efficiency of the SORC as illustrated in Figure 5. Figure 5 demonstrated that exergy efficiency of the SORC continuously increases with increase in the inlet pressure of SORC turbine. Results revealed that R600a has the maximum incremental variations in the overall exergy efficiency among the R152a and isobutane except for the toluene and cyclohexane due to abnormal behaviour of these fluids in the selected pressure range. It has been noticed that exergy efficiency of R600a based SORC increases from 87.95% at 8 MPa to 94.37% at 17 MPa. While, R152a based SORC shows that the exergy efficiency increases from 90.56% at 8 MPa to 93.13% at 17 MPa as shown in Figure 5. Therefore, it has been concluded that R152a shows better exergy performance than R600a between the specific pressure ranges of 8 MPa to 13 MPa. Conversely, both toluene and cyclohexane gives an increasing value of exergy performance up to 9 MPa pressure and beyond that both the fluids shows the decreasing behavior of exergy efficiency. Figure 5 also demonstrated the effect of inlet pressure of the SORC turbine on the total exergy destruction rate of the cycle. It has been observed from the results that exergy destruction rate has an inverse value of exergy efficiency. It implies that with an increase in the inlet pressure of SORC turbine, the total exergy destruction rate decreases. Figure 5 illustrates that R600a and R152a comparatively shows the minimum rate of total exergy destruction rate in the SORC in a certain pressure range, which is diminished from 2470 kW at 8 MPa to 1155 kW at 17 MPa for R600a based SORC. Also, for R152a based SORC, the total exergy destruction rate declining from approximately 1939 kW at 8 MPa to 1411 kW at 17 MPa. Conversely, isobutane based SORC possess the highest rate of total exergy destruction rate, i.e., decreases from 2962 kW at 8 MPa to 2265 kW at 17 MPa. Moreover, results revealed that maximum exergy destruction rate, which is around 80% to 85% of the total exergy destruction rate occurs in combined SPTC-SORC associated with only the solar collector field and it is due to the greater amount of exergy losses found in the SPTC field as illustrated in Figure 6 Therefore, it is essential to find out the causes behind the exergy losses due to the solar collector field for the improvement in design and working performance. Figure 6 demonstrates that R152a shows the minimum rate of total exergy destruction for SPTC combined SORC system, which is

Table 3. Detailed exergetic parameters of SORC for all the selected working fluids.

Exergetic parameters	System components	Selected fluids for SORC cycles				
		R600a	Toluene	R152a	Isobutane	Cyclohexane
IP (kW)	Solar collector	11,859	9582	7659	12,416	11,501
	Evaporator	61.84	29.22	17.42	53.32	42.68
	Solar pump	5.935	3.489	3.682	4.986	3.961
	SORC turbine	763.9	1801	1121	2055	2112
	SORC pump	6.223	3.364	2.801	4.947	3.799
	Recuperator	52.36	39.46	35.75	51.2	45.21
	Condenser	2.74	2.397	2.539	3.501	2.638
Y_{DEP}	Solar collector	0.579	0.4681	0.3746	0.6056	0.5612
	Evaporator	0.003046	0.001436	0.0008563	0.002624	0.002099
	Solar pump	0.0002898	0.0001704	0.0001801	0.0002432	0.0001933
	SORC turbine	0.03763	0.08852	0.05508	0.1011	0.1039
	SORC pump	0.0003065	0.001794	0.0001377	0.0002434	0.0001868
	Recuperator	0.002579	0.00194	0.03032	0.002519	0.002223
	Condenser	0.0001349	0.0001178	0.0001248	0.001615	0.001196
Y_{IR}	Solar collector	0.9296	0.8354	0.8658	0.8503	0.838
	Evaporator	0.06971	0.01558	0.01477	0.0246	0.01935
	Solar pump	0.0004652	0.0003042	0.0001801	0.0003414	0.0002886
	SORC turbine	0.8612	0.9603	0.9504	0.9479	0.9572
	SORC pump	0.007016	0.001794	0.002375	0.002282	0.001722
	Recuperator	0.05902	0.02104	0.03032	0.02362	0.9572
	Condenser	0.003088	0.001278	0.002153	0.001615	0.001196

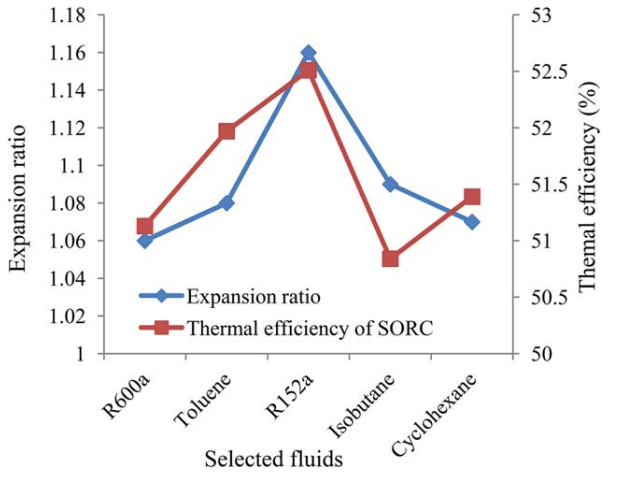


Figure 7. Variations in thermal efficiency and expansion ratio for the selected fluids. [Color figure can be viewed at **wileyonlinelibrary.com**]

declining from 15,136 kW at 8 MPa to 7959 kW at 17 MPa. On the other side, isobutane gives the highest rate of total exergy destruction for the SPTC combined SORC system, i.e., decreases from 24,915 kW at 8 MPa to 13,101 kW at 17 MPa, in which high amount of exergy destruction rate, i.e., around 12,452 kW is due to solar collector only as observed in Figure 6.

Outcomes of Exergy Analysis of the System Components

A detailed exergy analysis is conducted to find out the performance of the system components. Important parameters like fuel depletion ratio, improvement potential and irreversibility ratio was examined in this study and the calculated value of all these parameters are illustrated in Table 3. Furthermore, this study also described the variations

Table 4. Thermodynamic properties at the various stations for R600a based SORC.

Selected stations	P (bar)	T (K)	h (kJ/kg)	s (kj/kg-K)
SORC turbine inlet (5)	250	663	1464	4.894
Recuperator inlet (6)	152.4	548.6	1118	4.366
Condenser inlet (7)	152.4	328	465.8	2.921
SORC pump inlet (10)	152.4	299.5	395.6	2.687
Recuperator inlet (11)	200	393.3	709.2	3.452
Heat exchanger inlet (4)	200	339.6	545.4	3.012
SPTC inlet (2)	100	359.6	570.1	3.166
SPTC outlet (3)	100	663	1538	5.103

in expansion ratio and thermal efficiency of the SORC based on different working fluids as demonstrated in Figure 7. It has also been observed from the study that expansion ratio increases with an increase in the evaporating temperature of SORC. The Maximum value of expansion ratio and thermal efficiency is found to be 1.16 and 52.51% for R152a based SORC as shown in Figure 7. Improvement potential (IP) is an important exergy parameter to find out the possibility to improve the SORC performance up to certain limits. Solar collector shows the highest rate of exergy destruction; therefore it requires a better design to enhance the performance and to reduce the overall heat losses or exergy destruction of the system. Apart from this, evaporator or heat exchanger also has a major source of exergy destruction so that it needs a bigger area for the heat exchange. Also, fuel depletion ratio (Y_{DEP}) is an important parameter to enhance the performance of the SORC system components, and it is defined as the ratio of the exergy destruction rate to the inlet exergy. It has been analyzed that total exergy destruction rate in the solar collector is around 57.89% of the inlet exergy value. From the Table 3, it has been found that fuel depletion ratio in case of R600a based SORC is approximately 0.579, 0.03763, and 0.003046 for the solar collector, SORC turbine and evaporator, respectively. Furthermore, there is also an important exergetic parameter to examine the performance

of system components, i.e., irreversibility ratio, which is defined as the ratio of exergy destructed in a specific component to the total rate of exergy destruction rate in a complete system. As observed from the study, the highest value of the irreversibility ratio (Y_{IR}) is found in the solar collector, i.e., around 0.9296, and (Y_{IR}) for all other system components of different working fluid based SORC as listed in Table 3. Lastly, the thermodynamic properties for R600a based SPTC-SORC at the selected stations has been decribed in Table 4.

CONCLUSION

In the current study, the exergy and energy analysis of SPTC driven supercritical organic Rankine cycle (SORC) was conducted with the help of different refrigerants such as R600a, toluene, R152a, isobutene, and cyclohexane. Following results conclude from this study:

1. It has been observed that with the increase in solar irradiation intensity, exergy efficiency of the SORC also increases. The results concluded that R600a based SORC shows the maximum exergy efficiency, i.e., varies from 92.55% at 0.5 kW/m^2 to 96.09% at 0.95 kW/m^2 followed by R152a, toluene, isobutene, and cyclohexane occupy the minimum value of exergy efficiency. In addition, the exergy destruction rate has an inverse behavior from the exergy efficiency graph and cyclohexane has the highest exergy destruction rate, i.e., ranges from 3794 kW at 0.5 kW/m^2 to 1990 kW at 0.95 kW/m^2.
2. Moreover, the effect of inlet pressure of the SORC turbine on the exergy performance has been observed in this study. Findings revealed that both R600a and R152a comparatively showed the highest value of exergy efficiency among the others, which is around 94.37% and 93.13% at specified pressure of 17 MPa. Conversely, toluene and cyclohexane demonstrate the least value of exergy efficiency and highest value of the exergy destruction rate. Also, it has been observed that the major source of exergy destruction is the solar collector, in which 80% to 85% of the inlet exergy is destructed. Apart from the solar collector, SORC turbine, evaporator and recuperator accounts for the highest rate of exergy destruction.
3. Finally, this study concludes some important exergy performance parameters such as improvement potential, Fuel depletion ratio and the irreversibility ratio for the solar collector is around 92.6%, 0.579 and 0.9296. In addition, the expansion ratio and thermal efficiency for R152a based SORC is found to be 1.16 and 52.51%.

ACKNOWLEDGMENT

As an author, I (Harwinder Singh) would like to acknowledge the support provided by Delhi Technological University (Government of Delhi), India.

NOMENCLATURE

A_{ap}	area of the aperture, m^2
A_r	area of the receiver, m^2
A_c	area of the receiver cover, m^2
S	absorbed heat flux by receiver, W/m^2
$\dot{m}_a$	mass flow rate in the receiver, kg/s
U_l	overall heat loss coefficient, kW/K
W	width of collector, m
V	volume, m^3
$D_{r,o}$	outside diameter of cover, m
L	collector length, m
F	collector efficiency factor
D	diameter, m
F_R	collector heat removal factor
U_o	overall heat loss coefficient, kW/K
K_{air}	thermal conductivity, W/m-K
$\dot{E}x_d$	rate of exergy destruction, kW
Ex	exergy, kW
G_B	solar irradiation intensity, W/m^2
SORC	supercritical organic rankine cycle
$\dot{Q}_u$	useful heat gain per unit time
S	entropy kJ/kg-K
Ex_{inlet}	inlet exergy, kW
Q_{inl}	total inlet heat, kJ
$h_{cr,i}$	heat loss coefficient b/w receiver and cover, kW/m^{2}K
$h_{con,amc}$	convection heat loss coefficient b/w ambient and cover, kW/m^{2}K
$h_{rad,amc}$	radiation heat loss coefficient b/w ambient and cover, kW/m^{2}K
$h_{rad,cr}$	radiation heat loss coefficient b/w receiver and cover, kW/m^{2}K

Greek Letters

ρ_r	mirror reflectance
α	absorbance of receiver
γ	intercept factor
τ	cover transmittance
Km	incident angle modifier
η	efficiency
	emittance
σ	Stefan–Boltzmann constant, kW/m^{2}K^4
φ	expansion ratio

Subscripts

u	useful
o	outside
e	exit
i	inlet
0	environmental conditions
r	reciver
am	ambient
avg	average
ex	exergy per unit mass flow rate, kJ/kg

LITERATURE CITED

1. Sarangi, S.K., Barpujari, B., & Dawar, R. (2009). Emerging technology option for clean power generation - concentrated solar power (CSP). Petrotech-2009, New Delhi, India.
2. He, Y.L., Mei, D.H., Tao, W.Q., Yang, W.W., & Liu, H.L. (2012). Simulation of the parabolic trough solar energy generation system with organic Rankine cycle, Applied Energy, 97, 630–641.
3. Gao, W., Li, H., Xu, G., & Quan, Y. (2014). Working fluid selection and preliminary design of a solar organic rankine cycle system, Environmental Progress & Sustainable Energy, 34, 619–626.
4. Bamgbopa, M.O., & Uzgoren, E. (2013). Quasi-dynamic model for an organic Rankine cycle, Energy Conversion and Management, 72, 117–124.
5. Bryszewska-Mazurek, A., Wieboda, T.S., & Mazurek, W. (2011). Performance Analysis of a Solar-Powered Organic Rankine Cycle Engine, Journal of the Air & Waste Management Association, 61, 3–6.
6. Pei, G., Jing, L., & Ji, J. (2010). Analysis of low temperature solar thermal electric generation using regenerative organic Rankine cycle, Appied Thermal Engineering, 30, 998–1004.
7. Delgado-Torres, A.M., & García-Rodríguez, L. (2010). Analysis and optimization of the low-temperature solar organic Rankine cycle (ORC), Energy Conversion Management, 51, 2846–2856.
8. Al-Sulaiman, F.A., Hamdullahpur, F., & Dincer, I. (2012). Performance assessment of a novel system using parabolic trough solar collectors for combined cooling, heating, and power production, Renewable Energy, 48, 161–172.

9. Tunc, M., Sisbot, S., & Camdalib, U. (2012). Exergy analysis of electricity generation for the geothermal resources using organic rankine cycle: Kızıldere-denizli case, Environmental Progress & Sustainable Energy, 32, 830–836.
10. Wang, X., & Dai, X. (2016). Exergoeconomic analysis of utilizing the transcritical CO_2 cycle and the ORC for a recompression supercritical CO_2 cycle waste heat recovery: A comparative study, Applied Energy, 170, 193–207.
11. Kalra, C., Becquin, G., Jackson, J., Laursen, A.L., Chen, H., Myers, K., Hardy, A., Klockow, H., & Zia, J. (2012). High-potential power cycles & working fluids for next generation binary supercritical organic Rankine cycle for enhanced geothermal systems, Proceedings, Thirty-Seventh Workshop on Geothermal Reservoir Engineering, Stanford University, Stanford, California.
12. Chen, H., Goswami, D.Y., & Stefanakos, E.K. (2010). A review of thermodynamic cycles and working fluids for the conversion of low-grade heat, Renewable and Sustainable Energy Reviews, 14, 3059–3067.
13. Pan, L., Wang, H., & Shi, W. (2012). Performance analysis in near-critical conditions of organic Rankine cycle, Energy, 37, 281–286.
14. Xu, G., Song, G., Zhu, X., Gao, W., Li, H., & Quan, Y. (2015). Performance evaluation of a direct vapor generation supercritical ORC system driven by linear Fresnel reflector solar concentrator, Applied Thermal Engineering, 80, 196–204.
15. Zhou, C. (2014). Hybridisation of solar and geothermal energy in both subcritical and supercritical Organic Rankine Cycles, Energy Conversion and Management, 81, 72–82.
16. Yağlı, H., Koç, Y., Koç, A., Görgülü, A., & Tandiroğlu, A. (2016). Parametric optimization and exergetic analysis comparison of subcritical and supercritical organic Rankine cycle (ORC) for biogas fuelled combined heat and power (CHP) engine exhaust gas waste heat, Energy, 111, 923–932.
17. Rashidi, M.M., Galanis, N., Nazari, F., Basiri Parsa, A., & Shamekhi, L. (2011). Parametric analysis and optimization of regenerative Clausius and organic Rankine cycles with two feedwater heaters using artificial bees colony and artificial neural network, Energy, 36, 5728–5740.
18. Rashidi, M.M., Anwar Be, ́g., A., Basiri Parsa, A., & Nazari, F. (2011). Analysis and optimization of a transcritical power cycle with regenerator using artificial neural networks and genetic algorithms, Proceedings of the Institution of Mechanical Engineers, Part A: Journal of Power and Energy, 225, 701–717.
19. Rashidi, M.M., Ali, M., Freidoonimehr, N., & Nazari, F. (2013). Parametric analysis and optimization of entropy generation in unsteady MHD flow over a stretching rotating disk using artificial neural network and particle swarm optimization algorithm, Energy, 55, 497–510.
20. Basiri Parsa, A., Rashidi, M.M., Anwar Bég, O., & Sadri, S.M. (2013). Semi-computational simulation of magneto-hemodynamic flow in a semi-porous channel using optimal homotopy and differential transform methods, Computers in Biology and Medicine, 43, 1142–1153.
21. Bao, J., & Zhao, L. (2013). A review of working fluid and expander selections for organic Rankine cycle, Renewable and Sustainable Energy Reviews, 24, 325–342.
22. LUZ International Limited. (1990). Solar electric generating system IX technical description, Documentation, Los Angeles, CA: LUZ International Limited.
23. https://www.therminol.com/products/Therminol-VP1 (accessed on 16/11/2016).
24. Al-Sulaiman, F.A. (2014). Exergy analysis of parabolic trough solar collectors integrated with combined steam and organic Rankine cycles, Energy Conversion and Management, 77, 441–449.
25. Kalogirou, S. (2009). Solar energy engineering: Processes and systems (First edition), California: Academic Press/Elsevier.
26. Duffie, J., & Beckman, W. (2013). Solar engineering of thermal processes (4th edition), Hoboken, New Jersey: John Wiley & Sons, Inc.
27. Bejan, A., Tsatsaronis, G., & Moran, M. (1996). Thermal design and optimization (First edition), New York: John Wiley and Sons, Inc.
28. Petela, R. (2005). Exergy analysis of the solar cylindrical-parabolic cooker, Solar Energy, 79, 221–233.
29. Dudley, V.E., Koib, G.J., Mahoney, A.R., Mancini, T.R., Matthews, C.W., Sloan, M., & Keamey, D. (1994). SEGS LS-2 solar collector test results. Report of Sandia National Laboratories, SANDIA94–1884.
30. Facão, J., & Oliveira, A.C. (2009). Analysis of energetic, design and operational criteria when choosing an adequate working fluid for small orc systems, Proceedings of the ASME international mechanical engineering congress & Exposition.
31. Tchanche, B.F., Papadakis, G., Lambrinos, G., & Frangoudakis, A. (2009). Fluid selection for a low-temperature solar organic Rankine cycle, Applied Thermal Engineering, 29, 2468–2476.
32. Nouman, J. (2012). Comparative studies and analyses of working fluids for Organic Rankine Cycles - ORC. Master of Science Thesis, KTH School of Industrial Engineering and Management, STOCKHOLM.
33. Valenzuela, L., Zarza, E., Berenguel, M., & Camacho, E.F. (2005). Control concepts for direct steam generation in parabolic troughs. Sol Energy 78, 301–311.

Rock Mech Rock Eng
DOI 10.1007/s00603-017-1318-8

ORIGINAL PAPER

Physical Modeling of Shear Behavior of Infilled Rock Joints Under CNL and CNS Boundary Conditions

Amit Kumar Shrivastava[1,3] · **K. Seshagiri Rao**[2]

Received: 26 July 2016 / Accepted: 8 September 2017
© Springer-Verlag GmbH Austria 2017

Abstract Despite their frequent natural occurrence, filled discontinuities under constant normal stiffness (CNS) boundary conditions have been studied much less systematically, perhaps because of the difficulties arising from the increased number of variable parameters. Because of the lack of reliable and realistic theoretical or empirical relations and the difficulties in obtaining and testing representative samples, engineers rely on judgment and often consider the shear strength of the infilled material itself as shear strength of rock joints. This assumption leads to uneconomical and also sometimes the unsafe design of underground structures, slopes, rock-socketed piles and foundations. To study the effect of infill on the shear behavior of rock joints, tests were performed on the modeled infilled rock joint having different joint roughness under constant normal load (CNL) and CNS boundary conditions at various initial normal stress and varying thickness of the infilled material. The test results indicate that shear strength decreases with an increase in *t*/*a* ratio for both CNL and CNS conditions, but the reduction in shear strength is more for CNL than for CNS condition for a given initial normal stress. The detailed account of the effect of thickness of infilled material on shear and deformation behavior of infilled rock joint is discussed in this paper, and a model is proposed to predict shear strength of infilled rock joint.

Keywords CNL · CNS · Rock joint · Direct shear behavior · Infilled joint

List of Symbol

CNL	Constant normal load
CNS	Constant normal stiffness
i	Asperity angle
i'_{infill}	Effective infilled asperity angle
k_n	Stiffness of the surrounding rock mass
LVDT	Linear variation displacement transducer
P_i	Initial normal stress
$P_{n\ (t+\Delta t)}$	Normal load at any time interval $t + \Delta t$
P_n	Normal stress corresponding to peak shear stress
$P_{n(t)}$	Normal load at any time interval t
t/a	Thickness of infilled to a thickness of asperity ratio
X	Shear displacement
Y	Free dilation at any shear deformation
Y'	Dilation measured as the average of readings of four normal LVDTs placed on the top of the sample
$Y - Y'$	Dilation resisted by the surrounding rock mass
δ_{sp}	Shear displacement corresponding to peak shear stress
δ_{vp}	Dilation corresponding to peak shear stress
σ_{c}	Uniaxial compressive strength
τ_p	Peak shear stress of unfilled joint
$\tau_{p\text{infill}}$	Peak shear stress of infilled joint
φ	Friction angle of infilled joint
φ_{b}	Basic friction angle

✉ Amit Kumar Shrivastava
aksrivastava@dce.ac.in

K. Seshagiri Rao
raoks@civil.iitd.ac.in

[1] Present Address: Department of Civil Engineering, Delhi Technological University, Delhi, India

[2] Department of Civil Engineering, Indian Institute of Technology, Delhi, India

[3] E-11, Sector-18, Rohini, Delhi 110085, India

Published online: 18 September 2017

1 Introduction

Rock joints are mechanical discontinuities developed due to varied geological processes. These discontinuities are present in the form of joints, faults, bedding planes or other recurrent planar fractures in the rock mass. In general, strength and deformation behavior of these discontinuities are quite different from those of intact rock, and in many cases, the discontinuities completely dominate the shear and deformation behavior of the in situ rock mass in given stress condition. The main effect of the presence of these joints is to reduce the shear strength.

The presence of infilled or gouge material in these joints further reduces the shear strength. The sources of infilled material include products of weathering or overburden washed into open joint, water conducting in discontinuities, precipitation of minerals from the ground water, by-products of weathering alterations along joint walls, crushing of parent rock surfaces due to tectonic and localized shear displacements, and thin seams deposited during formation. In general, infilled materials may consist of partially loose to completely loose cohesionless soil or fine-grained clay. Normally, fine-grained clays are more frequently found as fillers and are more troublesome in terms of structural stability. The thickness of the infilled material varies from micrometers to several meters, and it plays a major role in shear behavior. In tectonically crushed zones, the infilled thickness may exceed several meters.

Despite their frequent natural occurrence, the filled discontinuities are less studied, perhaps because of the difficulties arising from the preparation of the sample and testing or due to increased number of variable controlling parameters. The major parameters influencing shear strength of rock joints are: (a) stiffness of the surrounding rock and joint, (b) shear rate, (c) joint roughness, (d) size of joint, i.e., scale effect, (e) joint condition, i.e., unfilled joint/infilled joint, (f) properties of the constituents infilled material, (g) thickness of the infilled material (Shrivastava and Rao 2009).

Due to limited research, it is a common practice to assume the shear strength of an infilled joint equal to the infilled material alone, regardless of its thickness. It may lead in most of the cases to uneconomical and unsafe design. Kanji (1974) reported that the shear strength of the infilled joint is lower than that of the infilled material. Hence, if the design is done using the above assumption, it may lead to unsafe designs.

Most of the conventional equipment used in the past by different researchers like Patton (1966), Goodman (1974), Ladanyi and Archambault (1970), Barton (1971, 1973), Barton and Choubey (1977), Bandis et al. (1981) and Hoek (1983) to predict the shear behavior of rock joints fail to correctly determine the shear behavior because of the limitation of boundary conditions. Conventional equipments used were working under constant normal load (CNL) boundary condition, and they are for unfilled or clean joints.

To overcome this limitation, either conventional equipments were modified by Obert et al. (1976) and Ooi and Carter (1987) or new equipment developed by Indraratna et al. (1998) or servo-controlled equipment developed by Jiang et al. (2004) and Kim et al. (2006) to conduct tests under CNS boundary conditions. The equipment modified or developed by Obert et al. (1976), Ooi and Carter (1987) and Indraratna et al. (1998) have difficulties to change the reaction rods, beams and stiffness plate to simulate different stiffness conditions of the surrounding rock mass, while changing there is also a chance that sample may fail before testing starts. These difficulties have been overcome by using servo-controlled equipment such as employed by Jiang et al. (2004), but this equipment is suitable for the comparatively smaller size of the sample, due to this influence of joint roughness cannot be well studied, and there is no facility to measure the rotation of the sample as well. The equipment developed by Kim et al. (2006) can test the samples only under two extreme conditions of the stiffness of the boundary, i.e., CNL (normal stiffness, $k_n = 0$) and infinite normal stiffness condition ($k_n = \infty$).

The shearing under CNL boundary condition is suitable for situations where the surrounding rock mass freely allows the joints to shear without restricting the dilation, thereby keeping normal stress constant during the shearing process. This mode of shearing is only applicable to planar rock joints and non-reinforced rock slopes where the normal load is constant during the shearing process. However, for non-planar discontinuities, shearing results in dilation as one asperity overrides another, and if the surrounding rock mass is unable to deform completely, an inevitable increase in the normal stress occurs during shearing. The increase in normal stress on the shearing plane depends upon the stiffness of the surrounding rock mass, and dilation resisted, hence shearing of rough joints takes place under variable normal load but constant normal stiffness (CNS) boundary conditions. As rock joints are always non-planar hence, a more typical behavior of joints would be achieved if the shear behavior is investigated under CNS conditions. De Toledo and De Freitas (1993) based on the review of the past work on infilled joints indicated the importance of CNS testing on the shear behavior of the infilled joints.

Most of the previous studies on infilled joints have been carried out on CNL condition which is applicable for planar, smooth and unreinforced rock joints, but as rock joints are usually non-planar, rough and are often reinforced, CNS boundary conditions are more suitable. Ladanyi and Archambault (1977), Phien-Wej et al. (1990), Papaliangas et al. (1990, 1993), De Toledo and De Freitas (1993), Pereira (1997), Fishman (2004) and Ong (2006) have investigated and proposed different models considering the CNL

boundary conditions for rough infilled rock joints. Seidel and Haberfield (2002) and Jiang et al. (2004) studied the effect of CNS boundary condition on clean joints without any infill.

The recent works carried out by Indraratna et al. (1998, 1999, 2010), Indraratna and Welideniya (2003) and Welideniya (2005) used equipment which can test infilled samples under CNS conditions. To simulate CNS boundary conditions, a stiffness plate of known stiffness was used, which need to be changed if the stiffness conditions of the rock mass are changed; while changing there is also a chance that sample may fail and hence, correct shear strength could not be determined.

Cheng et al. (1996) studied the effect of infill thickness on the shear behavior of concrete–rock joints under CNS conditions. They concluded that the shear response is purely frictional and is independent of the infill thickness. However, the test results from other researchers like Indraratna et al. (2005, 2008, 2012, 2013, 2014), Jahanian and Sadaghiani (2015) and Naghadehi (2015) indicate that shear behavior of rock joints is dependent on infill thickness. Sinha and Singh (2000) carried out unconsolidated undrained triaxial tests on samples filled with gouge of various thickness (t = 5–30 mm), dip angle (β = 5°–50°) at a strain rate (e = 5–80 mm/hr) for both undulation and planar type of joints. The test results are useful for providing satisfactory shear strength parameters for stability analysis and to develop constitutive relations. Indraratna et al. (2005) presented a model for predicting the shear strength of infilled joint on the basis of direct shear tests carried out under CNS conditions on model rock joints having asperity angles at 9.5° and 18°. They have used graphite and bentonite as the infilled material. The shear strength model explains the decrease in shear strength with increasing t/a ratio and highlights the role of the critical t/a ratio, beyond which no further reduction in shear strength normally occurs.

Indraratna et al. (2008) revised the model of Indraratna et al. (2005) for predicting the shear strength of the rough infilled joint, on the basis of consolidated undrained triaxial shear tests performed on idealized sawtoothed joints with natural silty clay as the infill material. The revised model describes the effect of over consolidation ratio on shear strength, pore water pressure development and critical t/a ratio. Indraratna et al. (2012) discussed with experimental data the effect of key governing parameters like joint wall roughness, infill type and thickness, boundary conditions and over consolidation ratio on the joint shear strength. Indraratna et al. (2013) conducted a series of triaxial tests on natural joint profiles having JRC of 10–12 at constant moisture content. Silty clay has been used as infill material, and moisture content of infill material is maintained by spreading the infill material on the water proof joints. The stress–strain curve exhibits two peaks for low t/a ratio, i.e., t/a = 0.26 and 0.51. The first peak corresponds to yielding of soil infill, and the second peak is largely influenced by a rock-to-rock contact. The double-peak phenomenon diminishes with an increase in infill thickness.

Indraratna et al. (2014) studied the influence of compacted (unsaturated) infill on the joint shear strength by conducting triaxial tests on idealized modeled and natural joints. The experimental results indicate that shear strength of infilled joint increases with a decrease in the degree of saturation. To incorporate the effect of infill saturation, the peak shear strength model proposed by Indraratna et al. (2005) has been modified. Jahanian and Sadaghiani (2015) conducted a series of direct shear tests on synthetic samples with infilled rough joint surface having different asperity and infill characteristics to study the effects of different factors influencing the shear strength of infilled joint with an emphasis on forward and reverse shearing. The test results indicate that joints with low asperity angle shows higher shear strength during the forward shearing cycle than the reverse shearing cycle. The joint with steeper asperity angle shows higher shear strength in reverse cycle than in forward cycle. Naghadehi (2015) conducted a series of direct shear strength tests under CNL condition on natural rock joints with clay, sand, and sand-clay as infill materials. Based on experimental results, an empirical prediction model has been proposed.

Hence, it is important to use the equipment for the study where boundary conditions can be changed easily and without disturbing the sample. This is possible only if an automatic servo-controlled testing machine is used where boundary conditions from CNL to CNS for any stiffness of the surrounding rock joints can be changed by just changing the input parameters in the direct shear test software and not by changing the plate of different stiffness. Hence, in the present study the servo-controlled large-scale direct shear testing machine designed by Shrivastava and Rao (2013) which is capable of conducting tests on large, jointed prismatic specimens through friction-free rigid platens under CNL and CNS boundary conditions is used to test the samples with different asperity angles and infill thickness to understand the effect of infill thickness on the shear behavior of such jointed materials. Based on the experimental studies, prediction models have been proposed.

2 Testing Equipment

A servo-controlled large-scale direct shear apparatus designed and developed by Shrivastava and Rao (2013) is used for testing the rock joint under CNL and CNS boundary conditions. The apparatus can perform the test on a sample of size 297 mm × 297 mm × 125 mm, and the normal and shear loads are applied through the actuator having the capacity of 500 and 1000 kN, respectively. Six linear

variation displacement transducers (LVDTs) are used for measurement of displacement.

In this apparatus, CNL and CNS conditions are achieved by an electrohydraulic servo-valve, which controls the application of hydraulic power to linear actuator to provide the programmed force on test specimens. The programmed force is calculated from Eq. (1) and this equation in made part of the direct shear software. The programmed force keeps changing depending upon the stiffness of the surrounding rock joint entered as input data in the direct shear software, and the dilation and horizontal displacement data are collected through sixteen channel data acquisition system. As discussed in Sect. 1, the CNL condition is applicable majorly in two cases (1) when rock is free to dilate, there is no restriction from the surrounding rock-or-rock bolts and anchor, in that case in Eq. (1), we have to substitute $k_n = 0$ and that Eq. (1) will lead to $P_{n\ (t+\Delta t)} = P_{n(t)}$; (2) when joints are planar, in that case $Y - Y' = 0$, and hence when it is substituted in Eq. (1), we will get $P_{n\ (t+\Delta t)} = P_{n(t)}$. Other joints are not free to dilate because of the stiffness of the surrounding rock mass (k_n) when substituted in Eq. (1) $P_{n\ (t+\Delta t)} \neq P_{n(t)}$, which has represented the case of CNS condition. Similarly, for rough joint $Y - Y' \neq 0$ when substituted in Eq. (1) will lead to $P_{n\ (t+\Delta t)} \neq P_{n(t)}$ which will be representing the CNS conditions. Hence, the same equipment can be used for conducting tests under both CNL and CNS conditions depending upon the joint and the applied load condition on the rock mass. The change in load during the progress of testing is calculated by the following equation (Rao et al. 2009; Shrivastava and Rao 2013):

$$P_{n(t+\Delta t)} = P_{n(t)} + k_n\left(Y - Y'\right) \tag{1}$$

where $P_{n\ (t+\Delta t)}$ = normal load at any time interval $t + \Delta t$, $P_n(t)$ = normal load at any time interval t, k_n = stiffness of the surrounding rock mass, $Y - Y'$ = dilation resisted by the surrounding rock mass.

The typical calculation for $(Y - Y')$ for a given asperity angle (i) can be explained with the help of Fig. 1, Y is the free dilation of the joint at any shear displacement, which can be calculated from $Y = X \tan(i)$, if the JRC values are known for the joint then, i can be calculated by the method suggested by Xie and Pariseau (1992) and Maksimovic (1996), where X = horizontal displacement measured as the average of two horizontal LVDTs' readings placed near the sample, Y' = dilation measured as the average of readings of four normal LVDTs placed on the top of the sample.

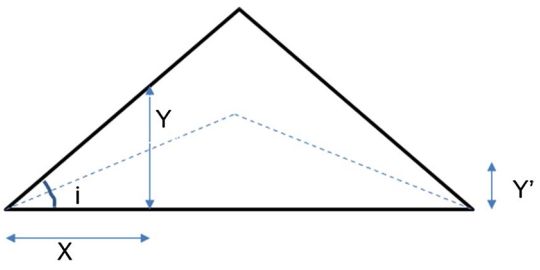


Fig. 1 Typical profile of asperity (Shrivastava and Rao 2015)

3 Experimental Investigation

3.1 Selection of Model Material

Plaster of Paris (POP) is selected as the model material for conducting a series of physical and mechanical tests, and a large number of specimens were prepared by mixing the prescribed quantity of water with plaster of Paris (POP) powder. The prescribed percentage of water is decided to achieve proper workability of the paste and required strength to simulate soft rock. Different water–cement (POP) ratios were tried to obtain the desired strength and workability. Based on the initial results, 0.60 ratio is selected.

The physical and engineering properties of the model material were determined in the laboratory as per the suggested methods by ISRM (1977, 1979). The average uniaxial compressive strength and tangent modulus at 50% of peak axial stress of model material at 0.60 water–cement (POP) ratio and after 14 days of air curing is 11.75 and 2281 MPa, respectively. Thus, the material can be classified as 'EL' based on (Deere and Miller 1966) classification chart, indicating that the material has very low strength (E) and low modulus ratio (L). The range of strength and modulus values obtained are suitable for physically and mechanically simulating the behavior of jointed rocks like siltstone, sandstone, friable limestone, clay shale and mudstone.

3.1.1 Selection of Infill Material

The rock joints are seldom clean; it is filled with weathered material from the parent rocks or transported material. The infill material is selected to simulate the field conditions. In the present work, combination of fine sand and mica dust, both passing through 425-micron sieve and plaster of Paris, is selected. The selected composition was 40% POP, 50% fine sand and 10% mica dust mixed with 45% water finally by weight of the total mass of the material. The uniaxial compressive strength of the 7 days air-cured infill material was 3.47 MPa, and the direct shear tests carried on the infilled material gave friction angle and cohesion, 28.8° and 0 MPa, respectively.

3.2 Sample Preparation

The asperity plates of different angles like 0°–0°,15°–15° and 30°–30° have been designed and fabricated to produce desired asperity in the sample (Rao et al. 2009). These asperity angles can easily be converted into joint roughness coefficient (JRC) value by use of method suggested by Xie and Pariseau (1992) and Maksimovic (1996).

Rock joint has two parts, namely upper and lower parts; both parts of the joint are prepared simultaneously to create properly mated joints. The casting molds with the suitable platform are placed and screwed on the vibrating table. The desired asperity plate is placed inside the mold facing the inclined asperity surface upwards. Plaster of Paris (POP) mixed with water thoroughly for 2 min before pouring into the casting mold, by maintaining the water POP ratio as 0.60 and the paste is then vibrated on a vibrating table for 1 min to compact and remove any entrapped air. The top surface of the specimen is properly leveled, and excess paste is removed. As the samples require 55 min to achieve final setting, it is removed from the mold only after elapse of 55 min, to ensure proper shape of the sample. All samples were allowed to cure in air for 14 days before testing. Different roughness conditions of the rock joints were simulated by preparing three types of specimen sets, namely 0°–0°, 15° –15° and 30°–30°.

3.2.1 Preparation of Infilled Joint

The infilled joint with a required thickness is made with the help of infilled mold as explained by Shrivastava and Rao (2013). The mold consists of upper and lower parts having the facility to hold the sample at required level with the help of four screws mounted on the sides of the mold. Both parts are open from the top and bottom, and the size of the mold is 0.5 mm greater than the size of the sample, so that the sample can easily be fit into the mold and during the placement of the infilled material, the excess infilled material can easily squeezed out from the space available between the mold and the sample. The guide rods on the mold ensure perfect positioning of the infilled material between the samples. The required thickness of the infilled is maintained with the help of the spacer bar and movable screw mounted on the top of the upper mold. The infill of any thickness can be created with this setup in the joint.

The samples are placed in the mold and tighten at a suitable point so that the required thickness of the infilled material is created (Fig. 2a). The infilled material is spread over the lower sample (Fig. 2b). Now, the asperity plate having the same angle as of the joint is put over the infilled material and compressed from the top with the help of C-clamps so that the uniform pressure is applied to the sample (Fig. 2c).

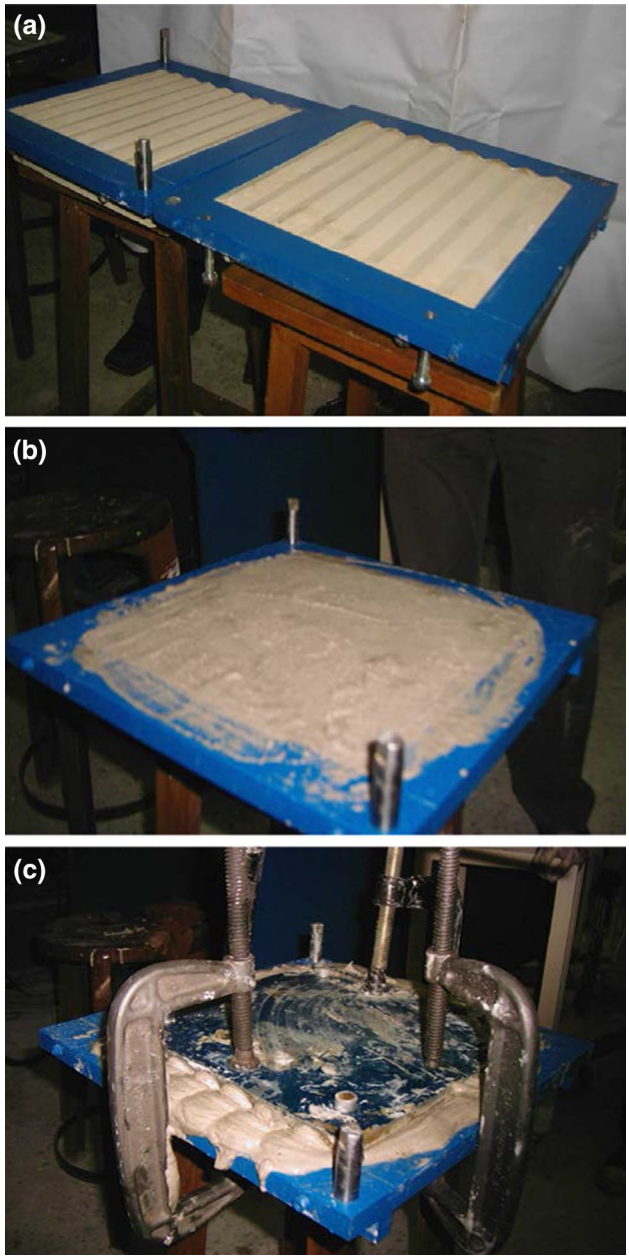


Fig. 2 Steps for placement of infill material

After 5 min the asperity plate is removed, and the lower sample will have infilled material as shown in Fig. 3a.

The upper mold is now placed over the lower mold. The required thickness of infilled material is ensured with the help of the guide rod and adjustable screw as shown in Fig. 3b. The whole assembly is now compressed from the top with the help of C- clamp, after 30 min the sample was removed from the mold and kept for air curing for 7 days before testing. The sample with 5 mm infilled thickness is shown in Fig. 3c.

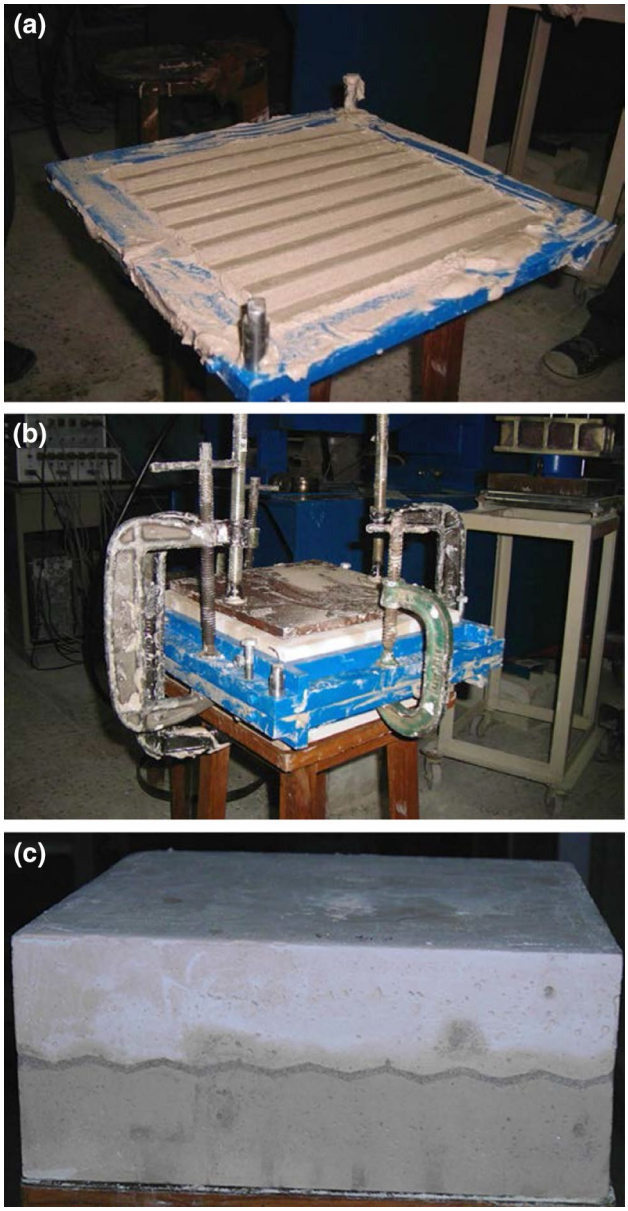


Fig. 3 Steps for preparation of infilled joint surface

3.3 Testing

The shear behavior of joints under CNL was investigated before joints were tested under CNS conditions. This has been carried out to assess the effect of boundary conditions and infilled thickness on the shear behavior. Hence, a series of tests were performed on the physically modeled rock joints with asperity angles 30°–30°, 15°–15° and varying the thickness of infilled from 0 mm to 10 mm making thickness (t) to asperity (a) ratio 0 to 2. To study the effect of the asperity on shear behavior, tests were also performed on planar joints with asperity angle 0°–0° in both the boundary conditions.

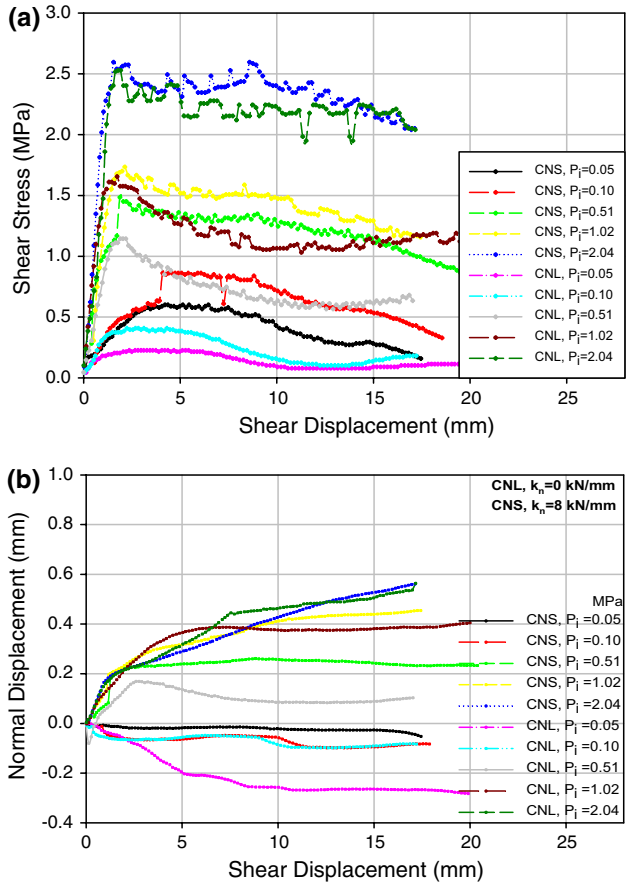


Fig. 4 **a** Shear and **b** dilation behavior of 30°–30° joint with $t/a = 0$

In the present study, 0.50 mm/min rate of shearing is selected, which is based on the study carried out by Shrivastava (2012) on similar type of physically modeled rock joints, where it has been concluded that there is no effect of shearing rate on peak shear stress up to shearing rate of 0.5 mm/min and at shearing rate more than 0.5 mm/min, the effect is to increase the peak shear stress for both the boundary conditions. The normal stiffness of the joint under CNS condition is selected as 8 kN/mm, which is based on results reported by Shrivastava (2012) for a similar type of rock joints. These tests were conducted at different initial normal stresses (P_i) ranging from 0.05 to 2.04 MPa, by keeping normal stiffness of the joint at 0 for CNL and 8 kN/mm for CNS condition.

3.3.1 Results and Discussion

3.3.1.1 Joint asperity 30°–30° Shear stress versus displacement characteristics of 30°–30° infilled joints under CNL and CNS conditions are presented in Figs. 4a, 5, 6, and 7a for infill material thickness 0, 5, 7 and 10 mm, respectively, making t/a ratio of 0, 1, 1.4 and 2. The test results indicate that the shear strength of the joint reduces due to the

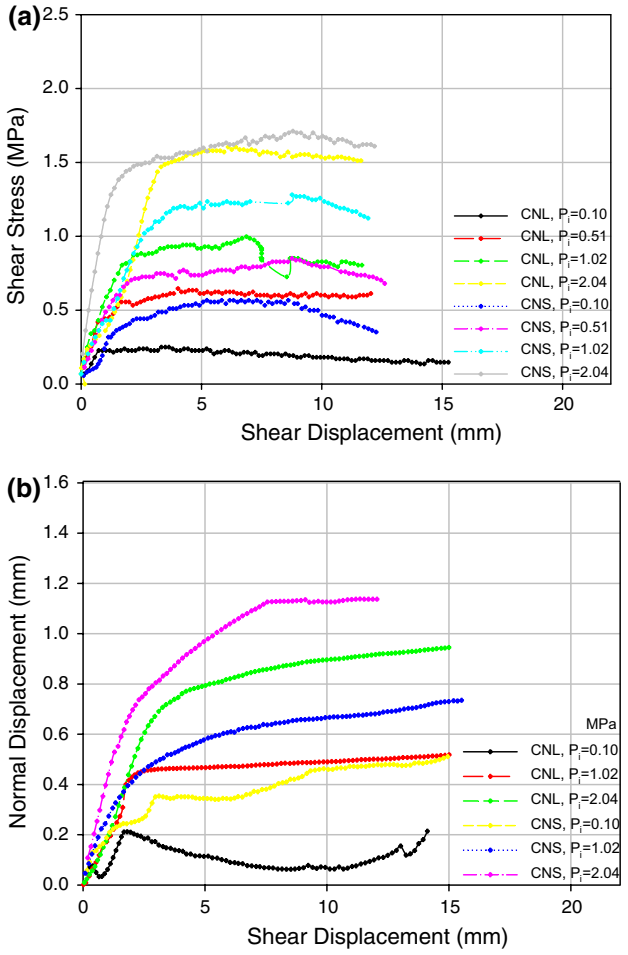


Fig. 5 **a** Shear and **b** dilation behavior of 30°–30° joint with $t/a = 1$

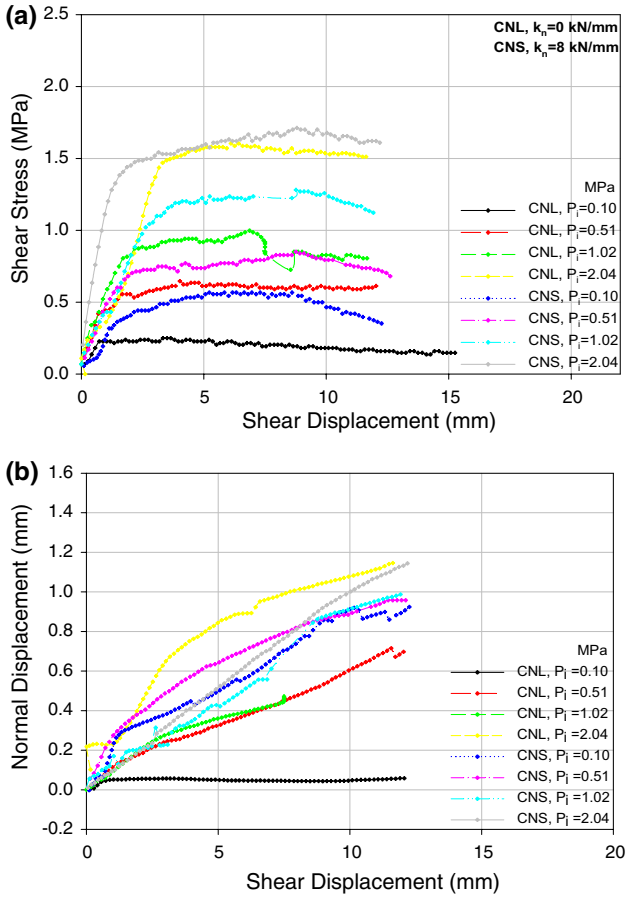


Fig. 6 **a** Shear and **b** dilation behavior of 30°–30° joint with $t/a = 1.4$

presence of the infilled material. The change in dilation with shear displacement for infill thickness 0, 5, 7 and 10 mm for different P_i under CNL and CNS conditions is as shown in Figs. 4b 5, 6, and 7b. The infill material causes positive dilation, i.e., compression for all range of P_i except at very low P_i under small horizontal displacement, and it increases with an increase in infill material thickness. The increase in infill thickness causes a reduction in participation of the asperity and shearing takes place predominantly through infill material which is more compressible. Hence, mostly positive dilation, i.e., compression of the sample takes place instead of dilation (negative) with shear displacement. It is also observed that the dilation is more for CNL than for CNS boundary conditions. This is due to the increase in normal stress for CNS conditions on a shearing plane which resulted into more dilation (positive) of the infilled samples.

The reduction in the shear strength is due to reduced contact between the joint asperities due to the presence of the infilled material. The percentage decrease in peak shear stress of infilled joint ($\tau_{p\text{infill}}$) is compared with that of the unfilled joint (τ_p) for different t/a ratio, and the same is presented in Fig. 8. The shear strength of infilled joint ($\tau_{p\text{infill}}$) decreases more rapidly with an increase in t/a ratio, and for $t/a = 2$, the reduction in $\tau_{p\text{infill}}$ is 80% of τ_p. Reduction in shear strength is higher at low normal stress, and it decreases with an increase in normal stress. It is because, at low normal stress, the infilled material is less compressed, resulting in reduced participation of joint in shearing phenomena. Hence, shear strength is mainly contributed by the infilled material than the joint surface and hence shear strength is greatly reduced. The increase in normal stress on the shearing plane causes compression of the infilled material which increases the participation of joint surface and hence less reduction in shear strength as compared to unfilled joints.

Similarly, the only shear strength of infilled material (τ_{infill}) is compared with $\tau_{p\text{infill}}$, a rapid reduction in shear strength can be observed (Fig. 9) with an increase in t/a ratio. The plot shows that at $t/a = 2$ the shear strength of the joint approaches to the shear strength of infilled material only and this ratio is defined as a critical ratio. Goodman (1970), Papaliangas et al. (1993) and Indraratna et al.

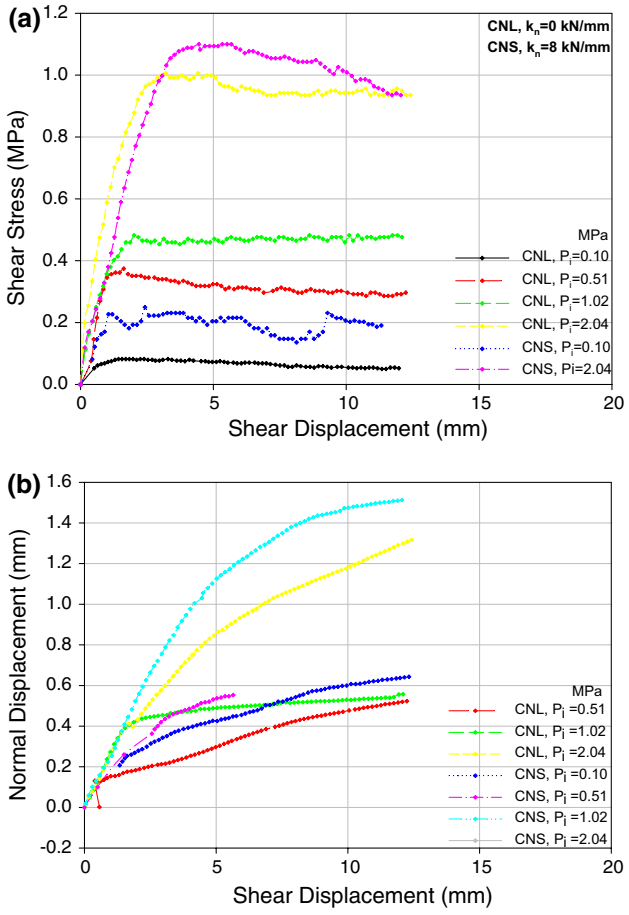


Fig. 7 **a** Shear and **b** dilation behavior of 30°–30° joint with $t/a = 2$

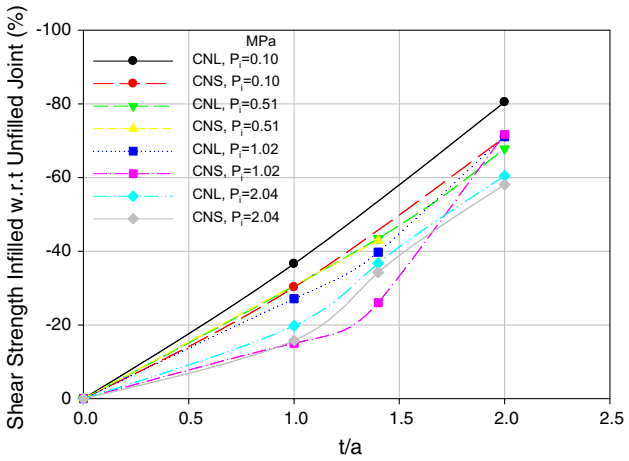


Fig. 8 Effect of t/a ratio on shear strength reduction of 30°–30° joint

(2005) reported that $(t/a)_{cr}$ depends upon the type of the infilled material and its value ≥ 1.

The reduction in shear strength is higher for CNL conditions compared to CNS. During the shearing process, the

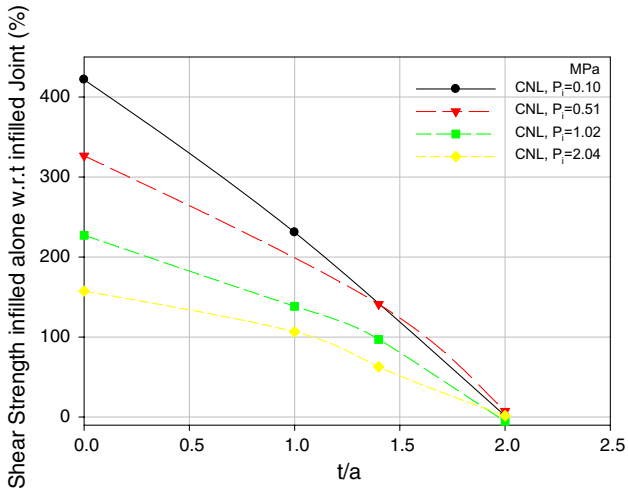


Fig. 9 Shear strength of 30°–30° joint compared with τ_{infill}

normal stress on the shearing plane increases with shear displacement under CNS condition, whereas it is constant for CNL condition for a given P_i. This increase in normal stress causes an increase in the compression of the infilled joint for CNS condition as compared to CNL at a given P_i. Due to the increase in the compression of the infill, the shearing plane will no longer pass through the infill alone, but it will start penetrating into the joint asperity also. As the shear strength of the infilled material is less than that of joints, the increase in the participation of joints will result into the increase in shear strength of the infilled joint. However, for CNL condition the participation of joint is less than that of CNS condition; hence, reduction in shear strength will be higher for CNL condition than in CNS condition. A close visual examination of the surface of the sheared joints also revealed that the asperities were subject to moderate–low-grade damage for an infill $t/a = 1.4$, i.e., thickness up to 7 mm, whereas no sign of asperity damage was observed for $t/a = 2.0$. The CNL conditions reflect only shearing of the infill material (Fig. 10a), whereas for CNS conditions, for the same $P_i = 0.10$ MPa and $t/a = 1$ the participations of the peak of joint surface can be seen easily in Fig. 6b.

De Toledo and De Freitas (1993) observed two peaks on the shear stress–displacement response while conducting tests on natural rock infilled joint under CNL conditions. The first peak is due to infilled, i.e., soil peak (gouge), and the subsequent peak is due to the natural rock joints, i.e., rock peak. Double-peak trend is not observed by Indraratna et al. (1999) while studying the influence of infilled on the simulated joint of gypsum plaster under CNS conditions. Welideniya (2005) while conducting the experiments on two types of infilled joint, i.e., 9.5° and 18.5° under CNS conditions observed a double peak only in the case of second joint, i.e., 18.5°, and the difference between peak shear

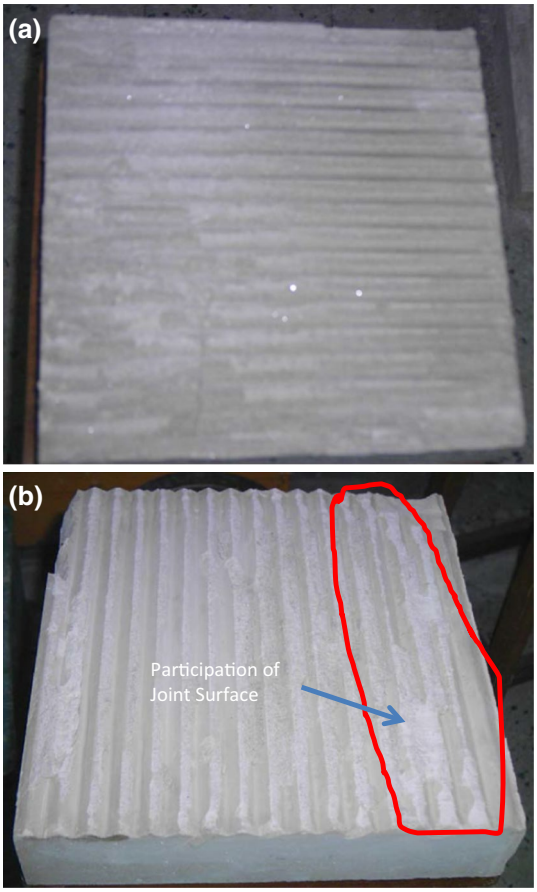


Fig. 10 Sheared sample at $P_i = 0.10$ MPa for $t/a = 1$ **a** CNL, **b** CNS conditions

stress is only marginal. Indraratna et al. (2013) observed a double peak at low t/a ratio ($t/a = 0.26$ and 0.51), the first peak corresponds to the yielding of soil infill and beyond this point asperity interference prevails, causing a significant increase in dilation. The second peak is largely influenced by a rock-to-rock contact. The double-peak phenomena become less pronounced as infill thickness increases. In the present work, single distinct peak is observed for all P_i at all t/a ratios under both CNL and CNS conditions. It is clear that the double peak is only noticed at $t/a \leq 1$, whereas for higher ratio the single peak is common.

The variation of shear displacement corresponding to peak shear stress (δ_{sp}) for different t/a ratio under CNL and CNS conditions is shown in Fig. 11. The effect of infilled material is to increase the δ_{sp} for $t/a \leq 1.4$ after that a sharp decrease in the value of δ_{sp} has been observed when t/a ratio approaches to $(t/a)_{cr}$. Similar behavior was also reported by Phien-Wej et al. (1990) for tests on infilled joint under CNL conditions and Indraratna and Haque (2000) for both CNL and CNS conditions. When $t/a \leq 1.4$, the cracking of infill takes place at smaller displacement and asperity starts providing shear resistance. But the increase in t/a ratio resulted

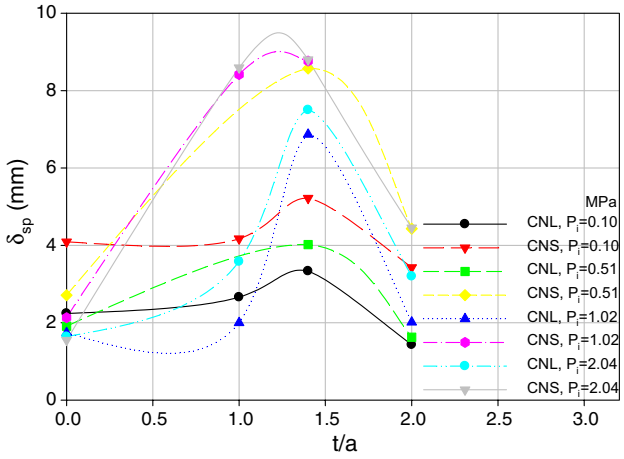


Fig. 11 Shear displacement of 30°–30° joint corresponding to peak shear stress

into more sliding to take place before cracking of the infill material and participation of the asperity in offering shear resistance. However, for $t/a \geq (t/a)_{cr}$ the shearing plane passes through infilled material alone, and joint does not participate in shearing and the peak shear stress is achieved at smaller shear displacement.

Similar to the unfilled joint, for infilled joint also peak shear stress under CNS boundary condition occurs at greater shear displacement than under CNL boundary condition (Shrivastava and Rao 2015).

The change in normal stress with shear displacement for $t/a = 1$ is presented Fig. 12. It is observed that there is no change in the normal stress with shear displacement for CNL conditions, whereas normal stress changes with shear displacement for CNS condition. The normal stress responses of infilled joints are similar to unfilled joints (Shrivastava and Rao 2010, 2011, 2015).

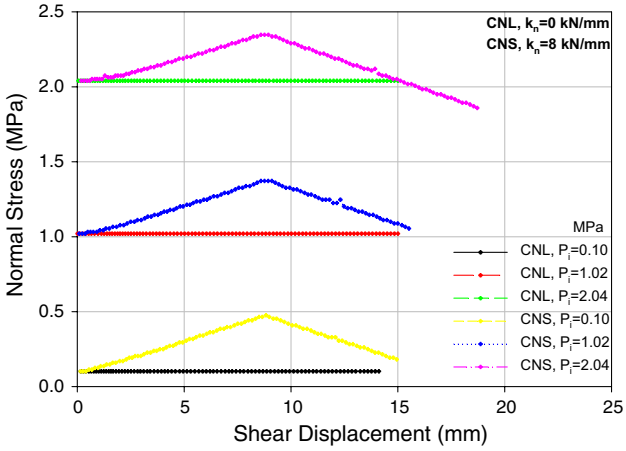


Fig. 12 Change in normal stress for $t/a = 1.0$ under CNL and CNS conditions 30°–30° joint

The results show that normal stress increases with shear displacement and reaches to the maximum value at shear displacement closure to peak of the asperity, i.e., 8.66 mm, and after that, the normal stress decreases to reach the minimum value equal to initial normal stress at shear displacement approximately equal to the length of one asperity, i.e., 17.32 mm. In the CNS boundary condition, the variation of normal stress exactly follows the shape of the asperity. Similar behavior is observed by Shrivastava and Rao (2015) for unfilled joints under CNS conditions.

The effects of infilled thickness on normal stress corresponding to peak shear stress (P_n) for different P_i values are presented in Fig. 13. The plots indicate that there is insignificant influence of infilled thickness on P_n value and it is almost constant for all t/a ratios. This is due to observed dilation (Y') at peak shear stress is same for unfilled and infilled joint. This may be because during shearing process the dry infill material gets crushed and deposits on the joint itself. No much loss of material from the sample is observed during the shearing process; hence, no change in volume takes place.

Probable strength envelope is obtained by joining the peak of different stress path for different t/a under CNL and CNS conditions. The strength envelopes of joint with different infilled thickness are compared with strength envelope of infilled material alone for CNL and CNS conditions as shown in Figs. 14 and 15, respectively. The effect of infill thickness on strength envelope is to change it from curvilinear to linear and reduce the shear strength with an increase in infill thickness for both CNL and CNS conditions, but the reduction in strength is more in the case of CNL condition than in the case of CNS condition. The reduction in shear strength is mostly due to the decrease in participation of the joint in shearing process with an increase in infilled material thickness. The infilled crushed material is deposited

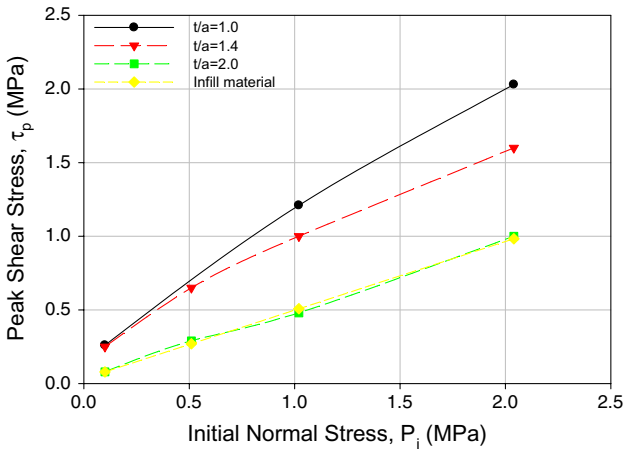


Fig. 14 Strength envelope of 30°–30° joint CNL conditions

on the joint during the shearing process, which reduces the frictional resistance and hence decreases the shear strength, even though the normal stress on a shearing plane is almost same with an increase in infill thickness. At $t/a = 2$, strength envelope of joint is similar to that of infilled material only, i.e., linear for both CNL and CNS conditions, and shear strength of the infilled joint is almost equal to that of infilled material alone. However, peak shear stress is more for CNS conditions than for CNL conditions for all levels of P_i at different t/a, due to increased normal stress on the shearing plane under CNS condition.

3.3.1.2 Joint asperity 15°–15° The shear tests at different P_i ranging from 0.10 to 2.04 MPa under CNL and CNS conditions for infilled joint ($t/a = 1$) show that the stress–strain response is almost similar to 30°–30° joint. However, the effect of infilled material on shear strength reduces with a decrease in asperity angle. The decrease in shear strength of

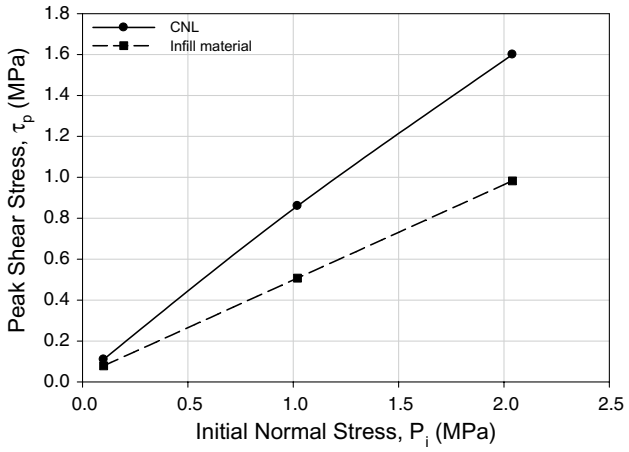


Fig. 13 Influence of t/a on peak normal stress under CNS condition for 30°–30° joint

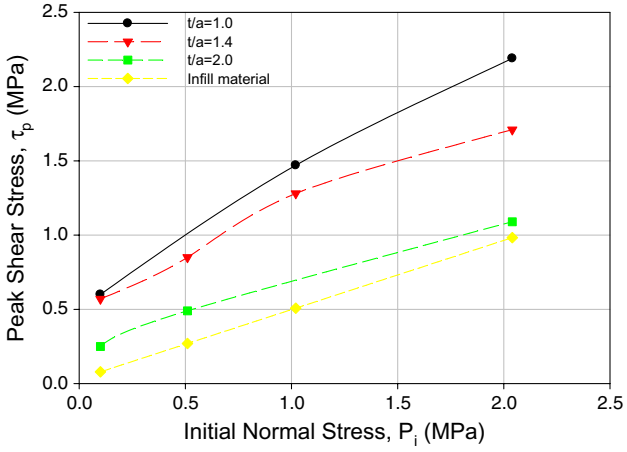


Fig. 15 Strength envelope of 30°–30° joint CNS conditions

15°–15° infilled joint as compared to the unfilled joint for $t/a = 1$ is maximum at 35.06% as compared to 43.48% for 30°–30° joint.

It is observed that the normal stress on the shear plane remains constant during testing for CNL conditions. However, for CNS conditions normal stress increases as the asperity slides over the other. Joint with asperity 15°–15° for CNS conditions shows that normal stress increases with shear displacement and reaches to the maximum value at shear displacement near to peak of the asperity and start decreasing; after that, the profile is similar to 30°–30° asperity joint.

The variation in shear stress with the normal stress for different P_i values is studied under CNL and CNS conditions, to obtain the stress path. The stress path is almost identical to 30°–30° infilled joint.

The shear strength envelopes for infilled joint having $t/a = 1$ and infilled material alone are presented in Fig. 16 for both CNL and CNS boundary conditions. The strength envelope of infilled joint can be approximated to the bilinear curve for both CNL and CNS conditions, which is curvilinear in the case of the unfilled joint as reported by Shrivastava and Rao (2015). The influence of the infilled material is to change the strength envelope from curvilinear to bilinear and the strength envelope for infilled joint changes approximately at $P_i = 0.70$ MPa.

3.3.1.3 Joint Asperity 0°–0° To study the effect of asperity on the infilled rock surface, the sample with planar infilled joints, i.e., asperity angle 0°–0°, is prepared.

The shear stress response for planar infilled joints under various P_i can be characterized by an increase in the shear stress with shear displacement till peak is reached and after that shear stress is constant, which is similar to unfilled joints as discussed in Shrivastava and Rao (2015).

The shear strength of infilled joint is always less than that of the unfilled joint. However, the increase in asperity angle increases the reduction in peak shear strength for the same thickness of infilled material. The maximum % decrease in shear strength is 25.23, 35.06 and 43.48, respectively, for 0°–0°, 15°–15° and 30°–30° infilled joints, respectively, for $t/a = 1$ for non-planar joint and $t = 5$ mm for the planar joint.

The shear and normal loads on the shearing plane are obtained from the respective load cells at a given interval of time. The peak shear stress at different initial normal stresses is obtained and plotted in Fig. 17 to obtain the strength envelope of infilled joint with $t/a = 1$ for non-planar joint and $t = 5$ mm for the planar joint.

The strength envelope is also compared with that of infilled material alone. The strength envelope is linear for both cases and also for the unfilled joint as discussed Shrivastava and Rao (2015). The only difference is a reduction in friction angle due to the presence of the infilled material. The presence of infilled material reduces the contact between the joint and hence decreases the peak shear strength.

3.4 Development of Shear Strength Model for Infilled Joint

Several models are available for the evaluation of shear parameters of clean rock joints under CNL and CNS conditions. Despite their frequent natural occurrence, filled discontinuities have been studied less, which may be because of the difficulties arising from the preparation of the sample and testing or due to an increased number of variable parameters as indicated earlier.

The commonly used models for predicting shear strength of the infilled joints are based on CNL test results, which were proposed by Lama (1978), Phien-Wej et al. (1990) and

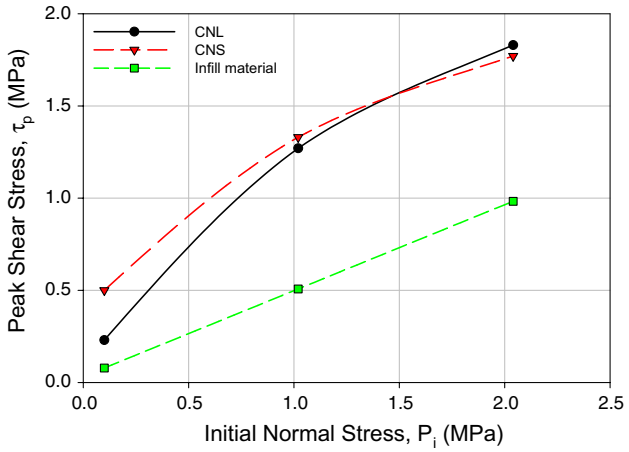


Fig. 16 Strength envelope of 15°–15° infilled joint $t/a = 1$ and infill material

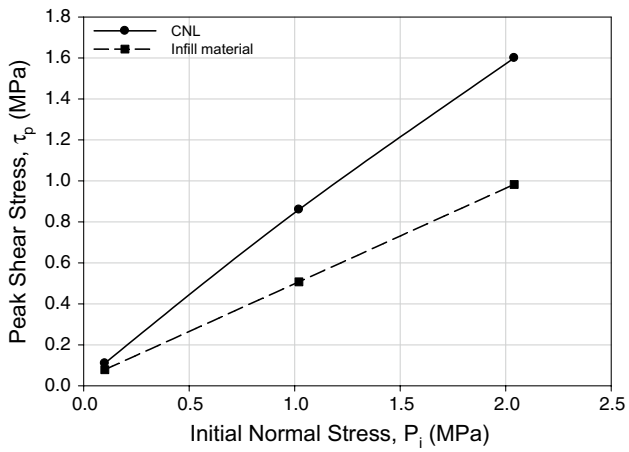


Fig. 17 Strength envelope of 0°–0° infilled joint $t = 5$ mm and infill material

Papaliangas et al. (1993). Due to unavailability of sufficient test results, limited shear strength models for infilled joints under CNS conditions are available in the literature because CNS shear tests on infilled rock joints are difficult and require complicated servo-controlled computerized equipment. Equipment developed by Shrivastava and Rao (2013) having these facilities has been used in the present work. The purpose of this section is to present a shear strength model based on test results that account for the boundary conditions and infilled material thickness on the shear strength of rock joints.

3.4.1 Prediction Model

The shear strength of the infilled joint cannot be described by an equation developed for unfilled joints as it does not take into account the effect of thickness of infilled material in reducing the shear strength.

The shear strength model for infilled joint is developed, which is based on observations made during the experimental investigation. The test results of planar and non-planar infilled joint are discussed in detail in Sect. 3.1. The influence of infilled material on strength envelope is to change from curvilinear to linear when infilled thickness reaches to a critical ratio, i.e., $t/a = (t/a)_{cr}$. This change in strength envelope is due to the reduced joint interference and the increased influence of infilled material because of the increase in the infilled thickness.

Hence, the shear strength of infilled joints can be broadly classified into two groups on the basis of t/a ratio. First, when t/a is $< (t/a)_{cr}$, both the asperity and infilled material will have control on the shear strength. Second, when $t/a > (t/a)_{cr}$ where the shear strength is governed by infilled material alone.

The bilinear strength model proposed by Patton (1966) for unfilled joint under CNL conditions is used as a basic model for the development of the new model for infilled joint. The basic Patton model is modified to take following limitations into the account:

1. normal stress on the shearing plane for CNS boundary conditions
2. decrease in the influence of the joint asperity due to an increase in the thickness of the infilled material.

Hence, Patton (1966) equation is modified to overcome the above limitations. It is developed by assuming that at peak shear stress under CNS condition, normal stress momentarily remains constant. The equation is given below:

$$\tau_{pinfill} = P_n \tan\left(\varphi_b + i'_{infill}\right) \quad (2)$$

where $\tau_{pinfill}$ = peak shear stress of infilled joint in MPa, P_n = normal stress corresponding to peak shear stress in MPa, φ_b = basic friction angle in degree, i'_{infill} = effective infilled asperity angle in degree.

3.4.1.1 Prediction Model for Normal Stress (P_n) There is no change in normal stress on a shearing plane for CNL conditions, but for CNS conditions it is governed by the stiffness of the surrounding rock joint and dilation resisted during shearing. The linear variation of the normal stress is observed during shearing in the present study, and similar observation is made by Jiang et al. (2004), Shrivastava and Rao (2015) for the unfilled joint. The variation of normal stress corresponding to peak shear stress with P_i for different asperity angles and stiffness at different t/a ratio is presented in Fig. 18. The test results indicate that there is only marginal influence of infill thickness and asperity angle on the normal stress of the joint corresponding to peak shear stress. The curve fitting of the test results indicates that there is a linear relationship between the normal stress corresponding to peak shear stress and P_i as shown by Eq. (3)

$$P_n = aP_i + b \quad (3)$$

where P_n = normal stress corresponding to the peak shear stress, P_i = initial normal stress in MPa, a and b = constants.

The regression analysis of data points of Fig. 18 indicates that the constant 'a' is almost insensitive to asperity angle and t/a ratio and can be approximated to $a = 1$, which is similar to unfilled joints. The coefficient 'b' varies from 0 to 0.36 for normal stiffness (k_n) = 0–8 kN/mm, which can be rewritten as $b = 0.045\ k_n$. The influence of infill thickness on normal stress corresponding to peak shear stress (P_n) is experimentally studied for 30°–30° joint and plotted in Fig. 19. The test results indicate that there is no effect of infill thickness on P_n. Hence for simplicity, constant b is approximated to Eq. (4) which is similar to the unfilled joint as proposed by Shrivastava and Rao (2015).

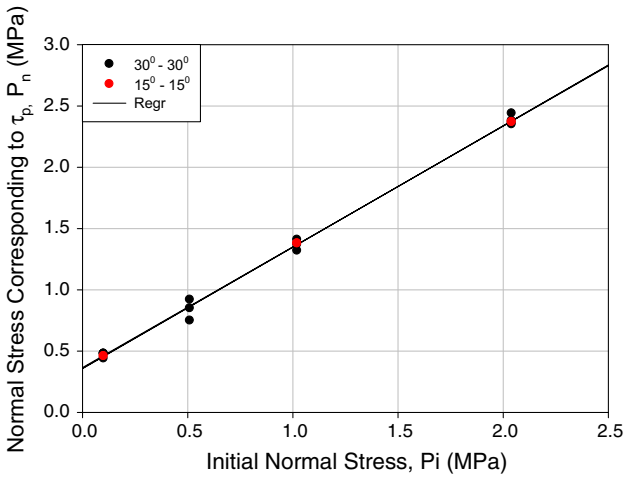


Fig. 18 Influence of infill thickness and asperity angle on P_n

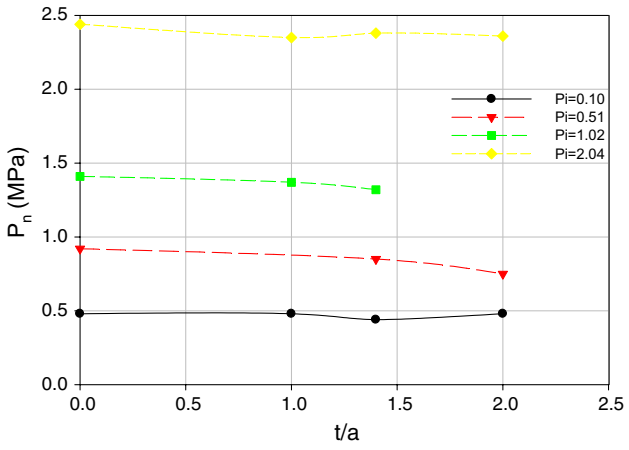


Fig. 19 Variation of P_n with infill thickness for 30°–30° joint for CNS condition

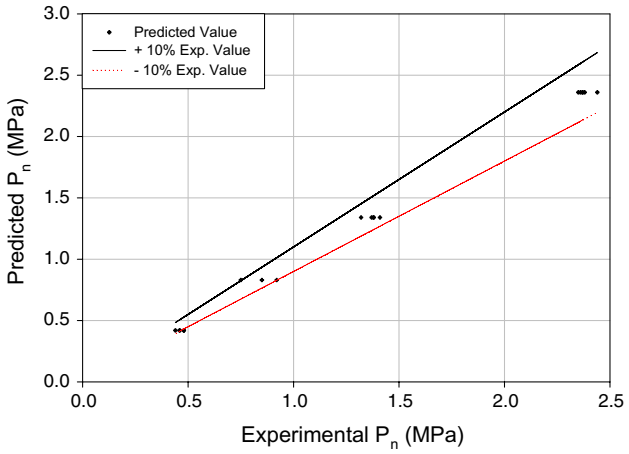


Fig. 20 Variation of predicted P_n from experimental results

$$b = 0.04\,k_n \tag{4}$$

The experimentally determined normal stress (P_n) is compared with the proposed model for different asperity joint and *t/a* ratio of infilled material. The variations of results are plotted in Fig. 20, and it can be seen that the variation of predicted results is ±10% of the experimental results.

3.4.1.2 Prediction Model for Effective Infilled Asperity Angle (i'_{infill}) A close visual examination of the surface of the sheared joints reveals that the asperities were subjected to moderate–low-grade damage for an infill *t/a* = 1.4, i.e., thickness up to 7 mm, whereas no sign of asperity damage was observed for *t/a* = 2.0. A detailed discussion about this is already presented in Sect. 3.1.1.

It indicates that the increase in *t/a* ratio causes the reduction in the participation of the asperity; hence, the term effective asperity angle for infilled joint (i'_{infill}) is introduced in Eq. (2). The reduction in the i'_{infill} depends upon P_n/σ_c ratio and *t/a* ratio for different asperity angles (i).

The dimensionless parameter i'_{infill}/i and P_n/σ_c are plotted for 30°–30° joint for *t/a* ratio 1.0, 1.4 and 2.0 to find out the decay rate of i'_{infill}, which is presented in Fig. 21a–d, respectively, and Fig. 22 for 15°–15° joint for *t/a* ratio 1.0. The decay rate is logarithmic and can be best represented by the equation given below:

$$i'_{\text{infill}}/i = x\ln(P_n/\sigma_c) + y \tag{5}$$

where i'_{infill} = effective asperity angle of infilled joint, i = initial asperity angle, P_n = normal stress corresponding to peak, shear stress calculated from Eq. (3), σ_c = uniaxial compressive strength in MPa, x and y = coefficients which depend upon *t/a* ratio and asperity angle.

The coefficients x and y along with the coefficient of determination (r^2) are given in Table 1 for different *t/a* ratios, and the intermediate value can be interpolated. It can be seen that at $t/a = 2$, i.e., at $t/a = (t/a)_{\text{cr}}$, the value of r^2 is low which will not result in a better prediction because shear strength for this case will completely depend on the shear strength of the infill alone. Hence, Eq. (5) will be valid for $t/a < (t/a)_{\text{cr}}$ and for $t/a \geq (t/a)_{\text{cr}}$ shear strength must be calculated from the shear strength of the infill only.

The calculated value of P_n and i'_{infill} from Eqs. (3) and (5) is substituted in Eq. (2) to predict the shear strength of infilled joint under both CNL and CNS conditions.

The predicted peak shear stress from proposed model is compared with the experimental results, and the variations of the results are plotted in Fig. 23 for 30°–30° joint with different *t/a* ratio. It can be seen that most of the predictions are within the tolerable variation of ±5%.

The above model will not be valid for planar infilled joint where asperity angle (i) = 0. The effect of infill material on the planar joint is to reduce friction angle (φ) in comparison with basic friction angle (φ_b). Hence, Eq. (2) is modified as given below:

$$\tau_p = P_n \tan\varphi \tag{6}$$

The dimensionless parameter φ/φ_b and P_n/σ_c are plotted for 0°–0° joint for t = 5 mm to find out the decay rate of φ, which is presented in Fig. 24. The decay rate is logarithmic and can be best represented by Eq. (7) as given below:

$$\varphi/\varphi_b = x\ln(P_n/\sigma_c) + y \tag{7}$$

where φ = friction angle of infilled joint, φ_b = basic friction angle, P_n = normal stress corresponding to peak shear stress calculated from Eq. (3) σ_c = uniaxial compressive strength in MPa x and y = coefficients which depend upon *t/a* ratio and asperity angle.

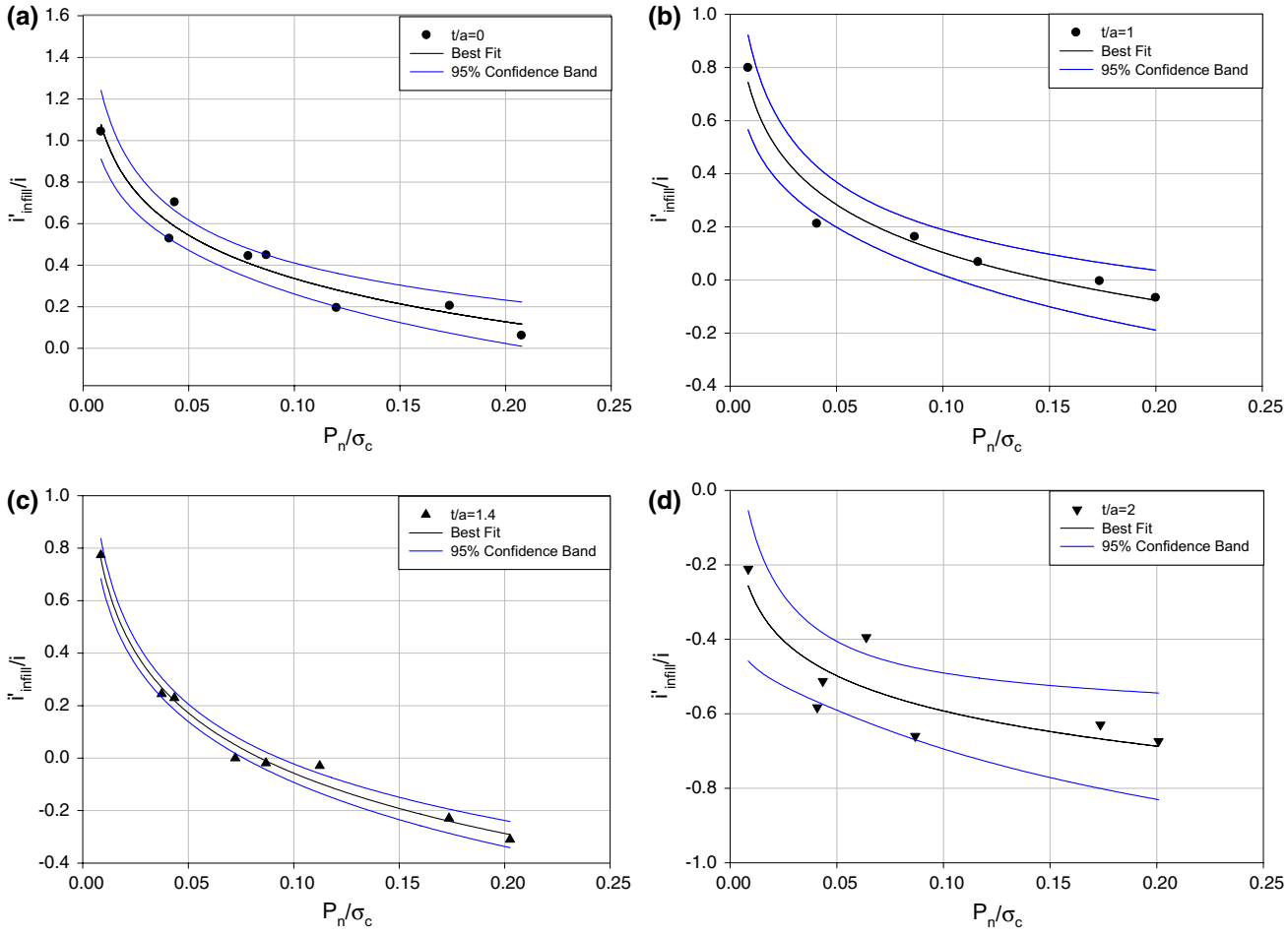


Fig. 21 Best fit curve for 30°–30° joint **a** $t/a = 0$, **b** $t/a = 1.0$, **c** $t/a = 1.4$, **d** $t/a = 2.0$

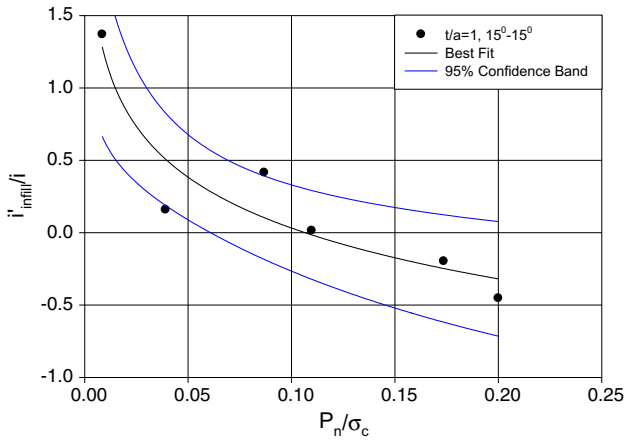


Fig. 22 Best fit curve for 15°–15° joint for $t/a = 1.0$

The coefficients x and y along with the coefficient of determination (r^2) are presented in Table 1. The calculated values of P_n and φ from Eqs. (3) and (7) are substituted in Eq. (6) to predict the shear strength of infilled joint under both CNL and CNS conditions. To predict it, the basic parameters like φ_b, σ_c and k_n are required for any rock joint, which can be easily determined in the laboratory having simple testing facility or data can be adopted from the literature. The asperity angle (i) is either measured or can be calculated from JRC values by the method suggested by Maksimovic (1996), which can be approximated to $i = 2\,X$ JRC. The predicted peak stress and normal stress for different boundary conditions, asperity angle and infill thickness are compared with the experimental results. The experimental results are

Table 1 Coefficients x and y

Asperity angle (i)	t/a	X	Y	$r2$
30°–30°	0	−0.30	−0.356	0.95
	1	−0.26	−0.494	0.96
	1.4	−0.33	−0.821	0.99
	2	−0.13	−0.906	0.75
15°–15°	1	−0.51	−1.14	0.88
0°–0°	$t = 5$ mm	−0.07	0.73	0.99

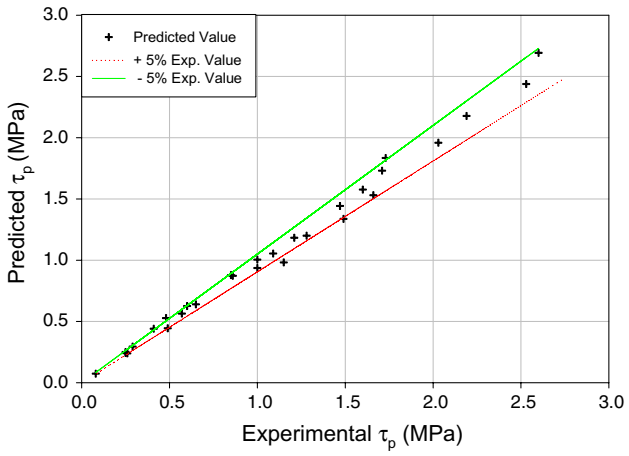


Fig. 23 Variation of τ_p predicted with experimental results for 30°–30° joint

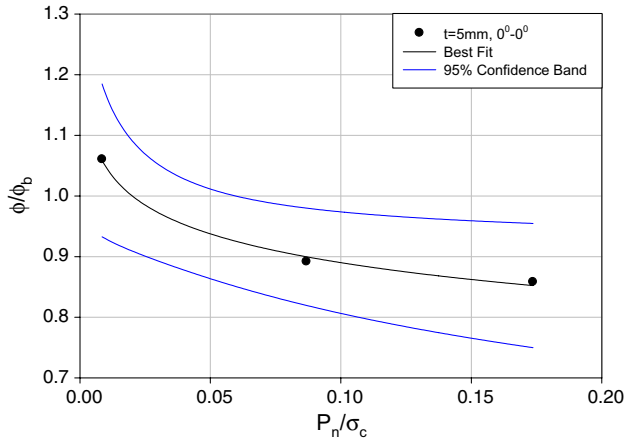


Fig. 24 Best fit curve for 0°–0° joint for $t/a = 1.0$

also compared with the prediction model proposed by Lama (1978), Fishman (2004) and Indraratna et al. (2005) which is presented in Table 2, the % variation in predicted result as compared to experimental results are also tabulated. It is observed that the Lama (1978) and Fishman (2004) models do not give any importance to joint roughness, joint compressive strength and degradation of the joint asperity during the shearing process; hence, very high variation between the predicted strength and experimental results has been observed, since these models proposed will be applicable to only joints which have been tested for development of the prediction model. Similarly, Indraratna et al. (2005) have considered the effect of joint roughness, degradation in the joint roughness and change in normal stress on the shearing plane during the shearing process, which has resulted into better prediction than earlier model, as the decay of joint roughness and decrease in the participation of joint in the shearing process since the increase in the thickness of infilled material is not well modeled. The % variation, in this case, is also higher than the acceptable limit of 10%. However, the proposed model has predicted the results mostly within 10% of the variation. The limitations of the current model are presented below:

1. The present study is done on model material representing the rock with very low strength and low modulus ratio. A future study may be extended to a different variety of model materials or natural rock simulating the joints from low to high strength.
2. Only triangular profile of asperity is investigated in the present study which gives 2D effect, but in field conditions asperities are wavy and 3D, hence examining the effect of wavy and irregular geometric patterns put further light on the shear behavior of infilled joints.
3. The testing has been performed under static conditions; the effect of dynamic loading will be important for infilled joints and extend the current knowledge of rock joints testing.
4. The role of different types of infill material and infill thickness on the joint shear response is imperative and must be investigated in more detail.
5. The joint and infill in dry conditions have been investigated in the present study, but in the field, joints are fully or partially saturated. Hence, it is important to examine the effect of changing water content of a given infill and shear strength analysis must be based on effective stress principle.

4 Conclusions

The influence of boundary conditions and thickness of the infill material on shear behavior of modeled joint with different asperities (30°–30° 15°–15° and 0°–0°) were systematically observed, and a new shear strength model is proposed based on experimental results for infilled joints with different infill thicknesses and asperity angles under CNL and CNS conditions.

The experimental results show that the shear strength of the joints decreases sharply with the addition of infill material for all values of P_i and asperity angle. When only shear strength of infill material (τ_{infill}) is compared with shear strength of infilled joints ($\tau_{p\text{infill}}$), a rapid reduction in shear strength is observed with the increase in t/a ratio, and it is observed that when $t/a = 2$, the shear strength of the joint approaches the shear strength of infill material only and this ratio is defined as the critical ratio.

A close visual examination of the surface of the sheared joints also reveals that the asperities were subjected to moderate–low-grade damage for an infill up to $t/a = 1.4$, i.e.,

Table 2 Comparisons of proposed model with available prediction model

i	k	t/a	P_i	P_n exp.	P_n prop.	P_n exp.	τ_P prop.	% variation	τ pred. Indraratna et al. (2005)	% variation	τ_{p1} pred. Fishman (2004)	% variation	τ_{p2} pred. Fishman (2004)	% variation	τ_p pred. Lama (1978)	% variation
30	0	1	0.1	0.1	0.1	0.26	0.24	7.95	0.12	55.69	0.14	46.15	0.06	75.38	0.04	85.26
30	0	1	1.02	1.02	1.02	1.21	1.18	2.28	1.17	2.89	1.43	−18.02	0.65	46.05	0.39	67.58
30	0	1	2.04	2.04	2.04	2.03	1.96	3.58	2.35	−15.76	2.86	−40.69	1.31	35.68	0.80	60.37
30	8	1	0.1	0.48	0.42	0.6	0.63	−4.31	0.12	80.80	0.59	2.00	0.31	48.80	0.18	69.99
30	8	1	1.02	1.37	1.34	1.47	1.44	1.93	1.17	20.07	1.88	−27.62	0.88	40.35	0.53	63.77
30	8	1	2.04	2.35	2.36	2.19	2.18	0.63	2.35	−7.31	3.30	−50.87	1.50	31.32	0.93	57.47
30	0	1.4	0.1	0.1	0.1	0.25	0.24	3.32	0.08	69.25	0.13	48.04	0.06	75.88	0.04	85.92
30	0	1.4	0.51	0.51	0.51	0.65	0.64	1.71	0.39	39.67	0.66	−1.93	0.31	52.69	0.18	72.13
30	0	1.4	1.02	1.02	1.02	1	1.00	−0.39	0.78	21.58	1.33	−32.50	0.62	38.50	0.37	62.53
30	0	1.4	2.04	2.04	2.04	1.6	1.58	1.51	1.57	1.97	2.65	−65.63	1.23	23.12	0.78	51.56
30	8	1.4	0.1	0.44	0.42	0.57	0.56	1.06	0.08	86.51	0.55	4.28	0.27	53.45	0.16	72.76
30	8	1.4	0.51	0.85	0.83	0.85	0.88	−3.20	0.39	53.87	1.08	−26.85	0.51	39.70	0.31	63.60
30	8	1.4	1.02	1.32	1.34	1.28	1.20	6.26	0.78	38.73	1.74	−36.00	0.80	37.82	0.49	61.63
30	8	1.4	2.04	2.38	2.36	1.71	1.73	−1.17	1.57	8.28	3.07	−79.29	1.44	16.08	0.91	46.74
30	0	2	0.1	0.1	0.1	0.08	0.07	7.87	0.05	41.75	0.12	−49.01	0.06	29.53	0.03	60.12
30	0	2	0.51	0.51	0.51	0.29	0.29	−1.70	0.24	18.04	0.61	−109.64	0.29	0.86	0.17	41.38
30	0	2	1.02	1.02	1.02	0.48	0.53	−9.86	0.48	0.97	1.22	−153.31	0.58	−19.80	0.36	25.83
30	0	2	2.04	2.04	2.04	1	0.94	6.45	0.95	4.93	2.43	−143.18	1.15	−15.01	0.74	25.62
30	8	2	0.1	0.48	0.42	0.25	0.25	−0.13	0.22	10.52	0.50	−100.27	0.27	−8.24	0.16	36.25
30	8	2	0.51	0.75	0.83	0.49	0.44	9.40	0.35	28.67	0.99	−101.92	0.42	13.71	0.26	47.66
30	8	2	2.04	2.36	2.36	1.09	1.05	3.29	1.10	−0.90	2.81	−158.10	1.33	−22.06	0.87	20.38
15	0	1	0.1	0.1	0.1	0.22	0.21	5.42	0.07	68.28	0.14	36.36	0.06	70.91	0.04	82.58
15	0	1	1.02	1.02	1.02	1.27	1.08	15.15	0.71	43.96	1.43	−12.44	0.65	48.60	0.39	69.11
15	0	1	2.04	2.04	2.04	1.84	1.79	2.69	1.42	22.64	2.86	−55.22	1.31	29.04	0.80	56.27
15	8	1	0.1	0.46	0.42	0.5	0.56	−12.93	0.07	86.04	0.59	−17.60	0.29	41.12	0.17	65.53
15	8	1	1.02	1.29	1.34	1.3	1.32	−1.25	0.71	45.25	1.88	−44.31	0.83	36.49	0.50	61.51
15	8	1	2.04	2.35	2.36	1.85	1.99	−7.65	1.42	23.05	3.30	−78.59	1.50	18.70	0.93	49.65

thickness up to 7 mm, whereas no sign of asperity damage was observed for $t/a = 2.0$.

The proposed shear strength model is applicable for the similar type of joint conditions; if it changes, the coefficients have to be determined by conducting tests. Hence, for wide application, a strong database is required to be developed for low–high-strength material, regular to irregular joint profile, varying infill material, varying infill thickness, varying infill compactness and saturation in both static and cyclic conditions.

References

Bandis S, Lumsden AC, Barton NR (1981) Experimental studies of scale effects on the shear behavior of rock joints. Int J Rock Mech Min Sci Geomech Abstr 18:1–21

Barton N (1971) Estimation of in situ shear strength from back analysis of failed rock slopes. In: Rock fracture; proc. int. syrup. rock mech., vol II. Nancy, p 27

Barton N (1973) Review of a new shear strength criterion for rock joints. Eng Geol 7:287–332

Barton N, Choubey V (1977) The shear strength of rock joint in theory and practice. Rock Mech 10:1–54

Cheng F, Haberfield CM, Seidel JP (1996) Laboratory study of bonding and wall smear in rock socketed piles. In: Jaska MB, Kaggwa WS, Cameron DA (eds) 7th Australia/New Zealand conference on geomechanics, Adelaide, Australia, The Institution of Engineers, Australia, pp 69–74

De Toledo PEC, De Freitas MH (1993) Laboratory testing and parameters controlling the shear strength of filled rock joints. Geotechnique 43:1–19

Deere DU, Miller RP (1966) Engineering classification and index properties of rock. Technical report no. AFNL-TR-65-116, Air Force Weapons Laboratory, Albuquerque

Fishman YA (2004) Shear resistance along rock mass discontinuities: results of large-scale field tests. Int J Rock Mech Min Sci Geomech 41:1029–1034

Goodman RE (1970) The deformability of joints, determination of the in situ modulus of deformation of rock. ASTM STP 447, American Society for Testing and Materials, pp 174–196

Goodman RE (1974) The mechanical properties of joints. In: Proc. 3rd congr., vol IA. ISRM, Denver, pp 127–140

Hoek E (1983) Strength of jointed rock masses. 23rd Rankine Lect Geotech 33(3):187–223

Indraratna B, Haque A (2000) Shear behavior of rock joints. Balkema, Rotterdam

Indraratna B, Welideniya HS (2003) Shear behavior of graphite infilled joints based on constant normal stiffness (CNS) test conditions. In: Proc. 10 th Congr., int. soc. rock mech—technology roadmap for rock mechanics, vol 1. Johannesburg, pp 569–574

Indraratna B, Haque A, Aziz N (1998) Laboratory modelling of shear behavior of soft joints under constant normal stiffness condition. J Geotech Geolog Eng 16:17–44

Indraratna B, Haque A, Aziz N (1999) Shear behavior of idealized joints under constant normal stiffness. Geotechnique 49(3):331–355

Indraratna B, Welideniya HS, Brown ET (2005) A shear strength model for idealised infilled joints under constant normal stiffness. Geotechnique 55(3):215–226

Indraratna B, Jayanathan M, Brown ET (2008) Shear strength model for over consolidated clay—infilled idealised rock joints. Geotechnique 58(1):55–65

Indraratna B, Oliveira DAF, Brown ET, Assis APD (2010) Effect of soil–infilled joints on the stability of rock wedges formed in a tunnel roof. Int J Rock Mech Min Sci 47:739–751

Indraratna B, Premadasa WN, Oliveira D (2012) Physical modeling of soil infilled discontinuities, ASCE. Geo Congr 2012:2312–2321

Indraratna B, Premadasa WN, Brown ET (2013) Shear behavior of rock joints with unsaturated infill. Geotechnique 63(5):1356–1360

Indraratna B, Premadasa WN, Brown ET, Gens A, Heitor A (2014) Shear strength of rock joint influenced by compacted infill. Int J Rock Mech Min Sci 70:296–307

ISRM (1977) Suggested method for determining water content, porosity, density, absorption and related properties and swelling and slake-durability index properties. In: Ulusay R, Hudson JA (eds) EUR 4, The complete ISRM suggestedmethods for rock characterization, testing and monitoring:1974-2006. ISRM Turkish National Group, Ankara, Turkey

ISRM (1979) Suggested method for determining the uniaxial compressive strength and deformability of rock materials. In: Ulusay R, Hudson JA (eds) EUR 4, The complete ISRM suggested methods for rock characterization, testing and monitoring:1974-2006. ISRM Turkish National Group, Ankara, Turkey

Jahanian H, Sadaghiani MH (2015) Experimental study on shear strength of sandy clay infilled regular rough rock joints. Rock Mech Rock Eng 48:907–922

Jiang Y, Xiao J, Tanabashi Y, Mizokami T (2004) Development of an automated servo-controlled direct shear apparatus applying a constant normal stiffness condition. Int J Rock Mech Min Sci 41:275–286

Kanji MA (1974) Unconventional laboratory tests for the determination of the shear strength of soil–rock contacts. In: Proceedings of the 3rd international congress of the international society for rock mechanics, vol 2. Denver, Colorado, pp 241–247

Kim DY, Chun BS, Yang JS (2006) Development of a direct shear apparatus with rock joints and its verification tests. Geotech Test J 29(5):1–9

Ladanyi B, Archambault G (1970) Simulation of shear behavior of a jointed rock mass. In: Proceedings of the 11th US symposium on rock mechanics. Berkeley, pp 105–125

Ladanyi B, Archambault G (1977) Shear strength and deformability of filled indented joints. In: Proc. int. symp. on geotechnics of structurally complex formations, Italian Geotech. Assoc., vol l. Capri, pp 317–326

Lama RD (1978) Influence of clay fillings on shear behavior of joints. In: Proc. 3rd congr. int. assoc. eng. geol., vol 2. Madrid, pp 27–34

Maksimovic M (1996) The shear strength components of a rough rock joint. Int J Rock Mech Min Sci Geomech. Abstr 33:769–783

Naghadehi MZ (2015) Laboratory study of the shear behavior of natural rough rock joints infilled by different soil. Period Polytech Civ Eng 59(3):413–421

Obert L, Brady BT, Schmechel FW (1976) The effect of normal stiffness on the shear resistance of rock. Rock Mech 8(2):57–72

Ong HY (2006) Behavior of filled joint under shear loading. M. Tech thesis, Universti Teknologi, Malaysia

Ooi LH, Carter PJ (1987) A constant normal stiffness direct shear device for static and cyclic loading. Geotech Test J 10(1):3–12

Papaliangas T, Lumsden AC, Hencher SR, Manolopoulou S (1990) Shear strength of modelled filled rock joints. In: Loen, N, Barton, N. Stephansson, O. (eds) Proceedings of the international symposium on rock joints. Balkema, A.A., Rotterdam, pp 275–282

Papaliangas T, Hencher SR, Lumsden AC, Manolopoulou S (1993) The effect of frictional fill thickness on the shear strength of rock discontinuities. Int J Rock Mech Min Sci Geomech Abst 30:81–91

Patton FD (1966) Multiple modes of shear failure in rock and related materials. PhD thesis, University of Illinois, Urbana

Pereira JP (1997) Rolling friction and shear behavior of rock discontinuities filled with sand. Int J Rock Mech Min Sci 34:3–4 **(Paper No. 244)**

Phien-wej N, Shrestha UB, Rantucci G (1990). Effect of infilled thickness on shear behavior of rock joints. In: Loen, N, Barton, N, Stephansson O (eds) Proceedings of the international symposium on rock joints. Balkema A.A., Rotterdam, pp 289–94

Rao KS, Shrivastava AK, Singh J (2009) Development of an automated large scale direct shear testing machine for rock. Indian Geotechnical Conference, Guntur, pp 238–244

Seidel JP, Haberfield CM (2002) A theoretical model for rock joints subjected to constant normal stiffness direct shear. Int J Rock Mech Min Sci Geomech 39(5):539–553

Shrivastava AK (2012) Physical and numerical modelling of shear behavior of jointed rocks under CNL and CNS boundary conditions. PhD thesis, IIT Delhi

Shrivastava AK, Rao KS (2009) Shear behavior of jointed rock: a state of art. Indian Geotechnical Conference, Guntur, pp 245–249

Shrivastava AK, Rao KS (2010) Estimation of contact area undergoing shearing for the rock mass. Indian Geotechnical Conference, Guntur, pp 891–894

Shrivastava AK, Rao KS (2011) Shear behavior of non planar rock joints. In: 14th ARC on soil mechanics and geotechnical engineering, 296_147, Hong Kong, China

Shrivastava AK, Rao KS (2013) Development of a large-scale direct shear testing machine for unfilled and infilled rock joints under constant normal stiffness conditions. Geotech Test J 36(5):670–679

Shrivastava AK, Rao KS (2015) Shear behavior of rock joints under CNL and CNS boundary conditions. Int J Geotech Geol Eng 33(3):1205–1220

Sinha UN, Singh B (2000) Testing of rock joints filled with gouge using a triaxial apparatus. Int J Rock Mech Min Sci 37:963–981

Welideniya HS (2005). Laboratory evaluation and modeling of shear strength of infilled joints under constant normal stiffness (CNS) conditions. PhD thesis, University of Wollongong, Australia

Xie H, Pariseau WG (1992) Fractal estimate of joint roughness coefficients. In: Proc. int. conf. on fractal and jointed rock masses, Lake Tahoe, California, USA, 3-5 June, pp 125–131

International Journal of Research in Engineering and Innovation (IJREI)
journal home page: http://www.ijrei.com
ISSN (Online): 2456-6934



Second law analysis of super critical power plant using entropy generation method

R.S Mishra, Prashant Bansal

Department of Mechanical, Production and Automobile Engineering, Delhi Technological University, Delhi, India

Abstract

The increasing demand of power has made the power plants of scientific interest, but most of the power plants are designed by the energetic performance criteria based on first law of thermodynamics only. The real useful energy loss cannot be justified by the fist law of thermodynamics, because it does not differentiate between the quality and quantity of energy. Energy analysis presents only quantities results while exergy analysis presents qualitative results about actual energy consumption. In this analysis shows exergy efficiency is less at each and every point of unit equipment's. Also presents major losses of available energy at combustor, superheater, economizer and air-pre heater section. In this article also shown energy exergy efficiency, exergy destruction and energy losses comparison charts. The primary objectives of this work is to analyze the system components separately and to identify and quantify the sites having largest energy and exergy losses at different load. A numerical code is established to perform the calculations required for the thermal and exergy plant analysis considering real variation ranges of the main operating parameters such as pressure, temperature and mass flow rate. The effects of theses parameters on the system performances are investigated. © 2017 ijrei.com. All rights reserved

Keywords: Second Law Analysis, Super Critical Power Plant, Thermodynamic Analysis, Irreversibility optimization

1. Introduction

A power plant is defined as the assembly of equipment that generates a flow of mechanical or electrical energy. The equipment used is known as the generator. Power plants are generally classified into two types: conventional power plants and non-conventional power plants, and they are classified based on the electricity generation devices and fuel. Power plants classified regarding the electricity generation devices such as turbines are called conventional power plants. Examples of conventional sources of energy include coal, natural gas, petroleum, and water power. The device that drives electricity generation determines the kind of power plant. For instance, steam turbine plants use the dynamic pressure generated by expanding steam to run the blades of a turbine. Some other kinds of the conventional power plants are: gas turbine plants, combined cycle plants, internal combustion plants, pulverized coal-fired power plants, circulating fluidized bed power plants, pressurized fluidized bed power plants, integrated gasification cycle power plants, hydro-electric power plants, nuclear power plants, diesel power plants, steam turbines, and steam engines. Among the above different kinds of power plants, steam turbines, steam engines, diesel power plants, and nuclear power plants are categorized as the thermal power plants because they convert heat into the electric energy. Power Plants that are classified based on fuel type are called non-conventional power plants. Some of the fuels used are biomass, solar, biogas, wind, tidal, and geothermal. Some examples of the power plants are thermo-electric generator, fuel cell power plants, photovoltaic solar cell power systems, fusion reactors, geothermal energy, plants, wind energy power systems, tidal wave plants, and biogas and biomass energy power system. In India electricity sector had an installed capacity of 303 GW as of 30 Jun2016. Renewable plants constituted 28% of total installed capacity and Non-

Corresponding author: R.S. Mishra
Email Id: rsmishradtu@gmail.com

Renewable Power Plants constituted the remaining 72%. The total electricity generated by utilities is 1,106 TWh (1,106,000 GWh) and 166 TWh by captive power plants till date. Gross electricity generation includes auxiliary power consumption of power generation plants. India became the world's third largest producer of electricity in the year 2013 with 4.8% global share in electricity generation surpassing Japan and Russia.
This paper mainly deals with followings

1. Detailed energy and exergy analysis of different component of super critical power plant
2. Parametric Studies of different parameters with respect to different factors like comparison of first law and second law efficiency with temperature and pressure.

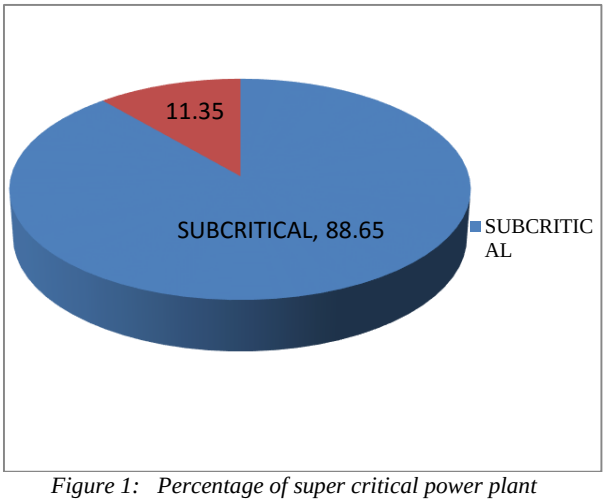


Figure 1: Percentage of super critical power plant

3. Variation of thermal performances with the changes in different component at different values of temperature and pressure.

2. Literature Review

The electricity sector in India supplies the world's 6th largest energy consumer, accounting for 3.4% of global energy consumption by more than 17% of the global population. Due to the fast paced growth of Indian economy there has been an average increase of 3.6% in the energy demand per annum over the last 30 years.
Mukesh gupta et.al [1] analyzed the exergy of a power plant as the way to approach the analysis of a power plant. The study points out that the boiler, combustor and turbine are the critical components where maximum exergy losses occur. The first law analysis shows major energy loss has been found to occur in condenser. The second law (Exergy) analysis shows that combustion chamber in both steam and gas turbine thermal power plants are main source of Irreversibility. The Irreversibility in condenser is insignificant, because in the condenser the low quality energy is lost. An Exergy method of optimization gives logical solution improving the power production opportunities in thermal power plants. Satyanarayana et.al [2] performed energy and exergy analyzes of the cycle in the pressure range between 200bar to 425 bar and temperature range are 5000C-8000C. First law analysis and second law analysis has carried out throw with and withot reheat. The irreversibility and fractional exergy loss are determined for the cycle with and without reheat. It is found that the cycle efficiency is high in reheat than the nonreheat supercritical cycle. It is also conclude that exergy efficiency is high in reheat than non-reheat supercritical cycle. It is found that nearly 20-25% irreversibility is reduced by using single reheat in the boiler, where as it is 12-15% in the turbine than the without reheating. Fractional exergy losses of all the components in the cycle is determined and compared with and without supercritical cycle..Pandey et.al.[3] concluded that the energy efficiency of the cycle increases as a result of using regeneration, open FWH and closed FWH. From the exergy analysis it is found that the exergy losses due to irreversibility were maximum in the boiler than in the turbine followed by the condenser. Further it was seen that the fractional irreversibility in the boiler increases with turbine inlet temperature whereas it decrease with increase in boiler pressure. In the present work a simple reheat-regenerative rankine cycle was considered for calculation of energy efficiency, exergy efficiency and the irreversible losses. S C kaushik et.al.[4] carried out the energetic and exergetic analysis on a 660 MWe coal fired supercritical thermal power plant at 100%, 80% and 60% of normal continuous rating (NCR) conditions under constant pressure as well as pure sliding pressure operation and to highlight the benefits of the latter over the former. The energetic input, energetic output, exergetic input, exergetic output, energetic and exergetic efficiencies of various components of the supercritical thermal power plant are estimated at 660 MWe, 528 MWe and 396 MWe load under both constant pressure as well as pure sliding pressure operation. Also the energy losses and exergy destruction in various components of a power plant i.e. Boiler, high pressure turbine (HPT), intermediate pressure turbine (IPT) , low pressure turbine (LPT), condenser, gland steam coolers, condensate extraction pumps, low pressure heaters (LPH), drip pumps (DP), deaerator (D), boiler feed pump (BFP) and high pressure heaters (HPH) have been calculated. The results have shown that the boiler has the maximum rate of exergy destruction than any other component in the power plant. After the boiler, turbine has the maximum rate of exergy destruction than any other component of the power plant. The study reveals that there is a significant reduction in the rate of exergy destruction at part load conditions for the turbine in case of sliding pressure operation in comparison to constant pressure operation. S

C kaushik et.al [5] carried out the energetic and exergetic analysis of natural gas fired combined cycle power plant, Linear Fresnel Reflecting Solar Concentrator and also solar aided natural gas fired combined cycle power plant. The exergetic analysis shows that combustion chamber subsystem followed by heat recovery steam generator (HRSG) is main source of exergy loss in a natural gas fired combined cycle power plant. The exergetic power loss in the condenser is less. In the analysis linear Fresnel reflecting solar concentrator (LFRSC) by increasing focal distance and decreasing width linear Fresnel reflector, total reflector area come close to actual reflector area. By the increasing of normal incidence beam solar radiation (Ib) both energetic and exergetic efficiencies increases. Increasing inlet temperature and decreasing the mass flow rate of thermic fluid exergetic efficiency is increased. Sandhya hasti et.al [6] performed exergy analysis for ultra-super-critical power plant. The analysis was carried out by means of process simulation using a computer model developed in Microsoft Excel .The model was based on the concepts of coal combustion, energy balances, enthalpy balances, entropy changes and heat transfer of the steam power cycle. After development, the validated model was used to simulate the hypothetical power plant combusting lignite coal with the net output of 422 MW. The exergy loss indicates that the highest concentration of losses appears to be the furnace followed by the turbine. M.K. Gupta et.al , [7] carried out energy and exergy analysis for the different components of a proposed conceptual direct steam generation (DSG) solar–thermal power plant (STPP). It has been found that the maximum energy loss is in the condenser followed by solar collector field.The maximum exergy loss is in the solar collector field while in other plant components it is small. The possibilities to further improve the plant efficiency are identified and exploited. For minimum exergy loss in receiver the inlet temperature of water to the receiver, which is governed by the number of feed water heaters (FWHs), bleed pressure and mass fraction of bleed steam, must be optimum. V. Siva Reddy et.al [8] carried out energetic and exergetic analysis for natural gas fired combined cycle power plant, Linear Fresnel Reflecting Solar Concentrator and also solar aided natural gas fired combined cycle power plant. The exergetic analysis shows that combustion chamber subsystem followed by heat recovery steam generator (HRSG) is main source of exergy loss in a natural gas fired combined cycle power plant. It is observed that the utilization of solar energy for feed water heating and low pressure steam generation is more effective based on exergetic analysis rather than energetic analysis. Ligang Wang et.al [9] performed exergy analysis on supercritical coal-fired power plant. The results show that the ratio of exogenous exergy destruction differs quite a lot from component to component. In general, almost 90% of the total exergy destruction within turbines comes from their endogenous parts, while that of feed water preheaters contributes more or less 70% to their total exergy destruction. Moreover, the boiler subsystem is proven to have a large amount of exergy destruction caused by the irreversibilities within the remaining components of the overall system. It is also found that the boiler subsystem still has the largest avoidable exergy destruction. S.K. Soma et.al [10] studies thermodynamic irreversibility and exergy analysis in the processes of combustion of gaseous, liquid and solid fuels. The need for such investigations in the context of combustion processes in practice is first stressed upon and then the various approaches of exergy analysis and the results arrived at by different research workers in the field have been discussed. It has been recognized that, in almost all situations, the major source of irreversibility's is the internal thermal energy exchange associated with high temperature gradients caused by heat release in combustion reactions. The primary way of keeping the exergy destruction in a combustion process within a reasonable limit is to reduce the irreversibility in heat conduction through proper control of physical processes and chemical reactions resulting in a high value of flame temperature but lower values of temperature gradients within the system. V. Raghavan et.al. [11] has performed entropy generation during the quasi-steady combustion of spherical liquid fuel particles .The effects of free stream velocity, particle diameter, ambient temperature and gravity, on the entropy generation rate, have been discussed in detail. In the range of subcritical freestream velocity, where an envelope flame is present, the entropy generation rate presents a minimum value. At a critical velocity, where the flame transition occurs, the entropy generation rate reaches a maximum value. Flame transition significantly affects the entropy generation rate, which suffers a sharp decrease in its value after the transition. Meeta Sharma et.al. [12] has performed exergy analysis of a dual pressure (DP) heat recovery steam generator (HRSG) having steam generation at high pressure (HP) and low pressure (LP) in the range of 50–70 bar and 2–6 bar respectively in the gas/steam combined cycle power plant for varying dead states. The in-operation plant data for this study are taken from a gas/steam combined cycle power plant at Auraiya (U.P.), India. Results have been obtained for exergy loss and exergy efficiency with varying dead state temperatures for different HP and LP steam generation states in different sections of HRSG. The exergy analysis for chosen conditions/parameters helps in locating the particular sections of the HRSG having maximum exergy loss. It is found that at varying steam generation pressures the HP and LP super heater sections and at higher dead state temperatures the HP evaporator are found to act as major source of irreversibilities. Cuneyt Uysal et.al [13] carried out the exergetic and thermo economic analyses of a coal-fired power plant with 160 MW capacity where located in Turkey were performed. Specific Exergy Costing (SPECO) and Modified Productive Structure Analysis (MOPSA) methods were separately applied to the system

to determine the unit exergy cost of electricity generated by the coal-fired plant. The differences of these methods were discussed. As a result, the exergy efficiency of coal-fired power plant is found to be 39.89%. The equipment having the highest improvement potential is determined as boiler. Ravinder Kumar[14] concluded that the maximum energy loss occurs in the condenser and next to it is boiler. The major exergy destruction has been found in the boiler. It was found that the cost of exergy destruction in the boiler and turbine is higher in comparison to the other components cost. In case of gas fired power plant, it was found that the combustor is the most inefficient apparatus and is the major destructor of exergy. In a combined cycle power plant the highest exergy destruction is caused by the combustion chamber using both conventional and advanced exergetic analyses. Ningning Si, et.al [15] evaluated the thermal performance of a 1000 MW double reheat ultra-supercritical power plant. An exergy analysis was performed to direct the energy loss distribution of this system. Based on the exergy balance equation, together with exergy efficiency, exergy loss coefficient, and exergy loss rate, the exergy distribution and efficiency of the unit were determined. Results show that the highest exergy loss in furnace is as high as 85%, which caused by the combustion of fuel and heat exchange of water wall. Kwang Y. Lee et.al [16] analyzed that ultra-super-critical (USC) boiler power plants are currently being developed to increase the efficiency of standard fossil fuel power plants. The modelling and control of a large-scale 1000 MW once-through type ultra-super-critical boiler power plant is investigated here. Larger more complicated power plants require more sophisticated methods to streamline the modelling process as well as more sophisticated control schemes that can be used to further enhance plant efficiency. Sairam Adibhatla et.al [17] carried out thermodynamic analysis of integrate solar aided feed water heating with a 500 MWe sub critical coal fired thermal power plant. Complete bleed steam substitution in high pressure heaters (HPH) has been attained by placing a feed water heat exchanger (FWHE) in parallel to the HPH group for solar aided feed water heating. Exergy and thermo economic analyses have been performed on both reference 500 MWe and conceptual solar aided 500 MWe thermal power plants. The exergy analysis has revealed that the solar field followed by boiler have the maximum exergy destruction ratios of 78.90% and 56.52% respectively. The corresponding second law efficiencies of solar field and boiler are 21.10% and 43.48% respectively. Thermo-economic analysis has been performed on both the plants by developing physical and productive structures for them. A set of linear equations have been developed and solved for finding the cost rates of different product streams. Many investigators have not carried out following.

1. Entropy generated in each component need to be calculated.
2. Factors affecting loss of exergy need to be analyzed
3. And actions to be defined to minimize the exergy loss.
4. Difference between first law and second law efficiency.

The present investigations mainly deals with mentioned above research gap identified.

3. Results and Discussions

After the analysis of different cycles on which the super critical thermal power plant work with respect to energy, exergy. The exergy destruction shows a loss that can be recovered by using the suitable design of the various parts of the system and also it confirms the best possible operation of the power plant according to second law of Thermodynamics. As the exergy destruction shows a loss, which can be quantify by analysis the system in mathematically. In the present work the analysis is done in the super critical steam power plant.

From Fig2 the network output from turbine will decrease with increase in boiler pressure as the temperature at inlet of turbine is constant and as a result the area under the curve will decrease.

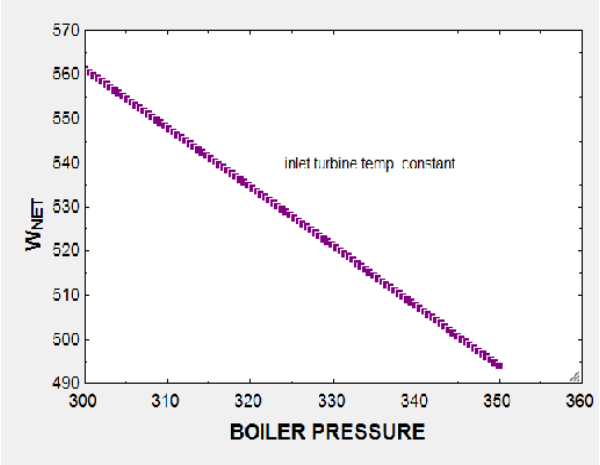


Figure 2: Variation of net-work output with boiler pressure

The first law efficiency of cycle will decrease as boiler pressure increases as net work output from turbine will decrease with increase in boiler pressure as the temperature at inlet of turbine is constant and as a result the area under the curve will decrease as shown in Fig-3 respectively. The area under the curve show the net work obtained and heat supplied is constant so efficiency of cycle will decrease.

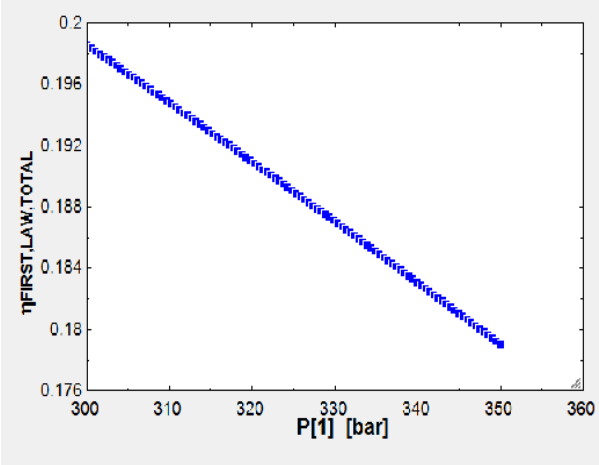


Figure 3: *Variation of first law efficiency with boiler pressure*

The variation of the boiler with T1 and P1 is shown in Fig. Exergy destruction increase with increase in T1 and P1. As exergy destruction is due to entropy generation and increase in temperature leads to more entropy generation hence more exergy destruction as shown in Fig-4

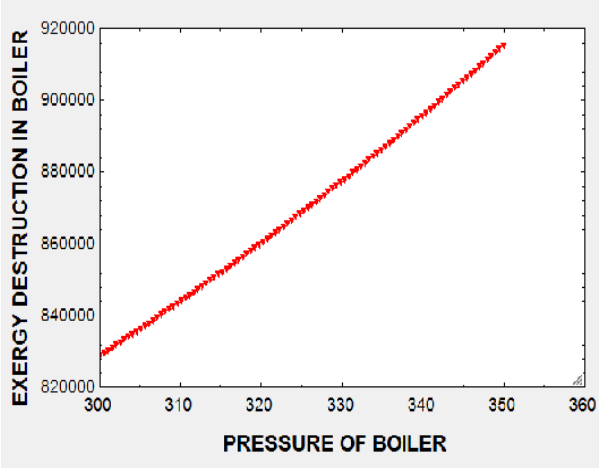


Figure 4: Variation of exergy loss in boiler with boiler pressure

The variation of the I_{cond} with T_1 and P_1 is shown in Fig. Exergy destruction increases with increase in T1 and P1. As exergy destruction is due to entropy generation and increase in temperature leads to more entropy generation hence more exergy destruction in the condenser as shown in Fig-5

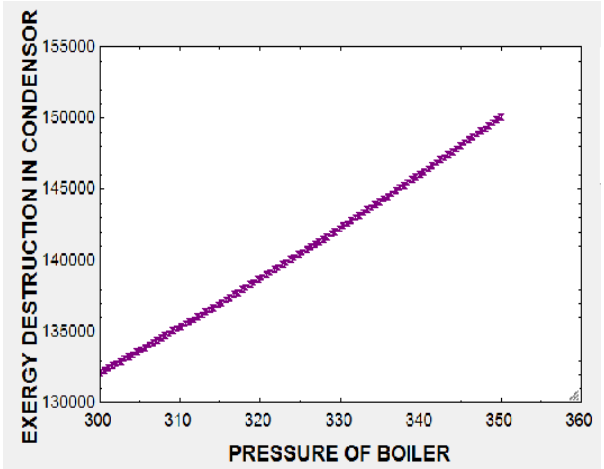


Figure 5: Variation of exergy loss in condenser with boiler pressure

As boiler pressure increases exergy loss also increases in turbine. As exergy destruction is due to entropy generation and increase in temperature leads to more entropy generation hence more exergy destruction in turbine as shown in Fig-6.

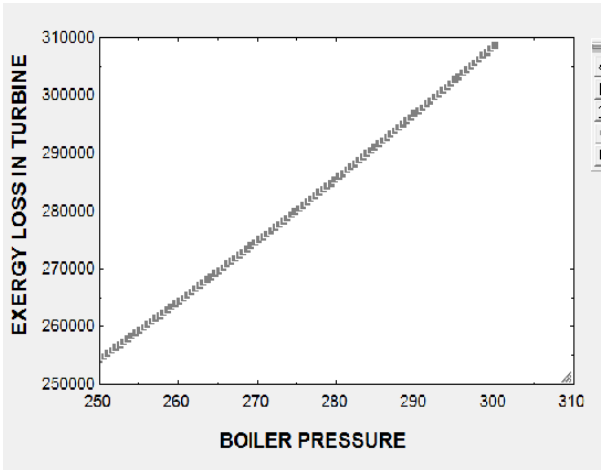


Figure 6: Exergy loss in turbine vs boiler pressure

Exergy loss in different component is calculated below. The maximum exergy loss occurs in boiler and then in turbine than in condenser but as per first law analysis maximum energy loss was in condenser but it was low energy loss. As shown in Fig-7.

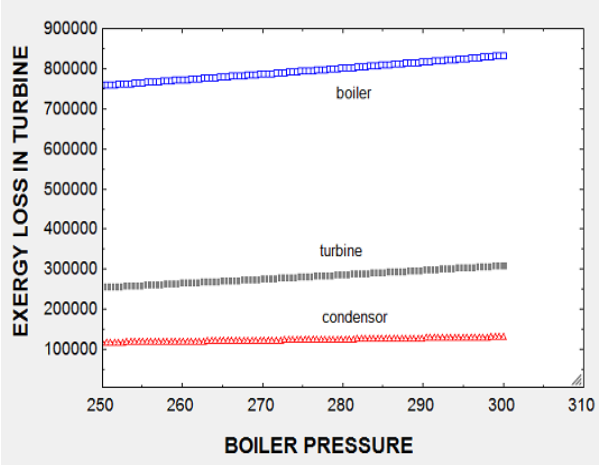


Figure 7: Variation of Exergy loss in different component

The variation of the W_t with T_1 is shown in Fig. Work output increases with increase in T1. As area under the curve increases. Hence net work output from turbine will increase as shown in Fig-8 respectively.

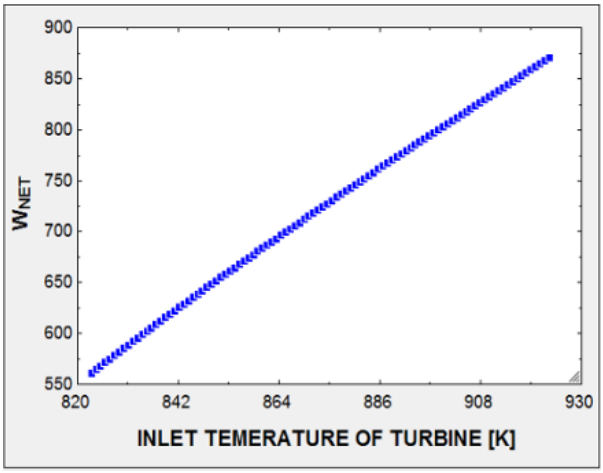


Figure 8: Variation of net work (W_net) with inlet temperature of turbine

The variation of the ηt1 with T1is shown in Fig. First law efficiency increases with increase in T1. As we have seen earlier in graph with temperature increase net work output will increase as compared to heat supplied as a result overall efficiency of cycle will increase as shown in Fig-9.

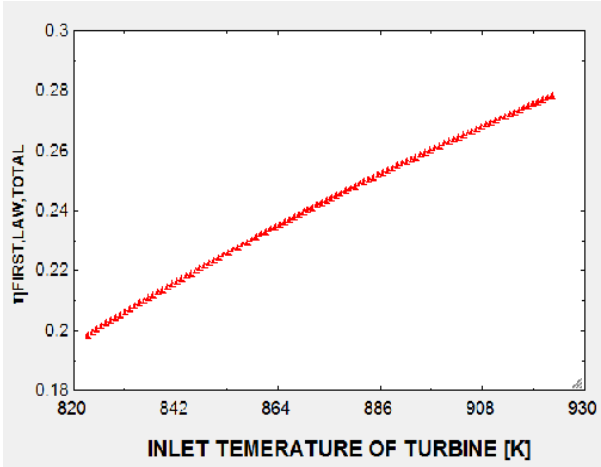


Figure 9: Variation of First law efficiency of cycle with inlet temperature of turbine

The variation of the η2t with T1 is shown in Fig. Second law efficiency decreases with increase in T1. As we increase the temperature, more entropy will be generated as a result more destruction of exergy hence efficiency will decrease as shown in Fig-10

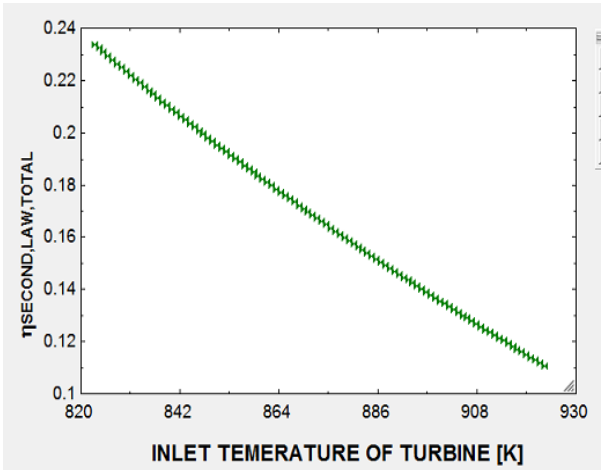


Figure. 10: Variation of second law efficiency of cycle vs inlet temperature of turbine

Fig-11 shows the Exergy destruction in boiler**.** As temperature increases more entropy will be generated as a result more exergy loss. Major exergy loss occurs in furnace part than in heat transfer part of boiler. So boiler is the main component where major exergy losses occur.

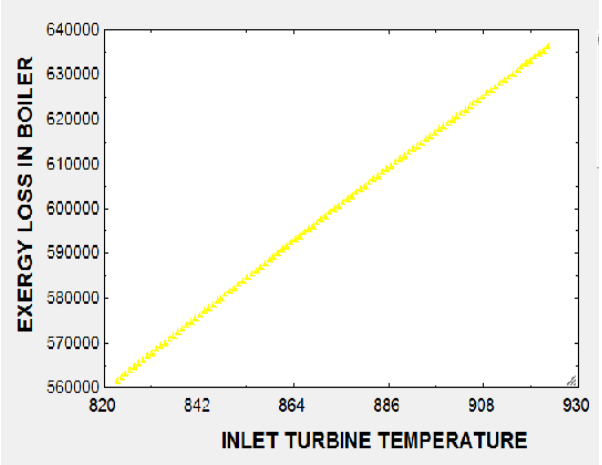


Figure 11: Variation of exergy loss in boiler with inlet temperature of turbine

The maximum exergy loss occurs in boiler and then in turbine than in condenser but as per first law analysis maximum energy loss was in condenser but it was low grade energy loss as shown in Fig-12.

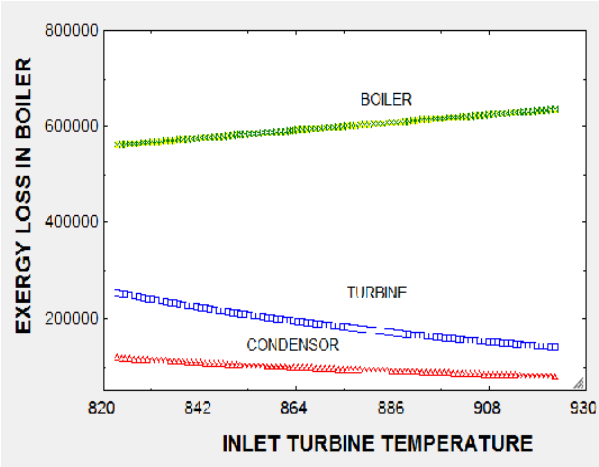


Figure 12: Variation of exergy loss in boiler vs inlet temperature of turbine

The variation of the W_t with mass flow rate is shown in Fig. Work output decrease with increase in mass flow rate. It is due to with high mass flow rate no. of losses in different component increases as a result overall performance decreases as shown in Fig-13

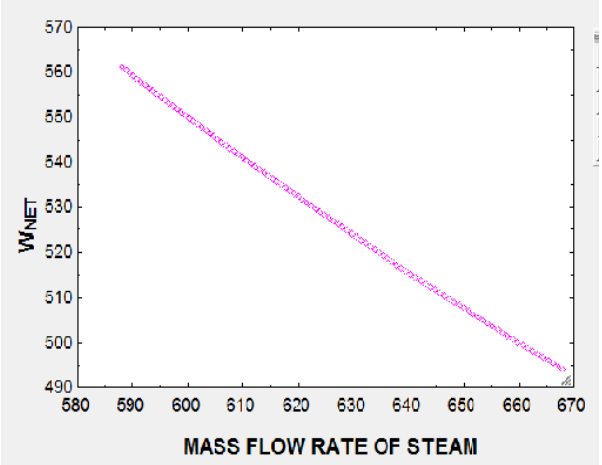


Figure 13: Variation of work output vs mass flow rate of steam

The variation of the second law efficiency in terms of exergetic efficiency (η2t) with mass flow rate is shown in Fig-14. . Second law efficiency decrease with increase in mass flow rate.

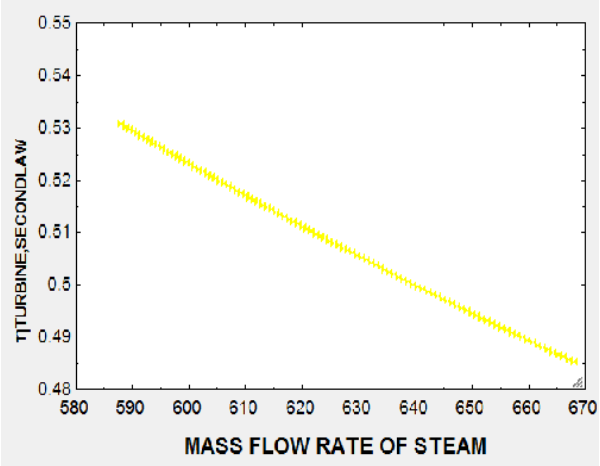


Figure 14: Variation of second law efficiency vs mass flow rate of steam

As mass flow rate increases first law efficiency decreases. It is due to with high mass flow rate no. of losses in different component increases as a result overall performance decreases. Therefore first law efficiency of cycle decreases as shown in Fig-15

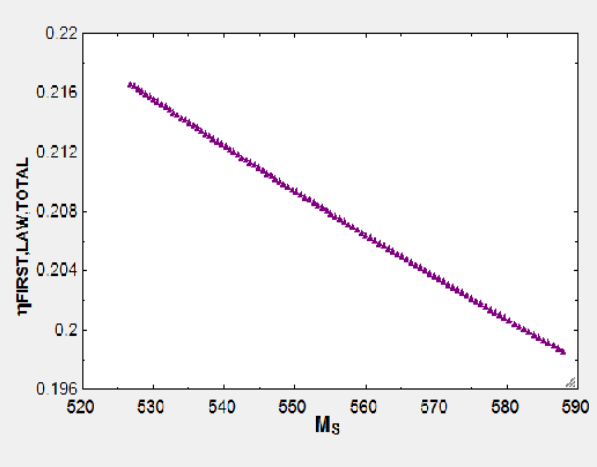


Figure 15: Variation of first law efficiency vs mass flow rate of steam

The maximum exergy loss occurs in boiler and then in turbine than in condenser but as per first law analysis maximum energy loss was in condenser but it was low grade energy loss.

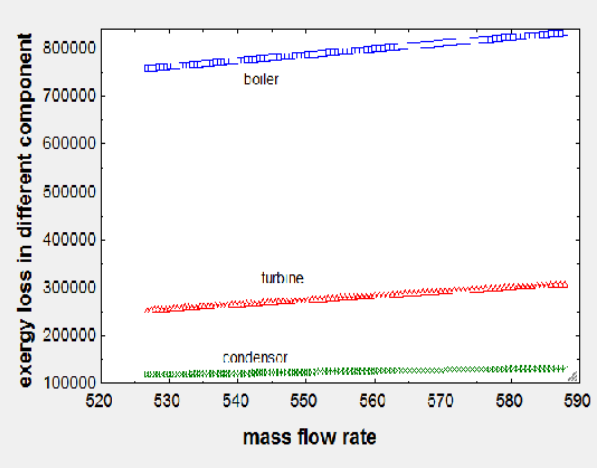


Figure 16: The variation of exergy loss in different component vs mass flow rate of steam

4. Conclusions and Recommendations

A second law of thermodynamic analysis was performed for a supercritical power plant to explore the performance of individual components. From the exergy analysis results obtained, the furnace was identified as having the highest exergy destruction. The turbines had the second highest exergy destruction rate.

Some of the conclusions regarding the exergy destruction of different components and options to reduce the exergy destruction in the furnace and turbine are given below:

1) Exergy destruction rate was greater in the combustor than the heat exchanger unit. The factors responsible for the furnace exergy losses were excess air percentage, preheated air temperature, and moisture content in the coal.

2) The exergy loss depends purely on the temperature range of the input and outlet stages of the turbine series. The exergetic efficiency increased in accordance with an increase in the reheating temperature.

3) As temperature of inlet turbine increases the exergy destruction in different component increases same happens with increase in pressure also. If exergy losses are avoided, overall efficiency can be increased.

The following are the recommendations for the future work: For the power plant to operate at a very high temperature and pressure, it is important to focus more on the plant design. An advanced material is required to design a steam turbine that can withstand high temperature that is around 700 C. The steam turbine has to be designed in such a way that it matches the furnace conditions. Future research should also focus on identifying a coating that can withstand the high temperature and pressure and protect the equipment from steam oxidation and erosion inside the turbines. Also, the material properties throughout the overall design of an ultra-supercritical power plant using coal as the fuel should be investigated.

References

[1] Habib, M.A. and Zubair, S.M. (1992), 2nd-law-based thermodynamic analysis of regenerative - reheat rankine-cycle power plants. Pergamon-Elsevier Science Ltd. Energy, 17, 295-301.

[2] Habib, M.A.; Said, S.A.M. and Al-Zaharna, I. (1995), Optimization of reheat pressuers in thermal power plants. Pergamon-Elsevier Science Ltd. Energy, 20(6), 555-565.

[3] Datta, A. and Som, S.K. (1999). Energy and exergy balance in a gas turbine combustor. J Power Energy—Proc Inst Mech Eng, 213A, 23–32.

[4] Drbal, L.F; Boston, P.G.; Westra, K.L. and Erickson, R.B. (1996). Power Plant Engineering. Ist Edition, Black & Veatech, Springer, New York.

[5] Kjaer, S. (2002). The advanced supercritical 700oC pulverized coal-fired power plant. VGB Power Tech, 7, 47-49.

[6] Kiga, T.; Yoshikawa, K.; Sakai, M. And Mochida, S. (2000). Characteristics of pulverized coal combustion in high temperature preheated air. Journal of propulsion and power, 16(4), 601-605.

[7] Kitto, J.B. (1996). Developments in pulverized coal-fired boiler technology, Babcock & Wilcox.

[8] Casarosa, C; Donatini, F. and Franco, A. (2004). Thermo economic optimization of heat recovery steam generators operating parameters for combined plants. Energy, 29, 389-414.

[9] Bejan, A. (2006). Advanced Engineering Thermodynamics, 3rd Edition. John Wiley & Sons: New York, NY, USA.

[10] Chaibakhsh, A. and Ghaffari, A. (2008). Simulation modeling practise and theory. Simulation Modelling Practice and Theory, 16, 1145–1162.

[11] Aljundi, I.H. (2009). Energy and exergy analysis of a steam power plant in jordan, Applied Thermal Engineering, 29, 324- 328.
[12] Bakhshesh, M. and Vosough, A. (2012). Boiler parametric study to decrease irreversibility. Indian Journal of Science and Technology, 5(4), 2534-2539.
[13] Cheng, L.; Guo, J.I.F. and Mingtian, X.u. (2010). Thermodynamic analysis of waste heat power generation system. Institute of Thermal Science and Technology, Energy, 35, 2824-2835.
[14] Datta, A. and Som, S.K. (1999). Energy and exergy balance in a gas turbine combustor. J Power Energy—Proc Inst Mech Eng, 213A, 23–32.
[15] Drbal, L.F; Boston, P.G.; Westra, K.L. and Erickson, R.B. (1996). Power Plant Engineering. Ist Edition, Black & Veatech, Springer, New York.
[16] Gwosdz, A.; Leisse, A. and Quenders, H.J. (2005). Pulverized coal firing system for the operation of steam generators with low excessive air. VGB Powertech. 85(11), 67-73.
[17] Hasan, H.E.; Ali, V.A; Burhanettin, A.D.; Suleyman, H.S.; Bahri, S.; Ismail, T.; Cengiz, G. and Selcuk, A. (2009). Comparative energetic and exergetic performance analyses for coal-fired thermal power plants in turkey. International Journal of Thermal Sciences, 48, 2179–86.
[18] Jayamaha. L. (2010). Energy efficient building systems. Handbook: 1st Edition. Mcgraw Hill eduaction, Europe.
[19] Kakaras, E.; Ahladas, P. and syrmopoulos, S. (2012). Computer simulation studies for the integration of dryer to coal power plant. Fuel, 81(5), 583-593.
[20] Kaushik, S.C.; SivaReddy, V. and Tyagi, S.K. (2013). Energy and exergy analyses of thermal power plants. A review, Renewable and Sustainable energy reviews, 15, 1857-1872.

This article has been accepted for publication in a future issue of this journal, but has not been fully edited. Content may change prior to final publication. Citation information: DOI 10.1109/TIA.2017.2752679, IEEE Transactions on Industry Applications

Soft Switched High Voltage Gain Boost Integrated Flyback Converter Interfaced Single-Phase Grid Tied Inverter for SPV Integration

Amardeep B. Shitole, *Student Member, IEEE,* Shelas Sathyan, H. M. Suryawanshi, *Senior Member, IEEE,* Girish G. Talapur, *Student Member, IEEE,* and Pradyumn Chaturvedi, *Senior Member, IEEE*

***Abstract*—A two-stage grid tied efficient solar photovoltaic (SPV) system with zero voltage switching (ZVS) and zero current switching (ZCS) at DC-DC converter stage and adaptive synchronization at inverter stage is proposed. In the first stage, an improved high step-up boost integrated flyback converter with quasi resonant voltage multiplier cell is proposed. ZVS turn-on of all MOSFETs and ZCS turn-off of all diodes of resonant voltage multiplier cell results in high efficient power conversion compared to the conventional boost integrated flyback converters. Small sized coupled inductor enhances magnetic utilization in this converter. Second stage consists of a single phase H-bridge grid interfaced inverter with variable band hysteresis current control technique. Amplitude adaptive notch filter (AANF) is used to extract fundamental unit voltage vector of grid voltage required for estimation of synchronized reference current for hysteresis controller. A 250W laboratory prototype is developed and experimentally evaluated. Experimental results demonstrate efficient renewable energy conversion at DC-DC converter stage and quality power injection at DC-AC inverter stage of the proposed grid tied SPV system under changing solar insulation levels.**

***Index Terms*—Two-stage, high step-up converter, soft switching, grid synchronization, variable band hysteresis current controller (VBHCC).**

I. Introduction

RECENTLY, two-stage grid connected efficient renewable energy conversion systems are gaining more popularity because of continuously increasing eco-friendly energy demand and unlimited availability of natural energy resources particularly solar energy [1]. Photovoltaic arrays are relatively low voltage DC power sources, hence research on efficient high gain DC/DC converters are at the center of attraction due to the numerous applications ranging from renewable energy integration, electronics ballast, un-interruptible power supply (UPS), laser systems, battery and ultra-capacitors based storage systems etc. [2], [3]. Boost converter is not an ample solution for aforesaid applications. This is because of its poor efficiency due to the parasitic elements, reverse recovery losses of the diode and high voltage stress at extreme duty cycle [4]. Voltage fed isolated converters like flyback, forward and full bridge converters are conventionally used for voltage step-up applications. However, in these converters, isolation transformer turns ratio need to be increased in order to achieve high step-up. MOSFETs and output diodes of these converters have high voltage stress. Instead of using conventional two-port isolated converters, three-port converter (TPC) topologies are researchers emerging attraction for PV integration due to its advantages such as, improved efficiency and power density with reduced cost. An improved three-port flyback-forward DC-DC converter topology with effective voltage regulation approach for stand-alone PV systems is presented in [5]. For high power (kW-level) PV applications where, isolation is mandatory, high frequency-AC (HFAC) link based converters are good choice. In [6], a soft switched HFAC converter with multiple PV input is proposed for application of kW-power level. These converters are voltage fed in nature and thus require large turns ratio to achieve high voltage gain. Current fed converters overcome these drawbacks of voltage fed converters [7]–[9]. In addition to the high frequency transformer, minimum one additional inductor is required in these converters. This increases the magnetic components count, size and weight etc. However, to clamp the voltage stress caused by the leakage inductance of the transformer, a lossless clamp circuit is necessary.

Due to higher efficiency, lower size and weight, non-isolated converters are good alternative for high voltage gain applications where isolation is not mandatory. Incorporating voltage multiplier circuit into the non-isolated converters, various high voltage gain converters are presented in [10]–[13]. However, more number of voltage multiplier cells along with the basic cell are required to obtain high voltage gain in these converters. This increases overall components count. In addition, all switches are hard switched which affect overall efficiency of the system. In order to achieve high voltage gain, an inductor of a conventional boost converter is replaced by a coupled inductor [14]. Coupled inductor provides an additional degree of freedom to the designer due to the flexibility of enhancing the voltage gain by duty ratio as well as turns ratio. However, the leakage inductance causes high voltage

Manuscript received March 08, 2017; revised June 10, 2017 and July 29, 2017; accepted September 07, 2017. Paper 2017-SECSC-0254.R2, presented at the 2016 IEEE International Conference on Power Electronics, Drives and Energy Systems, Trivandrum, India, December 14-17, and approved for publication in the IEEE TRANSACTIONS ON INDUSTRY APPLICATIONS by the Sustainable Energy Conversion Systems Committee of the IEEE Industry Applications Society. This work was supported by the Department of Science and Technology (DST), Government of India.

A. B. Shitole, H. M. Suryawanshi, G. G. Talapur and P. Chaturvedi are with the Department of Electrical Engineering, Visvesvaraya National Institute of Technology (VNIT), Nagpur 440011, India (e-mail: amardeep.shitole@gmail.com, hms_1963@rediffmail.com, girish223@gmail.com, pc220774@gmail.com).

S. Sathyan is with the Department of Electrical Engineering, Shiv Nadar University, Greater Noida, India. (e-mail: shelassathyan@yahoo.co.in).

0093-9994 (c) 2017 IEEE. Personal use is permitted, but republication/redistribution requires IEEE permission. See http://www.ieee.org/publications_standards/publications/rights/index.html for more information.

This article has been accepted for publication in a future issue of this journal, but has not been fully edited. Content may change prior to final publication. Citation information: DOI 10.1109/TIA.2017.2752679, IEEE Transactions on Industry Applications

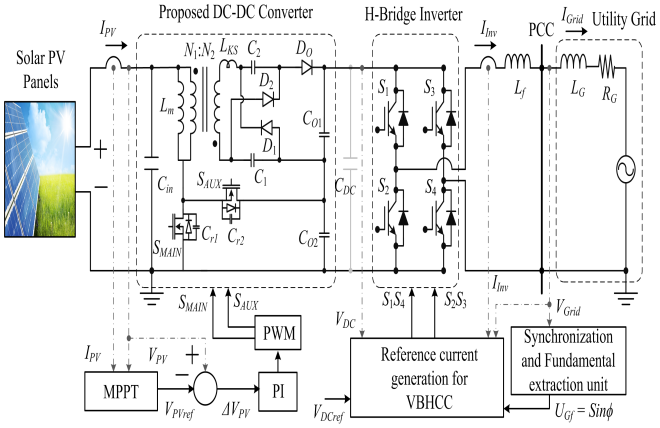


Fig. 1. Schematic diagram of the proposed two stage solar photovoltaic system.

stress and EMI problems which need to be addressed. To nullify voltage stress developed because of leakage energy of the coupled inductor, lossless clamp circuits are introduced in [15]. Even after addition of clamp circuit, output diode of this converter experiences higher voltage stress. Hence, it requires additional lossy snubber circuit (RCD) to clamp this voltage stress. To further enhance the converter voltage gain with reduced voltage stress on the devices, switched capacitors are introduced in combination with coupled inductor in [16]–[21].

In order to clamp the voltage stress across the switch, a technique of active clamping is introduced in [17]. With this technique it is possible to achieve ZVS turn-on of semiconductor switches. The converters proposed in [18]–[20] integrate flyabck converter with conventional boost converter where the function of boost inductor and flyback transformer is replaced by a single common coupled inductor. Moreover at the flyback side, switched-capacitor circuits are integrated to obtain high voltage gain operation. Here the output terminal of the flyback side is stacked with that of the boost converter which further enhances the converter voltage gain. Among these boost-flyback converters, converter presented in [20] has higher voltage gain and lower voltage stress. However all semiconductor switches are hard switched in this converter which affect the efficiency. In order to overcome these problems, ZVS and ZCS techniques should be incorporated in these converters to further improve the efficiency. A soft-switched DC-DC converter presented in [21] has higher voltage gain and lower voltage stress on the MOSFETs. Active clamp circuit is incorporated in [21] to achieve ZVS turn-on for both main and clamp switches. However, all the diodes of this converter are hard switched and also have high component count (5 capacitors, 4 diodes, 2 MOSFETs). In [22], a non-isolated resonant PWM DC-DC converter is proposed. This converter is able to achieve, ZVS of MOSFETs and ZCS of diodes. However, to have resonant operation and thus achieving soft switching, additional resonant inductor is required.

Keeping in mind the cost constraints of PV panels, maximum penetration of power generated by PV arrays is another crucial issue in designing two-stage grid connected solar energy conversion systems. To achieve maximum penetration of power generated by the PV arrays, MPPT control technique should be incorporated in the DC-DC control stage of a two stage system [23], [24]. In order to enhance the control performance and achieve efficient quality power injection capability, two-stage system should have: efficient high voltage gain DC-DC conversion stage with MPPT control, adaptive synchronization for accurate detection of utility voltage phase angle, adequate and improved current control technique for high quality current injection with appropriate switching strategy to drive interfacing inverter [25]–[30].

This paper presents, a two-stage grid tied efficient SPV system for low voltage solar PV based AC module application. First stage consist of a high step-up boost integrated flyback converter with quasi resonant voltage multiplier cell [31]. A bidirectional boost converter is stacked with a flyback converter which bypasses the leakage energy to the output capacitor and thus increases the voltage gain and provides ZVS turn-on of switches. At secondary side, resonant switched capacitor multiplier cell [32] is incorporated to achieve high voltage gain. A resonant circuit is formed between the secondary leakage inductance and the capacitors of this cell which provide ZCS turn-off of the diodes. This ZCS turn-off reduces the losses due to reverse recovery problem of the diodes. In addition, turn-off losses of the diodes are also reduced. Combination of coupled inductor and resonant voltage multiplier cell increases the voltage conversion gain without increasing the voltage stress on the switching devices. This ZVS and ZCS operation enhances the conversion efficiency. Second stage consist of a single phase H-bridge grid interfaced inverter with AANF based variable band hysteresis current control technique [33]. AANF is used because of its adaptive nature in extracting fundamental unit voltage vector of grid voltage required for estimation of synchronized reference current for hysteresis controller [34]–[36]. A 250W prototype is built in the laboratory and experimentally evaluated. Experimental results demonstrates the flexibility of the proposed solution for efficient solar PV generation system.

II. Proposed Two-Stage Solar Photovoltaic System Under Study

Schematic of the proposed two-stage solar PV system is represented in Fig. 1. The utility grid is modeled as a single phase voltage source with equivalent resistance (R_G) and inductance (L_G) till the point of common coupling (PCC) where two-stage inverter is connected. DC-DC stage of this system consist of proposed soft switched high voltage gain boost integrated flyback converter. Here, L_m is the primary referred magnetizing inductance of the coupled inductor. Equivalent leakage inductance is referred to the secondary side and is represented by L_{KS}. The switched capacitors C_1, C_2 and the diodes D_1, D_2 forms the resonant voltage multiplier circuit. Auxiliary MOSFET (S_{AUX}) and the output capacitor C_{O2} forms the active clamp circuit. This circuit clamps the voltage stress of the MOSFETs to V_{CO2} and also helps to achieve ZVS turn-on for both the MOSFETs. Second stage consist of a single phase H-Bridge grid interfaced inverter with AANF

0093-9994 (c) 2017 IEEE. Personal use is permitted, but republication/redistribution requires IEEE permission. See http://www.ieee.org/publications_standards/publications/rights/index.html for more information.

This article has been accepted for publication in a future issue of this journal, but has not been fully edited. Content may change prior to final publication. Citation information: DOI 10.1109/TIA.2017.2752679, IEEE Transactions on Industry Applications

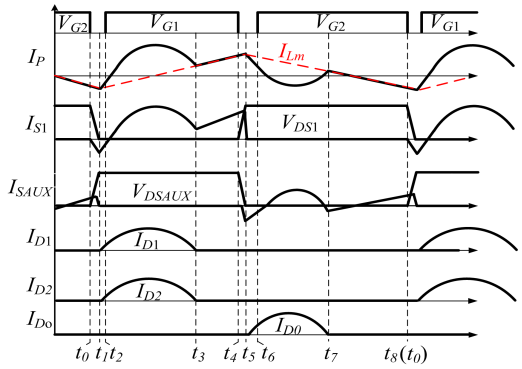


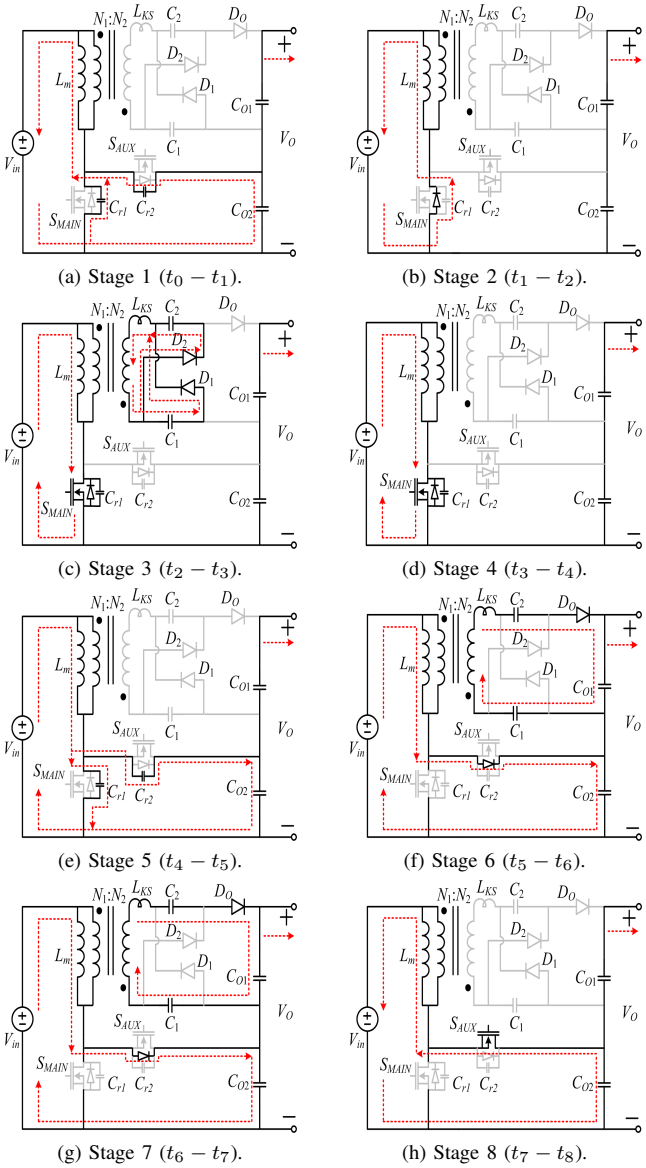
Fig. 2. Theoretical waveforms of the proposed DC-DC converter.

based VBHCC technique. AANF is used to achieve synchronization and to estimate the required synchronized reference current for hysteresis current controller. L_f represents the equivalent inductance of a passive filter connected at PCC. For simplicity, here programable DC-solar power emulator (MAGNA-POWER) is used as DC input power source to the proposed DC-DC converter. Interfacing inverter control circuit is designed such that it will only inject active power generated by PV source and maintains power factor close to UPF with improved injected current THD profile as per the IEEE 1547 standards. In the proposed system, H-Bridge inverter is operated with bipolar modulation technique. Hence, potential difference generated between the PV-panel and the system ground is not varying thus leakage current is significantly reduced. In addition, negative of the PV-panel is grounded which also reduces the problem of leakage current flowing through the parasitic capacitance to ground [1], [37].

A. Proposed DC-DC Converter Operation

Active clamp circuit formed by an auxiliary MOSFET (S_{AUX}) and capacitor C_{O2} clamps the voltage stress of MOSFETs to V_{CO2} and also helps to achieve ZVS turn-on for both the MOSFETs. Theoretical waveforms representing operating modes during each stage of operation of the proposed converter is shown in Fig. 2. Operating modes of the converter over a periodic cycle is shown in Fig. 3.

1) Stage 1 ($t_0 - t_1$): At t_0, an auxiliary switch S_{AUX} stops conducting. Therefore, primary current discharges capacitor C_{r1} to zero and the capacitor C_{r2} get charged to output capacitor voltage V_{CO2}. Output capacitors C_{O1} and C_{O2} continuously supplies their energy to the utility grid through interfacing inverter. The output capacitance of the MOSFETs (C_{r1} and C_{r2}) have small values hence discharges very soon. Therefore, duration of this stage is very small.
2) Stage 2 ($t_1 - t_2$): Output capacitance (C_{r1}) of main switch S_1 is completely discharged hence, primary currents conduction path shifts through the body diode of the main switch. This conduction mode ends at t_2 when the gate pulse for main switch S_{MAIN} is applied.
3) Stage 3 ($t_2 - t_3$): Switch S_{MAIN} turns on with ZVS at t_2. The energy of the secondary side charges the resonant switched capacitors C_1 and C_2 through the diodes D_1 and D_2 respectively in the multiplier cell. This resonating charging current have a quasi-sinusoidal nature.
4) Stage 4 ($t_3 - t_4$): Resonating diode currents become zero at t_3 . Hence diodes D_1 and D_2 turns off with ZCS.
5) Stage 5 ($t_4 - t_5$): Switch S_{MAIN} turns off at t_4. The primary current charges the output capacitance C_{r1} of S_{MAIN} to V_{CO2} and discharge C_{r2} of auxiliary MOSFET S_{AUX} to zero.
6) Stage 6 ($t_5 - t_6$): At t_5, primary current start to conduct through the body diode of S_{AUX}. Thus, voltage across switch S_{MAIN} is clamped to V_{CO2}. Switched capacitors C_1, C_2 and the secondary winding discharges their energy to the output capacitor C_{O1} connected in series.
7) Stage 7 ($t_6 - t_7$): At t_6, gate pulse to an auxiliary switch S_{AUX} is applied. Before applying the gate pulse, S_{AUX}



(a) Stage 1 ($t_0 - t_1$). (b) Stage 2 ($t_1 - t_2$).
(c) Stage 3 ($t_2 - t_3$). (d) Stage 4 ($t_3 - t_4$).
(e) Stage 5 ($t_4 - t_5$). (f) Stage 6 ($t_5 - t_6$).
(g) Stage 7 ($t_6 - t_7$). (h) Stage 8 ($t_7 - t_8$).

Fig. 3. Steady state operating stages of the proposed converter.

0093-9994 (c) 2017 IEEE. Personal use is permitted, but republication/redistribution requires IEEE permission. See http://www.ieee.org/publications_standards/publications/rights/index.html for more information.

This article has been accepted for publication in a future issue of this journal, but has not been fully edited. Content may change prior to final publication. Citation information: DOI 10.1109/TIA.2017.2752679, IEEE Transactions on Industry Applications

body diode was in conduction. Hence S_{AUX} turn-on with soft switching (ZVS).

8) Stage 8 ($t_7 - t_8$): The resonating secondary current becomes zero at t_7. Hence output diode D_O turns off with ZCS. The primary current changes its direction and conducts through S_{AUX} to the input source. This stage ends at t_8 where the gate signal to auxiliary switch S_{AUX} is removed.

B. Converter Steady State Analysis

1) Voltage Conversion Ratio: During stage 3, voltage across the magnetizing inductance and the switched-capacitors is expressed as,

$$V_{Lm}^{on} = V_{in} \tag{1}$$

$$V_{C1} = V_{C2} = \frac{N^2 L_m + L_{KS}}{N L_m} V_{in} \tag{2}$$

During Stage 6 we will get,

$$V_{Lm}^{off} = V_{in} - V_{CO2} \tag{3}$$

$$V_{CO1} = V_{C1} + V_{C2} - N V_{Lm}^{off} \tag{4}$$

Substituting (2) and (3) in (4) we get,

$$V_{CO1} = 2\frac{N^2 L_m + L_{KS}}{N L_m} V_{in} - N(V_{in} - V_{CO2}) \tag{5}$$

Applying Volt-Second balance on L_m we get,

$$V_{CO2} = \frac{V_{in}}{1-D} \tag{6}$$

Output voltage is expressed as,

$$V_O = V_{CO1} + V_{CO2} \tag{7}$$

Substituting (5) and (6) in (7), actual voltage conversion gain is obtained as,

$$\frac{V_O}{V_{in}} = \frac{1 + 2x(1-D) - N(1-D) + N}{1-D} \tag{8}$$

Where $x = \frac{N^2 L_m + L_{KS}}{N L_m}$. Since $L_{KS} \ll L_m$, ideal voltage ratio is given as,

$$\frac{V_O}{V_{in}} = \frac{1 + 2N - ND}{1-D} \tag{9}$$

2) Voltage Stress: Voltage across the output capacitor C_{O2} clamps the voltage stresses on the MOSFETs to,

$$V_{DS(MAIN)} = V_{DS(AUX)} = \frac{V_O}{1 + 2N - ND} \tag{10}$$

Voltage stress across the output diode D_O and multiplier cell diodes D_1 and D_2 are given as,

$$V_{DO} = V_{D1} = V_{D2} = \frac{N V_O}{1 + 2N - ND} \tag{11}$$

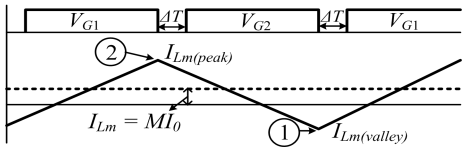


Fig. 4. Idealized magnetizing current waveform during switch turn-off period.

3) Selection of magnetizing Inductance: It is well known fact that, in case of two-stage grid-tied SPV systems, the soft switching performance of DC-DC converter is affected by the input solar power variation or output load variation. Hence, in order to achieve ZVS turn-on of MOSFETs, accurate design of magnetizing inductance of coupled inductor is very important. In the proposed converter, active clamp circuit is utilized to achieve ZVS of main and auxiliary switch. Compared to conventional active clamp technique, proposed converter makes use of bidirectional magnetizing current of coupled inductor to realize ZVS turn-on of main switch. This helps to achieve ZVS of main switch at light load without additional external inductor or large leakage inductance. Energy stored in the magnetizing inductance should be sufficiently large to charge and discharge the parasitic capacitance of the MOSFETs for its ZVS operation. Idealized magnetizing current waveform during switching transition showing positive peak and negative valley of the magnetizing current is shown in Fig. 4.

To achieve ZVS of main switch, the magnetizing current should reach the negative peak (valley) as shown in Fig. 4. Negative peak of magnetizing current is expressed as,

$$I_{Lm}(t)_{valley} = (I_{Lm} - \frac{\Delta I_{Lm}}{2}) < 0 \tag{12}$$

From Fig. 4, (12) can be written as,

$$M I_O - \frac{V_{in} D}{2 L_m f_{sw}} < 0 \tag{13}$$

Where, $M = \frac{1+2N-ND}{1-D}$. Hence, maximum value of magnetizing inductance to achieve ZVS of main switch is obtained as,

$$L_{m(max)} < \frac{V_{in} D_{max}(1 - D_{max})}{2(1 + 2N - N D_{max}) I_O f_{sw}} \tag{14}$$

The ZVS of main switch also depends on the load variation. As load current changes, the dc value or average value of magnetizing current changes. Hence, there is a change in the value of peak and valley of the magnetizing current. Therefore, value of L_m should be recalculated to achieve ZVS at desired load condition. To achieve ZVS at any load, at point (1) in Fig. 4, energy stored in the magnetizing inductance should be higher to discharge and charge the parasitic capacitance of MOSFETs. Therefore,

$$\frac{1}{2} L_m I_{Lm(valley)}^2 \geq \frac{1}{2} C_{r(eff)} V_{CO2}^2 \tag{15}$$

Where, $C_{r(eff)}$ is the effective value of C_{r1} and C_{r2}. From above relationship, the value of magnetizing inductance required to maintain ZVS at desired power/load condition is obtained as,

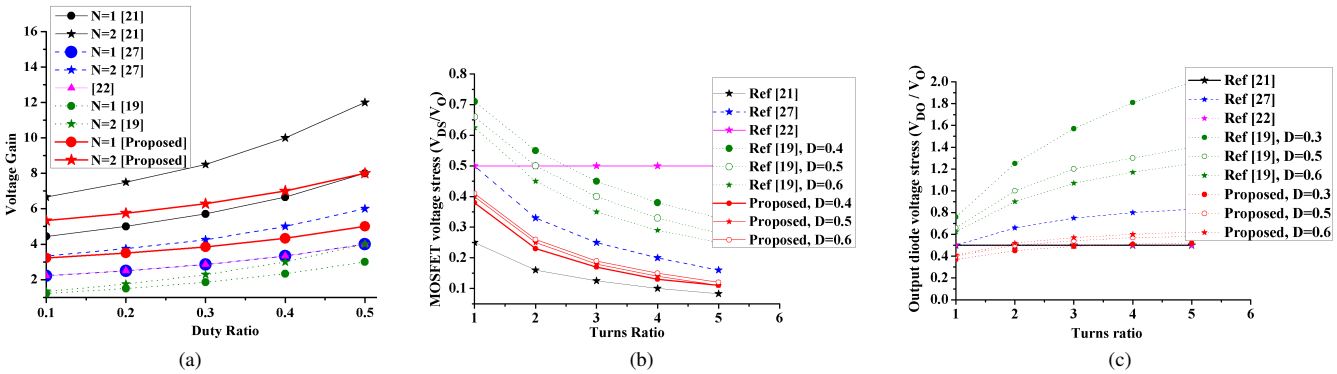
$$\sqrt{I_O} \geq \frac{C_{r(eff)} V_{CO2}^2}{L_m (M - \frac{R_O D}{2 M L_m f_{sw}})^2} \tag{16}$$

0093-9994 (c) 2017 IEEE. Personal use is permitted, but republication/redistribution requires IEEE permission. See http://www.ieee.org/publications_standards/publications/rights/index.html for more information.

This article has been accepted for publication in a future issue of this journal, but has not been fully edited. Content may change prior to final publication. Citation information: DOI 10.1109/TIA.2017.2752679, IEEE Transactions on Industry Applications

TABLE I
COMPARATIVE ANALYSIS OF THE CONVERTERS PRESENTED IN [21], [27], [22], [19] AND PROPOSED CONVERTER.

Converter Component	Converter in [21]	Converter in [27]	Converter in [22]	Converter in [19]	Proposed Converter
MOSFETs	2	1	2	1	2
Diodes	4	3	2	2	3
Voltage gain	$\frac{2(1+N)}{1-D}$	$\frac{1+N}{1-D}$	$\frac{2}{1-D}$	$\frac{1+ND}{1-D}$	$\frac{1+2N-ND}{1-D}$
Voltage stress on MOSFETs	$\frac{V_O}{2(1+N)}$	$\frac{V_O}{1+N}$	$\frac{V_O}{2}$	$\frac{V_O}{1+ND}$	$\frac{V_O}{1+2N-ND}$
Voltage stress on output diode	$\frac{V_O}{2}$	$\frac{NV_O}{1+N}$	$\frac{V_O}{2}$	$\frac{NV_O}{1+ND}$	$\frac{NV_O}{1+2N-ND}$
Soft switching of MOSFETs	ZVS	Hard switching	ZVS	Hard switching	ZVS
Soft switching of Diodes	Hard switching	Hard switching	ZCS	Hard switching	ZCS
Magnetic components count	1 (Large leakage inductance or external additional inductance is required to maintain ZVS at light load)	1	2	1	1



(a) (b) (c)

Fig. 5. The comparative analysis of proposed converter: (a) Voltage gain comparison for different duty ratio and turns ratio. (b) Voltage stress on MOSFETs. (c) Voltage stress on output diodes.

From (14) and (16), magnetizing inductance value is selected to maintain ZVS of main switch up to 10% of full load. Magnetizing current of the proposed converter have positive DC-bias component. Due to the positive DC-bias current, positive peak value of magnetizing current is higher than the valley point ($I_{Lm(peak)} > I_{Lm(valley)}$). Hence, during main switch off period at point (2) in Fig. 4, the magnetizing inductance energy is higher and hence achieves ZVS of auxiliary switch. In addition to the magnetizing inductance energy, stored energy of the leakage inductance also assist auxiliary switch to achieve ZVS. Hence S_{AUX} can naturally achieve ZVS for wide load range.

4) Selection of resonant switched capacitors C_1 and C_2: ZCS turn-off for the diodes D_1, D_2 and D_O are achieved by properly selecting the resonant period between the leakage inductance and the resonant switched capacitors C_1 and C_2. From (17) the capacitors C_1 and C_2 are selected in order to achieve ZCS turn-off for designed minimum duty cycle to maximum duty cycle (D=0.2 to 0.5) of the main switch. Hence, ZCS turn-off of the diodes is ensured for all operating condition between D_{min} to D_{max}.

$$C_1, C_2 < [\frac{(D_{min}T_s)^2}{\pi^2 L_{KS}}, \frac{(1-D_{max})^2 T_s^2}{\pi^2 L_{KS}}] \quad (17)$$

5) Selection of DC-Link capacitors: In the two stage system, both DC-DC and DC-AC stages are decoupled together with a DC-link capacitor. Here, the output capacitors C_{O1} and C_{O2} of the converter are functioning as DC-link capacitor. The value of the DC-link capacitors is determined considering many factors such as, ripple in the converter output voltage (ΔV_O), maximum output power capacity of the converter (P_{out}) and grid voltage natural frequency (ω). The minimum value of DC-link capacitor is determined as,

$$C_{DC} = \frac{P_{out}}{2\omega\ V_O\ \Delta V_O} \quad (18)$$

Where, DC-link capacitor is series combination of converter output capacitors (C_{O1} and C_{O2}) as $C_{DC} = \frac{C_{O1}C_{O2}}{C_{O1}+C_{O2}}$

C. Comparative Analysis of Proposed Converter

Comparative analysis of the proposed DC-DC converter with other high voltage gain DC-DC converters is summarized in Table I. Proposed converter belongs to the class of integrated boost flyback converter (IBFC) [19]. Such topologies have a single coupled inductor which works as a boost inductor as well as flyback transformer and hence improves the device utilization. However, [19] suffers from high voltage stress on output diodes and have low efficiency. In addition, the voltage gain of this converter is not adequate for high voltage step-up application. Hard switching of semiconductor devices like MOSFETs and diodes are limiting factor of this converter

0093-9994 (c) 2017 IEEE. Personal use is permitted, but republication/redistribution requires IEEE permission. See http://www.ieee.org/publications_standards/publications/rights/index.html for more information.

This article has been accepted for publication in a future issue of this journal, but has not been fully edited. Content may change prior to final publication. Citation information: DOI 10.1109/TIA.2017.2752679, IEEE Transactions on Industry Applications

to operate at high switching frequency. In order to alleviate high voltage stress on output diode, high voltage rated diodes or external snubber circuit is required in [19]. However, in the proposed converter, a bidirectional boost converter and flyback converter with switched capacitor voltage multiplier circuit is integrated to achieve high voltage gain. The switched capacitors are designed such that, it will resonate with leakage inductance of coupled inductor and shapes the diode currents to a quasi-sinusoidal nature. The resonant period is designed such that, all the diodes of proposed converter are turn-off with ZCS. This substantially reduces the reverse recovery losses and turn-off switching losses of power diodes. The bidirectional boost converter act as active clamp circuit which recycle the leakage energy of coupled inductor and clamp the voltage stress on MOSFETs. Hence low voltage switches having low on-state resistance can be utilized to improve the efficiency by reducing the conduction losses. In addition to this, both MOSFETs of proposed converter turn-on with ZVS. Hence switching losses are reduced. The voltage gain comparison, voltage stress on the power MOSFETs and output power diodes are plotted for various turns ratio and duty cycle as shown in Fig. 5. From these plots, it is evident that proposed converter has high voltage gain and low voltage stress on all MOSFETs and output diodes compared to [19], [22], [27].

An additional resonant inductor incorporated in [22] helps to achieve ZVS of MOSFETs and ZCS of diodes. This increases the magnetic components count in the circuit which adversely affects the power density of the converter. However, in proposed converter, no additional magnetic component is required to achieve soft switching operation. Precisely designed leakage inductance of the coupled inductor is sufficient to achieve soft switching operation. Converter presented in [21] has higher voltage gain and lower voltage stress on MOSFETs compared to the proposed converter. However, this converter have high component count (5 capacitors, 4 diodes and 2 MOSFETs). The component count increases the overall all cost of the converter. For low turns ratio (less than 2.5) and low duty cycle operation, voltage stress on output diode of proposed converter is lower than the converter presented in [21]. Converter [21] makes use of active clamp circuit to achieve ZVS turn-on of the MOSFETs. Here, ZVS characteristic is depending on the stored energy of leakage inductance alone. Hence at light load, to maintain ZVS of main MOSFET, converter in [21] needs large leakage inductance or additional external inductance. Increasing the leakage inductance value affects the duty cycle and thus reduces the overall voltage gain and efficiency of the converter. However, in the proposed converter, ZVS of main MOSFET is independent of the stored energy of leakage inductance. Proposed converter makes use of bidirectional nature of magnetizing current to achieve ZVS turn-on of MOSFETs. Hence, proposed converter can maintain ZVS turn on of main MOSFET without increasing leakage inductance or additional external inductor. In [21], all the diodes of converter are hard switched. Since all the diodes of proposed converter have ZCS turn-off, the reverse recovery losses of all diodes is lower than that the converter presented in [21]. High frequency-AC (HFAC) link based converter preferred for high power (kW-level) PV application requires large turns ratio to achieve high voltage gain [6]. However, increasing the turn's ratio causes high leakage inductance. In addition to this, variable frequency operation of this converter causes difficulty in designing the magnetic and filter components.

III. Two-Stage System Control Circuit Description

An overall control circuit depicted in Fig. 1 aims to inject maximum active power available from PV arrays into the utility grid in UPF mode. Both DC-DC and DC-AC conversion stages of the proposed system are controlled independently.

A. DC-DC Converter Control Stage

Low voltage input from solar panels is converted to high voltage DC input required for inverter using proposed DC-DC converter stage. The instantaneous maximum power from PV arrays with available irradiance and temperature variations is continuously extracted by controlling input impedance of PV array. A well-known perturb and observe (P&O) based MPPT technique is used to control the input impedance. The duty cycles for both main and auxiliary switches are controlled according to increment and decrement of PV array power and voltage. Actual PV array voltage (V_{PV}) is compared with reference PV voltage (V_{PVref}) calculated using MPPT technique and the voltage error is regulated using PI-regulator to generate modulating signal. The PWM pulses generated for main (S_{MAIN}) and auxiliary (S_{AUX}) switches are complementary to each other. As discussed in the earlier section, active clamp circuit formed by an auxiliary MOSFET (S_{AUX}) and capacitor C_{O2} clamps the voltage stress of MOSFETs to V_{CO2} and also helps to achieve ZVS turn-on for both the MOSFETs.

B. Inverter Control Stage

In order to penetrate the quality current generated by PV arrays into the utility grid at UPF mode, synchronization and extraction of fundamental component of utility voltage is mandatory. The fundamental unit voltage vector ($U_{Grid} = \sin\phi$) of the grid voltage at PCC ($V_{Grid} = V_{max}\ \sin\phi$), is extracted by using AANF developed in [34], [35].

1) AANF for Synchronization and Fundamental Extraction: An input grid voltage signal is represented as,

$$V_{Grid} = \sum_{i=1}^{n} V_{max_i} \sin\phi_i \quad where, \phi_i = \omega_i t + \varphi_i \tag{19}$$

Here, the frequencies ω_i and the phases φ_i, where, $i = 1, 2, 3, ..., n$, are both unknown quantities. To estimate these quantities an AANF structure is represented as,

$$\begin{aligned} \ddot{x} + \theta^2 x &= \sqrt{2}\theta e(t) \\ \dot{\theta} &= -\gamma x \theta e(t) \\ e(t) &= V(t) - \dot{x} \\ \gamma &= \frac{\epsilon}{(1+A^2)(1+\mu\theta^2)} \end{aligned} \tag{20}$$

Estimation accuracy of AANF depends on two real positive constants, damping ratio (ζ) and adaptation gain (γ). For a

0093-9994 (c) 2017 IEEE. Personal use is permitted, but republication/redistribution requires IEEE permission. See http://www.ieee.org/publications_standards/publications/rights/index.html for more information.

This article has been accepted for publication in a future issue of this journal, but has not been fully edited. Content may change prior to final publication. Citation information: DOI 10.1109/TIA.2017.2752679, IEEE Transactions on Industry Applications

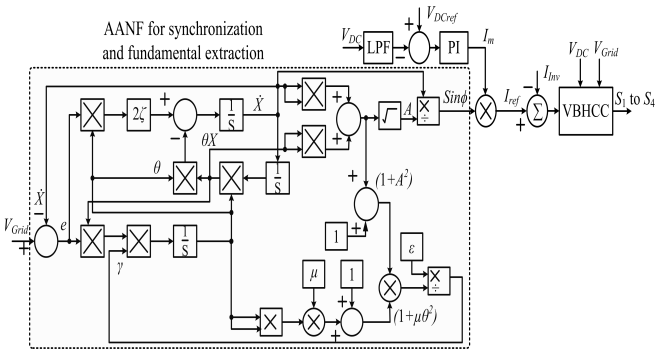


Fig. 6. Inverter control circuit.

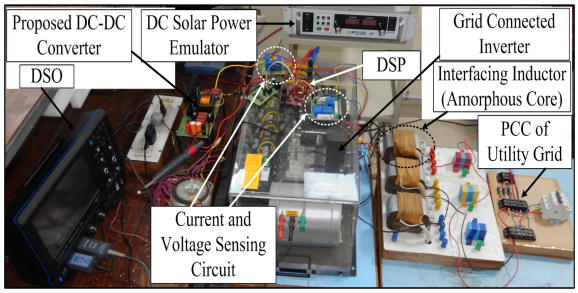


Fig. 7. Laboratory experimental setup.

fundamental frequency ω_1, the periodic orbit of AANF is located at,

$$(O) = \begin{pmatrix} x \\ \dot{x} \\ \theta \end{pmatrix} = \begin{pmatrix} \frac{-A_1}{\omega_1}\cos(\omega_1 t + \varphi_1) \\ A_1 \sin(\omega_1 t + \varphi_1) \\ \omega_1 \end{pmatrix} \quad (21)$$

Where, the element O gives the fundamental frequency ω_1, $\dot{x}$ is the fundamental component and $-\theta x$ is 90^o phase-shift component of the periodic input grid voltage signal. The amplitude of the fundamental component of grid voltage is determined as, $A_1 = \sqrt{(\dot{x}_1^2 + \theta^2 x_1^2)}$. Therefore, the fundamental unit voltage vector is $U_{Grid} = \frac{\dot{x}}{A_1} = \sin\phi$. This unit voltage vector is in synchronism with the utility grid voltage and hence used to achieve synchronization and generation of reference current component for VBHCC.

The instantaneous value of DC-link voltage (V_{DC}) decides the amount of active component of current to be injected into the utility grid. To extract this component, the sensed actual DC-link voltage (V_{DC}) is filtered using low pass filter (LPF) and compared with the reference DC-link voltage (V_{DCref}). The error signal (ΔV_{DC}) is then passed through PI-regulator which outputs active component of current (I_m) and regulates the DC-link voltage. To estimate synchronized modulating current component for VBHCC, this active component of current (I_m) is multiplied with fundamental unit voltage vector (U_{Grid}). The synchronized modulating reference current signal is then used to generate required current to be injected into the grid. To generate gate pulses (S_1 to S_4) required to drive the interfacing inverter, VBHCC developed in [33] is used. Inverter control circuit for proposed system is as shown in Fig. 6. VBHCC is used to avoid variable switching frequency related problem of increased switching losses and to achieve fast dynamic response. The synchronized reference current component is,

$$I_{ref}(t) = I_m \ \sin\phi \quad (22)$$

From the instantaneous value of this reference current, the current error (ΔI) required to estimate upper and lower band of VBHCC is given as [33],

$$\Delta I(t) = \frac{V_{DC}^2 - [V_{Grid}(t) + L_f \frac{dI_{ref}(t)}{dt}]^2}{4 L_f V_{DC} F_{sw}} \quad (23)$$

Where, L_f is the filter inductance and F_{sw} is the desired switching frequency of the inverter. The upper and lower band values of the current for VBHCC is,

$$I_{UB} = I_{ref}(t) + \Delta I(t) \quad (24)$$

$$I_{LB} = I_{ref}(t) - \Delta I(t) \quad (25)$$

TABLE II
PROPOSED TWO-STAGE SYSTEM PARAMETERS.

DC-DC converter stage	
Rated output power (P_{out})	250 W
Input voltage MPPT range (V_{in})	40V-55V
Output DC-link voltage (V_{DC})	380V
Turns ratio	1:2.5
Switching frequency (f_{sw})	60 KHz
Magnetizing inductance (L_m)	12μH
Leakage inductance (L_{ks})	3.2μH
Switched capacitors (C_1, C_2)	0.2μF
Output capacitors (C_{O1} and C_{O2})	100μF
DC-AC inverter stage	
Rated output power (P_{out})	250 W
Grid voltage (V_{Grid})	230 V
Grid frequency (f)	50 Hz
Desired switching frequency (F_{sw})	12 KHz
Filter inductance (L_f)	24 mH

IV. Experimental Results and Discission

To evaluate high step-up operation of the proposed DC-DC converter and to validate efficient maximum power injection capability of the proposed two stage system for low voltage PV sources, a 250W prototype of the DC-DC converter is developed and tested in the laboratory. Overall two-stage system parameters considered for laboratory experimentation are tabulated in Table II. Three-phase voltage source inverter fabricated using four SEMIKRON module legs is available in the laboratory of which, only two legs are used as a single-phase H-Bridge inverter. In general, for low voltage PV applications, crystalline silicon made PV arrays are used. Here, because of unavailability of PV arrays, MAGNA-XR LXI Programmable DC solar power emulator is used as PV source. Hall effect LEM current (LA-25p) and voltage (LV-25p) transducers are used to sense required current and voltage signals respectively. The control circuit of the proposed two stage system is implemented in dual core microcontroller TMS320F28379D. The laboratory experimental setup is as shown in Fig. 7. LeCroy and Tektronix digital oscilloscopes are used to analyze voltage and current waveforms.

0093-9994 (c) 2017 IEEE. Personal use is permitted, but republication/redistribution requires IEEE permission. See http://www.ieee.org/publications_standards/publications/rights/index.html for more information.

This article has been accepted for publication in a future issue of this journal, but has not been fully edited. Content may change prior to final publication. Citation information: DOI 10.1109/TIA.2017.2752679, IEEE Transactions on Industry Applications

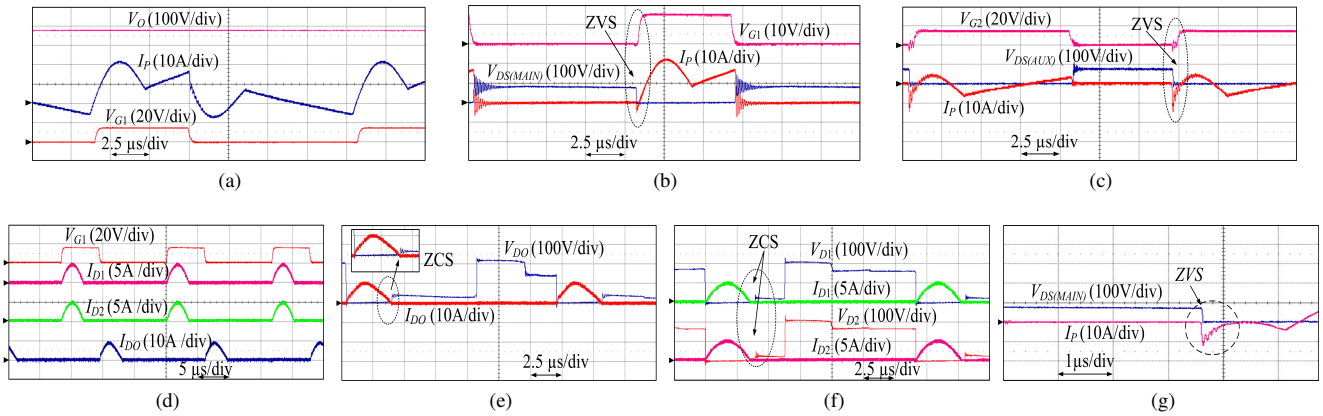


Fig. 8. Experimental results for $V_{in} = 48V$ and at full load: (a) Output DC-link voltage (V_{DC}), primary current (I_P) and main switch S_{MAIN} gate pulse (V_{G1}). (b) Gate pulse with voltage across and current through the main switch S_{MAIN} showing ZVS turn-on. (c) Gate pulse with voltage across and current through the auxiliary switch S_{AUX} showing ZVS turn-on. (d) Gate signal of main switch S_{MAIN} and all diode currents, (e) Voltage and current of output diode D_O with ZCS turn-off. (f) Voltages and currents of multiplier cell diodes D_1 and D_2 with ZCS turn-off. (g) Gate pulse with voltage across and current through the main switch S_{MAIN} with ZVS turn-on for $V_{in} = 48V$ and at 20% of full load.

A. Proposed DC-DC Converter Performance

Here, proposed converter performance to achieve high voltage step-up operation is verified under steady state condition as demonstrated in Fig. 8. In Fig. 8(a), output voltage of the converter, primary current and gate signal of main switch S_{MAIN} is shown for an input voltage of 48V at full load condition. These results demonstrates ability of the proposed converter to obtain higher voltage gain with lower duty cycle and hence are useful for low voltage solar PV based AC module applications. In Fig. 8(b), current flowing through the main switch S_{MAIN} and drain to source voltage (V_{DS1}) across the switch S_{MAIN} is shown along with gate triggering signal. Voltage stress across both the MOSFETs are clamped well below 120V due to the active clamp circuit formed by an auxiliary switch (S_{AUX}) and output capacitor C_{O2} as shown in Figs. 8(b) and 8(c). This also helps to achieve ZVS turn-on for both the switches. From Figs. 8(b) and 8(c) it is clearly visible that the voltage across the respective switches becomes zero before application of gate pulse and current starts to increase from zero. ZVS operation of both the MOSFETs helps to decrease the turn-on losses and thus improves the conversion efficiency. During this operation, current flowing through the diodes I_{D1}, I_{D2} and I_{DO} are depicted in Fig. 8(d). Quasi sinusoidal nature of diode current realizes zero current turn-off (ZCS) of the diodes. Voltage stresses (V_{DO}) across the output diode D_O and current through the diode (I_{DO}) is shown in Fig. 8(e) with ZCS turn-off. Diode voltage stress is less than 220V which is much below the converter output voltage. ZCS turn-off helps to diminish the problem of reverse recovery of the diodes and also reduce the diode turn-off losses. Voltage stress and the current through the multiplier cell diodes D_1 and D_2 are shown in Fig. 8(f). Both these diodes D_1 and D_2 are turn-off with ZCS. Their voltage stress is also lower. With the designed value of magnetizing inductance ($L_m = 12$ μH), ZVS turn-on of main switch is achieved at light load condition (20% of full load) is as shown in Fig. 8(g). Hence, proposed converter gives ZVS operation of main switch for wide range of load variation (10% to 100% of full load).

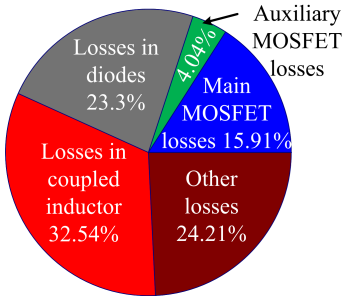


Fig. 9. Percentage loss of each component to the total power loss of proposed converter.

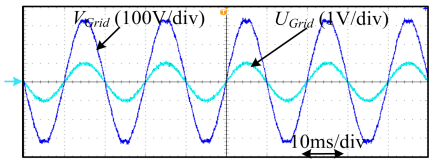


Fig. 10. The synchronized unit voltage vector for reference current generation.

TABLE III
PROPOSED CONVERTER COMPONENT LOSSES.

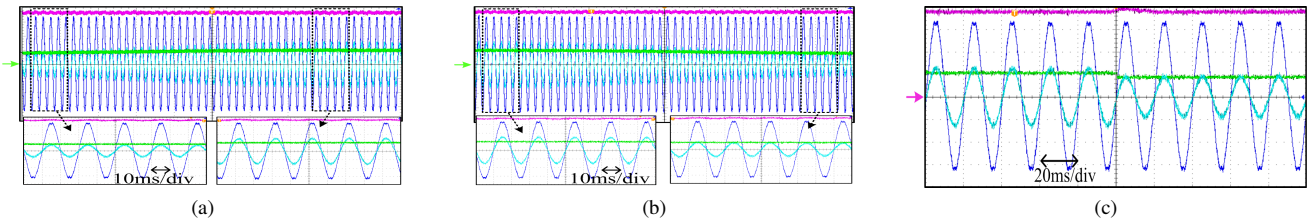
Component	Power Loss
Main MOSFET	1.81W (Conduction loss)
Auxiliary MOSFET	0.46W (Conduction loss)
Diodes	2.65W
Coupled Inductor	3.7W
Other Losses	2.75W
Total Loss	11.37W

B. Proposed Converter Components Loss Analysis

The component power losses of the proposed converter are estimated at full load for $V_{in} = 40V$. These losses are calculated by measuring required RMS values of currents

0093-9994 (c) 2017 IEEE. Personal use is permitted, but republication/redistribution requires IEEE permission. See http://www.ieee.org/publications_standards/publications/rights/index.html for more information.

This article has been accepted for publication in a future issue of this journal, but has not been fully edited. Content may change prior to final publication. Citation information: DOI 10.1109/TIA.2017.2752679, IEEE Transactions on Industry Applications



(a) (b) (c)

Fig. 11. Experimental results showing grid voltage with blue color (100V/div), input PV voltage with green color (50V/div), DC-link voltage with red color (100V/div) and injected inverter current with cyan color (1A/div) when: (a) Solar insolation increases. (b) Solar insulation decrease. (c) Solar insulation step change.

flowing through the switching devices using LeCroy DSO and selecting required parameter from the device data-sheet. Total power loss of the converter is calculated by measuring input and output power using power quality analyzer (Total loss = 11.37W). Low on-state resistance ($R_{DS(ON)} = 21m\Omega$) MOSFET (IRFP4227PbF) is used as main and auxiliary switch. From the known value of RMS current through the device and its on-state resistance, the estimated conduction loss of main MOSFET is 1.81W and auxiliary MOSFET is 0.46W. As ZVS operation of both the MOSFETs is achieved, the turn-on loss is negligible and turn-off loss is also very low. In order to calculate conduction losses of the hyper-fast power diode (BYC10D600), required parameters are selected from device data-sheet. The estimated conduction losses of the diodes are 2.65W. As ZCS of all the diodes is achieved, reverse recovery losses and turn-off losses are negligible. The power losses in the coupled inductor are estimated by measuring primary and secondary winding resistances of the coupled inductor using Fluke PM6304 R-C-L meter. From the known value of primary current and turns ratio, secondary winding current is calculated and total primary and secondary winding power losses are estimated as 3.7W. All the aforesaid losses (Main and auxiliary MOSFET losses, diode losses and coupled inductor losses) are subtracted from the overall total losses to estimate other losses. The other losses includes, core losses of magnetic components, losses in equivalent series resistances (ESR) of output capacitors C_{O1}, C_{O2}, switched capacitors C_1, C_2 and input filter capacitors, losses in the driver circuit and losses due to PCB track resistances. The estimated losses of various components are tabulated in Table III. Pie chart shown in Fig. 9 demonstrates percentage contribution of each component loss to the total power loss of the converter.

C. Overall Two-Stage System Performance

In order to validate the operation of overall two-stage solar PV system, proposed DC-DC converter output is coupled to a single phase H-Bridge inverter connected to the utility grid. Crystalline silicon PV-arrays are selected in the solar array emulation software of DC solar power emulator and two different profiles for winter cloudy and summer sunny conditions are created by selecting reference PV-array parameters. For winter and summer condition, temperature and irradiance levels are selected as $18^0C-600Watts/m^2$ and $38^0C-900Watts/m^2$ respectively. The input MPPT voltage range is selected as 40V-55V. Ideally, the environmental temperature and irradiance levels will not change dramatically. Hence, to achieve smooth transition between above two profiles, intermediate profiles are created for a time period of 2 Sec. Quality power injection capability of the proposed two-stage system is evaluated for changing solar insolation levels.

The synchronized unit voltage vector estimated by the synchronization unit is as shown in Fig. 10. This component is then used to generate reference current in phase with the utility grid voltage which represents the maximum power extracted from the solar input (excluding the power loss occurred at DC-DC stage). The amount of current injected into the utility grid under changing solar insolation levels is demonstrated in Fig. 11. Fig. 11(a) and Fig. 11(b) demonstrates performance of the proposed system during smooth transition of solar insulation for above two profiles for a period of 1 Sec. The PV-array voltage changes in the range of 40V-55V during increasing and decreasing solar insulation range. In order to verify the performance of proposed DC-DC converter during step change in the solar irradiance condition, irradiation level is dramatically changed from $900Watts/m^2$ to $600Watts/m^2$. The response of the proposed system for this condition is as shown in Fig. 11(c). From Fig. 11(c) it is observed that, the injected current suddenly decreased as soon as the irradiance level is changed. During this entire process, even though input PV voltage (V_{PV}) is changed, the DC-link voltage is maintained constant as shown in Fig. 11. Hence, proposed system works properly under transient condition also. In addition, the injected current is in phase with the grid voltage, hence ensures UPF operation of interfacing inverter. Also, the total harmonics distortions (THD) of the injected current measured by using an oscilloscope (DPO-3054) is 2.36% as shown in Fig. 12 which is well below the IEEE 1547 standards. Therefore, accurate extraction of fundamental unit voltage vector improves quality of the injected current.

To estimate conversion efficiency at first stage, proposed converter is separately tested and its efficiency is calculated at various output power levels as shown in Fig. 13. ZVS and ZCS operation of semiconductor switches, improves DC-DC conversion efficiency. Maximum conversion efficiency obtained for the proposed DC-DC converter is 96.77%. However, for rated output power its efficiency is 95.45%, which is much improved compared to hard switched converters. Efficiency of the proposed converter is compared with other hard switched boost-integrated flyback converters with high voltage gain capability [11], [20]. Proposed converters efficiency is plotted for an input voltage of 40V. From the efficiency plot, it is evident that, proposed converter have improved efficiency from

0093-9994 (c) 2017 IEEE. Personal use is permitted, but republication/redistribution requires IEEE permission. See http://www.ieee.org/publications_standards/publications/rights/index.html for more information.

This article has been accepted for publication in a future issue of this journal, but has not been fully edited. Content may change prior to final publication. Citation information: DOI 10.1109/TIA.2017.2752679, IEEE Transactions on Industry Applications

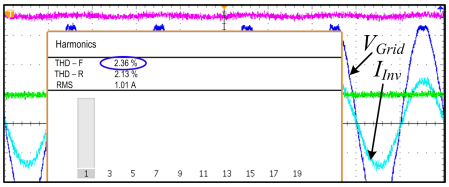


Fig. 12. Total harmonics distortions (THD) of the injected current.

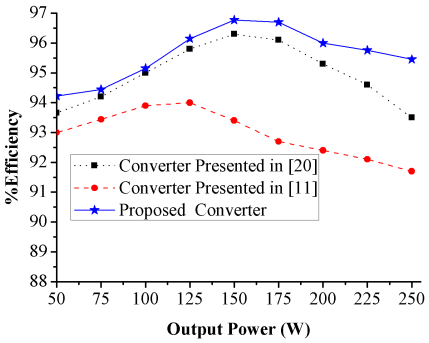


Fig. 13. Efficiency $Vs.$ output power.

light load to full load. More specifically, for almost all the output power ranges, proposed converter is able to operate with relatively good efficiency (more than 95%) as shown in Fig. 13. The overall two stage system efficiency will further reduce due to inverter losses. However, it is possible to achieve overall conversion efficiency between 90% to 95%.

V. Conclusion

Performance of a proposed two-stage grid tied low voltage solar PV system with efficient quality power injection capability is evaluated. At first stage, high voltage gain boost integrated flyback converter with quasi resonant voltage multiplier cell having soft-switching capabilities is presented. A bidirectional boost converter is stacked with a flyback converter which bypasses the leakage energy to the output capacitor and thus increases the voltage gain and provides ZVS turn-on of MOSFETs. Hence, reduces the high frequency switching losses. A resonant circuit is formed between the secondary leakage inductance and the capacitors of voltage multiplier cell which provide ZCS turn-off of all the diodes. ZVS and ZCS operation of all switching devices results in higher conversion efficiency compared to the conventional passive clamp boost integrated flyback converters. In the proposed converter, the voltage stress across the switches are clamped much below the output voltage, hence low voltage rating switches with lower on state resistances are used. At second stage, variable band hysteresis current control technique with adaptive synchronization unit for reference current extraction is presented. AANF is used because of its adaptive nature in extracting fundamental unit voltage vector of grid voltage required for estimation of synchronized reference current for hysteresis controller. Experimental results validates efficient quality current injection capability of the proposed two stage system under varying solar insulation level.

Appendix
Design Procedure of Magnetizing Inductance

From (14), the required magnetizing inductance is selected as $12\mu H$. The size of magnetic core is determined by the core area product $A_P = A_C * A_W$ which is proportional to the stored energy in the magnetic core [38].

$$A_P = \frac{2L_m I_{Lmp}^2}{K_u J B_{max}} \tag{26}$$

Where, magnetizing inductance ($L_m = 12\mu H$), peak magnetizing current ($I_{Lmp} = 20.1A$), window utilization factor ($K_u = 0.3$), current density ($J = 4A/mm^2$) and the maximum flux density ($B_{max} = 0.2T$). Ferrite Core EE42 having core area product ($A_P = 4.03cm^4$) and effective core cross-sectional area ($A_C = 2.33cm^2$) is selected for coupled inductor. Primary number of turns of coupled inductor is obtained as,

$$N_1 = \frac{L_m I_{Lmp}}{A_C B_{max}} \approx 5 \tag{27}$$

The secondary number of turns of coupled inductor is obtained as 12.5 from turns ratio relationship. Secondary number of turns is achieved by winding 12 full turns and a half turn. Magnetizing current of proposed converter have DC-bias component. This DC current may saturate the coupled inductor. Hence, air gap is necessary to avoid core saturation. The required air gap length considering free space permeability ($\mu_0 = 4\Pi * 10^{-7}$) is obtained as,

$$l_g = \frac{\mu_0 L_m I_{Lmp}^2}{A_C B_{max}^2} \approx 0.65mm \tag{28}$$

Primary and secondary winding is wound with litz wire to reduce the skin effect. The leakage and magnetizing inductance is measured through Fluke made R-L-C meter. The steps given in [39], are used to measure the parameters of coupled inductor. Estimating exact predetermined leakage inductance is very difficult in practice. By varying the air gap between the E-shape cores, the leakage inductance can be adjusted to the desired value.

References

[1] D. Meneses, F. Blaabjerg, O. Garcia, and J. A. Cobos, "Review and comparison of step-up transformerless topologies for photovoltaic ac-module application," *IEEE Trans. Power Electron.*, vol. 28, no. 6, pp. 2649–2663, June 2013.

[2] F. L. Tofoli, D. d. C. Pereira, W. J. de Paula, and D. d. S. Oliveira Junior, "Survey on non-isolated high-voltage step-up dc-dc topologies based on the boost converter," *IET Power Electronics*, vol. 8, no. 10, pp. 2044–2057, Oct. 2015.

[3] Y. Tang and T. Wang, "Study of an improved dual-switch converter with passive lossless clamping," *IEEE Trans. Ind. Electron.*, vol. 62, no. 2, pp. 972–981, Feb. 2015.

[4] R. W. Erickson and D. Maksimovic, *Fundamentals of power electronics*, 2nd ed. Norwell, MA, USA: Springer Science & Business Media, 2001.

[5] Y. Hu, W. Xiao, W. Cao, B. Ji, and D. J. Morrow, "Three-port dc-dc converter for stand-alone photovoltaic systems," *IEEE Trans. Power Electron.*, vol. 30, no. 6, pp. 3068–3076, June 2015.

[6] H. Keyhani and H. A. Toliyat, "Single-stage multistring pv inverter with an isolated high-frequency link and soft-switching operation," *IEEE Trans. Power Electron.*, vol. 29, no. 8, pp. 3919–3929, Aug 2014.

[7] U. R. Prasanna, A. K. Rathore, and S. K. Mazumder, "Novel zero-current-switching current-fed half-bridge isolated dc/dc converter for fuel-cell-based applications," *IEEE Trans. Ind. Appl.*, vol. 49, no. 4, pp. 1658–1668, July 2013.

0093-9994 (c) 2017 IEEE. Personal use is permitted, but republication/redistribution requires IEEE permission. See http://www.ieee.org/publications_standards/publications/rights/index.html for more information.

This article has been accepted for publication in a future issue of this journal, but has not been fully edited. Content may change prior to final publication. Citation information: DOI 10.1109/TIA.2017.2752679, IEEE Transactions on Industry Applications

[8] E. Adib and H. Farzanehfard, "Zero-voltage transition current-fed full-bridge pwm converter," *IEEE Trans. Power Electron.*, vol. 24, no. 4, pp. 1041–1047, April 2009.

[9] S. Lee, J. Park, and S. Choi, "A three-phase current-fed push pull dc-dc converter with active clamp for fuel cell applications," *IEEE Trans. Power Electron.*, vol. 26, no. 8, pp. 2266–2277, Aug. 2011.

[10] F. L. Luo and H. Ye, "Positive output multiple-lift push-pull switched-capacitor luo-converters," *IEEE Trans. Ind. Electron.*, vol. 51, no. 3, pp. 594–602, June 2004.

[11] J. W. Baek, M.-H. Ryoo, T.-J. Kim, D.-W. Yoo, and J.-S. Kim, "High boost converter using voltage multiplier," in *31st Annual Conference of IEEE Industrial Electronics Society, 2005. IECON 2005.*, Nov 2005, pp. 6 pp.–.

[12] M. Prudente, L. L. Pfitscher, G. Emmendoerfer, E. F. Romaneli, and R. Gules, "Voltage multiplier cells applied to non-isolated dc-dc converters," *IEEE Trans. Power Electron.*, vol. 23, no. 2, pp. 871–887, March 2008.

[13] C. M. Young, M. H. Chen, T. A. Chang, C. C. Ko, and K. K. Jen, "Cascade cockcroft walton voltage multiplier applied to transformerless high step-up dc-dc converter," *IEEE Trans. Ind. Electron.*, vol. 60, no. 2, pp. 523–537, Feb. 2013.

[14] M. N. Gitau, F. M. Mwaniki, and I. W. Hofsajer, "Analysis and design of a single-phase tapped-coupled-inductor boost dc–dc converter," *Journal of Power Electronics*, vol. 13, no. 4, pp. 636–646, 2013.

[15] Q. Zhao and F. C. Lee, "High-efficiency, high step-up dc-dc converters," *IEEE Trans. Power Electron.*, vol. 18, no. 1, pp. 65–73, Jan. 2003.

[16] R. J. Wai and R.-Y. Duan, "High step-up converter with coupled-inductor," *IEEE Trans. Power Electron.*, vol. 20, no. 5, pp. 1025–1035, Sept. 2005.

[17] S. Sathyan, H. M. Suryawanshi, M. S. Ballal, and A. B. Shitole, "Soft-switching dc-dc converter for distributed energy sources with high step-up voltage capability," *IEEE Trans. Ind. Electron.*, vol. 62, no. 11, pp. 7039–7050, Nov. 2015.

[18] K. C. Tseng and T. J. Liang, "Novel high-efficiency step-up converter," *IEE Proceedings-Electric Power Applications*, vol. 151, no. 2, pp. 182–190, Mar. 2004.

[19] T. J. Liang and K. C. Tseng, "Analysis of integrated boost-flyback step-up converter," *IEE Proceedings - Electric Power Applications*, vol. 152, no. 2, pp. 217–225, March 2005.

[20] T. J. Liang, S. M. Chen, L. S. Yang, J. F. Chen, and A. Ioinovici, "A single switch boost-flyback dc-dc converter integrated with switched-capacitor cell," in *Power Electronics and ECCE Asia (ICPE ECCE), 2011 IEEE 8th International Conference on*, May 2011, pp. 2782–2787.

[21] N. Molavi, E. Adib, and H. Farzanehfard, "Soft-switched non-isolated high step-up dc-dc converter with reduced voltage stress," *IET Power Electronics*, vol. 9, no. 8, pp. 1711–1718, 2016.

[22] Y. Park, B. Jung, and S. Choi, "Nonisolated zvzcs resonant pwm dc-dc converter for high step-up and high-power applications," *IEEE Trans. Power Electron.*, vol. 27, no. 8, pp. 3568–3575, Aug 2012.

[23] S. Jain and V. Agarwal, "Comparison of the performance of maximum power point tracking schemes applied to single-stage grid-connected photovoltaic systems," *IET Electric Power Applications*, vol. 1, no. 5, pp. 753–762, Sept. 2007.

[24] M. A. Elgendy, B. Zahawi, and D. J. Atkinson, "Assessment of perturb and observe mppt algorithm implementation techniques for pv pumping applications," *IEEE Trans. Sustain. Energy*, vol. 3, no. 1, pp. 21–33, Jan. 2012.

[25] M. Das and V. Agarwal, "Novel high-performance stand-alone solar pv system with high-gain high-efficiency dc-dc converter power stages," *IEEE Trans. Ind. Appl.*, vol. 51, no. 6, pp. 4718–4728, Nov. 2015.

[26] S. A. Arshadi, B. Poorali, E. Adib, and H. Farzanehfard, "High step-up dc-ac inverter suitable for ac module applications," *IEEE Trans. Ind. Electron.*, vol. 63, no. 2, pp. 832–839, Feb. 2016.

[27] M. Das and V. Agarwal, "Design and analysis of a high-efficiency dc-dc converter with soft switching capability for renewable energy applications requiring high voltage gain," *IEEE Trans. Ind. Electro.*, vol. 63, no. 5, pp. 2936–2944, May 2016.

[28] A. Elrayyah, Y. Sozer, and M. Elbuluk, "Microgrid-connected pv-based sources: A novel autonomous control method for maintaining maximum power," *IEEE Trans. Ind. Appl. Magazine*, vol. 21, no. 2, pp. 19–29, March 2015.

[29] R. Davoodnezhad, D. G. Holmes, and B. P. McGrath, "A fully digital hysteresis current controller for current regulation of grid connected pv inverters," in *2014 IEEE 5th International Symposium on Power Electronics for Distributed Generation Systems (PEDG)*, June 2014, pp. 1–8.

[30] Y. Hu, W. Cao, B. Ji, J. Si, and X. Chen, "New multi-stage dc-dc converters for grid-connected photovoltaic systems," *Renewable Energy*, vol. 74, pp. 247–257, 2015.

[31] S. Sathyan, H. M. Suryawanshi, A. B. Shitole, and G. G. Talapur, "Soft switched high voltage gain boost integrated flyback converter," in *2016 IEEE International Conference on Power Electronics, Drives and Energy Systems (PEDES)*, Dec 2016, pp. 1–6.

[32] S. Sathyan, H. M. Suryawanshi, B. Singh, C. Chakraborty, V. Verma, and M. S. Ballal, "Zvs-zcs high voltage gain integrated boost converter for dc microgrid," *IEEE Trans. Ind. Electron.*, vol. 63, no. 11, pp. 6898–6908, Nov. 2016.

[33] G. G. Talapur, H. M. Suryawanshi, A. B. Shitole, S. Sathyan, and V. V. Reddy, "Performance improvement of digital variable band hysteresis current control using dual processor microcontroller," in *IECON 2016 - 42nd Annual Conference of the IEEE Industrial Electronics Society*, Oct. 2016, pp. 2367–2371.

[34] G. Yin, L. Guo, and X. Li, "An amplitude adaptive notch filter for grid signal processing," *IEEE Trans. Power Electron.*, vol. 28, no. 6, pp. 2638–2641, June 2013.

[35] A. B. Shitole, H. M. Suryawanshi, and S. Sathyan, "Comparative evaluation of synchronization techniques for grid interconnection of renewable energy sources," in *Industrial Electronics Society, IECON 2015 - 41st Annual Conference of the IEEE*, Nov. 2015, pp. 001 436–001 441.

[36] A. Shitole, H. M. Suryawanshi, G. Talapur, S. Sathyan, M. Ballal, V. B. Borghate, M. Ramteke, and M. Chaudhari, "Grid interfaced distributed generation system with modified current control loop using adaptive synchronization technique," *IEEE Trans. Ind. Informat.*, vol. PP, no. 99, pp. 1–1, 2017.

[37] J. M. Shen, H. L. Jou, and J. C. Wu, "Novel transformerless grid-connected power converter with negative grounding for photovoltaic generation system," *IEEE Trans. Power Electron.*, vol. 27, no. 4, pp. 1818–1829, April 2012.

[38] M. K. Kazimierczuk, *High-Frequency Magnetic Components*, 2nd ed. U.K.: Wiley, November 2013.

[39] C. Basso, *How to Deal with Leakage Elements in Flyback Converters*, ON Semiconductor, September 2005, application Note, AN1679/D.



Amardeep B. Shitole received the B.E. degree in Electrical Engg. from Government College of Engg. Karad, India, in 2008 and M.Tech. degree in Power Systems (Electrical Engg.) from College of Engg. Pune, India, in 2012. Currently he is pursing Ph.D. degree in Electrical Engg. at VNIT, Nagpur, India. His research interests include power electronics, renewable energy integration, high power density converters, AC Micro-grid and power quality.



Shelas Sathyan received the B.Tech. degree in electrical and electronics engg. from the Government College of Engg. Kannur, India, in 2009, and M.Tech. and Ph.D. degree in electrical engg. from VNIT, Nagpur, India, in 2012 and 2017 respectively. He is currently an assistant Professor with the Department of Electrical Engg., Shiv Nadar University, Greater Noida, India. His research interests include dc-dc converters, soft switched converters and power factor correction.



Hiralal M. Suryawanshi (M'06-SM'12) received the B.E. degree in Electrical Engg. from Walchand College of Engg., Sangli, India, in 1988 and M.E. degree in Electrical Engg. from Indian Institute of Science, Bangalore, in 1994. He has been awarded Ph.D. degree by Nagpur University, Nagpur (India) in 1999. He is currently working as Professor in the Department of Electrical Engg., VNIT, Nagpur, (India). He is Chair Professor and Fellow of INAE. He is an Associate Editor of IEEE Transaction on Industrial Electronics. He has received IETE-Bimal Bose Award in 2009 and IETE-Biman Behari Sen Memorial Award in 2017 for his leadership in Power Electronics in India. His research interests include Power Electronics, resonant converters, power factor correction, active power filters, multilevel converters and electric drives.

0093-9994 (c) 2017 IEEE. Personal use is permitted, but republication/redistribution requires IEEE permission. See http://www.ieee.org/publications_standards/publications/rights/index.html for more information.

This article has been accepted for publication in a future issue of this journal, but has not been fully edited. Content may change prior to final publication. Citation information: DOI 10.1109/TIA.2017.2752679, IEEE Transactions on Industry Applications



Girish G. Talapur received the B.Tech. degree in electrical and electronics engineering from RGM College of Engineering and Technology, Nandyal, India in 2009; M.Tech. degree in power systems from Delhi Technological University, New Delhi, India in 2012. He is currently working towards Ph.D. degree in electrical engineering at VNIT, Nagpur, India. His research interests include high density power converters, distributed generation, AC Micro-grid, power quality and DC Micro-grid.



Pradyumn Chaturvedi (SM'2017) received the B.E., M.E. and Ph.D. degree in 1996, 2001 and 2010 respectively. He is currently working as Assistant Professor in the Department of Electrical Engineering, VNIT, Nagpur, India. He has published more than 70 research papers in International refereed Journals and refereed International/National Conferences. He is also actively involved in IEEE conferences as Track Chair (ITEC India 2017), Session Chair, Technical Program Committee and Advisory Committee. He is regular Reviewer of research articles for IEEE Transaction on Power Electronics, IEEE Transaction on Industrial Electronics, IEEE Transaction on Industrial Informatics. His research interests include Improved Power Factor Converter, Multilevel Converters, Renewable Energy Harvesting and Fault Tolerant Converters.

0093-9994 (c) 2017 IEEE. Personal use is permitted, but republication/redistribution requires IEEE permission. See http://www.ieee.org/publications_standards/publications/rights/index.html for more information.

INTERNATIONAL RESEARCH JOURNAL OF MULTIDISCIPLINARY STUDIES

Vol. 3, Issue 9, September, 2017 |ISSN (Online): 2454-8499 |Impact Factor: 1.3599(GIF), 0.679(IIFS)

SOLAR TECHNOLOGY , FACTORS AFFECTING ITS PERFORMANCE AND ITS POTENTIAL MARKET IN INDIA

ANADI SHANKAR JHA
Electrical Engineering (B.Tech), Delhi College Of Engineering
(Delhi Technological University), New Delhi, INDIA.

ABSTRACT-
Solar Energy is a renewable energy which is capable of generating thousands of MW of electricity. Developing countries like INDIA have framed policies inorder to help the genral public participate in this "GO SOLAR" movement. On one hand providing subsidies etc. is increasing the people's participation in this. While on the other, people are not able to optimize their systems due to lack of technical knowledge and awarness. India is capable of generating GW of solar power. However due to faulty installation process or by lack of self checking is decreasing the output of this potential market. Various government Ministries like the MNRE are training various groups of people.

The paper aims to cultivate a good feeling about Solar Power in the minds of the reader. It tells us that how much untapped solar energy is available in India. It gives an insight about the advantages of solar energy and how one has to follow certain standards and methodologies to bring out the best in an installed system. It highlights the best suppliers and their performance quality of waffers. It gives the layout of an ON-Grid System and the procedures like wiring,earthing,connections etc. to be followed inorder to smoothly operate the system. The functions and standards of each and every component like inverts , Panels , mounted structure etc. used are given here with respective to various Power Outputs. In this manner a person does not get cheated while buying products from the market and is well aware about the technique of setting up the Panels. For example Panel efficiency is often seen by looking at the parameters such as short circuit voltage , open circuit voltage etc. while buying. This indicates the performance factor. If this data is not convincing then type test certificates can be obtained whick would then give a clear idea about the waffers or Panels. The ranges of the Panel parameters are also given.

It also tells the main factors which need to be taken into consideration while maximizing the output of these cells like the percentage atmospheric absorption , Air mass etc. This helps in estimating the output of an installation from a given area.

CONTENTS-

Renewable Energy and Status of PV installation in INDIA
Photovoltatic Cells : types , specifications and suppliers
Residential Installation : Components and their standards
Connections
Key Ideas
Problem areas hampering performance and Output
Panels : performance parameters and types
Natural factors affecting irradiation on the Panels

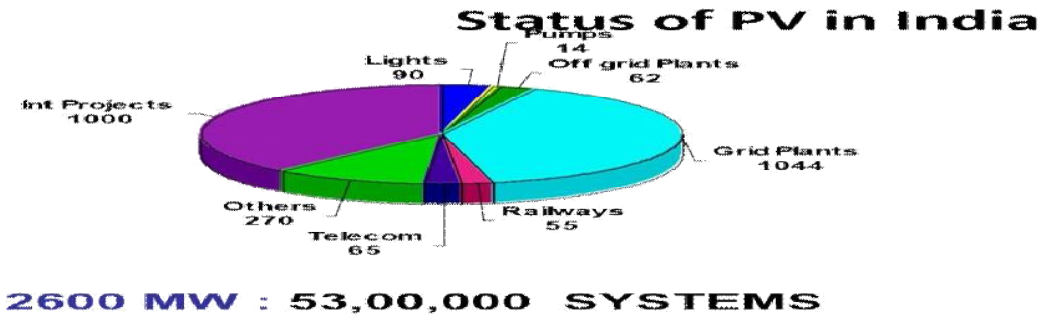
INTERNATIONAL RESEARCH JOURNAL OF MULTIDISCIPLINARY STUDIES
Vol. 3, Issue 9, September, 2017 |ISSN (Online): 2454-8499 |Impact Factor: 1.3599(GIF), 0.679(IIFS)

Renewable Energy

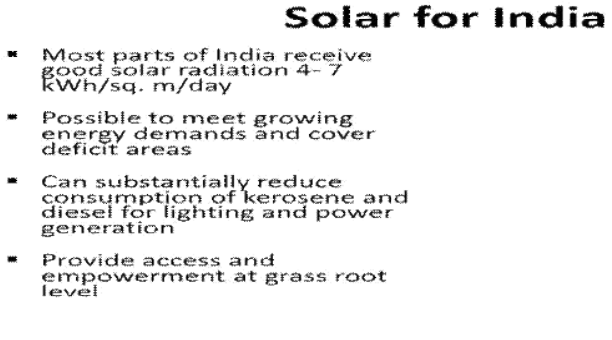
A country's economic progress majorly depends upon its energy resources. Highly developed countries like the USA and China have a high energy consumption rate compared to other developing nations of the world. It has been reported that India's absolute primary energy consumption is only 1/29th of that of the world, 1/7th of USA and 1/1.6 time of Japan. However, with the increasing danger posed by pollution, there is an urgent need to shun the excessive use of pollution releasing conventional sources of energy and switch over to environment friendly options like the renewable energy resources.

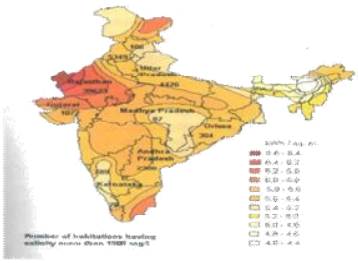
Renewable energy is the energy that comes from replenish able energy sources such as sunlight, wind, etc. There is a large potential for renewable energy in India. It has been estimated that India's renewable energy production amounts to a total of over 100,000 MW(excluding large hydro) There is a fully dedicated Ministry of New and Renewable Energy, assisted by a number of state nodal agencies that work to enhance India's position in the area of use of renewable energy sources.

Potential Market of INDIA



SOLAR FOR INDIA





Vol. 3, Issue 9, September, 2017 |ISSN (Online): 2454-8499 |Impact Factor: 1.3599(GIF), 0.679(IIFS)

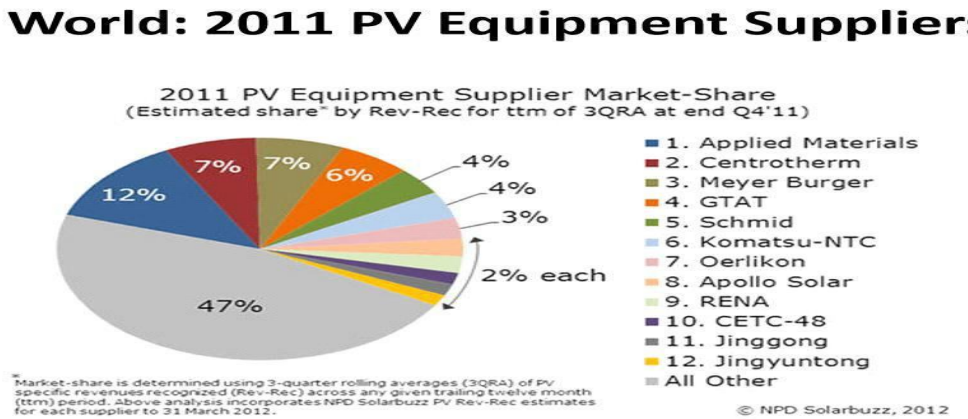
The map shows that the regions of Gujrat and Rajasthan recieve ample sunlight and is a potential market for Solar Energy. A major region of Kerela,being near the equator, is also useful for solar Power Installation.
Here we will first dicuss about Photovoltatic cells as they form the basic building blocks of the Panels. All the other components are discussed by taking the example of an Residential installation.

Photovoltatic cells -

PV Cell – The basic photovoltaic (PV) device that is the building block of PV modules. The cell is a thin wafer of silicon which changes light into electric current

- PV Modules - one solar cell produces 0.5 volts and 36 cells are connected together to charge 12 volt batteries, pumps and motors. The new standard is 72 cells per module for 24 volts and operating at about 30 volts. The module is the basic building block of systems. The PV cells are connected in series and/or parallel and encapsulated in an environmentally protective laminate
- Integrated PV Modules are often constructed to look like materials normally found in construction – i.e., shingles
- PV Array – A group of panels that comprises the complete direct current PV generating unit. (Sometimes referred to as a string).

DATA ON SUPPILERS



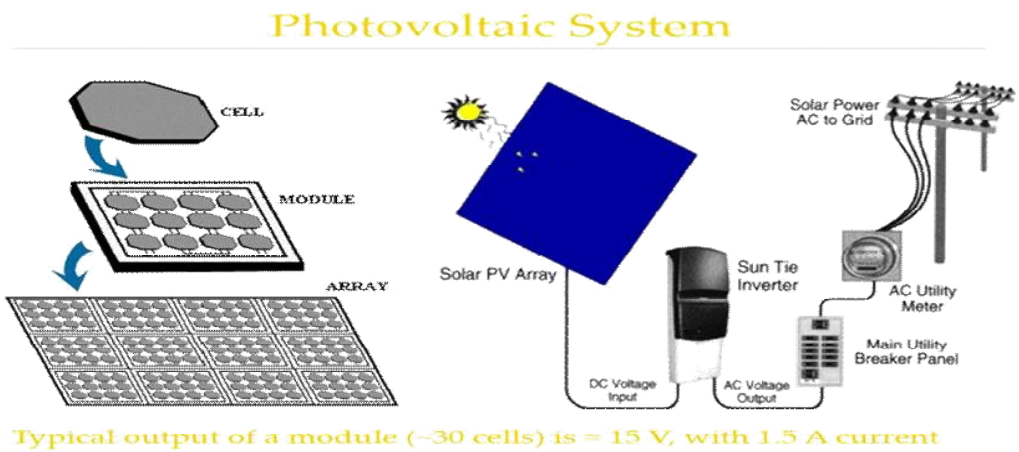
Specifications of Waffers
Type- Crystalline silicon
Origin- Manufactured in India
Efficiency- >= 13%
Fill factor- >= 70%
Degradation warranty Panel output (Wp) capacity to be >=90% of design nominal power after 10 years and >=80% of design nominal power after 25 years.
Module frame Non-corrosive and electrolytically compatible with the mounting structure material
Termination box Thermo-plastic, IP 65, UV resistant

Blocking diodes Schottky type
Module minimum rated power The nominal power of a single PV module shall not be less than 74Wp.
RF Identification tag -for each solar module
Shall be provided inside the module and must be able to withstand environmental conditions and last the lifetime of the solar module.
RF Identification tag data
a) Name of the manufacturer of PV Module
b) Name of the Manufacturer of Solar cells
c) Month and year of manufacture (separately for solar cells and module)
d) Country of origin (separately for solar cells and module)
e) I-V curve for the module
f) Wm, Im, Vm and FF for the module
g) Unique Serial No and Model No of the module
h) Date and year of obtaining IEC PV module qualification certificate
i) Name of the test lab issuing IEC
Specification of Solar PV Modules Solar PV modules shall be of the crystalline silicon type, manufactured in certificate
j) Other relevant information on traceability of solar cells and module as per ISO 9000 standard

Power output rating
To be given for standard test conditions (STC). I-V curve of the sample module shall be submitted.
Compliance with standards and codes
IEC 61215 / IS 14286 IEC 61730 Part 1 and 2
Salt Mist Corrosion Testing As per IEC 61701

Vol. 3, Issue 9, September, 2017 |ISSN (Online): 2454-8499 |Impact Factor: 1.3599(GIF), 0.679(IIFS)

RESIDENTIAL INSTALLATION
DIAGRAM FOR ON-GRID SYSTEMS



Typical roof top installation uses a rack mounting system, panels set in arrays or strings (multiple panels) and conduit for interconnection of panels. Example-- A cell or module is a single silicon unit and generators 0.5 volts.

The layout crew will measure the surface area of the roof and must check the exact location of the roof framing members beneath. Since the panels add a tributary load of between 3-5 psf, this extra dead load is minimal and should not require a structural engineer. However, the rack system requires that the anchors are embedded into the roof framing, not just the sheathing. Other factors such as the time of the day till the sun is available is also important. Days when the nights and days are equal are called as equinox days. Days when the day is the longest or the nights are longest are important so need to be taken into account for finding out the optimal power output. Environmental factors such as wind and heat are important for finding out the optimization of power output from the panel. Winds help to remove the heat and other dust matter. Heat hampers the performance of the system and hence needs to be minimized.

Track Systems

This standoffs or spacers of a typical Pro-Solar system is attached using approximately 5/8 diameter, long lag bolts through the metal roofing, ½ OSB and penetrating the 2-1/8 wide TJI top chord webs. The holes are pre-marked and drilled. Flashing sealant is often used to prevent roof leakage.

Verical Poles

The front rails have small restraining clips to hold the front of each panel. The vertical uprights [shown behind the rail] will elevate the panel to the desired angle for the specific latitude of the

project. The clips are adjustable from side-toside. For the vertical support legs (once cut to the correct length) also allow the installer to adjust the tilt of the legs. The angle of setting up of a system will depends upon a systems' latitude. This indicates the inclination of the sun and the optimal angle for it. In cases of some exceptions there are deviations. For examples where the regions are passing thorugh the equator the angle of inclination needs to be zero theoritically. However, we still give 4 to 5 degree inclination so that there is no deposition of dust and other particles.

Optimum Use of Space

The spacing between the solar PV arrays is critical. As the sun moves to the maximum height (azimuth) during the summer months to a lower height during the winter months, the panels must not shade each other. Partial vertical shading will only short circuit part of a panel; but horizontal shading will stop electrical production for the entire panel and thus the array. The spacing needs to be done during the design phase and prior to any installation. The legs get minor adjustments using flat washers to keep the bars level.

The boxes must be grounded; so there are several key considerations in using plastic boxes (weather proofing for snow and water) with metal conduit. The metal conduit here uses grounding lug end connectors and jumper wires (sized per Code) to keep the grounding and bonds of the conduit, rails, panels and boxes consistent. This is all connected to a grounding terminal in the box adjacent to the inverter. Sizing of the wire should be based upon the panel voltage requirements.

The a normal system would allow standard 12 gauge wiring; however, going to the next larger size (10 gauge) is more efficient and doesn't cause voltage loss to heat because the gauge is marginal or undersized. Because this is a metal roof installation, THWN 90 high heat wiring and insulation are used.

The inverter needs to be shaded and out of the weather. For this roof top installation, there are inverters which is mounted under an overhang. The inverter weighs 145 pounds and comes with a special mounting bracket. A normal mounting structure requires ¾ plywood backer that was supported by three vertical studs and secured with 12, evenly spaced 3 deck screws to hold the weight.Electrician checks grounding between conduit in plastic boxes.

PROTECTION FROM FAULTS

Earthing:

Earthing is done is as to protect the devices as well as life in case of faults. There are different types of earthing. A pit is dug in the ground upto a certain feet. Salt or some minerals are added . This is done inorder to increase the conductivity of the sand. The ground is then covered with silica . In some areas chemical treatment of the soil is also allowed. However this is not a healthy practice as this depletes the ground water table. In areas such as rocky mountains this is permissible.

For Earthing--

1 The PV module structure components shall be electrically interconnected and shall be grounded.

Vol. 3, Issue 9, September, 2017 |ISSN (Online): 2454-8499 |Impact Factor: 1.3599(GIF), 0.679(IIFS)

2 Earthing shall be done in accordance with IS 3043-1986, provided that earthing conductors shall have a minimum size of 6.0 mm2 copper, 10 mm2 aluminium or 70 mm2 hot dip galvanised steel. Unprotected aluminium or copper-clad aluminium conductors shall not be used for final underground connections to earth electrodes.

3 A minimum of two separate dedicated and interconnected earth electrodes must be used for the earthing of the solar PV system support structure with a total earth resistance not exceeding 5 Ohm.

4 The earth electrodes shall have a precast concrete enclosure with a removable lid for inspection and maintenance. The entire earthing system shall comprise non-corrosive components.

Surge Protection

1 Surge protection shall be provided on the DC side and the AC side of the solar panel system.

2 The DC surge protection devices (SPDs) shall be installed in the DC distribution box adjacent to the solar grid inverter.

3 The AC SPDs shall be installed in the AC distribution box adjacent to the solar grid inverter.

4 The SPDs earthing terminal shall be connected to earth through the above mentioned dedicated earthing system. The SPDs shall be of type 2 as per IEC 60364-5-53

Connections

The panels are active or capable of producing DC voltage the minute the sun light hits the panel.

Putting solar cell junction box at back of panels cabling for panels is carefully tucked into the rack channels [care to prevent crimping of connectors under panel edges] lightening arresting system installed in junction box ahead of inverter conduit down to photo voltaic meter at ground level.

Connection to Service panel

Feed breaker may not exceed 20% of the panel service size. This case, the house service was 200 amps, this limits the breaker to 40 amps; max. output for this system is 25 amps.

Conduit from roof to panel

Since this panel is exterior to the house (open to the environment), the panel needs to be connected through the bottom of the existing service panel. The bare copper wire is connected to the service panel grounding lug and uses the existing UFER to complete the ground.

Metering

A digital AC power production meter is installed after the lock out junction box for the system. The Utility Company (APS) wants this lock out accessible without going into a fenced backyard. The meter must be read once a year and the information sent to the Utility Company within 15 days.

The safety requirement for the metering is to prevent the customer from back feeding the grid system. If this disconnect wasn't there and APS had to work on the lines, then a person working on the line can get short circuited. Here the grid system will supply current to the grid.

Panel labels

More warning labels are required adjacent to the inverter and DC disconnect at the roof location. Once APS or the utility company authorizes the connection to the grid, a secondary

digital meter with remote reading capability will be added to the service panel. During a light usage day and with full sunlight, the service panel meter will run backwards .
APS (servering the Flagstaff Area) will require the owner of the system to read this meter once a year and report the total PV generating quantities. Now that the applicant is in a generator capacity, a log or notebook is probably going to be needed.
Key reminders

- If a solar panel is partially shaded vertically, then it only reduces the panel production by the
- percentage of cells shaded; however, shading the top or bottom of a panel horizontally will short out the entire panel and reduce the electricity produced. In this case the cells will behave as the load and entire heat is dissicipated across these cells. This reduces the performance. Heat is released in case of this resistive load.
- One of the leaders in authoring the Article 690, National Electric Code – Bill Brooks of Brooks Engineering, LLC [Bill@brooksolar.com; 707-332-0761] provides an excellent seminar through AZBO. Excellent source of information. [http://www.solarenergy.org/workshops/solarindustry.html]
- When sunlight hits the ground, each square meter (approximately 10 square feet) of earth is capable of producing 1000 watts. The basic formula is P=V*I (v=voltage and I = intensity or current).
- Factoid: Temperature affect voltage, so voltage increases as temperature drops and is reduced when it gets hotter. Light affect current (intensity) or the amperes.
- Photo voltaic systems are somewhere between 10-15% efficient (without intensifiers). Solar water heaters (thermal systems) are 40% or greater in efficiency.
- One silicon solar cell produces 0.5 volts. Electricity is produced when light knocks loose electrons from silicon atoms. The freed electrons have extra energy or voltage . Cells never run out of electrons.

Common Problem Areas

- Insufficient conductor ampacity and insulation – wiring is undersized for the load or the insulation type is not designed for hot locations. Roof tops often exceed 90 (F) degrees.
- Excessive voltage drop – DC (direct current) loss because of long distances to inverter.
- Unsafe wiring methods – inexperience by the installer.
- Lack of or improper placement of over current protection and disconnect devices
- Use of unlisted or improper application of listed equipment (i.e., AC in DC use)
- Lack of or improve equipment or system grounding
- Unsafe installation and use of batteries
- Improper mounting and connection of equipment and racks

After completed Solar Panel
From the street side, this roof top solar panel generating system (5.61 Kwh) awaits the City inspection and green tag . Once that it completed, APS is scheduled to replace the service panel

meter with a bi-direction digital meter and approve the installation for operation. Then during the peak months, the owner hopes to run the meter backwards as it generates more than used.

Panels
Solar Cells
• **Crystalli e Silico solar cells** - Single, Multi, Ribbon
• **Thi Fil solar cells** - Silicon, a-Si, m-Si, CdTe, CIGS
• **Co ce trati g solar cells** - Si, GaAs
• **Dye, Orga ic,a o aterials & other e ergi g solar cells**

Efficiency in photovoltaic solar panels is measured by the ability of a panel to convert sunlight into usable energy for human consumption. Knowing the efficiency of a panel is important in order to choose the correct panels for your photovoltaic system. For smaller roofs, more efficient panels are necessary, due to space constraints. How do manufacturers determine the maximum efficiency of a solar photovoltaic panel though? Read below to find out.

Efficiency Parameters of Panels -

Let there be a total of eleven (11) panels per array. Lets say, the Sharp 170 watt panel being used here is guaranteed for 25 years. The open current voltage is 43.2 volts, the Max power is 34.8 volts, the Max current is 4.9 amps and the model efficiency is 13.1% The panels weigh 37.8 pounds each and are 62 x32-1/2 x1-3/4 in size. (array configuration depends upon the maximum size of 600 Volts, DC)
So when you are determining what solar panels are right for you, think about how important the efficiency of panels are in paying a premium price. Perhaps you have a roof with a large area that would be ideal for the placement of solar panels, and therefore, lower cost and less efficient panels would work for you. If your rooftop area is limited though, you may want to determine the efficiency you will need for your panels to achieve the desired power output over a limited area.

Components and their specifications --

SPV Module

The photovoltaic modules should be Mono /Poly Crystalline with a total array capacity of i. For 1.0 KW SPV power plant- Power output under STC should be 1.0 KW ii. For 5.0 KW SPV power plant-Power output under STC should be 5.0 KW iii. For 10.0 KW SPV power plant-Power output under STC should be 10.0 KW

- The Photovoltaic modules must be qualified as per IEC 61215 (revised) / IS 14286 standards and in addition, the modules must conform to IEC 61730-1 requirements for construction & Part-2 requirements for testing, for safety qualification.
- The PV modules must be tested and approved from any of the NABL/IEC/ MNRE Accredited Testing Calibration Laboratories.

Vol. 3, Issue 9, September, 2017 |ISSN (Online): 2454-8499 |Impact Factor: 1.3599(GIF), 0.679(IIFS)

- The supplier shall provide performance guarantee for the PV modules used in the power plant must be warranted for their output peak watt capacity, which should not be less than 90% at the end of 10 years and 80% at the end of 25 years.
- The efficiency of the PV modules should be minimum 14%.
- Indigenously manufactured PV modules should be used.

Battery Bank

The battery bank should be

i. For 1.0 KW SPV power plant- 12 cells of 2 Volt, 300Ah Cells will be connected in series/ parallel to form 24 volt 300 Ah battery bank.

ii. For 5.0 KW SPV power plant- 60 cells of 2 Volt, 300Ah Cells will be connected in series/ parallel to form 120 volt 300 Ah battery bank.

iii. For 10.0 KW SPV power plant- 60 cells of 2 Volt, 600Ah Cells will be connected in series/ parallel to form 120 volt 600 Ah battery bank.

- VRLA tubular GEL type batteries conforming to National / international standards IEC-61427 & IS-15549 standards, low maintenance, stationery at C/10 rate).
- It will be staged in racks duly painted with acid resistant paint to cover less space.

Power Conditioning Unit with inbuilt charge controller Power conditioner unit with inbuilt charge controller of capacity 1.0 KW, 5.0 KW and 10 KW solar power plants should convert DC power in to AC power must confirm to standards IEC 61683 with following DC input and AC output voltages

i. For 1.0 KW solar power plant - 24 volt DC to 230 volt AC single phase

ii. For 5.0 KW solar power plant - 120 volt DC to 230 volt AC single phase

iii. For 10.0 KW solar power plant phase. - 120 volt DC to 440 (phase to phase) volt AC three

The PCU will have following features:

- MOSFET/ IGBT based MPPT / PWM charging
- Wide input voltage range
- Output voltage 220 + 2% of modified/ pure sine wave in case of 1.0 and 5.0 KW.
- Output voltage 440 + 2% (phase to phase) of modified/ pure sine wave in case of 10.0 KW.
- Output frequency: 50 Hz+0.5 Hz
- Capacity of PCU/ Inverter is specified at 0.8 lagging power factor.
- THD: less than 3%
- Efficiency: > 90% at full load
- Ambient Temp 50 degree Celsius (max)
- Operating humidity 95% maximum

Vol. 3, Issue 9, September, 2017 |ISSN (Online): 2454-8499 |Impact Factor: 1.3599(GIF), 0.679(IIFS)

- Protections: - Over voltage (automatic shut down) - Under voltage (automatic shut down) - Overload - Short circuit (circuit breaker & electronics protection against sustained fault). - Over Temperature - Battery, PV reverse polarity
- Indications: - Array on - MPPT/ PWM charger on - Battery connected, charging - Inverter ON - Load on solar/ battery

Grid charger on - Load on Grid - Grid on

- Display parameters - Charging current - Charging voltage - Voltage of PV panels - Output voltage - Grid voltage - Inverter loading - Output frequency
- Cooling: Air cooled
- When battery bank is fully charged, the PCU should have the feature to feed the power generated from solar to load and draw the additional power from main supply to meet the load requirements in the case load is more than solar energy produced.
- In case of 5.0 KW solar power plant if some manufacturer has different input voltage of PCU i.e. 48Volt and 96 Volt then the PCU should be able to deliver output of 230 Volt 50 Hz AC irrespective of what DC voltage input they are feeding to the PCU. The battery bank used should be of same watt hour capacity given above. The inbuilt Charge Controller shall be according to the system voltage selected for the PCU.

Junction boxes

- The junction boxes shall be dust and water proof and made of thermoplastic the terminals will be connected to copper lugs or bus-bar of proper sizes. The junction boxes will have suitable cable entry points fitted with the cables. Suitable markings shall be provided on the lugs or bus-bars for easy identification at cable ferrules will be fitted at the cable terminations points for identification. Each main junction box shall be fitted with appropriate rating reverse blocking diode. The junction boxes shall be of reputed make.
- The junction boxes shall have suitable arrangement for the following:

a) Combine groups of modules into independent charging sub-arrays that will be wired into the controller.
b) Provide arrangement for disconnection for each of the groups.
c) Provide a test point for each sub group for quick fault location.
d) To provide group array isolation.
e) The rating of the JBS shall be suitable with adequate safety factor to inter connect the Solar PV array. Structure for module frame

Modules shall be mounted on supporting structure made out of galvanized MS angle of required structural strength. (hot dip/galvanized) either on the roof top or at ground as per the site requirement Structure: -

Vol. 3, Issue 9, September, 2017 |ISSN (Online): 2454-8499 |Impact Factor: 1.3599(GIF), 0.679(IIFS)

1. The size of M.S. (Galvanized) angle should be 50 x 50 x 5 mm. The structures are to be fitted either on the roof top or at ground properly and south faced. It should withstand wind speed up to 120 Km/hour.
2. Foundation – The legs of the structure made with hot dip GI angles will be fixed and grouted in the RCC foundation columns of size 300mmx300mm made with 1:2:4 cement concrete. The minimum ground clearance from the lowest part of any module shall be 500 MM. While making foundation design due consideration will be given to wait of module assembly, maximum wind speed of 120 km per hour.
3. The work includes necessary excavation, concreting, back feeling, shoring and shuttering etc.
4. Brick paving of first class bricks with cement mortar (1:6) as per PWD specifications on edge type plate form is to be provided under the modules structure area with minimum 1 meter more than structure.

Connecting cables

I. For 1.0 KW solar power plant;- PVC insulated copper cables (ISI marked) for :

- Module interconnections (4.0 mm2 copper single core multi strand)
- Module parallel interconnection (6 mm2 copper single core multi strand)
- Array or AJB to PCU (10 mm2 copper two cores).
- Battery to PCU (16 mm2 copper single core multi strand) might be double cables if required
- PCU to load / change over switch (Single core copper cable 4.0 mm2 multi strand)
- distribution points (Single core copper cable 4.0 mm2 and 2.5 mm2 multi trand) and for further

II. For 5.0 KW solar power plant;-

- Module interconnections (4.0 mm2 copper single core multi strand)
- Module parallel interconnection (10mm2 copper single core multi strand)
- Array or AJB to PCU (16 mm2 copper two cores).
- Battery to PCU (16 mm2 copper single core multi strand) might be double cables if required PCU to load / change over switch (Single core copper cable 6.0 mm 2 multi strand) and for further distribution points (Single core copper cable 4.0 mm2 and 2.5 mm2 multi strand)

III. For 10.0 KW solar power plant;-

- Module interconnections (4.0 mm2 copper single core multi strand)
- Module parallel interconnection (10mm2 copper single core multi strand)
- Array or AJB to PCU (25 mm2 copper two cores).
- Battery to PCU (25 mm2 copper single core multi strand) might be double cables if required
- PCU to load / change over switch (Single core copper cable 10.0 mm2 multi strand) and for further distribution points (Single core copper cable 4.0 mm2 and 2.5 mm2 multi strand)

Vol. 3, Issue 9, September, 2017 |ISSN (Online): 2454-8499 |Impact Factor: 1.3599(GIF), 0.679(IIFS)

All cables to be supplied should be as per BIS and should have proper current carrying capacity and should not be heated. - All cables shall be adequately supported. - Outside of terminal/panels/enclosures shall be protected by conduits. Cables shall be provided with dry type compression glands wherever they enter junction boxes, panels, enclosures. Indoor wiring All indoor wiring is to be done in a casing capping system. As and when required flexible pipe may also be used. Load connection The supplier shall also ensure that main points of the building should be connected keeping in view the capacity of the plant. Lighting protection Suitable nos. of lighting arrestors shall be provided in the array field for the protection. Earthling protection Each array structure and all metal casings of the plant etc. shall be earthed properly. Tool Kit and Spares One necessary tools kit and spares will have to be provided by the supplier Energy meter Supplier shall provide energy meter to measure the DC power in KW hrs being fed to the plant.

2. CODES AND STANDARDS

The BoS items / components of the SPV power plant must conform to the latest edition of IEC/ equivalent BIS Standards as specified below: BoS item / component Standard Description Standard Number Power Conditioning Unit Inverter

BoS ite m / component Standard Description Standard Number Power Conditioning Unit Inverter

		equivalent BIS standard
Storage Batteries	General Requirements & Methods of Test	IEC 61427
	VRLA Tubular GEL type	IS 15549/ as per relevant BIS standard
Cables	General Test and Measuring Methods PVC insulated cables for working voltages upto and including 1100 V-Do-, UV resistant for outdoor installation	IEC 60227 IS 694 / IS 1554 (Pt I and II)
Switches / Circuit Breakers / Connectors	General Requirements	IEC 60947 part I, II & III/ IS 60947 part I II & II
	Connectors-safety	
	AC/DC	EN 50521
Junction Boxes/ Enclosures for inverters/ charge controller	General Requirements	IP54 (for outdoor) / IP/21 (for indoor) as per IEC 529

Power Conditioning Unit Inverter
Efficiency Measurements -- IEC61683/IS 61683
Environmental Testing -- IEC60068 2 (1, 2, 14, 30)/ equivalent BIS standard
Charge controller/ MPPT units*
Environmental Testing IEC60068 2 (1, 2, 14, 30)/ equivalent BIS standard

Vol. 3, Issue 9, September, 2017 |ISSN (Online): 2454-8499 |Impact Factor: 1.3599(GIF), 0.679(IIFS)

**In case if the Charge controller is in-built in the inverter, no separate IEC 62093 test is required and must additionally conform to the relevant national/international Electrical Safety Standards wherever applicable

IDENTIFICATION AND TRACEABILITY

Each PV modules used must use a RF identification tag (RFID), which must contain the following information.

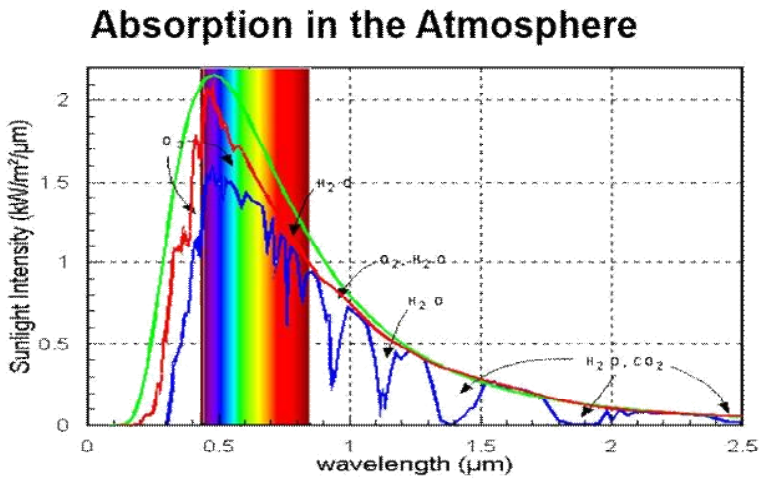
The RFID can be inside/ outside the module laminate, but must be able to withstand harsh environmental conditions.

(i) Name of the Manufacturer of PV Modules
(ii) Name of the Manufacturer of Solar Cells
(iii) Month and year of the manufacturer (separately for solar cells and module)
(iv) Country of origin (separately for solar cells and module)
(v) I-V curve for the module
(vi) Peak Wattage, lm, Vm and FF for the module
(vii) Unique Serial No and Model No of the module
(viii) Date and year of obtaining IEC PV module qualification certificate
(ix) Name of the test lab issuing IEC certificate
(x) Other relevant information on traceability of solar cells and module as per ISO 9000 series.

Factors affecting Solar Panel Installation with explanation --

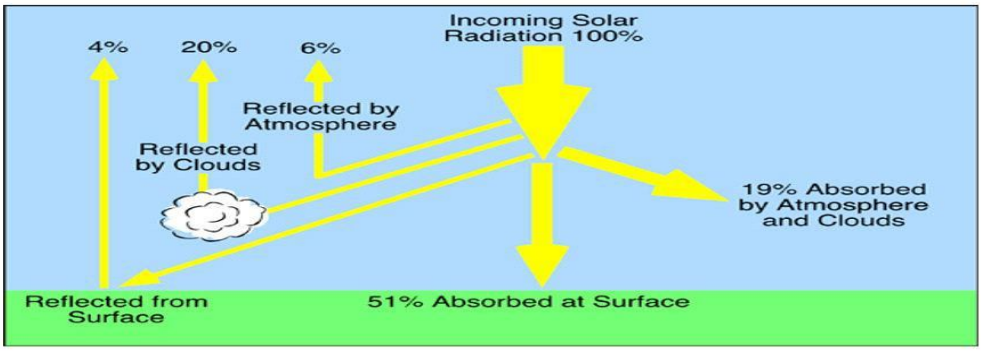
While the solar radiation incident on the Earth's atmosphere is relatively constant, the radiation at the Earth's surface varies widely due to:

- Atmospheric effects, including absorption and scattering When the sun is overhead, the absorption due to these atmospheric elements causes a relatively uniform reduction across the visible spectrum, so the incident light appears white. However, for longer path lengths, higher energy (lower wavelength) light is more effectively absorbed and scattered. Hence in the morning and evening the sun appears much redder and has a lower intensity than in the middle of the day

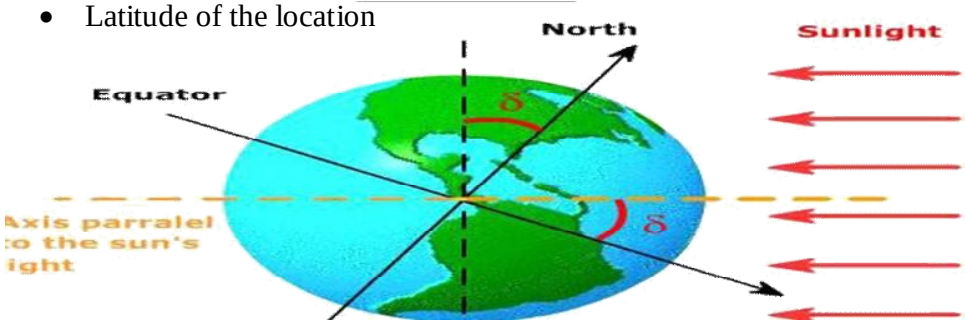


Vol. 3, Issue 9, September, 2017 |ISSN (Online): 2454-8499 |Impact Factor: 1.3599(GIF), 0.679(IIFS)

- Local variations in the atmosphere, such as water vapour, clouds, and pollution

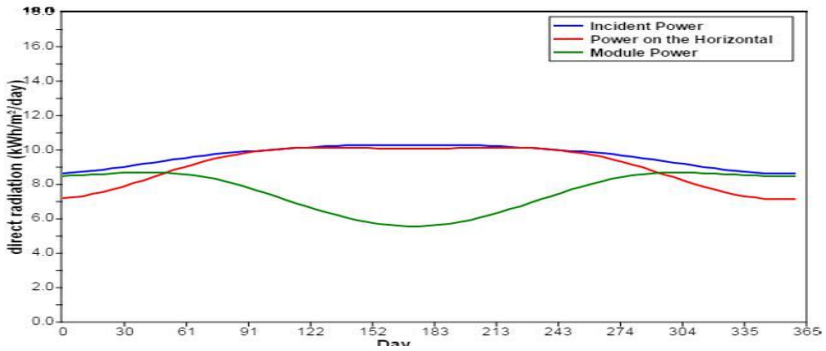


- Latitude of the location



- Tilt

The tilt angle has a major impact on the solar radiation incident on a surface. For a fixed tilt angle, the maximum power over the course of a year is obtained when the tilt angle is equal to the latitude of the location. However, steeper tilt angles are optimized for large winter loads, while lower title angles use a greater fraction of light in the summer.



References --

- *Jawaharlal Nehru National Solar Mission, Ministry of New and Renewable Energy, Government of India , February 2016.*
- *National Institute for Entrepreneurship and Small Business Development (NIESBUD), Noida, NCR of Delhi, U.P.,India. NPD, SolarBuzz ,2012.*
- *Solar Thermal and Photovoltaic Field Engineers Training course ,prepared by The Energy and Resources Institute, New Delhi, India .In association with Directorate General Of Employment And Training. .Under the Human Resources Development Programme of Ministry of New and Renewable Energy, Government of India (2010-2012).*
- *Title: RENEWABLE ENERGY ENGINEERING AND TECHNOLOGY Editor: V.V.N Kishore*
  Press. Publisher : TERI
- *Title: A Solar Future for Energy India. Editor: G.M.Pillai. Publisher : World Institute of Sustainable*
- *Title: From Sunlight to Electricity: a practical hand book on solar photovoltaic applications Editor: Suneel Deambi . Publisher: The Energy and Resources Institute (TERI).*

International Research Journal of Engineering and Technology (IRJET) e-ISSN: 2395-0056
Volume: 04 Issue: 09 | Sep -2017 www.irjet.net p-ISSN: 2395-0072

STATIC ANALYSIS AND MASS OPTIMIZATION OF AUTOMOTIVE VALVE SPRING

Anant Jindal[1], Aatresha Biswas[2]

[1,2] *Department of Mechanical Engineering, Delhi Technological University, Delhi*

Abstract - *Valve springs are an integral part of any IC engine's valve lift mechanism. Helical springs are used to serve the purpose. They are located on the input and output valves of the engine's cylinder and help the valve to remain in contact with the camshaft just like the spring of the follower helps it remain in contact with the cam. The springs undergo a lot of stresses as the valve is pushed open by the camshaft. Helical springs have an important dimensional parameter known as the spring index which is the ratio of spring mean diameter to the spring wire diameter. The present work aims at optimizing the spring index of a widely used automobile valve spring to reduce its mass with the same spring lift within specified stress limits. To validate the model used for structural analysis of the spring, the results were compared with numerical results using conventional formulas. Optimization yields a spring with same lift and strength with reduced mass which is better for the overall performance of the internal combustion engine.*

***Key Words*: Helical Springs, Spring Index, Torsional Shear Stress, Finite Element Analysis, Response Surface Study**

1. INTRODUCTION

A spring is defined as an elastic machine element, which deflects under the action of load and returns to its original shape when load is removed. Coil springs (helical spring), stores energy and releases it. It functions as a shock absorber. Springs are sometimes used to maintain contacting force between the surfaces. The helical springs are made up of a wire (usually of square cross section) coiled in the form of a helix and are intended for compressive or tensile loads. In helical spring, the helix angle is very small, it is usually less than 10 degrees. The major stresses produced in helical springs are torsional shear stresses due to twisting. The load may be applied parallel to or along the axis of the spring.
IC engine valve springs enable both the intake and exhaust valves to alternately open and close when the engine is in operation to permit intake and exhaust of air/fuel mixture or air. Rotation of the camshaft causes a valve to open and its spring to be compressed, so that the load on the spring is increased. The stored energy in the spring then forces the valve to close as the camshaft continues its rotation. This process occurs for each valve for each engine cycle, and over the lifetime of the engine, it occurs many millions of times. Automotive springs have to face very high working stresses. The structural reliability of the spring must therefore be ensured.



Fig - 1: Valves of IC engine

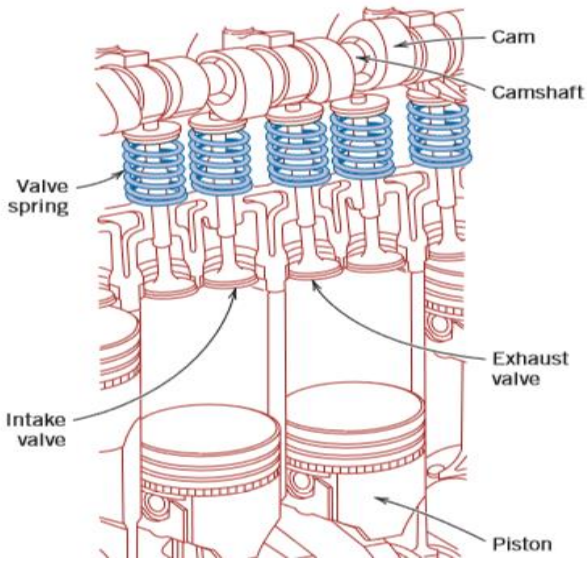


Fig - 2: Cutaway Drawing of a section of IC engine showing Valves and Valve springs

2. PROBLEM STATEMENT

The present work attempts to analyze the design and optimize the weight of a helical compression spring used in valves of engines. The spring is made up of chrome vanadium. The aim was to find the exact combination of

parameter values that will give the lowest mass for the same lift within the specified stress limits

3. LITERATURE REVIEW

- In 1678, Robert Hooke in his work "De Potentia Restitutiva" published. This simple statement, today known as Hooke's law yields the basic equation for spring design.
- In 1770, Lagrange analyzed the proportion of loads and deflection in springs.
- In 1813, A. Roever proposed a theory describing the maximum bending and shear stresses on spring coils.
- In 1902, French published formulas for calculating torsional elasticity and safe stress levels for different ratios of wire to coil diameters.
- In 1929, Arthur Wahl proposed a stress correction factor to take into account those additional stresses using torsion theory and carried out tests that were in good agreement with the values theoretically predicted.
- In 1947, Finniecome compared Roever's and Wahl's correction factors and determined that for springs with spring index above 3 Wahl's values were slightly higher than Roever's.
- Wahl (1939, 1949, 1963) analyzed the use of the curvature correction factor in springs with large deflections, with free and fixed ends, under fatigue loading and endurance.
- An excellent analysis of when and when not to use the stress correction factor was presented by Carlson in 1985.

4. DESIGN OF VALVE SPRING

Spring material

Chrome Vanadium Steel:

ASTM 232 chrome–vanadium steel is used. Spring wire is normally cold drawn to the desired diameter; so that the tensile strength increases with the amount of drawing. These materials are designed for springs that must withstand considerable shock, extreme heat and resistant to fatigue. Valve spring quality chrome vanadium has been eddy current tested to assure the finest possible surface in keeping with automotive industry requirements. The following table shows the composition of Chrome Vanadium Steel:

Table-1: Composition of Chrome Vanadium

COMPONENT	%
Carbon (C)	0.48 - 0.53
Manganese (Mn)	0.7 – 0.9
Phosphorus (P)	<0.04
Sulphur (S)	<0.04
Silicon (Si)	0.15- 0.35
Chromium (Cr)	0.8-1.1
Other (Ni, V etc)	< 0.15

Young's Modulus = 207000 MPa
Modulus of Rigidity = 87500 MPa
Density = 7800 kg /m3
Poisons ratio = 0.28
Tensile Strength (S_{ut}) = 169,000(d)^(-0.167) = 1618.08 MPa
Shear strength of material = 809.04 MPa

Other Specifications

1. Outer diameter of the coil (Do) = 22.542 mm
2. Inner diameter of the coil (Di) = 15.431 mm
3. Wire diameter (d) = 3.556 mm
4. Pitch (P) = 5.22 mm
5. Mean diameter of coil (D) = 18.9865 mm
6. Total number of coils (N) = 6
7. Number of active coils (Nt) = 4
8. Mass of the spring = 0.0326 kg
8. Free length (Lo) = 31.336 mm
9. Solid length (Ls) = 21.336 mm
10. Maximum Force (F) = 225 N
11. Spring Index (C) = 5.3392
12. Wahl's stress factor (Ks) =

$$\frac{4C-1}{4C-4}+\frac{0.615}{C}$$

= 1.288

13. Shear Stress (τ)

$$\tau = \frac{8FD}{\pi d^3} Ks$$

= 311.5 N/mm2

14. For cyclic loading
S_{ut} = 1618.08 N/mm2

Endurance Limit of the component subjected to fluctuating torsional shear stress (Sse) = 404.52MPa
Design stress (τd) = Sse /Fs = 404.52/1.2 = 337 N/mm^2

Hence, the design is safe as $\tau d > \tau$

5. MODELING AND STATIC ANALYSIS OF VALVE SPRING

5.1 CAD Model

The solid modeling of the helical spring is done using ANSYS DesignModeler. The characteristic parameter of the helical spring affects their behavior. The important dimension used for modeling the spring are wire diameter(d) and mean diameter(D), number of active loops(N) and the distance between two consecutive loops i.e. pitch(P).

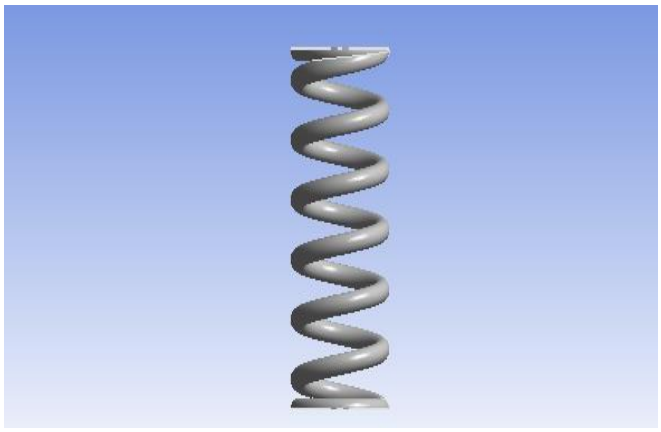


Fig - 3 CAD Model of valve spring

5.2 Meshing

The mesh was generated using proximity and curvature as an option. For the valve spring, the mesh was created as Triangular surface mesher. The minimum edge length was taken as 5.5858e-003 m and for checking the solutions the mesh was made finer and the solutions were obtained.

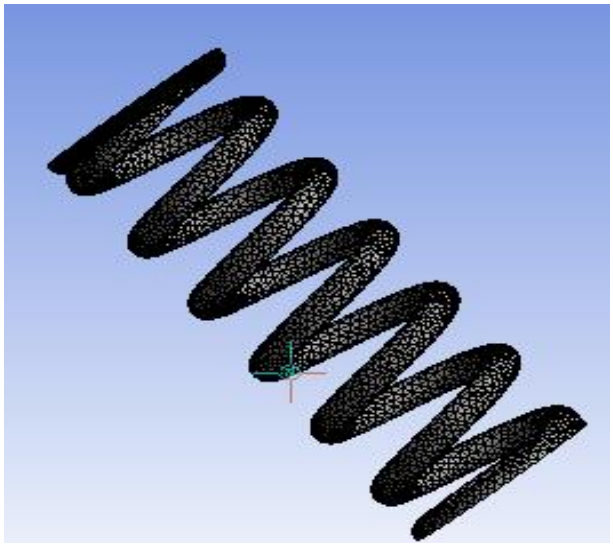


Fig – 4 Meshing of the CAD Model

5.3 Boundary Conditions and FEA

A force of 225N is applied in the Y direction and the boundary condition is applied at the end of the valve spring. Static analysis is carried out by using ANSYS WORKBENCH 14.5. The results for shear stress, total deformation are shown.



Fig – 5 Shear stress analysis of valve spring

Maximum shear stress for valve spring is 307 MPa.
We observe maximum shear stress occurs at the curvature of the spring.

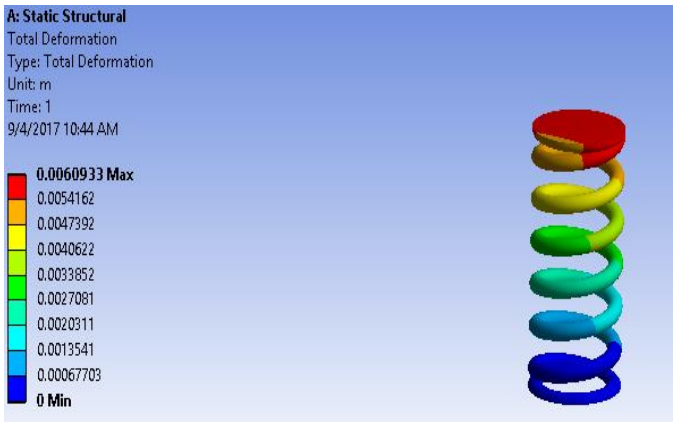


Fig – 6 Total deformation of valve spring

Maximum deformation for valve spring is 6 mm

Comparison of the results by Conventional Calculations and by Finite Element Analysis

Table-2: validation of results

	Result by Conventional Calculations	FEA results
Shear Stress	311.5 MPa	307 MPa

We observe the shear stress is much below the shear strength of material which is 809.04 MPa. The shear stress is also much below the endurance limit of the material which is 404.52 MPa which makes it resistant to fatigue.
Hence, the design of the automotive valve spring is safe.
Thus, the structural reliability of the automotive valve spring is ensured.

6. MASS OPTIMIZATION OF THE VALVE SPRING

6.1 Methodology

The objective is to reduce the mass of the valve spring within the defined stress limits and deformation. Spring Index (C) is defined as the ratio of mean coil diameter (D) to the wire diameter(d). Input parameters wire diameter (d) and the mean coil diameter (D) is varied to achieve reduction in weight and hence material costs. The goal is to find the exact combination of parameter values that will give the lowest mass within the specified stress limits.

While the initial designing, the original mass of the coil spring was 32.674 g

Response surface study in ANSYS WORKBENCH 14.5 is done for optimization of mass of the spring. A Central Composite Design DOE type and Auto Defined Design Type is selected, which optimizes the weight of the coil spring based on number of input parameters.

Input Parameters

1. Radius of spring coil
   Lower bound = 9 mm
   Upper bound = 10 mm
   Value = 9.4933 mm
2. Wire diameter
   Lower bound = 3 mm
   Upper bound = 4 mm
   Value = 3.556 mm

   ANSYS WORKBENCH response surface study gives the following output results.

Output Values

Response Surface Study in ANSYS WORKBENCH gives different values for Mass, Deformation and Shear stress according to the different combination of input parameters.

Table-3: Variation of output parameters w.r.t input parameters

Design Points	Radius of spring coil in mm	Wire diameter (d) in mm	Solid mass (kg)	Total Deformation(m)	Shear Stress maximum(Pa)
1	9.5	3.5	0.031795	0.0065135	3.228 E + 08
2	9	3.5	0.030358	0.005598	3.083 E + 08
3	10	3.5	0.033334	0.0075359	3.344 E + 08
4	9.5	3	0.024433	0.012187	5.002 E + 08
5	9.5	4	0.040276	0.0037777	2.227 E + 08
6	9	3	0.023388	0.010472	5.109 E + 08
7	10	3	0.025564	0.014105	5.1853 E + 08
8	9	4	0.038366	0.0032489	2.14 E + 08
9	10	4	0.042247	0.0043701	2.31 E + 08

The graph shows the variation of output values (solid mass and deformation) in accordance with input values

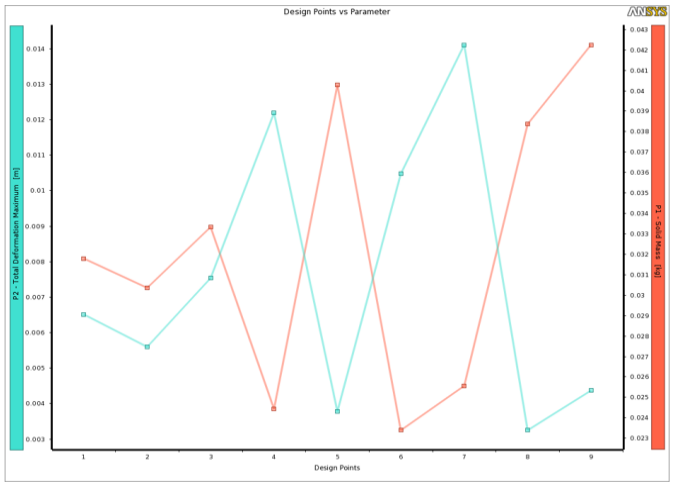


Chart - 1: Design point v/s parameter chart

In the design point v/s parameter chart we observe that design point 6 has minimum solid mass and has a deformation of 0.0104 m. Hence, this does not give us optimum results.

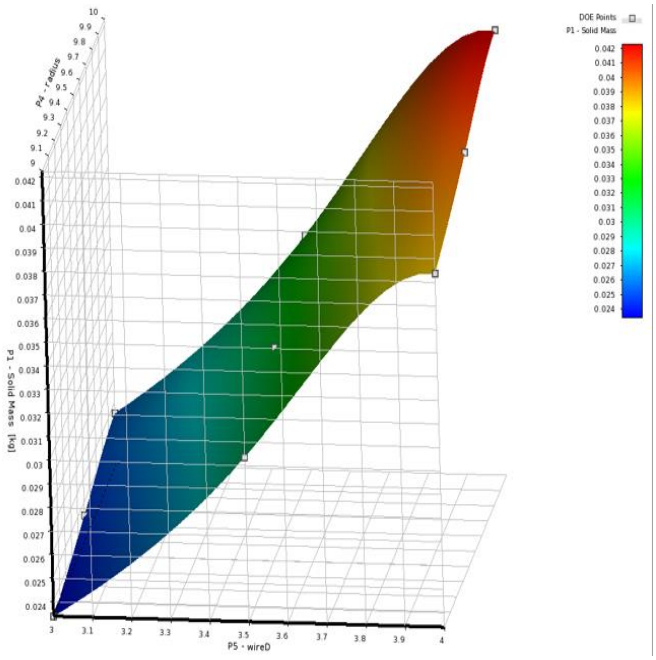


Chart – 2: Response surface chart

The response surface interpolates the values in multiple dimension. Response chart shows the variation of solid mass with changes in wire diameter(d) and coil radius(D).

6.2 Results

After the response surface study, a response surface optimization was obtained. Ansys Workbench 14.5 predicts the optimum combination of parameters to achieve this. Candidate points, where minimum mass of the spring is obtained within the specified stress limits and deformation are shown below:

Table-4: Results

Name	Coil radius (mm)	Wire diameter (mm)	Solid mass(kg) parameter value	Solid mass (kg)variation from reference	Total Deformation(m) Parameter value	Total deformation(m) Variation from reference	Shear stress (Pa) parameter value
Candidate point 1	9.0465	3.453625	0.029612	- 5.74 %	0.0060121	- 1.34 %	3.264E+08
Candidate Point 2	9.1905	3.4887812	0.030622	- 2.52 %	0.0060132	- 1.32 %	3.183E+08
Candidate Point 3	9.3215	3.5102656	0.031415	0.00 %	0.0060939	0.00 %	3.1437E+08

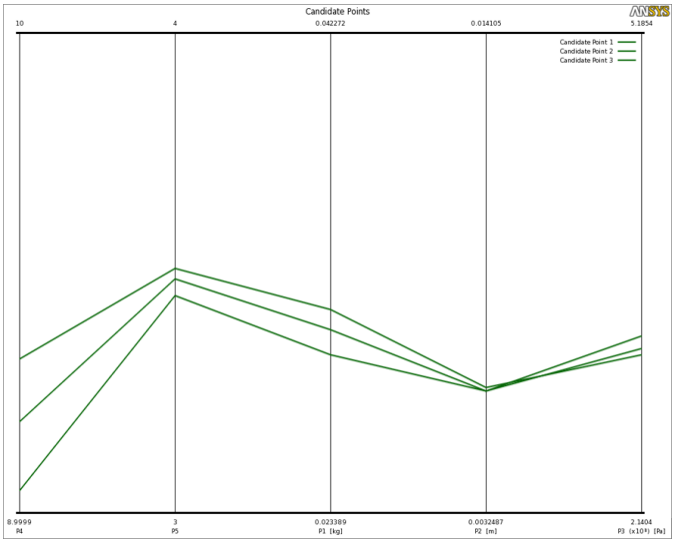


Chart -3: Output values obtained at different candidate points

Hence, we observe there is a reduction of 5.74 % of mass of the automotive spring at candidate point 1 where coil radius is 9.0465 mm and wire diameter is 3.453625 mm. At candidate point 2, a reduction of 2.52 % of mass is obtained with coil radius 9.19 mm and wire diameter 3.488mm.
We also observe the deformation and shear stress is well within limits at all the points predicted.
Hence, weight of the valve spring is optimized within the specified limits and input parameters.

7. CONCLUSIONS

The automotive valve spring is modeled, analyzed and its weight optimized in the present work. The automotive valve spring should be shock resistant, fatigue resistant and should be able to bear extreme heat. Theoretical and FEA analysis on ANSYS WORKBENCH 14.5 was carried out on the automotive valve spring to ensure the structural reliability. A response surface study was carried on ANSYS WORKBENCH 14.5 to optimize the weight of the valve spring. A reduction of 5.74% in weight of the valve spring is achieved by varying the Spring Index. The stress limits and deformation are well within range. Reduction in weight of valve spring would reduce material costs and increase efficiency of the engine. Hence, a better design of the valve spring was obtained.

REFERENCES

[1] Design of Machine Elements, 3rd Edition, V.B. Bhandari, McGraw Hill Publications.

[2] Wahl AW, “Mechanical springs” in McGrawHill Book Company,Inc.; 1963.

[3] Shigley J. Mechanical engineering design. New York: McGraw-Hill; 1981.

[4] Mehdi Bakhshesh and Majid Bakhshesh [5], in their research, had studied steel helical spring under uniform loading. They compared the Finite Element Analysis results with analytical solutions.

[5] Aurel P. STOICESCU, “On The Optimal Design of Helical Springs of An Automobile Suspension”, U.P.B. Sci. Bull., Series D, Vol. 71, Iss. 1, 2009, pp. 81-94.

International Journal of Research in Engineering and Innovation (IJREI)
journal home page: http://www.ijrei.com
ISSN (Online): 2456-6934

Thermo physical property of nano-refrigerant: preparation, thermal characteristics, and applications

R S Mishra[1], Rahul Jaiswal[2]

[1]Department of Mechanical Production and Automobiles Engineering, Delhi Technological University Delhi, India
[2]PhD Scholar, Department of Mechanical Production and Automobiles Engineering, Delhi Technological University Delhi, India

Abstract

Nano fluids, is a fluid/liquid containing nanometer-sized particles that are called nanoparticles. Similarly Nano refrigerant is a refrigerant which contains nanometer-sized particle. These refrigerant are engineered colloidal suspensions/mixture of nanoparticles in a base refrigerant. The nanoparticles used in Nano-refrigerant are typically made of oxides, metals, carbides, or carbon nanotubes. The refrigerant suspension of Nano nanomaterials, have shown many unpredicted properties, and the thermal characteristics offer unprecedented potential for many applications. This paper represent theoretical analysis of thermal characteristics of Nano refrigerant with respect to size and concentration of Nanoparticles and presents the broad range of current and future applications in different fields including mechanical, energy and biomedical fields. At last, the paper identifies the opportunities for future research.
© 2017 ijrei.com. All rights reserved
Keywords: Nano Refrigerants, Ecofriendly refrigerants, performance evaluation, Energy-Exergy analysis.

1. Introduction

Nano refrigerant are a new kind of fluids engineered by colloidal/mixture of nanometer-sized materials (nanofibers, nanotubes, nanoparticles, nanowires, Nano sheet, Nano rods, or droplets) in base refrigerant. In other words, Nano refrigerant are nanoscale colloidal suspensions containing condensed nanomaterials. Nano refrigerant have been found to possess enhanced thermo-physical properties such as thermal conductivity, density, dynamic viscosity, and convective heat transfer coefficients compared to those of base refrigerant like R134a, R407c, R404, R134a etc. It has demonstrated great potential applications in many fields.

For a two-phase system, there are some important issues we have to face. One of the most important issues is the stability of nano refrigerant, and it remains a big challenge to achieve desired stability of nano refrigerant. All of us we know that approx major refrigerant have vapour phase at atmospheric temperature, so it is a challenging work to mix nanoparticle into the base refrigerant. Refrigerant which have liquid phase at zero degree i.e. R114, R12 is easy to mix with nanoparticles. In this paper, we will theoretically analyze the performance characteristics of Nano refrigerant.

In recent years, Nano refrigerants have attracted more attention. The main driving force for Nano refrigerant research lies in a wide range of applications.

2. Preparation methods for Nano fluid

2.1. Two-Step Method

Two-step method is the most widely used method for preparing nano fluids. Nanoparticles, nanofibers, nanotubes, or other nanomaterials used in this method are first produced as dry powders by chemical or physical methods. Then, the Nano sized powder will be dispersed into a fluid in the second processing step with the help of intensive magnetic force agitation, ultrasonic agitation, high-shear mixing, homogenizing, and ball milling. Two-step method is the most economic method to produce Nano fluids in large scale, because Nano powder synthesis techniques have already been scaled up to industrial production levels. Due to the high surface area and surface activity, nanoparticles have the tendency to aggregate. The important technique to enhance the stability of nanoparticles in fluids is the use of surfactants. However, the functionality of the surfactants under high temperature is also a big concern, especially for high-temperature

Corresponding author: R.S. Mishra
Email Id: rsmishra@dce.ac.in

applications.
Due to the difficulty in preparing stable Nano fluids by two-step method, several advanced techniques are developed to produce Nano fluids, including one-step method. In the following part, we will introduce one-step method in detail.

2.2. One-Step Method

To reduce the agglomeration of nanoparticles, Eastman et al. developed a one-step physical vapor condensation method to prepare Cu/ethylene glycol Nano fluids [1]. The one-step process consists of simultaneously making and dispersing the particles in the fluid. In this method, the processes of drying, storage, transportation, and dispersion of nanoparticles are avoided, so the agglomeration of nanoparticles is minimized, and the stability of fluids is increased [2]. The one-step processes can prepare uniformly dispersed nanoparticles, and the particles can be stably suspended in the base fluid. The vacuum-SANSS (submerged arc nanoparticle synthesis system) is another efficient method to prepare Nano fluids using different dielectric liquids [3, 4]. The different morphologies are mainly influenced and determined by various thermal conductivity properties of the dielectric liquids. The nanoparticles prepared exhibit needle-like, polygonal, square, and circular morphological shapes. The method avoids the undesired particle aggregation fairly well.
One-step physical method cannot synthesize Nano fluids in large scale, and the cost is also high, so the one-step chemical method is developing rapidly. Zhu et al. resented a novel one-step chemical method for preparing copper Nano fluids by reducing $CuSO_4 \cdot 5H_2O$ with $NaH_2PO_2 \cdot H_2O$ in ethylene glycol under microwave irradiation [5]. Well-dispersed and stably suspended copper Nano fluids were obtained. Mineral oil-based Nano fluids containing silver nanoparticles with a narrow-size distribution were also prepared by this method [6]. The particles could be stabilized by Korantin, which coordinated to the silver particle surfaces via two oxygen atoms forming a dense layer around the particles. The silver nanoparticle suspensions were stable for about 1 month. Stable ethanol-based nanofluids containing silver nanoparticles could be prepared by microwave-assisted one-step method [7]. In the method, polyvinylpyrrolidone (PVP) was employed as the stabilizer of colloidal silver and reducing agent for silver in solution. The cationic surfactant octadecylamine (ODA) is also an efficient phase-transfer agent to synthesize silver colloids [8]. The phase transfer of the silver nanoparticles arises due to coupling of the silver nanoparticles with the ODA molecules present in organic phase via either coordination bond formation or weak covalent interaction. Phase transfer method has been developed for preparing homogeneous and stable graphene oxide colloids. Graphene oxide nanosheets (GONs) were successfully transferred from water to n-octane after modification by poleylamine, and the schematic illustration of the phase transfer process is shown in Figure 1 [9].

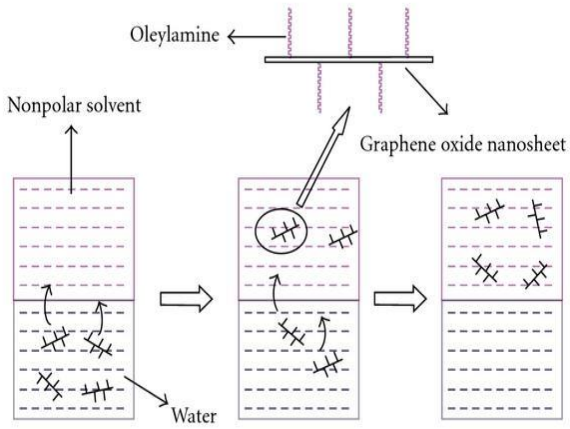


Figure 1: Schematic illustration of the phase transfer process

However, there are some disadvantages for one-step method. The most important one is that the residual reactants are left in the nanofluids due to incomplete reaction or stabilization. It is difficult to elucidate the nanoparticle effect without eliminating this impurity effect.

2.3. Other Novel Methods

Wei et al. developed a continuous-flow microfluidic micro reactor to synthesize copper Nano fluids. By this method, copper Nano fluids can be continuously synthesized, and their microstructure and properties can be varied by adjusting parameters such as reactant concentration, flow rate, and additive. CuO Nano fluids with high solid volume fraction (up to 10 vol%) can be synthesized through a novel precursor transformation method with the help of ultrasonic and microwave irradiation [10]. The precursor $Cu(OH)_2$ is completely transformed to CuO nanoparticle in water under microwave irradiation. The ammonium citrate prevents the growth and aggregation of nanoparticles, resulting in a stable CuO aqueous Nano fluid with higher thermal conductivity than those prepared by other dispersing methods. Phase-transfer method is also a facile way to obtain monodisperse noble metal colloids [11]. In a water-cyclohexane two-phase system, aqueous formaldehyde is transferred to cyclohexane phase via reaction with dodecylamine to form reductive intermediates in cyclohexane. The intermediates are capable of reducing silver or gold ions in aqueous solution to form dodecylamine-protected silver and gold nanoparticles in cyclohexane solution at room temperature. Feng et al. used the aqueous organic phase-transfer method for preparing gold, silver, and platinum nanoparticles on the basis of the decrease of the PVP's solubility in water with the temperature increase [12]. Phase-transfer method is also applied for preparing stable kerosene-based Fe_3O_4 Nano fluids. Oleic acid is successfully grafted onto the surface of Fe_3O_4 nanoparticles by chemisorbed mode, which lets Fe_3O_4nanoparticles have good compatibility

with kerosene [13]. The Fe_3O_4 Nano fluids prepared by phase-transfer method do not show the previously reported "time dependence of the thermal conductivity characteristic". The preparation of Nano fluids with controllable microstructure is one of the key issues. It is well known that the properties of Nano fluids strongly depend on the structure and shape of nanomaterials. The recent research shows that Nano fluids synthesized by chemical solution method have both higher conductivity enhancement and better stability than those produced by the other methods [14]. This method is distinguished from the others by its controllability. The Nano fluid microstructure can be varied and manipulated by adjusting synthesis parameters such as temperature, acidity, ultrasonic and microwave irradiation, types and concentrations of reactants and additives, and the order in which the additives are added to the solution.

3. Theoretical result of Nano refrigerant

A computational program has been developed to solve nonlinear equation related to Nano refrigerant and its thermal properties and various respective graph has been plotted with different concentration of nanoparticles and refrigerant shown below.

3.1. Thermo physical property of Nano refrigerant

In this section variation of thermo physical property of base refrigerant using nanoparticle suspended into base refrigerant at 5 Vol % are shown below.

3.1.1. Thermal conductivity of Nano refrigerant using different nanoparticle and base refrigerant

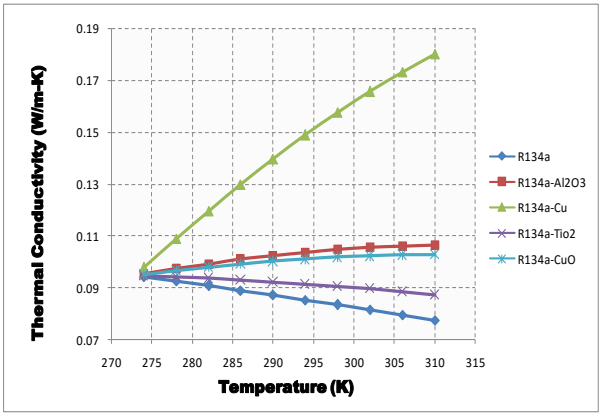


Fig.2. Variation of Thermal conductivity with Temperature of R134a using different nanoparticles

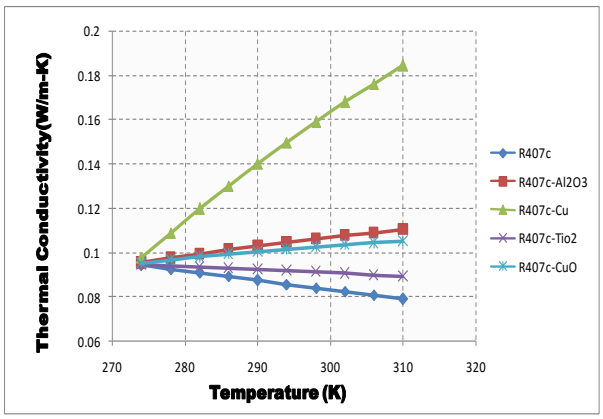


Fig.3. Variation of Thermal conductivity with Temperature of R407c using different nanoparticles

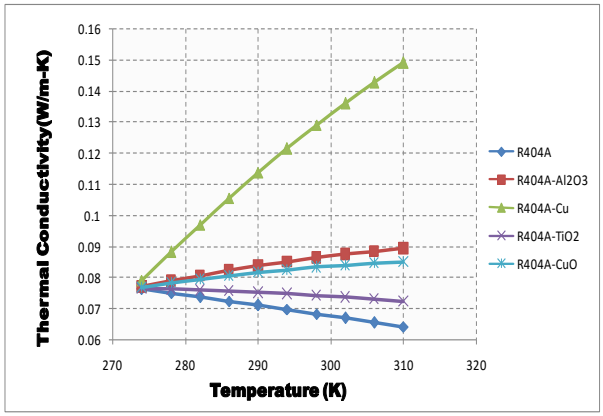


Fig.4. Variation of Thermal conductivity with Temperature of R404A using different nanoparticles

Fig.2. to Fig.4. Show the enhancement in thermal conductivity of Nano refrigerant when different kind of nanoparticle is suspended into the host refrigerant. The enhancement factor varies from 0.06 to 2 for different nanoparticle. From the Fig-4 we can see that cu nanoparticle have more EF at higher temperature which value is approx. 2.

3.1.2. Density of Nano refrigerant with different nanoparticle and base refrigerant

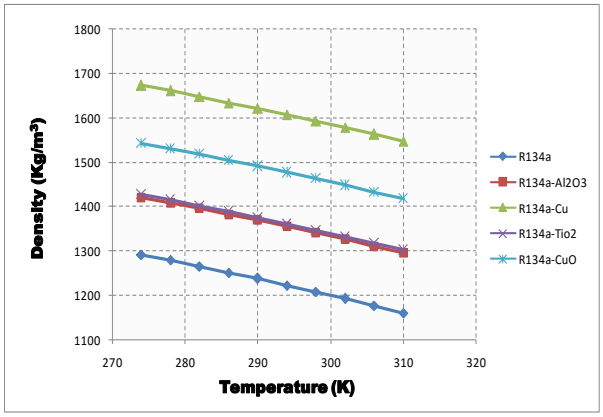


Fig.5. Variation of Density with Temperature of R134a using different nanoparticles

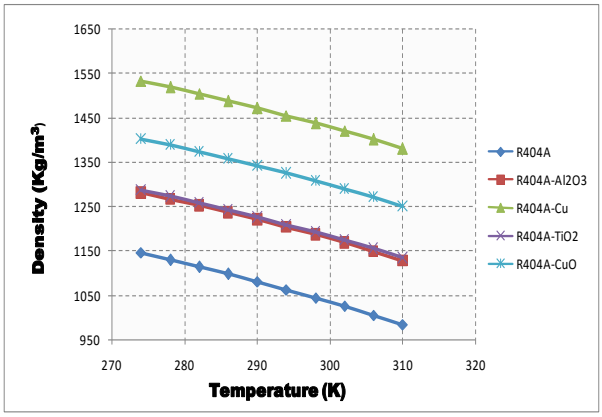


Fig.6. Variation of Density with Temperature of R404A using different nanoparticles

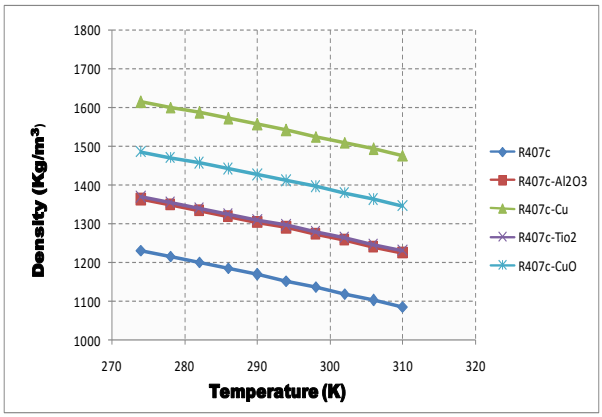


Fig.7. Variation of Density with Temperature of R407c using different nanoparticles

Fig.5. to fig.7. Shows variation in density of Nano refrigerant subject to temperature variation. Fig shows that density variation of Nano refrigerant is similar to pure refrigerant as higher temperature low density and lower temperature high.

3.1.3. Dynamic viscosity of Nano refrigerant using different nanoparticle and base refrigerant

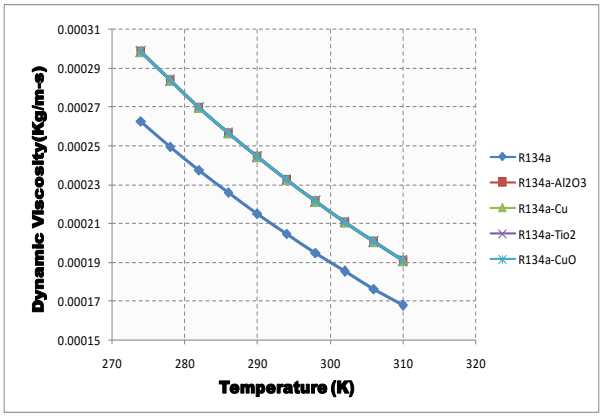


Fig.8. Variation of Dynamic viscosity with Temperature of R134a using different nanoparticles

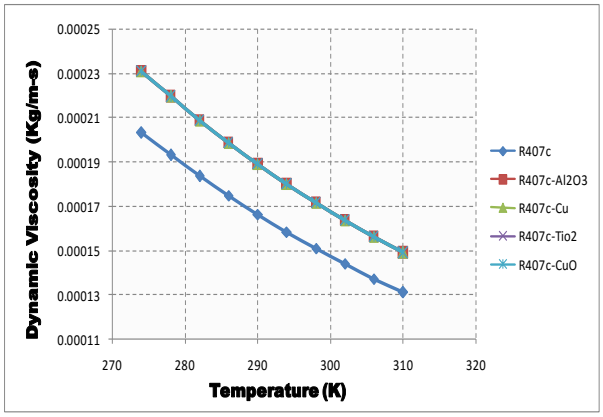


Fig.9. Variation of Dynamic viscosity with Temperature of R407c using different nanoparticles

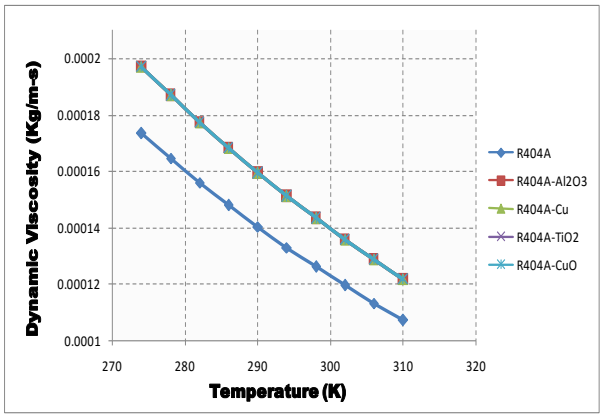


Fig.10. Variation of Dynamic viscosity with Temperature of R404A using different nanoparticles

Fig.8 to fig.10. Shows variation in Dynamic viscosity of Nano refrigerant subject to temperature variation. Fig shows that Dynamic viscosity variation of Nano refrigerant is similar to pure refrigerant as higher temperature low viscosity and lower temperature high.

3.1.4. Specific heat of Nano refrigerant using different nanoparticle and base refrigerant

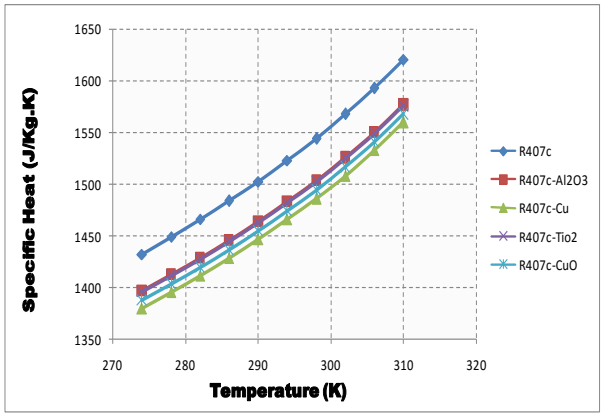


Fig.11. Variation of Specific heat with Temperature of R407c using different nanoparticles

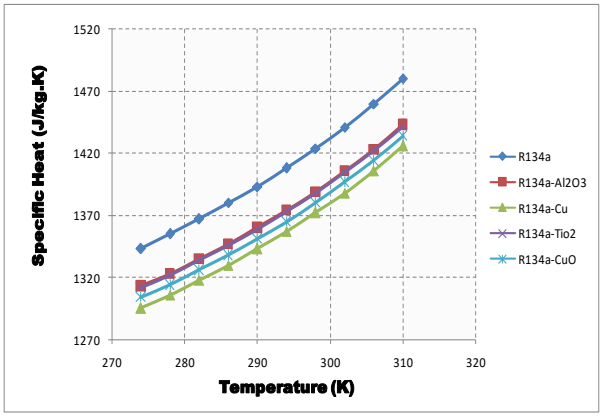


Fig.12. Variation of Specific heat with Temperature of R134a using different nanoparticles

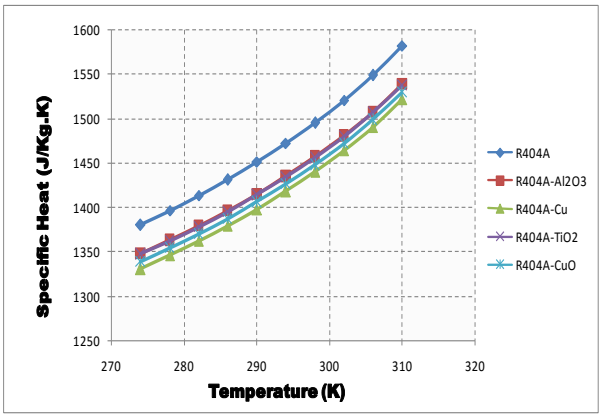


Fig.13. Variation of Specific heat with Temperature of R404A using different nanoparticles

Fig.11-13 shows variation in Specific heat of Nano refrigerant subject to temperature variation. Fig shows that Specific heat variation of Nano refrigerant is similar to pure refrigerant as higher temperature High Specific heat and lower temperature low. But when we go for higher vol % concentration of nanoparticle Specific heat will reduce.

3.1.5. *Effect of volume fraction on Thermo physical property of Nano refrigerant with different nanoparticle and base refrigerant (at 280K temperature)*

Density ratio shown Fig 14. is defined as the ratio of density of Nano refrigerant (nanoparticle mixed with pure refrigerant) to the density of pure refrigerant.
Thermal conductivity shown in Fig 17. is defined as the ratio of thermal conductivity of Nano refrigerant (pure refrigerant mixed with nanoparticle) to the thermal conductivity of pure refrigerant.

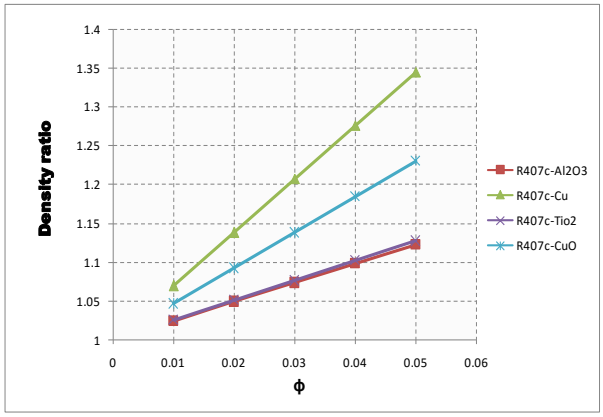


Fig.14. Variation of Density Ratio with volume fraction (ϕ) of R407c using different nanoparticles

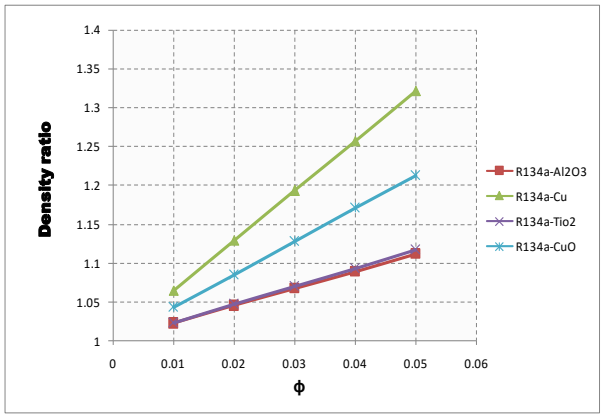


Fig.15. Variation of Density Ratio with volume fraction (ϕ) of R134a using different nanoparticles

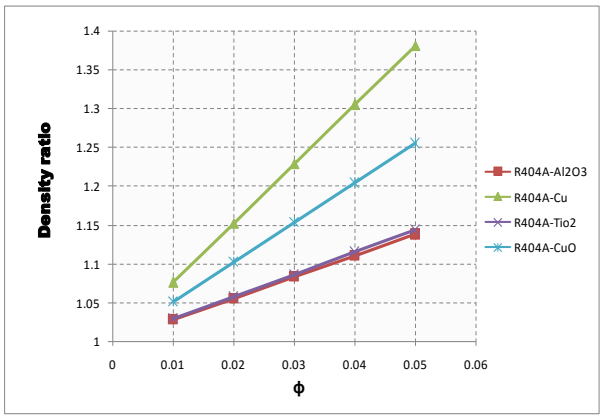


Fig.16. Variation of Density Ratio with volume fraction (ϕ) of R404A using different nanoparticles

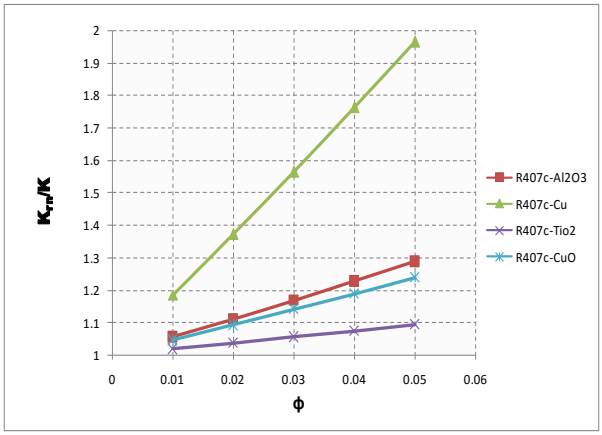


Fig.17. Variation of Thermal conductivity Ratio with volume fraction (ϕ) of R407c using different nanoparticles

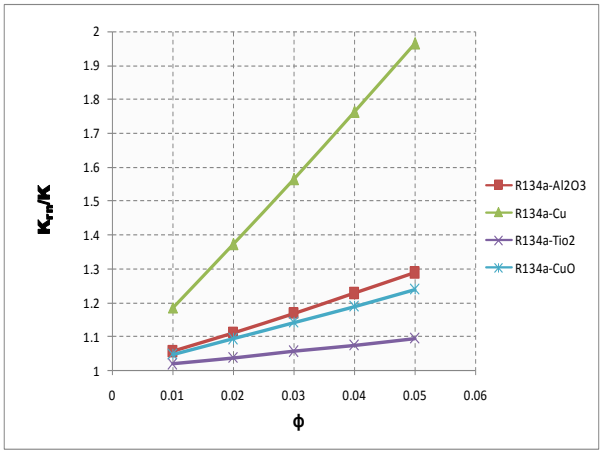


Fig.18. Variation of Thermal conductivity Ratio with volume fraction (ϕ) of R134a using different nanoparticles

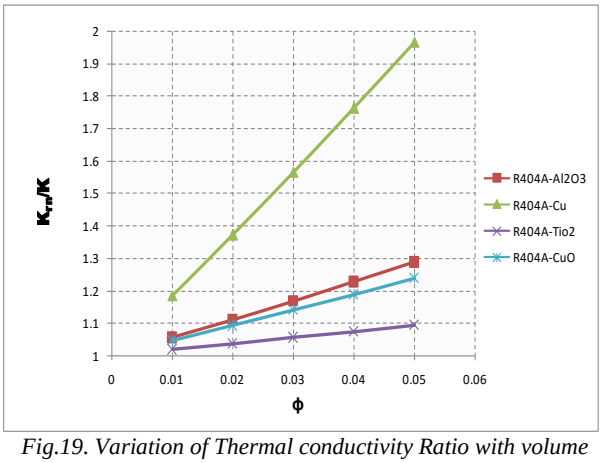


Fig.19. Variation of Thermal conductivity Ratio with volume fraction (ϕ) of R404A using different nanoparticles

Fig 17 to Fig. 19. Shows that conductivity ratio of pure refrigerant to Nano refrigerant increases with increasing concentration of nanoparticle into the host refrigerant. From the fig we can see that Cu nanoparticle based Nano refrigerant have higher cond. Ratio than other nanoparticle and have approx. two times higher than base refrigerant at 5 vol % concentration.

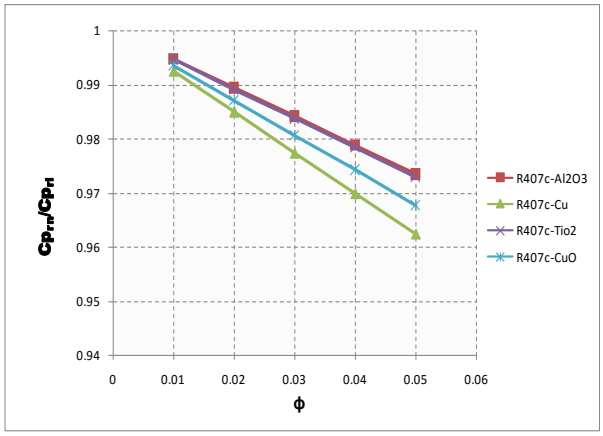


Fig.20. Variation of Specific heat ratio with volume fraction (ϕ) of R407c using different nanoparticles

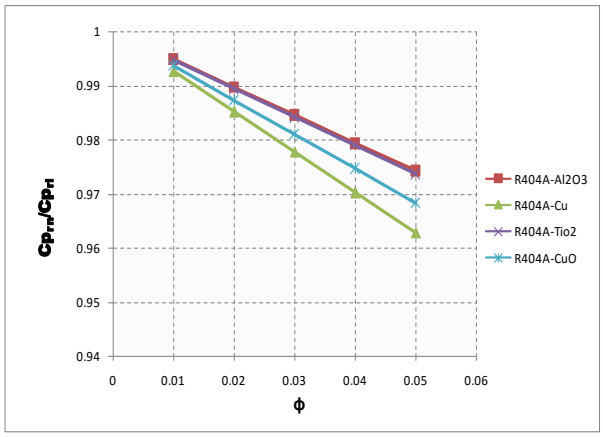


Fig.21. Variation of Specific heat ratio with volume fraction (ϕ) of R404A using different nanoparticles

Specific heat ratio shown in Fig 20-22. Is defined as the ratio of specific heat of Nano refrigerant (nanoparticle mixed with pure refrigerant) to the specific heat of pure refrigerant.

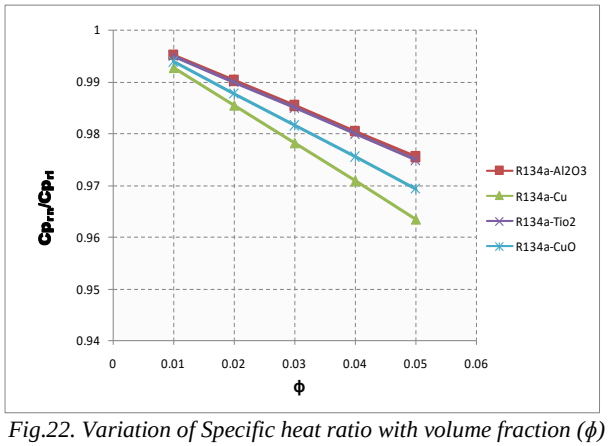


Fig.22. Variation of Specific heat ratio with volume fraction (ϕ) of R134a using different nanoparticles

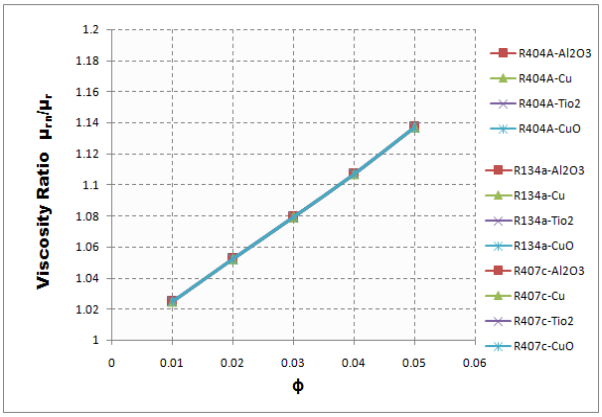


Fig.23. Variation of Viscosity ratio with volume fraction (ϕ) of all Nano refrigerant

Viscosity ratio shown in Fig 23 is defined as the ratio of Viscosity of Nano refrigerant (nanoparticle mixed with pure refrigerant) to the Viscosity of pure refrigerant.

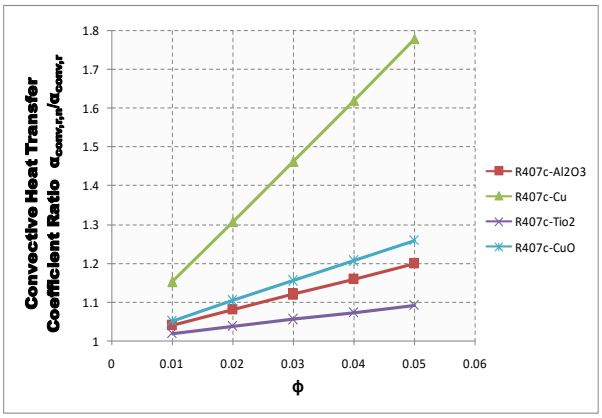


Fig.24.Variation of Convective heat transfer coefficient ratio with volume fraction (ϕ) of R407c using different nanoparticles

Convective heat transfer coefficient ratio shown in Fig 24, 25 and 26 is defined as the ratio of Convective heat transfer coefficient of Nano refrigerant (nanoparticle mixed with pure refrigerant) to the Convective heat transfer coefficient of pure refrigerant.

Heat transfer Enhancement Factor shown in Fig 27-29 is defined as the ratio of heat transfer coefficient of Nano refrigerant (nanoparticle mixed with pure refrigerant) to the heat transfer coefficient of pure refrigerant.

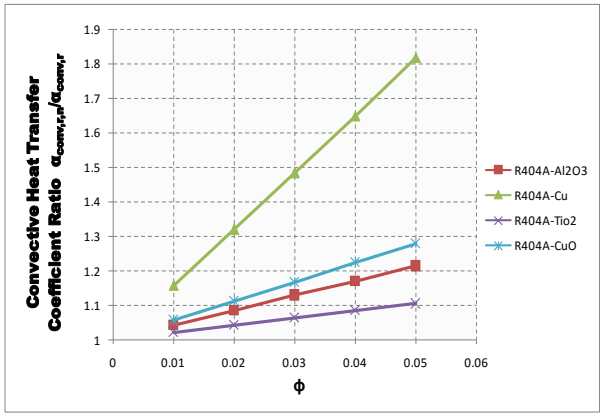


Fig.25. Variation of Convective heat transfer coefficient ratio with volume fraction (ϕ) of R404A using different nanoparticles

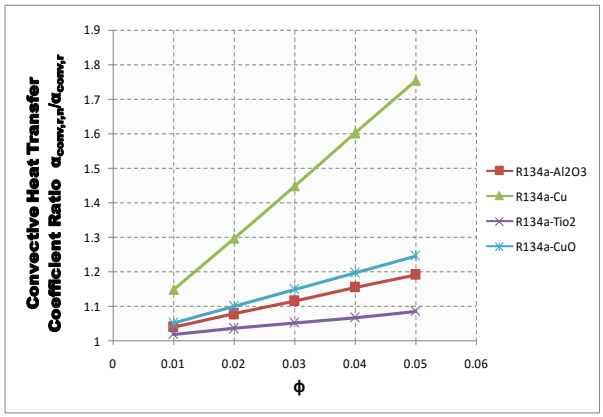


Fig.26. Variation of Convective heat transfer coefficient ratio with volume fraction (ϕ) of R134a using different nanoparticles

Fig 24-26 shows the convective heat transfer coefficient Ratio increases by increasing the concentration of nanoparticle. And copper nanoparticle based Nano refrigerant have highest convective heat transfer coefficient ratio than other particle its value ranges from 1 to 1.7.

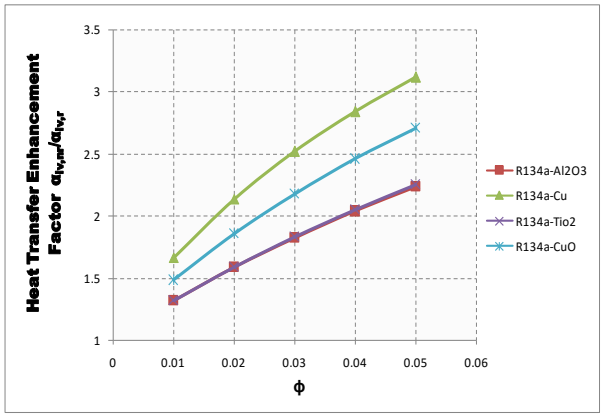


Fig.27. Variation of Heat transfer Enhancement Factor with volume fraction (ϕ) of R134a using different nanoparticles

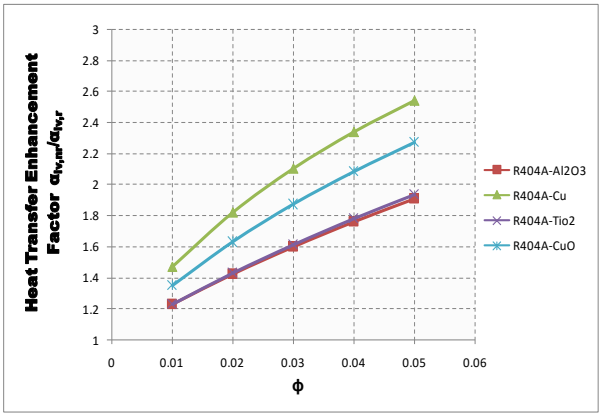


Fig.28. Variation of Heat transfer Enhancement Factor with volume fraction (ϕ) of R404A using different nanoparticles

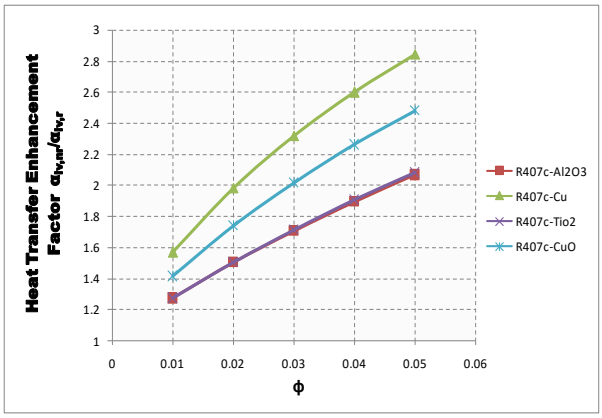


Fig.29. Variation of Heat transfer Enhancement Factor with volume fraction (ϕ) of R407c using different nanoparticles

Fig 27-29 show the heat transfer enhancement factor of Nano refrigerant with different nanoparticle its value ranges from 1.2 to 3.2. As it can be seen that R134 a with cu nanoparticle have highest EF approx. 3.2 at 5 vol %. EF increases with increasing vol %.

4. Conclusion and Future work

Following conclusions have been drawn from present investigations.

(i) The conductivity ratio of pure refrigerant to Nano refrigerant increases with increasing concentration of nanoparticle into the host refrigerant whereas Cu nanoparticle based Nano refrigerant have higher conductivity ratio as compared to other nanoparticle and have approx. two times higher than base refrigerant at 5 vol % concentration.

(ii) The ecofriendly R134a with cu nanoparticle have highest Effectiveness factor approx. 3.2 at 5 vol %. The Effectiveness Factor (EF) increases with increasing vol %.. and the copper nanoparticle based Nano refrigerant have highest convective heat transfer coefficient ratio than other nano particle

References

[1] J. A. Eastman, S. U. S. Choi, S. Li, W. Yu, and L. J. Thompson, "Anomalously increased effective thermal conductivities of ethylene glycol-based nanofluids containing copper nanoparticles," Applied Physics Letters, vol. 78, no. 6, pp. 718–720, 2001.

[2] Y. Li, J. Zhou, S. Tung, E. Schneider, and S. Xi, "A review on development of nanofluid preparation and characterization," Powder Technology, vol. 196, no. 2, pp. 89–101, 2009.

[3] C. H. Lo, T. T. Tsung, and L. C. Chen, "Shape-controlled synthesis of Cu-based nanofluid using submerged arc nanoparticle synthesis system (SANSS)," Journal of Crystal Growth, vol. 277, no. 1–4, pp. 636–642, 2005.

[4] C. H. Lo, T. T. Tsung, L. C. Chen, C. H. Su, and H. M. Lin, "Fabrication of copper oxide nanofluid using submerged arc nanoparticle synthesis system (SANSS)," Journal of Nanoparticle Research, vol. 7, no. 2-3, pp. 313–320, 2005.

[5] H. T. Zhu, Y. S. Lin, and Y. S. Yin, "A novel one-step chemical method for preparation of copper nanofluids," Journal of Colloid and Interface Science, vol. 277, no. 1, pp. 100–103, 2004.

[6] H. Bönnemann, S. S. Botha, B. Bladergroen, and V. M. Linkov, "Monodisperse copper- and silver-nanocolloids suitable for heat-conductive fluids," Applied Organometallic Chemistry, vol. 19, no. 6, pp. 768–773, 2005.

[7] A. K. Singh and V. S. Raykar, "Microwave synthesis of silver nanofluids with polyvinylpyrrolidone (PVP) and their transport properties," Colloid and Polymer Science, vol. 286, no. 14-15, pp. 1667–1673, 2008.

[8] A. Kumar, H. Joshi, R. Pasricha, A. B. Mandale, and M. Sastry, "Phase transfer of silver nanoparticles from aqueous to organic solutions using fatty amine molecules," Journal of Colloid and Interface Science, vol. 264, no. 2, pp. 396–401, 2003.

[9] W. Yu, H. Xie, X. Wang, and X. Wang, "Highly efficient method for preparing homogeneous and stable colloids containing graphene oxide," Nanoscale Research Letters, vol. 6, p. 47, 2011.

[10] H. T. Zhu, C. Y. Zhang, Y. M. Tang, and J. X. Wang, "Novel synthesis and thermal conductivity of CuO nanofluid," Journal of Physical Chemistry C, vol. 111, no. 4, pp. 1646–1650, 2007.

[11] Y. Chen and X. Wang, "Novel phase-transfer preparation of monodisperse silver and gold nanoparticles at room temperature," Materials Letters, vol. 62, no. 15, pp. 2215–2218, 2008.

[12] X. Feng, H. Ma, S. Huang et al., "Aqueous-organic phase-transfer of highly stable gold, silver, and platinum nanoparticles and new route for fabrication of gold nanofilms at the oil/water interface and on solid supports," Journal of Physical Chemistry B, vol. 110, no. 25, pp. 12311–12317, 2006.

[13] W. Yu, H. Xie, L. Chen, and Y. Li, "Enhancement of thermal conductivity of kerosene-based Fe3O4 nanofluids prepared via phase-transfer method," Colloids and Surfaces A, vol. 355, no. 1–3, pp. 109–113, 2010.

[14] L. Wang and J. Fan, "Nanofluids research: key issues," Nanoscale Research Letters, vol. 5, no. 8, pp. 1241–1252, 2010.

DOI:10.21276/sjeat

Saudi Journal of Engineering and Technology
Scholars Middle East Publishers
Dubai, United Arab Emirates
Website: http://scholarsmepub.com/

ISSN 2415-6272 (Print)
ISSN 2415-6264 (Online)

Original Research Article

Thermodynamic (Energy-Exergy) Analysis of Combined Coal based Thermal Power Plant and Solar Integrated Double Bed Vapor Adsorption System for Heat Recovery and Space Cooling

Kaushalendra Kumar Dubey[1,*], R.S. Mishra[1]
[*]Department of Mechanical Engineering, Sharda University, U.P., India
[1]Department of Mechanical Engineering, Delhi Technological University, New Delhi, India

***Corresponding Author:**
Kaushalendra Kumar Dubey
Email: dubey.kaushalendra@gmail.com

Abstract: The thermal performance of proposed model deals with combined double bed vapor adsorption refrigeration system and 9MW of Rankine thermal cycle .The provision of evacuated tube type solar collector (ETC) is available with adsorption system to support the system for continuous cooling effect. The energy-exergy analysis refers live operational data of thermal power plant, and proposed cooling system is adopted as per thermal gain from condenser and solar heater for adsorbent-adsorbate pair of adsorption system. Major units of combined plant (boiler, turbines, condenser, pump, solar collector, adsorption bed etc.) have been investigated in thermodynamic analysis. The main objective of energy-exergy modeling is to identify the magnitude of process, cause of losses and rectifying the components. The source temperatures available for both beds of Vapor Adsorption Refrigeration systems (VAdRS) from condenser exhaust and ETC solar system. The adsorbent and adsorbate pair for double bed VAdRS has been recommended by activated carbon as adsorbent and methanol and R134a as adsorbate respectively. This analysis shows the combination of adsorbent-adsorbate pair is suitable for low grade heat recovery with solar thermal integration for continuous cooling effect generation and applicable for space cooling purpose. The major findings of present work, the maximum irreversibility found in boiler as 47% in thermal power plant and solar generator as 12% of adsorption machine, whereas overall cooling effect from adsorption system is increasing by 15% in double bed combination. EES software is used for all analysis.

Keywords: Rankin power cycle, Vapor adsorption refrigeration system, $\eta_{rankine}$, COPth, SCP, Irreversibility, EES

INTRODUCTION

This paper focus on the performance analysis of double bed VADRS integrated with ETC type solar thermal system for heat recovery of condenser part and integrated for cooling of large space area with zero impact on environment. It is recognized that the energy is one of the key factors that required for social, economic and industrial development. The interdependency of energy sector with industrial development is major concern for developing countries. The infrastructure of industry determines the amount and form of energy needed. Similarly, the availability and cost of supplies energy has a major influence on industrial development. The world energy council (WEC) reported that energy generation is from fossil based resources are 76%, although it is decreases by 10-13% from 1993 by increases hydro power nuclear power and renewable energy technologies. Worldwide industrial sector energy consumption is to increase by an average of 1.2%/year, from 222 quadrillion Btu in 2012 to 309 quadrillion Btu in 2040 [1-2].Shah N. *et al* [3] presented over the decade 2010-2020, the incremental electricity demand in from commercial and as well as from residential ACs alone (600 TWh/yr) are estimated to consume more than half of the total generation. This additional electricity demand will put tremendous pressure on the power sector of countries. The growth of HVACs poses environmental issues due to the GHG emissions emitted during the production of electricity needed to power them, and due to the refrigerants that are used in their system. Askalany *et al* [4] described vapor compression refrigeration systems operated with refrigerants, such as CFCs, HCFCs or HFCs. When released into the atmosphere, such refrigerants

deplete the ozone layer and contribute to greenhouse effect. In the late 1980s,it was estimated that 33.3 % of greenhouse gas effect by using refrigeration machines and other heating/cooling thermal utilities, after this observation, the several protocols, like the Montreal protocol [28] and the Kyoto protocol [29] were established in order to reduce the emission of these refrigerants and introduce green concepts of heating/cooling technologies by using new trends of refrigerants, which has low ODP and GWP values for environmental safety aspects in Refrigeration & Air-Conditioning Industry. Turboden survey [5] shows the typical cement plant production capacity of 2000-8000 Tons/day consumes 3.5-5GJ of energy per ton. The energy produce by wastage heat recovery systems can account for 10-20% of total energy consumed by cement plant. The above described energy status and its future demand indicates the research and development in area of energy efficient technological development, its utilization with proper management in cost effective and eco-friendly nature for commercial, domestic and industrial purpose. The technology of vapor adsorption refrigeration system has potential for recover heat of low and high grade both, as well as integrated with solar thermal energy utilization. Many researches have been conducted in past, but implementation of technology and its development is still awaited. Kai Wang and A.Edward[6] explained basic adsorption cycle with the help of Chaperon diagram (Figure 1), it consists of four steps heating and pressurization, desorption and condensation, cooling and depressurization, and adsorption and evaporation. BaijuV.andMurleedharan C [7] tested cooling output is not continuous in single adsorption refrigeration cycle system. A minimum of two adsorbed is required to obtain a continuous cooling effect (when the first adsorbed is in the adsorption phase, the second adsorbed is in desorption phase). These absorbers will sequentially execute the adsorption-desorption process. The efficiency of the basic adsorption refrigeration cycle is low, and the cooling output is not continuous, many advanced adsorption refrigeration cycles (such as the heat recovery cycle, mass recovery cycle, thermal wave cycle, forced convective thermal wave cycle, etc.) have been developed by different investigators with improve efficiency and practicability [10,12,13,15]. The technology of solar adsorption refrigeration is satisfied the Montreal protocol and Kyoto protocol on ozone layer depletion and global warming concern [8]. The solar power based refrigeration system is simple and is adaptable for small, medium or large type low grade energy recovery systems because adsorption unit of solar adsorption refrigeration does not possess any problems of emission of greenhouse gases [9]. Since 1980's large efforts have been made to improve the performance of the adsorption refrigeration system. Sasha *et.al* [14] has analyzed two stage non-regenerative adsorption chiller prototype with experimental results show that the system operated with temperature range of 55-30 ^{0}C. Douses and Meniere [11] had reported experiments on two stage adsorptive heat pump. The cycle consisted of two adsorbed zeolite-water system at higher temperature stage and activated carbon-methanol at the low temperature stage. The COP of the system was reported as 1.06, which is higher than the COP of an intermittent cycle.

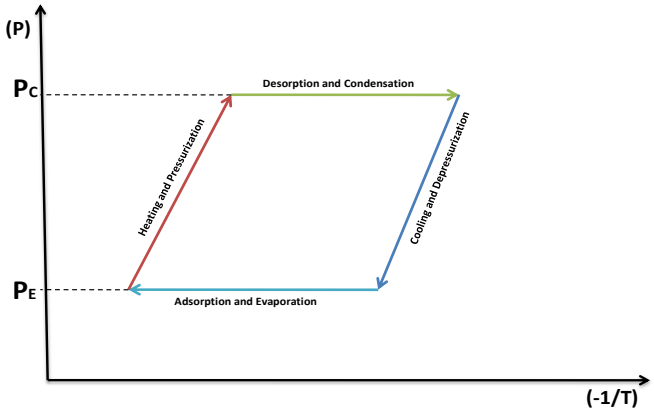


Fig-1: Chaperon diagram- Basic Adsorption cycle [6]

The projected VADRS model in present research work adopted from Mahesh and Kauirik [16] model, that model were used as single bed solar integrated, here double bed VADRS is proposed with two different pair of adsorbent &adsorbate under different source temperature level for more cooling effect with the source of low grade heat.

Many researches have been conducted in thermodynamic (energy-exergy) analysis of thermal utilities for actual performance estimation. Energy of system defines the true performance of system. Dicer and Rosen [19] stated that the exergy is the maximum rate of work, which is obtained from it and passes reversibly to the environmental state. Energy analysis is the theoretical limitations upon a system, clearly pointing out that no real system can conserve exergy and that only a portion of the input energy can be recovered. A. Began [20] introduce entropy generation minimization mechanism, if entropy production is minimized, than useful energy is maximized. Khaliq and Kaushik [21] concluded the combustion chamber exergy destruction is 50% of overall exergy destruction of cycle, and effect of intermediate pressure-ratio and effect two stage of reheating on combined GT-ST power cycle performance by using 2^{nd} law thermodynamic approach. Yang *et al* [22] compared conventional and advanced approach of exergy analysis of supercritical coal thermal power plant. Conventional approach identified exergy destruction of all components, whereas advanced exergyanalysis conclude thermodynamic interactions among thermal utilities for energy saving potential. Kaushalendra and Mishra found maximumexergy destruction in boiler part of thermal power plant analysis. Compressor of conventional refrigeration consumes larger amount of electrical energy with high destruction rate in VCRS, and author also summarize different thermodynamic systems for low to high grade energy recovery from industrial & power plant sector for combined heating-cooling and power generation by using new trends of working fluid in advanced thermal cycles like organic ranking cycle, kalian cycles supercritical organic ranking cycle etc. in efficient manner with environmental aspect [23-27]. More than 45% of energy generation supply to industrial purpose. The industrial sector (oil refineries, cement, glass, steel etc.) and power plant discard large amount of heat with useful energy generation or energy in production into the atmosphere. The novel concepts of wastage heat (low and high grade) recovery technology like ORC, Tri-Generation, Co-Generation, HRSG, Vapor absorption and adsorption refrigeration system with and without integration of solar energy utilization recover waste heat from several process like, kiln and clinker gas flow recovery in cement production plant, oven exhaust heat recovery in glass industry, pre-heating exhaust heat recovery of rolling process in steel industry, and produce power, heating and as well as cooling generation [26].

SYSTEM DESCRIPTIONS AND OPERATION.

The proposed Rankin cycle directly adopted from kaushalendra and Mishra energy-energy analysis of 9 MW thermal power plant[27]. The provision of double bed vapor adsorption system with ranking model in this paper consisted by two bed of vapor adsorption, first bed of VADRS filled by activated carbon-methanol type adsorbent-adsorbate (refrigerant) pair, which recover exhaust heat of condenser of unit and produce cooling effect, another bed of VADRSoccupied with activated carbon-R134a pair of adsorbent-adsorbate (refrigerant) and derive by solar water heater system. The selection of above pairs basically depend of source temperature for adsorption bed, and thermo physical properties of pair for required cooling load. The all components are shown in table-1 unit description. The main components of VADRS are generator for heating of bed (generators may be solar thermal system or any thermal utilities), adsorption bed, condenser, evaporator and chilling chamber. Stainless steel fabricated adsorption bed consisted of two chambers, inner chamber (9& 17), which is filled with activated carbon as adsorbent and methanol for first VADRS&activated carbon-R134a for second Verses a adsorb ate or refrigerant for adsorption cooling, and outer chamber (8& 16) for hot water chamber for desorption process of pair used, that hot water is supplied from condenser of unite bed-1, and similar from ETC solar thermal collector (24) to bed-2.In the inner chamber, one end was connected to the condenser (11 & 19,VAdRS condensers) to receive desorbed liquid condensed by the condenser. The outer chamber covers the inner chamber. The outer chamber consisted of two pipes. The two pipes were placed in the lower and upper sides of chamber (shown in fig.2). In the outer chamber, one end is connected to outlet of condenser for bed-1 and similar for bed-2, outer chamber end connected to outlet of ETC solar thermal collector. The hot water is circulated through the generators to adsorption bed (1 & 2 both)60 ^{0}C temperature of hot water from condenser caused the activated carbon to desorb the refrigerant in bed-1.Then refrigerant vapor was condensed with the help of a condenser and it was stored in the evaporator. The evaporator was placed inside the chilling chamber. Similar event happened in bed-2, during day time temperature of collector increased above 80 ^{0}C and hot water cause the desorb the R134a from activated carbon. For bed-1, valves v1 and v2 open for desorption, condensation and evaporation process and other hand valve v3 kept in close position, and during adsorption of refrigerant in adsorbent, v3 is open and v1 & v2 are closed. For bed-2, during daytime valves v4 and v5 open for same desorption, condensation and evaporation process and other hand valve v6 kept in close position. After sunset, collector temperature has been decreased to ambient temperature, the valves v4 & v5 were closed and the valve v6 kept open to allow refrigerant for adsorption process. Valves v7 & v8 regulate hot and cold water

respectively from solar collector to adsorption tank and its vice-versa is valid. Desorption process occurs here during day time and adsorption process took place during night. The provision of another valves v9 & v10 are specific here, solar integrated Vader's does not work during night, so hot water from condenser can help for desorption of refrigerant from adsorbent for cooling process, valves v9 is allow to hot water from condenser and v10 is pass the cold water from adsorption tank or bed-2 and water mixed with feed water pump line and pumped to the boiler. This circuit is important part of proposed model for effective cooling during night time.

PROPOSED MODEL OF COMBINED POWER AND VADRS SYSTEM

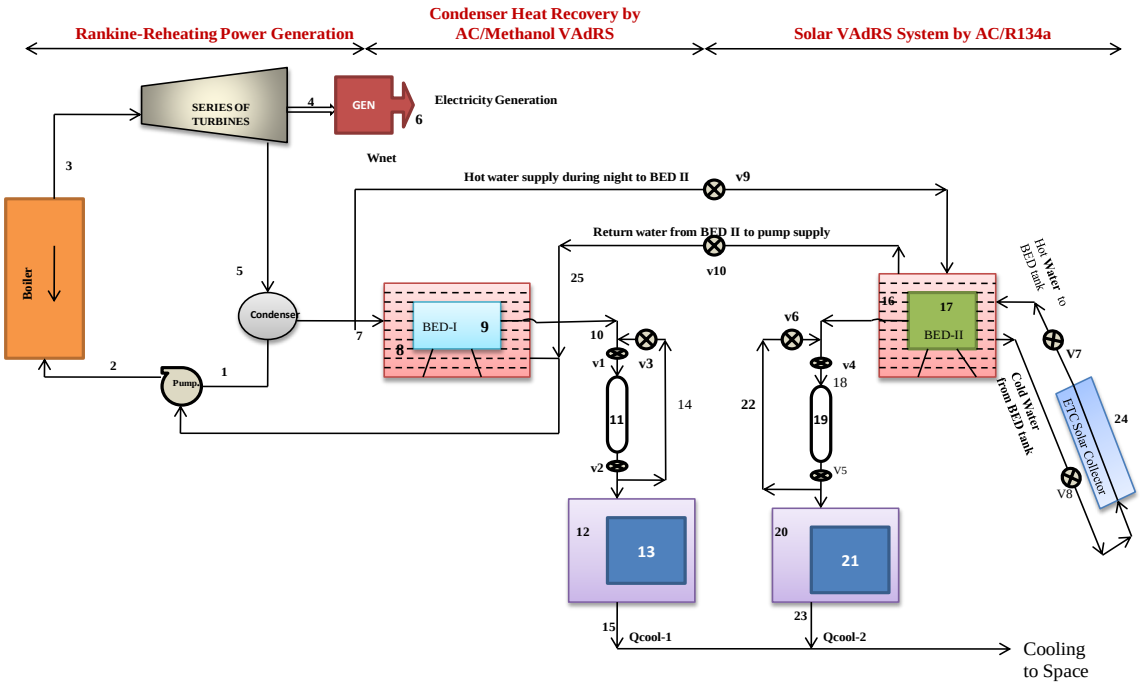


Fig-2: Schematic of combined power and VADRS system

Table-1Unit specification of combined plant

UNIT NO	SPECIFICATION	UNIT NO	SPECIFICATION
1	Condensed steam feed to pump	21	Chiller get to be cooled during evaporation
2	Feed water supply to boiler for steam formation	22	Evaporated refrigerant adsorbed in adsorbent bed
3	Steam from boiler supply to series of turbine	23	Chilled air supply to space where cooling is required through cooling line.
4	Turbine shaft work for electricity generation	24	ETC solar thermal water heater for hot water supply to BED-2.
5	Exhaust steam from turbine supply to condenser unit for condensation process	25	Return cold water from BED-2 and mixed with water line for pumping to boiler.
6	Generator work	v1	Valve 1 open and allow to vaporized

			refrigerant into condenser for condensation
7	Hot water proceeds to BED-1 and only during night to BED-2 for adsorption cooling process.	v2	Valve 2 allow Condensed refrigerant into evaporator and chiller unit.
8	Outer chamber of BED-1 for hot water collection, (need of hot water for adsorption of heat from adsorbate).	v3	Valve 3 open for adsorption of vapor refrigerant into adsorbent bed after evaporation.(v1 & v2 remain closed when adsorption is happening)
9	Inner chamber of bed -1, where Activated carbon-Methanol pair is filled, Its utilize condenser heat.	v4	Valve 4 open and allow to vaporized refrigerant into condenser for condensation
10	Vapor refrigerant (Methanol) supply to condenser of Vader's after desorption process.	v5	Valve 5 allow Condensed refrigerant into evaporator and chiller unit.
11	Refrigerant liquefy by using condenser	v6	Valve 6 open for adsorption of vapor refrigerant into adsorbent bed after evaporation.(v1 & v2 remain closed when adsorption is happening)
12	Liquid refrigerant get evaporation by evaporator	v7	Valve 7 open for hot water supply from ETC to BED-2 for desorption of refrigerant.(V9 & V10 are closed)
13	Chiller get to be cooled during evaporation	v8	Valve 8 open for cold water return in to ETC after desorption. (V9 & V10 are closed)
14	Evaporated refrigerant adsorbed in adsorbent bed	v9	V9 works during night, when ETC does not work. It opens for hot water supply from condenser exhaust to BED-2.
15	Chilled air supply to space where cooling is required through cooling line.	v10	V 10 allows return cold water from BED-2 after adsorption and water mixed with water line for pumping into boiler.
16	Outer chamber of BED-2 for hot water collection, (need of hot water for adsorption of heat from adsorbate).	Turbine	Series of High pressure turbine and low pressure turbine.
17	Inner chamber of bed -2, where Activated carbon-R134a pair is filled, Its utilize condenser heat.	GEN	Generator for electricity generation.
18	Vapor refrigerant (R134a) supply to condenser of V.Adms. After desorption process.	BOILER	Steam formation thermal utilities
19	Refrigerant liquefy by using condenser	CONDENSER	Condensation of exhaust steam and refrigerant vapor condensation process

THERMODYNAMIC ANALYSIS OF COMBINED RANKINE THERMAL AND VAPOR ADSORPTION SYSTEM

The thermodynamic analysis of the Combined Thermal and Vapor Adsorption Plant is consisting in the following parts as mentioned below.

ENERGY AND EXERGY ANALYSIS OF RANKINE CYCLE.

A simplified mathematical model of basic thermodynamic approaches is used in analysis. Mass and energy balance equations has been applied in all thermal utilities. In order to simplify

The analysis, some assumptions are generally made as follows:

A.The process is considering steady flow throughout working of system and thermal utilities also consider as a control volume (CV).

B.The state of the mass at every point within the control volume (CV) does not vary with time.
C.The mass flow rate into and out of the control volume does not vary with time.
D.The efficiencyof both turbines and pump assumed isentropic for analysis.
E.The thermodynamic equilibrium exits in the adsorbent bed at any given time.
F.The refrigerant is adsorbed uniformly in the adsorber and is liquid in the adsorbent,
G.The heat conduction from the adsorber to the condenser and to the evaporator through the metal is neglected.
H.The evaporating temperature is identical to the temperature of the liquid in the evaporator.
I.The specific heat of adsorbed adsorbateis equal to that of bulk liquid of adsorbate.
J.The resistances to the heat and mass transfers in the adsorbent are neglected.

All equations of analysis is fundamental approach of 1st law and 2nd law of thermodynamics, and properties (enthalpy,entropy,specificheat,specificvolume,etc) of steam formation referred from steam property table Data [17]as per steam condition (superheated and saturated) and working refrigerants fluid at different pressure-temperature level. [17]and[18] given energy-exergy equations for power-plant analysis as given below.
The thermal efficiency of plant is expressed by following equation

$\eta_{PLANT} = W_{NET} / Q_{BOILER}$ ……..…...(1)

Where Network done by plant is expressed as

$W_{NET}=W_{TURBINE_TOTAL}-W_{PUMP}$…….……...(2)

The Total work done by Turbine is a addition of work one by each turbine as given below

$W_{TURBINETOTAL}=W_{TURBINE_1}+W_{TURBINE_2}+W_{TURBINE_3}$…… (3)

$W_{TURBINE_1}$=m_dot_turbine1_steamflow (h_temp inlet_turbine1-h_temp exit_turbine1)…….…….,,,,,…… (4)

$W_{TURBINE_2}$=m_dot_turbine2_steam flow(h_tempinlet_turbine2-h_temp exit_turbine2)…….…..,,,,,…….…..(5)

$W_{TURBINE_3}$ = m_dot_turbine3_steamflow (h_temp inlet_turbine3- h_{2s})……..……..……,,,,.……....(6)

And Work done by pump=$W_{PUMP}=v\times dP=v\times(P_{BOILERLINE}-P_{CONDENSERLINE})$=m_dot_pump(h4s-hf3)……..(7)

From enthalpy and entropy balance equation the isentropic enthalpy at the inlet of condenser (h_{2s}) is expressed as
$h_{2s}=h_{f2}+x_2h_{fg2}$…… (8)
x_2 is steam dryness fraction at condenser
$s1=s_{2s}=s_{f2}+x_2\ s_{fg2}$…….…… (9)

Heat Generated by boiler

Q_{BOILER}=m_dot_boiler_steam_flow (h_boiler temp - h4s)……(10)

The energy balance in the condenser is expressed by following equations

$W_{TURBINETOTAL}–W_{PUMP}=Q_{BOILER} - Q_{CONDENSER}$……..……...(11)
$\eta_{Boiler}= Q_{BOILER} / Q_{FUEL}$……..…(12)

WhereQ_{FUEL}=(m_air+m_fuel)×fuelcalorificvalue…..(13)

THERMODYNAMIC MODELLING OF DOUBLE BED VAPOUR ADSORPTION REFRIGERATION SYSTEM

The desorbed of both beds are heated by the waste heat of condenser and solar collector to begin desorbing, and the condensation process occurs firstly in the evaporator because the evaporator temperature is lower than the condenser temperature at that time. Such process will continue until the evaporator temperature rises higher than the condenser temperature. Thereafter, the condenser will be in condensing mode, and the evaporator will be idle. Therefore, in the whole desorption process, the energy equilibrium equations can be described as: The total heat input to the system is estimation of energy liberated during adsorption is called esoteric heating and heat due to desorption [8].
The total energy input to the system is given by

$Q_{heat_total}=Q_{isosteric}+ Q_{desorption}$..... (14)

The total heat generated from vapour adsorber bed is given below [16]
$Q_{heat_total} = \sum m_{ad}[(Cp_{ad} + Cp_r*X_{max})(T_g - T_{ad}) + (Cp_{ad} + \Delta X/2)(T_{des} - T_g) + \Delta X*H_D]_{BED\text{-}1\ \&\ BED\text{-}2}$.....(15)

After condensation of desorbed refrigerant, the liquid refrigerant in the evaporator will absorb the heat of vaporization from liquid to be cooled, this cause the refrigeration effectand the refrigeration amount can be estimate as-
$Q_{Ref} = \sum [(m_{ad} *\Delta X * L_E)]_{BED\text{-}1\ \&\ BED\text{-}2}$.....(16)

The amount of energy used in cooling the evaporated absorb ate when passing through the condenser is given by-

$Q_{Cool}= \sum [(m_{ad} * \Delta X * Cp_r (T_C-T_E)]_{BED\text{-}1\ \&\ BED\text{-}2}$....(17)

The useful cooling of vapor adsorption system can be estimated by

$Q_{cool\ useful} = \sum m_{ad}[(L_E * \Delta X - Cp_r (T_C-T_E)]_{\ BED\text{-}1\&2}$. (18)

3.3 PERFORMANCE PARAMETERS INVOLVED IN THE DOUBLE BED VAPOUR ADSORPTION REFRIGERATION SYSTEM

The compactness of system is important parameter, Useful cooling per unit mass (specific cooling power) of adsorption system decide the compactness or size of system. Desorption and Adsorption time (second) play key role for cooling effect in the Vader's and its SCP sizing.

$\mathbf{SCP_{VADRS}} = Q_{cool\ useful\ } / m_{ad}$.....(19)

Or coefficient of performance of Vader's (is a ratio of useful cooling and total heat input for adsorption and desorption account the refrigeration capacity) is given by following expression

$\mathbf{COP_{VADRS}} = Q_{cool\ useful} / Q_{heat_total}$..... (20)

Similarly the solar thermal system COP is a ratio of refrigeration effect of solar vapor adsorption refrigeration system to the solar heat generation.

$\mathbf{COP_{SOLAR}}= Q_{cool\ useful} / Q_G$ ….....(21)
Where $Q_G = I * Ac$

3.4. EXERGY ANALYSIS OF COMBINED THERMAL AND VAPOR ADSORPTION PLANT
Exergy flow rate of inlet steam-

ϵ_{f_1n} = m_dot_steam × cp_boiler steam × to $[\frac{Tboiler}{To} - 1 - ln\frac{Tboiler}{TO}]$..... (22)
Exergy flow rate of exhaust steam-

ϵ_{f_out} = m_dot_steam × cp_boiler steam × to $[\frac{Tboiler}{To} - 1 - ln\frac{Tboiler}{TO}]$..... (23)

Rate of exergy increase of steam = Exergyutilization rate= $€_{f_Usefull}$

$€_{f_Usefull} = m_dot_steam\ [h1-h4s-To\ (s1-s4s)]$…… (24)

Exergy Destruction in boiler=$€_{Des_boiler}$ = Rate of exergy increase of steam - Rate of exergy decrease
Exergy flow rate of wet steam to condenser

$€_{wetsteam\ to\ condenser} = m_{}_{wet\ steam\ to\ condenser}\ [h2s-hf3-To\ (s_2-sf_3)]$…….……...…….(25)

Irreversibility estimation of each components-

I_{RR}= ToΣΔS = To (ΔS_{boiler}+ $\Delta S_{turbine}$+ $\Delta S_{condenser}$+ΔS_{pump}+ΔS_{Bed-1}+ΔS_{Bed-2}+ΔS_{solar})…….(26)

And ΔS = cpln($\frac{Tout}{Tin}$)……..(27)

(cp will vary with temperature and pressure condition of working fluid, putting all value of cp and Tout&Tin of components)

Now EDRratio = $\frac{ToΣΔS}{Qboiler}$……..……(28)

Exergetic efficiency = η_{EX} = 1- EDR_{ratio}……..…(29)

Exergy Destruction Rate = $\frac{ToΣΔS}{Wnet}$…… (30)

Rate of exergy loss in boiler= $\frac{€f_out}{€f\ in}$……. (31)

RESULTS AND DISCUSSIONS

The operational data of thermal power plant is provided in table-2(a) & (b), all data measured in February month2015 in daily basis, but for analysis average data is taken. (plant data referred from Adani Thermal Power Plant, Gujarat, India)

Table-2(a)-Plant Operational data (average data on daily basis)

Time	CW FLOW	Temperature		Ambient Conditions			Condenser		
		CW - IN	CW - OUT	DBT	RH%	WBT	Vacuum	Temp	Flow
	(m3/hr)	(ºC)	(ºC)	(ºC)	(%)	(ºC)	(Kg/cm2 g)	(ºC)	(TPH)
All day	**2376.22**	**28.67**	**39.89**	**28.00**	**50.00**	**20.30**	**-0.94**	**43.54**	**13.66**

Table-2(b)-Plant Operational data (average data on daily basis

Time	Inlet Steam			Extraction 1 & 2			Extraction 3			Generation
	Pressure	Temp	Flow	Pressure	Temp	Flow	Pressure	Temp	Flow	
	(Kg/cm2 g)	(ºC)	(TPH)	(Kg/cm2 g)	(ºC)	(TPH)	(Kg/cm2 g)	(ºC)	(TPH)	(MW)
All Day	**61.87**	**473.90**	**68.80**	**14.14**	**323.19**	**15.76**	**2.52**	**182.61**	**40.17**	**9.41**

h1=h_temp inlet_turbine3 = 2827.18 KJ/Kg….temp at 180 ^{0}C (inlet temp of turbine3)

s1=s2 = 7.353 kJ/kg-K from steam properties at condenser line pressure of 0.098 bar (absolute)

h3=hf3=hf2=184 kJ/kg from steam properties
s4=s3=sf2=0.629 kJ/kg-K
hfg2= 2397.95 kJ/kg

sfg2= 7.591 kJ/kg-
Sp Volume of saturated steam at condenser line v=0.001009 m3/kg
Put all values of entropy and get x2=0.91 and estimate h2s from eq. no7
h2s=2376KJ/kg
Now total turbine work (mass flow rate of steam for different turbine provide in plant data table-1 (a)&(b),providing all values of enthalpy as per inlet temperatures Values of turbines)
$W_{TURBINE\ TOTAL}$ = 960 kJ/kg or 8.5 MW (flow rate of steam varying daily with time)
h4s = 184.06 kJ/kg
W_{PUMP}=184 kJ/kg or 437KW at 8.5TPH of water flow through pump
W_{NET} = 8.2-0.43 = 7.77 OR 7.8MW
(Steam flow through boiler is 65TPH from data table)
$Q_{_BOILER}$ = 3196 kJ/Kg or 58627 KW
η_{PLANT} = 24.12%
(4620 kcal/kg as per data)
η_{Boiler} = 11%

(13 TPH of coal feeding with 97 TPH of air)
[Solar Irradiations (I) is taken 800-900 W/m^2 as per site, and aperture area of ETC is 6m^2 as per design]
(Steam generation inlet temperature is 485±5^{0}C, 75TPH and specific heat of steam 2.21 kJ/kg-k, atmospheric temp To is 298K)
$€_{f_1n}$ = 387 kJ/Kg or 7715KW

(Steam temperature exhaust is 320 ^{0}C, 75TPH and specific heat of steam 2.21 kJ/kg-k, atmospheric temp To is 298K)
$€_{f_out}$= 260 KJ/Kg or 5240KW

Rate of exergy decrease- $€_{f_1n}$ - $€_{f_out}$= 127 KJ/Kg or 2475 KW
Rate of exergy loss in boiler = $\frac{€f_out}{€f_in}$ = 0.47

$€_{f_Usefull}$= 1172.10 KJ/Kg or 23547.5KW
$€_{Des_boiler}$=1045.1 KJ/Kg or 21072.5 KW
(26THP of wet steam passing through condenser)
$€_{wet\ steam\ to\ condenser}$ = 188.25 KJ/Kg or 1350.44 KW
I_{RR_Boiler}= To(ΔS)$_{_boiler}$ = 1086 KJ/Kg
$I_{RR_turbine}$= To(ΔS)$_{_turbine}$ = 419 KJ/Kg
$I_{RR_condenser}$= To(ΔS)$_{_cond}$ = 124 KJ/Kg
I_{RR_pump}= To(ΔS)$_{_pump}$ = 61.17 KJ/Kg
I_{RR_Bed-1}= To(ΔS)$_{_Bed1}$ = 59.57KJ/Kg
I_{RR_Bed2}= To(ΔS)$_{_Bed2}$ = 59.31KJ/Kg
I_{RR_Solar}= To(ΔS)$_{_solar}$ = 364.77 KJ/Kg
EDR ratio = 0.63

η_{EX} = 1- EDR_{ratio}= 0.37

Exergy Destruction Rate = 2.8

The performance parameters of combined thermal power plant and VADRs are given in the tables 3(a), 3(b) and table no4.It is observed that COP of bed-2 is more than bed-1, because solar generator provides more temperature comparison to condenser, but maximum exergy destruction found in solar generator in exergy analysis of plant.

Table-3(a), Performance of Adsorption bed-1

COP_{TH}	Q_{COOL}(kJ)	Q_{HEAT}(kJ)	Q_{REF}(kJ)	SCP(kW/kg)	T_{GEN} (K)
0.488	854.6	33543	17222	23.32	328
0.4852	1688	58643	30139	40.53	333
0.4803	2687	84050	43056	57.51	338
0.4749	3850	109765	55973	74.25	343
0.4692	5179	135787	68890	90.76	348

Table-3(b), Performance of Adsorption bed-2

COP_{SOLAR}	COP_{TH}	I_G (W/m^2)	Q_{COOL}(kJ)	Q_{HEAT}(kJ)	Q_{REF} (kJ)	SCP (kW/kg)	T_{GEN}(K)
0.4811	0.507	750	1570	19858	11638	38.18	333
0.5529	0.482	775	1865	24804	13820	45.34	340.5
0.6202	0.4593	800	2159	30136	16002	52.49	348
0.6834	0.4387	825	2454	35855	18184	59.65	355.5
0.7429	0.4199	850	2748	41961	20366	66.81	363

Table-4, Parametric Results of VA pour adsorption Refrigeration system combined with Rankin Thermal power plant

Thermodynamics Parameters	**Computed Results**
Net Out Put (Wnet)	**7.8MW**
Total Turbine Out Put (Wturbine)	**8.5 MW**
Boiler Heat Generation (Qboiler)	**3196KJ/KG**
Plant Efficiency (η_{PLANT})	**24.12%**
Boiler Efficiency (η_{BOILER})	**11%**
Plant Exergy Destruction Rate	**2.8**
Plant Exergetic Efficiency (η_{EXERGY})	**37%**
COP of VAdRS ($COP_{COMBINEDVADRS}$)	**0.46 to 0.51 (13-15% increment in overall COP)**
Sp.Cooling Power ($SCP_{COMBINEDVADRS}$)	**70-90 W/kg (10-16% increment in overall SCP)**
COP gain by Solar energy (COP_{SOLAR})	**0.48-0.74 (most effective COP)**
Maximum Exergy Destruction of plant	**47% (during steam generation)**

The performance of proposed combined solar integrated vapor adsorption refrigeration system for condenser heat recovery is estimated using basic fundamental of thermodynamic. Parametric results of double bed vapor adsorption refrigeration system for heat recovery of Rankine condenser, the overall COP and SCP enhanced by 10-16% shown in figure 3(a) & (b). Solar based vapor adsorption bed gives more COP individually as compare to condenser connected vapor adsorption bed. The specific cooling power (SCP) of solar vapor adsorption bed is increasing but increasing of evaporation temperature will decrease the SCP of solar vapor adsorption bed due to conversion of solar gain into heating ($Q_{heat\text{-}solar}$) by double rate. The variation of SCP between solar and without solar (bed-1 and bed-2) shown in figure no4.

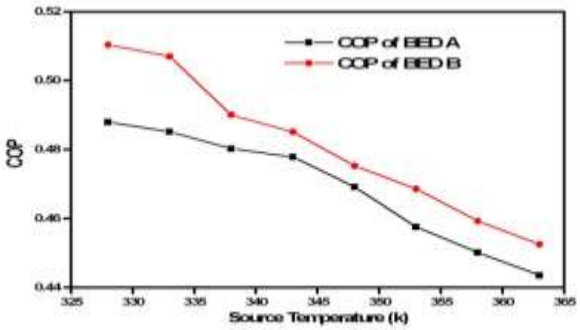


Fig-3(a), COP Vs. Source Temperature

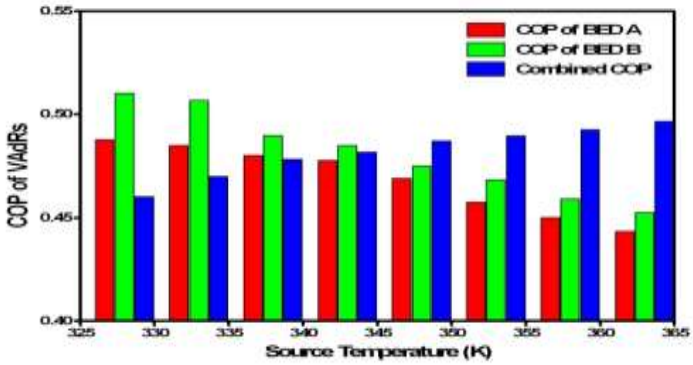


Fig-3(b), COP Vs. Source Temperature

A) **Chaperon diagram- Basic Adsorption cycle [6]**

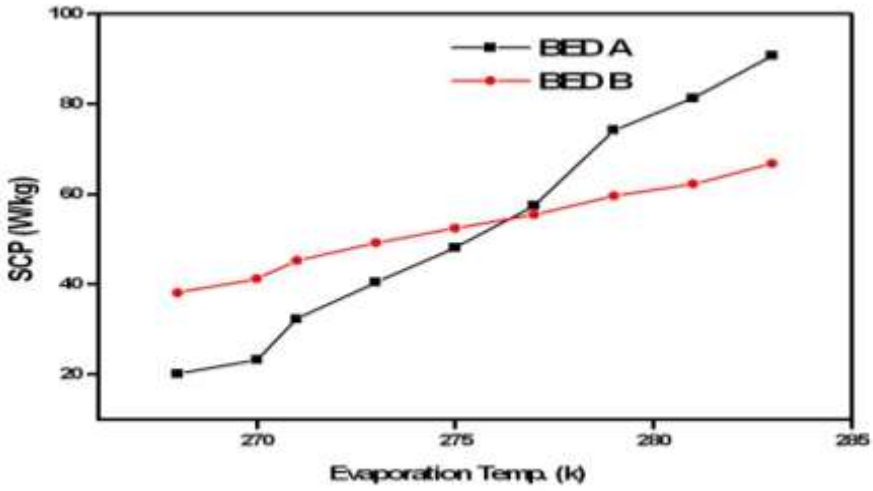


Fig-4, SCP and Evaporation Temperature

CONCLUSION

The conventional refrigeration technology VCRS have reached a significant state of maturity up with wide use for food retail and food preservation sectors. All of these systems consume precious fuel or electricity to achieve refrigeration. Increasing the attention on waste heat recovery through adsorption system. The advantages of solid sorption machines (noiseless, safety). In comparison with the vapor compression refrigeration and absorption refrigeration systems, the adsorption refrigeration system has its drawbacks, such as low mass and heat transfer performance, expansion and agglomeration phenomenon for chemical adsorbent, low coefficient of performance (COP) and low specific cooling power. Some advanced cycles have been proposed and investigated, such as the multi-bed cycles, the thermal wave cycle, and the forced convection cycle. Research has shown that solid-adsorption technology has a promising potential but still limited for commercialization and a under laboratory testing stages.

The present combination of adsorbent-adsorbate pair is suitable for low grade heat recovery with solar thermal integration for continuous cooling effect generation and applicable for space cooling purpose. The maximum irreversibility found in boiler in thermal power plant and solar generator of adsorption machine, whereas overall cooling effect from adsorption system is increasing by 15% in double bed combination. Some results have been found in present analysis.

1. The maximum energy destruction (irreversibility) found in boiler as 47% in thermal power plant and 12% estimated in solar generator of cooling plant...
2. Exergy Destruction is found to be 2.8 (which is the based on output analysis) and o.63 based on input.
3. The thermal power plant efficiency is 24.12%
4. The second law efficiency is 37%.
5. COP and specific cooling power is increased by 13-15% overall of combined bed system of adsorption machine.

The result of present analysis gives minimum energy wastage into environment with more power generation and cooing effect as outcome. These novel concepts helped to low grade waste heat recovery with eco-friendly solar refrigeration opportunities to mini and micro scale of power generating industry.

ACKNOWLEDGEMENT

The author would like to acknowledge Dr. Dibakar Rakshit, Professor, Centre of Energy Studies, Indian Institute of Technology, Delhi, India for their support, enlightening discussions and insights during summer research fellowship of May-July 2016.And also thanks to Dr. Gunjan Agarwal, Centre of Nano Science and Nano Technology (CNN), Jamia MilliaIslamia, New Delhi.

NOMENCLATURES

ETC-Evacuated Tube Collector
WEC-World Energy Council
COP-Coefficient of Performance
AC-Activated Charcoal
ORC-Organic Rankine Cycle
CFCs-Chlorofluorocarbons
HFCs-Hydrofluorocarbons
GWP-Global Warming Potential
CV-Control Volume
I=Solar Irradiation
EES-Engineering Equation Solver
VADRS-Vapour Adsorption Refrigeration System
BTU-British Thermal Unit
SCP-Specific Cooling Power
GHG-Green House Gas
HVAC-Heating Ventilation & Air-Conditioning
HCFCs–Hydro chlorofluorocarbons
ODP-Ozone Depletion Potential
HRSG-Heat Recovery Steam Generator
VCRS-VA pour Compression Refrigeration System
Ac=Aperture area of ETC

REFRENCES

1. Https: //www.worldenergy.org/wpcontent/uploads/2013/09/Complete_WER_2013_Survey.pdf.(cited by June 2016).
2. https://www.eia.gov/.../industrial.pdf. (Cited by June 2016).

3. Leventis, G., Shah, N. K., & McNeil, M. A. (2015). *Cooling the Growth of Air Conditioners Energy Consumption* (No. LBNL-184253). Lawrence Berkeley National Laboratory (LBNL), Berkeley, CA (United States).
4. Askalany, A. A., Salem, M., Ismael, I. M., Ali, A. H. H., Morsy, M. G., & Saha, B. B. (2013). An overview on adsorption pairs for cooling. *Renewable and sustainable energy reviews*, *19*, 565-572.
5. Goel, S., Herzog, O., Datta, A., Sonde, R., Deshpande, K., Fink, J., & Schumacher, T. (2014, June). Market potential study for organic rankine cycle technology in India: A publication on industrial energy efficiency. In *Indo-German Energy Forum*.
6. Kanade, A. V., Kulkarni, A. V., & Deshmukh, D. A. (2015). Solar power adsorption ice maker system. *Int. Res. J. Eng. Technol*, *2*, 477-486.
7. Baiju, V., & Muraleedharan, C. (2011). Performance study of a two stage solar adsorption refrigeration system. *International Journal of Engineering Science and Technology*, *3*(7).
8. Anyanwu, E. E. (2000). Environmental pollution: restructuring the refrigeration industry as a way out. *Environment Protection Engineering*, *26*(4), 17-27.
9. Anyanwu, E. E. (2003). Review of solid adsorption solar refrigerator I: an overview of the refrigeration cycle. *Energy conversion and Management*, *44*(2), 301-312.
10. Critoph, R. E., & Thorpe, R. (1996). Momentum and heat transfer by forced convection in fixed beds of granular active carbon. *Applied Thermal Engineering*, *16*(5), 419-427.
11. Douss, N., & Meunier, F. (1989). Experimental study of cascading adsorption cycles. *Chemical Engineering Science*, *44*(2), 225-235.
12. Holman, J. P., & Gajda, W. J. (2001). *Experimental methods for engineers* (Vol. 7). New York: McGraw-Hill.
13. Pons, M. (1997). Analysis of the adsorption cycles with thermal regeneration based on the entropic mean temperatures. *Applied Thermal Engineering*, *17*(7), 615-627.
14. Saha, B. B., Akisawa, A., & Kashiwagi, T. (2001). Solar/waste heat driven two-stage adsorption chiller: the prototype. *Renewable Energy*, *23*(1), 93-101.
15. Sumathy, K., & Zhongfu, L. (1999). Experiments with solar-powered adsorption ice-maker. *Renewable Energy*, *16*(1-4), 704-707.
16. Mahesh, A., & Kaushik, S. C. (2013). Solar adsorption refrigeration system using different mass of adsorbents. *Journal of thermal analysis and calorimetry*, *111*(1), 897-903.
17. Pabla, A. S. (2007). *Electrical power distribution*. Tata McGraw-Hill Education.
18. Dubey, K. K., & Mishra, R. S. Thermodynamic (Energy-Exergy) Analysis Of Nine MW Coal Based Thermal Power Plant Using Entropy Generation Principle.
19. Rosen, M. A., & Dincer, I. (2003). Exergoeconomic analysis of power plants operating on various fuels. *Applied Thermal Engineering*, *23*(6), 643-658.
20. Bejan, A. (2002). Fundamentals of exergy analysis, entropy generation minimization, and the generation of flow architecture. *International Journal of Energy Research*, *26*(7), 0-43.
21. Khaliq, A., & Kaushik, S. C. (2004). Second-law based thermodynamic analysis of Brayton/Rankine combined power cycle with reheat. *Applied Energy*, *78*(2), 179-197.
22. Yang, Y., Wang, L., Dong, C., Xu, G., Morosuk, T., & Tsatsaronis, G. (2013). Comprehensive exergy-based evaluation and parametric study of a coal-fired ultra-supercritical power plant. *Applied energy*, *112*, 1087-1099.
23. Dubey, K. K., & Mishra, R. S. (2016). Thermodynamic (Energy-Exergy) Analysis of Solar Assisted Power-Cooling Combined Generation Systems. *International Journal*, *4*(1), 129-135.
24. Dubey, K. K., & Mishra, R. S. (2017). Condenser Heat Recovery For Combined Cooling-Heating and Power Generation using Isentropic Fluid. *European Journal of Engineering Research and Science*, *2*(6), 18-26.
25. Mishra, K. K. D. R. Thermodynamic study of R134a in Vapour Compression Refrigeration System in Summer Climate.
26. Tripathi, K., Mani, C., Somasagara, R. R., Clark, D. W., Ananthapur, V., Vinaya, K., & Palle, K. (2017). Detection and evaluation of estrogen DNA-adducts and their carcinogenic effects in cultured human cells using biotinylated estradiol. *Molecular carcinogenesis*, *56*(3), 1010-1020.
27. Das, S., Vasisht, S., Das, N., Srivastava, L. M., Dubey, K. K., & Watal, G. (2000). Correlation between total antioxidant status and lipid peroxidation in hypercholesterolemia. Current science-Bangalore-, *78*(4), 486-486.
28. Protocol, M. (1987). Montreal protocol on substances that deplete the ozone layer. Washington, DC: US Government Printing Office, 26.
29. Grubb, M., Vrolijk, C., & Brack, D. (1997). *The Kyoto Protocol: a guide and assessment*. Royal Institute of International Affairs Energy and Environmental Programmed.

Asian Journal of Applied Science and Technology (AJAST)
Volume 1, Issue 7, Pages 38-46, August 2017

Time Kinetics Studies of Enzyme Catalyzed Hydrolysis of Triolein and Transesterifications of Olive Oil for the Synthesis Major Olive Oil Methyl Esters Using Pseudomonas Aeruginosa Lipase

Vineet Kumar Goswami[1] and Jai Gopal Sharma[2]

[1,2]*Laboratory of Environmental and Industrial Biotechnology, Department of Biotechnology, Delhi Technological University, Delhi, India.*

Article Received: 20 July 2017 *Article Accepted: 05 August 2017* *Article Published: 08 August 2017*

ABSTRACT

The enzyme lipase (triacylglycerol ester hydrolase, EC 3.1.1.3) is a special class of esterase enzyme that acts on fats and oils and hydrolyze them into the respective glycerides and fatty acids, and finally on complete hydrolysis into glycerol and fatty acid. The hydrolysis of triolein and olive oil using Pseudomonas aeruginosa lipase has been carried out under controlled conditions at 60°C and 200 rpm for varied time intervals (3- 72hrs). The analysis of the triolein hydrolytic products on TLC plates showed the presence of glycerol, triolein, diolein, monoolein and oleic acid in 15hrs as compared to 24hrs for the production of oleic acid and glycerol. However, complete hydrolysis of triolein took place in 24hrs but the synthesis of methyl oleate and methyl linoleate by transesterification of olive oil in presence of methanol as acyl donor was initiated as early as 3hrs and it reached to its maximum level of respective methyl ester synthesis just in 6hrs.

Keywords: Catalysis, Gas chromatography, Lipase, Methyl linoleate, Methyl oleate, Olive oil and Transesterification.

1. INTRODUCTION

Lipases (triacylglycerol ester hydrolases E.C.3.1.1.3) are hydrolytic enzymes [1&2]. They are special class of esterase enzymes that act on fats and oil and hydrolyze them into the respective glycerides and fatty acids, and finally on complete hydrolysis into glycerol and fatty acid. Lipases are used as versatile biocatalysts in modern organic chemistry especially for modifications of fats and oils via hydrolysis, esterification, transesterification, interesterification reactions [3,4 & 5] and as a tool for nano-biosensor [6]. On the other hand, this enzyme can efficiently carry out the reverse reaction of synthesis under water limiting conditions [7].

Olive oil is the primary edible oil of Spain, Italy and several other countries. The approved limits for its various constituent fatty acids have been published by European Union (European Community Regulation, 1991; 2001) and International Olive Oil Council. The respect of these limits does not characterize olive oil (especially extra virgin and virgin as largely defined). Fatty acid composition differs from sample to sample and is influenced by the olive variety, production zone, climate and stage of maturity of the drupes when they are collected. The composition of major fatty acids, oleic acid and linoleic acid in olive oil varies from 49-79% and 3.1-24% respectively depending upon the session of harvest and region of

© 2017 AJAST All rights reserved.

cultivation of crop [8&9]. In the present study, the rate of hydrolysis and the rate of transesterification reactions catalyzed by the immobilized lipase enzyme produced by *Pseudomonas aeruginosa* were studied for the analysis of time kinetics of hydrolysis of triolein and for the transesterification kinetics of olive oil into respective methyl esters.

2. MATERIAL AND METHODS

A natural isolate of *Pseudomonas aeruginosa* produced 22,000 IU/L lipase at share flask level on a defined media with composition (%): Casein Acid Hydrolysate (2.000), Tween 80 (1.000), KH_2PO_4 (0.300), KH_2PO_4 (0.100), $MgSO_4.7H_2O$ (0.085), NaH_2PO_4 (0.680) and pH 6.3±0.2. The crude enzyme from fermentation broth was concentrated and partially purified by 60% ammonium sulfate precipitation followed by dialysis against pH 9.0 Tris-HCl buffer and was further concentrated using 60kDa membrane and was immobilized onto the alumina before its use in biocatalysis. Product analysis was carried out using Thin Layer Chromatography (TLC) and Gas Chromatography (GC) and percent yield was determined by titration of initial and residual fatty acids contents according to the procedure [10]. Olive oil (Figaro brand) was purchased from the local market at Delhi and the standards of methyl oleate and methyl linoleate were procured from Sigma Aldrich, USA.

One International Unit (IU) of lipase activity is defined as the amount of enzyme required to release one micro-mole of fatty acid per ml per minute under the standard assay conditions.

Triolein hydrolysis was carried out in the aqueous system at 60ºC and 200 rpm for varied time (3-72hrs). 1 ml of triolein and 2000 IU of immobilized *Pseudomonas aeruginosa* lipase and 4 ml of Tris- HCl buffer pH 9.0 were incubated at 60°C for 72hrs with shaking at 200 rpm and aliquots of 200µl were withdrawn at a regular interval of time upto 72hrs and the reaction were terminated using 5ml of diethyl ether each time. The products were analyzed by thin layer chromatography (Silica Gel 60 F_{254}, Merck, Germany) using the solvent system consisted of petroleum ether: diethyl ether: acetic acid in ratio of 80:30:1. Spots were visualized in a saturated iodine chamber.

For the synthesis of major olive oil methyl esters (methyl oleate and methyl linoleate) under non- aqueous conditions by transesterification, 5ml of olive oil and 5ml of methanol was allowed to react in presence of 2000 IU of immobilized *Pseudomonas aeruginosa* lipase at

© 2017 AJAST All rights reserved. Online ISSN: 2456-883X Publication Impact Factor: 0.825 Website: www.ajast.net

60°C and 200 rpm for varied time intervals (3- 72hrs) and the final volume of methanol was raised to 15ml by adding additional first dose 5 ml of methanol at one-third time of termination time and second dose of 5 ml methanol at two-third time of termination time so as to reach the final equimolar concentration of free fatty acid and methanol and to minimize the deactivation of lipase in presence of methanol. The reaction was terminated by collection of solvent layer after separation by centrifugation at 15000g and 4°C for 5 minutes using Eppendorf® 5810R centrifuge (Eppendorf, Germany). Excess of solvent was evaporated by vacuum evaporation and the residue was dissolved in 1.0ml of n-hexane for GC analysis. The percentage yield was also estimated and percent yield was expressed as the percentage molar conversion of olive oil to ester after titrating the residual fatty acid against 0.01 N KOH using phenolphthalein as an indicator.

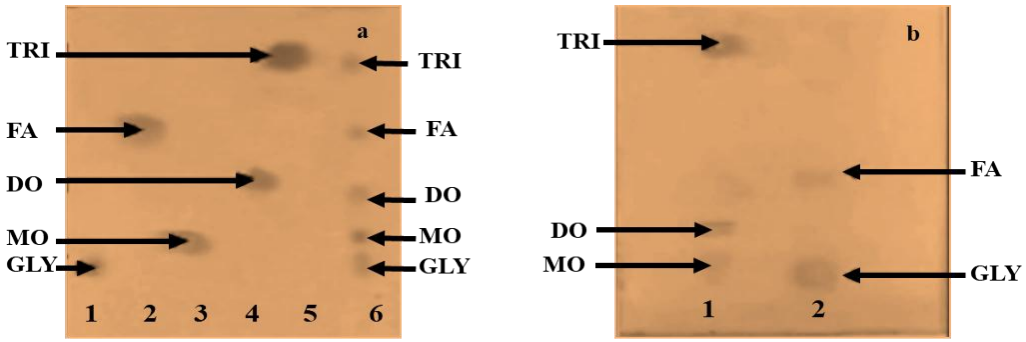
2.1 GC Analysis

A1.0 µl aliquot of the sample was injected onto capillary column using AOC- 20i auto injector in split mode on a Shimadzu GC-2010 Gas Chromatograph (Shimadzu, Japan). The GC was equipped with Restek® Rxi®-5Sil MS capillary column with 30-meter column length and 0.25 mm ID which was having a coating of 5% diphenyl and 95% dimethyl polysiloxane as stationary phase with phase/ film thickness of 0.25µm. The column pressure cut off was held at 130.0 kPa and a constant flow rate of 1.2 mL/min was maintained. The initial column oven temperature was held at 140°C and the final temperature was raised to 280°C for a total run time of 40 min. The FID detector was used which was set at 270°C and hydrogen was used as carrier gas and the helium was used as makeup gas while air flow was maintained at 400ml/min.

3. RESULTS AND DUISCUSSION

The hydrolysis of triolein using *Pseudomonas aeruginosa* lipase was studied in relation to time. The analysis of the hydrolytic products on TLC plates showed the presence of free fatty acid, glycerol, triolein, diolein, monoolein and oleic acid at the reaction time of 15hrs (Fig. 1a) but no free fatty acid was observed on TLC plate for initial 3hrs sample (Fig. 1b) indicating very poor or no hydrolysis during initial 3hrs while for 24hrs sample, only glycerol and free fatty acid could be spotted on TLC plate indicating complete hydrolysis of triolein in 24hrs (Fig 1b) after which the concentration of oleic acid did increased in the reaction system (Fig. 2 & table 1).

© 2017 AJAST All rights reserved.



Lane 1- 5: Standards **Lane 1: 3hrs.**
Lane 6: Triolein hydrolysis at 15hrs. **Lane 2: 24hrs.**
TRI=Triolein, FA= Fatty acid, DO= Diolein, MO=Monoolein, GLY= Glycerol

Fig. 1: TLC analysis of hydrolysis products of triolein using *Pseudomonas aeruginosa* lipase

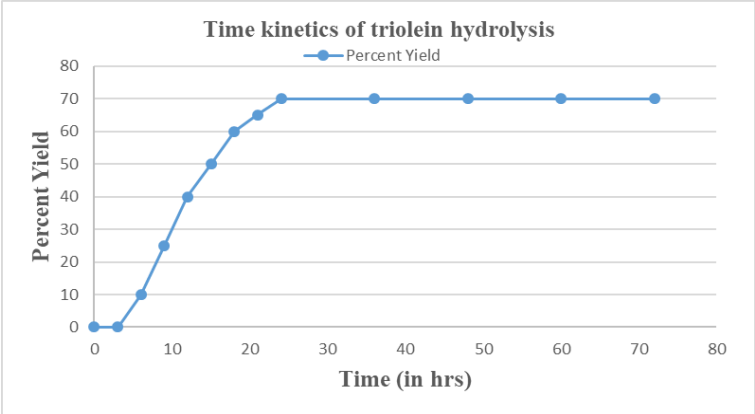


Fig. 2: Time kinetics of triolein hydrolysis by *Pseudomonas aeruginosa* lipase

Table 1: Triolein hydrolysis profile and time kinetics of percent yield

S.No.	Time (hrs)	Triolein Hydrolysis	
		Compounds (Seen on TLC)	Percent yield
1.	3	TO, DO, MO	--
2.	6	DO, MO, FA	10
3.	9	DO, MO, FA	25
4.	12	DO, MO, FA	40
5.	15	MO, FA, GLY	50
6.	18	MO, FA, GLY	60
7.	21	MO, FA, GLY	65
8.	24	FA, GLY	70

© 2017 AJAST All rights reserved. Online ISSN: 2456-883X Publication Impact Factor: 0.825 Website: www.ajast.net

9.	36	FA, GLY	70
10.	48	FA, GLY	70
11.	60	FA, GLY	70
12	72	FA, GLY	70

TO=Triolein, DO=Diolein, MO=Monoolein, FA=Fatty acid, GLY=Glycerol

This showed that *Pseudomonas aeruginosa* lipase could very efficiently catalyze the hydrolysis of triolein and it converts all the TO, DO, MO into free oleic acid and glycerol within 24hrs and no further increase in free oleic acid concentration was observed after 24hrs, indicating complete hydrolysis within 24hrs.

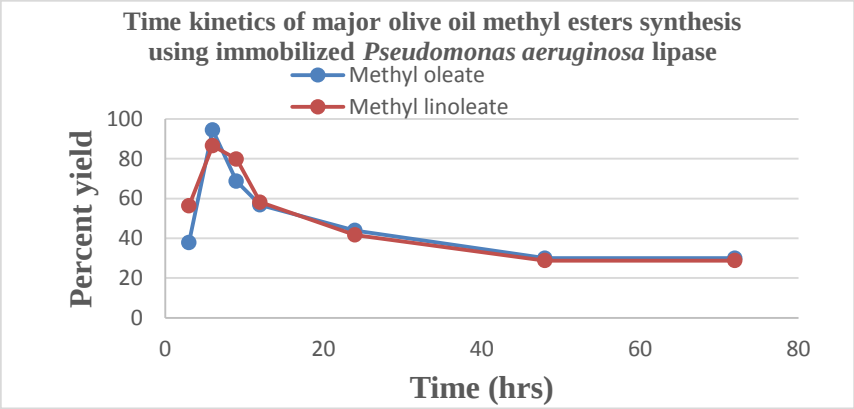


Fig. 2: Time kinetics of major olive oil methyl esters synthesis using immobilized Pseudomonas aeruginosa lipase

For the transesterification of major constituent fatty acids (oleic acid and linoleic acid) of olive oil with the help of immobilized *Pseudomonas lipase* into their respective methyl esters, it was observed that the reaction proceeded in forward direction very rapidly and 37.76% of methyl oleate could be synthesized within initial 3hrs and the transesterification reaction reaches to its maximum level (94%) within 6hrs (Fig. 2), after which reaction proceeded in backward direction leading to the decrease in the overall production of methyl oleate (table 2). For the synthesis of methyl linoleate, a similar pattern to that of methyl oleate synthesis was observed and the maximum transesterification (86%) was observed in 6hrs (Fig. 2) after which reaction went into reverse direction and the lowest catalytic turnover (37%) was observed in 72hrs (table 2). However, it is evident from the results that the *Pseudomonas*

© 2017 AJAST All rights reserved. Online ISSN: 2456-883X Publication Impact Factor: 0.825 Website: www.ajast.net

aeruginosa lipase could successfully mediate the esterification reactions for the synthesis of methyl oleate and methyl linoleate but if the product is not withdrawn from the reaction mixture on regular interval then reaction can proceed in backward direction leading to the hydrolysis of methyl oleate and methyl linoleate into their respective fatty acids.

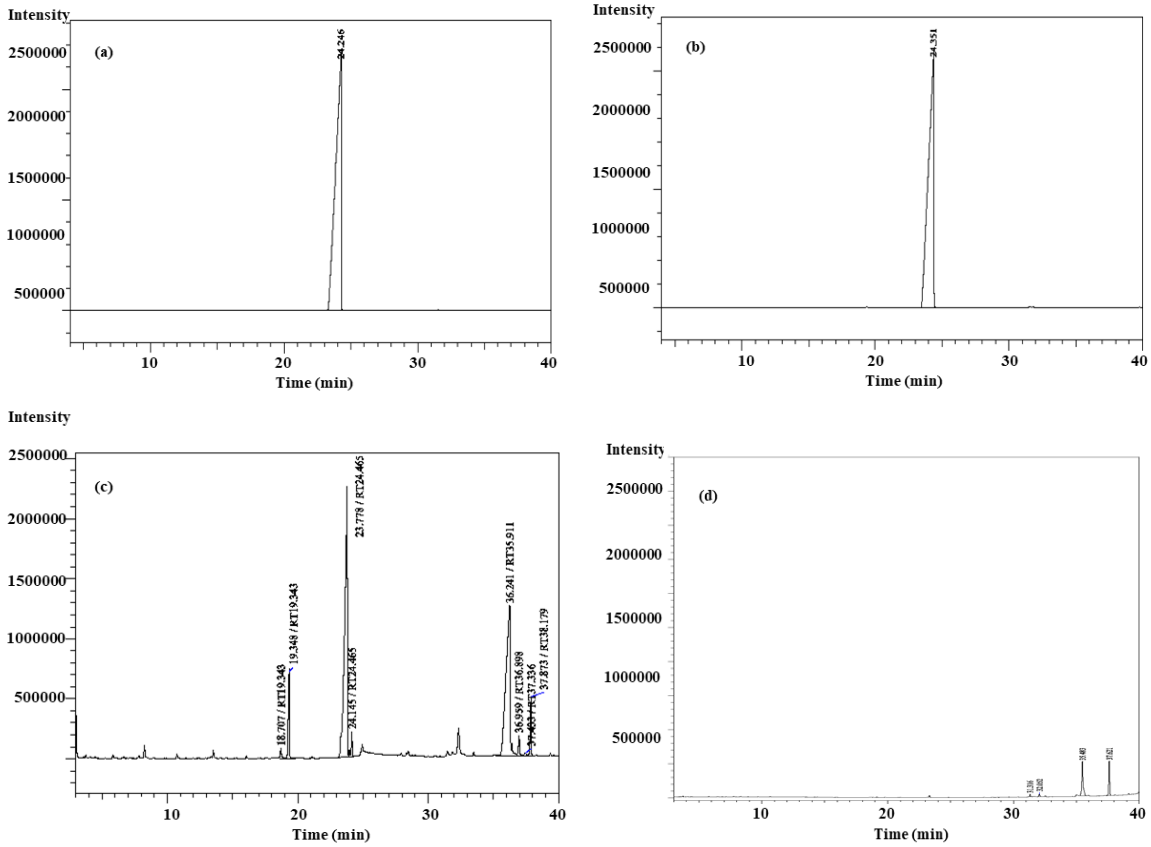


Fig 3: GC chromatogram of (a) standard methyl oleate (b) standard methyl linoleate (c) test 6hrs (d) control 6hrs

Table 2: Synthesis of major olive oil methyl esters using immobilized *Pseudomonas aeruginosa* lipase

S.No.	Time (hrs)	Products	Percent yield
1.	3	Methyl oleate	37.76
		Methyl linoleate	56.28
2.	6	Methyl oleate	94.460
		Methyl linoleate	86.53
3.	9	Methyl oleate	68.66
		Methyl linoleate	79.83
4.	12	Methyl oleate	56.80
		Methyl linoleate	58.15
5.	24	Methyl oleate	43.89
		Methyl linoleate	41.67

© 2017 AJAST All rights reserved. Online ISSN: 2456-883X Publication Impact Factor: 0.825 Website: www.ajast.net

6.	48	Methyl oleate	30.00
		Methyl linoleate	28.82
7.	72	Methyl oleate	30.00
		Methyl linoleate	28.82

Slight variations in retention time (RT) was observed for pure/ standard and synthesized methyl oleate and methyl linoleate which was correlated and confirmed by co-elution of standards with test sample. GC chromatograms for standards, test and control sample are placed in figure 3.

Catalytic potential of lipase lies in the fact that they act on fats and oils on oil- water interface and through the series of intermediates it finally breaks the oil into respective fatty acids and glycerol [11]. There are several reports wherein successful efforts have been made to hydrolyze triolein using lipase in macroemulsion [12 & 13], mono-phase reaction system containing cyclodextrin [14], immobilized lipase [15] and all these reports advocates the effect of the initial enzyme concentration, the interfacial area and the initial concentrations of triolein and a fatty acid on the entire process of the triolein hydrolysis.

Synthesis of olive oil esters using various alcohols over a range of temperature (10- 90°C) have been reported by [16] wherein they could achieve a maximum of 17.0% methyl oleate synthesis at 50°C in 3hrs while [17] reported 90.90% yield of methyl oleate using nano-bioconjugates *Candida rugusa* lipase. However, in this study we have not used lipase in emulsion or in aqueous phase which is otherwise inhibitory for ester synthesis due to high water activity but our results are in concurrence of the previous reports [11-17].

4. CONCLUSION

Esters, such as methyl oleate, are functionally important compounds in many industrial sectors, mainly as components for manufacturing of emulsifiers, detergents, intermediate stabilizers and wetting agents. This study has established that the lipase produced by the laboratory isolate of *Pseudomonas aeruginosa* shows both the lipolytic (hydrolytic) and esterolytic activity as evident from its efficacy to hydrolyze triolein and to synthesize the oleic acid methyl esters by transesterification. Owning to this property it can be inferred that the lipase from this new isolate of *Pseudomonas aeruginosa* may have vast industrial application. Other industrially important aspects such as enantio-selectivity and regio-

© 2017 AJAST All rights reserved.

specificity of this lipase need to further investigated for its commercialization so that its applicability for other industrial uses can be ascertain.

5. ACKNOWLEDGMENTS

Authors acknowledge the financial support from Delhi Technological University to carry out this investigation.

REFERENCES

1. Raku, T., Kitagawa, M., Shimakawa, H., and Tokiwa, Y. J., Enzymatic synthesis of trehalose esters having lipophilicity, *Biotechnol*., **100,** (2003), 203-208.
2. Shintre, M. S., Ghadge, R. S. S., and Sawant, S. B., Kinetics of esterification of lauric acid with fatty alcohols by lipase: Effect of fatty alcohol, *J. Chem. Technol. Biotechnol*., **77**, 10, (2002) 1114-1121.
3. Nagayama, K., Yamasaki, N., and Imai, M., Fatty acid esterification catalyzed by *Candida rugosa* lipase in lecithin microemulsion-based organogels, *Biochem. Eng*. J., **12, (**2002), 231-236.
4. Piao, J., Kobayashi, T., Adachi, S., Nakanishi, K., and Matsuno, R., Synthesis of mono- and dioleoyl erythritols through immobilized-lipase-catalyzed condensation of erythritol and oleic acid in acetone, *Biochem. Eng. J*., **14**, (2003), 79-84.
5. Lu, X., Luo, Z., Yu, S. and Fu, X., Lipase catalyzed synthesis of starch palmitate in mixed ionic liquids, *J. Agric. Food. Chem*., **60**, (2012), 9273-9279.
6. Ansary A. E. and Faddah L.M., Nanoparticles as biochemical sensors, *Nanotechnology Science and Applications*, **3**, (2010);65-76.
7. Kidwai, M., Mishra, P., Bhushan, K. R., Saxena, R. K., Gupta, R. and Singh, M., Synthesis of novel antibacterial cephalosporin derivatives using microwaves, *Indian J. Chem*., **38**, (1999), 993-997.
8. Mailer, R., Testing olive oil quality: chemical and sensory methods, *Primefacts*, **231**, (2008), 1-5.
9. Poiana, M., and Mincione, A., Fatty acids evolution and composition of olive oils extracted from different olive cultivars grown in Calabrian area *Mincione*, *Grasas y Aceites*, *International J. of Fats and Oils*, **55,** 3, (2004), 282-290.

© 2017 AJAST All rights reserved.

10. Naka, Y. and Nakamura, T., The effect serum albumin and related amino acids on pancreatic lipase and bile salts inhibited microbial lipases, *Biosci. Biotechnol. Biochem.* **56**, (1992), 1066-70.
11. Saxena, R. K., Ghosh, P. K., Gupta, R., Davidson, W. S., Bradoo, S. and Gulati, R, Microbial lipases potential biocatalysts for the future industry, *Curr. Sci.,* **77**, (1999), 101-115.
12. Burrier, R. E. and Brecher, P., Hydrolysis of triolein in phospholipid vesicles and microemulsions by a purified rat liver acid lipase, *The J. of Biol. Chem*., **258,** 19, (1983), 12043-12050.
13. Jing, F., Ana, X. and Shen, W., The characteristics of hydrolysis of triolein catalyzed by wheat germ lipase in water-in-oil microemulsions, *Journal of Molecular Catalysis B: Enzymatic*, **24-25**, (2003), 53-60.
14. Lee, H. Y., Kim, T. K., Shin, H. D. and Park, D. C., Enzymatic hydrolysis of hydrophobic triolein by lipase in a mono-phase reaction system containing cyclodextrin; Reaction characteristics, *Biotechnol. Bioprocess Eng*. **3**, (1998), 103-108.
15. Plou, F. J., Barandiaran, M., Calvo, M. V., Ballesteros, A. and Pastor, E., High yield production of mono- and di-oleylglycerol by lipase-catalyzed hydrolysis of triolein, *Enzyme and Microbial Technology*, 1996, **18,** 66-71.
16. Kenz, Z., Leitgeb, M., Zavrsnik, D. and Lavric, B., Synthesis of oleic acid esters with immobilized lipase, *Fat Sci Technol.*, **92,** 4, (1990), 169-172.
17. Marzuki, N. H. C., Huyop, F., Enein, H. Y. A., Mahat N. A. and Wahab, R.A., Modelling and optimization of *Candida rugosa* nanobioconjugates catalysed synthesis of methyl oleate by response surface methodology, *Biotechnology & Biotechnological Equipment*, **29,** 6, (2015), 1113-1127.

© 2017 AJAST All rights reserved.